TECHNISCHE
UNIVERSITÄT
DARMSTADT

Colour Superconductivity and the Equation of State of Dense Matter

vom Fachbereich Physik
der Technischen Universität Darmstadt

zur Erlangung des akademischen Grades
Doctor rerum naturalium
(Dr. rer. nat.)

genehmigte Dissertation von
Benedikt Paul Schallmo, M. Sc.

Referent: Prof. Dr. Jens Braun
Korreferent: PD Dr. Kai Hebeler

Darmstadt 2024

Colour Superconductivity and the Equation of State of Dense Matter
Farbsupraleitung und die Zustandsgleichung von dichter Materie

Dissertation von Benedikt Paul Schallmo

Referent: Prof. Dr. Jens Braun
Korreferent: PD Dr. Kai Hebeler

Tag der mündlichen Prüfung: 05. Juni 2024
Jahr der Veröffentlichung: 2024

Darmstadt, Technische Universität Darmstadt

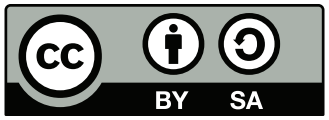

Abstract

It is widely accepted that dense strong-interaction matter at low temperatures is governed by a colour-superconducting ground state. To study the emergence of colour superconductivity in dense strong-interaction matter at zero temperature for two massless quark flavours from first principles, we employ a renormalisation group approach. For this purpose, we construct a new class of regulators for functional renormalisation group studies that is designed to handle issues arising from the presence of a Cooper instability governing the dynamics at intermediate and high densities.

We examine the dynamical formation of diquark states in the low-energy regime from the fundamental quark and gluon degrees of freedom that govern the dynamics at high energies. This includes a computation of the (chirally symmetric) diquark condensate, which is associated with a gap in the excitation spectrum of the quarks, and describes pairing of the two-flavour colour-superconducting type. We study the dependence of the gap on the chemical potential and the strong coupling and find a new scaling behaviour of the gap expected to be valid at intermediate densities. Effects of different approximations entering our calculation and possible extensions are discussed. Furthermore, we use the results from our first-principles renormalisation group flows to construct a new simple low-energy model for dense strong-interaction matter.

We demonstrate the application of this low-energy model by computing the zero-temperature thermodynamics of isospin-asymmetric matter with two massless quark flavours at high densities and zero temperature. For trajectories relevant for astrophysical applications, we find indications for a first-order phase transition from a colour-superconducting phase to an ungapped quark-matter phase when the density is increased. This phase transition appears to be absent for isospin-symmetric matter. To provide an estimate for the speed of sound in neutron-star matter, we include constraints from beta equilibrium, electric-charge neutrality, and colour-charge neutrality. Coming from high densities, we find an increase in the speed of sound towards lower densities and that it even exceeds the value associated with the noninteracting quark gas.

In addition to our explicit calculations of the properties of dense strong-interaction matter, we also discuss the thermodynamics at high densities on general grounds. To this end, we consider an expansion of the equation of state of isospin-symmetric matter in the presence of a colour-superconducting gap. This allows us to identify mechanisms underlying qualitatively different behaviours of the speed of sound. For very high densities, we find that the speed of sound approaches its value in the noninteracting limit from below, in agreement with perturbative studies which do not take into account a superconducting gap in the excitation spectrum of the quarks. However, towards lower densities, our general analysis indicates that gap-induced contributions lead to an increase in the speed of sound that eventually exceeds the value associated with a noninteracting quark gas, in agreement with our numerical renormalisation group results. We find that, even for small gap-induced contributions, the existence of a colour-superconducting phase leads to a qualitative change in the behaviour of the speed of sound. Taking into account results from studies based on chiral effective field theory at low densities, these findings suggest the existence of a maximum in the speed of sound at supranuclear densities for densities below ten times the nuclear saturation density.

Kurzfassung

Es ist allgemein anerkannt, dass dichte, stark wechselwirkende Materie bei tiefen Temperaturen von einem farbsupraleitenden Grundzustand beherrscht wird. Um die Entstehung von Farbsupraleitung in dichter, stark wechselwirkender Materie bei verschwindender Temperatur für zwei masselose Quark-Flavours von fundamentalen Prinzipien ausgehend zu untersuchen, verwenden wir einen Renormierungsgruppenansatz. Zu diesem Zweck konstruieren wir eine neue Klasse von Regulatoren für funktionale Renormierungsgruppenstudien, die entworfen wurde, um Probleme zu behandeln, die sich aus dem Vorhandensein einer Cooper-Instabilität ergeben, welche die Dynamik bei mittleren und hohen Dichten bestimmt.

Wir untersuchen die dynamische Bildung von Diquark-Zuständen im Niederenergie-Regime ausgehend von den fundamentalen Quark- und Gluon-Freiheitsgraden, die die Dynamik bei hohen Energien bestimmen. Dies beinhaltet die Berechnung des (chiral-symmetrischen) Diquark-Kondensats, das mit einer Energielücke im Anregungsspektrum der Quarks assoziiert ist. Wir untersuchen die Abhängigkeit der Energielücke vom chemischen Potential und der starken Kopplung und finden ein neues Skalierungsverhalten dieser Energielücke, welches für mittlere Dichten gültig sein sollte. Die Auswirkungen verschiedener Näherungen, die in unserer Berechnung verwendet werden, und mögliche Erweiterungen werden diskutiert. Darüber hinaus verwenden wir die Ergebnisse dieser Renormierungsgruppenrechnungen, um ein neues und einfaches Niederenergiemodell für dichte, stark wechselwirkende Materie zu konstruieren.

Wir demonstrieren die Anwendung dieses Niederenergie-Modells, indem wir die Thermodynamik von isospin-asymmetrischer Materie mit zwei masselosen Quark-Flavourn bei hohen Dichten und verschwindender Temperatur berechnen. Für Trajektorien, die für astrophysikalische Anwendungen relevant sind, finden wir Hinweise auf einen Phasenübergang erster Ordnung von einer farbsupraleitenden Phase zu einer ungekoppelten Quark-Materie-Phase, wenn die Dichte erhöht wird. Dieser Phasenübergang scheint in isospin-symmetrischer Materie nicht aufzutreten. Um die Schallgeschwindigkeit in Neutronensternmaterie abzuschätzen, berücksichtigen wir Randbedingungen durch das Betagleichgewicht, die elektrische Ladungsneutralität und die Farbladungsneutralität. Wir stellen fest, dass die Schallgeschwindigkeit von hohen Dichten zu niedrigen Dichten zunimmt und sogar den Wert übersteigt, der mit einem nicht wechselwirkenden Quarkgas assoziiert wird.

Zusätzlich zu unseren expliziten Berechnungen der Eigenschaften dichter, stark wechselwirkender Materie diskutieren wir die Thermodynamik bei hohen Dichten auf Basis allgemeinerer Überlegungen. Zu diesem Zweck untersuchen wir eine Entwicklung der Zustandsgleichung für isospin-symmetrische Materie in Gegenwart einer farbsupraleitenden Energielücke. Dies ermöglicht die Identifizierung der Mechanismen, die dem qualitativ unterschiedlichen Verhalten der Schallgeschwindigkeit zugrunde liegen. Bei sehr hohen Dichten nähert sich die Schallgeschwindigkeit ihrem Wert im nicht-wechselwirkenden Limit von unten an, was mit perturbativen Studien übereinstimmt, die eine supraleitende Energielücke im Anregungsspektrum der Quarks nicht berücksichtigen. In Richtung niedrigerer Energien zeigt unsere allgemeine Analyse jedoch, dass Beiträge, die durch die Bindungslücke induziert werden, zu einem Anstieg der Schallgeschwindigkeit führen, sodass

diese schließlich den Wert übersteigt, der mit einem nicht-wechselwirkendem Quarkgas assoziiert ist. Diese Beobachtung stimmt auch mit unseren numerischen Renormierungsgruppenergebnissen überein. Wir stellen fest, dass selbst bei kleinen durch die Bindungslücke induzierten Beiträgen die Existenz einer farbsupraleitenden Phase zu einer qualitativen Änderung des Verhaltens der Schallgeschwindigkeit führt. Unter Berücksichtigung der Ergebnisse von Studien, die auf chiralen effektiven Feldtheorien bei niedrigen Dichten basieren, deuten diese Erkenntnisse auf die Existenz eines Maximums der Schallgeschwindigkeit bei supranuklearen Dichten unter dem Zehnfachen der nuklearen Sättigungsdichte hin.

Danksagung

Die Arbeit an der Forschung für die vorliegende Dissertation hat einen großen Teil meines Lebens in den letzten Jahren eingenommen und mir zahlreiche wertvolle Erfahrungen gebracht. Diese herausfordernde, manchmal auch frustrierende Reise hat letztendlich zu einem doch lohnenswerten Abschluss geführt. Viele Menschen haben mich auf diesem Weg unterstützend begleitet.

Mein besonderer Dank gilt Jens Braun, der mir bei jedem Problem zur Seite gestanden hat und mir viele hilfreiche Anregungen gegeben hat. Deine Fähigkeit, meinen persönlichen Arbeitsstil und mein Potential einzuschätzen, war mir eine große Hilfe. Durch Deine Anleitung konnte diese Dissertation zu einem erfolgreichen Abschluss gebracht werden. Deine Unterstützung war von unschätzbarem Wert und hat wesentlich zur Qualität meiner Arbeit beigetragen.

An dieser Stelle möchte ich mich auch bei meinem Zweitbetreuer Kai Hebeler für die wissenschaftlichen Diskussionen und die Übernahme des Zweitgutachtens bedanken.

Ein weiterer großer Dank geht an Andreas Geißel, mit dem ich während eines Großteils meiner Zeit als Doktorand das Büro geteilt habe. Unsere zahlreichen Diskussionen innerhalb und außerhalb der Physik sowie die gemeinsame Arbeit an Projekten haben nicht nur mein Verständnis erweitert, sondern auch zu einer angenehmen Arbeitsatmosphäre beigetragen. Ich weiß es sehr zu schätzen, dass wir die Ersten waren, die nach langer Zeit im Homeoffice wieder ins Büro gekommen sind.

Des Weiteren möchte ich mich bei meinen Koautoren bedanken, mit denen ich in den letzten Jahren gemeinsam an einigen Forschungsprojekten und Veröffentlichungen gearbeitet habe, die auch für die vorliegende Arbeit wichtig waren. Zusätzlich möchte ich mich bei meinen anderen aktuellen und ehemaligen Bürokollegen und Gruppenmitgliedern bedanken, die stets zur Gemeinschaft beigetragen haben.

Mein Dank gilt auch Daniel Derr und Catharina Brase für ihre hilfreichen Kommentare und fachlichen Diskussionen.

Nicht zuletzt möchte ich mich bei meiner Familie und insbesondere bei meinen Eltern bedanken, die mich stets unterstützt und ermutigt haben (auch wenn sie oft nicht verstanden haben, was ich genau gemacht habe). Ohne Euch wären mein Physikstudium und dieser Abschluss nicht möglich gewesen. Auch meinen Onkel möchte ich dankend erwähnen, der mich schon während meiner Schulzeit für die Naturwissenschaften zu begeistern wusste, sowie meinen Bruder, der mir beratend und motivierend zur Seite gestanden hat.

Contents

Introduction

Physics serves as the cornerstone of natural sciences, as its name already suggests, since it can be translated as the "study of Nature". Its goal is to gain a deeper understanding of the phenomena occurring in Nature and to comprehend the existence of the Universe in its current state. A central goal is to discover and describe the inherent orders and laws governing the Cosmos. By the end of the 19th century, classical physics was mostly explored and understood, setting the stage for the most important pillars of modern physics that were developed in the 20th century.

The development of the theory of relativity in the beginning of the 20th century and quantum mechanics in the first half of the 20th century fostered a dramatically different perspective of the Universe and led to numerous scientific advancements. In the second half of the 20th century, additional advancements allowed to further explore the fundamental nature of matter, resulting in a more comprehensive and unified understanding of the laws that govern the Cosmos. It is now well-established that four fundamental interactions are observed in the Universe. These interactions are the strong interaction, the weak interaction, the electromagnetic interaction, and gravity. The first three are described by the Standard Model of physics which was developed in the latter half of the 20th century. It introduces elementary particles whose dynamics is governed by quantum mechanics. Twelve matter particles, namely six quarks (the up, down, charm, strange, top, and bottom) and six leptons (the electron, muon, tau, and three neutrinos), which are all fermions with spin 1/2, interact with force particles, the gauge bosons (the photon, gluon, $W^{\pm}$ bosons, Z boson, and Higgs boson) which are spin-one particles. The Standard Model describes these three interactions in terms of the theoretical framework of quantum field theory. However, only the weak interaction acts on all matter particles, whilst the strong interaction only acts on the quarks and the electromagnetic interaction does not act on the electrically neutral neutrinos.

Quantum field theory was initially developed in the beginning of the 20th century incorporating concepts from quantum mechanics, classical field theory, and special relativity. However, it only became an essential part of modern physics with the introduction of renormalisation techniques. This development was necessary for quantum electrodynamics to become the well-established quantum field theory describing the electromagnetic interaction. In particular, quantum electrodynamics became manageable because the corresponding small coupling constant allows for perturbative calculations. These calculations first appeared to be the only ones possible within this approach. In particular, the description of the strong interaction with a quantum field theory was plagued by issues due to the strength of the corresponding coupling and the self-interactions of the force carriers. Both of these aspects are absent in quantum electrodynamics. However, the development of nonperturbative methods led to the possibility to describe the strong interaction via a quantum field theory, specifically quantum chromodynamics. Finally, within the Standard Model, the weak, electromagnetic, and strong interaction were all successively described by a renormalisable quantum field theory. Notably, Sheldon Glashow, Abdus Salam, and Steven Weinberg were able to unify the electromagnetic force and the weak interaction by introducing the electroweak interaction [1–3].

As the theory of the strong interaction, quantum chromodynamics describes interactions between the quarks themselves and their antiparticles, the antiquarks, mediated by the exchange of force carriers, the gluons. Quarks are the elementary constituents of hadrons that are held together by the strong interaction. The quark model and the idea that hadrons consist of quarks were originally proposed by Murray Gell-Mann [4] (who also coined the name "quark") and George Zweig [5, 6]. It was preceded by the "eightfold way" proposed by Murray Gell-Mann [7] and Yuval Ne'eman [8] that classifies and structures the hadrons based on the symmetry group SU(3). Hadrons are generally classified into mesons and baryons. Baryons consist of three quarks, while mesons consist of a quark and an antiquark. The most prominent examples for baryons are the proton and the neutron. Although the strong interaction is short-ranged, it extends slightly beyond the "edge" of the proton and the neutron allowing them to interact and form atomic nuclei. Interestingly, the observed masses of the hadrons mostly result from the strong interaction and not the mass of their constituent quarks.

In quantum chromodynamics, quarks and gluons come in three different colour charges, namely red, green, and blue. Correspondingly, antiquarks come in colour charges antired, antiblue, and antigreen. The additional quantum number, later named colour [9], was first proposed by Oscar Wallace Greenberg [10] and Moo-Young Han and Yoichiro Nambu [11]. It is important to note that hadrons are colourless, i.e., the colour charges have to add up to "white". This is fulfilled by combining three quarks where each quark has a different colour. Alternatively, a quark can be paired with an antiquark which has the anticolour of the quark. Therefore, hadrons are said to be colour-neutral. The phenomenon that no observed particles have been experimentally found carrying a colour charge is referred to as colour confinement [12–14]. Quarks also carry other charges, such as the electric charge. Based on the concept of colour, quantum chromodynamics was developed by Harald Fritzsch, Heinrich Leutwyler, and Murray Gell-Man [15] based on the Yang-Mills theory introduced by Chen Ning Yang and Robert Mills [16, 17] with coloured quarks and gluons, the force carriers of quantum chromodynamics. In contrast to the photon, which is the force carrier of quantum electrodynamics, the gluons interact with each other because they also carry a colour charge. In addition to that, quantum chromodynamics is an asymptotically free theory implying that the strength of the interaction decreases with increasing energy and vice versa so that the interaction becomes strong at low energies. This phenomenon was discovered in quantum chromodynamics by David Gross, Frank Wilczek, and David Politzer [18, 19].

Of special interest in research in recent years has been the phase diagram of quantum chromodynamics which is shown in a simplified version in Fig. 1 spanned by the quark chemical potential μ, which is closely related to the total baryon density, and the temperature T. In particular, the existence and properties of different phases have been of significant interest, see Refs. [20–23] for reviews. Indeed, interesting phenomenological aspects arise at finite chemical potential and temperature, and various phases of strongly interacting matter are expected to appear.

Since quantum chromodynamics is an asymptotically free theory, quarks and gluons exist as a gas of almost free particles at high energies. This regime is deconfined since the strong interaction is weak enough so that quarks are not bound (in hadrons). As the system is effectively probed at energies of the order of μ and T at high densities and temperature, respectively, these regions of the phase diagram are governed by a weak strong interaction. The corresponding phase is referred to as the quark-gluon plasma [24–26] and it is expected to behave like a dense and thin fluid [27]. However, this phase requires temperatures of over 1500 billion Kelvin (corresponding to $\sim 150\,\mathrm{MeV}$). It is expected that a quark-gluon plasma existed for a short period of time in the early Universe. Experimentally, this region can be accessed in heavy-ion collision experiments such as at the Relativistic Heavy Ion Collider (RHIC) or the Large Hadron Collider (LHC) where conditions similar to the ones in the early Universe can be generated [28–32]. After the temperature decreased in the early Universe, quarks "condensed" into hadrons. At these low energies (associated with

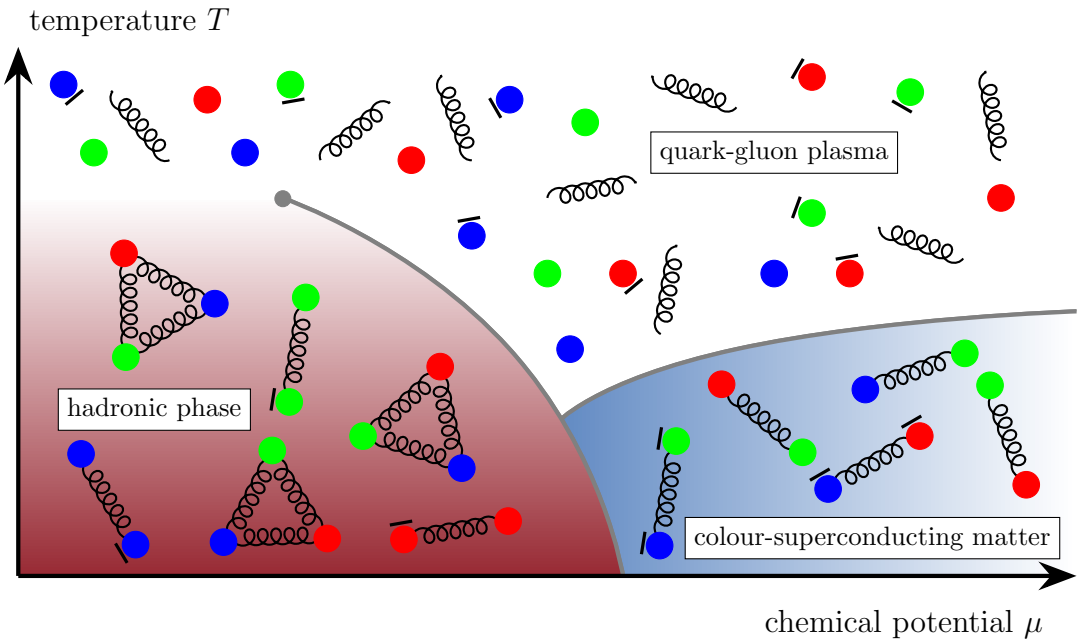

Figure 1: Simplified schematic phase diagram of quantum chromodynamics spanned by the quark chemical potential μ and the temperature T, where quarks are represented by coloured circles, antiquarks are represented by coloured circles with an overline, and gluons are represented by curled lines. For high energies, associated with high densities and temperatures, strong-interaction matter exists as a quark-gluon plasma. Going to lower energies, a phase transition occurs where quarks and gluons start to become bound in hadrons characterising the hadronic phase. In this phase, strong-interaction matter is made up of mesons, which consist of a quark and an antiquark, and baryons which consist of three quarks. The line separating the quark-gluon plasma from the hadronic phase represents a first-order phase transition with a critical endpoint (represented by the grey circle) exhibiting a second-order phase transition. For high densities but low temperatures a colour-superconducting ground state is expected where quarks form diquark-like Cooper pairs, see main text for details.

temperatures below $\sim 150\,\mathrm{MeV}$ and densities below $\sim 350\,\mathrm{MeV}$), where the interaction between the quarks becomes strong, quarks only appear as bound states, i.e., confined in hadrons. The corresponding phase is referred to as the hadronic phase. Consequently, no free quarks or gluons propagate in the vacuum, i.e., at zero temperature and density. Since the hadronic phase represents a confined phase there has to be a phase transition from the deconfined quark-gluon plasma to the confined hadronic phase [33, 34]. Additionally, a second phase transition exists where chiral symmetry is restored, the so-called chiral phase transition [33–37]. It essentially describes a transition from heavy constituent quarks to light current quarks. The line representing the first-order phase transition between the hadronic phase and the quark-gluon plasma is drawn in Fig. 1 up to the possibly-existing critical point where a second-order phase transition is expected to occur [38–40]. For smaller chemical potential, the transition is expected to be a crossover. In the hadronic phase, there is also a nuclear liquid-gas transition [41–45], which we do not show in Fig. 1. Of particular interest, regarding the studies in the present work, is the region in the phase diagram associated with large chemical potentials but sufficiently low temperatures where a colour-superconducting phase is expected to exist [20, 46–56]. We shall come back to this aspect below. Interestingly, this phase may be governed by a multitude of different types of so-called colour superconductors giving rise to a rich phase structure.

The different regions in the phase diagram are associated with different symmetries and the spontaneous breakdown of these symmetries. Spontaneous symmetry breaking refers to the phenomenon that the ground state is not invariant under a symmetry transformation although the action of the theory under consideration and the resulting equations of motion are invariant. This phenomenon is an essential part of modern physics. For example, in quantum chromodynamics, chiral symmetry breaking [57, 58], referring to the spontaneous breaking of the chiral symmetry, is responsible for the masses of the hadrons. The two lightest quarks (up and down quark) are almost massless and their respective current masses are insufficient to explain the masses of the observed hadrons. However, quarks acquire a mass due to chiral symmetry breaking, leading to constituent quark masses of $\sim 300 - 350\,\mathrm{MeV}$ for the up and down quark [59, 60]. As it turns out, the concept of symmetry breaking can be transferred to explain various phenomena in physics, such as the Anderson-Higgs mechanism in particle physics, which explains the generation of gauge boson masses in the electroweak sector of the Standard Model [61–66].

Outside of particle physics, the concept of spontaneous symmetry breaking appears, e.g., in the description of superconductivity in condensed matter physics. Interestingly, the Anderson-Higgs mechanism in particle physics was proposed based on and preceded by research in superconductivity [67, 68]. The exploration of superconductivity can be traced back to the beginning of the 20th century when Heike Kamerlingh Onnes noticed that mercury suddenly loses all its electrical resistance if a temperature of $4.2\,\mathrm{K}$ is subceeded and thereby discovered superconductivity in metals. The classical understanding of conductivity in metals cannot explain this phenomenon. Attempts to find an explanation were made by, e.g., Fritz and Heinz London [69] and Lev Landau and Vitaly Ginzburg [70]. However, it took approximately 50 years, after the first discovery of superconductivity, to develop a complete microscopic theory. Leon Cooper developed the idea that in the presence of a Fermi sea, two electrons can form a bond at its surface [71]. These two-electron bound states, referred to as Cooper pairs, exist for an arbitrarily small attractive interaction. This instability towards the formation of fermion pairs is known as the Cooper instability [71]. Building on this idea, John Bardeen, Leon Cooper, and John Robert Schrieffer developed the so-called Bardeen–Cooper–Schrieffer (BCS) theory [72, 73]. While Cooper's idea only considers two electrons at the Fermi surface, in the BCS theory many particles interacting at the Fermi surface are considered. Analogous to Cooper's idea, according to the BCS theory, a system with at least a weak attractive interaction becomes unstable towards the formation of Cooper pairs. For electrons in a metal, this attractive interaction is mediated by electron-phonon interactions which were first proposed by Herbert Fröhlich [74, 75]. Since the Cooper pairs are effectively bosonic, they can condense in the same state so that they have the same macroscopic wavefunction. This results in the macroscopic occupation of a coherent ground state. Since, at the Fermi surface, it is energetically favoured for the electrons to form Cooper pairs, the energy of this new ground state is, in the range of the Fermi energy, energetically lowered compared to the normal ground state. Consequently, an energy gap between the ground state and excited quasiparticle states, i.e., Cooper pairs, arises resulting in a gap in the excitation spectrum. The formation of this new ground state corresponds to the emergence of a superconducting phase. Therefore, superconductivity in metals is explained by the formation of a suprafluid in an electron gas and the resulting emergence of a macroscopic quantum state. However, the Cooper pairs in the superconducting phase can be broken up by thermal fluctuations, which explains why superconductivity has only been observed at low temperatures. Although the BCS theory was originally developed to explain superconductivity in metals, it turns out that it is possible to generalise it by extending it to the formation and condensation of pairs of fermions in general. Therefore, it can be applied to different fermionic systems such as liquids like helium-3 [76, 77] or cold atomic gases in a trap like lithium-6 or potassium-40 [78].

Interestingly, the superconducting ground state exhibits spontaneous symmetry breaking associated with a nonzero value of the expectation value of the pairing field, namely the Cooper pairs. Considering superconductivity in metals, where the Cooper pairs consist of electrons, the electromagnetic gauge symmetry, i.e.,

the U(1) symmetry of electrodynamics, is broken. According to Goldstone's theorem [79, 80], by breaking a continuous symmetry so-called Goldstone modes emerge, which are massless excitations. The particles corresponding to these excitations are called Goldstone bosons. However, loosely speaking, by breaking a symmetry that is gauged, these Goldstone bosons are absorbed by the gauge bosons which then consequently acquire a mass. These gauge bosons that "eat up" the Goldstone modes are the ones corresponding to the broken generators of the underlying symmetry group. This generation of mass for gauge bosons is referred to as the aforementioned Anderson-Higgs mechanism [61–66]. In condensed matter physics, by breaking the electromagnetic U(1) gauge symmetry, one Goldstone boson would be generated, which is however absorbed by the gauge boson of electrodynamics, namely the photon. Consequently, the initially massless photon effectively acquires a mass, causing the electromagnetic field to become short ranged. This leads to the expulsion of magnetic flux in the interior of a superconductor [67], a phenomenon known as the Meissner-Ochsenfeld effect [81]. In particle physics, the role of the Cooper pairs is played by the Higgs boson which couples to the gauge bosons of the weak interaction. Consequently, the $W^{\pm}$ and Z bosons appear massive analogous to the photon in condensed matter superconductors.

In the context of quantum chromodynamics, taking into account that quarks are fermions, the existence of a superconducting phase of quarks is expected since certain interactions are already attractive, indicating the existence of a Cooper instability at the Fermi surface. Therefore, the phase diagram of quantum chromodynamics, see Fig. 1, is expected to be governed by a colour-superconducting ground state at high densities but low temperatures. The existence of such a ground state in quantum chromodynamics at supranuclear densities was first discussed in the 1970s, see Ref. [55] for an early review. However, this phase attracted little interest until it was found that colour-superconductivity and the resulting formation of sizeable pairing gaps $\sim 100\,\mathrm{MeV}$ may considerably affect quantum chromodynamics at low temperatures, see Refs. [20, 46–54]. These studies suggest the emergence of a plethora of symmetry-breaking patterns [40, 82–92]. With this, the interest in quantum chromodynamics at supranuclear densities flourished. In contrast to conventional superconductivity, where Cooper pairs are formed by electrons with opposite spins, the Cooper pairs are diquark-like states. In addition to that, instead of the electric charge, the corresponding charge is the colour charge as the name already suggests. For colour-superconducting matter to occur, very specific conditions have to be met. Densities have to be high enough so that quarks are not bound in hadrons and temperatures low enough so that the diquark-like states (corresponding to Cooper pairs) are not broken up by thermal fluctuations. Therefore, this state of matter is only expected to exist in strong-interaction matter in the region of the phase diagram corresponding to high densities but low temperatures where quarks are expected to form a Fermi liquid. Currently, it is not possible to experimentally investigate strong-interaction matter under such extreme conditions. However, a colour-superconducting ground state is speculated to govern the state of quark matter found in the core of neutron stars [46, 47, 50, 55, 93].

Neutron stars provide an excellent link between nuclear physics, particle physics, and astrophysics [94–96] to test our understanding of physics in many ways. To this end, they provide a link between physics at two very different regions across many length scales. At very small length scales, corresponding to microscopic properties, the dynamics is governed by quarks and gluons, which are expected to be the relevant degrees of freedom in the core of neutron stars. These fundamental dynamics influence the physics at very large length scales where macroscopic properties such as the equation of state or the mass-radius relation are an essential part of describing the properties of neutron stars. This connection enables us to test theories under extreme conditions since the small-scale dynamics significantly determines the properties of neutron stars. As we shall see, we encounter this connection between different length scales in several places throughout the present thesis.

Stars with a mass greater than approximately eight times that of the sun are unable to support their own weight once their fusion processes have depleted and the gas and radiation pressure is insufficient. As a

result, they undergo a process known as core-collapse supernova, which produces remnants such as black holes and neutron stars [97]. Neutron stars represent the most extreme and densest *stable* object known in the Universe, only surpassed by black holes. They have a mass of one to two solar masses and a radius of approximately $\sim 10\,\mathrm{km}$ [98], resulting in extremely high densities within the core of the star. The cores of the exploded stars from which neutron stars emerge are mostly composed of iron. After the collapse, due to gravitational pressure, the electrons are pushed into the protons, resulting in the formation of neutrons through an inverse beta decay (electron-capture process) until beta equilibrium is reached. Therefore, neutron stars are expected to consist mostly of neutron-rich matter, with a small fraction of protons and electrons. Consequently, the neutron star is partially supported against collapse by the Fermi pressure of the neutrons (in addition to, e.g., repulsive forces from the strong interaction). However, the relevant degrees of freedom may be even more complex, particularly towards the core of the neutron star, where densities up to ten times the nuclear saturation density are expected [96]. In particular, the explanation of the existence of two-solar mass neutron stars [99–102] remains a problem that is not conclusively solved and still under investigation, indicating that there is a lot that needs to be understood. Different states of matter and phenomena that govern the dynamics inside neutron stars may exist [96]. At the densities present inside neutron stars, it is expected that neutrons will dissolve into their composites, namely quarks and gluons. This suggests the existence of deconfined quark matter [103–105]. Furthermore, the densities are high enough so that strange quarks may become relevant. Therefore, a possible state of matter present in the core of a neutron star is strange matter, such as hyperon-dominated matter [106–109], where hyperons refer to baryons consisting of one or more strange quarks. Alternatively, the ground state in neutron stars may be governed by colour superconductivity already discussed above. Indeed, the densities and temperatures present in neutron stars suggest that strong-interaction matter, as realised in the core of neutron stars, is represented by the region in the phase diagram along the chemical potential axis, see Fig. 1.

The impressive and recent advancements in the observation of neutron stars because of the first detection of gravitational-wave signals of a neutron-star merger [110, 111], the ongoing missions aiming at the first direct neutron star radius measurements [112–117], and the precise mass measurements of heavy neutron stars [99, 100, 102, 118], have sparked the interest in the exploration of neutron stars from a theoretical perspective. This particularly challenges our understanding of the dynamics of dense strong-interaction matter and has led to new interest in the phase diagram of quantum chromodynamics, especially in the region relevant for the description of the properties of neutron stars, i.e., at supranuclear densities.

Indeed, the understanding of the properties of neutron stars requires knowledge about the equation of state of dense strong-interaction matter across a wide range of densities. The recent breakthroughs in the observation of neutron stars provide constraints for the equation of state and challenge the theoretical description of dense matter and require quantitative results for densities up to ten times the nuclear saturation density or even higher [119]. Information about the temperature dependence of the equation of state up to $\sim 100\,\mathrm{MeV}$ are additionally needed for a description of neutron-star mergers. Therefore, constraints from the theoretical point of view are indeed urgently needed. Another property, related to the equation of state, which can be used to characterise matter is the speed of sound which serves as an indicator of the stiffness of matter and the equation of state. It is a very sensitive quantity regarding changes in the density dependence of the pressure, such that already small corrections to the pressure can lead to significant changes in the speed of sound. The observed neutron-star masses suggest the existence of a maximum in the speed of sound which exceeds the asymptotic value in the noninteracting limit [103, 119–124]. This maximum is expected to be below $n/n_0 \approx 10$ (where n_0 is the nuclear saturation density and n is the total baryon density). A detailed knowledge about the equation of state and particularly the speed of sound across a wide density and temperature range is very challenging because it requires to consider regimes where very different low-energy dynamics with many different effective degrees of freedom are involved.

From a theoretical standpoint, these regions with different effective degrees of freedom and the complex phase structure require to explore the phase diagram of quantum chromodynamics with many different approaches. Depending on the considered density and temperature, certain approaches may be more applicable than others. In the low-density regime, where the effective degrees of freedom are nucleons and pions and the dynamics is governed by chiral symmetry breaking, low-energy models that incorporate the relevant features of quantum chromodynamics are applied. For the properties of nuclear matter, chiral effective field theories provide strong constraints for the equation of state at low densities (associated with densities around $n/n_0 \lesssim 2-3$) [125–129]. For example, for the speed of sound, these studies predict a rapid increase with the density. In addition to chiral effective field theories, functional renormalisation group studies of the equation of state based on nucleon-meson and quark-meson models also exist for low to moderate densities and low temperatures [130–136]. For vanishing density, the phase diagram can be successfully explored up to high temperatures through studies based on lattice calculations [137–141] and functional methods [142–150]. However, for finite densities, lattice studies suffer from the so-called sign problem [151–153]. For very high densities, where quantum chromodynamics is expected to be weakly coupled and the dynamics is governed by quarks and gluons, studies based on perturbative calculations (perturbative quantum chromodynamics) provide constraints for the equation of state [154–163]. This approach is valid as long as possibly existing condensates, such as a colour-superconducting gap in the excitation spectrum of the quarks, are small compared to the chemical potential. The situation in terms of the phase structure becomes more complicated when considering the intermediate density regime. Quantum chromodynamics becomes strongly coupled and identifying the dominant effective degrees of freedom is less straightforward. In fact, many interaction channels and condensates associated with different symmetry-breaking patterns become relevant [130–132, 135, 164–169]. Therefore, chiral and perturbative expansions of quantum chromodynamics are expected to break down. In this regime, the chiral symmetry is at least effectively restored. However, the ground state is still complex and is expected to be governed by colour superconductivity emerging from the presence of a Cooper instability. The existence of this colour-superconducting ground state at low temperatures and high densities has already been proposed by early low-energy models and first-principles studies in the weak-coupling limit [40, 83, 85–88]. Because of the complex phase structure and the various dominant effective degrees of freedom governing the dynamics, the equation of state and speed of sound are still plagued by large uncertainties. Interestingly, this region is of special interest for astrophysical applications.

Renormalisation group methods present a well-suited approach for studying these aspects as they study physics across many scales. This is particularly useful for addressing problems arising in strong-interaction matter at intermediate densities which require to include different degrees of freedom that become important on different scales. These methods enable the study of the effective action of quantum chromodynamics under a variation of the resolution [126, 142, 143, 146, 170–178]. They also play an important role in studies of the equation of state and symmetry-breaking patterns. In addition to that, they are widely used to study phase structures, the dynamics of a Cooper instability associated with the formation of a pairing gap, and the impact of quark-gluon dynamics on the equation of state, see, e.g., Refs. [82, 83, 91, 134, 143, 145, 146, 165, 179–192]. The *functional* renormalisation group is particularly useful for studying condensation effects and the formation of diquark fields, which are associated with the emergence of a colour-superconducting ground state. The aim of this work is to analyse dense strong-interaction matter using the functional renormalisation group approach by analysing the formation of a colour-superconducting ground state and its effects on the equation of state, starting from the fundamental interactions that govern the dynamics of quantum chromodynamics.

The present work builds on previous work on the analysis of dense strong-interaction matter with the functional renormalisation group approach [126, 165, 179, 193, 194]: In particular, it utilises results from a Fierz-complete calculation of four-quark interaction channels for two massless quark flavours where the four-

quark interactions are induced by the underlying quark-gluon dynamics, see Ref. [179]. This study allowed for an analysis of the symmetry-breaking patterns governing the ground state of quantum chromodynamics and the dominant degrees of freedom across a wide range of densities for low to intermediate temperatures. It was shown that, for low densities, the scalar-pseudoscalar channel becomes dominant indicating the onset of chiral symmetry breaking. However, for high densities, the diquark channel was found to become dominant. The divergence of this channel is associated with the formation of a chirally symmetric diquark condensate indicating the formation of a two-flavour colour superconductor. The existence of this colour-superconducting ground state in dense strong-interaction matter is in accordance with several studies, ranging from low-energy models, including only the most relevant degrees of freedom, to first-principles studies at high densities utilising that the strong coupling is small [40, 82–90, 92]. In between the two density regimes close to the nucleonic low-density regime, many interaction channels become important exhibiting roughly the same strength. This indicates a complicated phase structure and ground state [130–132, 135, 164–169]. Consequently, for quantitative calculations, the inclusion of many interaction channels may eventually be required which might also qualitatively alter the equation of state.
Building on the Fierz-complete study in Ref. [179], constraints for the equation of state for isospin-symmetric two-flavour strong-interaction matter were provided over a wide range of densities in Ref. [126]. By comparing these results towards the low-density regime with constraints obtained from chiral effective field theory [125, 126], it was found that the calculations show a remarkable consistency. Interestingly, the speed of sound as a function of the density as obtained from the Fierz-complete study has a maximum at supranuclear densities [126]. This maximum exceeds the value of the speed of sound for asymptotically high densities associated with a noninteracting quark gas. Notably, also the aforementioned advances in the observation of neutron stars and constraints from neutron-star masses suggest that a maximum exists in the speed of sound at least for neutron-rich matter [103, 119–122]. Recall that colour superconductivity is connected to the formation of a gap in the excitation spectrum of the quarks. From perturbative calculations for very high densities where the gap in the excitation spectrum is expected not to contribute significantly, the speed of sound is expected to approach the noninteracting limit from below, see Refs. [126, 157–162].

Outline of the Thesis

The focus of the present thesis is on the study of the region of the phase diagram of quantum chromodynamics where the ground state is expected to be governed by colour superconductivity. In particular, we explore strong-interaction matter at supranuclear densities examining the underlying phase structure and study the implications on thermodynamic quantities such as the speed of sound. For this purpose, the thesis is divided into three main chapters.
In Chap. 1, we discuss the theoretical framework for our investigation of strong-interaction matter which is based on renormalisation group methods. Starting with an introduction to the theory of the strong interaction, i.e., quantum chromodynamics, in Sec. 1.1, we present the action of quantum chromodynamics and its subtleties, leading to the procedure of quantisation and gauge fixing necessary within the path integral approach to quantum field theory. In addition to that, we take a closer look at the aforementioned theory of renormalisation in Sec. 1.2, focussing on the functional renormalisation group which is the primary method employed throughout the present work for analysing dense strong-interaction matter. Particularly, we introduce a renormalisation group flow equation for the effective action, known as the Wetterich equation. In Sec. 1.3, we discuss challenges in renormalisation group studies of dense relativistic systems, particularly those arising from the presence of a Cooper instability. In view of our intention to employ the so-called derivative expansion in the matter sector of quantum chromodynamics in the subsequent chapters, we address issues

that are specific to this expansion. As it turns out, in order to ensure that the correct scaling behaviour is recovered, fluctuations should be integrated out around the Fermi surface. This requires the introduction of a regularisation scheme capable of handling the arising issues which is at least needed for calculations based on the derivative expansion. We demonstrate the capabilities of this regularisation scheme by applying it to a widely-used quark-diquark model.

After establishing the necessary field-theoretical tools, we start with the analysis of dense strong-interaction matter from first principles which is the focus of Chap. 2. In particular, we start by only considering the fundamental interactions of quantum chromodynamics and see how, only from those interactions, diquarks emerge as dynamic degrees of freedom. Starting from the action of quantum chromodynamics, we motivate the ansatz for the effective action in Sec. 2.1 by qualitatively examining the trajectory along the renormalisation group flow equation from high to low momentum scales. The description of the low-energy dynamics may be more efficient in terms of suitably chosen degrees of freedom in the long-range limit. In case of dense strong-interaction matter, this suggests to use diquark fields as low-energy effective degrees of freedom which can be traced back to quark interactions at high momentum scales. Diquark fields, as composites of two quarks, have a nontrivial colour structure which we shall discuss in detail. The ansatz for the effective action is presented in Sec. 2.2, summarising the insight gained from our qualitative analysis of the renormalisation group trajectory. We present the resulting flow equations in Sec. 2.3 which requires to introduce the so-called dynamical bosonisation technique. In Sec. 2.4, we show the results for the renormalisation group flows which allow us to study the dynamical formation of diquark fields in the low-energy limit and allow us to gain an insight into the dynamics of quantum chromodynamics over a wide range of densities. At the heart of Chap. 2 is the calculation of the diquark gap which is shown in Sec. 2.5. It represents a gap in the excitation spectrum of the quarks signalling the emergence of a colour-superconducting ground state. Lastly, we investigate the influence of fluctuations of the diquark fields and the emergence of the gluon-diquark interactions in Sec. 2.6. In particular, we improve the approximations underlying the analysis in the remaining chapter. In summary, Chap. 2 establishes the field-theoretical foundations for first principles studies of the equation of state of strong-interaction matter at supranuclear densities.

Based on the findings of the previous chapter, we analyse and narrow down the uncertainties of thermodynamic quantities in Chap. 3. In particular, we analyse the density dependence of the speed of sound at zero temperature. The speed of sound is a suitable quantity to probe the density dependence of the pressure of dense strong-interaction matter. For this purpose, we use the results for the diquark gap obtained in Chap. 2 to constrain a low-energy model for two massless quark flavours at intermediate to high densities in Sec. 3.1. We improve the model by extending it to finite isospin asymmetry which is ultimately needed for astrophysical applications. However, it does not represent a first-principles study of asymmetric strong-interaction matter. In addition to that, we only consider the zero-temperature limit. Using the low-energy model, we estimate the zero-temperature phase diagram of asymmetric strong-interaction matter for $n/n_0 \gtrsim 10$ and investigate the implications on neutron-star matter by taking into account constraints from beta equilibrium, electric-charge neutrality, and colour-charge neutrality.

In Sec. 3.2, we consider the speed of sound from a more general point of view by employing an expansion of the equation of state in the presence of a colour-superconducting gap for isospin-symmetric matter. We analyse the speed of sound for two massless quark flavours and identify mechanisms underlying qualitatively different behaviours of the speed of sound. For example, this shall allow us to relate the size of the colour-superconducting gap to a specific density value where, coming from high densities, the speed of sound exceeds the asymptotic value of the speed of sound, indicating the existence of a maximum of the speed of sound above the value of the free quark gas.

Finally, we summarise the results and discuss possible extensions in the Summary and Outlook. In particular, we discuss relevant contributions and improvements to the first-principles study discussed in Chap. 2.

List of Publications

The results presented this thesis have been obtained together with different collaborators. The publications that have been completed during my time working on this thesis have been published in journals:

[195] Title: "Renormalization group studies of dense relativistic systems"
Authors: Jens Braun, Timon Dörnfeld, Benedikt Schallmo, and Sebastian Töpfel
Published in: Phys. Rev. D 104, 096002 (2021)
e-Print: arXiv:2008.05978 [hep-ph]

[196] Title: "From quarks and gluons to color superconductivity at supranuclear densities"
Authors: Jens Braun and Benedikt Schallmo
Published in: Phys. Rev. D 105, 036003 (2022)
e-Print: arXiv:2106.04198 [hep-ph]

[197] Title: "Zero-temperature thermodynamics of dense asymmetric strong-interaction matter"
Authors: Jens Braun and Benedikt Schallmo
Published in: Phys. Rev. D 106, 076010 (2022)
e-Print: arXiv:2204.00358 [nucl-th]

[198] Title: "Speed of sound in dense strong-interaction matter"
Authors: Jens Braun, Andreas Geißel, and Benedikt Schallmo
Published in: SciPost Phys. Core 7, 015 (2024)
e-Print: arXiv:2206.06328 [nucl-th]

Texts and figures in the present work that are taken from and based on these references are not marked specifically. In particular, Sec. 1.3 is based on and includes figures from Ref. [195] which mainly focuses on issues that arise in the study of relativistic dense matter. In addition to that it introduces a regularisation scheme that is capable to handle these issues. The first-principles study of dense strong-interaction matter, primarily the analysis and results presented in Secs. 2.1–2.5, are based on and include figures from Ref. [196]. The analysis of a low-energy model including isospin asymmetry presented in Sec. 3.1 is based on and includes figures from Ref. [197]. The analysis of the density dependence of the speed of sound underlying an expansion of the equation of state in Sec. 3.2 is based on and includes figures from Ref. [198].

1

Fundamentals

In this chapter, we discuss the field-theoretical framework for our analysis of dense strong-interaction matter in Chap. 2 and Chap. 3. The commonly-accepted theory of the strong interaction, one of the four known fundamental interactions, is quantum chromodynamics (QCD), which is part of the Standard Model of particle physics and describes the strong interaction between quarks via the exchange of gluons, the so-called gauge fields of QCD. We introduce the fundamentals of QCD in Sec. 1.1. As we have already discussed in the Introduction, the phase diagram of QCD can be investigated by many different approaches. As it turns out, nonperturbative methods are needed in the regime considered in the present work, i.e., the intermediate density regime where the coupling strength becomes large and the ground state is governed by the formation of condensates. Phase transitions are associated with regimes where perturbative methods are no longer applicable. The functional renormalisation group (fRG), which is a nonperturbative functional method, appears to be very promising for intermediate densities. We introduce this method, which utilises the path-integral approach to quantum field theory, in Sec. 1.2. However, the investigation of dense matter within the fRG framework requires the introduction of a so-called regularisation scheme which is suitable to handle divergences that appear in relativistic systems, particularly at finite densities. Therefore, we discuss aspects of regularisation schemes in Sec. 1.3.

1.1 Quantum Chromodynamics

Quantum chromodynamics is a Yang-Mills gauge theory with an underlying SU(3) symmetry and is therefore a non-Abelian gauge theory [16, 17]. The fundamental particles of QCD are the so-called quarks which are spin-1/2 fermions and are represented by Dirac fields in the fundamental representation of the colour group SU(3). There are six known species of quarks that are commonly referred to as flavours. These six flavours are up (u), down (d), strange (s), charm (c), bottom (b), and top (t). The quarks are the elementary building blocks of the hadrons which are the particles that are held together by the strong interaction. One

distinguishes between mesons, which have integer spin and consist of an even number of quarks (one quark and one antiquark), and baryons which have half-integer spin and consist of an odd number of quarks (three quarks). Prominent examples of baryons are the proton and the neutron, while examples of mesons are the pion or the rho meson. For each quark, there exists an antiquark that has opposite charges and lives in the conjugate representation of SU(3). Quarks come in three colours where colour charge is a quantum number specific to the strong interaction, loosely comparable to the electric charge in quantum electrodynamics. In general, Yang-Mills gauge theories can be constructed for N_c colours where the underlying symmetry is the SU(N_c) symmetry. The introduction of the colour charge allows to construct the observed hadrons while still fulfilling the Pauli exclusion principle. It was first needed to explain the existence of, e.g., the Delta baryon Δ^{++} which consists of three up quarks and could therefore not exist without an additional degree of freedom, namely the colour charge. The three colour charges are referred to as red, green, and blue. Note that the underlying colour symmetry SU(3) appears to be exactly realised in Nature. This is connected to the observation that colours "weigh" the same, i.e., the mass of each flavour of quarks does not depend on its colour charge. In the Standard Model, quarks carry an electric charge (either $-1/3$ or $+2/3$ times the elementary charge) and a weak charge additionally to the aforementioned colour charge and flavour degree of freedom. However, QCD is restricted to the consideration of colour and flavour charges. The quark flavours can be loosely categorised by their corresponding masses. Generally, three heavy quarks (charm, bottom, and top quark), two light quarks (up and down quark), and one intermediate-mass quark, the strange quark, are distinguished. The two light quarks are frequently considered to be massless since their respective masses are significantly smaller than the energy scales that are typically employed. For most applications, the three heavy quark flavours are neglected because their masses are much bigger than the arising energy scales.

Interactions between the quarks are described via the exchange of gluons that are massless spin-one bosons and are the so-called gauge fields (gauge bosons) of SU(3). There exist eight gluons that live in the adjoint representation of the SU(3) colour-symmetry group. For a general Yang-Mills gauge theory with N_c colours, there are N_c^2-1 gauge fields corresponding to the number of generators of the underlying symmetry group. In contrast to the photon, which is the gauge boson of quantum electrodynamics, gluons interact directly among themselves because they carry a colour charge themselves. This is a consequence of SU(3) being a non-Abelian symmetry group and, therefore, QCD being a non-Abelian gauge theory. Gluon self-interactions also imply that QCD is short-ranged. Note that gluons have no flavour, no electric charge, and do not "participate" in the weak interaction. To conclude, all elementary particles participating in the strong interaction, i.e., quarks and gluons, and their masses and quantum numbers are summarised in Fig. 1.1.

Before turning to the description of QCD in terms of the action and the path integral, we highlight some important aspects. Recall that QCD is a non-Abelian gauge theory so that it follows that the gauge fields interact among themselves. Closely related is the behaviour of the interaction strength in terms of the coupling constant g which we shall refer to as the strong coupling. As it turns out, the coupling decreases towards high energies whereas it becomes large for low energies. The opposite behaviour is observed in quantum electrodynamics. It follows that quarks behave like free particles at very high energies. The phenomenon that the coupling constant becomes weaker at high energies is called asymptotic freedom, a property of non-Abelian gauge theories [199], and has been discovered in QCD by David Gross, Frank Wilczek, and David Politzer [18, 19]. Further, as it turns out, the gluon self-interactions are directly responsible for asymptotic freedom. Its appearance in the theory also implies that perturbative methods [200–203] may be used at very high energies. However, as the energy is decreased, QCD becomes strongly coupled. This comes along with another phenomenon, called colour confinement that experimentally no observed particles carry colour charge [12, 13]. Therefore, at least at low energies where the coupling is large enough, quarks only appear as bound states, i.e., confined within hadrons which are necessarily colourless, and only colour-singlet states are observed.

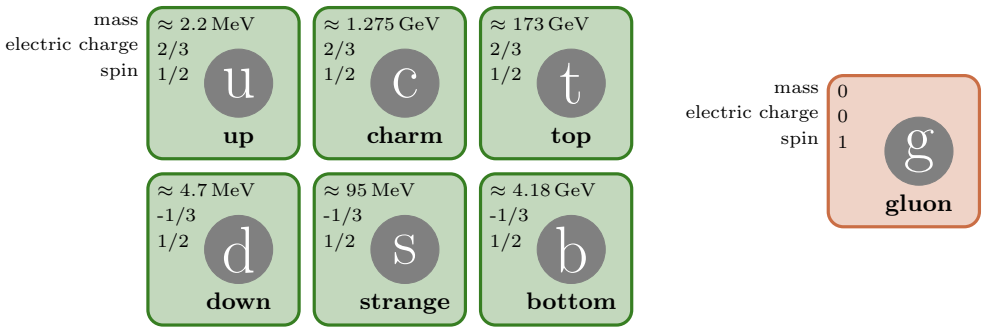

Figure 1.1: Illustration of the elementary particles participating in the strong interaction with their respective mass, electric charge, and spin: The six quark flavours are up (u), down (d), strange (s), charm (c), bottom (b), and top (t) and the gauge boson that mediates the interaction between the quarks is the gluon (g). For each quark, there exists an antiquark with opposite charges. Masses taken from [60].

Since QCD is strongly coupled at low energies, standard perturbative methods are not applicable in this region. Alternatives are lattice QCD [204–207], functional methods which we shall introduce in Sec. 1.2, and effective theories such as chiral effective field theory [208–213]. Effective field theories use the experience that the effective degrees of freedom of QCD at low energies are no longer quarks and gluons but are rather represented by hadrons.

With the general aspects of QCD provided, we can start to introduce the action of QCD and quantise the theory with the path integral formulation. The introduction to QCD and the following considerations are based on textbooks covering this topic, see Refs. [214–219]. For the motivation of the QCD action, we start with the action S of a free Dirac field with mass m given by

$$S[\bar{\psi},\psi] = \int_x \bar{\psi}(\mathrm{i}\partial\!\!\!/ + \mathrm{i}m)\psi\,. \tag{1.1}$$

We use the Feynman slash notation, i.e., $\partial\!\!\!/ \equiv \partial_\mu\gamma_\mu$. If not stated otherwise, we exclusively work in Euclidean spacetime. We do so because the corresponding path integral, which we shall introduce in the following, is then closely related to the partition function from statistical physics, see, e.g., Refs. [200, 214, 215, 220–222] for an introduction into this aspect. We only note that this relation allows for the calculation of physical observables such as the pressure, density, and the speed of sound. In QCD, the quark fields, represented by Dirac spinors $\bar{\psi}$ and ψ, respectively, carry colour and flavour indices. Quarks with the same flavour but different colour are assumed to have the same mass. Since colour and flavour are independent degrees of freedom, the action for each one of the flavours can be considered separately and is represented by Eq. (1.1) with $\psi = (\psi_\mathrm{r}, \psi_\mathrm{g}, \psi_\mathrm{b})^T$ and $\bar{\psi} = (\bar{\psi}_\mathrm{r}, \bar{\psi}_\mathrm{g}, \bar{\psi}_\mathrm{b})$ where m is the mass corresponding to the considered flavour. Now, ψ and $\bar{\psi}$ are three-component vectors representing the three colours r (red), g (green), and b (blue) where each element itself is a four-component Dirac spinor. The symmetry group associated with the colour degrees of freedom is the aforementioned SU(3). The SU(3) transformations of the quark fields $\psi \mapsto \psi' = U\psi$ with $U \in \mathrm{SU}(3)$ leave the physics invariant, i.e., the action is invariant under global SU(3) transformations. The exponential representation of the group elements U is given by

$$U = \exp\left(\mathrm{i}g\theta^a T^a\right). \tag{1.2}$$

Here, T^a with the colour indices $a = 1, ..., 8$ are the generators of the group SU(3). Their definition can be found in App. A.2. Additionally, g is the strong coupling and $\theta^a \in \mathbb{R}$. We now require that the SU(3) symmetry not only holds globally but also locally, i.e., θ now depends on spacetime: $\theta \mapsto \theta(x)$ $(U \mapsto U(x))$.

A priori, there is no argument why we should assume that the transformation has to hold locally. However, as it turns out, this requirement of local gauge invariance leads to QCD, the well-established theory of the strong interaction, and it may therefore be considered as a new principle of physics, see, e.g., Ref. [59]. The transformations of the Dirac fields are given by

$$\psi \mapsto \psi^{(\theta)} = \exp\bigl(\mathrm{i}g\theta^a(x)T^a\bigr)\psi \qquad \text{and} \qquad \bar{\psi} \mapsto \bar{\psi}^{(\theta)} = \bar{\psi}\exp\bigl(-\mathrm{i}g\theta^a(x)T^a\bigr)\,. \tag{1.3}$$

Locally, for infinitesimal θ^a, these transformations can be written as

$$\psi \mapsto \psi^{(\theta)} = \psi + \mathrm{i}g\theta^a(x)T^a\psi \qquad \text{and} \qquad \bar{\psi} \mapsto \bar{\psi}^{(\theta)} = \bar{\psi} - \mathrm{i}g\theta^a(x)\bar{\psi}T^a\,. \tag{1.4}$$

We find that the action (1.1) is not invariant under these local transformations. However, an action that is invariant can be obtained by replacing the conventional derivative with the covariant derivative

$$D_\mu = \partial_\mu - \mathrm{i}gA_\mu\,. \tag{1.5}$$

Here, $A_\mu = A_\mu^a T^a$ is the vector field which is the so-called gauge field of QCD. It is matrix-valued in colour space so that D_μ is matrix-valued as well. We further note that there are eight gauge fields, the aforementioned gluons, which carry colour charge. The covariant derivative (1.5) introduces a coupling of the quark fields to the gauge fields A_μ. To ensure that the action is invariant under the gauge transformations (1.4), the gauge fields have to transform according to

$$A_\mu \mapsto U(x)\Bigl[A_\mu + \frac{\mathrm{i}}{g}\partial_\mu\Bigr]U^\dagger(x)\,. \tag{1.6}$$

Locally, for infinitesimal θ^a this transformation can be written as

$$A_\mu^a \mapsto A_\mu^{a,(\theta)} = A_\mu^a + \partial_\mu\theta^a(x) + gf^{abc}A_\mu^b\theta^c(x) = A_\mu^a + \bar{D}_\mu^{ab}\theta^b(x)\,, \tag{1.7}$$

where $\bar{D}_\mu^{ab} = \partial_\mu\delta^{ab} - gf^{abc}A_\mu^c$. With the transformations of the gauge fields (1.6) and the quark fields (1.3), we indeed find that $\bar{\psi}\mathrm{i}\not{D}\psi$ is gauge invariant. Therefore, we replace the derivative $\not{\partial}$ in Eq. (1.1) with the covariant derivative $\not{D}$, where $\not{D} \equiv D_\mu\gamma_\mu$.

Lastly, we would like to introduce a gauge-invariant kinetic term for the gauge fields to describe their dynamics. The corresponding term in the action can be constructed from the so-called field strength tensor $F_{\mu\nu}^a$, which is given by

$$F_{\mu\nu}^a = \partial_\mu A_\nu^a - \partial_\nu A_\mu^a + gf^{abc}A_\mu^b A_\nu^c\,. \tag{1.8}$$

We indeed find that $F_{\mu\nu}^a F_{\mu\nu}^a$ is gauge invariant. It not only includes a term corresponding to a kinetic term for the gauge fields but also self-interactions of these gauge fields, i.e., three- and four-gluon self-interactions, which are mediated by the strong coupling g. The self-interactions are a result of the underlying non-Abelian group structure, which is tightly connected to the phenomenon of asymptotic freedom, and are accordingly also responsible for the finite range of the strong interaction, which is well-observed in Nature. In conclusion, the resulting gauge-invariant action is given by

$$S[A_\mu^a, \bar{\psi}, \psi] = \int_x \left\{\bar{\psi}(\mathrm{i}\not{D} + \mathrm{i}m)\psi + \frac{1}{4}F_{\mu\nu}^a F_{\mu\nu}^a\right\}\,. \tag{1.9}$$

The gauge invariance comes at the cost of the introduction of the gauge fields A_μ. Note that terms other than those in Eq. (1.9) are not permitted. A mass term for the gauge fields $\sim m_\mathrm{A}^2 A_\mu^a A_\mu^a$ is not permitted since it is not a gauge-invariant quantity. It follows that the gauge fields are massless. Other gauge-invariant terms also exist. However, these terms can be ruled out by identifying symmetries that have to be obeyed by the action because they are realised in Nature. Additionally, the requirement for renormalisability, which we shall go into more detail in Sec. 1.2, also excludes additional terms. In conclusion, the QCD action (1.9) only includes three interactions, i.e., the quark-gluon interaction and three- and four-gluon self-interactions.

Recall that we have considered the action for each of the quark flavours separately since colour and flavour are independent degrees of freedom. Therefore, the action (1.9) represents the QCD action for one quark flavour with mass m so that in total six actions are needed to represent six flavours. Alternatively, the action can be generalised by considering that the elements in the vectors $\psi = (\psi_\mathrm{r}, \psi_\mathrm{g}, \psi_\mathrm{b})^T$ and $\bar{\psi} = (\bar{\psi}_\mathrm{r}, \bar{\psi}_\mathrm{g}, \bar{\psi}_\mathrm{b})$, representing the different coloured states, are themselves vectors that contain fields to represent each of the six quark flavours, i.e., $\psi_c = (\psi_{c,\mathrm{u}}, \psi_{c,\mathrm{d}}, \psi_{c,\mathrm{s}}, \psi_{c,\mathrm{c}}, \psi_{c,\mathrm{b}}, \psi_{c,\mathrm{t}})^T$ and $\bar{\psi}_c = (\bar{\psi}_{c,\mathrm{u}}, \bar{\psi}_{c,\mathrm{d}}, \bar{\psi}_{c,\mathrm{s}}, \bar{\psi}_{c,\mathrm{c}}, \bar{\psi}_{c,\mathrm{b}}, \bar{\psi}_{c,\mathrm{t}})$. This yields $\psi = (\psi_{\mathrm{r,u}}, \ldots, \psi_{c,f}, \ldots, \psi_{\mathrm{b,t}})^T$ and $\bar{\psi} = (\bar{\psi}_{\mathrm{r,u}}, \ldots, \psi_{c,f}, \ldots, \bar{\psi}_{\mathrm{b,t}})$. Here, c is the colour index representing the three colours $c = \mathrm{r}, \mathrm{g}, \mathrm{b}$ and f is a flavour index, representing the six flavours, i.e., $f = \mathrm{u}, \mathrm{d}, \mathrm{s}, \mathrm{c}, \mathrm{b}, \mathrm{t}$. Therefore, ψ and $\bar{\psi}$ are vectors with 18 components where each component is a four-component Dirac spinor. To account for the flavours having different masses, m becomes a matrix with different masses on its diagonal.

1.1.1 Quantisation and Gauge Fixing

To quantise the theory of the strong interaction, gauge fixing is essential. Therefore, we shall discuss it in more detail in the following. There are essentially two possibilities to quantise a theory: In the so-called canonical quantisation, fields are described by operators that are subject to commutation relations [215]. On the other hand, the path-integral formalism works with classical fields instead of operators by introducing a high-dimensional integral. Throughout the present work, we use the path integral approach to quantum field theory. It is based on the action principle from classical mechanics where the solutions of the equations of motion follow from requiring that the action S is stationary, which is called Hamilton's principle, $\delta S = 0$. In other words, a particle travelling from A to B takes a trajectory that makes the action stationary. In contrast to that, in quantum mechanics not only the path that makes the action stationary but all paths are relevant, i.e., it is assumed that a particle going from A to B can take every possible trajectory. They do not, however, contribute equally but weighted by a complex phase factor that is determined by the classical action S and that is, in Minkowski space, given by $\mathrm{e}^{\mathrm{i}S/\hbar}$. The contributions from the various trajectories along which a system can evolve are then added up by integrating over all functions (corresponding to the position x of the particle changing with time t) that describe the paths from A to B, represented by $\int \mathcal{D}x(t)$. This yields

$$\int \mathcal{D}x(t)\, \mathrm{e}^{\mathrm{i}S/\hbar}\,. \tag{1.10}$$

Note that we included $\hbar$ (although we use "natural units", see App. A.6, for the remainder of the present work and therefore set $\hbar$ to one in the following) to indicate that classical physics is recovered from quantum mechanics by taking the limit $\hbar \to 0$. The path integral for quantum mechanics then allows for the calculation of transition amplitudes where each trajectory described by the classical action S contributes. Interestingly, the exponential factor $\mathrm{e}^{\mathrm{i}S/\hbar}$ can be related to the Boltzmann factor $\mathrm{e}^{-\hat{H}/(k_\mathrm{B}T)}$ (where $\hat{H}$ is the Hamilton operator and k_B is the Boltzmann constant) allowing for a connection between the path integral and statistical physics. For a detailed discussion of this aspect and a general introduction to the path integral, see, e.g., Refs. [200, 214–216, 218–223].

Describing QCD in terms of the path integral requires to move away from quantum mechanics towards quantum field theory. Integrating over all functions that describe the change of the position of a particle travelling from A to B is replaced by integrating over all possible field configurations, i.e., the position depending on time $x(t)$ is replaced by fields that depend on spacetime. We restrict ourselves to Euclidean spacetime so that the path integral formulation of QCD can, at least naively, be represented by the functional integral

$$\int \mathcal{D}\bar{\psi}\mathcal{D}\psi\mathcal{D}A_\mu^a \, \exp\left(-S[A_\mu^a, \bar{\psi}, \psi]\right). \tag{1.11}$$

Here, S is the Euclidean QCD action given by Eq. (1.9) and the integration runs over all possible field configurations. However, this naive approach is plagued by problems since QCD exhibits gauge degrees of freedom, i.e., the field strength tensor is invariant under the gauge transformation (1.7). Therefore, the path integral (1.11) is ill-defined for gauge-invariant quantities since the integration includes physically equivalent gauge-field configurations, i.e., for each physically unique configuration there may be many configurations given by the choice of gauge. However, only physically inequivalent field configurations and not redundant ones should be considered, leading to the necessity to (gauge) constrain the path integral. This is provided by the aforementioned gauge-fixing procedure.

In the following, we shall use a trick put forward by Faddeev and Popov in Ref. [224]. See also Refs. [173, 214–216, 218] on which the following discussion is based on for further details. We first introduce the gauge-fixing condition by defining the functional G which is set to zero as the gauge-fixing condition: $G^a[A^a_\mu] = 0$. It is convenient to use

$$G^a[A^a_\mu] = g^a[A^a_\mu] - f^a(x)\,. \tag{1.12}$$

Here, f^a is some arbitrary scalar function and for the functional g^a, we choose

$$g^a[A^a_\mu] = \partial_\mu A^a_\mu(x)\,. \tag{1.13}$$

Setting $G^a[A^a_\mu] = 0$ is a generalisation of the Lorenz gauge condition: $\partial_\mu A^a_\mu = f^a(x)$. Then, the usual Lorenz gauge condition is recovered by setting $f^a = 0$. Note that other choices for g^a are possible but we shall restrict ourselves to classes of gauges enforced by Eq. (1.13).

The observation, that many field configurations lead to the same value of the action, is related to the propagator of the gauge fields (gluon propagator) being ill-defined. For example, the free gluon propagator is given by the inverse of $M_{\mu\nu} = p^2\delta_{\mu\nu} - p_\mu p_\nu$ which originates from the kinetic term of the gluons in the action (1.9). We indeed find that $M_{\mu\nu}$ exhibits an eigenvector k_μ with eigenvalue zero so that it is not invertible.

The implementation of the gauge-fixing condition, which constrains the integral by restricting it to configurations with $G^a[A^a_\mu] = 0$, can be achieved by introducing a delta functional such as $\delta(G^a[A^a_\mu])$. Following the work of Faddeev and Popov, this is accomplished by inserting the following 'one' into the path integral:

$$1 = \int \mathcal{D}\theta\, \delta\Big(G\big[A^{a,(\theta)}_\mu\big]\Big) \det\left(\frac{\delta G\big[A^{a,(\theta)}_\mu\big]}{\delta\theta}\right) = \Delta_\mathrm{f}[A^a_\mu] \int \mathcal{D}\theta\, \delta\Big(G\big[A^{a,(\theta)}_\mu\big]\Big)\,. \tag{1.14}$$

Here, $A^{a,(\theta)}_\mu$ is the gauge-transformed field and we have defined the so-called Faddeev-Popov determinant $\Delta_\mathrm{f}[A^a_\mu] = \det(\delta G[A^{a,(\theta)}_\mu]/\delta\theta)$ which is gauge invariant. As it turns out, only infinitesimal gauge transformations are relevant in the latter expression. With this, we can assume that the gauge transformations can be written as an expression linear in θ so that the gauge fields transform as given in Eq. (1.7): $A^{a,(\theta)}_\mu = A^a_\mu + \bar{D}^{ab}_\mu\theta^b$. As long as the gauge transformations are linear, the Faddeev-Popov determinant is independent of θ so that it can indeed be pulled out of the integral. However, for non-Abelian gauge theories, such as QCD, it still depends on the gauge fields. Using that the Faddeev-Popov determinant Δ_f, the path integral measure $\mathcal{D}A^a_\mu = \mathcal{D}A^{a,(\theta)}_\mu$, and the action $S[A^{a,(\theta)}_\mu, \bar\psi^{(\theta)}, \psi^{(\theta)}] = S[A^a_\mu, \bar\psi, \psi]$ are gauge-invariant, yields

$$\int \mathcal{D}\theta \times \int \mathcal{D}\bar\psi\mathcal{D}\psi\mathcal{D}A^a_\mu\, \Delta_\mathrm{f}[A^a_\mu]\delta(G[A^a_\mu]) \exp\left(-S[A^a_\mu, \bar\psi, \psi]\right). \tag{1.15}$$

In doing so, we have achieved that the second factor is independent of θ so that $\int\mathcal{D}\theta$ can be identified with the volume of the gauge group (integration over the gauge group) which can be absorbed in a normalisation constant and cancels out in the calculation of correlation functions. Therefore, we only have to consider

$$\int \mathcal{D}\bar\psi\mathcal{D}\psi\mathcal{D}A^a_\mu\, \Delta_\mathrm{f}[A^a_\mu]\delta(G[A^a_\mu]) \exp\left(-S[A^a_\mu, \bar\psi, \psi]\right). \tag{1.16}$$

The path integral is now restricted by the delta distribution to only include inequivalent field configurations as required. However, let us bring the Faddeev-Popov determinant and the aforementioned delta distribution into a more convenient expression to work with in the path integral formalism. For this purpose, we start by rewriting the delta distribution. Recall that f^a, which appears in Eq. (1.12), is some arbitrary function so that the condition holds for all f^a. Therefore, we can integrate over them using a Gaussian weight function by inserting another 'one' which is given by

$$1 = \int \mathcal{D}f \, \exp\left(-\frac{1}{2\xi} \int_x f^a f^a \right) . \tag{1.17}$$

Here, we have introduced the so-called gauge parameter ξ.
By inserting the latter expression into the path integral (1.16) and using the expression for the functional G given in Eq. (1.12) together with the generalised Lorenz gauge enforced by Eq. (1.13), we obtain

$$\begin{aligned} &\int \mathcal{D}\bar{\psi}\mathcal{D}\psi\mathcal{D}A^a_\mu \, \Delta_\mathrm{f}[A^a_\mu] \int \mathcal{D}f \exp\left(-\frac{1}{2\xi} \int_x f^a f^a \right) \delta\Big(\partial_\mu A^a_\mu - f^a\Big) \exp\left(-S[A^a_\mu, \bar{\psi}, \psi]\right) \\ &= \int \mathcal{D}\bar{\psi}\mathcal{D}\psi\mathcal{D}A^a_\mu \, \Delta_\mathrm{f}[A^a_\mu] \, \exp\left(-\frac{1}{2\xi} \int_x \left(\partial_\mu A^a_\mu\right)^2 \right) \exp\left(-S[A^a_\mu, \bar{\psi}, \psi]\right) . \end{aligned} \tag{1.18}$$

Next, we turn to the calculation of the Faddeev-Popov determinant Δ_f. As we shall see in the following, it depends on the gauge fields which is a detail specific to non-Abelian gauge theories. In contrast to that, in Abelian gauge theories such as quantum electrodynamics, the Faddeev-Popov determinant does not depend on the gauge fields and can therefore be absorbed in a normalisation constant. However, considering generalised Lorenz gauge and the transformation of the gauge fields according to Eq. (1.7), we find

$$\Delta_\mathrm{f}[A^a_\mu] = \det\left(\frac{\delta G\big[A^{a,(\theta)}_\mu\big]}{\delta\theta} \right) = \det\left(\partial_\mu \bar{D}^{ab}_\mu \right) = \int \mathcal{D}\bar{c}\,\mathcal{D}c \, \exp\left(-\int_x \bar{c}^a \partial_\mu \bar{D}^{ab}_\mu c^b \right) . \tag{1.19}$$

In the last step, we have used that a determinant can be written as the path integral over Grassmann numbers. For this purpose, we have introduced the so-called Faddeev-Popov ghosts $\bar{c}$ and c that belong to the adjoint representation of the gauge group. Note that the ghosts are anticommuting Lorentz scalars, so that they have no Lorentz indices, and there exists one ghost and one antighost for each gauge field. In addition to that, the ghosts are unphysical virtual states because they violate the spin-statistic theorem and are an artefact of the gauge-fixing procedure. The ghosts cancel the unphysical degrees of freedom in the gauge fields and, in terms of Feynman diagrams, they only appear as internal lines. Since the Faddeev-Popov determinant depends on the gauge fields, the ghost term introduces, besides a kinetic term for the ghosts, a new interaction, i.e., the interaction between ghosts and gauge fields (ghost-antighost-gluon interaction). It is also possible to consider axial gauges where ghost fields are absent. Recall that gauge fixing also has to be done in quantum electrodynamics. However, interactions between ghosts and gauge fields only appear in non-Abelian gauge theories so that the ghosts can simply be integrated out in Abelian gauge theories. In any case, we end up with the following expression for the path integral for QCD:

$$\int \mathcal{D}\bar{\psi}\mathcal{D}\psi\mathcal{D}A^a_\mu\mathcal{D}\bar{c}\,\mathcal{D}c \, \exp\left(-S[A^a_\mu, \bar{\psi}, \psi] - \frac{1}{2\xi} \int_x \left(\partial_\mu A^a_\mu\right)^2 - \int_x \bar{c}^a \partial_\mu \bar{D}^{ab}_\mu c^b \right) . \tag{1.20}$$

In conclusion, the gauge-fixing procedure leads to two additional terms in the path integral that can be absorbed into a redefinition of the action S which is then given by

$$\bar{S}[A^a_\mu, \bar{\psi}, \psi, \bar{c}, c] = S[A^a_\mu, \bar{\psi}, \psi] + S_\mathrm{gf}[A^a_\mu] + S_\mathrm{gh}[A^a_\mu, \bar{c}, c] . \tag{1.21}$$

Here, S is the QCD action given in Eq. (1.9), S_gf is the gauge-fixing term, and S_gh is the ghost term:

$$S_\mathrm{gf}[A^a_\mu] = \frac{1}{2\xi} \int_x \left(\partial_\mu A^a_\mu\right)^2 \qquad \text{and} \qquad S_\mathrm{gh}[A^a_\mu, \bar{c}, c] = \int_x \bar{c}^a \partial_\mu \bar{D}^{ab}_\mu c^b . \tag{1.22}$$

Recall that the original version of the path integral suffers from an ill-defined gauge-field propagator. This problem is cured since the propagator is now given by the inverse of $M_{\mu\nu} = p^2\delta_{\mu\nu} - \big(1 - 1/\xi\big)p_\mu p_\nu$, which is well-defined and given by $M^{-1}_{\mu\nu} = (\delta_{\mu\nu} + (\xi - 1)p_\mu p_\nu/p^2)/p^2$. Two commonly employed values for the parameter ξ are $\xi = 0$ (Landau gauge) and $\xi = 1$ (Feynman gauge).
With this at hand, we can finally define the generating functional Z for QCD which reads

$$Z[J] = \int \mathcal{D}\bar{\psi}\mathcal{D}\psi\mathcal{D}A^a_\mu\mathcal{D}\bar{c}\,\mathcal{D}c\,\exp\left(-\bar{S}[A^a_\mu,\bar{\psi},\psi,\bar{c},c] + \int_x \left(J^a_\mu A^a_\mu + \bar{\eta}\psi + \bar{\psi}\eta + \bar{\mu}^a c^a + \bar{c}^a\mu^a\right)\right). \tag{1.23}$$

The gauge-fixed action $\bar{S}$ is defined in Eq. (1.21) and we have introduced sources corresponding to the different fields appearing in the action: J^a_μ, $\bar{\eta}$, η, $\bar{\mu}^a$, and μ^a are the sources corresponding to A^a_μ, ψ, $\bar{\psi}$, c^a, and $\bar{c}^a$.
The action $\bar{S}$ is no longer gauge invariant since the gauge-fixing term S_{gf} breaks gauge invariance. However, as it turns out, it is possible to use the ghosts and the corresponding ghost term S_{gh} to construct a new symmetry that is not present in the classical action $\bar{S}$ which is the so-called Becchi-Rouet-Stora-Tyutin symmetry [225–228] (BRST symmetry), see also Refs. [215, 216, 219, 229] for an introduction. To introduce this symmetry, we replace the gauge parameter θ^a in the gauge transformations for the quarks (1.4) and the gauge fields (1.7) with $\theta^a \mapsto \lambda c^a$, where c^a are the Grassmann-valued ghosts and λ is a Grassmann-valued parameter so that $\lambda c^a = -c^a\lambda$. Note that the indices of the ghosts are the same as the ones from the gauge parameter θ^a. For the gauge fields, we therefore find

$$A^a_\mu \mapsto A^{a,(\lambda)}_\mu = A^a_\mu + \lambda\partial_\mu c^a + \lambda g f^{abc}A^b_\mu c^c = A^a_\mu + \lambda\bar{D}^{ab}_\mu c^b\,. \tag{1.24}$$

For the quark fields, we find

$$\psi \mapsto \psi^{(\lambda)} = \psi + \mathrm{i}g\lambda c^a T^a\psi \qquad \text{and} \qquad \bar{\psi} \mapsto \bar{\psi}^{(\lambda)} = \bar{\psi} - \mathrm{i}g\lambda c^a\bar{\psi}T^a\,. \tag{1.25}$$

Therefore, the transformations of the gauge fields and the fermion fields are simply local gauge transformations where the gauge parameter is taken to be proportional to the ghost fields. The transformations of the ghosts are now chosen such that they cancel out the transformation of the gauge-fixing term $\sim(\partial_\mu A^a_\mu)^2/(2\xi)$ while simultaneously ensuring that $\bar{D}^{ab}_\mu c^b$ is gauge invariant. The corresponding transformations are given by

$$c^a \mapsto c^{a,(\lambda)} = c^a - \lambda\frac{1}{2}gf^{abc}c^b c^c \qquad \text{and} \qquad \bar{c}^a \mapsto \bar{c}^{a,(\lambda)} = \bar{c}^a - \lambda\frac{1}{\xi}\partial_\mu A^a_\mu. \tag{1.26}$$

The transformations for c^a and $\bar{c}^a$ can be chosen independently because, in contrast to $\bar{\psi}$ and ψ, there is no relation between the two restricting the respective transformation behaviour. We indeed find that $\bar{S}$ is invariant by simultaneously applying Eqs. (1.24)–(1.26), i.e., under the so-called BRST transformation. The BRST transformation highlights the purpose of the introduction of the ghost fields since it shows that unphysical states of the non-Abelian gauge theory are cancelled by the Faddeev-Popov ghosts. The remnants of transformations associated with terms that are not gauge invariant are cancelled by the corresponding transformations of the ghosts. Therefore, the BRST symmetry can be interpreted as a generalisation of the gauge invariance present in the classical theory to the quantised theory.

1.2 Renormalisation and the Functional Renormalisation Group

In the section, we begin with a brief introduction to the theory of renormalisation and the renormalisation group (RG) in Sec. 1.2.1. This leads to the discussion of the functional renormalisation group (fRG) in Sec. 1.2.2 which is the main method employed in the present work for our analysis of dense strong-interaction matter. For more details on the theory of renormalisation and the renormalisation group, we refer the reader to textbooks covering this topic in more detail, on which the following general considerations are based on, see, e.g., Refs. [215, 216, 218, 229–233].

1.2.1 General Considerations

Quantum field theories such as QCD (introduced in Sec. 1.1) owe much of their success to the framework provided by the theory of renormalisation and modern developments would be unimaginable without it. Already early studies of quantum field theories were plagued by the existence of infinities arising from "diverging quantities". Historically, infinities already appeared in, e.g., classical electrodynamics when dealing with point particles: For instance, the electron has an infinite electromagnetic "self-mass" since it is given by $\sim 1/r_\mathrm{e}$ (where r_e is the electron radius) so that this self-mass diverges for a point particle $r_\mathrm{e} \to 0$ [231, 234]. These issues with infinities extend to quantum field theories, e.g., as divergences in the calculation of so-called n-point correlation functions or loop diagrams within perturbative calculations. The calculation of correlation functions is a central aspect in quantum field theories, as knowledge about all correlation functions implies a complete understanding of the theory under investigation. Therefore, addressing the problems of divergences was a critical step forward for quantum field theories.

First steps towards solving the discussed issues were taken by observing that the appearance of divergences turns out to be unproblematic if they do not appear in predictions for physical observables [235–243]. It was found, for example, that the aforementioned divergence of the self-mass can be eliminated by reformulating the theory in terms of the parameter representing the experimentally measured electron mass. In this sense, the infinity appears only in a so-called *bare* electromagnetic mass. Here, the bare mass is simply a parameter appearing in the corresponding equations which is not directly related to a measurable physical quantity and is therefore not realised in experiments. This parameter is subsequently replaced with the so-called *renormalised* mass which has been adjusted so that it corresponds to a measurable quantity.

These discoveries inspired the development of the theory of renormalisation. In quantum field theories, the phenomena of divergences typically appear when dealing with high energy scales and the divergences are therefore called ultraviolet (UV) divergences. More precisely, momentum integrals are encountered that diverge in the region where the momentum is sent to infinity so that the full momentum integral diverges. To address this problem, a so-called regulator is introduced which is, e.g., a cutoff Λ corresponding to a large momentum scale (or very small distance scale). Subsequently, the integrals are then only performed up to the scale Λ which is large but finite. In doing so, effects originating below the length scale $\approx 1/\Lambda$ are effectively neglected. These types of UV cutoffs can also be encountered more naturally in physical systems concerning, e.g., condensed matter systems where effects originating from scales below the size of an atom are disregarded. Therefore, the physics on larger scales can be understood from considering physics at the scale corresponding to the size of an atom, which serves as the natural cutoff in such systems. However, considering fundamental particles and the corresponding theories, the existence of a smallest scale appears less intuitive rendering the introduction of the cutoff somewhat arbitrary. The introduction of the cutoff Λ is usually referred to as *regularisation*, which only constitutes the first step to handle the UV divergences, since the results, e.g., correlation functions, now depend on the UV cutoff Λ. The subsequent step, referred to as *renormalisation*, can be summarised as follows: Since the aforementioned cutoff is somewhat arbitrary, it needs to be removed so that observables are insensitive to it and measurable quantities remain finite for $\Lambda \to \infty$. This can be achieved by first recognising that the parameters appearing in the theory under consideration, e.g., in the action, do not correspond to actual physical observables. Therefore, the theory is, e.g., defined by a so-called bare action with bare parameters. The divergent parts are split off from these parameters to obtain manageable finite (renormalised) quantities. Alternatively, additional terms originating in the renormalisation procedure can be added to the theory as so-called counterterms. In this manner, the appearing infinities are assimilated into practically unobservable parameters and the theory is reformulated in terms of measurable quantities (i.e., so-called renormalised quantities) that remain finite and are independent of the regulator, e.g., the cutoff Λ. Renormalisation can therefore be summarised as an adjustment of the parameters of the

theory. The artificial cutoff that has been introduced to regularise the theory is eliminated. Subsequently, the renormalised parameters describe observables that are encountered in Nature and that can be measured. In contrast to that, the bare parameters are not directly related to physical observables. Therefore, regularisation and renormalisation not only serve as tools to treat divergences appearing in the theory under consideration but are also about constructing a theory that describes Nature. In practice, one calculates observables by tuning the theory by means of other observables that are experimentally measured. In this spirit, the short-distance physics is hidden in the observables that determine the theory from experiment.
With these considerations, it also becomes possible to classify quantum field theories with respect to their renormalisability. If only a fixed number of physical observables from experiment are needed to remove all UV divergences, the theory is called renormalisable. This is required for the theory having predictive power. In contrast to that, if infinitely many parameters are needed, the theory is called nonrenormalisable. Note that a fundamental theory that aspires to describe Nature is expected to be renormalisable. Therefore, renormalisability became an important criterion in the development of the Standard Model that describes the weak, electromagnetic, and strong interaction by a renormalisable quantum field theory. For example, QCD introduced in Sec. 1.1 is a renormalisable field theory.
An alternative approach that is closely related to the concept discussed so far, is the so-called renormalisation group, which originated in the field of condensed matter physics. Within this field, Leo Kadanoff introduced the so-called block-spin renormalisation group [244, 245]. He found that it is possible to introduce "coarse graining" for atoms with spin on an evenly spaced lattice (with lattice spacing $\sim 1/\Lambda$) at a given temperature T. Only neighbouring atoms interact via a spin-spin interaction. Coarse graining can be thought of as looking at the system under a variation of the resolution. For the aforementioned lattice, this corresponds to introducing so-called block spins. This means that groups (blocks) of atoms with spin are constructed and a single spin value is assigned to each block. Thereby, multiple spin values are combined in a single block with a single spin value. The process is illustrated in Fig. 1.2. The key idea is that physical observables should remain unchanged when using the average spin over a group of spins instead of using the individual spins of the atoms. Other strategies, beyond using the average spin, can be employed to assign a single spin value to a block of spins. The introduction of block spins leads to a reduction of nearby degrees of freedom to a single effective degree of freedom for neighbouring atoms. However, when considering blocks of spins rather than individual spins, it is necessary to adjust the interaction strength, i.e., the value of the spin-spin interaction. This adjustment has to be done in a way such that the resulting physics stays the same. The renormalisation group implements a way to systematically coarse grain a system by introducing so-called RG transformations. Renormalisation group approaches have and still are an important part of condensed matter physics, see, e.g., [246–249].
A continuum representation was implemented by Kenneth G. Wilson. It is usually referred to as Wilson's approach to renormalisation [250, 251]. In the renormalisation group approach, instead of removing the cutoff Λ, it becomes part of the theory. The cutoff is then chosen such that the corresponding length scale $\sim 1/\Lambda$ is much smaller than the typical length scale of the physics that is examined. Macroscopic properties of quantum-statistical systems are determined by their microscopic fluctuations. Since Λ is a parameter of the theory, it is also reasonable to conceive of the parameters of the theory at Λ to be part of the theory as well. Subsequently, they are adapted so that they already include effects originating from larger scales than Λ. In this sense, they are then "determined" by a theory that is defined for larger scales.
Wilson's approach starts with a given microscopic theory where the dynamics is, for example, defined by a "classical" action S. From there, all fluctuations are successively integrated out from high to low momentum scales [250–252]. By integrating out all fluctuations, macroscopic information about the system under consideration can be extracted. The integration of the fluctuations is performed gradually. The change in the scale when going towards the low-momentum regime is compensated by adjusting the parameters (i.e., the

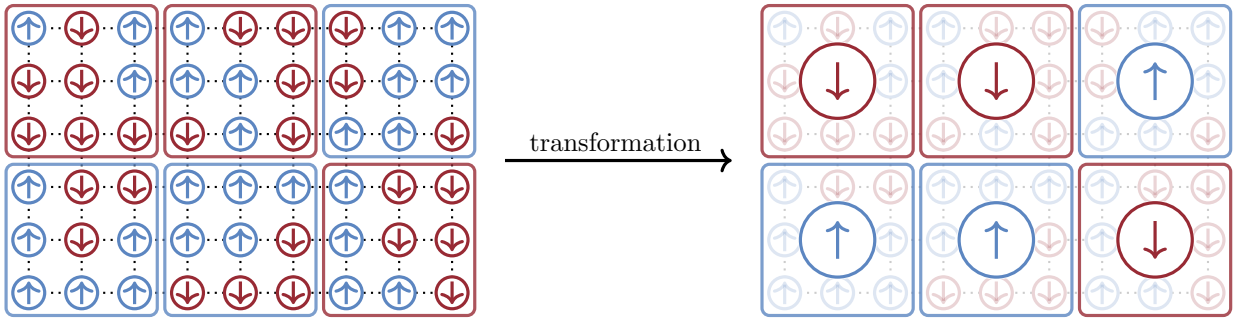

Figure 1.2: Illustration of coarse graining by introducing block spins in a system of atoms with spin up and down arranged on an evenly spaced two-dimensional lattice with lattice spacing $\sim 1/\Lambda$. The atoms only interact via next-neighbour spin-spin interactions. In this example, atoms with spin are grouped into blocks containing nine atoms. After the transformation, a single spin value is assigned to each of the blocks where we have used the most common spin value in each of the blocks. The process of introducing block spins is not unique and other strategies can be employed to assign a single spin value to the block. To ensure that the transformation does not change the underlying physics, the coupling between the effective spins is adjusted and thus different from the coupling between the original spins.

couplings) of the theory so that physical observables remain invariant. Therefore, the couplings $\{g_i(\Lambda)\}$ of the theory under consideration have to be functions of the cutoff Λ so that the parameters become scale dependent. The piecewise integration of fluctuations is performed from Λ to $k = \Lambda/b$ where the parameter $b > 1$ is associated with looking at different momentum scales. Choosing $b > 1$ ensures that the long-range limit (small-momentum limit) is considered which corresponds to going from microscopic to macroscopic scales, i.e., going from small to large length scales. This corresponds to the coarse graining procedure that we have already encountered in the block-spin renormalisation group. Here, coarse graining is implemented in a continuous system in momentum space. The integration of fluctuations corresponds to a so-called RG transformation. The renormalisation group is used to analyse how the parameters of the theory change with changes in the momentum scale or more generally, with changes of the "scale of interest". Therefore, the transformation $\{g_i(\Lambda)\} \mapsto \{g_i(\Lambda/b)\} = \{g_i(k)\}$ is considered. Here, k plays the role of a scale that connects the microscopic $k = \Lambda$ with macroscopic scales $k \to 0$. We shall refer to this scale as the RG scale. Using Wilson's approach, differential equations can be obtained for the couplings that describe their change under a variation of the scale. Then, the rescaling of the couplings leads to the couplings "travelling" along the so-called RG trajectory (in the space spanned by the coupling constants) which is often referred to as RG flow. Along this RG flow, going from the microscopic to the macroscopic scale, the number of relevant degrees of freedom is reduced. The renormalisation group explores changes of the physical system under consideration at different scales while the observables remain invariant under the changes of the parameters of the theory. The scale dependence of the couplings is given by the so-called beta functions $\{\beta_i(g_i)\}$ [216, 232, 253]. For example, for a theory with a single coupling g, this beta function is given by $\beta(g) = -(\mathrm{d}g)/(\mathrm{d}\ln(b))$. In terms of the scale k and by introducing $t = \ln(k/\Lambda)$, we find $\beta(g) = (\mathrm{d}g)/(\mathrm{d}t) = k(\mathrm{d}g)/(\mathrm{d}k)$. Therefore, the beta function describes the behaviour of the coupling under a variation of the RG scale k.

To conclude this short introduction, we would like to highlight some interesting aspects that arise when applying the renormalisation group. The introduction of the beta functions allows us to define so-called fixed points in the RG flow. Considering, for example, the beta function for a theory with a single coupling g, a fixed point g^* is given by $\beta(g = g^*) = 0$. For theories with N couplings $\{g_i\}$ (where $i = 1, \ldots, N$), a fixed point is defined by $\beta_i(\{g_i\}) = 0$. Exactly at the fixed point the system is scale invariant so that,

loosely speaking, the system "looks" the same independently of the resolution. To illustrate this, let us again consider the spin model shown in Fig. 1.2: If the spins are in complete disorder (associated with $T \to \infty$), the system looks identical on all scales, representing a fixed point. Alternatively, a fixed point exists if all spins are aligned in the same direction (associated with $T \to 0$) so that the system again looks identical on all resolutions. A system can have multiple fixed points and the number of fixed points does not depend on the applied renormalisation scheme but is a universal property. In addition to that, fixed points may be repulsive or attractive. For attractive fixed points, the coupling "flows" towards its value at the fixed point whereas the couplings are driven away from a repulsive fixed point. The Gaussian fixed point is associated with points where all couplings are zero so that the system is described by a free theory. In this case, the path integral becomes an exact Gaussian integral.
Some fixed points can be associated with critical points, i.e., points at which a phase transition occurs. This indicates that the theory of renormalisation is closely related to phase transitions. It is noteworthy that theories, which might describe two different physical systems with many different degrees of freedom, behave very similarly in the vicinity of a (critical) fixed point, i.e., in the vicinity of a phase transition. It turns out that only a few variables and scaling relations are relevant to describe the systems quantitatively, regardless of the details of the interactions and the phenomenology of the system. Only the underlying symmetries of the theories under consideration are important. Furthermore, the slope, referred to as the critical exponent, of the beta function near a (critical) fixed point is universal. The qualitatively identical behaviour of different theories close to a (critical) fixed point is called universality.
Based on the preceding considerations and implementation of the renormalisation group, we consider the so-called functional renormalisation group in the following. It is a nonperturbative approach which is required for calculations in strongly-interacting systems, such as QCD.

1.2.2 The Functional Renormalisation Group

As we have seen, from the viewpoint of the renormalisation group, macroscopic properties (which correspond to long-range physics) of quantum-statistical systems are determined by microscopic fluctuations. To obtain macroscopic information about the system, one has to integrate over all microscopic fluctuations. The renormalisation group is a tool to understand what happens between the two extremes and how the parameters of the theory evolve such that observables are invariant. For example, going from the microscopic dynamics to the long-range limit, a weak coupling might turn into a strong coupling, different degrees of freedom become relevant at different scales, or the symmetries of the system under consideration might change.
The functional renormalisation group is a nonperturbative approach to the renormalisation group that allows for calculations using the path-integral formulation of quantum field theory. Its functional nature offers a convenient and practical approach in comparison to other methods based on the renormalisation group. At the core of the functional renormalisation group is the Wetterich equation, an evolution equation of the so-called effective average action Γ_k [254, 255]. We shall derive this equation in the following. The derivation and discussion in the present section are based on [172, 173, 256].
The Wetterich equation connects the microscopic physics given by the "classical" action S with the low-energy regime associated with the full effective action Γ. Regarding statistical physics and thermodynamics in terms of thermal field theory, we note that the full effective action is closely connected to macroscopic properties, such as pressure, density, or speed of sound. The effective average action Γ_k depends on the RG "time" $t = \ln(k/\Lambda)$ where k is the RG scale which connects the high-energy scales ($k \to \Lambda$) with the low-energy regime ($k \to 0$). The initial condition $\Gamma_{k=\Lambda}$ is fixed at the scale Λ. By taking the limit $k \to 0$, we recover the full effective action $\Gamma = \Gamma_{k=0}$. Before turning to the calculation of the evolution equation of Γ_k,

we start by defining the infrared-regulated (IR-regulated) functional $Z_k[J_k]$:

$$Z_k\left[J_k\right] = \exp\left(W_k[J_k]\right) = \int \mathcal{D}\phi \, \exp\left(-S[\phi] - \Delta S_k[\phi_k] + \int J_k^a \phi_k^a\right). \tag{1.27}$$

The integration runs over all possible field configurations. Note that the generating functional is closely related to the partition function in classical statistical mechanics. We modified the usual definition of the generating functional to contain the functional $\Delta S_k[\phi_k]$ carrying a regulator function R_k. The latter depends on the scale k and can be interpreted as a momentum-dependent mass term that ensures infrared regularisation. In momentum space, it is given by

$$\Delta S_k[\phi_k] = \frac{1}{2}\int_p \int_q \phi_k^a(-p) R_k^{ab}(q) \phi_k^b(q) (2\pi)^n \delta^{(n)}(p-q) = \frac{1}{2}\int_p \int_q \phi_k^a(-p) \tilde{R}_k^{ab}(p,q) \phi_k^b(q)\,. \tag{1.28}$$

A suitable form for the regulator function R_k^{ab} has to be chosen. We shall come back to this aspect below. For convenience, we exclusively work in momentum space in the following. However, the derivation can also be performed analogously in position space. We have also introduced k-dependent fields into the Wetterich equation which provides a powerful extension to the usually employed Wetterich equation [146, 170–175, 178, 257]. For this purpose, we have included the k-dependent fields ϕ_k^a which are a functional of the k-independent fields $\phi_k^a = \phi_k^a[\phi]$. We have not yet specified a field, but included the superfields ϕ_k^a, which include fermionic and bosonic fields so that the index a is either a "fermionic" index corresponding to ϕ_k^a being a fermionic field or a "bosonic" index corresponding to ϕ_k^a being a bosonic field. Additionally, the index a may consist of a multitude of indices, such as Lorentz, colour, or flavour indices. The corresponding source terms, which are also k-dependent, are given by J_k. Since ϕ_k^a and J_k may represent fermionic degrees of freedom, which are represented by Grassmann-valued fields, one has to be careful with the order of the fields and the corresponding derivatives.

From the generating functional $Z_k[J_k]$, we obtain correlation functions, which play a very prominent role in quantum field theories, by taking functional derivatives with respect to the corresponding source J_k. For example, for the two-point correlation function, we find

$$\frac{1}{Z_k[J_k]} \frac{\delta}{\delta J_k^a(p)} \frac{\delta}{\delta J_k^b(-q)} Z_k[J_k] = \left\langle \phi_k^a(-p) \phi_k^b(q) \right\rangle_J . \tag{1.29}$$

Therefore, $Z_k[J_k]$ is called the generating functional of correlation functions. Note that correlation functions are generally defined by setting the source term to zero $J_k = 0$. However, for the purpose of the present work, we use the correlation function in the presence of a source as indicated by the subscript 'J' in order to derive the flow equation for the effective action. The two-point correlation function as introduced in Eq. (1.29) is the product of two field operators with different momenta and averaged over all possible field configurations and is therefore given by

$$\left\langle \phi_k^a(-p) \phi_k^b(q) \right\rangle_J = \frac{1}{Z_k[J_k]} \int \mathcal{D}\phi \, \phi_k^a(-p) \phi_k^b(q) \exp\left(-S[\phi] - \Delta S_k[\phi_k] + \int J_k^a(p) \phi_k^a(-p)\right). \tag{1.30}$$

Higher-order correlation functions, i.e., n-point correlation functions, as the product of n fields averaged over all possible field configurations, can be obtained by taking additional derivatives with respect to the source J_k. Correlation functions are closely related to scattering amplitudes in physical processes and play a prominent role in statistical mechanics and quantum field theories. We have also introduced the generating functional of the connected correlation functions $W_k[J_k] \equiv \ln(Z_k[J_k])$ where the terminology becomes clear when again considering derivatives with respect to the source J_k:

$$\frac{\delta}{\delta J_k^a(p)} \frac{\delta}{\delta J_k^b(-q)} W_k[J_k] = \left\langle \phi_k^a(-p) \phi_k^b(q) \right\rangle_J - \left\langle \phi_k^a(-p) \right\rangle \left\langle \phi_k^b(q) \right\rangle_J = \left\langle \phi_k^a(-p) \phi_k^b(q) \right\rangle_{J,\mathrm{c}} = G_k^{ba}(q,p)\,. \tag{1.31}$$

Here, G_k^{ba} is the so-called full connected propagator. The functional $W_k[J_k]$ only generates connected correlation functions as indicated by the subscript 'c'. Speaking in terms of Feynman diagrams, in contrast to "normal" correlation functions, connected correlation functions do not include diagrams where external lines are not connected to all other external lines. To derive an evolution equation for Γ_k, we calculate the derivative of the generating functional $W_k[J_k]$ with respect to the RG "time" $\partial_t = k\partial_k$ which yields

$$\begin{aligned}\partial_t W_k[J_k] = \frac{1}{Z_k[J_k]}\partial_t \exp\Big(W_k[J_k]\Big) = -\frac{1}{2}\int_p\int_q \tilde{R}_k^{ab}(p,q)\Big(\left\langle\big(\partial_t\phi_k^a(-p)\big)\phi_k^b(q)\right\rangle_J + \left\langle\phi_k^a(-p)\partial_t\phi_k^b(q)\right\rangle_J\Big) \\ + \int_p J_k^a(p)\left\langle\partial_t\phi_k^a(-p)\right\rangle_J - \frac{1}{2}\int_p\int_q\Big(\partial_t\tilde{R}_k^{ab}(p,q)\Big)\left\langle\phi_k^a(-p)\phi_k^b(q)\right\rangle_J \\ + \int_p\Big(\partial_t J_k^a(p)\Big)\left\langle\phi_k^a(-p)\right\rangle_J\,. \qquad (1.32)\end{aligned}$$

In the following, we utilise

$$\left\langle\phi_k^a(-p)\big(\partial_t\phi_k^b(q)\big)\right\rangle_J = \left(\frac{\delta}{\delta J_k^a(p)} + \left\langle\phi_k^a(-p)\right\rangle_J\right)\left\langle\partial_t\phi_k^b(q)\right\rangle_J\,, \qquad (1.33)$$

$$\left\langle\big(\partial_t\phi_k^a(-p)\big)\phi_k^b(q)\right\rangle_J = (-1)^{ab}\left(\frac{\delta}{\delta J_k^b(-q)} + \left\langle\phi_k^b(q)\right\rangle_J\right)\left\langle\partial_t\phi_k^a(-p)\right\rangle_J\,. \qquad (1.34)$$

In addition to that, we use that the regulator is supposed to be chosen such that $R_k^{ab}(p) = (-1)^{ab}R_k^{ba}(-p)$ and that it does not mix fermionic and bosonic degrees of freedom, i.e., it is zero if a is a fermionic index an b is a bosonic index or vice versa. Only if a and b correspond to the same fermionic fields or the same bosonic fields, the regulator is nonzero. Here, we have also introduced the factor $(-1)^{ab}$ which accounts for possible Grassmann-valued fields. For fermionic fields, represented by anticommuting Grassmann numbers, the order of the fields matters and it is $(-1)^{ab} = -1$ (for a and b fermionic). For bosonic fields, we have $(-1)^{ab} = 1$ (for a or b bosonic). This yields

$$\begin{aligned}\partial_t W_k[J_k] = -\int_p\int_q\left(\tilde{R}_k^{ab}(p,q)\left(\frac{\delta}{\delta J_k^a(p)} + \left\langle\phi_k^a(-p)\right\rangle_J\right)\left\langle\partial_t\phi_k^b(q)\right\rangle_J\right) + \int_p J_k^a(p)\left\langle\partial_t\phi_k^a(-p)\right\rangle_J \\ - \frac{1}{2}\int_p\int_q\Big(\partial_t\tilde{R}_k^{ab}(p,q)\Big)G_k^{ba}(q,p) - \frac{1}{2}\int_p\int_q\Big(\partial_t\tilde{R}_k^{ab}(p,q)\Big)\left\langle\phi_k^a(-p)\right\rangle_J\left\langle\phi_k^b(q)\right\rangle_J \\ + \int_p\Big(\partial_t J_k^a(p)\Big)\left\langle\phi_k^a(-p)\right\rangle_J\,. \qquad (1.35)\end{aligned}$$

Here, we have also replaced the two-point correlation function $\left\langle\phi_k^a(-p)\phi_k^b(q)\right\rangle_J$ with the expression for the connected propagator presented in Eq. (1.31). The class of correlation functions can conveniently be further reduced. Recall that $W_k[J_k]$ is the generating functional of connected correlation functions. Therefore, we now define the generating functional of one-particle irreducible (1PI) correlation functions, the effective (average) action $\Gamma_k[\varphi_k]$, which is the Legendre transformation of the generating functional of connected correlation functions $W_k[J_k]$ with respect to the source J_k:

$$\Gamma_k[\varphi_k] = \sup_J\left(\int_p J_k^a(p)\varphi_k^a(-p) - W_k[J_k]\right) - \Delta S_k[\varphi_k]\,. \qquad (1.36)$$

In contrast to the well-known definition of the (full) effective action, i.e., $\Gamma = \sup_J(\int J\varphi - W[J])$ [218], it depends on the RG scale k and includes the regulator term ΔS_k that we have already introduced in the functional $Z_k[J_k]$ in Eq. (1.27). In the limit $k \to 0$, we require that we recover the full effective action. Therefore, the regulator needs to fulfil some requirements that we shall discuss below in the present section. Note that $\Gamma_k[\varphi_k]$ is a functional of the scale-dependent so-called classical field φ_k, which is the expectation

value of the field ϕ_k in the presence of the source J_k as given by

$$\varphi_k^b(q) = \frac{\delta}{\delta J_k^b(-q)} W_k[J_k] = \langle \phi_k^b(q) \rangle_J \,. \tag{1.37}$$

We emphasise that J_k is chosen such that $\int J_k \varphi_k - W_k[J_k]$ approaches its supremum as indicated by '$\sup_J$'. In the following, we therefore assume that the source J_k has been evaluated at this supremum. Taking the derivative with respect to the RG "time" of the effective action (1.36) and inserting Eq. (1.35) yields

$$\begin{aligned}
\partial_t \Gamma_k[\varphi_k] &= \int_p \partial_t J_k^a(p) \varphi_k^a(-p) - \partial_t W_k[J_k] - \partial_t \Delta S_k[\varphi_k^a] \\
&= \int_p J_k^a(p) \Big(\partial_t \varphi_k^a(-p) - \langle \partial_t \phi_k^a(-p) \rangle_J \Big) + \int_p \int_q \tilde{R}_k^{ab}(p,q) \varphi_k^a(-p) \Big(\langle \partial_t \phi_k^b(q) \rangle_J - \partial_t \varphi_k^b(q) \Big) \\
&\quad + \frac{1}{2} \int_p \int_q \Big(\partial_t \tilde{R}_k^{ab}(p,q) \Big) G_k^{ba}(q,p) + \int_p \int_q \tilde{R}_k^{ab}(p,q) \frac{\delta}{\delta J^a(p)} \langle \partial_t \phi_k^b(q) \rangle_J \,.
\end{aligned} \tag{1.38}$$

Recall that we have included k-dependent fields ϕ_k^a in the definition of the regulator term $\Delta S_k[\phi_k]$ and the functional $Z_k[J_k]$. In the latter expression, this k dependence appears as derivatives of the fields with respect to the RG "time" in terms of their expectation value $\langle \partial_t \phi_k^a \rangle_J$. A specific form for $\partial_t \phi_k^a$ has not yet been assumed. However, in practice, the derivative of the field $\partial_t \phi_k^a$ is chosen such that $\langle \partial_t \phi_k^a \rangle_J = \partial_t \varphi_k^a$. Therefore, the effective action simplifies to

$$\begin{aligned}
\partial_t \Gamma_k[\varphi_k] &= \frac{1}{2} \int_p \int_q \Big(\partial_t \tilde{R}_k^{ab}(p,q) \Big) G_k^{ba}(q,p) + \int_p \int_q \tilde{R}_k^{ab}(p,q) \frac{\delta}{\delta J^a(p)} \partial_t \varphi_k^b(q) \\
&= \frac{1}{2} \int_p \int_q \Big(\partial_t \tilde{R}_k^{ab}(p,q) \Big) G_k^{ba}(q,p) + \int_p \int_q \int_{q'} \tilde{R}_k^{ab}(p,q) G_k^{ca}(q',p) \frac{\delta \partial_t \varphi_k^b(q)}{\delta \varphi_k^c(q')} \,.
\end{aligned} \tag{1.39}$$

Here, we have replaced the derivative with respect to the source J_k with a more suitable expression in terms of the connected propagator G_k^{ab}, which reads

$$\frac{\delta}{\delta J_k^a(p)} \partial_t \varphi_k^b(q) = \int_{q'} \frac{\delta \varphi_k^c(q')}{\delta J_k^a(p)} \frac{\delta \partial_t \varphi_k^b(q)}{\delta \varphi_k^c(q')} = \int_{q'} G_k^{ca}(q',p) \frac{\delta \partial_t \varphi_k^b(q)}{\delta \varphi_k^c(q')} \,. \tag{1.40}$$

In conclusion, we find

$$\begin{aligned}
\partial_t \Gamma_k[\varphi] + \int_{p'} \frac{\delta \Gamma_k[\varphi_k]}{\delta \varphi_k^a(p')} \partial_t \varphi_k^a(p') = \partial_t \Gamma_k[\varphi_k] &= \frac{1}{2} \int_p \int_q \Big(\partial_t \tilde{R}_k^{ab}(p,q) \Big) G_k^{ba}(q,p) \\
&\quad + \int_p \int_q \int_{q'} \tilde{R}_k^{ab}(p,q) G_k^{ca}(q',p) \frac{\delta \partial_t \varphi_k^b(q)}{\delta \varphi_k^c(q')} \,.
\end{aligned} \tag{1.41}$$

To obtain an equation for the Wetterich equation for k-independent fields $\partial_t \Gamma_k[\varphi] = \partial_t|_\varphi \Gamma_k[\varphi_k]$ we compare the left- and right-hand side of Eq. (1.41). For the expression on the left-hand side, we have simply taken the derivative of Γ_k with respect to the RG "time" by considering that Γ_k and ϕ_k depend on k, respectively. The right-hand side is the expression for $\partial_t \Gamma_k$ as obtained from Eq. (1.39). We have introduced k-dependent fields to provide an extension to the typically employed Wetterich equation. This leads to additional terms that have to be compensated since the fields present in the underlying theory are still k independent. We do so by employing $\partial_t \Gamma_k[\varphi]$ in the following. Therefore, the (modified) Wetterich equation used in the present work is given by

$$\begin{aligned}
\partial_t \Gamma_k[\varphi] &= \frac{1}{2} \int_p \int_q \Big(\partial_t \tilde{R}_k^{ab}(p,q) \Big) G_k^{ba}(q,p) + \int_p \int_q \int_{q'} \tilde{R}_k^{ab}(p,q) \frac{\delta \partial_t \varphi_k^b(q)}{\delta \varphi_k^c(q')} G_k^{ca}(q',p) \\
&\quad - \int_{p'} \frac{\delta \Gamma_k[\varphi_k]}{\delta \varphi_k^a(p')} \partial_t \varphi_k^a(p') \,.
\end{aligned} \tag{1.42}$$

Here, the first term in the latter expression represents the typically employed Wetterich equation. The second and third term take into account a possible k-dependence of the field φ_k^a.

The Wetterich equation is generally written as a differential equation for the effective action Γ_k. Therefore, we shall replace the connected propagator G_k^{ab} with a more suitable expression in terms of the effective action Γ_k. To this end, we start by taking the derivative of the effective action (1.36) with respect to the classical field φ_k from the right-hand side. This yields

$$\begin{aligned}\Big(\Gamma_k[\varphi_k]+\Delta S_k[\varphi_k]\Big)\frac{\overleftarrow{\delta}}{\delta\varphi_k^a(q)} &= J_k^a(-q)+(-1)^{ab}\int_p J_k^b(p)\frac{\overleftarrow{\delta}}{\delta\varphi_k^a(q)}\varphi_k^b(-p)-W_k[J_k]\frac{\overleftarrow{\delta}}{\delta\varphi_k^a(q)} \\ &= J_k^a(-q)+(-1)^{ab}\int_p J_k^b(p)\frac{\overleftarrow{\delta}}{\delta\varphi_k^a(q)}\varphi_k^b(-p)-\int_p\frac{W_k[J_k]\overleftarrow{\delta}}{\delta J_k^b(p)}\frac{J_k^b(p)\overleftarrow{\delta}}{\delta\varphi_k^a(q)}=J_k^a(-q)\,.\end{aligned} \tag{1.43}$$

This can be viewed as the quantum equation of motion with a regulator modification, i.e., the well-known quantum equation of motion follows by dropping the regulator term $\Delta S_k[\varphi_k]$ and setting the source J_k to zero. Taking the derivative of the modified quantum equation of motion with respect to the classical field from the left-hand side yields

$$\frac{\overrightarrow{\delta}}{\delta\varphi_k^b(-p)}\Big(\Gamma_k[\varphi_k]+\Delta S_k[\varphi_k]\Big)\frac{\overleftarrow{\delta}}{\delta\varphi_k^a(q)}=\frac{\overrightarrow{\delta}}{\delta\varphi_k^b(-p)}J_k^a(-q)\,. \tag{1.44}$$

With this expression at hand, we now consider

$$\begin{aligned}\delta^{ac}(2\pi)^n\delta^{(n)}(p'-q)=\frac{\overrightarrow{\delta}}{\delta J_k^c(-p')}J_k^a(-q)&=\int_p\frac{\overrightarrow{\delta}\varphi_k^b(-p)}{\delta J_k^c(-p')}\frac{\overrightarrow{\delta}J_k^a(-q)}{\delta\varphi_k^b(-p)} \\ &=(-1)^{bc}\int_p G_k^{cb}(p',p)\frac{\overrightarrow{\delta}}{\delta\varphi_k^b(-p)}\Big(\Gamma_k[\varphi_k]+\Delta S_k[\varphi_k]\Big)\frac{\overleftarrow{\delta}}{\delta\varphi_k^a(q)}\,.\end{aligned} \tag{1.45}$$

Here, the connected propagator enters the latter expression by using the condition for the classical field φ_k determined by the Legendre transformation (1.37) which yields $\delta\varphi_k^b(q)/\delta J_k^a(p)=G_k^{ba}(q,p)$. Additionally, we have used that $G_k^{bc}(-q,-p)=\langle\phi_k^c(p)\phi_k^b(-q)\rangle_{J,\mathrm{c}}=(-1)^{bc}G_k^{cb}(p,q)$. Recall that we have $(-1)^{ab}=-1$ for a and b corresponding to fermionic fields and $(-1)^{ab}=1$ for a or b corresponding to a bosonic field. Therefore, the connected propagator is given by the inverse of the regulated functional derivative of the effective action:

$$G_k^{ba}(q,p)=(-1)^{ab}\Big(\Gamma_k^{(1,1)}[\varphi_k,q,p)+\tilde{R}_k(q,p)\Big)^{-1}_{ba}\,. \tag{1.46}$$

Here, we have defined the $(1+1)$-point function

$$\Gamma_{k,ba}^{(1,1)}[\varphi_k,q,p)=\frac{\overrightarrow{\delta}}{\delta\varphi_k^b(-q)}\Gamma_k[\varphi_k]\frac{\overleftarrow{\delta}}{\delta\varphi_k^a(p)}\,. \tag{1.47}$$

From the modified Wetterich equation (1.42), we can recover the conventionally employed Wetterich equation without scale-dependent fields by setting $\partial_t\varphi_k^a=0$:

$$\partial_t\Gamma_k[\varphi]=\frac{1}{2}\int_p\int_q\Big(\partial_t\tilde{R}_k^{ab}(p,q)\Big)G_k^{ba}(q,p)=\frac{1}{2}\mathrm{STr}\Big\{\Big(\partial_t\tilde{R}_k(p,q)\Big)\Big[\Gamma_k^{(1,1)}[\varphi,q,p)+\tilde{R}_k(q,p)\Big]^{-1}\Big\}\,. \tag{1.48}$$

The minus sign that accounts for the presence of fermionic Grassmann-valued fields has been absorbed into the "super trace" operator STr. In addition to a trace over the fields and a summation over indices, it includes the momentum integration or, alternatively, an integration over coordinates since the Wetterich equation can also be adopted in position space.

The Wetterich equation describes the evolution of the effective action and therefore of correlation functions with the change of the scale k that connects macroscopic physics with microscopic interactions. In doing so, the influence of fluctuations is analysed by considering the effective action at different scales. It is noteworthy that the Wetterich equation is an exact flow equation for the effective action. The solution of the Wetterich

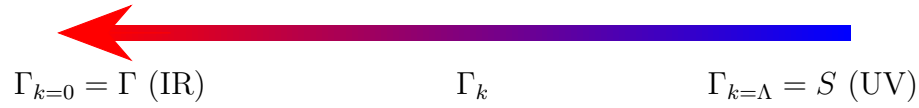

Figure 1.3: Illustration of the trajectory described by the solution of the Wetterich equation. The effective average action interpolates between the microscopic (ultraviolet, UV) where the interactions are known and the theory is defined by the action S and macroscopic properties and phenomena that can be extracted from the full effective action Γ (infrared, IR).

equation describes a trajectory in theory space that interpolates between the infrared (IR) and the ultraviolet (UV), see Fig. 1.3. Here, "infrared" refers to physics on large length scales and "ultraviolet" to physics on small length scales. The initial condition of this trajectory is given for small length scales by $\Gamma_{k=\Lambda} = S$. Here, Λ corresponds to the initial RG scale as a high UV cutoff scale. The trajectory is followed until the full quantum effective action is recovered for $k \to 0$: $\Gamma_{k=0} = \Gamma$ in the long-range limit. The advantage compared to the path integral representation is that the Wetterich equation does not require to compute a functional integral explicitly. Instead, it is a functional differential equation of the effective average action Γ_k. Flow equations of higher-order n-point functions can be obtained by taking the corresponding derivatives but, e.g., the flow equation for $\Gamma_k^{(n)}$ requires knowledge about $\Gamma_k^{(n+1)}$ and $\Gamma_k^{(n+2)}$. In general, this results in an infinite number of coupled differential equations. This corresponds to saying that Γ_k should contain all possible interactions that are consistent with the symmetries of the theory under consideration. In practice, an inclusion of all possible interactions in an ansatz for Γ_k is not feasible at least in general. Therefore, an ansatz with the most relevant degrees of freedom is usually employed. For example, in Chap. 2, we choose an ansatz that includes the most relevant degrees of freedom for QCD considering the high-density regime. Alternatively, in Sec. 3.1, we include the relevant low-energy degrees of freedom for the model that we shall employ. In addition to only considering the relevant degrees of freedom, e.g., higher-order correlations are also neglected and the momentum dependence is simplified. Finding the relevant degrees of freedom by including the correct terms in the ansatz to obtain the correct physics is perhaps the most challenging part of the Wetterich equation. More details about the properties of the Wetterich equation can be found in, e.g., Refs. [172, 173, 258, 259].

The connection between the functional renormalisation group and the conventional renormalisation group discussed above can be seen in the effective average action Γ_k. It is a generalisation of the effective action Γ since Γ_k only includes fluctuations with $q^2 \gtrsim k^2$ at least if the regulator function is chosen accordingly. Therefore, it is closely related to the coarse-graining procedure discussed above and Γ_k resembles a coarse-grained free energy. The coarse-graining length scale is given by $\sim k^{-1}$. For large scales k, fluctuations are suppressed so that the effective average action is close to the microscopic action. By lowering the scale k, more and more fluctuation effects are successively included until the full effective action Γ is recovered for $k \to 0$, allowing for an investigation of the theory on larger and larger length scales.

Let us now turn to the role and some of the properties of the regulator that has been introduced as a modification to the functional $Z_k[J_k]$ in Eq. (1.27). Firstly, the regulator is supposed to implement infrared regularisation which is ensured by

$$\lim_{q^2/k^2 \to 0} R_k(q) > 0\,. \tag{1.49}$$

This is especially important for massless theories as the regulator generates a mass-like term for small momenta and, therefore, ensures infrared regularisation which is reflected in the Wetterich equation, see Eq. (1.48), where the inverse of the $(1 + 1)$-point function is modified by the regulator term, resulting

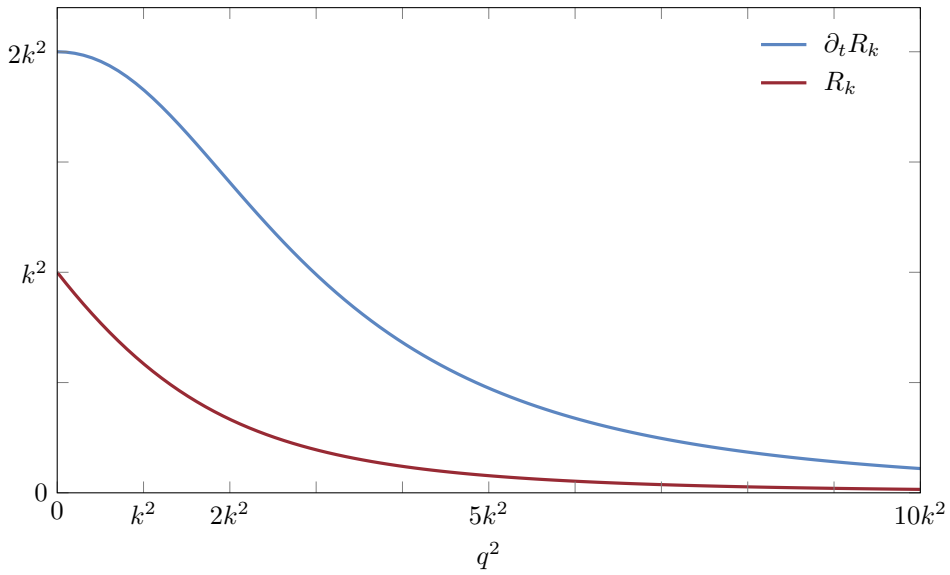

Figure 1.4: Example for a regulator R_k and derivative of the regulator $\partial_t R_k$ with respect to the RG time for a regulator commonly used for bosonic degrees of freedom: $R_k(q) = q^2 r(q^2/k^2)$. For the regulator shape function, we have used a four-dimensional polynomial regulator adapted for bosonic degrees of freedom, see App. B.2 for their definition. For $q^2/k^2 \to 0$, we find $R_k(q) \to k^2$ and for $q^2/k^2 \to \infty$, we find $R_k(q) \to 0$.

in a k-dependent connected propagator. The regulator consequently guarantees that this propagator does not diverge in the infrared. Secondly, the full quantum effective action is supposed to be recovered when considering the limit $k \to 0$. Therefore, we require that the regulator vanishes in the aforementioned limit:

$$\lim_{k^2/q^2 \to 0} R_k(q) = 0\,. \tag{1.50}$$

With this requirement imposed on the regulator, the full effective action is recovered from the modified version (1.36) for $k \to 0$ since the regulator and the resulting k-dependence drop out in the generating functional $W_{k\to 0}[J] = W[J]$ and the effective action $\Gamma_{k\to 0}[\varphi] = \Gamma[\varphi]$, respectively. In addition to that, the action S which defines the microscopic properties of the system under consideration is supposed to be recovered in the UV, i.e., for $k^2 \to \Lambda^2 \to \infty$: $\Gamma_{k\to\Lambda}[\varphi] = S[\varphi]$. This is ensured by

$$\lim_{k^2 \to \Lambda^2 \to \infty} R_k(q) \to \infty\,, \tag{1.51}$$

which leads to a suppression of fluctuations for $k \to \infty$ as required. Ultraviolet regularisation is provided by the contribution $\partial_t R_k$ to the Wetterich equation (1.48) since contributions from large momenta are suppressed. In addition to that, it resembles Wilson's approach to the renormalisation group because fluctuations close to k provide the largest contributions. This becomes apparent by considering an example for the regulator as done in the following. Note that the regulator is often written in terms of a dimensionless regulator shape function r, e.g., $R_k(q) \sim r(q^2/k^2)$. For example, for bosonic degrees of freedom, we may use $R_k^{\mathrm{b}}(q) = q^2 r(q^2/k^2)$ or $R_k^{\mathrm{b}}(q) = \vec{q}^{\,2} r(\vec{q}^{\,2}/k^2)$ only regularising the spatial momenta (referred to as three-dimensional regulators). The requirements for the regulator translate to the regulator shape function. We introduce different regulator shape functions that comply with the aforementioned requirements in App. B.2. As an example, we show the regulator and its derivative with respect to the RG time t employing a polynomial regulator shape function in Fig. 1.4. Notably, for $q^2/k^2 \to 0$, we find that $R_k(q) \to k^2$ which corresponds to the mass-like term that guarantees infrared regularisation. The other two requirements for

the regulator are also reflected in Fig. 1.4, i.e., for $k^2/q^2 \to 0$ ($q^2/k^2 \to \infty$), the regulator tends to zero and it diverges for $k \to \infty$. We add that, for fermionic degrees of freedom, the regulator is often chosen such that $R_k^\psi(q) = -\not{q}\, r(q^2/k^2)$ or $R_k^\psi(q) = -\vec{\not{q}}\, r(\vec{q}^2/k^2)$ only regularising the spatial momenta (referred to as three-dimensional regulators) [260–263]. The challenges we are encountering in the present work, which arise due to the presence of a chemical potential, require a more elaborate method to introduce a regulator for fermionic degrees of freedom that is suitable for such systems. Therefore, we shall discuss these issues in more detail and introduce a regulator that is capable of treating them in Sec. 1.3.

We would also like to point the reader to the fact that different regulators correspond to different trajectories in theory space. The full effective action which is recovered for $k \to \infty$ should be independent of the specific choice for the regulator. However, as soon as approximations or an ansatz are employed, the trajectory and result may depend on the specific choice for the regulator.

We conclude the discussion of the Wetterich equation by pointing out its connection to perturbation theory which becomes evident by replacing Γ_k with S in the effective action [173] so that

$$\partial_t \Gamma_k^{\text{1-loop}}[\varphi] = \frac{1}{2}\text{STr}\left\{\left(\partial_t R_k\right)\cdot\left[S^{(1,1)}[\varphi] + R_k\right]^{-1}\right\} = \frac{1}{2}\partial_t\,\text{STr}\ln\left(S^{(1,1)}[\varphi] + R_k\right). \tag{1.52}$$

The latter expression can then be integrated from Λ to zero so that

$$\Gamma^{\text{1-loop}}[\varphi] = S + \frac{1}{2}\text{STr}\ln\left(S^{(1,1)}[\varphi]\right) + \text{const.}\,, \tag{1.53}$$

which is nothing but the standard one-loop result for the effective action.

1.3 Regularisation in Dense Relativistic Systems

The present work focuses on exploring the phase structure and thermodynamics of strong-interaction matter at supranuclear densities using the fRG approach. In the following, we address issues arising in dense relativistic systems, particularly within the fRG approach.

As we have already discussed before, strong-interaction matter is expected to be governed by a colour-superconducting ground state at supranuclear densities, see Refs. [20, 46–56] for reviews. The related Cooper instability [71] leads to potential issues in calculations. In particular, the calculation of the effective action requires to introduce a suitable regularisation and renormalisation scheme with a suitably chosen class of regulators. As discussed in the previous section, fluctuations are usually integrated out successively from high-momentum scales to low-momentum scales. Then, the regulator is employed to regularise divergences around a given point in momentum space which appear in the low-energy limit at least for vanishing chemical potential. In the following, we do not aim to discuss the issues arising in calculations governed by a Cooper instability in detail but refer to Ref. [195] for details on the aspects that are only summarised in the following. However, we present the regularisation scheme for fRG studies that allows us to systematically handle the issues arising from the Cooper instability in Sec. 1.3.1 and we provide an example by applying it to a simple quark-diquark model that demonstrates the abilities of the regularisation scheme in Sec. 1.3.2. A quantitative understanding of relativistic fermions in a dense environment is not only essential for studying dense strong-interaction matter but also for applications in, e.g., condensed matter physics, nuclear physics, and high-energy physics. For the present work, we shall use this regularisation scheme in the subsequent chapters for fRG studies of the theory of the strong interaction.

Any RG approach requires to define suitable renormalisation and regularisation schemes. However, these schemes are not entirely at our disposal but are implicitly defined by certain aspects underlying the theory under consideration. Theories with a finite chemical potential exhibit the so-called Silver-Blaze property [264].

As it turns out, partition functions and observables do not depend on the chemical potential up to some critical value. This statement is valid as long as the regularisation scheme does not violate the underlying Silver-Blaze symmetry. With the inclusion of a chemical potential, the action is invariant under a set of transformations that are referred to as Silver-Blaze transformations reflecting the Silver-Blaze symmetry. See Refs. [184, 264–266] for a detailed discussion of the Silver-Blaze property. It should be noted that the Silver-Blaze property is no coincidence but can be understood from a phenomenological standpoint: The chemical potential can be related to the change in the free energy when fermions are added or removed from the system. For noninteracting fermions, a lower bound for this change in the free energy is the fermion mass. Therefore, the fermion density can only become finite for chemical potentials greater than the corresponding fermion mass. For chemical potentials below the fermion mass, this results in a partition function which does not depend on the chemical potential at zero temperature.

The calculation of the effective action usually involves approximations. An approximation scheme that is used throughout the present work is the derivative expansion [267–269], see also Refs. [172, 259, 270] for reviews. This corresponds to an expansion of correlation functions in terms of their external momenta and therefore requires to choose an expansion point. The derivative expansion is often used because resolving the full momentum dependence of correlation functions is very costly. It is now intuitive, to choose a Silver-Blaze symmetric point in the calculation of the effective action within a derivative expansion. Indeed, to preserve the Silver-Blaze property, an expansion in external momenta performed around a point that preserves the Silver-Blaze symmetry is needed. This point is given by $(p_0 + \mathrm{i}F\mu, \vec{p}) = (0,0)$ instead of the conventional expansion point $(p_0, \vec{p}) = (0,0)$ [184, 266]. Here, F is the fermion number where, e.g., diquark fields composed of two quarks or two antiquarks carry fermion number $|F| = 2$ and mesons composed of quark and antiquark carry fermion number $F = 0$. However, this expansion point leads to issues as we shall elaborate in the following. Concerning RG studies where fluctuations are integrated out successively, it should be emphasised that the Silver-Blaze property is only preserved if the regularisation and renormalisation scheme are chosen accordingly. In terms of the Wetterich equation [255], this requires to appropriately choose the momentum dependence of the regulator functions, i.e., the regulator term for fermions should obey $R_k^{\psi}(\mathrm{i}p_0, \mathrm{i}\vec{p}, \mu) = R_k^{\psi}(\mathrm{i}(p_0 - \mathrm{i}\mu), \mathrm{i}\vec{p}, 0)$ and the regulator for bosons composed of fermions should obey $R_k^{\mathrm{b}}(\mathrm{i}p_0, \mathrm{i}\vec{p}, \mu) = R_k^{\mathrm{b}}(\mathrm{i}(p_0 - \mathrm{i}F\mu), \mathrm{i}\vec{p}, 0)$. In summary, an expansion around the point $(p_0, \vec{p}) = (0,0)$ and regulator terms that do not obey these rules break the invariance under Silver-Blaze transformations. Therefore, to preserve the Silver-Blaze property in a derivative expansion of the effective action, these two aspects have to be followed.

Another important aspect of the regularisation scheme is that it should not violate the scaling behaviours for physical observables that are required to be recovered in, e.g., dense systems and the corresponding BCS-type models. As it turns out, this scaling behaviour of physical observables is influenced by the expansion point. For example, in BCS-type models a specific choice of expansion point may lead to a decrease in physical observables $\mathcal{O}$ with increasing chemical potential although an increase is expected according to a BCS-type scaling behaviour $\mathcal{O} \sim \exp(-c/\mu^2)$, where $c > 0$ is a positive constant [40, 82, 84–86]. Therefore, an expansion in the derivative expansion with a Silver-Blaze symmetric expansion point is not suitable to recover the expected BCS-type scaling behaviour. To be more explicit, considering the quark-diquark model that we shall consider in Sec. 1.3.2 as an example, using a Silver-Blaze symmetric expansion point does not lead to the expected behaviour for, e.g., the diquark gap which is expected to scale as $|\bar{\Delta}_0| \sim \exp(-c/\mu^2)$. Consequently, an expansion around a Silver-Blaze symmetric point is not always the correct choice especially from a phenomenological perspective. Instead, one could argue that the expansion point should be given by $(p_0, \vec{p}) = (0,0)$. However, this expansion point comes with a new problem. Using a Silver-Blaze symmetric regulator without using a Silver-Blaze symmetric expansion point may result in ill-defined loop integrals. These ill-defined loop integrals originate from poles appearing in the calculation, see, e.g., Ref. [193].

Therefore, the flow of the couplings also becomes ill-defined when fluctuations are integrated out from the high-energy scale ($k = \Lambda$) to the low-energy limit ($k = 0$). In RG studies using the conventionally employed class of regulator functions [172, 255], this pole is therefore always approached from one side. It should be noted that the existence of these poles is not inherently problematic but a consequence of a Cooper instability present in the system. Nevertheless, the treatment with conventional regularisation schemes is problematic. To recover the correct BCS-type scaling behaviour in the presence of a Cooper instability and to render the loop integrals well-defined, we need to introduce a new regularisation scheme. It turns out that the poles can be cured by effectively gapping fluctuations around the Fermi surface. This is also the approach in Refs. [82, 84], where the correct scaling behaviour has been recovered, by implementing a sharp cutoff around the Fermi surface. Notably, integrating around a scale set by the chemical potential is conventionally done in dense nonrelativistic matter and ultracold atomic gases [247–249, 271–274]. A systematic implementation of integrating out fluctuations around the Fermi surface to recover the expected scaling behaviour of observables, at least in studies based on the derivative expansion, is provided by the regularisation scheme introduced in Sec. 1.3.1 below. It provides a more applicable approach, especially for calculations underlying more complex approximations, since the sharp cutoff comes with problems due to nonlocality and it leads to ambiguities in the computations [172, 275]. A related class of regulators has already been introduced in nonrelativistic theories, e.g., condensed matter physics and ultracold atomic gases, see Refs. [247–249, 271–274]. It is important to emphasise that the regularisation scheme introduced in Sec. 1.3.1 breaks the Silver-Blaze symmetry explicitly because it relies on regularising the chemical potential alongside the spatial momentum as we shall see. Recall that it is necessary to break the Silver-Blaze symmetry anyhow by using an expansion point that does not obey this symmetry to recover the correct BCS-type scaling behaviour. Therefore, breaking the Silver-Blaze symmetry with the regulator may not be considered unreasonable. However, it should be noted that the regulator vanishes in the low-energy limit. Still, if the regulator breaks Silver-Blaze invariance, this breaking is also reflected in the low-energy limit even if a Silver-Blaze symmetric expansion point is used in the derivative expansion.

1.3.1 Quasi-Particle Regularisation Scheme

The presence of a Cooper instability requires the introduction of a suitable regularisation scheme that can handle the poles appearing in the fermion propagators. In the following, we refer to this regularisation scheme as the "quasi-particle regularisation scheme" because it introduces projectors onto positive and negative energy solutions of the free Dirac equation which can be related to particle and antiparticle states. We shall come back to this aspect in more detail in the following. The two aforementioned projectors are given by

$$P_\pm \equiv P_\pm(\vec{p}) = \frac{1}{2}\left(\gamma_0 \mp \frac{\mathrm{i}\vec{\not{p}}}{|\vec{p}|}\right)\gamma_0 \,. \tag{1.54}$$

We use the slash notation $\vec{\not{p}} = p_i\gamma_i$. The projectors obey the following rules:

$$\begin{gathered} P_+ + P_- = \mathbb{1}, \qquad P_+P_- = P_-P_+ = 0, \qquad P_+P_+ = P_+, \qquad P_-P_- = P_- \,, \\ P_-\gamma_0 = \gamma_0 P_+ \,, \qquad \text{and} \qquad P_+\gamma_0 = \gamma_0 P_- . \end{gathered} \tag{1.55}$$

The free Dirac equation comes with two solutions with positive energy and two with negative energy which is reflected by $\mathrm{Tr}\big(P_\pm\big) = 2$. These solutions are related to particle and antiparticle states. Similar versions of these projectors have already been introduced in, e.g., Refs. [218, 276, 277]. Similar to the free Dirac equation, the projectors can be used to split the kinetic term for the fermions that comes with the corresponding action, e.g., the action (1.76) defined in the following, see Sec. 1.3.2.

The kinetic term is given by

$$S_{\bar{\psi}\psi} = \int_p \bar{\Psi}(p)\big(-(p_0 + \mathrm{i}\mu)\gamma_0 - \not{p}\big)\Psi(p)\,. \tag{1.56}$$

Here, we have performed a Fourier transformation of the kinetic term so that $\bar{\Psi}$ and Ψ are the Fourier transforms of the fields $\bar{\psi}$ and ψ, respectively. The kinetic term suggests to introduce the kinetic operator

$$T = -(p_0 + \mathrm{i}\mu)\gamma_0 - \not{p}\,. \tag{1.57}$$

Indeed, this definition is convenient in the calculation of loop diagrams and for calculations using the Wetterich equation where the inverse of T appears. The kinetic operator T can be conveniently rewritten by utilising the two projectors:

$$T = T\big(P_+ + P_-\big) = -\big(p_0 + \mathrm{i}\,(\mu - |\vec{p}|)\,\big)P_-\gamma_0 - \big(p_0 + \mathrm{i}\,(\mu + |\vec{p}|)\,\big)P_+\gamma_0 = C_-P_-\gamma_0 + C_+P_+\gamma_0\,. \tag{1.58}$$

For convenience, we have introduced $C_\pm = (p_0 + \mathrm{i}(\mu \pm |\vec{p}|))$. This decomposition allows us to split the kinetic term (1.56) of the fermions into two contributions:

$$S_{\bar{\psi}\psi} = \int_p \bar{\Psi}C_-P_-\gamma_0\Psi + \int_p \bar{\Psi}C_+P_+\gamma_0\Psi\,. \tag{1.59}$$

As we shall see, these contributions resemble modes with positive and negative energy values relative to the Fermi surface.

At this point, some comments concerning the symmetries are in order. Firstly, we notice that the two contributions in Eq. (1.59) are separately invariant under chiral transformation and separately invariant under Silver-Blaze transformations as well. Secondly, the contributions are not separately invariant under charge conjugation which is broken anyway at finite chemical potential. However, also for $\mu = 0$, the two contributions are not invariant under charge conjugation because the projectors split them into particle and antiparticle contributions. In contrast to that, $\int_p \bar{\Psi}T\Psi$ is invariant under charge conjugation for vanishing chemical potential $\mu = 0$.

Using the relations for the projectors, the expression for the kinetic operator T can be inverted:

$$T^{-1} = -\frac{P_+\gamma_0}{p_0 + \mathrm{i}\,(\mu - |\vec{p}|)} - \frac{P_-\gamma_0}{p_0 + \mathrm{i}\,(\mu + |\vec{p}|)} = C_-^{-1}P_+\gamma_0 + C_+^{-1}P_-\gamma_0\,. \tag{1.60}$$

From the latter expression the necessity for a suitable regularisation scheme for the problems arising in the present work can be easily understood. We note that C_+ is invertible since $C_+ \neq 0$ (for any finite μ) so that C_+^{-1} is finite. In contrast to that, C_- becomes zero at $p_0 = 0$ and $|\vec{p}| = \mu$ so that C_-^{-1} exhibits a pole at that position. Recall that $|\vec{p}| = \mu$ corresponds to the Fermi surface. We conclude that the kinetic operator T is not invertible, at least in general. For vanishing chemical potential, the pole corresponds to a vanishing four-momentum which is conventionally taken care of by a mass-like regularisation scheme. However, this regularisation scheme does not cure the corresponding pole at the Fermi surface for finite chemical potential. In the presence of a chemical potential, the vanishing of the four-momentum is screened by μ. This is sufficient for C_+ to be invertible at finite chemical potential. In contrast to that, the pole of C_-^{-1} at $p_0 = 0$ and $|\vec{p}| = \mu$ is not cured in this way. In the next step, we therefore introduce a regularisation scheme to address the problematic pole.

Before introducing the corresponding regulator term, we analyse the poles of the kinetic operator T from an alternative viewpoint. For this particular consideration, we switch to Minkowski spacetime which can be recovered by considering $p_0 \mapsto -\mathrm{i}p_0$. Consequently, the kinetic propagator exhibits poles at $p_0 = \omega_\pm$ where

$$\omega_\pm = \mu \pm |\vec{p}|\,, \tag{1.61}$$

which is nothing but the quasi-particle dispersion relations of relativistic (quasi-)particles in the presence of a chemical potential. This dispersion relation gives the energy of the (anti-)fermions relative to the Fermi surface.

To effectively handle both, the positive and negative, energy solutions in terms of the quasi-particle dispersion relations, a regulator has to treat the modes associated with the two terms in the decomposed kinetic term differently. The regularisation of the two energy states separately ensures that poles in C_-^{-1} can be removed without introducing new poles in C_+^{-1}. An exception to this is the sharp regulator (e.g., introducing a sharp cutoff around the Fermi surface), which has the ability to handle the task but at the expense of additional issues, e.g., leading to ambiguities in the evaluation of loop integrals. Therefore, it is preferable to implement the regularisation scheme that we are introducing in the present section. It is important to note that the modes should only be treated differently in the presence of a chemical potential, but should be handled in the same manner in the limit of vanishing chemical potential. In the latter case, the regulator regularises divergences in the low-momentum limit, ensuring that the charge conjugation symmetry remains unaffected for $\mu = 0$. In addition to that, the regulator should not break the chiral symmetry of the theory. A general regulator term that fulfils these requirements is given by

$$R_k^\psi = -\mathrm{i}\big(\mu - |\vec{p}\,|\big) r_- P_- \gamma_0 - \mathrm{i}\big(\mu + |\vec{p}\,|\big) r_+ P_+ \gamma_0 \,. \tag{1.62}$$

Here, we have introduced two different regulator functions $r_\pm$ that deal with the positive and negative modes. In the following, we use regulator functions of the form

$$r_\pm \equiv r\,(x_\pm) \qquad \text{with} \qquad x_\pm = (\mu \pm |\vec{p}\,|)^2/k^2 \,. \tag{1.63}$$

Here, r is a dimensionless regulator shape function. The subscript '$\pm$' indicates that we regularise the solutions associated with positive and negative energy values separately. The two different regulator functions $r_\pm$ only differ by the argument of the regulator shape function r. This ensures that the two modes are regularised identically for vanishing chemical potential. The regulator shape functions used throughout the present work are found in App. B.2.

It should be emphasised that the regulator term (1.62) breaks Silver-Blaze symmetry explicitly in contrast to conventionally employed three-dimensional regularisation schemes. This results from integrating out fluctuations around the Fermi surface which requires to couple the spatial momentum and the chemical potential by regularising them together. However, the breaking of the Silver-Blaze symmetry appears to be necessary anyhow to recover the correct BCS-type scaling behaviour in the derivative expansion as discussed in the beginning of this section. In addition to that, conventionally employed three-dimensional regularisation schemes with an expansion point that breaks the Silver-Blaze symmetry lead to ill-defined loop diagrams in the presence of a Cooper instability, see Ref. [195]. Note that although regulators vanish in the infrared limit ($k \to 0$), the possible breaking of the Silver-Blaze symmetry by the regulator is reflected in the low-range limit even if a Silver-Blaze symmetric expansion point is chosen.

Recall that we have introduced requirements that have to be fulfilled by the regulator in Sec. 1.2 which translate to conditions that have to be imposed on the regulator shape functions. These conditions are slightly adapted to account for the presence of a chemical potential. In general, we consider shape functions that fulfil $(1+r) \geq 0$ so that no artificial divergences emerge in the calculation of loop diagrams. In order to guarantee that the regulator vanishes in the long-range limit $k \to 0$ for fixed momentum and in the limit $|\vec{p}\,| \to \infty$ for fixed k, we require

$$\lim_{x\to\infty} r(x) = 0 \,. \tag{1.64}$$

In addition to that, we consider regulator shape functions for which

$$\lim_{x\to 0} \sqrt{x}\, r(x) > 0 \,. \tag{1.65}$$

To be precise, for regulators employed in the present work we find $\lim_{x\to 0}\sqrt{x}\,r(x) = 1$ so that

$$r(x_\pm) = \frac{k}{|\mu \pm |\vec{p}||} + \cdots \tag{1.66}$$

in the limit $x \to 0$. This condition ensures that poles around the Fermi surface, i.e., around $|\vec{p}| = \mu$, appearing in the inverse of C_- and therefore in the kinetic operator T are regularised. Fermionic regulator shape functions that exhibit these properties are found in App. B.2.
Adding the regulator to the kinetic term leads to a regularised kinetic operator given by

$$T + R_k^\psi = -\big(p_0 + \mathrm{i}\epsilon_-\big)P_-\gamma_0 - \big(p_0 + \mathrm{i}\epsilon_+\big)P_+\gamma_0\,. \tag{1.67}$$

Here, we have introduced

$$\epsilon_\pm = \big(\mu \pm |\vec{p}\,|\big)\big(1 + r_\pm\big)\,, \tag{1.68}$$

which resembles a regularised "quasi-particle dispersion relation". The inverse of the kinetic operator can be calculated using the relations for the projectors which yields

$$\left(T + R_k^\psi\right)^{-1} = -\frac{P_+\gamma_0}{p_0 + \mathrm{i}\epsilon_-} - \frac{P_-\gamma_0}{p_0 + \mathrm{i}\epsilon_+}\,. \tag{1.69}$$

This inverse is now well-defined for all p_0 and $\vec{p}$. The effect of the regularisation can be illustrated by considering the effect of the regulator on the "quasi-particle dispersion relation" associated with the negative energy mode ϵ_-. We find that $\epsilon_- > 0$ for $\mu > |\vec{p}|$ and $\epsilon_- < 0$ for $\mu < |\vec{p}|$. Therefore, it changes its sign at the Fermi surface so that, close to the Fermi surface, it is given by $\epsilon_- = k\,\mathrm{sgn}(\mu - |\vec{p}|) + \cdots$. Consequently, fluctuations around the Fermi surface are gapped by the regulator with a gap given by $\sim k$. In the long-range limit $k \to 0$, this gap disappears so that all fluctuations are integrated out around the Fermi surface. In contrast to that, we find $\epsilon_+ > 0$, where the chemical potential effectively acts as a regulator, even for $k \to 0$. Recall that we constructed the quasi-particle regularisation scheme such that, for vanishing chemical potential, the positive and negative energy modes are regularised in the same manner. Therefore, for $\mu = 0$ it is identical to the standard three-dimensional regularisation scheme because the regulator term reduces to $R_k^\psi = \mathrm{i}\,|\vec{p}\,|\,P_-\gamma_0 r - \mathrm{i}\,|\vec{p}\,|\,P_+\gamma_0 r = -\not{p} r$ [260–263]. Then, the regularised kinetic operator becomes

$$T + R_k^\psi = -p_0\gamma_0 - \not{p}\,(1 + r)\,. \tag{1.70}$$

The regulator shape function $r \equiv r(x)$ comes with the argument $x = \vec{p}^{\,2}/k^2$. It is useful to note that the standard three-dimensional regularisation scheme for finite chemical potential (with $R_k^\psi = -\not{p} r$ [260–263]) can be recovered from the quasi-particle regularisation scheme by setting $\epsilon_\pm \to (\mu \pm |\vec{p}\,|\,(1 + r))$ in Eq. (1.67) so that

$$T + R_k^\psi = -(p_0 + \mathrm{i}\mu)\gamma_0 - \not{p}\,(1 + r)\,. \tag{1.71}$$

We conclude this section on the introduction of the quasi-particle regularisation scheme that is suitable for handling systems in the presence of a Cooper instability by putting it into context with the functional renormalisation group. To do so, we show some useful relations for explicit calculations of flow equations. Using the result for the inverse of the kinetic propagator (1.69), we find

$$\left(T + R_k^\psi\right)^{-1}\big(\partial_t R_k^\psi\big) = \frac{\mathrm{i}\,(\mu - |\vec{p}\,|)\,(\partial_t r_-)}{p_0 + \mathrm{i}\epsilon_-}P_+ + \frac{\mathrm{i}\,(\mu + |\vec{p}\,|)\,(\partial_t r_+)}{p_0 + \mathrm{i}\epsilon_+}P_-\,. \tag{1.72}$$

The properties of the projectors allow us to solve the trace over Dirac space (indicated by the subscript 'D') resulting in

$$\mathrm{Tr}_\mathrm{D}\left\{\left(T + R_k^\psi\right)^{-1}\big(\partial_t R_k^\psi\big)\right\} = \frac{2\mathrm{i}\,(\mu - |\vec{p}\,|)\,(\partial_t r_-)}{p_0 + \mathrm{i}\epsilon_-} + \frac{2\mathrm{i}\,(\mu + |\vec{p}\,|)\,(\partial_t r_+)}{p_0 + \mathrm{i}\epsilon_+}\,. \tag{1.73}$$

We find that derivatives with respect to the regulator only appear together with the corresponding energy modes, i.e., the quasi-particle dispersion relations. More precisely, the scale derivative of the regulator $r_\pm$ appears together with the corresponding dispersion relation $\epsilon_\pm$. Additionally, these two contributions are conveniently split into two terms which can be handled separately. For applications of the Wetterich equation, it is also useful to consider the complex conjugate of the kinetic operator which is given by

$$\big(T\big)^* = -\left(p_0 - \mathrm{i}\mu\right)\gamma_0^T - \vec{\not{p}}^T = -\big(p_0 - \mathrm{i}\left(\mu + |\vec{p}|\right)\big)\gamma_0 P_-^T - \big(p_0 - \mathrm{i}\left(\mu - |\vec{p}|\right)\big)\gamma_0 P_+^T \,. \tag{1.74}$$

With the complex conjugate of the regulator term $\big(R_k^\psi\big)^*$ the inverse of the regulated kinetic operator becomes

$$\Big(\big(T\big)^* + \big(R_k^\psi\big)^*\Big)^{-1} = -\frac{\gamma_0 P_+^T}{p_0 - \mathrm{i}\epsilon_+} - \frac{\gamma_0 P_-^T}{p_0 - \mathrm{i}\epsilon_-} \,. \tag{1.75}$$

The expressions for the inverse of the regulated kinetic propagators, see Eqs. (1.69) and (1.75), can be transferred to define the so-called propagator matrix we use in our fRG studies, see App. C for details. Note that the regularisation scheme can be extended to account for an isospin asymmetry in the system, i.e., the existence of different chemical potentials for the up and down quarks, and also to include colour chemical potentials. This extension is required for the calculations in Sec. 3.1 and can be found in App. B.1.

1.3.2 Example: Diquark Condensation

Using the quasi-particle regularisation scheme, we demonstrate its application in the following by employing a simple quark-diquark model (commonly used for dense strong-interaction matter, see, e.g., Refs. [46–50]) with two quark flavours and three colours at finite chemical potential which is represented by the following ansatz for the effective action:

$$\Gamma_k = \int_x \Big\{ \bar{\psi}\big(\mathrm{i}\partial\!\!\!/ - \mathrm{i}\gamma_0\mu\big)\psi - \frac{1}{2}\big(\bar{\psi}\tau_2 \mathrm{i}\Delta_a^* \epsilon_a \gamma_5 \mathcal{C}\bar{\psi}^T\big) + \frac{1}{2}\big(\psi^T \mathcal{C}\gamma_5\tau_2 \mathrm{i}\Delta_a \epsilon_a \psi\big) + U_k(\Delta_a^*, \Delta_a)\Big\} \,. \tag{1.76}$$

The quark fields ψ and $\bar{\psi}$ carry two flavour degrees of freedom. The index $a = 1, 2, 3$ is a colour index and the definitions of all matrices, i.e., colour, flavour, and Dirac matrices, can be found in App. A. We do not go into detail about the construction and the motivation of the terms included in the action but refer to Sec. 2.1 where diquark fields are included from the fundamental quark-gluon interaction of QCD. Here, we only note that the present ansatz (1.76) can be viewed as a low-energy effective model of the action underlying the calculations in Chap. 2.

The diquark fields Δ_a are complex-valued and carry fermion number $|F| = 2$. They represent states $\Delta_a \sim (\bar{\psi}\tau_2\epsilon_a\gamma_5\mathcal{C}\bar{\psi}^T)$ with $J^P = 0^+$ where J is the angular momentum and P the parity. The diquark potential U_k entering the ansatz for the effective action (1.76) is given by

$$U_k(\Delta_a^*, \Delta_a) = \bar{\nu}_k^2 \Delta_a^* \Delta_a + \bar{\lambda}_k \big(\Delta_a^* \Delta_a\big)^2 \,. \tag{1.77}$$

At the initial RG scale, the effective action is given by the classical action $S = \Gamma_{k=\Lambda}$ where $U_\Lambda(\Delta_a^*, \Delta_a) = \bar{\nu}_\Lambda^2 \Delta_a^* \Delta_a$. We emphasise that U_k contains diquark self-interaction channels but it should in general not be confused with the effective potential which is given by Γ_k/V_4 evaluated on constant fields. We drop a possible scale dependence of the Yukawa-type interaction term and the wavefunction renormalisation factors in the ansatz (1.76), see also Ref. [194]. The couplings $\bar{\nu}_k^2$ and $\bar{\lambda}_k$ at the initial RG scale are external control parameters of the model that can be used to determine the ground-state properties. The emergence of two different ground states is possible in the vacuum, i.e., for $\mu = 0$, see, e.g., Refs. [85, 165, 179, 193] for a general fixed-point analysis and mean-field analysis. Firstly, the ground state might already be governed by symmetry breaking and the resulting formation of a finite diquark gap. Secondly, the symmetry can only

be broken at finite μ while it is intact in the vacuum. Setting the four-diquark coupling $\bar{\lambda}_k$ to zero at the initial RG scale so that it is only induced in the RG flow, the initial value for $\bar{\nu}_k^2$ determines which of the two possible ground states is realised in the vacuum. For sufficiently large $\bar{\nu}_\Lambda^2$ the symmetry is only broken for finite chemical potential whereas for small $\bar{\nu}_\Lambda^2$, the symmetry is already broken in the vacuum. These two scenarios are separated by a critical value $\bar{\nu}_*^2$.

In the following, we do not aim to provide a detailed discussion of the quark-diquark model, since it is a frequently used low-energy model for dense strong-interaction matter (see, e.g., Refs. [46–50]), but only demonstrate the abilities of the quasi-particle regularisation scheme. We especially show that the correct BCS-type scaling behaviour is recovered. Therefore, we only consider the running of the parameter $\bar{\nu}_k^2$ and the four-diquark coupling $\bar{\lambda}_k$.

The parameter $\bar{\nu}_k^2$ represents the curvature of the diquark potential at the origin. It is therefore an indicator for the onset of spontaneous symmetry breaking. At the initial RG scale $k = \Lambda \gg \mu$, the starting point is given by the classical action S which is invariant under $\mathrm{U}(1)_V$ (where V stands for vector) transformations. Therefore, for large scales, we have $\bar{\nu}_k^2 > 0$. However, towards the long-range limit, the curvature of the potential, which serves as an indicator of the breakdown of the $\mathrm{U}(1)_V$ symmetry, may eventually change its sign determining the symmetry-breaking scale k_{SB}. Note that $\bar{\nu}_k^2$ is related to the inverse of a four-quark interaction, see Sec. 2.1 and also Ref. [165, 179, 193] for details about this aspect. We add that, for the present illustrative study, we only consider purely fermionic loops for simplicity and use the expansion point $(p_0, \vec{p}) = (0, 0)$.

We calculate the flow of the curvature $\bar{\nu}_k^2$ and the four-diquark coupling $\bar{\lambda}_k$ using the quasi-particle regularisation scheme and the Wetterich equation. For this, we identify the complex-valued diquark fields Δ_a in the ansatz (1.76) with homogeneous background fields $\bar{\Delta}_a$: $\Delta_a = \bar{\Delta}_a$. Then, the flow equation of the curvature of the diquark potential $\bar{\nu}_k^2$ is given by

$$\partial_t \bar{\nu}_k^2 = \frac{1}{V_4} \left(\frac{\partial}{\partial(\bar{\Delta}_1^* \bar{\Delta}_1)} \partial_t \Gamma_k \right)_{\mathrm{gs}} . \tag{1.78}$$

Here, $V_4 = \int \mathrm{d}^4 x$ is the four-dimensional volume and the subscript 'gs' indicates that we evaluate on the ground state, i.e., $\bar{\Delta}_a = 0$. At this point, we should note that terms $\sim \mu^2 \Delta_a^* \Delta_a$ are generated in the RG flow. These terms are related to the kinetic term of the diquark fields. However, these contributions are effectively included in the running of the parameter $\bar{\nu}_k^2$, see also our discussion in Sec. 2.1 below.

Similarly to the flow equation of the curvature of the diquark potential, we calculate the flow equation of the four-diquark coupling $\bar{\lambda}_k$ using

$$\partial_t \bar{\lambda}_k = \frac{1}{2V_4} \left(\frac{\partial^2}{\partial(\bar{\Delta}_1^* \bar{\Delta}_1)^2} \partial_t \Gamma_k \right)_{\mathrm{gs}} . \tag{1.79}$$

Alternatively, we can define the flow equation of the parameter $\bar{\nu}_k^2$ and the four-diquark coupling $\bar{\lambda}_k$ with a derivative with respect to $(\bar{\Delta}_2^* \bar{\Delta}_2)$ or $(\bar{\Delta}_3^* \bar{\Delta}_3)$, respectively. We employ an expansion of the Wetterich equation $\partial_t \Gamma_k$, see App. C for details. With these projection rules, the set of flow equations in the symmetric regime is given by:

$$\partial_t \bar{\nu}_k^2 = -4 \int_p \tilde{\partial}_t \left(\frac{1}{p_0^2 + (\mu + |\vec{p}|)^2 (1 + r_+)^2} + \frac{1}{p_0^2 + (\mu - |\vec{p}|)^2 (1 + r_-)^2} \right) \tag{1.80}$$

and

$$\partial_t \bar{\lambda}_k = 2 \int_p \tilde{\partial}_t \left(\frac{1}{(p_0^2 + (\mu + |\vec{p}|)^2 (1 + r_+)^2)^2} + \frac{1}{(p_0^2 + (\mu - |\vec{p}|)^2 (1 + r_-)^2)^2} \right) . \tag{1.81}$$

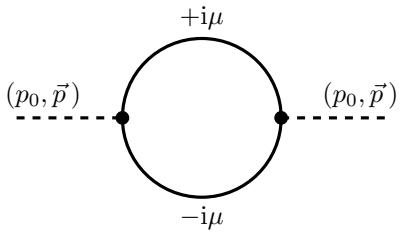

Figure 1.5: Loop diagram contributing to the running of the curvature $\bar{\nu}_k$. The solid lines are associated with fermions and the dashed lines are associated with diquark fields with external momenta $(p_0, \vec{p})$. We use $(p_0, \vec{p}) = (0, 0)$ as the expansion point in the derivative expansion.

Here, $\tilde{\partial}_t = (\partial_t r_+)\partial/\partial r_+ + (\partial_t r_-)\partial/\partial r_-$. The integral on the right-hand side of the flow equation (1.80) for the parameter $\bar{\nu}_k$ corresponds, in terms of Feynman diagrams, to the loop diagram shown in Fig. 1.5 where the external momenta have been evaluated according to $(p_0, \vec{p}) = (0, 0)$.
We also find that the flow equations (1.80) and (1.81) are decoupled, at least within the present approximation, as we have dropped fluctuation effects. Therefore, to calculate the symmetry-breaking scale, we only have to consider Eq. (1.80) since the parameter $\bar{\nu}_k^2$ serves as an indicator for the spontaneous breakdown of the $\mathrm{U}(1)_V$ symmetry associated with the formation of a gap in the excitation spectrum of the fermions referred to as diquark gap [165, 179, 193]. In the symmetric regime, $\bar{\nu}_k^2 > 0$ which is realised for at least a certain range of values $k \leq \Lambda$. At the symmetry-breaking scale k_{SB}, depending on the initial condition $\bar{\nu}_\Lambda^2$, the parameter $\bar{\nu}_k^2$ may change its sign so that we can extract the scaling behaviour of the symmetry-breaking scale from Eq. (1.80). For example, by using a linear shape function $r(x) = (1/\sqrt{x} - 1)\theta(1 - x)$ [263, 278, 279], the right-hand side of the flow equation can be solved analytically so that we find

$$\partial_t \bar{\nu}_k^2 = 2k^2/(3\pi^2) + 2\mu^2/\pi^2 \,. \tag{1.82}$$

For the scaling behaviour, it follows $k_{\mathrm{SB}} \sim \exp(-c/\mu^2)$ with $c > 0$ which is independent of the chemical potential and determined by the initial condition $\bar{\nu}_\Lambda^2$. Here, we have assumed that $k_{\mathrm{SB}} \ll \Lambda$ which is required anyhow. Consequently, the expected BCS-type scaling behaviour (as expected from relativistic models, see Refs. [40, 84–86]) is recovered. Since the symmetry-breaking scale sets the scale for low-energy observables $\mathcal{O}$, the scaling behaviour is passed down to physical observables in the infrared limit leading to $\mathcal{O} \sim \exp(-c/\mu^2)$, see also Ref. [82] for the scaling behaviour.
The onset of spontaneous symmetry breaking is associated with the emergence of a nontrivial ground state. While the diquark potential in the symmetric regime ($k \geq k_{\mathrm{SB}}$) is given by Eq. (1.77), we expand the action in the phase governed by spontaneous symmetry breaking around the scale-dependent ground state, i.e., the diquark condensate $|\bar{\Delta}_0|^2$. Therefore, the diquark potential for $k \leq k_{\mathrm{SB}}$ is given by

$$U_k(\Delta_a^*, \Delta_a) = \bar{\lambda}_k(\Delta_a^*\Delta_a - |\bar{\Delta}_0|^2)^2 \,. \tag{1.83}$$

For convenience, we choose the diquark condensate to point in the three-direction in colour space without loss of generality, i.e., $\Delta_{a,0} = |\bar{\Delta}_0|\delta_{a,3}$. In addition to that, $\bar{\Delta}_0$ is assumed to be homogeneous and real-valued. We calculate the flow equation of the diquark condensate $|\bar{\Delta}_0|^2$ and the four-diquark coupling $\bar{\lambda}_k$ by identifying the diquark fields Δ_a in the ansatz (1.76) with homogeneous background fields $\bar{\Delta}_a$. However, in contrast to the symmetric phase, we decompose the background field such that $\Delta_a = \bar{\Delta}_a = \delta\bar{\Delta}_a + \bar{\Delta}_3\delta_{a,3}$. Using this decomposition, the flow equation of the diquark condensate $|\bar{\Delta}_0|^2$ is obtained from

$$\partial_t|\bar{\Delta}_0|^2 = -\frac{1}{2\bar{\lambda}_k V_4}\left(\frac{\partial}{\partial(\delta\bar{\Delta}_1^*\delta\bar{\Delta}_1)}\partial_t\Gamma_k\right)_{\mathrm{gs}} . \tag{1.84}$$

Here, the subscript 'gs' indicates that we evaluate on the ground state which is given by evaluating $\delta\bar{\Delta}_a = 0$ and $\bar{\Delta}_3 = |\bar{\Delta}_0|$. Alternatively, we can define the flow equation of the diquark condensate $|\bar{\Delta}_0|^2$ with a derivative with respect to $(\delta\bar{\Delta}_2^*\delta\bar{\Delta}_2)$. However, a straightforward calculation by differentiating with respect to $(\delta\bar{\Delta}_3^*\delta\bar{\Delta}_3)$ is not possible since $V_4^{-1}(\partial/\partial(\delta\bar{\Delta}_3^*\delta\bar{\Delta}_3)\partial_t\Gamma_k)_{\mathrm{gs}} = -2\bar{\lambda}_k\partial_t|\bar{\Delta}_0|^2 + 2|\bar{\Delta}_0|^2\partial_t\bar{\lambda}_k$. Therefore, we also differentiate with respect to $(\delta\bar{\Delta}_1^*\delta\bar{\Delta}_1)$ or $(\delta\bar{\Delta}_2^*\delta\bar{\Delta}_2)$ to define the flow equation of the four-diquark coupling $\bar{\lambda}_k$ so that

$$\partial_t\bar{\lambda}_k = \frac{1}{2V_4}\left(\frac{\partial^2}{\partial(\delta\bar{\Delta}_1^*\delta\bar{\Delta}_1)^2}\partial_t\Gamma_k\right)_{\mathrm{gs}}. \tag{1.85}$$

Employing these projection rules, the set of flow equations in the phase governed by spontaneous symmetry breaking is given by

$$\partial_t|\bar{\Delta}_0|^2 = \frac{2}{\bar{\lambda}_k}\int_p\tilde{\partial}_t\left(\frac{1}{p_0^2+(\mu+|\vec{p}|)^2(1+r_+)^2+|\bar{\Delta}_0|^2}+\frac{1}{p_0^2+(\mu-|\vec{p}|)^2(1+r_-)^2+|\bar{\Delta}_0|^2}\right) \tag{1.86}$$

and

$$\partial_t\bar{\lambda}_k = 2\int_p\tilde{\partial}_t\left(\frac{1}{(p_0^2+(\mu+|\vec{p}|)^2(1+r_+)^2+|\bar{\Delta}_0|^2)^2}+\frac{1}{(p_0^2+(\mu-|\vec{p}|)^2(1+r_-)^2+|\bar{\Delta}_0|^2)^2}\right). \tag{1.87}$$

We apply the set of differential equations (1.80), (1.81), (1.86) and (1.87) to calculate the symmetry-breaking scale and the diquark condensate (diquark gap) for a specific example. In order to achieve this, the initial conditions have to be specified. Firstly, we require that, at the initial RG scale Λ, the four-diquark interaction vanishes so that $\bar{\lambda}_\Lambda = 0$. Secondly, the initial condition for the curvature $\bar{\nu}_k^2$ is chosen so that the quarks are gapped by a diquark condensate for finite chemical potential while they remain ungapped for $\mu = 0$ on all scales. Therefore, the underlying $\mathrm{U}(1)_V$ symmetry is only broken at finite chemical potential but remains intact in the vacuum limit for all scales. The emergence of the diquark condensate for finite chemical potential is then only generated due to the Cooper instability present in the system. For this purpose, we choose $(\bar{\nu}_\Lambda/\bar{\nu}_*)^2 = 4/3$, where $\bar{\nu}_*^2$ represents the value of $\bar{\nu}_k^2$ at the non-Gaussian fixed point. In the following, we set the UV scale to $\Lambda = 0.6\,\mathrm{GeV}$ (which is a typically used scale in low-energy models, see, e.g., Refs. [48, 280]) and use a polynomial regulator shape function with $N = 4$. Then, we find $\bar{\nu}_*^2/\Lambda^2 \approx 0.065$ so that $\bar{\nu}_\Lambda^2/\Lambda^2 \approx 0.087$. The initial condition for the curvature of the diquark potential has to be fine-tuned so that the $\mathrm{U}(1)_V$ symmetry is broken at finite chemical potential. The Yukawa interaction is introduced into the action artificially. In contrast to that, in Chap. 2, the Yukawa interaction will be introduced via a four-quark interaction and generated dynamically from first principles in QCD so that no fine-tuning of the parameter representing the curvature of the potential is required, see also Ref. [179].

We show the numerical results for the symmetry-breaking scale k_{SB} and the diquark condensate $|\bar{\Delta}_0|$ in the long-range limit $k \to 0$ as a function of the chemical potential in Fig. 1.6. We find that the diquark condensate and the symmetry-breaking scale exhibit the same behaviour. This is expected since the symmetry-breaking scale sets the scale for low-energy observables, i.e., $k_{\mathrm{SB}} \sim |\bar{\Delta}_0|$. By increasing the chemical potential, the symmetry-breaking scale and the diquark condensate increase monotonically. Towards $\mu \to 0$, we find an exponential decrease. Therefore, we find the expected BCS-type scaling behaviour as a function of the chemical potential which is given by $k_{\mathrm{SB}} \sim |\bar{\Delta}_0| \sim \exp(-c/\mu^2)$, where $c > 0$ is a positive constant. Note that these results only present an example to illustrate the capabilities of the quasi-particle regularisation scheme and to introduce the corresponding prerequisites for our analysis of dense strong-interaction matter. Indeed, we shall come back to the scaling behaviour of the diquark condensate in a more detailed calculation in Chap. 2 where the diquark condensate is obtained from a first-principles calculation of QCD.

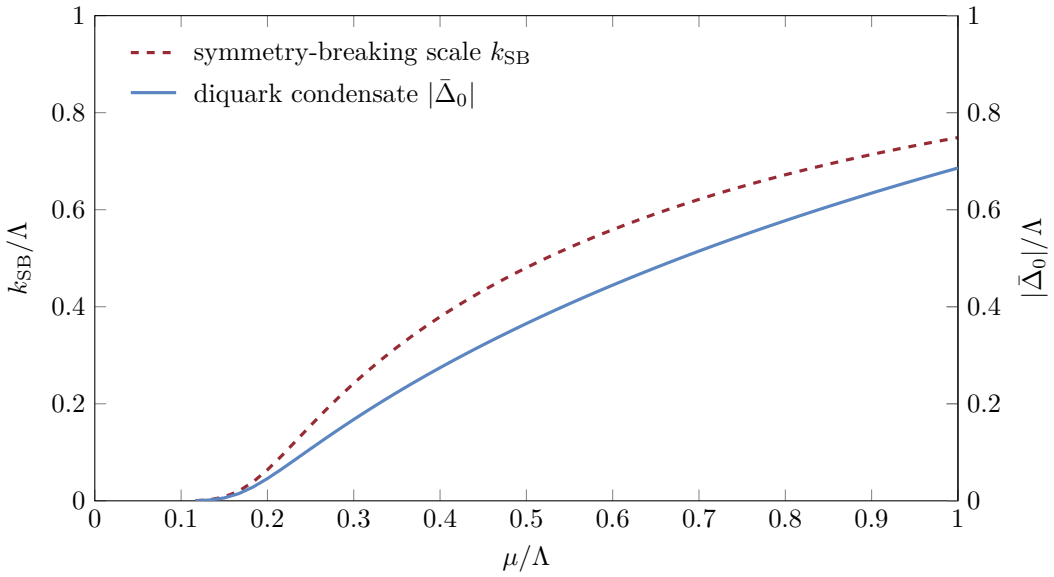

Figure 1.6: Symmetry-breaking scale k_{SB} and diquark condensate $|\bar{\Delta}_0|/\Lambda$ as a function of the chemical potential μ normalised by the UV scale Λ. We set the UV scale to $\Lambda = 0.6\,\mathrm{GeV}$ and use a polynomial regulator shape function with $N = 4$. The expected BCS-type scaling behaviour is reflected in the numerical results: The symmetry-breaking scale and the diquark condensate increase monotonically for increasing chemical potential and decrease exponentially for $\mu \to 0$.

With respect to the capabilities of the quasi-particle regularisation scheme, we note that it is suitable to handle calculations concerning systems with a Cooper instability. Indeed it leads to well-defined loop integrals in the presence of a chemical potential, see Eqs. (1.80), (1.81), (1.86) and (1.87). In addition to that, the kinetic term of the fermions in the action is conveniently split into two contributions resembling modes with positive and negative energy values relative to the Fermi surface. By using this regularisation scheme, the correct BCS-type scaling behaviour for observables is recovered. However, it breaks the Silver-Blaze symmetry explicitly. It should be emphasised that the regularisation scheme is, therefore, only suitable for systems that are governed by a Cooper instability since recovering the correct scaling behaviour requires to break the Silver-Blaze symmetry anyway.

In contrast to that, for systems and regimes governed by the Silver-Blaze property, a regularisation scheme that does not break the Silver-Blaze property explicitly should be employed while simultaneously choosing an expansion point in the derivative expansion that maintains the Silver-Blaze symmetry. For example, a regime for which the quasi-particle regularisation scheme is not well-suited is the small chemical potential regime which is governed by chiral symmetry breaking. The dynamics of QCD is governed by the Silver-Blaze property for baryon chemical potentials of the order and below the mass of the nucleon. Therefore, observables should not depend on the baryon chemical potential as long as it is smaller than the nucleon mass. Therefore, an expansion around the Fermi surface is not suitable since the system does not depend on the chemical potential (for small chemical potential and temperature). In contrast to that, at high densities the dynamics is expected to be dominated by a Cooper instability [71], which makes an expansion around the Fermi surface preferable. In conclusion, the choice of a regularisation scheme has to be adjusted with regard to the relevant degrees of freedom underlying the system under consideration. Considering QCD, this leads to the necessity to switch from one regularisation scheme to the other one when considering different density regimes in the QCD phase diagram at least in a derivative expansion.

2

From Quarks and Gluons to Colour Superconductivity

Exploring the properties and dynamics of strong-interaction matter over a wide range of temperatures and densities has been of special interest of research in recent years and still presents a formidable challenge. Of particular significance, especially within the context of the present work, is the investigation of the high density regime where QCD is governed by an interesting phase structure. Indeed, at sufficiently high densities strong-interaction matter is expected to exist as quark matter instead of hadronic matter. Combined with sufficiently low temperatures, this suggests the existence of a colour-superconducting ground state, see Refs. [20, 46–56] for reviews. This potentially existing ground state may significantly influence the dynamics of QCD at sufficiently low temperatures and large chemical potential, thereby challenging our current understanding and revealing new insight into the nature of strong-interaction matter. Therefore, the present chapter focuses on investigating the emergence of colour-superconductivity from the most fundamental degrees of freedom of QCD, namely quarks and gluons.

The theory that provides an explanation for the occurrence of superconductivity was originally developed to be applied to electrons in metals. However, as it turns out, this so-called BCS theory [72, 73] can be extended to different systems consisting of fermions to describe the formation of fermion pairs and their condensation into a macroscopically occupied state. The condensation occurs because the fermion pairs are effectively bosonic. They are referred to as Cooper pairs which form if a weak attractive interaction between the fermions exists at the Fermi surface. This results in the emergence of an energy gap in the excitation spectrum of the fermions that separates the ground state from the excited quasiparticle states. Correspondingly, the dispersion relation of the quasiparticle excitations is given by $E = \sqrt{(\epsilon_p - \mu)^2 + |\Delta|^2}$, where $\epsilon_p = \sqrt{\vec{p}^2 + m^2}$ is the single-particle energy and $|\Delta|$ is the energy gap [48, 49, 281] which is also viewed as the order parameter of the superconducting phase. The emergence of this phenomenon is associated with the spontaneous breakdown of a local symmetry present in the system before the formation of a gap. In the following, we shall concentrate on the formation of a superconducting ground state in dense quark matter. For further details about the BCS theory in general, see, e.g., Refs. [281–284].

In dense quark matter, the Cooper pairs consist of two quarks, i.e., they are given by diquark states which have fermion number $F = \pm 2$ (or baryon number $B = \pm 2/3$). Therefore, we refer to the energy gap in the excitation spectrum as the diquark gap in the following. Since these states carry colour degrees of freedom, the phenomenon of superconductivity in quark matter is referred to as colour superconductivity. Interestingly, diquark states have, besides the colour charge, additional degrees of freedom. This opens up the possibility for different Cooper pairs. The diquark gap is given by the expectation value $\langle \psi^T \mathcal{O} \psi \rangle$ where $\mathcal{O}$ is an operator in colour, flavour, and Dirac space: $\mathcal{O} = \mathcal{O}_{\text{colour}} \otimes \mathcal{O}_{\text{flavour}} \otimes \mathcal{O}_{\text{Dirac}}$. Then, superconductivity occurs if this expectation value of diquark states as the product of two quark fields becomes finite. From the Pauli exclusion principle, it follows that the operator $\mathcal{O}$ has to be antisymmetric, i.e., $\mathcal{O}^T = -\mathcal{O}$. Still, the colour, flavour, and Dirac structure of the operator $\mathcal{O}$ opens up the possibility for different diquark condensates by combining colour, flavour, and Dirac matrices. Notably, in QCD, certain channels of gluon exchange are attractive, indicating the existence of a colour-superconducting phase in cold deconfined quark matter [56]. Since quarks belong to the colour-triplet representation of the colour-symmetry group, the interaction between quarks occurs in two channels, the (antisymmetric) antitriplet or the (symmetric) sextet: $\mathbf{3}_c \otimes \mathbf{3}_c = \bar{\mathbf{3}}_c \oplus \mathbf{6}_c$. As we shall elaborate in Sec. 2.1, it follows that diquark states can form an antitriplet (associated with an antisymmetric colour wavefunction) and a sextet (associated with a symmetric colour wavefunction). At least in the perturbative regime where the strong coupling is weak and the interaction between quarks is mediated by the exchange of gluons, it follows from an analysis of the relevant interaction that the antitriplet channel is attractive. Therefore, diquark fields are expected to condense in the colour antitriplet channel. It should, however, be noted that this argument becomes unreliable if we do not consider asymptotically high densities. For asymptotically high densities, the diquark gap has been calculated in Refs. [82, 83, 87, 88, 90].

Recall that diquark fields carry colour charge, i.e., they cannot be colour singlets. Therefore, their condensation in terms of a finite expectation value breaks the local colour gauge symmetry SU(3) which effectively drives the onset of colour superconductivity. At this point, it should be emphasised that it is well-known that a local gauge symmetry cannot be truly broken spontaneously [285]. However, the existence of a gap in the excitation spectrum is a gauge-invariant statement. Additionally, the spontaneous breakdown of remnants of the gauge symmetry can happen after fixing the gauge [286, 287]. This situation is similar to classical superconductivity where the U(1) gauge symmetry of electrodynamics is broken spontaneously or the Anderson-Higgs mechanism in the electroweak sector of the Standard Model responsible for the mass generation [61–66].

Apart from the colour wavefunction, diquark states can be classified by their total spin $J = L + S$ where L is the angular momentum and S is the spin of the particle. It appears that spin-zero condensates are favoured which can be traced back to the fact that pairing can occur in a larger phase space. For spin-zero, i.e., $J = 0$, the spin group is totally antisymmetric so that colour and flavour together have to be symmetric. Assuming further that diquark fields favour to condense in a colour antisymmetric state (as indicated by the attractive interaction at sufficiently high densities), the flavour wavefunction has to be antisymmetric as well. Under these prerequisites, at least two quark flavours have to be considered which can be decomposed into a flavour triplet and a flavour singlet: $\mathbf{2}_f \otimes \mathbf{2}_f = \mathbf{1}_f \oplus \mathbf{3}_f$. Importantly, the resulting flavour-singlet is antisymmetric. In conclusion, this leads to a diquark condensate which is antisymmetric in flavour, colour, and Dirac space. Therefore, the conventionally employed diquark condensate for two flavours is given by

$$\Delta_k \sim \epsilon_{\alpha\beta}\epsilon_{ijk} \langle \psi^T_{\alpha,i} \mathcal{C}\gamma_5 \psi_{\beta,j} \rangle \ . \tag{2.1}$$

Here, α and β are flavour indices corresponding to up and down quarks and i, j, and k are colour indices corresponding to the three colours red, green, and blue. The Dirac indices have been suppressed. This condensate is a chirally symmetric spin-zero condensate with $J^P = 0^+$ (where P represents the parity) which is expected to be the most attractive channel for two-flavour QCD. To construct a spin-zero condensate, we

have used the Lorentz scalar $\mathcal{C}\gamma_5$. Alternatively, the Lorentz scalar $\mathcal{C}$ corresponds to a spin-zero condensate with negative parity which, however, appears to be disfavoured and would also indicate that parity is broken at high densities. Additionally, this condensate would break chiral symmetry. Indeed, various studies (see, e.g., Refs. [40, 83, 85–88]) agree that for two flavours, quarks prefer to pair in the colour antitriplet and flavour singlet condensate given by Eq. (2.1). Because of the antisymmetric flavour structure, the condensate represents pairs consisting of one up and one down quark so that this mechanism is referred to as two-flavour colour superconductivity (2SC) [55, 85]. The condensate is a vector in colour space which can be rotated by SU(3) colour transformation which allows us to always rotate the vector into, for example, the three-direction $\Delta = \Delta_k \delta_{k3}$, which is the direction usually chosen. Identifying the colour indices with the three colours, the explicit colour and flavour structure of the condensate yields

$$\Delta \sim \langle \psi^T_{\mathrm{u,r}} \mathcal{C}\gamma_5 \psi_{\mathrm{d,g}} \rangle - \langle \psi^T_{\mathrm{u,g}} \mathcal{C}\gamma_5 \psi_{\mathrm{d,r}} \rangle - \langle \psi^T_{\mathrm{d,r}} \mathcal{C}\gamma_5 \psi_{\mathrm{u,g}} \rangle + \langle \psi^T_{\mathrm{d,g}} \mathcal{C}\gamma_5 \psi_{\mathrm{u,r}} \rangle \ . \tag{2.2}$$

We have identified the three-direction with the colour blue so that only red and green quarks participate in the condensation. Consequently, blue quarks remain ungapped. Note, that it may be possible for the remaining blue quarks to form a different condensate which only pairs blue quarks and therefore has a symmetric colour structure. This may possibly lead to a spin-one condensate [288–293]. However, the corresponding gap is expected to be much weaker.

Condensation is indicated by a nonvanishing expectation value in Eq. (2.1). This condensate breaks the local SU(3) colour symmetry, but it does not break the symmetry completely. An SU(2) colour symmetry remains intact, i.e., it remains intact in the subgroup of the red- and green-coloured quarks. Therefore, the symmetry-breaking mechanism is SU(3) $\to$ SU(2). Consequently, five Nambu-Goldstone bosons emerge. However, these bosons are "eaten up" by five of the eight gluons which acquire a mass according to the Anderson-Higgs mechanism [61–66] where the masses are of the order of the gap. Then, only three of the eight gluons remain massless. In general, the number of massive gluons depends on the form of the condensate. The condensate (2.1) also breaks the $\mathrm{U}(1)_V$ symmetry (associated with baryon number conservation), and interestingly, the electromagnetic gauge symmetry is also broken. However, since there exists a rotated electromagnetic symmetry given by a linear combination of the electric charge and the eight generators of the colour group SU(3), there is no additional electromagnetic superconductivity present in the system [56].

So far, we have only discussed the case for two quark flavours. At zero temperature only up, down, and strange quarks are expected to play a role for densities reached in the Universe, e.g., in neutron stars. Other quark species are too heavy, exceeding a mass of 1 GeV. Although the present work focuses on two quark flavours, we shall briefly comment on the case for three flavours. The most important condensate is then given by

$$\Delta_{\delta,k} \sim \epsilon_{\alpha\beta\delta} \epsilon_{ijk} \langle \psi^T_{\alpha,i} \mathcal{C}\gamma_5 \psi_{\beta,j} \rangle \ . \tag{2.3}$$

Here, α, β, and δ are flavour indices corresponding to up, down, and strange quarks and i, j, and k are colour indices. Similar to the two-flavour case, it is a spin-zero condensate with an antisymmetric flavour and colour structure. However, for three flavours, quarks can be decomposed into a flavour antitriplet and a flavour sextet ($\mathbf{3}_f \otimes \mathbf{3}_f = \bar{\mathbf{3}}_f \oplus \mathbf{6}_f$) where the antitriplet is antisymmetric. In this case, different flavours of quarks are paired in the condensate. In particular, down-strange, up-strange, and up-down pairing exist. Therefore, the condensate not only depends on a colour index, but also on a flavour index. Now, a possible condensate has the form $\Delta_{\delta,k}\delta_{k,\delta}$ effectively coupling colour and flavour indices, i.e., for the condensate to stay invariant, transforming the colour degrees of freedom requires to also transform the flavour degrees of freedom. This is referred to as colour-flavour locking (CFL) [294]. Here, all colours participate in the condensation process. In this case, all gluons become massive since the colour symmetry is completely broken. Alternatively, the

condensate can have the form $\Delta_{\delta,k}\delta_{k,3}\delta_{\delta,3}$ which is similar to the 2SC phase in two-flavour QCD since only red and green up and down quarks participate while blue up, blue down, and strange quarks remain ungapped. Here, we have again identified the colour index three with the colour blue. The choice of which colour remains ungapped is arbitrary. In this case, five of the eight gluons acquire a mass. However, the CFL case appears to be favoured since all quarks participate in the condensation resulting in a bigger energy gain. Note that other condensates are also possible but the ones discussed here appear to be the most important ones that are most likely realised in Nature. See Refs. [46–50, 56, 295], on which the present short introduction is based on, for further details about colour superconductivity.

Although strange quarks may potentially become important at the densities considered in the present work, we leave them aside and consider only two quark flavours, namely up and down quarks, since the inclusion of strange quarks complicates the analysis considerably. However, the present work provides a starting point for future systematic and nonperturbative studies of dense strong-interaction matter, and we expect that it already gives useful insight into the dynamics of matter at such extreme conditions. In addition to two quark flavours, we concentrate on the diquark condensate in Eq. (2.1) which is the only possible condensate if we require that it is a chirally symmetric spin-zero condensate belonging to the antisymmetric colour antitriplet. Based on these findings, we discuss the formalism underlying our RG analysis in Sec. 2.1. In particular, we explain how diquarks emerge as dynamic degrees of freedom from the fundamental quark and gluon dynamics. Following this, we present the ansatz for the effective action required for the RG analysis in Sec. 2.2. The resulting flow equations are presented in Sec. 2.3, the corresponding RG flows are then studied in Sec. 2.4, and results for the aforementioned diquark gap as a function of the quark chemical potential are shown in Sec. 2.5. We improve upon the approximations used up to this point in Sec. 2.6. In particular, we investigate the influence of fluctuations of the diquark fields and the emergence of the gluon-diquark interaction. The conclusions can be found in Sec. 2.7. In summary, we demonstrate that our RG approach is suitable to study the dynamical formation of diquark fields in the low-energy limit allowing us to gain insight into the dynamics of dense strong-interaction matter.

2.1 From the Quark-Gluon Interaction to Diquark Fields as the Effective Degrees of Freedom

In the present work, we intend to perform a first-principles study of QCD for intermediate and high densities. Therefore, we start with the classical Euclidean QCD action S with two massless quark flavours coming in three colours which is given by

$$S = \int_x \left\{ \frac{1}{4} F^a_{\mu\nu} F^a_{\mu\nu} + \bar{\psi}\Big(\mathrm{i}\not{D} - \mathrm{i}\mu\gamma_0\Big)\psi \right\} . \tag{2.4}$$

Here, $F^a_{\mu\nu} = \partial_\mu A^a_\nu - \partial_\nu A^a_\mu + \bar{g} f^{abc} A^b_\mu A^c_\nu$ is the field strength tensor where the gluon fields A^a_μ come with Lorentz (Greek letters; $\mu, \nu = 0, \ldots, 3$) and colour (Roman letters; $a = 1, \ldots, 8$) indices. Furthermore, f^{abc} are the structure constants of the SU(3) colour symmetry. The gluon fields are coupled to the quark fields ψ via the covariant derivative which is given by $D_\mu = \partial_\mu - \mathrm{i}\bar{g} A^a_\mu T^a$. The strong coupling is given by $\bar{g}$ and the quarks have a chemical potential μ. The quark fields carry colour and flavour components so that $\psi = (\psi_{\mathrm{r,u}}, \psi_{\mathrm{r,d}}, \psi_{\mathrm{g,u}}, \psi_{\mathrm{g,d}}, \psi_{\mathrm{b,u}}, \psi_{\mathrm{b,d}})^T$ and $\bar{\psi} = (\bar{\psi}_{\mathrm{r,u}}, \bar{\psi}_{\mathrm{r,d}}, \bar{\psi}_{\mathrm{g,u}}, \bar{\psi}_{\mathrm{g,d}}, \bar{\psi}_{\mathrm{b,u}}, \bar{\psi}_{\mathrm{b,d}})$ are six-component vectors representing all combinations of the two flavours u (up) and d (down) and colour r (red), g (green), and b (blue) where each element itself is a four-component Dirac spinor. For further details on the QCD action, see Sec. 1.1. Note that we exclusively work with three colours $N_\mathrm{c} = 3$ and two flavours $N_\mathrm{f} = 2$.

In the following, we use the Wetterich equation [255] for the analysis of properties of dense strong-interaction matter. The Wetterich equation is an evolution equation for the effective action Γ_k which depends on the RG scale k, see Sec. 1.2 for an introduction. The initial condition for the scale-dependent effective action $\Gamma_{k=\Lambda}$ is fixed at the scale Λ by the classical QCD action (2.4). In practice, we choose Γ_Λ such that we at least start in the vicinity of the QCD action, see Sec. 2.4.1 for details on fixing the initial conditions. Note that we choose $\Lambda \gg \mu$ so that it is guaranteed that the RG flow is initialised in the perturbative high-energy regime. Solving the Wetterich equation usually requires an ansatz for the scale-dependent effective action Γ_k which captures the dynamics at high momentum scales, represented by the classical QCD action, as well as relevant contributions in the low-energy sector in terms of effective degrees of freedom. We shall motivate the necessary contributions to describe quark matter at intermediate to high densities in the following.
The only interaction present at the initial scale Λ, besides gluon self-interactions, is the quark-gluon vertex. Following the RG flow from the initial RG scale Λ towards the low-energy regime, we find that the quark-gluon vertex generates a plethora of interaction channels, e.g., quark self-interactions that are important for the study of ground-state properties. Of particular importance are four-quark interactions which are already generated at one-loop level by the exchange of two gluons as depicted in Fig. 2.1. Higher-order quark interactions that are generated from the quark-gluon vertex along the RG flow are parametrically suppressed at high momentum scales. The inclusion of four-quark interactions requires the inclusion of different interaction channels in the ansatz for the effective action Γ_k in terms of

$$\sum\nolimits_i \bar{\lambda}_i \left(\bar{\psi}\mathcal{O}_i\psi\right)^2 . \tag{2.5}$$

Here, $\bar{\lambda}_i$ are the bare four-quark couplings associated with the four-quark interaction with the operator $\mathcal{O}_i$ which is an operator in colour, flavour, and Dirac space. Notably, the four-quark interactions are therefore generated from first principles rather than being introduced as input parameters, as commonly seen in low-energy models. We shall return to this aspect in Sec. 3.1 where we employ a low-energy model based on findings in the current chapter. As the four-quark interactions are generated by the exchange of two gluons, as depicted in Fig. 2.1, we observe that $\bar{\lambda}_i \sim \bar{g}^4$. It is worth noting that the interaction channels that are included in the ansatz for the effective action have to be consistent with the symmetries of the underlying theory. Therefore, if the theory under consideration respects fewer symmetries, the number of possible interaction channels increases, which is, for example, the case when introducing a chemical potential. The inclusion of all possible interaction channels is beyond the scope of the present work. However, a study of the dominance of different four-quark interaction channels for different density ranges has been carried out in Ref. [179] in a so-called Fierz-complete setting which allows for the identification of relevant interaction channels in different density regimes. This study has shown that for small chemical potentials, the so-called scalar-pseudoscalar channel associated with pion dynamics is dominant which suggests the formation of a chiral condensate. This is in accordance with QCD RG flows in the vacuum limit, see Refs. [176, 177]. In contrast to that, in the large chemical potential regime which is relevant for the present work $\mu \gtrsim 350\,\mathrm{MeV}$, the so-called diquark channel becomes dominant which suggests the formation of a chirally symmetric diquark condensate [179]. It is invariant under $\mathrm{SU}(3) \otimes \mathrm{SU}_L(2) \otimes \mathrm{SU}_R(2) \otimes \mathrm{U}(1)_V$ transformations. This formation is associated with pairing of the two-flavour colour superconductor (2SC) type, which is in agreement with early studies of dense QCD matter [40, 83, 85–88]. The objective of the present work is to analyse the properties of dense QCD matter. As the aforementioned diquark channel becomes dominant in this regime, we only include this four-quark interaction in the ansatz for the effective action:

$$\frac{\bar{\lambda}_{\mathrm{csc}}}{2}\left(\bar{\psi}\tau_2 \mathrm{i}\epsilon_a \gamma_5 \mathcal{C}\bar{\psi}^T\right)\left(\psi^T \mathcal{C}\gamma_5 \tau_2 \mathrm{i}\epsilon_a \psi\right) . \tag{2.6}$$

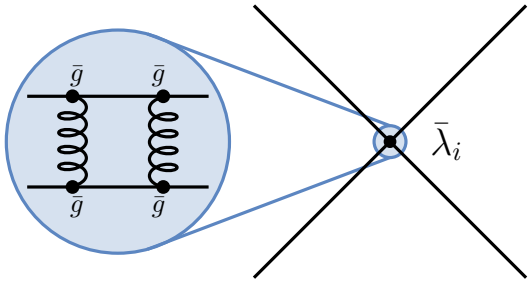

Figure 2.1: The quark-gluon vertex generates four-quark interactions via the exchange of two gluons already at one-loop level. Therefore, the four-quark interaction with the coupling $\bar{\lambda}_i$ has to be considered in the ansatz for the effective action. Here, the solid lines represent quark fields and the curled lines represent gluon fields. The quark-gluon vertex is proportional to the strong coupling $\bar{g}$ so that $\bar{\lambda}_i \sim \bar{g}^4$.

Here, $\bar{\lambda}_{\mathrm{csc}}$ represents the four-quark coupling associated with the diquark channel. Note that we have introduced the totally antisymmetric matrix ϵ_a in colour space where the entries of the matrix are defined by the Levi-Civita tensor: $(\epsilon_a)_{bc} = \epsilon_{abc}$ with the colour indices $a, b, c = 1, 2, 3$ (alternatively represented by $a, b, c = \mathrm{r}, \mathrm{g}, \mathrm{b}$) so that the indices b and c couple to the colour degrees of freedom of ψ and $\bar{\psi}$. Alternatively, the colour structure can be expressed in terms of antisymmetric Gell-Mann matrices. Additionally, τ_2 and $\gamma_5\mathcal{C}$ are antisymmetric matrices in flavour and Dirac space, respectively. Therefore, the combination in colour, flavour, and Dirac space is also antisymmetric which is needed to fulfil the Pauli exclusion principle, as we have also discussed at the beginning of this chapter. However, in contrast to that discussion of the 2SC superconductor, we use the second Pauli matrix to represent the antisymmetric flavour structure, i.e., $(\tau_2)_{\alpha\beta} = -\mathrm{i}\epsilon_{\alpha\beta}$.

In the following, we intend to perform an expansion around the point-like limit which we expect to already provide insight into symmetry-breaking patterns, see Refs. [179, 273, 296–298]. However, studies in the point-like limit are only applicable up to some symmetry-breaking scale k_{SB}. In this setting, symmetry breaking is indicated by the divergence of a four-quark interaction at the symmetry-breaking scale k_{SB} associated with spontaneous symmetry breaking. In case of the diquark channel, the divergence of the corresponding coupling $\bar{\lambda}_{\mathrm{csc}}$ signals that the $\mathrm{U}(1)_V$ symmetry is broken. The breaking of this symmetry indicates the formation of a colour-superconducting ground state associated with the formation of a gap in the fermionic excitation spectrum. Going beyond the symmetry-breaking scale requires to resolve momentum dependences of the quark correlation functions because it encodes information about bound states and the formation of condensates. Accessing this regime can also be conveniently done by employing a so-called Hubbard–Stratonovich transformation [299, 300] of at least the most dominant channel. However, since we only include a single channel, namely the diquark channel, in the present study, we only have to transform this channel. For this, we first consider the Hubbard–Stratonovich transformation and apply it to the effective average action in the next step. For this purpose, let us first consider the simple NJL-type (Nambu–Jona-Lasinio-type) fermionic model for dense QCD matter with the action

$$S_{\mathrm{M}} = \int_x \left\{ \bar{\psi}\left(\mathrm{i}\partial\!\!\!/ - \mathrm{i}\mu\gamma_0\right)\psi + \frac{\bar{\lambda}_{\mathrm{csc}}}{2}\left(\bar{\psi}\tau_2\mathrm{i}\epsilon_a\gamma_5\mathcal{C}\bar{\psi}^T\right)\left(\psi^T\mathcal{C}\gamma_5\tau_2\mathrm{i}\epsilon_a\psi\right)\right\}. \tag{2.7}$$

We have only included the diquark channel in the action S_{M} along with a kinetic term for the quarks. Following this, we consider the generating functional Z which is given by

$$Z = \mathcal{N}\int \mathcal{D}\psi\mathcal{D}\bar{\psi}\, \exp\left(-S_{\mathrm{M}}\right). \tag{2.8}$$

Here, $\mathcal{N}$ ensures normalisation. Next, we include a 'one' in the generating functional which is given by

$$1 = \exp\Big(- \int_x \tilde{m}^2 \Delta_a'^* \Delta_a' \Big) \,. \tag{2.9}$$

Here, we have introduced so-called diquark fields Δ_a' with a mass $\tilde{m}^2$. The diquark fields are complex-valued and carry colour indices $a = 1, 2, 3$ (alternatively represented by $a = \mathrm{r}, \mathrm{g}, \mathrm{b}$). This yields

$$Z = \mathcal{N} \int \mathcal{D}\Delta_a' \mathcal{D}\Delta_a'^* \mathcal{D}\psi \mathcal{D}\bar{\psi} \, \exp\Big(- S_\mathrm{M} - \int_x \tilde{m}^2 \Delta_a'^* \Delta_a' \Big) = \mathcal{N} \int \mathcal{D}\Delta_a' \mathcal{D}\Delta_a'^* \mathcal{D}\psi \mathcal{D}\bar{\psi} \, \exp\Big(- S_\mathrm{M}' \Big) \tag{2.10}$$

with a redefined action S_M' that now includes diquark degrees of freedom. To associate the recently introduced diquark fields with the four-quark interaction, we shift the diquark fields according to

$$\Delta_a'^* = \Delta_a^* + \frac{\bar{h}}{2\tilde{m}^2} \Big(\psi^T \mathcal{C} \gamma_5 \tau_2 \mathrm{i} \epsilon_a \psi \Big), \tag{2.11}$$

$$\Delta_a' = \Delta_a - \frac{\bar{h}}{2\tilde{m}^2} \Big(\bar{\psi} \tau_2 \mathrm{i} \epsilon_a \gamma_5 \mathcal{C} \bar{\psi}^T \Big) \,. \tag{2.12}$$

Here, we have introduced the real-valued Yukawa coupling $\bar{h}$ as an a priori arbitrary variable so that we find

$$S_\mathrm{M}' = \int_x \Big\{ \bar{\psi} \Big(\mathrm{i} \partial\!\!\!/ - \mathrm{i} \mu \gamma_0 \Big) \psi + \tilde{m}^2 \Delta_a^* \Delta_a - \frac{\bar{h}}{2} \Big(\bar{\psi} \tau_2 \mathrm{i} \Delta_a^* \epsilon_a \gamma_5 \mathcal{C} \bar{\psi}^T \Big) + \frac{\bar{h}}{2} \Big(\psi^T \mathcal{C} \gamma_5 \tau_2 \mathrm{i} \Delta_a \epsilon_a \psi \Big) \Big\} \,. \tag{2.13}$$

Since the Yukawa coupling $\bar{h}$ is an arbitrary variable, it is at our disposal and we have chosen it so that

$$\bar{\lambda}_\mathrm{csc} = \frac{\bar{h}^2}{2\tilde{m}^2} \,. \tag{2.14}$$

In doing so, the four-quark interaction has been replaced by an equivalent description in terms of bosonic degrees of freedom. Consequently, a new interaction between quarks and diquarks as effective degrees of freedom emerges, the so-called Yukawa interaction $\sim \bar{h}$. From the action S_M', the equations of motion for the diquark fields can be extracted:

$$\Delta_a^* = - \frac{\bar{h}}{2\tilde{m}^2} \Big(\psi^T \mathcal{C} \gamma_5 \tau_2 \mathrm{i} \epsilon_a \psi \Big) \qquad \text{and} \qquad \Delta_a = \frac{\bar{h}}{2\tilde{m}^2} \Big(\bar{\psi} \tau_2 \mathrm{i} \epsilon_a \gamma_5 \mathcal{C} \bar{\psi}^T \Big) \,. \tag{2.15}$$

In this sense, the interactions of the fermions are described via bosonic degrees of freedom. This is reasonable since the macroscopic properties of a fermionic system are often described in terms of bosonic degrees of freedom. Indeed, we can connect the fundamental particles (quarks) with bound states (diquarks), which become important in the low-energy regime. In doing so, we connect the fundamental parameters of QCD in the short-range regime with the low-energy momentum scale. As mentioned before, a diverging four-quark coupling signals spontaneous symmetry breaking. In this case, the divergence of the diquark coupling $\bar{\lambda}_\mathrm{csc}$ indicates the spontaneous breakdown of the $\mathrm{U}(1)_V$ symmetry. In the description via the Yukawa interaction, this can be translated as the mass $\tilde{m}^2$ becoming zero. Then, symmetry breaking implies that Δ_a^* or Δ_a obtain a finite vacuum expectation value, respectively. For more details on the Hubbard–Stratonovich transformation, we refer the reader to Refs. [214, 299–301].

This simple model can already be used to study symmetry breaking. In a slightly more elaborate way, we shall do so in Sec. 3.1 by including additional chemical potentials to differentiate between different quark species and different colours. In this chapter, we are more interested in the emergence of a gap in the fermionic excitation spectrum from the fundamental interactions. In the following, we shall refer to this gap as the diquark gap. We now leave behind the simple model and return to the QCD action and the formulation in terms of the functional renormalisation group. Recall that the quark-gluon vertex generates four-quark interactions already at one-loop level via the exchange of two gluons, see Fig. 2.1. Hence, the four-quark

interaction (2.6) has to already be included in the ansatz for the effective action after an infinitesimal RG step δk. We only include the diquark channel which can be translated into low-energy effective degrees of freedom via a Hubbard–Stratonovich transformation. Performing the Hubbard–Stratonovich transformation requires to include the following term in the ansatz for the effective action:

$$\tilde{m}^2\Delta_a^*\Delta_a - \frac{\mathrm{i}\bar{h}}{2}\left(\bar{\psi}\tau_2\Delta_a^*\epsilon_a\gamma_5\mathcal{C}\bar{\psi}^T\right) + \frac{\mathrm{i}\bar{h}}{2}\left(\psi^T\mathcal{C}\gamma_5\tau_2\Delta_a\epsilon_a\psi\right). \tag{2.16}$$

In this way, the four-quark interaction associated with the diquark channel can be remapped onto the Yukawa interaction with the coupling $\bar{h}$ and a term bilinear in the diquark fields corresponding to a mass term $\sim\tilde{m}^2$. Consequently, the four-quark interaction is removed. However, the situation in terms of constructing an ansatz for the scale-dependent effective action is more involved compared to the simple model. The use of the Hubbard–Stratonovich transformation results in a new interaction, namely the Yukawa interaction. This aspect has to be carefully considered when determining the interactions to be included in an ansatz for the scale-dependent effective action. Considering the next RG step, after performing the Hubbard–Stratonovich transformation, the quark-gluon vertex and the newly emerged Yukawa interaction give rise to a four-quark interaction again, as illustrated in Fig. 2.2. Therefore, although the four-quark vertex has been rewritten by introducing diquark fields, it still has to be considered in the ansatz for the effective action. Since the interactions associated with the couplings $\bar{h}$ and $\bar{\lambda}_{\mathrm{csc}}$ are only generated during the RG flow, they should be set to zero at the initial RG scale.

The Hubbard–Stratonovich transformation of gluon-induced four-quark interactions can still be used to gain insight into the low-energy dynamics. For example, the transformation can be performed at a scale $\Lambda_0 > k_{\mathrm{SB}}$ (where k_{SB} is the symmetry-breaking scale) as done in Ref. [126]. However, the introduction of such a scale introduces an artificial dependence on the scale Λ_0. This leads to additional uncertainties for the low-energy observables. Further, it limits the range of chemical potentials that is accessible within this framework to $\mu \lesssim \Lambda_0$ and the scale is also expected to depend on the chemical potential itself. This μ-dependence is at least a priori difficult to determine. Removing this (artificial) scale Λ_0 can be conveniently done by introducing the so-called dynamical bosonisation technique, see Refs. [146, 170–175, 178, 257] for an introduction and recent developments. It essentially introduces a continuous Hubbard–Stratonovich transformation of the gluon-induced four-quark interactions in the RG flow which works as follows: The four-quark interaction is generated by the fundamental quark-gluon vertex already after an infinitesimal RG step. As discussed above, we only take into account the diquark channel. This channel is removed by rewriting it in terms of diquark degrees of freedom by performing a Hubbard–Stratonovich transformation already once it is generated. However, in the next infinitesimal RG step, the four-quark interaction is regenerated by the quark-gluon interaction and the Yukawa interaction. Consequently, the Hubbard–Stratonovich transformation can be performed again, which modifies the Yukawa coupling $\bar{h}$ and the mass $\tilde{m}^2$ of the diquark fields by removing the four-quark interaction. As visualised in Fig. 2.3, this procedure of generating the four-quark interaction and immediately mapping it onto the Yukawa interaction and a term bilinear in the fields, is repeated until the low-energy regime is finally reached. Formally, this continuous application of Hubbard-Stratonovich transformations can be performed with the dynamical bosonisation technique. Using the dynamical bosonisation method, we continuously follow the RG flow from high momentum scales associated with the classical QCD action (governed by quarks and gluons) down to the low-energy regime which is governed by the formation of bound states and condensates. As we shall see in Sec. 2.3.1, this can be conveniently implemented by introducing k-dependent fields as we have done in the derivation of the Wetterich equation, see Sec. 1.2 and also Refs. [146, 170–175]. The modification of the Yukawa coupling and the mass of the diquark fields is then cast into flow equations for the corresponding couplings which shall be derived in Sec. 2.3.1. Note that the complex-valued diquark fields Δ_a^* are now quark composites of the form $\sim\left(\psi^T\mathcal{C}\gamma_5\tau_2\mathrm{i}\epsilon_a\psi\right)$. We emphasise again that we only consider diquark fields as low-energy degrees of freedom because the diquark channel

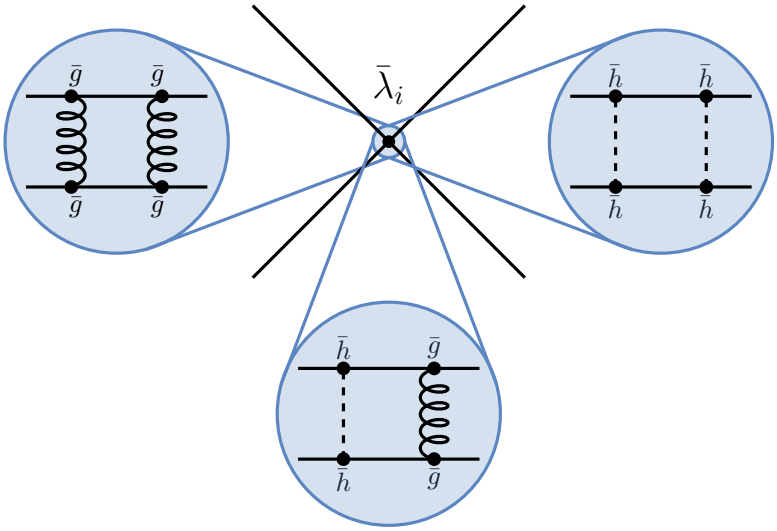

Figure 2.2: The quark-gluon vertex and the newly generated Yukawa interaction generate four-quark interactions. The curled lines represent the gluon fields, the solid lines represent the quark fields, and the dashed lines represent the diquark fields. Therefore, the four-quark interaction $\bar{\lambda}_i$ not only consists of contributions from the strong coupling $\bar{g}$ but also from the Yukawa coupling $\bar{h}$.

has been found to be the most dominant in the density regime relevant for the present work [179]. The inclusion of, e.g., the scalar-pseudoscalar channel associated with pion dynamics would, in principle, require the introduction of additional low-energy degrees of freedom. However, useful information might already be extracted by investigating the effect of the scalar-pseudoscalar channel above the symmetry-breaking scale. Since we do not take into account the scalar-pseudoscalar channel, the present work does not allow us to study the transition from a colour-superconducting state at high to intermediate densities to a phase governed by chiral symmetry breaking. A study of this transition region is anyway complicated since many four-quark interaction channels become important indicating a complicated phase structure [166, 179].
In the process of bosonising the four-quark interaction, we introduced diquark fields. These fields become dynamic degrees of freedom during the RG flow. This requires the inclusion of a kinetic term which is also dynamically generated along the RG flow. Since diquarks consist of two quarks or two antiquarks, they are associated with a chemical potential. The kinetic term is, therefore, given by

$$\begin{aligned}&\Big[\big(\partial_0 - 2\mu\big)\Delta_a^*\Big]\Big[\big(\partial_0 + 2\mu\big)\Delta_a\Big] + \big(\partial_j \Delta_a^*\big)\big(\partial_j \Delta_a\big)\\ &= \big(\partial_\mu \Delta_a^*\big)\big(\partial_\mu \Delta_a\big) + 2\mu\Big[\Delta_a \partial_0 \Delta_a^* - \Delta_a^* \partial_0 \Delta_a\Big] - 4\mu^2 \Delta_a^* \Delta_a \,. \end{aligned} \tag{2.17}$$

Note that the last term in the latter expression effectively belongs to the potential of the diquark fields and not to the kinetic term. Therefore, we absorb it into a "modified" mass $\tilde{m}^2 = \bar{m}^2 - 4Z_\Delta \mu^2$ which we, conveniently, have already introduced in Eq. (2.16). Now, $\bar{m}^2$ is the mass of the diquark fields and $\tilde{m}^2$ represents the curvature of the potential. At the initial UV scale Λ, the diquark sector has to decouple from the fermion sector. Hence, the kinetic term associated with the diquark wavefunction renormalisation in the ansatz for the effective action has to be set to zero at the initial RG scale Λ. This corresponds to "making" the renormalised mass parameter infinitely large for $k \to \Lambda$: $\tilde{m}^2/Z_\Delta \to \infty$. Since the chemical potential is finite and $\Lambda \gg \mu$, this corresponds to $\bar{m}^2/Z_\Delta \to \infty$ so that the contribution from the chemical potential in $\tilde{m}^2$ corresponds to a negligible contribution at Λ. If the mass of the diquark fields is large and positive, they are nondynamic, noninteracting, and heavy at the UV scale Λ. Consequently, they effectively decouple

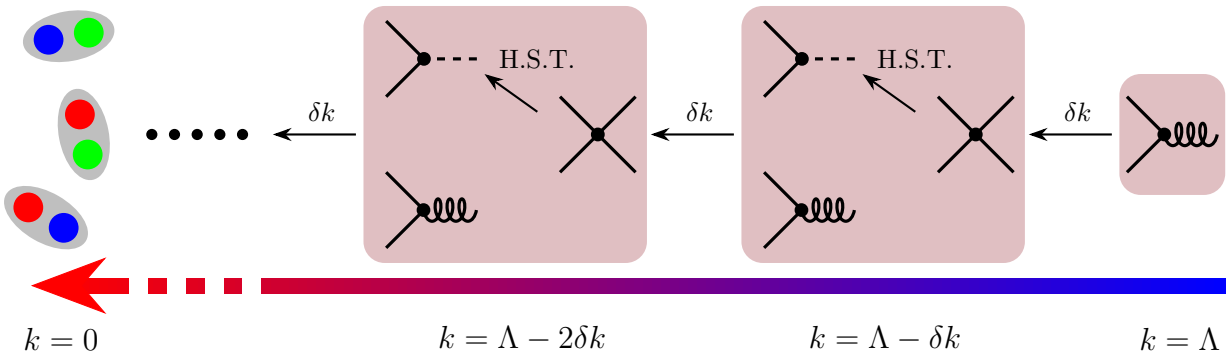

Figure 2.3: Illustration of the dynamical bosonisation technique to be understood from right (associated with the initial scale Λ) to left (low-energy regime $k = 0$): After the first RG step δk, the quark-gluon interaction generates four-quark interactions, i.e., we only include the so-called diquark channel. The four-quark interaction is, by introducing so-called diquark fields and using a Hubbard–Stratonovich transformation (H.S.T.), replaced by a Yukawa interaction. In the next RG step, the four-quark interaction is again generated, now by the quark-gluon vertex and the Yukawa interaction. Again, the four-quark interaction is replaced. This cycle repeats until the low-energy regime associated with $k = 0$ is reached which is governed by the formation of ground states and condensates.

from the fermion sector. However, as soon as the diquark wavefunction renormalisation becomes finite, the diquark fields become dynamic degrees of freedom, solely as a consequence of the underlying quark-gluon dynamics. To ensure the decoupling of the diquark degrees of freedom from the fermion sector at the initial RG scale, we shall choose the initial conditions, according to the present discussion, in Sec. 2.4.1.
Because diquark-like eight-quark interactions can already become important at scales relevant for the present work, we include a four-diquark interaction. We shall verify this statement in Sec. 2.4. Therefore, the diquark potential V becomes

$$V(|\Delta|^2) = \tilde{m}^2 \Delta_a^* \Delta_a + \bar{\lambda}_\Delta \left(\Delta_a^* \Delta_a \right)^2 . \tag{2.18}$$

Here, $|\Delta|^2 = \Delta_a^* \Delta_a$. The coupling $\bar{\lambda}_\Delta$ corresponds to the interaction between four diquark fields and is generated dynamically by the Yukawa interaction using the dynamical bosonisation technique. The potential also includes the "modified" mass $\tilde{m}^2$. Note that we have only included diquark self-interactions up to the order four. However, the potential can, in principle, be expanded to arbitrary order in the diquark fields by introducing higher orders:

$$V(|\Delta|^2) = \tilde{m}^2 \Delta_a^* \Delta_a + \bar{\lambda}_\Delta \left(\Delta_a^* \Delta_a \right)^2 + \bar{\lambda}_6 \left(\Delta_a^* \Delta_a \right)^3 + \cdots . \tag{2.19}$$

Here, $\bar{\lambda}_6$ is the coupling associated with the six-diquark interaction. For simplicity and since we expect the interaction to be subdominant at high scales ($\bar{\lambda}_6 \sim g^{12}$), we only take into account diquark self-interactions up to the fourth order, see Eq. (2.18), in the following. We add that higher-order diquark self-interactions can be related to quark self-interactions with a nontrivial momentum structure, for example, the four-diquark interaction is associated with an eight-quark interaction.
Recall that a diverging four-quark coupling signals the onset of spontaneous symmetry breaking. In terms of diquark degrees of freedom, the curvature of the diquark potential $\tilde{m}^2$ becoming zero signals the breakdown of the aforementioned $\mathrm{U}(1)_V$ symmetry. We can analyse this aspect further by considering what happens to the diquark potential when the curvature becomes zero and eventually negative. For this, we consider the

nontrivial minimum $|\Delta_0|^2$ of the diquark potential (2.18) which is given by

$$\left.\frac{\partial V(|\Delta|^2)}{\partial|\Delta|^2}\right|_{|\Delta|^2=|\Delta_0|^2} \stackrel{!}{=} 0 \qquad \Rightarrow \qquad |\Delta_0|^2 = -\frac{\tilde{m}^2}{2\bar{\lambda}_\Delta}\,. \tag{2.20}$$

Assuming that $\bar{\lambda}_\Delta$ is strictly positive so that for $\tilde{m}^2 > 0$, only the trivial minimum at $|\Delta|^2 = 0$ exists, see left-hand side of Fig. 2.4. As soon as the mass becomes zero, we enter a phase with a finite minimum and thereby enter the symmetry-broken phase, which corresponds to $\tilde{m}^2 < 0$, see the right-hand side of Fig. 2.4. Therefore, in the broken phase, it is convenient to rewrite the potential by replacing the mass of the diquark fields with the minimum of the diquark potential:

$$V(|\Delta|^2) = -2\bar{\lambda}_\Delta|\Delta_0|^2\Delta_a^*\Delta_a + \bar{\lambda}_\Delta\big(\Delta_a^*\Delta_a\big)^2 = \bar{\lambda}_\Delta\big(\Delta_a^*\Delta_a - |\Delta_0|^2\big)^2 - \bar{\lambda}_\Delta|\Delta_0|^4. \tag{2.21}$$

Note that the last term in the latter expression is simply a constant, which does not need to be considered in an ansatz for the effective action. With the Hubbard–Stratonovich transformation, we have related the coupling $\bar{\lambda}_{\mathrm{csc}}$ to the diquark mass $\tilde{m}^2$. Consequently, the divergence of the coupling $\bar{\lambda}_{\mathrm{csc}} \to \infty$ or a vanishing diquark mass $\tilde{m}^2 \to 0$ signals the spontaneous symmetry breaking, which for the present considerations, is the breaking of the $\mathrm{U}(1)_V$ symmetry. The emerging diquark condensate breaks the $\mathrm{U}(1)_V$ symmetry but leaves the chiral symmetry intact. The expectation value of diquark field becomes finite in the spontaneously broken phase: $\langle\Delta_a\rangle \neq 0$. In terms of quark fields, a finite expectation value for $\langle\psi\mathcal{O}\psi\rangle$ or $\langle\bar{\psi}\mathcal{O}\bar{\psi}\rangle$ arises. Here, $\mathcal{O}$ is a matrix in colour, flavour, and Dirac space which has to be antisymmetric due to the Pauli-exclusion principle. In the symmetric high-momentum regime, the ground state is at the origin which may become unstable and tend towards a lower stable minimum at Δ_0 in the low-momentum regime. This minimum can be related to a so-called diquark gap Δ_{gap}. Considering spontaneous chiral symmetry breaking instead, the finite expectation value of a corresponding bosonic field corresponds to the quarks becoming massive. In contrast to that, the occurrence of a finite expectation value of the diquark field leads to the formation of the so-called diquark gap, analogous to the gap in the excitation spectrum of a conventional superconductor. The scale at which the curvature of the potential becomes zero, indicating the onset of spontaneous symmetry breaking, is the so-called symmetry-breaking scale k_{SB}. Recalling the discussion about superconductivity in two-flavour QCD at the beginning of this chapter, we emphasise that diquark fields considered in this discussion are of the form $\sim \big(\psi^T\mathcal{C}\gamma_5\tau_2\mathrm{i}\epsilon_a\psi\big)$. Recall that $(\tau_2)_{\alpha\beta} = -\mathrm{i}\epsilon_{\alpha\beta}$ and $(\epsilon_a)_{bc} = \epsilon_{abc}$ where α and β are flavour indices and a, b, and c are colour indices. Therefore, a finite expectation value of these diquark fields is associated with pairing of the two-flavour colour superconductor (2SC) type.

The diquark fields are not colour-neutral as they consist of two quark fields (and not a quark and an antiquark field). Therefore, they interact directly with gluons. To determine the interaction of diquark fields and gluons, we derive their transformation in colour space starting from the transformation of the quarks. Additionally, we discuss the effect of colour in QCD by commenting on the colour wavefunctions for mesons and gluons. In QCD, all quark fields carry a colour charge of red, green, or blue (r, g, b) and antiquarks carry a colour anticharge of antired, antigreen, or antiblue ($\bar{r}$, $\bar{g}$, $\bar{b}$). The strong interaction is invariant under rotations in colour space due to the underlying SU(3) colour symmetry. The generators T^a of the SU(3) symmetry are defined in App. A.2. We can use the eigenstates of T^3 and T^8 as the basis vectors to represent the three colour states by:

$$|r\rangle = \begin{pmatrix}1\\0\\0\end{pmatrix}, \qquad |g\rangle = \begin{pmatrix}0\\1\\0\end{pmatrix}, \qquad \text{and} \qquad |b\rangle = \begin{pmatrix}0\\0\\1\end{pmatrix}. \tag{2.22}$$

The anticolour basis vectors are represented in the dual representation.

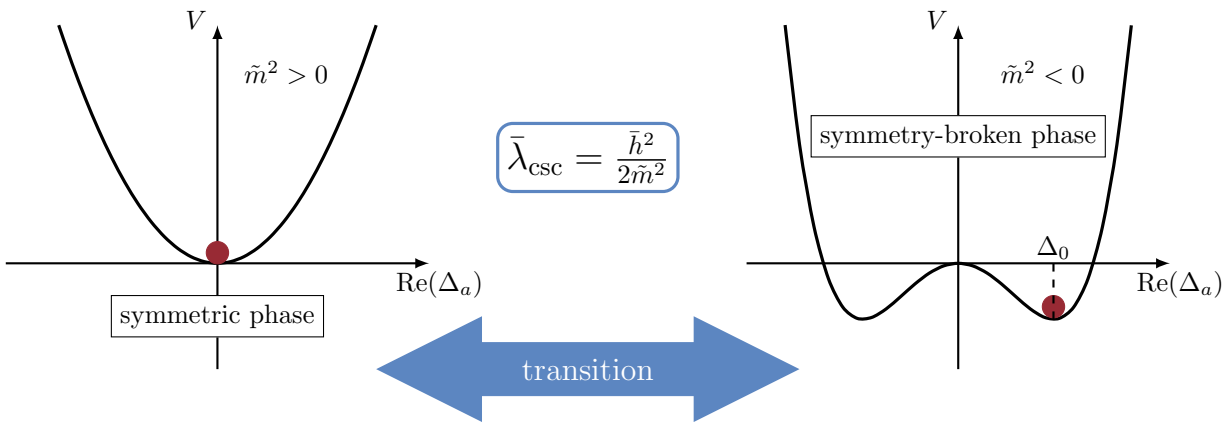

Figure 2.4: Illustration of the diquark potential V for $\mathrm{Im}(\Delta_a) = 0$. The symmetric phase (left-hand side) is characterised by $\tilde{m}^2 > 0$ while the symmetry-broken phase (right-hand side), where a finite expectation value exists for the diquark gap, is associated with a negative mass $\tilde{m}^2 < 0$. At vanishing diquark mass $\tilde{m}^2 = 0$, the coupling $\bar{\lambda}_{\mathrm{csc}}$ diverges which corresponds to a transition between the symmetric and the symmetry-broken phase. Symmetry breaking suggests the formation of a chirally symmetric diquark condensate of the two-flavour colour-superconductor (2SC) type characterised by an expectation value $\langle\psi\psi\rangle$ or $\langle\bar{\psi}\bar{\psi}\rangle$, respectively.

In the following, we use the analogy of the SU(3) colour symmetry to the approximate SU(3) flavour symmetry for three quark flavours (u, d, s) used in the quark model to construct baryons and mesons. The quark model was originally proposed by Murray Gell-Mann [4] and George Zweig [5, 6] and was preceded by the "eightfold way" proposed by Murray Gell-Mann [7] and Yuval Ne'eman [8] classifying and structuring the hadrons based on the symmetry group SU(3). Notably, the SU(3) symmetry is an extension of the SU(2) isospin symmetry. This symmetry was introduced by Werner Heisenberg and was originally used to describe proton and neutron as different states of the same particle [302]. See also Refs. [59, 303] for introductions about the construction of mesons and baryons and the quark model.

In contrast to the approximate SU(3) flavour symmetry (which is approximate because of the different masses of different quark flavours), the colour symmetry is an exact SU(3) symmetry. In analogy to the quark model, where isospin and hypercharge are introduced, we define a colour isospin I_3^{c} and a colour hypercharge Y^{c}. The colour isospin is given by the eigenvalue of T^3 and the colour hypercharge is the eigenvalue of $2/\sqrt{3}T^8$. These quantum numbers of the colour states and the anticolour states are shown in Fig. 2.5. The colour states can be understood as a colour triplet and the anticolour states as a colour antitriplet. It is convenient, to introduce the (ladder) operators $T_\pm = T^1 \pm \mathrm{i}T^2$, $U_\pm = T^6 \pm \mathrm{i}T^7$, and $V_\pm = T^4 \pm \mathrm{i}T^5$ which, together with T^3 and $2/\sqrt{3}T^8$, are also a representation of the SU(3) symmetry group. Notably, the operators $T_\pm$, $U_\pm$, and $V_\pm$ shift the states as depicted in Fig. 2.5. The states for antiquarks are represented by the basis vectors of the dual representation and corresponding ladder operators $\bar{T}_\pm$, $\bar{U}_\pm$, and $\bar{V}_\pm$ can be defined. For a discussion of colour in QCD, see, e.g., Ref. [59, 303].

With this at hand, we can construct colour wavefunctions for mesons, consisting of one quark and one antiquark, and for gluons. This is identical to the construction of flavour wavefunctions with three flavours u, d, and s where quark and antiquarks are combined. We start with the construction of a product state consisting of the colour triplet and the colour antitriplet. The states can then be constructed by starting with one state and by applying the ladder operators. The resulting colour wavefunctions are shown in Fig. 2.6. In doing so, we find a coloured octet and a colour-neutral singlet which is invariant under SU(3) transformations. We

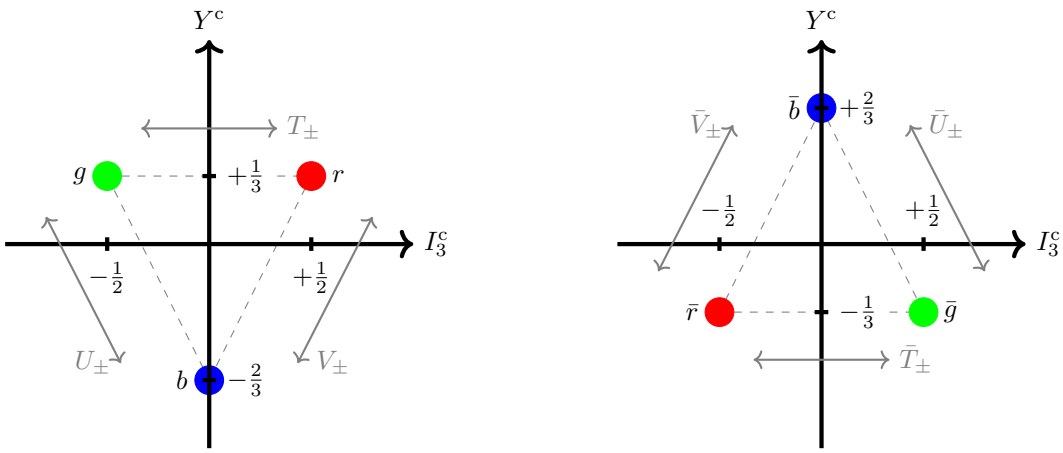

Figure 2.5: Illustration of the quark colour triplet (left-hand side) and the antiquark colour antitriplet (right-hand side) in the plane spanned by the colour isospin I_3^c and the colour hypercharge Y^c. The ladder operators $T_\pm$, $U_\pm$, and $V_\pm$ (for quarks) and $\bar{T}_\pm$, $\bar{U}_\pm$, and $\bar{V}_\pm$ (for antiquarks) shift the states along the respective axes (represented by the dashed lines).

write $\mathbf{3}_c \otimes \bar{\mathbf{3}}_c = \mathbf{8}_c \oplus \mathbf{1}_c$. Here and in the following, the subscript 'c' indicates that we consider the representation of the colour-symmetry group instead of, e.g., the flavour-symmetry group. It is strongly expected that free particles can only exist as colourless states, i.e., asymptotic quark states, which would carry a net colour charge, have never been observed. This aspect is known as colour confinement which is a well-established phenomenon in QCD. Two of the particles in the octet are colour-neutral. However, they are not invariant under SU(3) colour transformation. Only the singlet state is invariant under the aforementioned symmetry transformation and, therefore, represents the only reasonable choice for the colour wavefunction of confined matter, i.e., mesons. In contrast to that, we can also construct the gluon colour wavefunction by combining the colour triplet and the colour antitriplet. However, a colour-singlet gluon cannot exist because it would be colour-neutral and would behave like a strongly interacting photon. In Nature, there is no infinite-range strong interaction, which contradicts the existence of a strongly interacting photon. Hence, the gluon colour wavefunctions are given by the octet, indicating the existence of eight gluons [59].

In the present work, we are interested in the construction of the colour wavefunction for diquark fields Δ_a^* (antidiquarks Δ_a) which consist of two antiquarks (quarks). This can be done by combining the colour triplet (colour antitriplet) with another colour triplet (colour antitriplet). Similarly to the derivation of the meson and gluon colour wavefunctions, we can employ the ladder operators to construct the diquark colour wavefunctions. From the combination of two triplets, we find an (antisymmetric) antitriplet and a (symmetric) sextet. The colour wavefunctions of the antitriplet are totally antisymmetric under the exchange of colour whereas the sextet is totally symmetric. We write $\mathbf{3}_c \otimes \mathbf{3}_c = \bar{\mathbf{3}}_c \oplus \mathbf{6}_c$. The resulting states are shown in Fig. 2.7. We can also combine two colour antitriplets and find an (antisymmetric) triplet and a (symmetric) antisextet. Therefore, for diquark fields there are no colour singlets.

In this chapter, we have introduced diquark fields that are antisymmetric in colour space and can, therefore, be identified with the colour triplet and antitriplet, respectively, which also represent antisymmetric colour states. Following the discussion at the beginning of this chapter, we expect that diquark fields preferably condense in the colour antitriplet channel (at least for two quark flavours) so that we only consider diquark fields pairing in this channel in the present study. Note that the colour triplet for the diquarks is identical to the colour antitriplet for the antiquarks, which becomes apparent when comparing Fig. 2.7 and Fig. 2.5 (right

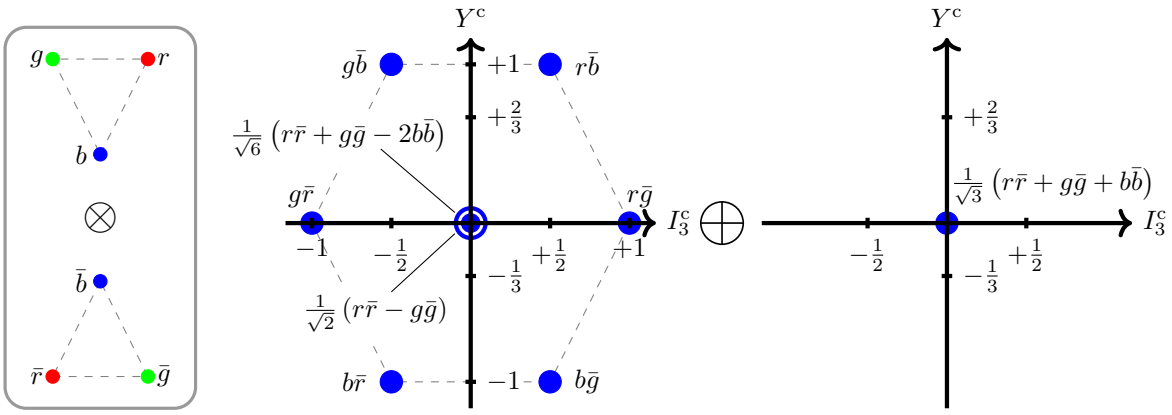

Figure 2.6: Colour wavefunctions as obtained by combining the colour triplet and the colour antitriplet. The resulting nine states exist as an octet (left-hand side) and a singlet (right-hand side). The singlet state is a colourless state with quantum numbers $I_3^{\mathrm{c}} = Y^{\mathrm{c}} = 0$. Applying the ladder operators to the singlet state yields zero for each operator. Furthermore, it is invariant under SU(3) colour transformations.

panel). Therefore, the antisymmetric colour states transform like an antiquark triplet, and antisymmetric diquarks (antidiquarks) consisting of two quarks (consisting of two antiquarks) behave like antiquarks (quarks) in colour space. By describing the behaviour of the diquarks as a quark or antiquark, we can also associate a single colour with each diquark state: For example, an antisymmetric diquark(quark-quark) consisting of r and g behaves like an antiquark with the colour $\bar{b}$. This can also be explained more visually: The combinations diquark-quark or antidiquark-antiquark are colour-neutral states similar to the colour-neutral states antiquark-quark or quark-antiquark. In one case, baryons are built, while in the other case, mesons are built. However, the behaviour in colour space appears to be "identical". In the above example, this means that the diquark which behaves like a $\bar{b}$ antiquark coupled to a b quark yields a colour-neutral state as it would if we directly coupled quarks with colours r, g, and b. The important information that can be explained by this is that diquarks couple to gluons like a quark or an antiquark. Note that in our convention Δ_a consists of two antiquarks and Δ_a^* consists of two quarks. Therefore, Δ_a couples to a gluon like a quark and Δ_a^* couples to a gluon like an antiquark. Consequently, the diquark Δ_a^* (antidiquark Δ_a) transforms as an antitriplet (triplet) in colour space.

Let us now directly consider the behaviour of the diquark fields used in the present work under SU(3) colour transformations. Employing the transformations of the quark and antiquark under the local SU(3) transformations, introduced in Sec. 1.1, and considering that the diquark fields are composites of quark fields according to $\Delta_a \sim \left(\bar{\psi}\tau_2 \mathrm{i}\epsilon_a \gamma_5 \mathcal{C}\bar{\psi}^T\right)$ and $\Delta_a^* \sim \left(\psi^T \mathcal{C}\gamma_5 \tau_2 \mathrm{i}\epsilon_a \psi\right)$, yields

$$\Delta_a \mapsto \left(\delta_{ae} + \mathrm{i}\theta^s(x) T^s_{ae}\right)\Delta_e \qquad \text{and} \qquad \Delta_a^* \mapsto \Delta_e^*\left(\delta_{ae} - \mathrm{i}\theta^s(x) T^s_{ea}\right). \tag{2.23}$$

It follows that the antidiquarks Δ_a transform like quarks and the diquarks Δ_a^* transform like antiquarks under colour transformations, as expected from our analysis of the colour wavefunctions of the diquark fields. To ensure gauge invariance of the effective action, we therefore have to replace the derivatives with respect to diquark fields with the covariant derivative

$$D_\mu^{ab} = \partial_\mu \delta_{ab} - \mathrm{i}\bar{g}_\Delta A_\mu^c T_{ab}^c, \tag{2.24}$$

where a, b, and c are colour indices and $\bar{g}_\Delta$ is the strong coupling via which the diquark fields couple to the gluons. We indeed find that $\left(D_\mu^{ca}\Delta_a\right)\left(D_\mu^{cb}\Delta_b\right)^*$ and $\left(\Delta_a\left(D_0^{ab}\Delta_b\right)^* - \Delta_a^*\left(D_0^{ab}\Delta_b\right)\right)$ are gauge-invariant.

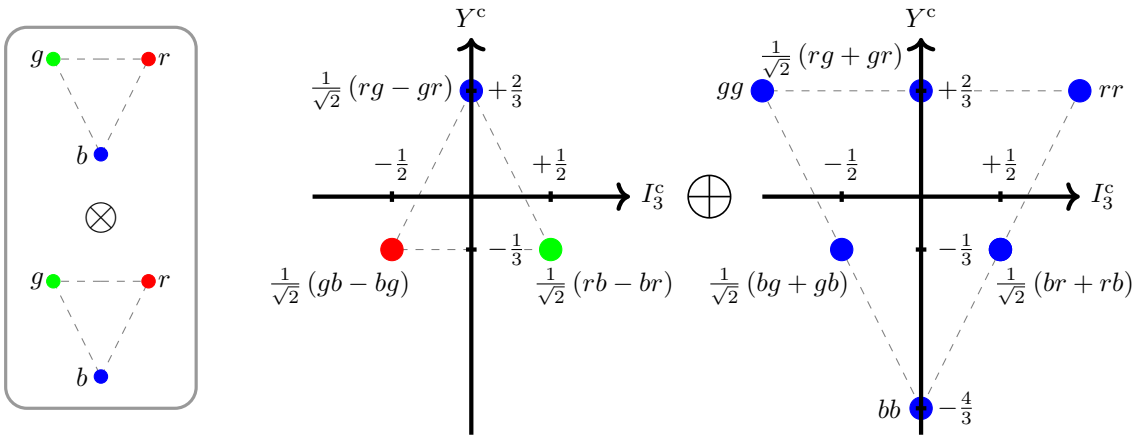

Figure 2.7: Colour wavefunction as obtained by combining the colour triplet with a colour triplet. We find that the nine states exist as an antitriplet (left-hand side) and a sextet (right-hand side). Notably, the triplet looks like the colour antitriplet in Fig. 2.5. However, none of the states are colour-neutral. A similar representation arises from the combination of the colour antitriplet with another colour antitriplet.

We close this section by noting that we include the diquark fields as effective degrees of freedom. Diquark fields consist of either two quarks or two antiquarks so that they are not colour-neutral. Since we have expanded the action in $\Delta_a^*\Delta_a$, which is a gauge-invariant object and since we have included the gauge-invariant derivative, the action itself is gauge invariant. However, the dynamical generation of a finite expectation value for the diquark fields is not a gauge-invariant statement and it would break the SU(3) colour symmetry. It is well-known that local gauge invariance cannot be truly broken [285]. Nevertheless, our prescription is suitable for the formation of a gap $\sim \Delta_a^*\Delta_a$ in terms of diquarks as the effective degrees of freedom which only presents a convenient approach to access the low-energy dynamics [46]. The existence of such a gap in the excitation spectrum of the fermions in colour-superconducting systems is a gauge-invariant statement since $\Delta_a^*\Delta_a$ is a gauge-invariant quantity. In future studies, it may be possible to calculate the aforementioned gap without relying on diquark fields as effective low-energy degrees of freedom. Instead, a direct computation of the full momentum dependence of fermionic correlation functions in a vertex expansion and a resulting gap may be possible. At the present, we consider our approach as a feasible way to study colour superconductivity at high densities.

2.2 Ansatz for the Scale-Dependent Effective Action

With the considerations from the preceding section, we can write down an ansatz for the effective action in our present study. Our effective action represents a combination of the classical QCD action (2.4) and an ansatz including the relevant contributions in the low-energy sector, see the preceding section for details. By also including wavefunction renormalisations for the respective fields, we find

$$\begin{aligned}\Gamma_k = \int_x \Big\{ & Z_\psi \bar{\psi}\Big(\mathrm{i}\partial\!\!\!/ - \mathrm{i}\mu\gamma_0\Big)\psi + \bar{g}\bar{\psi}\gamma_\mu A_\mu^a T^a \psi + \frac{\bar{\lambda}_{\mathrm{csc}}}{2}\Big(\bar{\psi}\tau_2 \mathrm{i}\epsilon_a \gamma_5 \mathcal{C}\bar{\psi}^T\Big)\Big(\psi^T \mathcal{C}\gamma_5\tau_2 \mathrm{i}\epsilon_a \psi\Big) \\ & + Z_\Delta\Big(D_\mu^{ca}\Delta_a\Big)\Big(D_\mu^{cb}\Delta_b\Big)^* + 2\mu Z_\Delta\Big(\Delta_a\big(D_0^{ab}\Delta_b\big)^* - \Delta_a^*\big(D_0^{ab}\Delta_b\big)\Big) + V(|\Delta|^2) \\ & + \frac{\mathrm{i}\bar{h}}{2}\Big(\psi^T\mathcal{C}\gamma_5\tau_2\Delta_a\epsilon_a\psi\Big) - \frac{\mathrm{i}\bar{h}}{2}\Big(\bar{\psi}\gamma_5\tau_2\Delta_a^*\epsilon_a\mathcal{C}\bar{\psi}^T\Big) + \frac{1}{4}Z_A F_{\mu\nu}^a F_{\mu\nu}^a\Big\} + \Delta\Gamma_{\mathrm{gf}} + \Delta\Gamma_{\mathrm{gh}}\,. \end{aligned} \tag{2.25}$$

Terms associated with covariant derivatives with respect to diquark fields include two-gluon two-diquark interactions, one-gluon two-diquark interactions, and a kinetic term for the diquark fields. In practice, we replace terms with a covariant derivative with respect to diquark fields by considering

$$\begin{aligned} &Z_\Delta \left(D_\mu^{ca}\Delta_a\right)\left(D_\mu^{cb}\Delta_b\right)^* + 2\mu Z_\Delta\left(\Delta_a\left(D_0^{ab}\Delta_b\right)^* - \Delta_a^*\left(D_0^{ab}\Delta_b\right)\right) \\ &\to Z_\Delta\left(\partial_\mu\Delta_a\right)\left(\partial_\mu\Delta_a^*\right) + 2\mu Z_\Delta\left(\Delta_a\partial_0\Delta_a^* - \Delta_a^*\partial_0\Delta_a\right) + 4\mu \mathrm{i}\bar{g}_{\Delta,1}A_0^c\Delta_a^*T_{ab}^c\Delta_b + \bar{g}_{\Delta,2}^2A_\mu^cA_\mu^d\Delta_b^*T_{bc}^cT_{ca}^d\Delta_a\,. \end{aligned} \tag{2.26}$$

Here, the first two terms are kinetic terms, the third term represents a one-gluon two-diquark interaction associated with the coupling $\bar{g}_{\Delta,1}$, and the fourth term represents a two-gluon two-diquark interaction associated with the coupling $\bar{g}_{\Delta,2}^2$ which, however, may be related by gauge invariance. In doing so, we have explicitly introduced different couplings for the different interactions. We dropped possible interactions that explicitly depend on the momentum, which would require to include additional interactions that also explicitly depend on the momentum.

For the diquark potential V, we differentiate between the symmetric phase and the regime governed by spontaneous symmetry breaking which are separated by the symmetry-breaking scale k_{SB} so that

$$V(|\Delta|^2) = \begin{cases} \tilde{m}^2\Delta_a^*\Delta_a + \bar{\lambda}_\Delta\left(\Delta_a^*\Delta_a\right)^2, & \text{symmetric phase } (k \geq k_{\mathrm{SB}}) \\ \bar{\lambda}_\Delta\left(\Delta_a^*\Delta_a - |\Delta_0|^2\right)^2, & \text{phase governed by symmetry breaking } (k \leq k_{\mathrm{SB}}) \end{cases}. \tag{2.27}$$

Note that $\Delta\Gamma_{\mathrm{gf}}$ is the gauge-fixing term and $\Delta\Gamma_{\mathrm{gh}}$ represents the ghost term where we rely on the background field approach to gauge theories [304, 305] within background covariant gauges and employ the background field approximation. For details and applications, see also Refs. [179, 192, 306–315].

The ansatz for the effective action is spanned by the set of wavefunction renormalisations (Z_ψ, Z_A, Z_Δ) and couplings $(\bar{g}, \tilde{m}^2, \bar{\lambda}_\Delta, \bar{h}, \bar{\lambda}_{\mathrm{csc}}, \bar{g}_{\Delta,1}, \bar{g}_{\Delta,2})$. The wavefunction renormalisations and couplings are k-dependent but we do not show this dependence explicitly. In the phase governed by spontaneous symmetry breaking, we replace the curvature of the potential $\tilde{m}^2$ with the minimum of the potential $|\Delta_0|^2$. We can express the couplings in terms of dimensionless renormalised couplings, i.e., the renormalised strong coupling $g^2 = Z_A^{-1}Z_\psi^{-2}\bar{g}^2$, the renormalised dimensionless curvature of the potential $\epsilon = \tilde{m}^2Z_\Delta^{-1}k^{-2}$, the renormalised diquark interaction $\lambda_\Delta = \bar{\lambda}_\Delta Z_\Delta^{-2}$, the renormalised Yukawa coupling $h = \bar{h}Z_\psi^{-1}Z_\Delta^{-1/2}$, the renormalised dimensionless four-quark interaction $\lambda_{\mathrm{csc}} = \bar{\lambda}_{\mathrm{csc}}k^2Z_\psi^{-2}$, and renormalised strong couplings associated with gluon-diquark interactions, $g_{\Delta,2}^2 = Z_A^{-1}Z_\Delta^{-1}\bar{g}_{\Delta,2}^2$ and $g_{\Delta,1} = Z_A^{-1/2}Z_\Delta^{-1}\bar{g}_{\Delta,1}$. In the broken phase, the renormalised dimensionless minimum of the potential is $\kappa = Z_\Delta|\Delta_0|^2k^{-2}$.

2.3 RG Flow Equations

In the beginning of this chapter, we established that the four-quark interaction emerges in each RG step due to the quark-gluon vertex and the quark-diquark vertex. While the Hubbard-Stratonovich transformation can be applied at a specific scale, it does not eliminate the four-quark interaction across all scales. Instead, a continuous Hubbard-Stratonovich transformation can be utilised to eliminate the four-quark interaction after each RG step. In the RG framework, a scale-dependent transformation is naturally feasible as it can be accomplished by, for example, introducing scalar fields that depend on the scale k, such as scale-dependent diquark fields $\Delta_{a,k}$. By modifying the diquark fields, the four-quark interaction can be absorbed continuously as a function of the RG scale, a process referred to as the dynamical bosonisation technique. We employ this technique in this study. In doing so, the four-quark interaction is eliminated at all scales which would not be the case with only a single Hubbard–Stratonovich transformation since four-quark interactions would be

regenerated in the RG flow. More precisely, the information of the four-quark interaction is assimilated into the Yukawa interaction in each step. In doing so, the translation of the four-quark interaction is recast into flow equations for the remaining couplings. For additional information and an introduction, see Refs. [146, 170–175, 178, 257] as the following discussion is based on their findings.

In the following, we derive the relations required for the application of the dynamical bosonisation technique. For this purpose, we consider k-dependent diquark fields $\Delta_{a,k}$ while the remaining fields are scale independent. We exclusively work in momentum space with the four-momentum given by $p = (p_0, \vec{p}\,)$ and correspondingly for q, p', q'. Then, the super field φ_k as used in the derivation of the Wetterich equation for k-dependent fields in Sec. 1.2 becomes, for the purpose of the present work, $\varphi_k(q) = \left(A^a_\mu(q), \Delta^*_{a,k}(q), \Delta_{a,k}(-q), \psi^T(q), \bar{\psi}(-q)\right)^T$. The introduction of k-dependent fields leads to a modification of the Wetterich equation which is shown in Eq. (1.42), see Sec. 1.2 for details on its derivation. The modified version of the Wetterich equation consists of a term that is simply the conventionally employed Wetterich equation for k-independent fields and terms that represent corrections stemming from the scale dependence of the fields. Specifically, it includes a term that shall modify the diquark anomalous dimension and a term that is used in the following to implement the dynamical bosonisation in terms of recasting the flow of the four-quark interaction into the flow of the remaining couplings. Before deriving the corresponding equations in Sec. 2.3.1, we start with the scale dependence of the diquark fields $\Delta_{a,k}$. In principle, this scale dependence is at our disposal. However, a suitable choice is needed to rewrite the four-quark interaction. Considering the quark-composite nature of the diquark fields, i.e., diquarks consisting of two quarks or two antiquarks, it is reasonable that this is also reflected in their scale dependence. Therefore, we choose

$$\partial_t \Delta_{a,k}(p') = \frac{1}{2}\int_p \int_q \Big(\bar{\psi}(p)\gamma_5\tau_2 \mathrm{i}\epsilon_a \mathcal{C}\bar{\psi}^T(q)(2\pi)^4\delta^{(4)}\left(p'-p-q\right)\Big)\partial_t\alpha_k(p') - \Delta_{a,k}(p')\partial_t\beta_k(p')\,, \tag{2.28}$$

$$\partial_t \Delta^*_{a,k}(p') = -\frac{1}{2}\int_p \int_q \Big(\psi^T(p)\mathcal{C}\gamma_5\tau_2 \mathrm{i}\epsilon_a \psi(q)(2\pi)^4\delta^{(4)}\left(p'-p-q\right)\Big)\partial_t\alpha_k(p') - \Delta^*_{a,k}(p')\partial_t\beta_k(p')\,. \tag{2.29}$$

Note that the first part reflects the aforementioned quark-composite nature of the diquark fields which would already suffice to rewrite the four-quark interaction associated with the diquark channel in terms of diquark self-interactions and the Yukawa interaction in the following. However, the second term in the latter expression, which takes into account a possible general scale dependence or rescaling of the diquark fields, can be used to impose additional constraints. For now, the functions α_k and β_k are arbitrary functions that depend on the scale k. In the following, see Sec. 2.3.1, these functions are chosen such that the four-quark coupling vanishes at all scales, the Yukawa coupling $\bar{h}$ is momentum-independent, and the running of the diquark wavefunction renormalisation is given by $\partial_t Z_\Delta(p_0 = 0, |\vec{p}\,| = k) = -\eta_\Delta Z_\Delta$. A similar determination of the functions α_k and β_k has been discussed in Refs. [170, 171, 173, 175] for the chiral regime.

Taking into account the scale dependence of the diquark fields in Eqs. (2.28) and (2.29), the modified Wetterich equation (1.42) reduces to

$$\partial_t \Gamma_k[\varphi] = \partial_t \bar{\Gamma}_k[\varphi] - \int_{p'} \left\{ \frac{\delta\Gamma_k[\varphi_k]}{\delta\Delta^*_{a,k}(p')}\partial_t\Delta^*_{a,k}(p') + \frac{\delta\Gamma_k[\varphi_k]}{\delta\Delta_{a,k}(p')}\partial_t\Delta_{a,k}(p') \right\}. \tag{2.30}$$

The first part of the latter expression is the original Wetterich equation for scale-independent diquark fields but with a shifted diquark anomalous dimension:

$$\partial_t \bar{\Gamma}_k[\varphi] = \frac{1}{2}\mathrm{STr}\left\{ \left(\partial_t \tilde{R}_k(p,q)\right)\left[\Gamma_k^{(1,1)}[\varphi,q,p) + \tilde{R}_k(q,p)\right]^{-1} \right\}\Big|_{\eta_\Delta \to \eta_\Delta + 2\partial_t\beta_k}. \tag{2.31}$$

The resulting flow equations are derived in Sec. 2.3.2. The shift in the diquark anomalous dimension $\eta_\Delta \to \eta_\Delta + 2\partial_t\beta_k$ stems from the second term on the right-hand side of Eq. (1.42). In the part representing the

original Wetterich equation, we have replaced the full propagator G_k^{ba} with a more suitable expression for our purposes below which is in terms of derivatives of the effective action Γ_k:

$$\Gamma_k^{(1,1)}[\varphi_k, q, p) = \frac{\overrightarrow{\delta}}{\delta\varphi_k^T(-q)}\Gamma_k[\varphi_k]\frac{\overleftarrow{\delta}}{\delta\varphi_k(p)}\,. \tag{2.32}$$

The derivative of the effective action $\Gamma_k^{(1,1)}$ includes derivatives with respect to diquark fields, quark fields, and gluons. For more details, we refer the reader to App. C. A suitably chosen regulator function is given by

$$\tilde{R}_k(p,q) = \begin{pmatrix} R_A(q) & 0 & 0 & 0 & 0 \\ 0 & 0 & R_\Delta(q) & 0 & 0 \\ 0 & R_\Delta(q) & 0 & 0 & 0 \\ 0 & 0 & 0 & 0 & -R_\psi^T(-q) \\ 0 & 0 & 0 & R_\psi(q) & 0 \end{pmatrix} (2\pi)^4\delta^{(4)}\,(p-q)\,. \tag{2.33}$$

The entries of this matrix are given by

$$R_A(q) = Z_A\vec{q}^{\,2}r_{\mathrm{B}}\big(\vec{q}^{\,2}/k^2\big)\Big(A_{\mu\nu} + B_{\mu\nu} + P^L_{\mu\nu}/\xi\Big)\delta^{ab}\,, \tag{2.34}$$

$$R_\Delta(q) = Z_\Delta\vec{q}^{\,2}r_{\mathrm{B}}\big(\vec{q}^{\,2}/k^2\big)\delta_{ab}\,, \tag{2.35}$$

$$R_\psi(q) = -Z_\psi\mathrm{i}\big(\mu - |\vec{q}\,|\big)P_-\gamma_0 r_\psi\big((\mu-|\vec{q}\,|)^2/k^2\big) - Z_\psi\mathrm{i}\big(\mu + |\vec{q}\,|\big)P_+\gamma_0 r_\psi\big((\mu+|\vec{q}\,|)^2/k^2\big)\,. \tag{2.36}$$

The regulator shape functions r_{B} and r_ψ can be found in App. B. We use three-dimensional regulators and, for the fermions, we use a regulator shape function that regularises around the Fermi surface, see Sec. 1.3 for an introduction to this regularisation scheme.

In the phase governed by spontaneous symmetry breaking, we employ a homogeneous background for the expansion of the diquark fields. In practice, we choose the background field $\bar{\Delta}_3$ to point into the three-direction such that $\Delta_a \mapsto \Delta_a + \delta_{a3}\bar{\Delta}_3$. Note that we do not study a potentially existing dependence of our results on our choice of picking the three-direction for the background field. In the calculation of the flow equations, we ultimately evaluate the background field at the minimum. With this, we basically choose to evaluate the minimum in the three-direction: $|\Delta_0|^2 = \sum_a |\Delta_{0,a}|^2$ with $\Delta_{0,a} = \delta_{a3}\Delta_0$. Consequently, the diquark gap is constructed from the gauge-invariant object $\sum_a \Delta_a^*\Delta_a$.

2.3.1 Dynamical Bosonisation

The introduction of k-dependent diquark fields $\Delta_{a,k}$ leads to a modification of the Wetterich equation according to Eq. (2.30). In particular, the flow equations of the couplings that span the ansatz for the effective action (2.25) are altered by the second part of Eq. (2.30). The scale dependence of the k-dependent diquark fields, see Eqs. (2.28) and (2.29), is chosen such that it is possible to recast the continuous change of the four-quark interaction into flow equations for the couplings. We shall do so in the following. For this purpose, we have introduced a priori arbitrary functions α_k and β_k.

For the Yukawa coupling, the modified Wetterich equation yields

$$\partial_t\bar{h} = \partial_t\bar{h}\big|_{\bar{\Gamma}} + \big(\tilde{m}^2 + Z_\Delta p^2 + 4\mathrm{i}\mu Z_\Delta p_0\big)\partial_t\alpha_k(p) + \bar{h}\partial_t\beta_k(p)\,. \tag{2.37}$$

Here and in the following, we use the subscript '$\bar{\Gamma}$' to indicate the contribution to the running couplings from the part of the Wetterich equation for scale independent fields given in Eq. (2.31). For the mass and the wavefunction renormalisation, we have the combined expression

$$\partial_t\big(\tilde{m}^2 + Z_\Delta p^2 + 4\mathrm{i}\mu Z_\Delta p_0\big) = \partial_t\big(\tilde{m}^2 + Z_\Delta p^2 + 4\mathrm{i}\mu Z_\Delta p_0\big)\big|_{\bar{\Gamma}} + 2\big(\tilde{m}^2 + Z_\Delta p^2 + 4\mathrm{i}\mu Z_\Delta p_0\big)\partial_t\beta_k(p)\,. \tag{2.38}$$

We can extract the contribution to the mass $\tilde{m}^2$ by setting $p^2 = 0$ and $p_0 = 0$ in the latter expression so that

$$\partial_t \tilde{m}^2 = \partial_t \tilde{m}^2\big|_{\bar{\Gamma}} + 2\tilde{m}^2 \partial_t \beta_k(0)\,. \tag{2.39}$$

With this, we can also identify

$$\partial_t Z_\Delta\big(p^2 + 4\mathrm{i}\mu p_0\big) = \partial_t Z_\Delta\big|_{\bar{\Gamma}}\big(p^2 + 4\mathrm{i}\mu p_0\big) - 2\tilde{m}^2 \partial_t \beta_k(0) + 2\big(\tilde{m}^2 + Z_\Delta p^2 + 4\mathrm{i}\mu Z_\Delta p_0\big)\partial_t \beta_k(p)\,. \tag{2.40}$$

For the diquark coupling $\bar{\lambda}_\Delta$ and the quark coupling $\bar{\lambda}_{\mathrm{csc}}$, we find

$$\partial_t \bar{\lambda}_\Delta = \partial_t \bar{\lambda}_\Delta\big|_{\bar{\Gamma}} + 4\bar{\lambda}_\Delta \partial_t \beta_k(p)\,, \tag{2.41}$$

$$\partial_t \bar{\lambda}_{\mathrm{csc}} = \partial_t \bar{\lambda}_{\mathrm{csc}}\big|_{\bar{\Gamma}} - \bar{h}\partial_t \alpha_k(p)\,. \tag{2.42}$$

We also find corrections to the running of the strong coupling associated with gluon-diquark interactions:

$$\partial_t \bar{g}^2_{\Delta,2} = \partial_t \bar{g}^2_{\Delta,2}\big|_{\bar{\Gamma}} + 2\bar{g}^2_{\Delta,2} \partial_t \beta_k(p)\,, \tag{2.43}$$

$$\partial_t \bar{g}_{\Delta,1} = \partial_t \bar{g}_{\Delta,1}\big|_{\bar{\Gamma}} + 2\bar{g}_{\Delta,1} \partial_t \beta_k(p)\,. \tag{2.44}$$

Note that the functions α_k and β_k depend on the external momentum p. Since $\partial_t \alpha_k(p)$ is an arbitrary function, we can choose it so that the four-quark interaction $\bar{\lambda}_{\mathrm{csc}}$ vanishes at all scales by requiring

$$\partial_t \bar{\lambda}_{\mathrm{csc}} = \partial_t \bar{\lambda}_{\mathrm{csc}}(p)\big|_{\bar{\Gamma}} - \bar{h}\partial_t \alpha_k(p) \stackrel{!}{=} 0 \qquad \Rightarrow \qquad \partial_t \alpha_k(p) = \frac{1}{\bar{h}} \partial_t \bar{\lambda}_{\mathrm{csc}}(p)\big|_{\bar{\Gamma}}\,. \tag{2.45}$$

This condition, together with the initial condition $\bar{\lambda}_{\mathrm{csc}} \to 0$ for $k \to \Lambda$, ensures that the four-quark interaction corresponding to the diquark channel vanishes at all scales in the RG flow: $\lambda_{\mathrm{csc}} = 0$. The contributions to the running of the four-quark coupling from the fundamental quark-gluon interaction are still generated but are now mapped onto the diquark sector. From here on, $\partial_t \bar{\lambda}_{\mathrm{csc}}(p)$ is the flow equation of the four-quark coupling associated with the part of the Wetterich equation for scale independent fields.

In practice, we project the couplings onto zero external momentum. However, in general, the couplings depend on the external momentum. Therefore, we keep the momentum dependence of the running of the four-quark coupling for now. The choice of the vanishing four-quark interaction modifies the flow equation for the Yukawa coupling which becomes

$$\partial_t \bar{h} = \partial_t \bar{h}\big|_{\bar{\Gamma}} + \frac{1}{\bar{h}}\big(\tilde{m}^2 + Z_\Delta p^2 + 4\mathrm{i}\mu Z_\Delta p_0\big)\partial_t \bar{\lambda}_{\mathrm{csc}}(p) + \bar{h}\partial_t \beta_k(p)\,. \tag{2.46}$$

From the latter expression, it is obvious that the running of the four-quark interaction directly influences the flow of the Yukawa coupling. This is expected since the general aim was to translate the emerging four-quark interaction via a Yukawa interaction and scalar fields. This becomes more visible now: The flow of the four-quark interaction which "measures" the emergence of the four-quark interaction at each RG step is now recast into the flow equation for the Yukawa interaction.

Besides α_k, we have also introduced β_k as an arbitrary function because the field configuration is not fixed uniquely, and we allow for a general rescaling of the diquark fields. In doing so, we can use the contribution from $\beta_k(p)$ to absorb the momentum dependence of the Yukawa coupling. For this, we choose

$$\partial_t \beta_k(p) = -\frac{\tilde{m}^2 + Z_\Delta p^2 + 4\mathrm{i}\mu Z_\Delta p_0}{\bar{h}^2} \partial_t \bar{\lambda}_{\mathrm{csc}}(p) + f(k)\,, \tag{2.47}$$

where $f(k)$ is a p-independent function which only depends on the scale k. It can be seen that, with this choice, the running of the Yukawa coupling $\bar{h}$ does not depend on the momentum p any more:

$$\partial_t \bar{h} = \partial_t \bar{h}\big|_{\bar{\Gamma}} + \bar{h} f(k)\,. \tag{2.48}$$

In doing so, we ensure that the diquark gap is also momentum independent in the low-energy regime.

The momentum-independent part $f(k)$ can be used to guarantee that the wavefunction renormalisation Z_Δ is momentum independent as well. This is required to render our assumption, that the wavefunction renormalisation is momentum independent, self-consistent. Consequently, we choose the momentum independent function $f(k)$ to read

$$f(k) = \frac{1}{Z_\Delta k^2 \bar{h}^2}\Big[\left(Z_\Delta k^2 + \tilde{m}^2\right)^2 \partial_t \bar{\lambda}_{\mathrm{csc}}(p_0 = 0, |\vec{p}| = k) - \tilde{m}^4 \partial_t \bar{\lambda}_{\mathrm{csc}}(p_0 = 0, |\vec{p}| = 0)\Big] \tag{2.49}$$

so that

$$k^2 \partial_t Z_\Delta(p_0 = 0, |\vec{p}| = k) = k^2 \partial_t Z_\Delta\big|_{\bar{\Gamma}}\,. \tag{2.50}$$

It follows

$$\begin{aligned}\partial_t \beta_k(p) = -\frac{\tilde{m}^2 + Z_\Delta p^2 + 4\mathrm{i}\mu Z_\Delta p_0}{\bar{h}^2}\partial_t \bar{\lambda}_{\mathrm{csc}}(p) + \frac{1}{Z_\Delta k^2 \bar{h}^2}\Big[\left(Z_\Delta k^2 + \tilde{m}^2\right)^2 \Big(\partial_t \bar{\lambda}_{\mathrm{csc}}(p_0 = 0, |\vec{p}| = 0) + \partial_t \Delta\bar{\lambda}_{\mathrm{csc}}\Big) \\ - \tilde{m}^4 \partial_t \bar{\lambda}_{\mathrm{csc}}(p_0 = 0, |\vec{p}| = 0)\Big]\,.\end{aligned} \tag{2.51}$$

Here, we have introduced the difference $\Delta\bar{\lambda}_{\mathrm{csc}} = \bar{\lambda}_{\mathrm{csc}}(p_0 = 0, |\vec{p}| = k) - \bar{\lambda}_{\mathrm{csc}}(p_0 = 0, |\vec{p}| = 0)$. Note that $\Delta\bar{\lambda}_{\mathrm{csc}}/\bar{\lambda}_{\mathrm{csc}}(p_0 = 0, |\vec{p}| = 0) < 0$ and it is supposed to be small. This difference measures the suppression of λ_{csc} for large momenta, i.e., it measures the decay of the four-fermion interaction with the momentum. For the case of vanishing external momentum (point-like limit), it is given by $\Delta\bar{\lambda}_{\mathrm{csc}}/\bar{\lambda}_{\mathrm{csc}}(p_0 = 0, |\vec{p}| = 0) = 0$ where the decay becomes maximal. As this represents the point-like limit, we choose $\Delta\bar{\lambda}_{\mathrm{csc}} = 0$ in the following. This approximation has only a negligible effect on the symmetry-breaking scale and the diquark gap as we have checked. Additionally, the four-quark interaction $\bar{\lambda}_{\mathrm{csc}} = \bar{h}^2/2\tilde{m}^2$ is unaffected by the difference. It only affects the position of (pseudo-)fixed points in the RG flow of the couplings. More information and a discussion of this approximation can be found in Refs. [170, 171].

The initially arbitrary functions $\alpha_k(p)$ and $\beta_k(p)$ are now uniquely determined by the stated requirements. In conclusion, this leads to a coupled system of differential equations for the running of the renormalised squared Yukawa coupling $h^2 = Z_\psi^{-2} Z_\Delta^{-1} \bar{h}^2$, the renormalised dimensionless mass $\epsilon = Z_\Delta^{-1} k^{-2} \tilde{m}^2$, and the renormalised four-diquark coupling $\lambda_\Delta = Z_\Delta^{-2} \bar{\lambda}_\Delta$:

$$\partial_t h^2 = Z_\psi^{-2} Z_\Delta^{-1} \partial_t \bar{h}^2\big|_{\bar{\Gamma}} + 2(1 + 2\epsilon) k^2 Z_\psi^{-2} \partial_t \bar{\lambda}_{\mathrm{csc}}(0) + h^2 \eta_\Delta + 2h^2 \eta_\psi\,, \tag{2.52}$$

$$\partial_t \lambda_\Delta = Z_\Delta^{-2} \partial_t \bar{\lambda}_\Delta\big|_{\bar{\Gamma}} + \frac{4\lambda_\Delta(1 + \epsilon)}{h^2} k^2 Z_\psi^{-2} \partial_t \bar{\lambda}_{\mathrm{csc}}(0) + 2\eta_\Delta \lambda_\Delta\,, \tag{2.53}$$

$$\partial_t \epsilon = k^{-2} Z_\Delta^{-1} \partial_t \tilde{m}^2\big|_{\bar{\Gamma}} + \frac{2\epsilon(1 + \epsilon)}{h^2} k^2 Z_\psi^{-2} \partial_t \bar{\lambda}_{\mathrm{csc}}(0) + (\eta_\Delta - 2)\epsilon\,. \tag{2.54}$$

For convenience, we have replaced the flow equation of the Yukawa coupling h with the flow of the squared Yukawa coupling h^2. In addition to that, the flow equations of the renormalised strong couplings, $g_{\Delta,2}^2 = Z_A^{-1} Z_\Delta^{-1} \bar{g}_{\Delta,2}^2$ and $g_{\Delta,1} = Z_A^{-1/2} Z_\Delta^{-1} \bar{g}_{\Delta,1}$, associated with gluon-diquark interactions read

$$\partial_t g_{\Delta,2}^2 = Z_A^{-1} Z_\Delta^{-1} \partial_t \bar{g}_{\Delta,2}^2\big|_{\bar{\Gamma}} + \frac{2g_{\Delta,2}^2(1 + \epsilon)}{h^2} k^2 Z_\psi^{-2} \partial_t \bar{\lambda}_{\mathrm{csc}}(0) + \big(\eta_A + \eta_\Delta\big) g_{\Delta,2}^2\,, \tag{2.55}$$

$$\partial_t g_{\Delta,1} = Z_A^{-1/2} Z_\Delta^{-1} \partial_t \bar{g}_{\Delta,1}\big|_{\bar{\Gamma}} + \frac{2g_{\Delta,1}(1 + \epsilon)}{h^2} k^2 Z_\psi^{-2} \partial_t \bar{\lambda}_{\mathrm{csc}}(0) + \frac{1}{2}\big(\eta_A + 2\eta_\Delta\big) g_{\Delta,1}\,. \tag{2.56}$$

The function $\partial_t \beta_k$ is, in the point-like limit, given by

$$\partial_t \beta_k(0) = \frac{1}{\bar{h}^2}\left[Z_\Delta k^2 + \tilde{m}^2\right] \partial_t \bar{\lambda}_{\mathrm{csc}}(0) = \frac{1 + \epsilon}{h^2} k^2 Z_\psi^{-2} \partial_t \bar{\lambda}_{\mathrm{csc}}(0)\,. \tag{2.57}$$

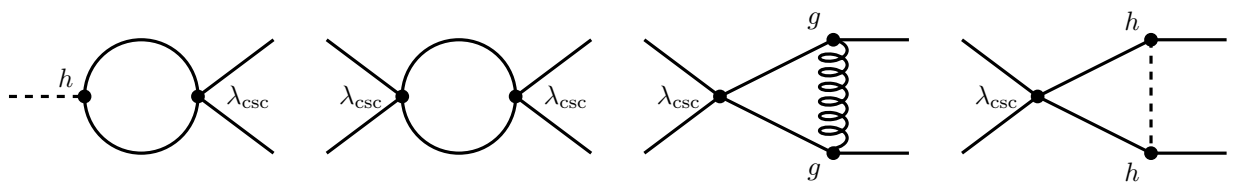

(a) (b) (c) (d)

Figure 2.8: Schematic representation of terms that drop out in the calculation while only considering one channel, i.e., the diquark channel associated with the coupling $\bar{\lambda}_{\mathrm{csc}}$. This coupling vanishes at all scales due to the dynamical bosonisation which is used to ensure $\bar{\lambda}_{\mathrm{csc}} = 0$. The contribution to the Yukawa interaction (a) and contributions to the four-quark interaction (b–d) drop out. However, by considering more than only the diquark channel in the ansatz for the scale-dependent effective action, similar diagrams would still appear with other four-quark couplings.

Here, we have evaluated the couplings in the point-like limit, i.e., on vanishing external momenta $p = (p_0, \vec{p}) = (0, 0)$. The wavefunction renormalisation of the diquark fields only enters the set of differential equations in terms of the diquark anomalous dimension η_Δ which is determined by Eq. (2.50) so that $\partial_t Z_\Delta(p_0 = 0, |\vec{p}| = k) = -\eta_\Delta Z_\Delta$. The four-quark interaction now enters the set of differential equations only in terms of its running $\partial_t \bar{\lambda}_{\mathrm{csc}}$ and not as an additional differential equation. Furthermore, the four-quark interaction itself $\bar{\lambda}_{\mathrm{csc}}$ vanishes at all scales. As a consequence, $\partial_t \bar{\lambda}_{\mathrm{csc}}$ only consists of diagrams emerging from the fundamental quark-gluon interaction and the Yukawa interaction. Contributions corresponding to diagrams that depend on λ_{csc} drop out by construction. These diagrams are shown in Fig. 2.8. In practice, this means that diagrams that contribute to the flow equation of (a) the Yukawa coupling and (b–d) the four-quark interaction drop out.

The set of differential equations derived so far describes the system in the high-momentum regime where the curvature of the effective potential ϵ is positive. Following the RG flow towards smaller scales, we shall find that the curvature decreases and eventually becomes zero at the so-called symmetry-breaking scale k_{SB}, see Sec. 2.4.2. In this regime governed by a spontaneously broken $\mathrm{U}(1)_V$ symmetry, the diquark field obtains a finite expectation value associated with a nontrivial minimum of the diquark potential so that the set of differential equations changes.

The derivation of the modifications to the running couplings due to the introduction of scale-dependent diquark fields in the regime governed by spontaneous symmetry breaking is very similar to the derivation in the symmetric phase. Therefore, we keep it brief and only show the relevant changes in the derivation. In contrast to the symmetric phase, in the regime governed by spontaneous symmetry breaking, we only consider the fields $\Delta_{\bar{a}}$ and $\Delta^*_{\bar{a}}$ to be scale dependent. Here, $\bar{a} = 1, 2$ is a reduced colour index, i.e., it does not include the three-direction. This choice for the scale dependence of the diquark fields is motivated by the following consideration for mapping onto the diquark gap: While the different directions of the diquark field used in the projection for the curvature of the diquark potential in the symmetric phase are all equivalent, the three-direction of the diquark fields is different in the phase governed by spontaneous symmetry breaking. Recall that we choose the background field $\bar{\Delta}_3$ to point into the three-direction such that $\Delta_a \mapsto \Delta_a + \delta_{a3}\bar{\Delta}_3$. With this, the flow equation of the diquark condensate $|\bar{\Delta}_0|^2$ can be obtained from $-2\bar{\lambda}_\Delta \partial_t |\bar{\Delta}_0|^2 = V_4^{-1}(\partial/\partial(\Delta_1^*\Delta_1)\partial_t \Gamma_k)_{\mathrm{gs}}$. Here, the subscript 'gs' indicates that we evaluate on the ground state which is given by evaluating on $\Delta_a = 0$ and $\bar{\Delta}_3 = |\bar{\Delta}_0|$ where $|\bar{\Delta}_0|$ is the minimum of the diquark potential. Alternatively, we can define the flow equation of the diquark condensate $|\bar{\Delta}_0|^2$ with a derivative with respect to $(\bar{\Delta}_2^*\bar{\Delta}_2)$ which is equivalent to using a derivative with respect to $(\bar{\Delta}_1^*\bar{\Delta}_1)$. However, a straightforward calculation by differentiating with

respect to $(\bar{\Delta}_3^*\bar{\Delta}_3)$ is not possible since $V_4^{-1}(\partial/\partial(\delta\bar{\Delta}_3^*\delta\bar{\Delta}_3)\partial_t\Gamma_k)_{\mathrm{gs}} = -2\bar{\lambda}_\Delta\partial_t|\bar{\Delta}_0|^2 + 2|\bar{\Delta}_0|^2\partial_t\bar{\lambda}_\Delta$. Here, we obtain additional contributions that cannot be identified with the flow of the diquark condensate $|\bar{\Delta}_0|^2$. Therefore, a projection onto all three directions simultaneously would be inconsistent and we map only by differentiating with respect to $(\bar{\Delta}_1^*\bar{\Delta}_1)$ and $(\bar{\Delta}_2^*\bar{\Delta}_2)$. Since we also differentiate with respect to diquark fields in the second term of the modified Wetterich equation (2.60), a differentiation with respect to the three-direction would also lead to additional terms. To solve this issue, we only consider the diquark fields in the one- and two-direction to be scale dependent. Therefore, also the scale dependence of the diquark fields is adapted to read

$$\partial_t\Delta_{\bar{a},k}(p') = \frac{1}{2}\int_p\int_q \bar{\psi}(p)\gamma_5\tau_2\mathrm{i}\epsilon_{\bar{a}}\mathcal{C}\bar{\psi}^T(q)(2\pi)^4\delta^{(4)}(p'-p-q)\,\partial_t\alpha_k(p') - \Delta_{\bar{a},k}(p')\partial_t\beta_k(p')\,, \tag{2.58}$$

$$\partial_t\Delta^*_{\bar{a},k}(p') = -\frac{1}{2}\int_p\int_q \psi^T(p)\mathcal{C}\gamma_5\tau_2\mathrm{i}\epsilon_{\bar{a}}\psi(q)(2\pi)^4\delta^{(4)}(p'-p-q)\,\partial_t\alpha_k(p') - \Delta^*_{\bar{a},k}(p')\partial_t\beta_k(p')\,. \tag{2.59}$$

Consequently, the modified Wetterich equation is given by

$$\partial_t\Gamma_k[\varphi] = \partial_t\bar{\Gamma}_k[\varphi] - \int_{p'}\left\{\frac{\delta\Gamma_k[\varphi_k]}{\delta\Delta^*_{\bar{a},k}(p')}\partial_t\Delta^*_{\bar{a},k}(p') + \frac{\delta\Gamma_k[\varphi_k]}{\delta\Delta_{\bar{a},k}(p')}\partial_t\Delta_{\bar{a},k}(p')\right\}. \tag{2.60}$$

Here, the first term in the latter expression is still given by Eq. (2.31).
For the Yukawa coupling $\bar{h}$, we find

$$\partial_t\bar{h} = \partial_t\bar{h}\big|_{\bar{\Gamma}} + \big(Z_\Delta p^2 + 4\mu\mathrm{i}Z_\Delta p_0\big)\partial_t\alpha_k(p) + \bar{h}\partial_t\beta_k(p)\,. \tag{2.61}$$

Instead of a flow equation for the mass, we find a flow equation for the minimum of the diquark potential $|\Delta_0|^2$ which is notably not directly affected by the contributions from the scale dependence of the diquark fields:

$$-2\bar{\lambda}_\Delta\partial_t|\Delta_0|^2 = -2\bar{\lambda}_\Delta\partial_t|\Delta_0|^2\big|_{\bar{\Gamma}}\,. \tag{2.62}$$

The running of the diquark wavefunction renormalisation can be extracted from

$$\partial_t\big(Z_\Delta p^2 + 4\mu\mathrm{i}Z_\Delta p_0\big) = \partial_t\big(Z_\Delta p^2 + 4\mu\mathrm{i}Z_\Delta p_0\big)\big|_{\bar{\Gamma}} + 2\big(Z_\Delta p^2 + 4\mu\mathrm{i}Z_\Delta p_0\big)\partial_t\beta_k(p)\,. \tag{2.63}$$

Since $\partial_t\alpha_k(p)$ is an arbitrary function, we can choose it so that the four-quark interaction $\bar{\lambda}_{\mathrm{csc}}$ vanishes at all scales by requiring $\partial_t\alpha_k(p) = \partial_t\bar{\lambda}_{\mathrm{csc}}(p)\big|_{\bar{\Gamma}}/\bar{h}$. It follows that $\partial_t\alpha_k$ remains unchanged in the broken phase compared to the symmetric phase. However, $\partial_t\beta_k$ changes which is, besides $\alpha_k(p)$, also an arbitrary function because the field configuration is not fixed uniquely. Therefore, we can use the contribution of $\beta_k(p)$ to absorb the momentum dependence of the Yukawa coupling. As in the symmetric phase, we can also use $\beta_k(p)$ to ensure that the wavefunction renormalisation Z_Δ is momentum independent. For this purpose, we choose

$$\partial_t\beta_k(p) = -\frac{Z_\Delta p^2 + 4\mu\mathrm{i}Z_\Delta p_0}{\bar{h}^2}\partial_t\bar{\lambda}_{\mathrm{csc}}(p) + \frac{Z_\Delta k^2}{\bar{h}^2}\partial_t\bar{\lambda}_{\mathrm{csc}}(p_0=0,|\vec{p}|=k)\,. \tag{2.64}$$

Here, the first part guarantees that the Yukawa coupling is momentum independent and the second (p-independent) part guarantees that the wavefunction renormalisation Z_Δ is momentum independent as well:

$$k^2\partial_t Z_\Delta(p_0=0,|\vec{p}|=k) = k^2\partial_t Z_\Delta\big|_{\bar{\Gamma}}\,. \tag{2.65}$$

As in the symmetric phase, we introduced the difference $\Delta\bar{\lambda}_{\mathrm{csc}} = \bar{\lambda}_{\mathrm{csc}}(p_0=0,|\vec{p}|=k) - \bar{\lambda}_{\mathrm{csc}}(p_0=0,|\vec{p}|=0)$. As it also represents the point-like limit, we choose $\Delta\bar{\lambda}_{\mathrm{csc}} = 0$ in the following. The initially arbitrary functions $\alpha_k(p)$ and $\beta_k(p)$ are now uniquely determined by the stated requirements. As in the symmetric phase, the four-quark interaction now enters the set of differential equations only in terms of its running $\partial_t\bar{\lambda}_{\mathrm{csc}}$

and not as an additional differential equation. Furthermore, the four-quark interaction itself $\bar{\lambda}_{\text{csc}}$ vanishes on all scales.

In conclusion, this leads to a coupled system of differential equations for the running of the renormalised squared Yukawa coupling $h^2 = Z_\psi^{-2} Z_\Delta^{-1} \bar{h}^2$, the renormalised dimensionless minimum $\kappa = Z_\Delta k^{-2} |\Delta_0|^2$, and the renormalised four-diquark coupling $\lambda_\Delta = Z_\Delta^{-2} \bar{\lambda}_\Delta$:

$$\partial_t h^2 = Z_\psi^{-2} Z_\Delta^{-1} \partial_t \bar{h}^2 \big|_{\bar{\Gamma}} + 2k^2 Z_\psi^{-2} \partial_t \bar{\lambda}_{\text{csc}}(0) + h^2 \eta_\Delta + 2h^2 \eta_\psi \,, \tag{2.66}$$

$$\partial_t \kappa = Z_\Delta k^{-2} \partial_t |\Delta_0|^2 \big|_{\bar{\Gamma}} - \kappa \eta_\Delta - 2\kappa \,, \tag{2.67}$$

$$\partial_t \lambda_\Delta = Z_\Delta^{-2} \partial_t \bar{\lambda}_\Delta \big|_{\bar{\Gamma}} + 4 \frac{\lambda_\Delta}{h^2} k^2 Z_\psi^{-2} \partial_t \bar{\lambda}_{\text{csc}}(0) + 2\lambda_\Delta \eta_\Delta \,. \tag{2.68}$$

In contrast to the symmetric phase, the flow equation of the curvature of the potential has been replaced by the flow of the minimum of the potential. However, the flow of the minimum does not receive contributions originating from the use of the dynamical bosonisation technique.

2.3.2 Flow Equations

In this section, we turn to the first part of the modified Wetterich equation (2.30) which is simply the conventionally employed Wetterich equation with a shifted diquark anomalous dimension $\eta_\Delta \to \eta_\Delta + 2\dot{\beta}$. For a first calculation, we start with some assumptions and simplifications. Note, however, that the derivation of the corrections to the flow equations derived in the preceding section does not rely on these assumptions. We shall improve upon the following calculation in Sec. 2.6. In this section, we set the wavefunction renormalisation of the quarks to one $Z_\psi = 1$ since it is expected to depend only mildly on the RG scale at least for small densities [142, 146, 171, 175–177, 316]. Nevertheless, we take it into account in the next step. We also drop bosonic fluctuations by effectively dropping kinetic terms of the diquark fields in the ansatz for the Wetterich equation (2.25). By dropping bosonic fluctuations, the flow of different diquark self-interaction couplings effectively decouple. Therefore, the inclusion of, e.g., a six-diquark interaction associated with the coupling λ_6 (and higher-order diquark self-interactions) would not influence the flow equations of the remaining couplings. However, the wavefunction renormalisation Z_Δ is still generated in the RG flow already from purely fermionic loop diagrams. Furthermore, we use Feynman gauge for convenience. For a first analysis, we shall also set gluon-diquark interactions to zero $g_{\Delta,1} = g_{\Delta,2}^2 = 0$. We shall include them alongside the other improvements of the current truncation in Sec. 2.6. In contrast to the gluon-ghost and higher-order gluon self-interactions, there is no argument that they should be equal to the quark-gluon interaction even at one loop, see Sec. 2.6 for details. We emphasise that $\bar{\lambda}_{\text{csc}} = 0$ because of the dynamical bosonisation, see Sec. 2.3.1. In the following, we evaluate the couplings in the point-like limit. For more details on the derivation of the running couplings, we refer to App. C.

Schematic representations of the terms that contribute to the running couplings are shown in Fig. 2.9. Consequently, the running of the modified mass $\tilde{m}^2 = \bar{m}^2 - 4Z_\Delta \mu^2$ as the curvature of the diquark potential can be obtained for $k \geq k_{\text{SB}}$ by considering

$$\partial_t \tilde{m}^2 \big|_{\bar{\Gamma}} = \frac{1}{3V_4} \left(\frac{\partial}{\partial \Delta_a^*} \frac{\partial}{\partial \Delta_a} \partial_t \bar{\Gamma}_k[\varphi] \right)_{\text{gs}} = -8 Z_\Delta k^2 h^2 \mathcal{L}_{\text{ff}}^{(2)} \left(\frac{\mu}{k}, 0, \rho_\psi \right) \,. \tag{2.69}$$

Here, $V_4 = \int \mathrm{d}^4 x$ is the four-dimensional volume of Euclidean spacetime. and we have adapted the subscript '$\bar{\Gamma}$' from the preceding section to indicate that we only consider the first part of the modified Wetterich equation (2.30). As we have already mentioned before, by following the RG flow towards lower scales, we find that the curvature of the potential eventually becomes zero. Below the symmetry-breaking scale $k \leq k_{\text{SB}}$, the curvature of the diquark potential, given by the modified mass $\tilde{m}^2$, becomes negative and a colour superconducting ground state is formed. Then, we replace the flow equation of the curvature with the flow of

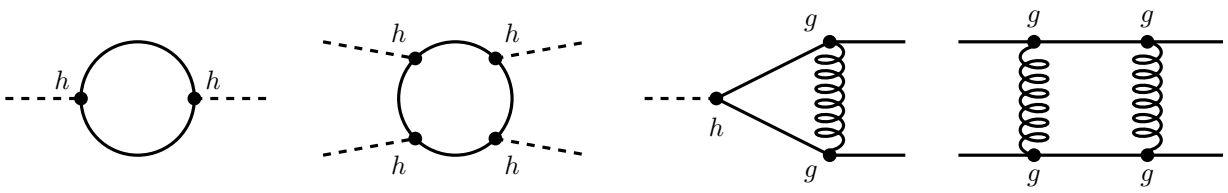

(a) (b) (c) (d)

Figure 2.9: Schematic representations of the contributions to the different flow equations of the couplings with the current approximations. One diagram contributes to the (a) curvature of the potential (modified mass) $\tilde{m}^2$, (b) the diquark coupling $\bar{\lambda}_\Delta$, (c) the Yukawa coupling $\bar{h}$, and (d) the four-quark interaction $\bar{\lambda}_{\text{csc}}$, respectively. Note that, although the four-quark interaction $\bar{\lambda}_{\text{csc}}$ has been eliminated with the dynamical bosonisation, its flow is still generated and contributes to the remaining couplings.

the minimum of the diquark potential $|\Delta_0|^2 = \sum_a |\Delta_{0,a}|^2$ which is given by

$$\partial_t |\Delta_0|^2\big|_{\bar{\Gamma}} = -\frac{1}{4\bar{\lambda}_\Delta V_4}\left(\frac{\partial}{\partial\Delta^*_{\bar{a}}}\frac{\partial}{\partial\Delta_{\bar{a}}}\partial_t\bar{\Gamma}_k[\varphi]\right)_{\text{gs}} = Z_\Delta^{-1}\frac{4h^2}{\lambda_\Delta}k^2\mathcal{L}^{(2)}_{\text{ff}}\left(\frac{\mu}{k}, h^2\kappa, \rho_\psi\right). \tag{2.70}$$

Recall that we use a homogeneous background field for the expansion of the diquark fields in the phase governed by spontaneous symmetry breaking. We choose this background field $\bar{\Delta}_3$ to point into the three-direction so that $\Delta_a \mapsto \Delta_a + \delta_{a3}\bar{\Delta}_3$. Following the discussion above Eq. (2.58), differentiating with respect to diquark fields in the three-direction to map onto the minimum of the diquark potential is not straightforward. Therefore, we only only differentiate with respect to diquark fields in the one- and two-direction by using the reduced colour index $\bar{a} = 1, 2$. The subscript 'gs' indicates that we evaluate on the ground state, i.e., on vanishing fields for $k \geq k_{\text{SB}}$. For $k \leq k_{\text{SB}}$, the ground state is given by evaluating on $\Delta_a = 0$ and $\bar{\Delta}_3 = |\bar{\Delta}_0|$ while the remaining fields are set to zero. This effectively leads to an expansion of the diquark condensate in the three-direction: $\Delta_{0,a} = \Delta_0\delta_{a,3}$. The so-called threshold function $\mathcal{L}^{(2)}_{\text{ff}}$ corresponds to a loop diagram with two internal fermion lines as depicted in Fig. 2.9a.
The running of the four-diquark coupling $\bar{\lambda}_\Delta$ is for $k \geq k_{\text{SB}}$ given by

$$\partial_t\bar{\lambda}_\Delta\big|_{\bar{\Gamma}} = \frac{1}{24V_4}\left(\frac{\partial}{\partial\Delta^*_a}\frac{\partial}{\partial\Delta_a}\frac{\partial}{\partial\Delta^*_b}\frac{\partial}{\partial\Delta_b}\partial_t\bar{\Gamma}_k[\varphi]\right)_{\text{gs}} = 4Z_\Delta^2 h^4\mathcal{L}^{(2)}_{\text{ffff}}\left(\frac{\mu}{k}, 0, \rho_\psi\right). \tag{2.71}$$

For consistency, we also differentiate with respect to the one- and two-direction in the calculation of the diquark coupling in the phase governed by symmetry breaking. Therefore, for $k \leq k_{\text{SB}}$ the running of the diquark coupling is $\bar{\lambda}_\Delta$ given by

$$\partial_t\bar{\lambda}_\Delta\big|_{\bar{\Gamma}} = \frac{1}{12V_4}\left(\frac{\partial}{\partial\Delta^*_{\bar{a}}}\frac{\partial}{\partial\Delta_{\bar{a}}}\frac{\partial}{\partial\Delta^*_{\bar{b}}}\frac{\partial}{\partial\Delta_{\bar{b}}}\partial_t\bar{\Gamma}_k[\varphi]\right)_{\text{gs}} = 4h^4 Z_\Delta^2\mathcal{L}^{(2)}_{\text{ffff}}\left(\frac{\mu}{k}, h^2\kappa, \rho_\psi\right). \tag{2.72}$$

Here, the threshold function $\mathcal{L}^{(2)}_{\text{ffff}}$ corresponds to a loop diagram with four internal fermion lines as depicted in Fig. 2.9b.
For the running of the Yukawa coupling $\bar{h}$ for $k \geq k_{\text{SB}}$, we find

$$\partial_t\bar{h}\big|_{\bar{\Gamma}} = \frac{1}{V_4}\left(\frac{2}{\mathrm{i}\psi^T\mathcal{C}\gamma_5\tau_2\Delta_a\epsilon_a\psi - \mathrm{i}\bar{\psi}\gamma_5\tau_2\Delta^*_a\epsilon_a\mathcal{C}\bar{\psi}^T}\partial_t\bar{\Gamma}_k[\varphi]\right)_{\text{gs}} = \frac{8}{3}Z_\psi Z_\Delta^{1/2}g^2h\mathcal{L}^{(2)}_{\text{bff}}\left(\frac{\mu}{k}, 0, \rho_\psi, \rho_A\right). \tag{2.73}$$

For $k \leq k_{\text{SB}}$, we find

$$\partial_t\bar{h}\big|_{\bar{\Gamma}} = \frac{1}{V_4}\left(\frac{2}{\mathrm{i}\psi^T C\gamma_5\tau_2\Delta_{\bar{a}}\epsilon_{\bar{a}}\psi - \mathrm{i}\bar{\psi}\gamma_5\tau_2\Delta^*_{\bar{a}}\epsilon_{\bar{a}}C\bar{\psi}^T}\partial_t\bar{\Gamma}_k[\varphi]\right)_{\text{gs}} = \frac{8}{3}Z_\psi Z_\Delta^{1/2}g^2h\mathcal{L}^{(2)}_{\text{bff}}\left(\frac{\mu}{k}, h^2\kappa, \rho_\psi, \rho_A\right). \tag{2.74}$$

Note that the notation is somewhat sloppy. In practice, we have compared the left- and right-hand side of the Wetterich equation to identify the coefficients that contribute to the running of the Yukawa coupling and dropped the remaining terms. Following the mapping of the minimum $|\Delta_0|^2$ and the diquark coupling λ_Δ in $\bar{a} = 1, 2$ direction, we also consider the Yukawa coupling associated with this direction in the broken phase. We further assume that the Yukawa coupling associated with the $\bar{a} = 1, 2$ direction is identical to the one in the three-direction. The threshold function $\mathcal{L}^{(2)}_{\text{bff}}$ is associated with a loop diagram with two internal fermion lines and one internal gluon line as depicted in Fig. 2.9c.
Recall that the four-quark interaction λ_{csc} has been eliminated with the aid of the dynamical bosonisation technique so that there are no contributions to the running couplings that depend on λ_{csc}, see Fig. 2.8 for a selection of such diagrams. However, the running of the four-quark interaction $\partial_t \lambda_{\text{csc}}$ contributes to the remaining couplings that span the ansatz for the effective action (2.25). For $k \geq k_{\text{SB}}$, it is given by

$$\partial_t \bar{\lambda}_{\text{csc}}\big|_{\bar{\Gamma}} = \frac{1}{V_4}\left(\frac{2}{\bar{\psi}\tau_2 \mathrm{i}\epsilon_a \gamma_5 \mathcal{C}\bar{\psi}^T \psi^T \mathcal{C}\gamma_5 \tau_2 \mathrm{i}\epsilon_a \psi}\partial_t \bar{\Gamma}_k[\varphi]\right)_{\text{gs}} = k^{-2} Z_\psi^2 g^4 \mathcal{L}^{(A)}_{\text{bbff}}\left(\frac{\mu}{k}, 0\right) \tag{2.75}$$

and for $k \leq k_{\text{SB}}$, it is given by

$$\partial_t \bar{\lambda}_{\text{csc}}\big|_{\bar{\Gamma}} = \frac{1}{V_4}\left(\frac{2}{\bar{\psi}\tau_2 \mathrm{i}\epsilon_{\bar{a}} \gamma_5 \mathcal{C}\bar{\psi}^T \psi^T \mathcal{C}\gamma_5 \tau_2 \mathrm{i}\epsilon_{\bar{a}} \psi}\partial_t \bar{\Gamma}_k[\varphi]\right)_{\text{gs}} = k^{-2} Z_\psi^2 g^4 \mathcal{L}^{(A)}_{\text{bbff}}\left(\frac{\mu}{k}, h^2\kappa\right) . \tag{2.76}$$

Similar to the Yukawa coupling, we have mapped onto the running of the four-quark interaction by comparing the left- and right-hand side of the Wetterich equation to identify the coefficients that contribute. The diquark channel does not directly appear on the right-hand side of the Wetterich equation since only terms $\sim (\bar{\psi}\ldots\psi)(\bar{\psi}\ldots\psi)$ appear. Consequently, we have performed a so-called Fierz transformation which then allows us to map onto the diquark channel. However, after performing the Fierz transformation a multitude of four-quark channels $\sim (\bar{\psi}\ldots\bar{\psi}^T)(\psi^T\ldots\psi)$ appears on the right-hand side of the Wetterich equation. In the present study, we only map onto the diquark channel and drop the remaining terms. A rigorous analysis would require to include a Fierz-complete set of four-quark interactions, see, e.g., Refs. [179]. The Fierz transformations can be found in App. A. Similarly to the mapping of the Yukawa interaction, we use the four-quark interaction in the $\bar{a} = 1, 2$ direction. The threshold function $\mathcal{L}^{(A)}_{\text{bbff}}$ is associated with a loop diagram with two internal fermions and one internal gluon line as depicted in Fig. 2.9d and consists of three contributions:

$$\begin{aligned}\mathcal{L}^{(A)}_{\text{bbff}}\left(\frac{\mu}{k}, h^2\kappa\right) = \frac{5}{36}\mathcal{L}^{(1)}_{\text{bbff}}\left(\frac{\mu}{k}, h^2\kappa, \rho_\psi, \rho_A, \rho_A\right) + \frac{4}{9}\mathcal{L}^{(2)}_{\text{bbff}}\left(\frac{\mu}{k}, h^2\kappa, \rho_\psi, \rho_A, \rho_A\right) \\ + \frac{5}{48}\mathcal{L}^{(4)}_{\text{bbff}}\left(\frac{\mu}{k}, h^2\kappa, \rho_\psi, \rho_A, \rho_A\right) .\end{aligned} \tag{2.77}$$

The definitions of all threshold functions used in the present work can be found in App. B.3. Note that they entail the regularisation scheme. In the present study, we employ a three-dimensional regularisation scheme with a polynomial regulator shape function which has been adapted to integrate out fermion fluctuations around the Fermi surface. We have introduced this regularisation scheme in Sec. 1.3. The threshold functions may also entail a possible temperature dependence, but in the present work, we work in the zero-temperature limit. The argument ρ_ψ entails all possible arguments from fermion propagators. The diquark gap is an argument of the fermion propagator which appears in the regime governed by spontaneous symmetry breaking in the threshold functions in terms of the quantity $h^2\kappa$ which is closely related to the diquark gap $\Delta^2_{\text{gap}} = k^2 h^2 \kappa$. Although the fermion propagators depend on this quantity, to better distinguish the threshold functions in the symmetric phase and the regime governed by spontaneous symmetry breaking, we do not include the diquark gap in ρ_ψ but keep it as a separate argument in the threshold functions. Therefore, the only argument of the fermion propagator in the present study is the anomalous dimension η_ψ: $\rho_\psi = [\eta_\psi]$. Note also

that we have set $Z_\psi = 1$ so that $\eta_\psi = 0$ but still keep their dependences in the equations. The argument ρ_A collects all possible arguments coming from gluon propagators which in the present study is only the gluon anomalous dimension η_A: $\rho_A = \{\eta_A\}$. In defining the threshold functions with "collective" arguments, we can directly extend them to include, e.g., gluon masses. See Sec. 2.6.1 for the inclusion of gluon masses in the flow equations.

With the contributions from the dynamical bosonisation, i.e., effectively employing Eqs. (2.52)–(2.54), the coupled set of flow equations in the symmetric phase $k \geq k_{\mathrm{SB}}$ reads

$$\partial_t \lambda_\Delta = 4h^4 \mathcal{L}^{(2)}_{\mathrm{ffff}}\Big(\frac{\mu}{k}, 0, \rho_\psi\Big) + \frac{4\lambda_\Delta(1+\epsilon)}{h^2} g^4 \mathcal{L}^{(A)}_{\mathrm{bbff}}\Big(\frac{\mu}{k}, 0, \rho_\psi, \rho_A, \rho_A\Big) + 2\eta_\Delta \lambda_\Delta \,, \tag{2.78}$$

$$\partial_t \epsilon = -8h^2 \mathcal{L}^{(2)}_{\mathrm{ff}}\Big(\frac{\mu}{k}, 0, \rho_\psi\Big) + \frac{2\epsilon(1+\epsilon)}{h^2} g^4 \mathcal{L}^{(A)}_{\mathrm{bbff}}\Big(\frac{\mu}{k}, 0, \rho_\psi, \rho_A, \rho_A\Big) + (\eta_\Delta - 2)\epsilon \,, \tag{2.79}$$

$$\partial_t h^2 = \frac{16}{3} g^2 h^2 \mathcal{L}^{(2)}_{\mathrm{bff}}\Big(\frac{\mu}{k}, 0, \rho_\psi, \rho_A\Big) + 2(1+2\epsilon) g^4 \mathcal{L}^{(A)}_{\mathrm{bbff}}\Big(\frac{\mu}{k}, 0, \rho_\psi, \rho_A, \rho_A\Big) + h^2\eta_\Delta + 2h^2\eta_\psi \,. \tag{2.80}$$

In the regime governed by spontaneous symmetry breaking $k \leq k_{\mathrm{SB}}$, the system is described by

$$\partial_t h^2 = \frac{16}{3} g^2 h^2 \mathcal{L}^{(2)}_{\mathrm{bff}}\Big(\frac{\mu}{k}, h^2\kappa, \rho_\psi, \rho_A\Big) + 2g^4 \mathcal{L}^{(A)}_{\mathrm{bbff}}\Big(\frac{\mu}{k}, h^2\kappa, \rho_\psi, \rho_A, \rho_A\Big) + h^2\eta_\Delta + 2h^2\eta_\psi \,, \tag{2.81}$$

$$\partial_t \kappa = \frac{4h^2}{\lambda_\Delta} \mathcal{L}^{(2)}_{\mathrm{ff}}\Big(\frac{\mu}{k}, h^2\kappa, \rho_\psi\Big) - \kappa\eta_\Delta - 2\kappa \,, \tag{2.82}$$

$$\partial_t \lambda_\Delta = 4h^4 \mathcal{L}^{(2)}_{\mathrm{ffff}}\Big(\frac{\mu}{k}, h^2\kappa, \rho_\psi\Big) + 4\frac{\lambda_\Delta}{h^2} g^4 \mathcal{L}^{(A)}_{\mathrm{bbff}}\Big(\frac{\mu}{k}, h^2\kappa, \rho_\psi, \rho_A, \rho_A\Big) + 2\lambda_\Delta\eta_\Delta \,. \tag{2.83}$$

As already mentioned, there is no flow equation for the four-quark coupling which is a consequence of the dynamical bosonisation technique [146, 170–175, 178, 257]. However, it enters the flow equations for λ_Δ, ϵ, and h^2 as an additional contribution continuously generated in the flow by the elimination of the running of the four-quark interaction. In the flow equations this is represented by the contribution $\sim g^4$ entering the flow of λ_Δ, ϵ, and h^2. Notably, there is no contribution to the flow of the curvature κ. The contribution $\sim g^4$ originally originates from a two-gluon exchange box diagram, see Fig. 2.9d. Additional contributions $\sim h^4$ and $\sim h^2 g^2$ might be generated when including diquark fluctuations in Sec. 2.6.

Lastly, we turn to the scale dependence of the diquark anomalous dimension and the gluon anomalous dimension. Their corresponding contributions are shown in Fig. 2.10. The scale dependence of the diquark anomalous dimension is given for $k \geq k_{\mathrm{SB}}$ by

$$\eta_\Delta = -Z_\Delta^{-1}\partial_t Z_\Delta = -\frac{1}{3V_4} Z_\Delta^{-1}\left(\frac{\partial}{\partial P_0^2}\frac{\partial}{\partial \Delta_a^*(P)}\frac{\partial}{\partial \Delta_a(P)}\partial_t \bar{\Gamma}_k[\varphi]\right)_{\mathrm{gs,P=0}} = 8h^2\, \mathcal{D}^{(2)}_{\mathrm{ff}}\Big(\frac{\mu}{k}, 0, \rho_\psi\Big) \,. \tag{2.84}$$

For $k \leq k_{\mathrm{SB}}$, it is given by

$$\eta_\Delta = -Z_\Delta^{-1}\partial_t Z_\Delta = -\frac{1}{2V_4} Z_\Delta^{-1}\left(\frac{\partial}{\partial P_0^2}\frac{\partial}{\partial \Delta_{\bar{a}}^*(P)}\frac{\partial}{\partial \Delta_{\bar{a}}(P)}\partial_t \bar{\Gamma}[\varphi]\right)_{\mathrm{gs,P=0}} = 8h^2\, \mathcal{D}^{(2)}_{\mathrm{ff}}\Big(\frac{\mu}{k}, h^2\kappa, \rho_\psi\Big) \,. \tag{2.85}$$

Here, we have defined the diquark anomalous dimension by differentiating with respect to the zeroth component of the external four-momentum. A definition with a derivative with respect to the spatial component of the external four-momentum is also possible. The inclusion of a chemical potential requires to differentiate between the zeroth and the spatial component so that it is, in principle, necessary to consider both definitions of the wavefunction renormalisation. In addition to the chemical potential, also the use of a three-dimensional regularisation scheme generates this splitting as it breaks Lorentz invariance [317]. Therefore, already for $k \gg \mu$, we expect a difference in the wavefunction renormalisations of the corresponding definitions which should be absent for a four-dimensional regularisation scheme. However, this distinction is beyond the scope of the present work so that we approximate by assuming that both directions are equal

(a) (b)

Figure 2.10: Schematic representation of the contributions to the scale dependence of the (a) diquark anomalous dimension η_Δ and (b) the gluon anomalous dimension η_A.

and by taking the derivative with respect to the zeroth component of the external momentum as already mentioned. In practice, this choice also simplifies the calculation because the regulator in a three-dimensional setting does not depend on the zeroth component of the external momentum. The threshold function $\mathcal{D}_{\text{ff}}^{(2)}$ corresponds to the loop diagram shown in Fig. 2.10a.
In the present work, the gauge sector only enters via the running of the strong coupling g which is, in the background-field formalism [304, 305] underlying the present work, given by

$$\partial_t g^2 = \eta_A g^2 \,. \tag{2.86}$$

The gluon anomalous dimension consists of two contributions [296–298]: the pure gluonic part η_A^{glue} and the quark contribution η_A^{quark} so that

$$\eta_A = -Z_A^{-1}\partial_t Z_A = \eta_A^{\text{glue}} + \eta_A^{\text{quark}} \,. \tag{2.87}$$

For the gluon contribution to the anomalous dimension η_A^{glue}, we use results from previous fRG studies where it has been calculated nonperturbatively within the background field formalism, see Ref. [297, 298, 311]. This approach also underlies the present work. For further details on the strong coupling see App. D. For the quark contribution to the anomalous dimension η_A^{quark} for $k \geq k_{\text{SB}}$, we find

$$\eta_A^{\text{quark}} = -\frac{1}{24V_4} Z_A^{-1} \left(\frac{\partial}{\partial P_0^2} P_T^{\mu\nu}(P) \frac{\delta}{\delta A_\mu^a(P)} \frac{\delta}{\delta A_\nu^a(-P)} \partial_t \bar{\Gamma}_k[\varphi] \right)_{\text{gs},P=0,\text{quarkloop}} = \frac{8}{3} g^2 D_{\text{ff}}^{(1)}\left(\frac{\mu}{k}, 0, \rho_\psi\right) \,. \tag{2.88}$$

Here, we project onto the transverse momentum by introducing $P_T^{\alpha\beta} = \delta_{\alpha\beta} - P_\alpha P_\beta / P^2$. Further, the only contribution considered in the latter expression is the quark loop shown in Fig. 2.10b as indicated by the subscript 'quarkloop'. For vanishing chemical potential $\mu \to 0$, we find $\eta_A^{\text{quark}} \simeq g^2/(6\pi^2)$, which is the standard one-loop contribution of the quark fields to the running of the strong coupling. In the regime governed by spontaneous symmetry breaking $k \leq k_{\text{SB}}$, we find

$$\begin{aligned} \eta_A^{\text{quark}} &= -\frac{1}{24V_4} Z_A^{-1} \left(\frac{\partial}{\partial P_0^2} P_T^{\mu\nu}(P) \frac{\delta}{\delta A_\mu^a(P)} \frac{\delta}{\delta A_\nu^a(-P)} \partial_t \bar{\Gamma}_k[\varphi] \right)_{\text{gs},P=0,\text{quarkloop}} \\ &= \frac{8}{3} g^2 \left(D_{\text{ff}}^{(1)}\left(\frac{\mu}{k}, h^2\kappa, \rho_\psi\right) + D_{\text{ff}}^{(3)}\left(\frac{\mu}{k}, h^2\kappa, \rho_\psi\right) \right) . \end{aligned} \tag{2.89}$$

Note that the expansion of the diquark fields into the three-direction leads to different contributions if mapping on different gluons. However, we do not aim to resolve this issue but simply average over the different gluons for the quark contribution to the gluon anomalous dimension.
As already mentioned, we drop bosonic fluctuations in the present study. These fluctuations are associated with loop diagrams with at least one internal diquark line. These contributions are, at least for scales above the symmetry-breaking scale, parametrically suppressed since the curvature of the potential, entering the

propagators of the diquark fields in terms of a modified mass, is large and only becomes small close to the symmetry-breaking scale, see Sec. 2.4.2. Nevertheless, we shall include diquark fluctuations in Sec. 2.6 alongside further improvements of the present calculation, at least in the symmetric phase.
In the regime governed by spontaneous symmetry breaking ($k \leq k_{\mathrm{SB}}$) fluctuation effects may become important. However, since the diquark fields are not expected to be massless below the symmetry-breaking scale, fluctuation effects may be suppressed below k_{SB} as well. Still, the situation is more involved in this regime since diquark fields carry a net colour charge. This requires the consideration of an Anderson-Higgs-type mechanism associated with the symmetry-breaking pattern $\mathrm{SU}(3) \to \mathrm{SU}(2)$ in colour space. We expect that only three of the eight gluons remain massless below the symmetry-breaking scale. Loosely speaking, by "eating up" Goldstone modes in the diquark spectrum, the remaining five gluons become massive and are, consequently, similar to the quarks, gapped in the phase governed by spontaneous symmetry breaking [50]. In the present work, we do not intend to resolve this issue but drop diquark fluctuations below the symmetry-breaking scale. However, we at least aim to estimate the effect of the Anderson-Higgs-type mechanism and the resulting gluon gapping, see Sec. 2.4.2.

2.4 RG Flow of Dense Strong-Interaction Matter

We turn to the RG flows of dense strong-interaction matter which are given by the set of differential equations (2.78)–(2.80) in the symmetric phase $k \geq k_{\mathrm{SB}}$ and (2.81)–(2.83) in the regime governed by spontaneous symmetry breaking $k \leq k_{\mathrm{SB}}$. The diquark anomalous dimensions enter the set of differential equations via (2.84) and (2.85) and the gluon anomalous dimension via (2.87). Furthermore, the flow equation of the strong coupling is given by Eq. (2.86). In practice, we follow the RG flow given by Eqs. (2.78)–(2.80) coming from large scales. We find that the curvature of the potential ϵ decreases and eventually becomes zero which defines the symmetry-breaking scale k_{SB}. This indicates the formation of a colour-superconducting ground state associated with the formation of a gap in the fermionic excitation spectrum. We refer to this gap as the diquark gap, which is closely related to the minimum of the potential. Therefore, at the symmetry-breaking scale, we replace the flow equation of the curvature of the potential ϵ with that of its renormalised dimensionless minimum κ, which is then dynamically generated in the RG flow. As a result, the RG flow is given by (2.81)–(2.83) until the long-range limit ($k \to 0$) is reached. Before showing results for the RG flows in Sec. 2.4.2, we start with a discussion of the initial conditions in Sec. 2.4.1.

2.4.1 Fixing the Initial Conditions

The discussion of the flow equations requires to fix the initial conditions at the UV scale first. This initial RG scale Λ has to be chosen such that $\Lambda \gg \mu$. For the purpose of the present study, we choose $\Lambda = 10\,\mathrm{GeV}$ which allows us to cover a reasonable range of chemical potentials. It is important to emphasise that the only external input parameter in the present study is the initial condition for the strong coupling g which at $\Lambda = 10\,\mathrm{GeV}$ is given by $g^2(\Lambda) = 4\pi\alpha(\Lambda) = 4\pi \cdot (0.179 \pm 0.004)$. This corresponds to the experimental value $\alpha(m_\tau) = 0.330 \pm 0.014$ at the tau-mass scale m_τ [318]. The experimental error can be used to examine the corresponding uncertainties in the following discussion. As the only input parameter, the strong coupling sets the scale for all dimensionful quantities. To this end, we define Λ_{QCD} as the deflection point of the strong coupling in the vacuum limit which we use in the following to express all dimensionful quantities. We find $\Lambda_{\mathrm{QCD}} \approx 209\,\mathrm{MeV}$ resulting in, e.g., $\Lambda/\Lambda_{\mathrm{QCD}} \approx 47.8$.

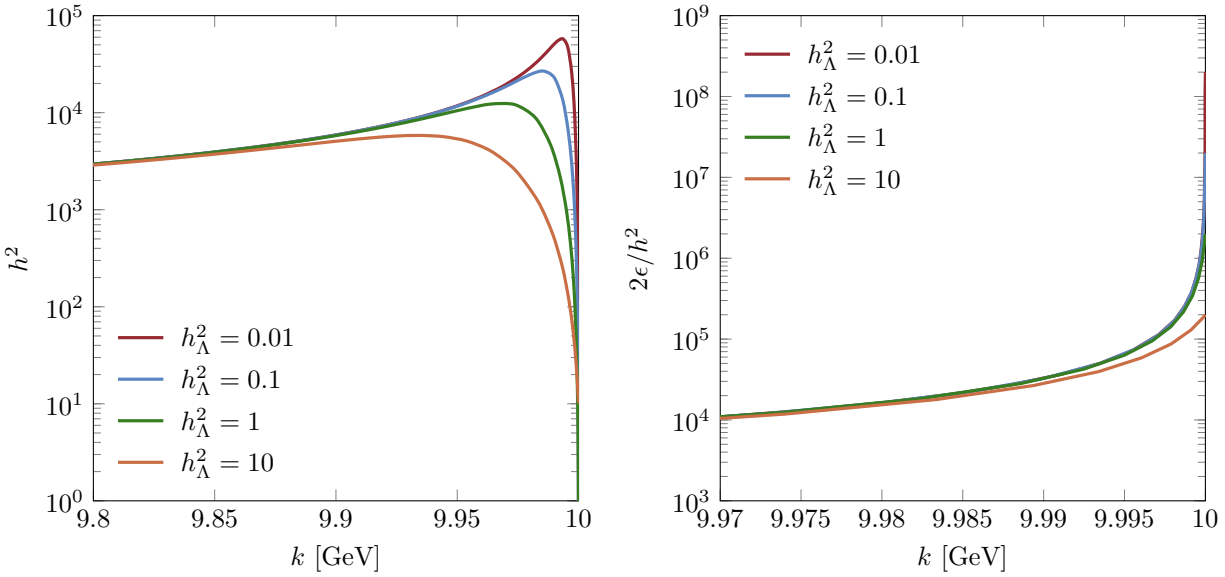

Figure 2.11: As an example of the effect of the initial conditions, we show the squared Yukawa coupling h^2 (left panel) and the inverse of the four-quark interaction $2\epsilon/h^2$ (right panel) as a function of the scale k for $\mu/\Lambda_{\mathrm{QCD}} = 2$. We only show k-values close to the initial RG scale $\Lambda = 10\,\mathrm{GeV}$. Note that we have varied the initial condition for the Yukawa coupling $h_\Lambda^2 = 0.01, 0.1, 1, 10$. Similar results are obtained by varying the initial condition for the renormalised dimensionless mass ϵ while ensuring $\lambda_{\mathrm{csc}} = h^2/(2\epsilon) \ll 1$ (or $2\epsilon/h^2 \gg 1$, see right panel). It turns out that the initial condition only has an impact on the flow of the couplings at scales (very) close to the initial RG scale $\Lambda = 10\,\mathrm{GeV}$. After almost "no RG time" has passed, an effect due to the different initial conditions cannot be seen in the flow any more. This effect is even smaller for the inverse of the four-quark coupling $2\epsilon/h^2$, see the reduced range of axis in the right panel.

Although the strong coupling is the only input parameter, we still need to determine the initial conditions for the remaining couplings at the UV scale Λ. However, these initial conditions arise from the way these couplings have been introduced into the ansatz (2.25) and the fact that, at the scale $k = \Lambda$, the effective action is expected to be given by the classical QCD action: $\Gamma_{k=\Lambda} = S$. As we have already mentioned before, the diquark sector has to decouple from the fermion sector at the initial RG scale. Accordingly, the diquark wavefunction renormalisation is expected to vanish $Z_\Delta \to 0$ at $k = \Lambda$ corresponding to $\epsilon \to \infty$. In this sense, the diquark fields are nondynamic, noninteracting, and heavy at Λ and effectively decouple from the fermion sector. In practice, we choose $Z_\Delta = 10^{-6}$ and $\epsilon = 10^6$ for the dimensionless renormalised curvature. Consequently, the dimensionful mass is of the order of the initial RG scale $\tilde{m}^2 = \Lambda^2$ at $k = \Lambda$. Note that this corresponds to $\bar{m}^2 = \tilde{m}^2 + 4Z_\Delta\mu^2 \approx \Lambda^2$ at $k = \Lambda$. Recall that $\Lambda \gg \mu$. However, the necessary initial condition is the one for $\tilde{m}^2$ anyhow since it represents the curvature of the diquark potential. For the squared Yukawa coupling, we set $h^2 = 0.01$. This choice ensures that the four-quark coupling associated with the diquark channel is small at the UV scale. Indeed, since it can be related to the renormalised diquark mass and the Yukawa interaction by $\lambda_{\mathrm{csc}} = h^2/(2\epsilon)$ and we have $\epsilon \gg h^2$, it is small at $k = \Lambda$. By doing so, the RG flow is initialised very close to the Gaussian fixed point of the four-quark interaction λ_{csc}. Lastly, we choose $\lambda_\Delta = 0$ at $k = \Lambda$. These initial conditions indeed guarantee that we consider QCD-like scenarios by initialising the system at least in the vicinity of the QCD action (2.4).
However, to assess and illustrate the impact of changes in the initial conditions on the couplings, we have varied the initial condition for the squared Yukawa coupling h^2 in Fig. 2.11. Our findings indicate that the

specific details of the initial conditions only affect the flow of the couplings very close to the initial RG scale. Furthermore, it seems as if the RG flow "forgets" about the details of the initial conditions after almost "no RG time" has passed. The behaviour originates from the appearance of pseudo-fixed points in the RG flow of the gluon-induced four-quark interaction channels, see Refs. [146, 171, 173–175] for a discussion for QCD in the vacuum limit. Provided that $k_{\mathrm{SB}} \ll \Lambda$, the effect of the initial conditions is indeed remarkably negligible. Therefore, the couplings and especially the diquark gap exhibit only a weak dependence on the initial conditions, if any at all. Moreover, it turns out that the important initial condition is to ensure that λ_{csc} is small at $k = \Lambda$ which is guaranteed by our choice for the initial conditions.
Another uncertainty, apart from the experimental error of the strong coupling, arises because of the regulator. In the present study, we use polynomial regulator shape functions. With these, we can conveniently assess the impact of the regulator by varying the order of the polynomial shape function. In practice, we use $N = 4$, 6, and 8. The corresponding shape functions can be found in App. B.2. However, it turns out that uncertainties from the variation of the order of the polynomial regulator are negligible compared to the ones from the experimental error of the strong coupling, see Fig. 2.17 in Sec. 2.5 for an illustration of the error from the variation of the regulator.

2.4.2 RG Flows

Finally, we turn to the discussion of the results from the solution of the flow equations. We show the flow of the (squared) renormalised Yukawa coupling h^2, the renormalised four-diquark coupling λ_Δ, and the renormalised strong coupling $\alpha = g^2/(4\pi)$ over a wide range of scales for two different chemical potentials, $\mu/\Lambda_{\mathrm{QCD}} = 2$ and $\mu/\Lambda_{\mathrm{QCD}} = 10$, in Fig. 2.12. We also show the flow of the renormalised dimensionless curvature ϵ for $k \geq k_{\mathrm{SB}}$ and the diquark gap $\Delta_{\mathrm{gap}} = hk\sqrt{\kappa}$ for $k \leq k_{\mathrm{SB}}$ for $\mu/\Lambda_{\mathrm{QCD}} = 2$ in Fig. 2.13 and for $\mu/\Lambda_{\mathrm{QCD}} = 10$ in Fig. 2.14. Here, we have defined the diquark gap which is the gap in the fermionic excitation spectrum and appears in the quark propagators. For $\mu/\Lambda_{\mathrm{QCD}} = 2$, the symmetry-breaking scale is given by $k_{\mathrm{SB}}/\Lambda_{\mathrm{QCD}} \approx 1.09$ and for $\mu/\Lambda_{\mathrm{QCD}} = 10$, the symmetry-breaking scale is given by $k_{\mathrm{SB}}/\Lambda_{\mathrm{QCD}} \approx 1.61$. Symmetry breaking is indicated by a diverging four-quark interaction which translates into a vanishing curvature ϵ, see Fig. 2.13 and Fig. 2.14. In the present section, we have fixed the strong coupling with $g^2(\Lambda) = 4\pi \cdot 0.179$. However, we shall include the experimental error of the strong coupling (along with uncertainties from a variation of the regularisation scheme) in results for the diquark gap and the long-range limit for the couplings in Sec. 2.5.
Let us begin our discussion with the couplings in the symmetric phase. Note that both, the squared Yukawa coupling h^2 and the diquark coupling λ_Δ, seem to have large values at the initial RG scale. However, this apparent behaviour is simply a consequence of the existence of pseudo-fixed points in the RG flow [146, 171, 173–175]. In reality, both couplings start with very small values at Λ but rapidly increase in the RG flow already in the vicinity of the initial scale Λ, see also our discussion above. This behaviour can, for the (squared) Yukawa coupling, be seen in Fig. 2.11 (left panel). Towards the long-range limit, the couplings decrease again, and the curvature of the diquark potential ϵ eventually "hits" zero. This indicates the onset of the spontaneous breakdown of the $\mathrm{U}(1)_V$ symmetry associated with the symmetry-breaking scale k_{SB}. This behaviour is driven by gluon-exchange diagrams associated with the strong coupling g which increases towards smaller scales. The existence of a colour-superconducting ground state associated with spontaneous symmetry breaking of the $\mathrm{U}(1)_V$ symmetry should, however, not rely on *strong* gauge fluctuations. Instead, the existence of a Cooper instability in the system should trigger the aforementioned symmetry breaking, even for an arbitrarily small strong coupling [85, 165, 193]. The gauge fluctuations enhance the formation of the colour-superconducting ground state. In this sense, *strong* gauge fluctuations also increase the symmetry-breaking scale k_{SB} and the diquark gap $\Delta_{\mathrm{gap}} \sim k_{\mathrm{SB}}$.

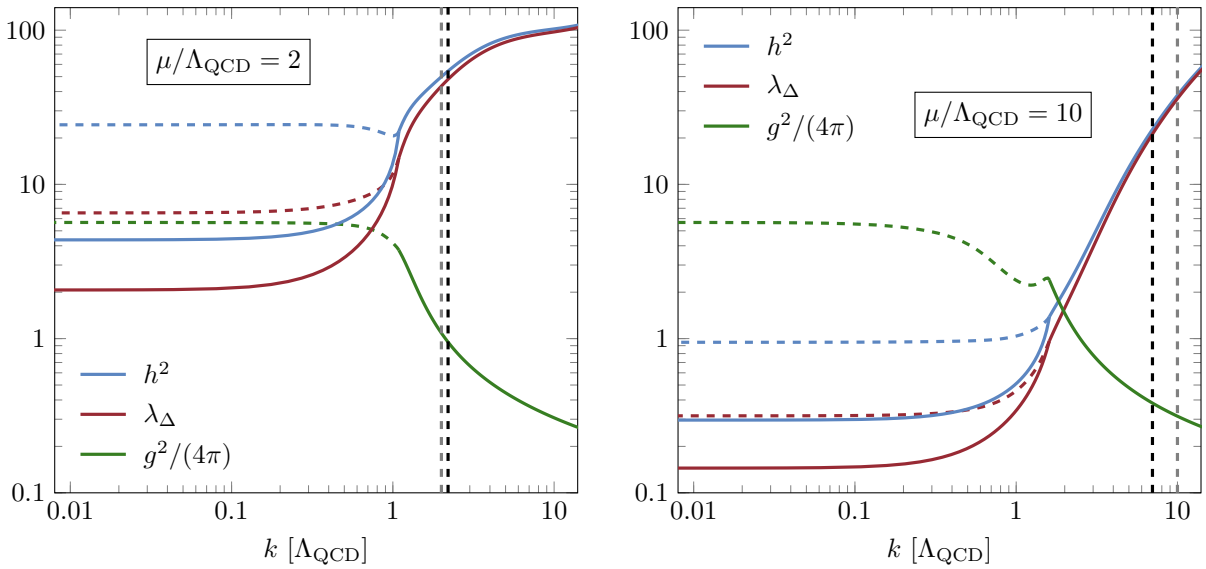

Figure 2.12: Flow of the renormalised (squared) Yukawa coupling h^2, four-diquark coupling λ_Δ, and strong coupling $\alpha = g^2/(4\pi)$ for two different chemical potentials, namely $\mu/\Lambda_{\mathrm{QCD}} = 2$ (left panel) and $\mu/\Lambda_{\mathrm{QCD}} = 10$ (right panel). The grey (vertical) dashed line is associated with the scale $k = \mu$ and the black (vertical) dashed line is associated with the scale $k = k_{\mathrm{m}}$, which is the scale where gluon screening masses exceed the scale k, see main text for details. The couplings are given by solid and dashed lines. The dashed lines represent results where the gluons remain ungapped and do not acquire a mass according to the Anderson-Higgs-type mechanism. Solid lines have been obtained by fully decoupling gluons from the matter sector for $k < k_{\mathrm{SB}}$, effectively "infinitely" gapping all gluons.

We have not included any gluon screening masses in our present calculation. However, we discuss their qualitative impact in the following. For this purpose, we introduced the scale k_{m} which is an estimate for the scale at which the gluon screening masses exceed the scale k in Figs. 2.12–2.14 (black vertical dashed lines). For the gluon screening mass m_{g} in the high-energy symmetric regime $k > k_{\mathrm{SB}}$, we use $m_{\mathrm{g}} = g(k)\mu/\pi$ [319, 320]. Note that we do not distinguish between electric and magnetic masses here. The estimate for the scale k_{m} is then obtained by considering $m_{\mathrm{g}} = g(k_{\mathrm{m}})\mu/\pi = k_{\mathrm{m}}$. However, these quantities are scheme dependent. A more qualitative discussion of the effect of gluon screening masses on our present results will be postponed to future studies. In Sec. 2.6.1, we shall at least present the RG flow equations in the symmetric high-energy regime including gluon screening masses.

For $\mu/\Lambda_{\mathrm{QCD}} = 2$, the scale, where the screening masses of the gluons exceed the scale k, is given by $k_{\mathrm{m}}/\Lambda_{\mathrm{QCD}} \approx 2.20$. Therefore, we find a clear hierarchy of scales: $k_{\mathrm{SB}} < \mu < k_{\mathrm{m}}$. In the range $k > k_{\mathrm{m}}$, we do not expect that the inclusion of gluon screening masses influences the RG flows of the various couplings significantly because the corresponding effects are suppressed as $m_{\mathrm{g}}/k < 1$. Further, effects from the appearance of the quark chemical potential in the quark propagators are even more suppressed: $\mu/k < m_{\mathrm{g}}/k < 1$. However, in the regime $k_{\mathrm{SB}} < k < k_{\mathrm{m}}$, we expect that effects from the inclusion of gluon screening masses become relevant because $m_{\mathrm{g}}/k > 1$. Therefore, at least one internal gluon line is suppressed. Because gluons drive the spontaneous symmetry breaking, we expect that gluon screening masses lower the symmetry-breaking scale and the diquark gap compared to our present study. However, considering that the scale where gluon screening effects become important for small chemical potential, e.g., $k_{\mathrm{m}}/\Lambda_{\mathrm{QCD}} \approx 2.20$ (for $\mu/\Lambda_{\mathrm{QCD}} = 2$), is not much greater than the symmetry-breaking scale, e.g., $k_{\mathrm{SB}}/\Lambda_{\mathrm{QCD}} \approx 1.09$ (for $\mu/\Lambda_{\mathrm{QCD}} = 2$), we expect

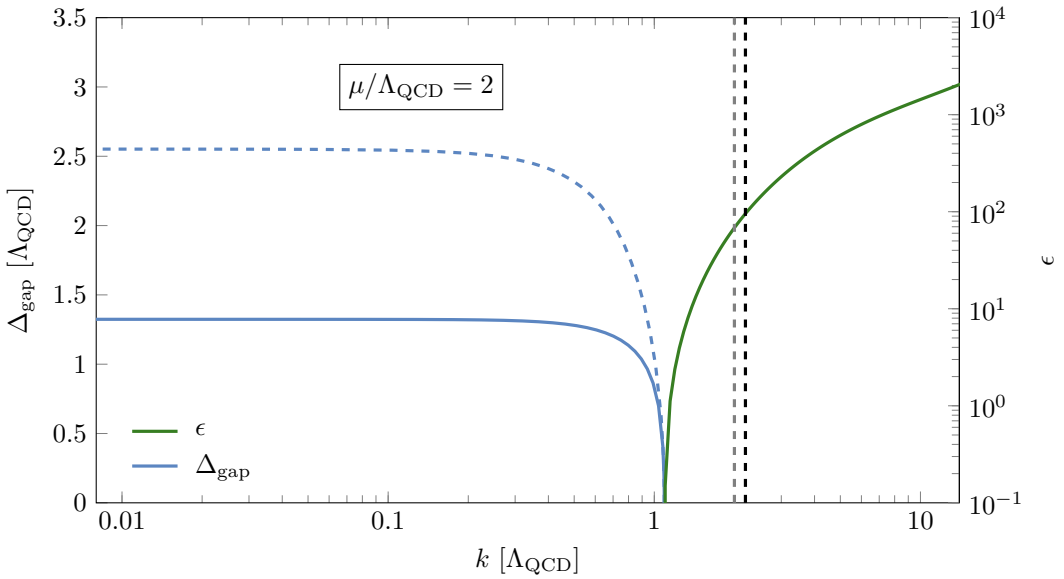

Figure 2.13: Renormalised dimensionless curvature ϵ for $k \geq k_{\mathrm{SB}}$ and the diquark gap $\Delta_{\mathrm{gap}} = hk\sqrt{\kappa}$ for $k \leq k_{\mathrm{SB}}$ for $\mu/\Lambda_{\mathrm{QCD}} = 2$. The grey (vertical) dashed line is associated with the scale $k = \mu$. The black (vertical) dashed line is associated with the scale $k = k_{\mathrm{m}}$, see main text for details. The symmetry-breaking scale for $\mu/\Lambda_{\mathrm{QCD}} = 2$ is given by $k_{\mathrm{SB}}/\Lambda_{\mathrm{QCD}} \approx 1.09$. Below the symmetry-breaking scale, the diquark gap is given by solid and dashed lines, respectively. Dashed lines represent the results where the gluons remain ungapped whereas solid lines correspond to "infinitely" gapped gluons where they have effectively been decoupled from the matter sector for $k < k_{\mathrm{SB}}$.

that our results do not suffer too much from neglecting gluon screening effects, at least when considering small chemical potentials. Indeed, the range in the RG flow where gluon screening effects become important is comparatively small.

In contrast to that, for larger chemical potentials, we find that screening effects have to be considered over a larger range in the RG flow. For example, for $\mu/\Lambda_{\mathrm{QCD}} = 10$, the scale where the screening masses of the gluons exceed the scale k is given by $k_{\mathrm{m}}/\Lambda_{\mathrm{QCD}} \approx 6.99$. Compared to the symmetry-breaking scale which does not depend too much on the chemical potential, so that $k_{\mathrm{SB}}/\Lambda_{\mathrm{QCD}} \approx 1.61$, we find that a larger range in the RG flow may be affected by gluon screening effects. Furthermore, the hierarchy of scales changes so that we find $k_{\mathrm{SB}} < k_{\mathrm{m}} < \mu$. It follows that the effect of the quark chemical potential in the quark propagators is now greater than effects from gluon screening masses over a wide range of scales. However, the gluon screening masses scale roughly linearly with μ. Therefore, by going to larger chemical potentials, also the gluon screening masses increase. This suggests a stronger suppression of gluonic contributions at large chemical potential compared to small chemical potential and a stronger impact of gluon screening effects over a larger range of scales. We therefore expect that our results may become less reliable for larger chemical potentials where gluon screening effects have a stronger impact. Indeed, this may potentially lead to a decrease in the symmetry-breaking scale (and consequently the diquark gap) for very large chemical potentials in contrast to the conventional increase according to the BCS-type scaling at lower densities [40, 82, 84–86]. However, for even larger chemical potentials (beyond those considered in the present work) it is expected that the diquark gap increases as a function of the chemical potential again, see Refs. [82, 83, 87, 88, 90]. Motivated by this discussion, we focus on $\mu/\Lambda_{\mathrm{QCD}} \leq 5$ in the following. Note, however, that the inclusion of gluon screening effects shall be discussed in Sec. 2.5 in more detail.

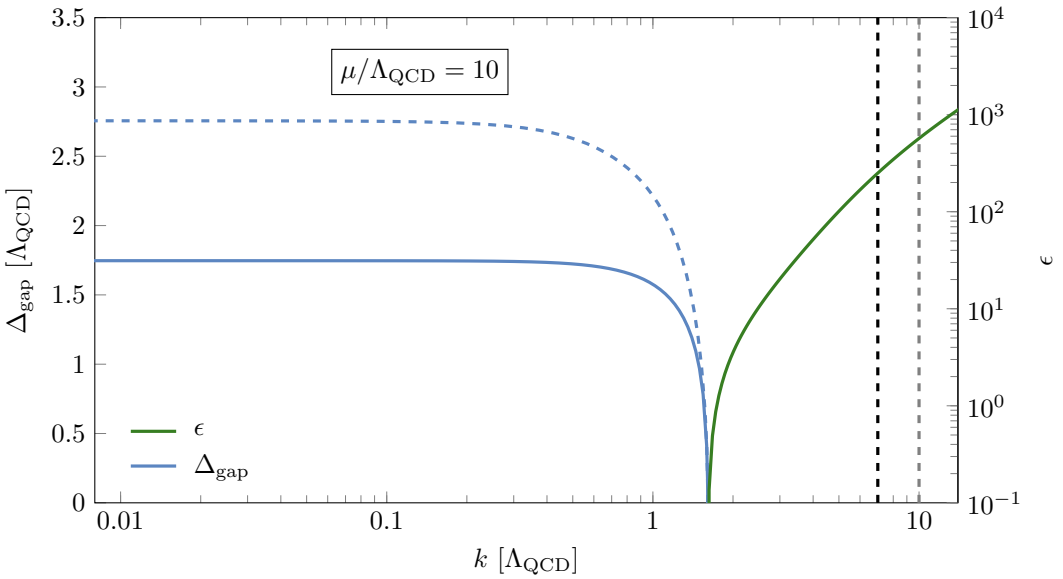

Figure 2.14: Renormalised dimensionless curvature ϵ for $k \geq k_{\mathrm{SB}}$ and the diquark gap $\Delta_{\mathrm{gap}} = hk\sqrt{\kappa}$ for $k \leq k_{\mathrm{SB}}$ for $\mu/\Lambda_{\mathrm{QCD}} = 10$. The grey (vertical) dashed line is associated with the scale $k = \mu$. The black (vertical) dashed line is associated with the scale $k = k_{\mathrm{m}}$, see main text for details. The symmetry-breaking scale for $\mu/\Lambda_{\mathrm{QCD}} = 10$ is given by $k_{\mathrm{SB}}/\Lambda_{\mathrm{QCD}} \approx 1.61$. Below the symmetry-breaking scale, the diquark gap is given by solid and dashed lines, respectively. Dashed lines represent the results where the gluons remain ungapped whereas solid lines correspond to "infinitely" gapped gluons where they have effectively been decoupled from the matter sector for $k \leq k_{\mathrm{SB}}$.

The situation becomes even more involved below the symmetry-breaking scale. As already mentioned before, the emergence of a diquark gap for $k \leq k_{\mathrm{SB}}$ requires the inclusion of an Anderson-Higgs-type mechanism [61–66] associated with the symmetry breaking SU(3) to SU(2) in colour space. Then, only three of the eight gluons are massless while the others effectively acquire a screening mass which is related to the diquark gap. In this sense, five of the eight gluons are "gapped" below the symmetry-breaking scale. However, an inclusion of this effect is beyond the scope of the present work. Instead, we consider two approximations for $k \leq k_{\mathrm{SB}}$ in the following so that we can assess the effects of gluon gapping and already gain an insight into the effect of gluon screening in the long-range limit. Firstly, we assume that all gluons remain ungapped for $k \leq k_{\mathrm{SB}}$ and, therefore, do not acquire a mass in contrast to what is expected according to the Anderson-Higgs-type mechanism. In the following, we refer to this approximation as "ungapped" gluons. Secondly, we decouple the gluons from the matter sector which can be viewed as "infinitely" gapping the gluons for $k \leq k_{\mathrm{SB}}$. Therefore, we refer to this as "gapped" gluons in the following. In our calculation, we have implemented this by effectively dropping the quark-gluon interaction by setting the strong coupling to zero for $k \leq k_{\mathrm{SB}}$. The results for the couplings resulting from these two approximations are given as solid and dashed lines for $k \leq k_{\mathrm{SB}}$, respectively. Dashed lines represent the running of these quantities for "ungapped" gluons whereas solid lines show the results for "gapped" gluons, where the gluons have been fully decoupled from the matter sector for $k \leq k_{\mathrm{SB}}$. Notably, when comparing "gapped" gluons with "ungapped" gluons, the diquark gap is approximately reduced by a factor of two for $\mu/\Lambda_{\mathrm{QCD}} = 2$ and by roughly a factor of 1.5 for $\mu/\Lambda_{\mathrm{QCD}} = 10$. This result can also be observed in the result for the diquark gap as a function of the chemical potential in the subsequent section. In addition to that, also the couplings shown in Fig. 2.12 are (significantly) smaller for "gapped" gluons. This is also present in the results for the couplings in the long-range limit as a function

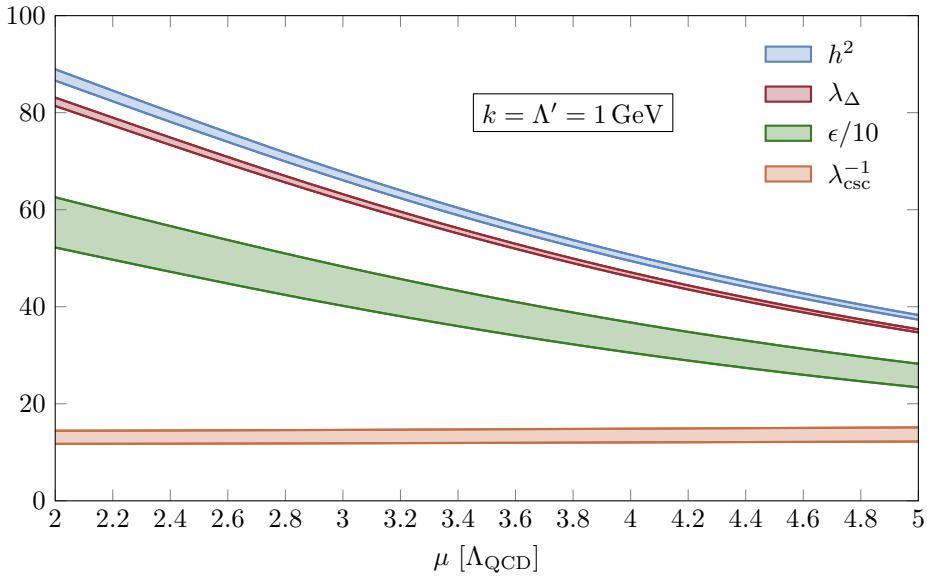

Figure 2.15: Diquark coupling λ_Δ (green band), squared Yukawa coupling h^2 (blue band), renormalised dimensionless curvature of the diquark potential ϵ (red band), and inverse of the four-quark interaction $\lambda_{\mathrm{csc}}^{-1} = 2\epsilon/h^2$ (orange band) as a function of the chemical potential. Here, we have evaluated the couplings at a scale $k = \Lambda' = 1\,\mathrm{GeV} \approx 4.8\Lambda_{\mathrm{QCD}}$ above the symmetry-breaking scale: $\Lambda' > k_{\mathrm{SB}}$. The bands represent the uncertainties from the experimental error of the strong coupling and a variation of the regularisation scheme.

of the chemical potential shown in the subsequent section. This behaviour can already be understood from considering that gluons boost the formation of the colour-superconducting ground state. By gapping/screening the gluons, these effects are effectively suppressed which leads to a smaller diquark gap.
To conclude this section, we show the couplings at a scale above the symmetry-breaking scale in Fig. 2.15. The values of the couplings can be used to, e.g., extract parameters for low-energy models. However, this task can be difficult because the couplings are in general scheme-dependent quantities. In practice, it might therefore be easier to fix the model parameters at observables obtained in the long-range limit $k \to 0$ such as the diquark gap. Nevertheless, the qualitative behaviour of the couplings at a scale above the symmetry-breaking scale might still be of interest. We shall include these results in the considerations underlying the construction of a low-energy model in Sec. 3.1. As shown in Fig. 2.15, we find that the diquark coupling λ_Δ, the squared Yukawa coupling h^2, and the dimensionless curvature of the diquark potential ϵ show the same qualitative behaviour and decrease towards higher chemical potentials. Notably, the inverse of the four-quark interaction is almost constant for the entire range of chemical potentials considered in the present study.

2.5 Diquark Gap and Low-Energy Couplings

At the heart of the present study is the calculation of the diquark gap which corresponds to a gap in the excitation spectrum of the quarks closely connected to the formation of a colour-superconducting ground state. We show the results for the symmetry-breaking scale k_{SB} and the diquark gap $\Delta_{\mathrm{gap}} = \bar{h} Z_\psi^{-1} |\Delta_0| = h\sqrt{\kappa} k$ in the limit $k \to 0$ in Fig. 2.16. As in the preceding section, we consider two approximations below the symmetry-breaking scale: Dashed lines represent "ungapped" gluons and solid lines represent "gapped" gluons. Further details regarding these approximations can be found in Sec. 2.4.2. Within the range of chemical potentials considered in the present study, we find that the diquark gap and the symmetry-breaking scale, as a function of

the chemical potential, in both approximations, are consistent with the standard BCS-type scaling behaviour (as expected from relativistic models, see Refs. [40, 82, 84–86]), i.e., it increases as a function of the chemical potential. As discussed in the preceding section, we find that the gap is approximately twice as big in the case for "ungapped" gluons compared to "gapped" gluons.

It is also possible to find an analytic estimate for the scaling behaviour of the symmetry-breaking scale and the diquark gap, at least for small chemical potential, based on the following considerations: We can recover the running of the four-quark interaction $\lambda_{\text{csc}} = h^2/(2\epsilon)$ above the symmetry-breaking scale from the running of the curvature of the potential ϵ, see Eq. (2.79), and the squared Yukawa coupling h^2, see Eq. (2.80), which yields

$$\partial_t \lambda_{\text{csc}} = 2\lambda_{\text{csc}} + 16\lambda_{\text{csc}}^2 \mathcal{L}_{\text{ff}}^{(2)} + \frac{16}{3} g^2 \lambda_{\text{csc}} \mathcal{L}_{\text{bff}}^{(2)} + g^4 \mathcal{L}_{\text{bbff}}^{(A)} . \tag{2.90}$$

Provided that the strong coupling g is sufficiently small, the RG flow is governed by two fixed points for large scales k which can be translated into fixed points for the Yukawa coupling h and the curvature ϵ, see Ref. [273]. At the initial RG scale Λ, the four-quark interaction is small $\lambda_{\text{csc}} \approx 0$ which corresponds to $\epsilon \gg h^2$. Therefore, the RG flow is dominated by the two-gluon exchange diagram $\sim g^4$ whereas the remaining contributions are initially subleading so that the flow equation reduces to

$$\partial_t \lambda_{\text{csc}} = 2\lambda_{\text{csc}} + g^4 \mathcal{L}_{\text{bbff}}^{(A)} . \tag{2.91}$$

In the region where this approximation is feasible, we have $\mathcal{L}_{\text{bbff}}^{(A)} < 0$. In the following, we assume that we can split the RG flow above the symmetry-breaking scale into two regions separated by some scale $\bar{k}$: For $k > \bar{k}$, the RG flow is dominated by two-gluon exchange $\sim g^4$ so that the flow equation for the four-quark interaction is given by (2.91). For $k < \bar{k}$, however, the four-quark interaction has become strong enough so that it dominates its own flow. In this region ($k < \bar{k}$), contributions from the quark-gluon interaction, $\sim g^4$ and $\sim g^2$, can be dropped in Eq. (2.90) so that the flow equation for the four-quark interaction is given by

$$\partial_t \lambda_{\text{csc}} = 2\lambda_{\text{csc}} + 16\lambda_{\text{csc}}^2 \mathcal{L}_{\text{ff}}^{(2)} . \tag{2.92}$$

Note that $\mathcal{L}_{\text{ff}}^{(2)} < 0$. We expect that the aforementioned scale $\bar{k}$ exists such that the approximations underlying Eqs. (2.91) and (2.92) are reasonable, at least for sufficiently small chemical potential. With these assumptions, we find an estimate for the symmetry-breaking scale k_{SB}. For this, we start by assuming that the dependence on the chemical potential of the two-gluon exchange diagram is negligible for $k > \bar{k}$, so that Eq. (2.91) can be integrated analytically from $k = \Lambda$ to $k = \bar{k}$ which yields

$$\lambda_{\text{csc}}(\bar{k}) = -\frac{1}{2} \mathcal{L}_{\text{bbff}}^{(A)} g^4(\bar{k}) + \mathcal{O}(g^6) . \tag{2.93}$$

Here, we have dropped terms that are small for $\Lambda \gg \bar{k}$ and terms from higher-order gluon interactions. In the region, where the RG flow is dominated by four-quark interactions ($k < \bar{k}$), the flow equation of the four-quark interaction is given by Eq. (2.92). This flow equation is valid up to the symmetry-breaking scale and its initial condition at $k = \bar{k}$ is given by Eq. (2.93). The symmetry-breaking scale is given by the scale k at which the curvature of the diquark potential ϵ becomes zero, causing the four-quark interaction $\lambda_{\text{csc}} = h^2/(2\epsilon)$ to diverge: $1/\lambda_{\text{csc}}(k_{\text{SB}}) = 0$. Moreover, for $k < \bar{k}$ the RG flow enters a regime in which the loop diagram $\sim \lambda_{\text{csc}}^2$ appearing in Eq. (2.92) can be estimated by $\mathcal{L}_{\text{ff}}^{(2)} \sim -c_\psi(\mu^2/k^2)$ for $\mu > k$, where c_ψ is a dimensionless scheme-dependent constant. With these assumptions, we can now integrate (2.92) and identify the estimate for the symmetry-breaking scale: $k_{\text{SB}} \sim \bar{k} \exp(-\bar{k}^2/(16 c_\psi \lambda_{\text{csc}}(\bar{k})\mu^2))$. With the relation for $\lambda_{\text{csc}}(\bar{k})$, see Eq. (2.93), we obtain an estimate for the scaling behaviour of the symmetry-breaking scale. Taking further into account that the symmetry-breaking scale sets the scale for low-energy observables, such as the diquark gap, we find

$$\Delta_{\text{gap}} \sim k_{\text{SB}} \sim \exp\left(-\frac{\bar{c}}{g^4 \mu^2}\right) , \tag{2.94}$$

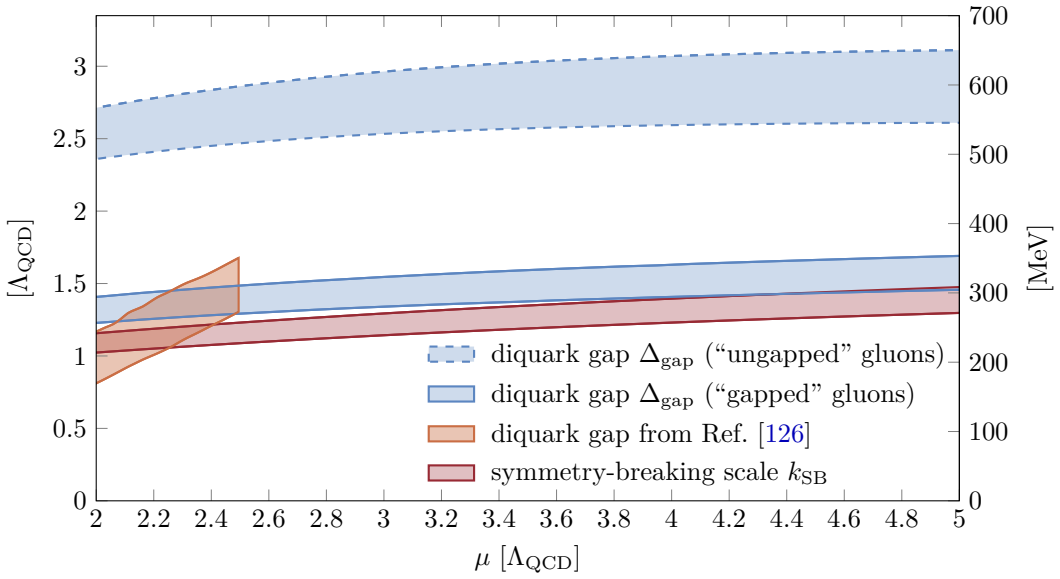

Figure 2.16: Diquark gap Δ_{gap} and symmetry-breaking scale k_{SB} (red band) as a function of the chemical potential in units of the QCD scale $\Lambda_{\mathrm{QCD}} = 209\,\mathrm{MeV}$. We show the diquark gap for two different approximations: The dashed blue band (“ungapped” gluons) represents the result where we have left the gluons ungapped in the broken phase $k \leq k_{\mathrm{SB}}$ whereas we have “infinitely” gapped the gluons for the solid blue band (“gapped” gluons) and thereby have decoupled them from the matter sector for $k \leq k_{\mathrm{SB}}$. We compare these results, obtained in the present work, with a previous fRG study from Ref. [126] (orange band) where the range of chemical potentials shown is associated with densities $n/n_0 \approx 6 \ldots 12$. Here, n_0 is the nuclear saturation density. The bands for the gap and the symmetry-breaking scale (apart from the orange band) represent the uncertainty of the strong coupling at the initial RG scale where we have used $g^2(\Lambda) = 4\pi \cdot (0.179 \pm 0.004)$. Further, they include a variation of the regularisation scheme in terms of the order of the polynomial regulator. However, the dependence on the regulator scheme is negligible compared to the uncertainties arising from the strong coupling, see Fig. 2.17. The orange band represents an estimate for the theoretical uncertainties in the corresponding study, see Ref. [126] and main text for details.

where $\bar{c} = -\bar{k}^2/(8c_\psi \mathcal{L}^{(A)}_{\mathrm{bbff}})$ is a positive constant and the strong coupling is evaluated at $\bar{k}$. The relation between the symmetry-breaking scale and the diquark gap is also reflected in our numerical results, see Fig. 2.16. Furthermore, as also indicated by the numerical results and the estimate (2.94), the diquark gap seems to saturate with increasing chemical potential.

Comparing our analytic estimate for the diquark gap with other studies, we find that it differs from the one in, e.g., Refs. [82, 84, 321, 322]. There, it was found that $\Delta_{\mathrm{gap}} \sim k_{\mathrm{SB}} \sim \exp(-\bar{c}'/(g^2\mu^2))$, where $\bar{c}'$ is a positive constant. Although the dependence on the chemical potential is identical, the dependence on the strong coupling is different. The dependence on the strong coupling $\sim g^2$ can be traced back to the assumption $\lambda_{\mathrm{csc}} \sim g^2$ which is associated with a tree-level consideration involving a one-gluon exchange. In contrast to that, loop contributions to λ_{csc} in the present work lead to a dependence $\sim g^4$. As a result, the gap as considered in the present work increases more rapidly coming from small chemical potentials. As we have already observed, the assumptions underlying the analytic estimate for the diquark gap are only valid for small chemical potential. Going beyond chemical potentials considered in the present work to very large chemical potentials, it is expected that the gap increases according to $\Delta_{\mathrm{gap}} \sim \mu \exp(-\bar{c}''/g)$, where $\bar{c}''$ is a positive constant. However, $\Delta_{\mathrm{gap}}/\mu$ is expected to decrease, see Refs. [50, 82].

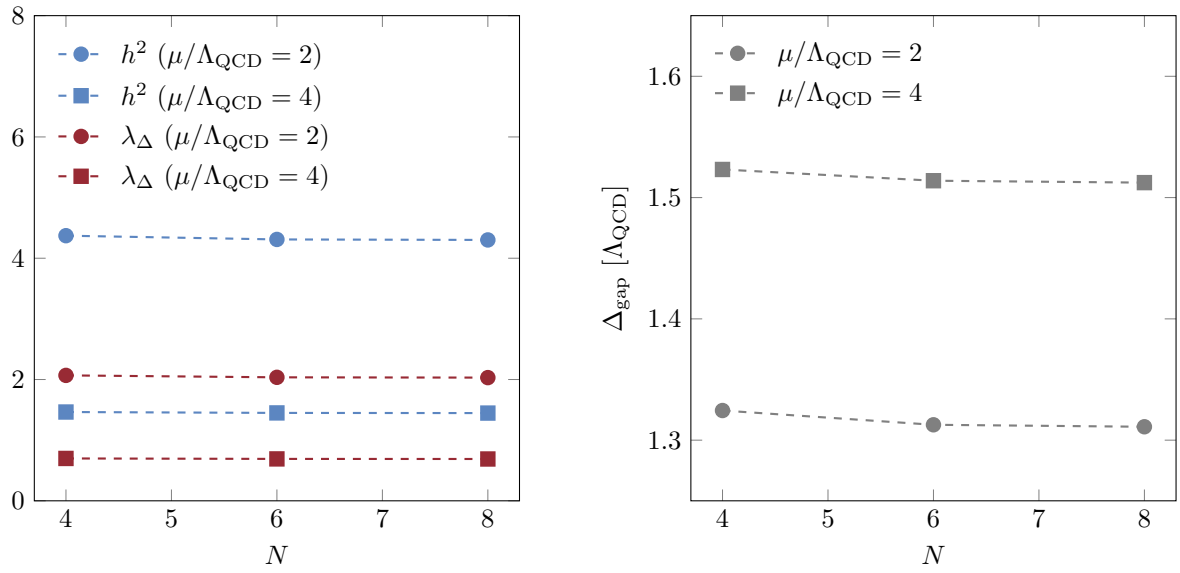

Figure 2.17: Regulator dependence of the infrared values of the (squared) Yukawa coupling h^2 and the diquark coupling λ_Δ (left panel) and the diquark gap Δ_{gap} (right panel) for two values of the chemical potential. The parameter N specifies the order of the polynomial regulator, see App. B.2 for the definition of the fermionic and bosonic regulator shape functions. We show the regulator dependence for the approximation referred to as "gapped" gluons and used $g^2(\Lambda) = 4\pi \cdot 0.179$ for the value of the strong coupling at the initial RG scale. We find that the regulator dependence is small compared to uncertainties arising from a variation of the strong coupling at the initial RG scale.

A more quantitative comparison of our present results for the diquark gap can be done by considering results from a previous fRG calculation where they have also started from the underlying quark-gluon dynamics and have, in contrast to the present work, used a Fierz-complete ansatz, see Fig. 2.16 (orange band) [126]. It should be emphasised that a comparison is difficult because it requires the diquark gap as a function of the density. The calculation of the diquark gap as a function of the density requires the pressure as a function of the chemical potential, which is not accessible in the present study. However, we shall come back to this comparison in Sec. 3.1 where the consideration of a low-energy model allows us to estimate the density. Nonetheless, a comparison at this point might already provide insight into the underlying dynamics.
For this, we compare our results for the diquark gap from a computation with "gapped" gluons with the results from the previous fRG study [126]. We consider the results for "gapped" gluons because gluonic contributions are at least partially suppressed below the symmetry-breaking scale due to the Anderson-Higgs-type mechanism resulting in a gap for the gluons. Only considering the diquark channel, as done in the present work, seems to have less of an impact at large chemical potential in contrast to employing a Fierz-complete ansatz. This result has been expected since, in the large chemical potential regime, the diquark channel has been found to be the most dominant [179]. Consequently, for chemical potentials with diquark channel dominance, the results are remarkably consistent. However, for small chemical potential, the present results exceed the results from the aforementioned previous fRG calculation. For small chemical potential, the scalar-pseudoscalar channel becomes dominant, and the dominance pattern becomes even more involved in the transition region [167–169, 179]. Therefore, our results become less reliable towards the small chemical potential regime, and Fierz completeness becomes more and more important. In practice, we find that our present results for the diquark gap exceed those from Ref. [126] for $\mu/\Lambda_{\mathrm{QCD}} \lesssim 2.1$. However,

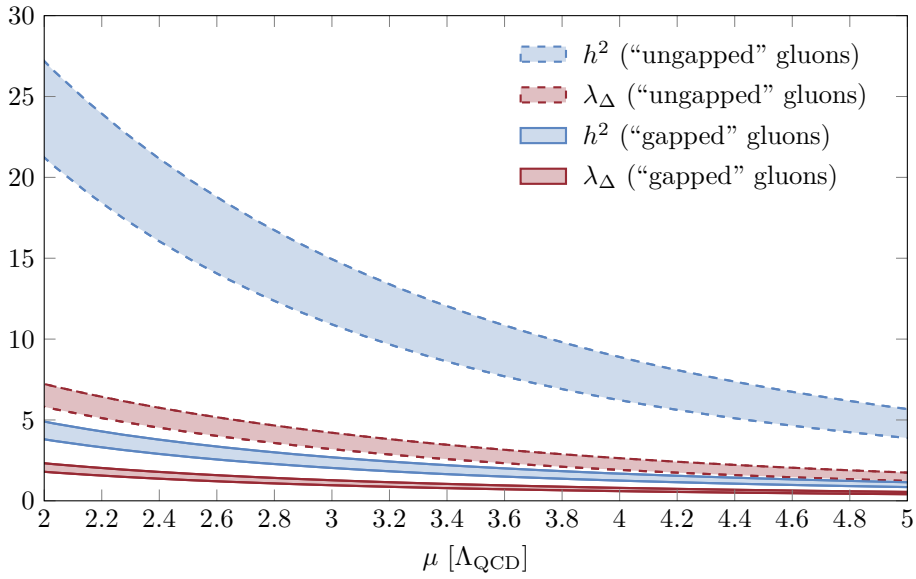

Figure 2.18: Squared Yukawa coupling h^2 and diquark coupling λ_Δ as a function of the chemical potential μ in units of the QCD scale $\Lambda_{\mathrm{QCD}} = 209\,\mathrm{MeV}$. We show results for "gapped" gluons (dashed lines) and for "ungapped" gluons (solid lines). The bands represent the error resulting from the uncertainties in the strong coupling and a variation of the regularisation scheme in terms of the order of the polynomial regulator. However, the dependence on the regulator scheme is much smaller compared to the uncertainties arising from the strong coupling, see Fig. 2.17.

towards larger chemical potentials, the range of chemical potentials accessible in the present work is only restricted by $\mu \ll \Lambda$. In contrast to that, in Ref. [126], the transition between high-energy degrees of freedom and the effective low-energy regime in terms of a Hubbard–Stratonovich transformation has been performed at a fixed scale Λ_0. This scale introduces a new artificial uncertainty, see Fig. 2.16 (orange band), and restricts the range of chemical potentials that is accessible within this framework to $\mu \lesssim \Lambda_0$. Notably, this artificial dependence on the scale Λ_0 has been removed in the present work by implementing the dynamical bosonisation technique in which the aforementioned transition from high-energy degrees of freedom to the effective low-energy regime is performed continuously. This is a powerful extension of the fRG results from Ref. [126] and already gives meaningful results at least in the chemical potential range that is dominated by the diquark channel. An extension to cover a larger range towards the small chemical potential regime by including at least the scalar-pseudoscalar channel is also expected to be possible, but it is beyond the scope of the present work. We close this discussion of the diquark gap by remarking that, towards smaller chemical potentials associated with densities $n/n_0 \lesssim 5$, the results from Ref. [126] are consistent with results from early low-energy models, see, e.g., Ref. [85]. There, it has been found that for $n/n_0 \approx 5$ the diquark gap is given by $\Delta_{\mathrm{gap}} \approx 70 \ldots 160\,\mathrm{MeV}$.

Finally, we would like to comment on the low-energy couplings ($k \to 0$). We show results for the squared Yukawa coupling h^2 and the diquark coupling λ_Δ in the long-range limit $k \to 0$ in Fig. 2.18. These couplings are often used in the construction of low-energy models although they are scheme-dependent quantities. As before, we show the results for two approximations: Dashed lines represent "ungapped" gluons and solid lines represent "gapped" gluons. See Sec. 2.4.2 for more details on the approximation. We find, as also observed for the diquark gap, that the couplings are bigger in the case of "ungapped" gluons compared to

the approximation with "gapped" gluons. However, their qualitative behaviour as a function of the chemical potential agrees and they decrease by increasing the chemical potential. Note that increasing the chemical potential leads to a decrease in the four-diquark interaction λ_Δ and it also leads to an increase in the minimum of the potential towards larger values. This effect of an increasing minimum is almost cancelled by the fact that the Yukawa coupling decreases with increasing chemical potential so that the diquark gap Δ_{gap} is almost constant across the range of chemical potentials considered in the present work and saturates towards larger chemical potentials. In addition to that, the decreasing couplings indicate that the interactions between quarks and diquarks and among diquarks themselves become weaker when the chemical potential is increased. Therefore, the system is expected to turn into weakly coupled colour-superconducting matter at (very) high densities (associated with large chemical potentials).

2.6 The Influence of Diquark Fluctuations and the Emergence of the Gluon-Diquark Interaction

In the previous sections, we have used some approximations and assumptions in the calculation of the gap and the symmetry-breaking scale. In the following, we improve some of these approximations and test whether the corresponding assumptions have been justified. Although we do not overcome all the assumptions, we expect that, with the present section, we can demonstrate that the foundations laid in the present work allow us to systematically improve nonperturbative studies of dense strong-interaction matter. Additionally, we provide further insight into the dynamics of dense strong-interaction matter by giving updates for the RG flow of dense matter and by comparing the symmetry-breaking scale and the diquark gap.
Since the diquark fields carry a net colour charge and consequently transform under SU(3) colour transformations similar to the quarks, they interact with the gluons. This requires to introduce gluon-diquark interactions and to take into account the flow of the corresponding couplings, which we consequently consider in the following. So far, we have dropped diquark fluctuations since they are expected to be suppressed at least in the symmetric phase where we include them anyway in the following. Below the symmetry-breaking scale, their inclusion would require to consider an Anderson-Higgs-type mechanism [61–66] which effectively suppresses gluonic contributions. However, this is beyond the scope of the present work. Therefore, in the broken phase, we apply the approximations from the previous section and decouple the matter sector from the gauge sector by effectively infinitely gapping the gluons. In addition to these improvements, we also include the quark anomalous dimension, which modifies the quark propagators, and we investigate the influence of the gauge parameter ξ on the results. In particular, we compare Landau and Feynman gauge.
These extensions are already taken into account in the derivation of the dynamical bosonisation in Sec. 2.3.1. In the following section, we present updates of our RG formalism. In particular, Sec. 2.6.1 provides updates for the flow equations presented Sec. 2.3.2 and Sec. 2.6.2 for the RG flows shown in Sec. 2.4.2. In Sec. 2.6.3, new results for the diquark gap are presented and compared with the results from Sec. 2.5.

2.6.1 Flow Equations

In the following, we provide updates for the RG flow equations presented in Sec. 2.3.2 by including diquark fluctuations and the running of the gluon-diquark couplings. In contrast to the aforementioned section, we also include the running of the wavefunction renormalisation of the fermions and derive the flow equations without specifying the gauge parameter ξ. In addition to that, we also include gluon (screening) masses in the flow equations. As in Sec. 2.3.2, the flow equations shown here represent the first part of the modified Wetterich equation (2.30), which is simply the conventionally used Wetterich equation with a shifted diquark

anomalous dimension, $\eta_\Delta \to \eta_\Delta + 2\dot{\beta}$, which appears in diquark propagators. In the following, we evaluate the couplings in the point-like limit. More details on the derivation of the running couplings can be found in App. C. Recall that with the help of the dynamical bosonisation technique, the four-quark interaction λ_{csc} vanishes on all scales. However, the corresponding flow equation $\partial_t \lambda_{\text{csc}}$ contributes to the flow of the remaining couplings. Note that we only consider the flow equations in the symmetric regime in the following. In the phase governed by spontaneous symmetry breaking, we use the approximation with infinitely gapped gluons, see Sec. 2.4.2 for details on this approximation. In addition, we also drop bosonic fluctuations in the regime below the symmetry-breaking scale. The inclusion of these two effects would require to consider the Anderson-Higgs-type mechanism, which is beyond the scope of the present work, see Sec. 2.4.2 for details on this aspect. Therefore, we can reuse the flow equations in the phase below the symmetry-breaking scale from our studies above. Unless stated otherwise, we use the same projection rules as already used in Sec. 2.3.2.

We start with the running of the curvature of the diquark potential in terms of the modified mass $\tilde{m}^2$ which consists of contributions from four different loop diagrams that are depicted in Fig. 2.19. In the symmetric phase, it is therefore given by

$$\begin{aligned} Z_\Delta^{-1} k^{-2} \partial_t \tilde{m}^2\big|_{\bar{\Gamma}} = &-8h^2 \mathcal{L}^{(2)}_{\text{ff}}\left(\frac{\mu}{k}, 0, \rho_\psi\right) \\ &+ \frac{64}{3}\left(\frac{\mu}{k}\right)^2 g^2_{\Delta,1}\left(\mathcal{L}^{(1,0)}_{2\times\text{b}}\left(\frac{\mu}{k}, \rho^+_\Delta, \rho^D_A\right) + \xi \mathcal{L}^{(0,1)}_{2\times\text{b}}\left(\frac{\mu}{k}, \rho^+_\Delta, \rho^L_A\right)\right) \\ &+ 8\lambda_\Delta \mathcal{L}^{(0,0)}_{1\times\text{b}}\left(\frac{\mu}{k}, \rho^+_\Delta\right) \\ &+ \frac{4}{3} g^2_{\Delta,2}\left(\mathcal{L}^{(0,0)}_{1\times\text{b}}\left(\frac{\mu}{k}, \rho^D_A\right) + 2\mathcal{L}^{(0,0)}_{1\times\text{b}}\left(\frac{\mu}{k}, \rho^M_A\right) + \xi \mathcal{L}^{(0,0)}_{1\times\text{b}}\left(\frac{\mu}{k}, \rho^L_A\right)\right). \end{aligned} \tag{2.95}$$

Here, we have used the subscript '$\bar{\Gamma}$' from Sec. 2.3.1 to indicate that we only consider the first part of the modified Wetterich equation (2.30). In Fig. 2.19, the threshold function $\mathcal{L}^{(2)}_{\text{ff}}$ corresponds to a loop diagram with two internal fermion lines (a), the threshold functions $\mathcal{L}^{(1,0)}_{2\times\text{b}}$ and $\mathcal{L}^{(0,1)}_{2\times\text{b}}$ correspond to loop diagrams with two internal bosonic lines (b), and the threshold function $\mathcal{L}^{(0,0)}_{1\times\text{b}}$ corresponds to loop diagrams with one internal bosonic line (c and d).

Whether the internal bosonic lines represent gluon or diquark fields is determined by the argument of the corresponding threshold function. Here and in the following, an argument $\rho_A^{D,M,L}$ indicates that the corresponding loop diagram has an internal gluon line and $\rho^\pm_\Delta$ indicates an internal diquark line. There is no distinction between different internal fermion lines, which are therefore always indicated by the argument ρ_ψ appearing in the corresponding threshold functions. Note that ρ_ψ, $\rho_A^{D,M,L}$, and $\rho^\pm_\Delta$ are "collective" arguments that entail all possible dependences of the respective propagator corresponding to internal lines in the loop diagrams. The diquark gap is also an argument of the fermion propagator. However, in order to better distinguish the threshold functions in the symmetric phase and in the regime governed by spontaneous symmetry breaking, we do not include the diquark gap in ρ_ψ but keep it as a separate argument of the threshold functions. Therefore, the only argument of the fermion propagator in the present study, concerning only the symmetric phase, is the anomalous dimension η_ψ: $\rho_\psi = [\eta_\psi]$. The argument $\rho_A^{D,M,L}$ collects all possible arguments coming from gluon propagators, which, in the present study, are the gluon anomalous dimension η_A and the gluon screening masses: $\rho^D_A = \{\epsilon_D, \eta_A\}$, $\rho^M_A = \{\epsilon_M, \eta_A\}$, and $\rho^L_A = \{\epsilon_L, \eta_A\}$. Here, $\epsilon_M = \bar{m}^2_M/(Z_A k^2)$ corresponds to the so-called Meissner mass $\bar{m}^2_M$, $\epsilon_D = \bar{m}^2_D/(Z_A k^2)$ corresponds to the so-called Debye mass $\bar{m}^2_D$, and $\epsilon_L = \xi \bar{m}^2_L/(Z_A k^2)$ is related to the so-called longitudinal mass $\bar{m}^2_L$. Lastly, diquark propagators depend on the fermion number $|F| = 2$ (which corresponds to the baryon number $|B| = 2/3$), the anomalous dimension η_Δ, and the curvature of the diquark potential in terms of the dimensionless quantity ϵ so that $\rho^\pm_\Delta = \{\pm 2, \epsilon, \eta_\Delta\}$.

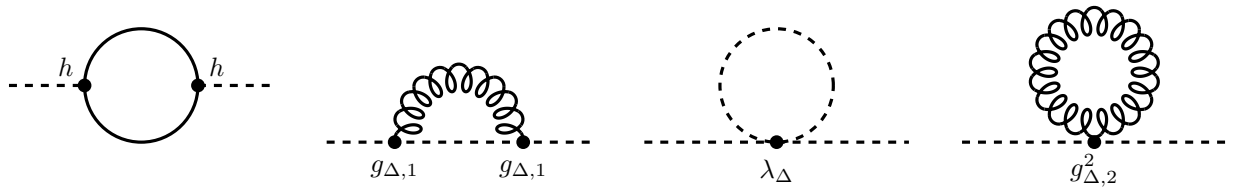

(a) (b) (c) (d)

Figure 2.19: Schematic representation of contributions in terms of loop diagrams to the flow equation of the curvature of the diquark potential, i.e., the modified mass $\tilde{m}^2$, originating from (a) the Yukawa interaction, (b) the one-gluon two-diquark interaction, (c) the four-diquark coupling, and (d) the two-gluon two-diquark interaction. Note that the diagrams (a) and (b) also contribute to the anomalous dimension of the diquark fields. Without including diquark fluctuations and the gluon-diquark interactions, only diagram (a) contributes to the flow equation of the curvature of the diquark potential, at least if terms coming from the dynamical bosonisation technique are disregarded, see Sec. 2.3.2.

The threshold functions can, in principle, also be temperature dependent, but in the present study, we work exclusively in the zero-temperature limit. In addition, they also depend on the regularisation scheme. As before, we employ a three-dimensional regularisation scheme with a polynomial regulator shape function such that fluctuations around the Fermi surface of the fermion propagators are integrated out successively. For further details and the definitions of the threshold functions, see App. B.3.
The running of the four-diquark coupling $\bar{\lambda}_\Delta$ consists of contributions coming from six different loop diagrams that are shown in Fig. 2.20. In the symmetric phase, it is therefore given by

$$
\begin{aligned}
Z_\Delta^{-2}\partial_t\bar{\lambda}_\Delta\big|_{\bar{\Gamma}} = -\frac{64}{9}\Big(\frac{\mu}{k}\Big)^4 g_{\Delta,1}^4\Big(&11\mathcal{L}^{(2,0)}_{4\times\mathrm{b}}\Big(\frac{\mu}{k},\rho_\Delta^+,\rho_\Delta^+,\rho_A^D,\rho_A^D\Big)+2\mathcal{L}^{(2,0)}_{4\times\mathrm{b}}\Big(\frac{\mu}{k},\rho_\Delta^+,\rho_\Delta^-,\rho_A^D,\rho_A^D\Big)\\
&+11\xi^2\mathcal{L}^{(0,2)}_{4\times\mathrm{b}}\Big(\frac{\mu}{k},\rho_\Delta^+,\rho_\Delta^+,\rho_A^L,\rho_A^L\Big)+2\xi^2\mathcal{L}^{(0,2)}_{4\times\mathrm{b}}\Big(\frac{\mu}{k},\rho_\Delta^+,\rho_\Delta^-,\rho_A^L,\rho_A^L\Big)\\
&+22\xi\mathcal{L}^{(1,1)}_{4\times\mathrm{b}}\Big(\frac{\mu}{k},\rho_\Delta^+,\rho_\Delta^+,\rho_A^D,\rho_A^L\Big)+4\xi\mathcal{L}^{(1,1)}_{4\times\mathrm{b}}\Big(\frac{\mu}{k},\rho_\Delta^+,\rho_\Delta^-,\rho_A^D,\rho_A^L\Big)\Big)\\
-\frac{13}{36}g_{\Delta,2}^4\Big(&\mathcal{L}^{(0,0)}_{2\times\mathrm{b}}\Big(\frac{\mu}{k},\rho_A^D,\rho_A^D\Big)+2\mathcal{L}^{(0,0)}_{2\times\mathrm{b}}\Big(\frac{\mu}{k},\rho_A^M,\rho_A^M\Big)+\xi^2\mathcal{L}^{(0,0)}_{2\times\mathrm{b}}\Big(\frac{\mu}{k},\rho_A^L,\rho_A^L\Big)\Big)\\
-\frac{104}{9}\Big(\frac{\mu}{k}\Big)^2 g_{\Delta,1}^2 g_{\Delta,2}^2\Big(&\mathcal{L}^{(1,0)}_{3\times\mathrm{b}}\Big(\frac{\mu}{k},\rho_\Delta^+,\rho_A^D,\rho_A^D\Big)+\xi^2\mathcal{L}^{(0,1)}_{3\times\mathrm{b}}\Big(\frac{\mu}{k},\rho_\Delta^+,\rho_A^L,\rho_A^L\Big)\Big)\\
-\frac{32}{3}\Big(\frac{\mu}{k}\Big)^2 g_{\Delta,1}^2\lambda_\Delta\Big(&5\mathcal{L}^{(1,0)}_{3\times\mathrm{b}}\Big(\frac{\mu}{k},\rho_\Delta^+,\rho_\Delta^+,\rho_A^D\Big)+\mathcal{L}^{(1,0)}_{3\times\mathrm{b}}\Big(\frac{\mu}{k},\rho_\Delta^+,\rho_\Delta^-,\rho_A^D\Big)\\
&+5\xi\mathcal{L}^{(0,1)}_{3\times\mathrm{b}}\Big(\frac{\mu}{k},\rho_\Delta^+,\rho_\Delta^+,\rho_A^L\Big)+\xi\mathcal{L}^{(0,1)}_{3\times\mathrm{b}}\Big(\frac{\mu}{k},\rho_\Delta^+,\rho_\Delta^-,\rho_A^L\Big)\Big)\\
-2\lambda_\Delta^2\Big(&6\,\mathcal{L}^{(0,0)}_{2\times\mathrm{b}}\Big(\frac{\mu}{k},\rho_\Delta^+,\rho_\Delta^+\Big)+\mathcal{L}^{(0,0)}_{2\times\mathrm{b}}\Big(\frac{\mu}{k},\rho_\Delta^+,\rho_\Delta^-\Big)\Big)+4h^4\mathcal{L}^{(2)}_{\mathrm{fff}}\Big(\frac{\mu}{k},0,\rho_\psi\Big)\,. \qquad (2.96)
\end{aligned}
$$

In Fig. 2.20, the threshold function $\mathcal{L}^{(0,0)}_{2\times\mathrm{b}}$ corresponds to loop diagrams with two internal bosonic lines (a and b), the threshold functions $\mathcal{L}^{(1,0)}_{3\times\mathrm{b}}$ and $\mathcal{L}^{(0,1)}_{3\times\mathrm{b}}$ correspond to loop diagrams with three internal bosonic lines (c and d), the threshold function $\mathcal{L}^{(2)}_{\mathrm{fff}}$ corresponds to loop diagrams with four internal fermionic lines (e), and the threshold functions $\mathcal{L}^{(2,0)}_{4\times\mathrm{b}}$, $\mathcal{L}^{(1,1)}_{4\times\mathrm{b}}$, and $\mathcal{L}^{(0,2)}_{4\times\mathrm{b}}$ correspond to loop diagrams with four internal bosonic lines (f).

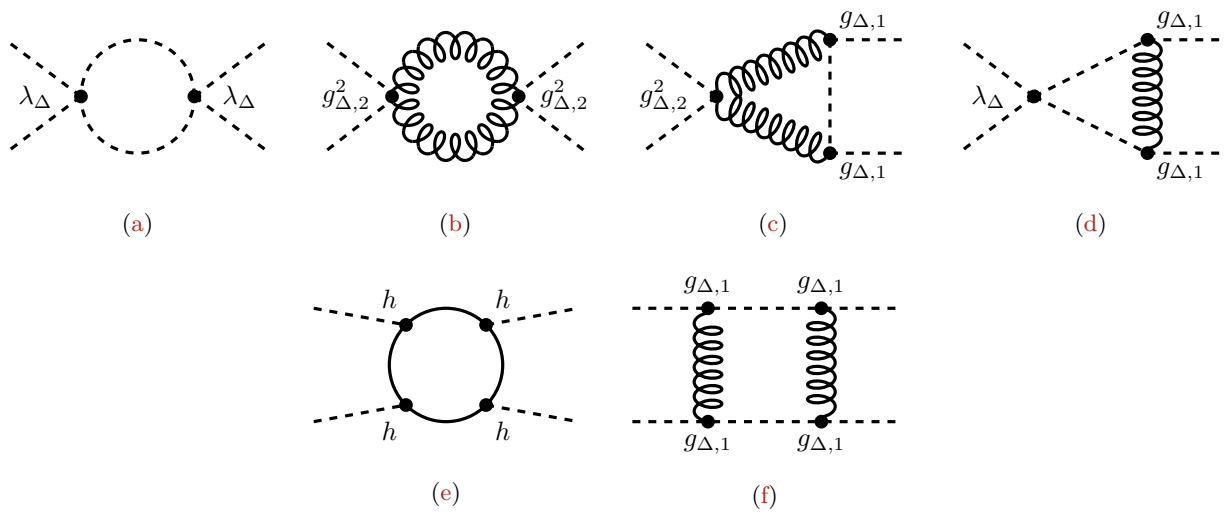

(a) (b) (c) (d) (e) (f)

Figure 2.20: Schematic representation of contributions in terms of loop diagrams to the flow equation of the four-diquark coupling $\bar{\lambda}_\Delta$ originating from (a) the four-diquark coupling itself, (b, c, and f) gluon-diquark interactions, (e) the Yukawa interaction, and (d) a combination of the gluon-diquark interaction and the four-diquark interaction. Without including diquark fluctuations and the gluon-diquark interactions, only diagram (e) contributes to the flow equation of the four-diquark coupling, at least if terms coming from the dynamical bosonisation technique are disregarded, see Sec. 2.3.2.

The running of the Yukawa coupling $\bar{h}$ consists of contributions from two different loop diagrams that are shown in Figs. 2.21a and 2.21b.. In the symmetric phase, this yields

$$Z_\psi^{-1} Z_\Delta^{-1/2} \partial_t \bar{h}|_{\bar{\Gamma}} = \frac{8}{3} g^2 h \left(\frac{1}{2} \mathcal{L}^{(2)}_{\mathrm{bff}} \left(\frac{\mu}{k}, 0, \rho_\psi, \rho_A^M \right) + \frac{1}{4} \mathcal{L}^{(2)}_{\mathrm{bff}} \left(\frac{\mu}{k}, 0, \rho_\psi, \rho_A^D \right) + \frac{\xi}{4} \mathcal{L}^{(2)}_{\mathrm{bff}} \left(\frac{\mu}{k}, 0, \rho_\psi, \rho_A^L \right) \right) - \frac{8}{3} \left(\frac{\mu}{k} \right) g_{\Delta,1} g h \left(\mathcal{L}^{(1)}_{\mathrm{bbf}} \left(\frac{\mu}{k}, 0, \rho_\psi, \rho_\Delta^+, \rho_A^D \right) + \xi \mathcal{L}^{(3)}_{\mathrm{bbf}} \left(\frac{\mu}{k}, 0, \rho_\psi, \rho_\Delta^+, \rho_A^L \right) \right). \tag{2.97}$$

The threshold function $\mathcal{L}^{(2)}_{\mathrm{bff}}$ corresponds to loop diagrams with two internal fermionic and one internal bosonic line, see Fig. 2.21a, and the threshold function $\mathcal{L}^{(1)}_{\mathrm{bbf}}$ corresponds to loop diagrams with two internal bosonic lines and one internal fermionic line, see Fig. 2.21b.
The running of the four-quark interaction $\bar{\lambda}_{\mathrm{csc}}$ consists of contributions from two different loop diagrams that are shown in Figs. 2.21c and 2.21d. In the symmetric phase, it is given by

$$\begin{aligned} Z_\psi^{-2} k^2 \partial_t \bar{\lambda}_{\mathrm{csc}} = {} & \frac{4}{9} g^4 \left(\frac{1}{16} \mathcal{L}^{(2)}_{\mathrm{bbff}} \left(\frac{\mu}{k}, 0, \rho_\psi, \rho_A^D, \rho_A^D \right) + \frac{\xi^2}{16} \mathcal{L}^{(2)}_{\mathrm{bbff}} \left(\frac{\mu}{k}, 0, \rho_\psi, \rho_A^L, \rho_A^L \right) + \frac{1}{4} \mathcal{L}^{(2)}_{\mathrm{bbff}} \left(\frac{\mu}{k}, 0, \rho_\psi, \rho_A^M, \rho_A^M \right) \right. \\ & \left. + \frac{\xi}{8} \mathcal{L}^{(2)}_{\mathrm{bbff}} \left(\frac{\mu}{k}, 0, \rho_\psi, \rho_A^D, \rho_A^L \right) + \frac{1}{4} \mathcal{L}^{(2)}_{\mathrm{bbff}} \left(\frac{\mu}{k}, 0, \rho_\psi, \rho_A^D, \rho_A^M \right) + \frac{\xi}{4} \mathcal{L}^{(2)}_{\mathrm{bbff}} \left(\frac{\mu}{k}, 0, \rho_\psi, \rho_A^L, \rho_A^M \right) \right) \\ & + \frac{5}{36} g^4 \left(\frac{1}{4} \mathcal{L}^{(1)}_{\mathrm{bbff}} \left(\frac{\mu}{k}, 0, \rho_\psi, \rho_A^D, \rho_A^D \right) + \frac{\xi}{2} \mathcal{L}^{(1)}_{\mathrm{bbff}} \left(\frac{\mu}{k}, 0, \rho_\psi, \rho_A^D, \rho_A^L \right) + \frac{\xi^2}{4} \mathcal{L}^{(1)}_{\mathrm{bbff}} \left(\frac{\mu}{k}, 0, \rho_\psi, \rho_A^L, \rho_A^L \right) \right. \\ & \left. - \mathcal{L}^{(3)}_{\mathrm{bbff}} \left(\frac{\mu}{k}, 0, \rho_\psi, \rho_A^D, \rho_A^M \right) + \xi \mathcal{L}^{(3)}_{\mathrm{bbff}} \left(\frac{\mu}{k}, 0, \rho_\psi, \rho_A^L, \rho_A^M \right) \right) \\ & + \frac{2}{3} g^2 h^2 \left(- \frac{1}{2} \mathcal{L}^{(3)}_{\mathrm{bbff}} \left(\frac{\mu}{k}, 0, \rho_\psi, \rho_\Delta^+, \rho_A^D \right) + \frac{\xi}{2} \mathcal{L}^{(3)}_{\mathrm{bbff}} \left(\frac{\mu}{k}, 0, \rho_\psi, \rho_\Delta^+, \rho_A^L \right) \right. \\ & \left. + \frac{1}{2} \mathcal{L}^{(1)}_{\mathrm{bbff}} \left(\frac{\mu}{k}, 0, \rho_\psi, \rho_\Delta^+, \rho_A^D \right) + \frac{\xi}{2} \mathcal{L}^{(1)}_{\mathrm{bbff}} \left(\frac{\mu}{k}, 0, \rho_\psi, \rho_\Delta^+, \rho_A^L \right) \right). \end{aligned} \tag{2.98}$$

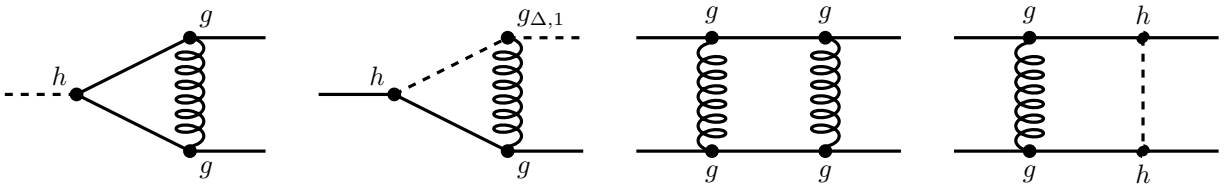

Figure 2.21: Schematic representation of contributions in terms of loop diagrams to the flow equation of the Yukawa coupling $\bar{h}$ (a and b) and the four-quark interaction $\bar{\lambda}_{\mathrm{csc}}$ (c and d). Note that a box diagram with two internal diquark lines is present in the calculation. However, it drops out at least in the symmetric phase. Similarly, a diagram contributing to the Yukawa coupling similar to (a) but with an internal diquark line instead of a gluon line does not exist, at least in the symmetric phase. Without diquark fluctuations and the gluon-diquark interactions, only diagram (a) contributes to the flow equation of the Yukawa interaction and diagram (c) to the flow equation of the four-quark interaction, at least if terms coming from the dynamical bosonisation technique are disregarded, see Sec. 2.3.2.

The threshold functions $\mathcal{L}^{(1)}_{\mathrm{bbff}}$, $\mathcal{L}^{(2)}_{\mathrm{bbff}}$, and $\mathcal{L}^{(3)}_{\mathrm{bbff}}$ correspond to loop diagrams with two internal fermionic and two internal bosonic lines. Note that a loop diagram contributing a term $\sim h^4$ to the flow equation, i.e., a loop diagram with two internal diquark lines, is not present although it might be expected. However, such a diagram drops out in the calculation of the running of the four-quark interaction, at least in the symmetric phase.

Since we include gluon-diquark interactions, we have to consider the corresponding running couplings, as they are different from the coupling associated with the quark-gluon interaction. We shall discuss this in more detail in Sec. 2.6.2. The running of the coupling $\bar{g}_{\Delta,1}$ can be calculated from the Wetterich equation by considering

$$\partial_t \bar{g}_{\Delta,1} = \frac{1}{16V_4}\frac{1}{\mu \mathrm{i}}\left(T^c_{ab}\frac{\delta}{\delta A^c_0}\frac{\delta}{\delta \Delta^*_b}\frac{\delta}{\delta \Delta_a}\partial_t \bar{\Gamma}_k[\varphi]\right)_{\mathrm{gs}} . \tag{2.99}$$

Here, $V_4 = \int \mathrm{d}^4x$ is the four-dimensional volume of Euclidean spacetime and the subscript 'gs' indicates that we evaluate on the ground state. In the symmetric phase, this projection yields

$$\begin{aligned} Z_A^{-1/2} Z_\Delta^{-1} \partial_t \bar{g}_{\Delta,1}\big|_{\bar{\Gamma}} = \frac{8}{3}\left(\frac{\mu}{k}\right)^2 g^3_{\Delta,1}\left(\mathcal{L}^{(1,0)}_{3\times \mathrm{b}}\left(\frac{\mu}{k},\rho^+_\Delta,\rho^+_\Delta,\rho^D_A\right) + \xi \mathcal{L}^{(0,1)}_{3\times \mathrm{b}}\left(\frac{\mu}{k},\rho^+_\Delta,\rho^+_\Delta,\rho^L_A\right)\right) \\ + \frac{1}{2}\frac{k}{\mu} h^2 g \mathcal{L}^{(2)}_{\mathrm{fff}}\left(\frac{\mu}{k},0,\rho_\psi\right) \\ - 2 g_{\Delta,1}\lambda_\Delta \mathcal{L}^{(0,0)}_{2\times \mathrm{b}}\left(\frac{\mu}{k},\rho^+_\Delta,\rho^+_\Delta\right) \\ - \frac{7}{3} g_{\Delta,1} g^2_{\Delta,2}\left(\mathcal{L}^{(1,0)}_{2\times \mathrm{b}}\left(\frac{\mu}{k},\rho^+_\Delta,\rho^D_A\right) + \xi \mathcal{L}^{(0,1)}_{2\times \mathrm{b}}\left(\frac{\mu}{k},\rho^+_\Delta,\rho^L_A\right)\right) . \end{aligned} \tag{2.100}$$

It follows that the one-gluon two-diquark coupling $\bar{g}_{\Delta,1}$ consists of contributions from four different loop diagrams. These loop diagrams are shown in Figs. 2.22a–2.22d. The threshold functions $\mathcal{L}^{(1,0)}_{3\times \mathrm{b}}$ and $\mathcal{L}^{(0,1)}_{3\times \mathrm{b}}$ correspond to loop diagrams with three internal bosonic lines (a), the threshold function $\mathcal{L}^{(2)}_{\mathrm{fff}}$ corresponds to loop diagrams with three internal fermionic lines (b), and the threshold functions $\mathcal{L}^{(0,0)}_{2\times \mathrm{b}}$, $\mathcal{L}^{(1,0)}_{2\times \mathrm{b}}$, and $\mathcal{L}^{(0,1)}_{2\times \mathrm{b}}$ correspond to loop diagrams with two internal bosonic lines (c and d). Interestingly, at large scales where diquark fluctuations are parametrically suppressed, the running of $\bar{g}_{\Delta,1}$ is dominated by contributions from the strong coupling $\sim g^5$ which follows from an analysis of the corresponding interaction in terms of the

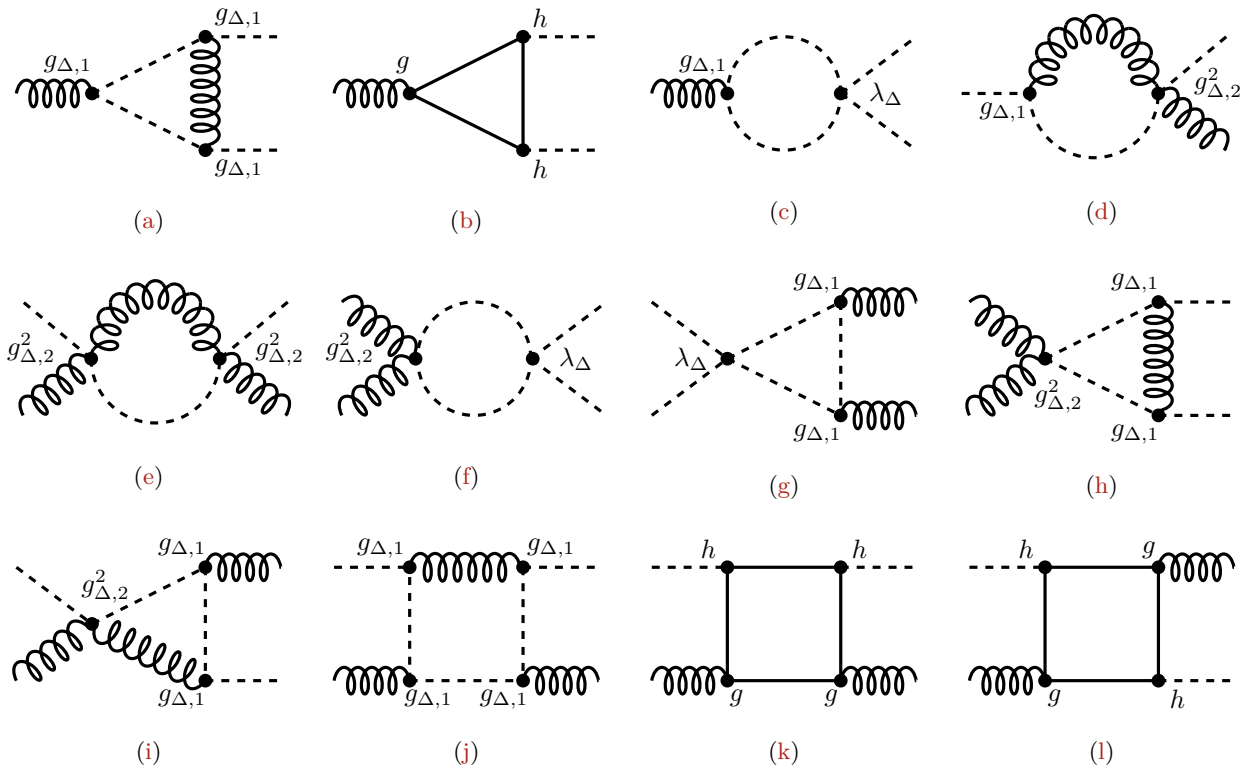

Figure 2.22: Schematic representation of contributions in terms of loop diagrams to the flow equation of the one-gluon two-diquark interaction $\bar{g}_{\Delta,1}$ (a–d) and the two-gluon two-diquark interaction $\bar{g}_{\Delta,2}$ (e–l).

underlying fundamental quark-gluon interaction (i.e., $h^2 g \sim g^5$ because $h \sim g^2$). Since the strong coupling g is small at large scales, the running of $\bar{g}_{\Delta,1}$ is expected to also be suppressed.
The situation for the two-gluon two-diquark interaction is more involved. Considering the corresponding term in the ansatz for the effective action we observe that

$$\begin{aligned}\bar{g}^2_{\Delta,2} A^a_\mu A^b_\mu \Delta^*_b T^b_{bc} T^a_{ca} \Delta_a &= \frac{1}{6}\bar{g}^2_{\Delta,2} A^a_\mu A^a_\mu \Delta^*_a \Delta_a + \frac{1}{2}\bar{g}^2_{\Delta,2} d_{abc} A^a_\mu A^b_\mu \Delta^*_b T^c_{ba} \Delta_a \\ &\to \frac{1}{6}\bar{g}^2_{\Delta,2,\mathrm{a}} A^a_\mu A^a_\mu \Delta^*_a \Delta_a + \frac{1}{2}\bar{g}^2_{\Delta,2,\mathrm{b}} d_{abc} A^a_\mu A^b_\mu \Delta^*_b T^c_{ba} \Delta_a \,. \end{aligned} \tag{2.101}$$

As it turns out, the two-gluon two-diquark interaction consists of two terms. In order to map everything that is generated on the right-hand side of the Wetterich equation, we consider these two contributions separately by introducing $\bar{g}^2_{\Delta,2,\mathrm{a}}$ and $\bar{g}^2_{\Delta,2,\mathrm{b}}$. The running of these two contributions can be calculated from the Wetterich equation by considering

$$\partial_t \bar{g}^2_{\Delta,2,\mathrm{a}} = \frac{1}{32}\left(\frac{\delta}{\delta\Delta^*_a}\frac{\delta}{\delta\Delta_a}\frac{\delta}{\delta A^b_\nu}\frac{\delta}{\delta A^b_\nu}\partial_t \bar{\Gamma}_k[\varphi]\right)_{\mathrm{gs}} \tag{2.102}$$

and

$$\partial_t \bar{g}^2_{\Delta,2,\mathrm{b}} = \frac{3}{80}\left(d^{a'b'c'} T^{c'}_{ab}\frac{\delta}{\delta\Delta^*_b}\frac{\delta}{\delta\Delta_a}\frac{\delta}{\delta A^{a'}_\nu}\frac{\delta}{\delta A^{b'}_\nu}\partial_t \bar{\Gamma}_k[\varphi]\right)_{\mathrm{gs}} . \tag{2.103}$$

However, the inclusion of both contributions separately is beyond the scope of the present work and we do not aim to resolve this difference here since we do not expect it to have a significant impact. Nevertheless,

it should be noted that $\bar{g}^2_{\Delta,2,\mathrm{a}}$ and $\bar{g}^2_{\Delta,2,\mathrm{b}}$ may be related via gauge invariance and the corresponding Ward-Takahashi identities. Therefore, we calculate the running of $\bar{g}^2_{\Delta,2}$ by averaging over the two contributions:

$$\partial_t \bar{g}^2_{\Delta,2} = \frac{\partial_t \bar{g}^2_{\Delta,2,\mathrm{a}} + \partial_t \bar{g}^2_{\Delta,2,\mathrm{b}}}{2} \,. \tag{2.104}$$

The running of the two-gluon two-diquark interaction in the symmetric phase is then given by

$$\begin{aligned} Z_A^{-1} Z_\Delta^{-1} \partial_t \bar{g}^2_{\Delta,2}\big|_{\bar{\Gamma}} = &-\frac{19}{48} g^4_{\Delta,2} \left(\mathcal{L}^{(0,0)}_{2\times\mathrm{b}}\left(\frac{\mu}{k}, \rho^+_\Delta, \rho^D_A\right) + 2\mathcal{L}^{(0,0)}_{2\times\mathrm{b}}\left(\frac{\mu}{k}, \rho^+_\Delta, \rho^M_A\right) + \xi \mathcal{L}^{(0,0)}_{2\times\mathrm{b}}\left(\frac{\mu}{k}, \rho^+_\Delta, \rho^L_A\right) \right) \\ &- 5\lambda_\Delta g^2_{\Delta,2} \mathcal{L}^{(0,0)}_{2\times\mathrm{b}}\left(\frac{\mu}{k}, \rho^+_\Delta, \rho^+_\Delta\right) \\ &- 20\left(\frac{\mu}{k}\right)^2 g^2_{\Delta,1} \lambda_\Delta \mathcal{L}^{(0,0)}_{3\times\mathrm{b}}\left(\frac{\mu}{k}, \rho^+_\Delta, \rho^+_\Delta, \rho^+_\Delta\right) \\ &- \frac{17}{3}\left(\frac{\mu}{k}\right)^2 g^2_{\Delta,2} g^2_{\Delta,1} \left(\mathcal{L}^{(1,0)}_{3\times\mathrm{b}}\left(\frac{\mu}{k}, \rho^+_\Delta, \rho^+_\Delta, \rho^D_A\right) + \xi \mathcal{L}^{(0,1)}_{3\times\mathrm{b}}\left(\frac{\mu}{k}, \rho^+_\Delta, \rho^+_\Delta, \rho^L_A\right) \right) \\ &- \frac{112}{3}\left(\frac{\mu}{k}\right)^4 g^4_{\Delta,1} \left(\mathcal{L}^{(1,0)}_{4\times\mathrm{b}}\left(\frac{\mu}{k}, \rho^+_\Delta, \rho^+_\Delta, \rho^+_\Delta, \rho^D_A\right) + \xi \mathcal{L}^{(0,1)}_{4\times\mathrm{b}}\left(\frac{\mu}{k}, \rho^+_\Delta, \rho^+_\Delta, \rho^+_\Delta, \rho^L_A\right) \right) \\ &+ g^2 h^2 \left(\mathcal{L}^{(1)}_{\mathrm{fff}}\left(\frac{\mu}{k}, 0, \rho_\psi\right) + \mathcal{L}^{(2)}_{\mathrm{fff}}\left(\frac{\mu}{k}, 0, \rho_\psi\right) + \mathcal{L}^{(3)}_{\mathrm{fff}}\left(\frac{\mu}{k}, 0, \rho_\psi\right) \right) . \end{aligned} \tag{2.105}$$

It follows that the running of the two-gluon two-diquark interaction consists of contributions from eight different loop diagrams that are shown in Figs. 2.22e–2.22l. The threshold function $\mathcal{L}^{(0,0)}_{2\times\mathrm{b}}$ corresponds to loop diagrams with two internal bosonic lines (e and f), the threshold functions $\mathcal{L}^{(0,0)}_{3\times\mathrm{b}}$, $\mathcal{L}^{(1,0)}_{3\times\mathrm{b}}$, and $\mathcal{L}^{(0,1)}_{3\times\mathrm{b}}$ correspond to loop diagrams with three internal bosonic lines (g, h and i), the threshold functions $\mathcal{L}^{(1,0)}_{4\times\mathrm{b}}$ and $\mathcal{L}^{(0,1)}_{4\times\mathrm{b}}$ correspond to a loop diagram with three internal bosonic lines (j), and the threshold functions $\mathcal{L}^{(1)}_{\mathrm{fff}}$, $\mathcal{L}^{(2)}_{\mathrm{fff}}$, and $\mathcal{L}^{(3)}_{\mathrm{fff}}$ correspond to loop diagrams with four internal fermionic lines (k and l). Interestingly, at large scales where diquark fluctuations are parametrically suppressed, the running of $\bar{g}_{\Delta,2}$ is dominated by contributions from the strong coupling $\sim g^6$ which follows from an analysis of the corresponding interaction in terms of the underlying fundamental quark-gluon interaction (i.e., $h^2 g^2 \sim g^6$ because $h \sim g^2$). Since the strong coupling g is small at large scales, the running of $\bar{g}_{\Delta,2}$ is also expected to be suppressed.

Finally, we turn to the anomalous dimensions of the gluon, quark, and diquark fields. The diquark anomalous dimension η_Δ is given by contributions from the loop diagrams depicted in Figs. 2.19a and 2.19b so that

$$\eta_\Delta = -Z_\Delta^{-1} \partial_t Z_\Delta = 8h^2 \mathcal{D}^{(2)}_{\mathrm{ff}}\left(\frac{\mu}{k}, 0, \rho_\psi\right) - \frac{64}{3}\left(\frac{\mu}{k}\right)^2 g^2_{\Delta,1} \left(\mathcal{D}^{(1,0)}_{2\times\mathrm{b}}\left(\frac{\mu}{k}, \rho^+_\Delta, \rho^D_A\right) + \xi \mathcal{D}^{(0,1)}_{2\times\mathrm{b}}\left(\frac{\mu}{k}, \rho^+_\Delta, \rho^L_A\right) \right) . \tag{2.106}$$

The threshold function $\mathcal{D}^{(2)}_{\mathrm{ff}}$ corresponds to a loop diagram with two internal fermionic lines and the threshold functions $\mathcal{D}^{(1,0)}_{2\times\mathrm{b}}$ and $\mathcal{D}^{(0,1)}_{2\times\mathrm{b}}$ correspond to a loop diagram with two internal bosonic lines. In both cases, the threshold functions include a derivative with respect to the external momentum. The projection rule for η_Δ is identical to that in Sec. 2.3.2, see Eq. (2.84). Recall that we have defined the anomalous dimensions by differentiating with respect to the zeroth component of the external four-momentum.

In the first part of this chapter, we have set the anomalous dimension of the quarks to zero by setting $Z_\psi = 1$ for all scales. In the following, we consider the quark anomalous dimension η_ψ which is calculated from

$$\eta_\psi = -Z_\psi^{-1} \partial_t Z_\psi = Z_\psi^{-1} \frac{1}{4V_4} \left(\frac{\partial}{\partial P_0} \mathrm{Tr}_{\mathrm{D}} \left[\gamma_0 \cdot \frac{\overrightarrow{\delta}}{\delta \bar{\psi}(P)} \partial_t \Gamma_k \frac{\overleftarrow{\delta}}{\delta \psi(P)} \right] \right)_{\mathrm{gs}, P=0} . \tag{2.107}$$

Note that we have defined the anomalous dimensions by differentiating with respect to the zeroth component of the external four-momentum. The subscript '$P = 0$' indicates that we evaluate on vanishing external momenta after differentiation. The inclusion of a finite chemical potential (and the fact that three-dimensional

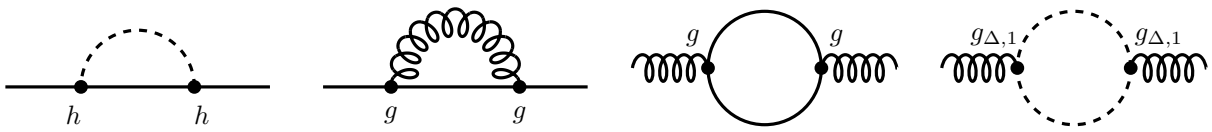

(a) (b) (c) (d)

Figure 2.23: Schematic representation of contributions in terms of loop diagrams to the anomalous dimension of the quark fields (a and b) and the contributions to the anomalous dimension of the gluon fields (c and d).

regulator schemes break Lorentz invariance [317]) leads to a difference in the anomalous dimension when differentiating with respect to the zeroth or the spatial component so that it is, in principle, necessary to consider both contributions separately. However, we do not attempt to resolve this difference here and simply identify both anomalous dimensions with Eq. (2.107). For large scales k, where $\mu/k \lll 1$, this may be justified, since both anomalous dimensions are identical at $\mu = 0$, at least in the case of a four-dimensional regularisation scheme. The contributions from loop diagrams to the quark anomalous dimension are shown in Figs. 2.23a and 2.23b. The corresponding flow equation reads

$$\begin{aligned}\eta_\psi = -\frac{4}{3}g^2\Big(&\mathcal{D}^{(3)}_{\mathrm{bf}}\Big(\frac{\mu}{k},0,\rho_\psi,\rho^D_A\Big) - \xi\mathcal{D}^{(3)}_{\mathrm{bf}}\Big(\frac{\mu}{k},0,\rho_\psi,\rho^L_A\Big) - \frac{1}{2}\mathcal{D}^{(1)}_{\mathrm{bf}}\Big(\frac{\mu}{k},0,\rho_\psi,\rho^D_A\Big)\\ &+ \frac{\xi}{2}\mathcal{D}^{(1)}_{\mathrm{bf}}\Big(\frac{\mu}{k},0,\rho_\psi,\rho^L_A\Big) - \mathcal{D}^{(1)}_{\mathrm{bf}}\Big(\frac{\mu}{k},0,\rho_\psi,\rho^M_A\Big)\Big) + h^2\mathcal{D}^{(1)}_{\mathrm{bf}}\Big(\frac{\mu}{k},0,\rho_\psi,\rho^+_\Delta\Big)\,.\end{aligned} \tag{2.108}$$

Here, the threshold functions $\mathcal{D}^{(1)}_{\mathrm{bf}}$ and $\mathcal{D}^{(3)}_{\mathrm{bf}}$ correspond to loop diagrams with one internal fermionic and one internal bosonic line, see Figs. 2.23a and 2.23b. Note that they include a differentiation with respect to the external momentum.

The gluon self-interactions only enter our present study only via the running of the strong coupling g which is in the background-field formalism [304, 305] underlying the present work given by

$$\partial_t g^2 = \eta_A g^2\,. \tag{2.109}$$

The gluon anomalous dimension consists of three contributions, namely the quark contribution η_A^{quark}, the diquark contribution $\eta_A^{\mathrm{diquark}}$, and the purely gluonic contribution η_A^{glue} so that

$$\eta_A = -Z_A^{-1}\partial_t Z_A = \eta_A^{\mathrm{quark}} + \eta_A^{\mathrm{diquark}} + \eta_A^{\mathrm{glue}}\,. \tag{2.110}$$

For the gluon contribution η_A^{glue} to the anomalous dimension, we use results from previous fRG studies where it has been calculated nonperturbatively within the background-field formalism, see Ref. [297, 298, 311]. This approach also underlies the present work. The loop diagram contributing to η_A^{quark} is shown in Fig. 2.23c and the loop diagram contributing to $\eta_A^{\mathrm{diquark}}$ is shown in Fig. 2.23d. Combining these two contributions yields

$$\eta_A^{\mathrm{quark}} + \eta_A^{\mathrm{diquark}} = \frac{8}{3}g^2\mathcal{D}^{(1)}_{\mathrm{ff}}\Big(\frac{\mu}{k},0,\rho_\psi\Big) + 4\Big(\frac{\mu}{k}\Big)^2 g^2_{\Delta,1}\mathcal{D}^{(2)}_{2\times\mathrm{b}}\Big(\frac{\mu}{k},\rho^+_\Delta,\rho^+_\Delta\Big)\,. \tag{2.111}$$

The threshold function $\mathcal{D}^{(1)}_{\mathrm{ff}}$ corresponds to the loop diagram with two internal fermion lines and the threshold function $\mathcal{D}^{(2)}_{2\times\mathrm{b}}$ corresponds to the loop diagram with two internal bosonic lines. Note that both functions include a derivative with respect to the external momentum.

With the contributions from the dynamical bosonisation, i.e., effectively employing Eqs. (2.52)–(2.54), as derived in Sec. 2.3.1, the coupled set of flow equations in the symmetric phase $k \geq k_{\mathrm{SB}}$ reads

$$\partial_t h^2 = 2hZ_\psi^{-1} Z_\Delta^{-1/2} \partial_t \bar{h}\big|_{\bar{\Gamma}} + 2(1+2\epsilon) k^2 Z_\psi^{-2} \partial_t \bar{\lambda}_{\mathrm{csc}} + h^2 \eta_\Delta + 2h^2 \eta_\psi \,, \tag{2.112}$$

$$\partial_t \lambda_\Delta = Z_\Delta^{-2} \partial_t \bar{\lambda}_\Delta\big|_{\bar{\Gamma}} + \frac{4\lambda_\Delta(1+\epsilon)}{h^2} k^2 Z_\psi^{-2} \partial_t \bar{\lambda}_{\mathrm{csc}} + 2\eta_\Delta \lambda_\Delta \,, \tag{2.113}$$

$$\partial_t \epsilon = k^{-2} Z_\Delta^{-1} \partial_t \tilde{m}^2\big|_{\bar{\Gamma}} + \frac{2\epsilon(1+\epsilon)}{h^2} k^2 Z_\psi^{-2} \partial_t \bar{\lambda}_{\mathrm{csc}} + (\eta_\Delta - 2)\epsilon \,. \tag{2.114}$$

For convenience, we have not explicitly inserted the running of the couplings coming from the first part of the modified Wetterich equation (2.30), as indicated by the subscript $\bar{\Gamma}$. However, they are given by Eqs. (2.95)–(2.98). Taking the contributions from the dynamical bosonisation into account, see Eqs. (2.55) and (2.56), the running of the gluon-diquark couplings for $k \geq k_{\mathrm{SB}}$ are given by

$$\partial_t g_{\Delta,2}^2 = Z_A^{-1} Z_\Delta^{-1} \partial_t \bar{g}_{\Delta,2}^2\big|_{\bar{\Gamma}} + \frac{2g_{\Delta,2}^2(1+\epsilon)}{h^2} k^2 Z_\psi^{-2} \partial_t \bar{\lambda}_{\mathrm{csc}} + \big(\eta_A + \eta_\Delta\big) g_{\Delta,2}^2 \,, \tag{2.115}$$

and

$$\partial_t g_{\Delta,1} = Z_A^{-1/2} Z_\Delta^{-1} \partial_t \bar{g}_{\Delta,1}\big|_{\bar{\Gamma}} + \frac{2g_{\Delta,1}(1+\epsilon)}{h^2} k^2 Z_\psi^{-2} \partial_t \bar{\lambda}_{\mathrm{csc}} + \frac{1}{2}\big(\eta_A + 2\eta_\Delta\big) g_{\Delta,1} \,. \tag{2.116}$$

The running of the gluon-diquark couplings stemming from the first part of the modified Wetterich equation (2.30), as indicated by the subscript $\bar{\Gamma}$, are given by Eqs. (2.100) and (2.105). The anomalous dimensions are for $k \geq k_{\mathrm{SB}}$ given by Eqs. (2.106), (2.108) and (2.110), respectively.

Below the symmetry-breaking scale $k \leq k_{\mathrm{SB}}$, the consideration of diquark fluctuations and the quark-gluon dynamics is more involved since diquark fields carry a net colour charge. As already discussed above, this requires the consideration of an Anderson-Higgs-type mechanism associated with the symmetry-breaking pattern SU(3) $\to$ SU(2) in colour space. According to this, we expect that only three of eight gluons remain massless below the symmetry-breaking scale. The remaining five gluons become massive and are, consequently, similar to the quarks, gapped in the phase governed by spontaneous symmetry breaking. Considering this aspect is beyond the scope of the present work. Therefore, we drop bosonic fluctuations and decouple the matter sector from the gauge sector by effectively "infinitely gapping" the gluons as already done in the previous section. Then, we can reuse the flow equations from Sec. 2.3.2, so that

$$\partial_t h^2 = h^2 \eta_\Delta + 2h^2 \eta_\psi \,, \tag{2.117}$$

$$\partial_t \kappa = \frac{4h^2}{\lambda_\Delta} \mathcal{L}_{\mathrm{ff}}^{(2)}\Big(\frac{\mu}{k}, h^2\kappa, \rho_\psi\Big) - \kappa\eta_\Delta - 2\kappa \,, \tag{2.118}$$

$$\partial_t \lambda_\Delta = 4h^4 \mathcal{L}_{\mathrm{ffff}}^{(2)}\Big(\frac{\mu}{k}, h^2\kappa, \rho_\psi\Big) + 2\lambda_\Delta \eta_\Delta \,. \tag{2.119}$$

Note that by dropping diquark fluctuations below k_{SB}, the four-quark interaction is only regenerated from the fundamental quark-gluon dynamics. Since we decouple the matter sector from the gauge sector below the symmetry-breaking scale, the running of the four-quark coupling effectively vanishes. Therefore, the terms in the flow equation that originate from the dynamical bosonisation also drop out of the calculation. Additionally, the quark anomalous dimension also vanishes:

$$\eta_\psi = 0 \,. \tag{2.120}$$

The diquark anomalous dimension for $k \leq k_{\mathrm{SB}}$ is given by

$$\eta_\Delta = 8h^2 \mathcal{D}_{\mathrm{ff}}^{(2)}\Big(\frac{\mu}{k}, h^2\kappa, \rho_\psi\Big) \,. \tag{2.121}$$

2.6.2 RG Flows

We turn to the RG flows of the couplings that span our ansatz of the effective action which are given by Eqs. (2.112)–(2.116) in the symmetric phase $k \geq k_{\mathrm{SB}}$ and Eqs. (2.117)–(2.119) in the phase governed by spontaneous symmetry breaking $k \leq k_{\mathrm{SB}}$. The anomalous dimensions are given by Eqs. (2.106), (2.108) and (2.110) and Eqs. (2.120) and (2.121), respectively. The running of the strong coupling is given by Eq. (2.109). The present section should be viewed as an update of the RG flows presented in Sec. 2.4, where we now include the gluon-diquark interactions and diquark fluctuations at least in the symmetric phase. Furthermore, we include the anomalous dimension of the quarks and use Landau gauge $\xi = 0$. The latter is preferred to minimise truncation errors since Landau gauge represents a fixed point in the RG flow and is therefore preferred over Feynman gauge. However, we shall compare the results for the symmetry-breaking scale and the diquark gap for Landau and Feynman gauge in Sec. 2.6.3. Moreover, we shall also discuss the effects of the diquark fluctuations on the symmetry-breaking scale and the diquark gap in the aforementioned section. Note that we still set the gluon masses to zero although they are included in the flow equations in Sec. 2.6.1 and postpone their inclusion to future studies. For a discussion of the effects of gluon masses, we refer to the analysis in Sec. 2.4.2 which can be directly transferred to the present section.

We follow the RG flow given by Eqs. (2.112)–(2.116) coming from large scales until the curvature of the diquark potential ϵ becomes zero, indicating the formation of a colour-superconducting ground state. Below the symmetry-breaking scale k_{SB}, we then replace the flow of the curvature of the potential with the minimum of the potential κ which is then closely related to the so-called diquark gap Δ_{gap}. The emergence of a diquark gap for $k \leq k_{\mathrm{SB}}$ requires the inclusion of an Anderson-Higgs-type mechanism associated with the symmetry breaking SU(3) to SU(2) in colour space. Then, only three of the eight gluons are massless while the others effectively acquire a screening mass so that five of the eight gluons are effectively "gapped". However, the inclusion of "gluon gapping" is beyond the scope of the present work. Therefore, we decouple the matter sector from the gauge sector by effectively "infinitely" gapping the gluons. For a detailed discussion of this aspect and the effect of including the gauge sector by leaving all gluons ungapped below the symmetry-breaking scale, we refer to Sec. 2.5. The following results correspond to what we refer to as "gapped" gluons in the aforementioned section. In doing so, no gluon dynamics appears in the RG flow equations that determine the RG flows in the phase governed by spontaneous symmetry breaking. We also add that the dynamics below the symmetry-breaking scale becomes even more involved when also trying to consider diquark fluctuations, as the diquarks themselves acquire a gap. Therefore, we also discard diquark fluctuations in the phase governed by spontaneous symmetry breaking. This is indeed a reasonable approximation since, in contrast to the phase associated with chiral symmetry breaking, there are no Goldstone modes in this case and fluctuation effects are expected to be suppressed.

Before turning to the results for the RG flows, we have to discuss the initial conditions. We employ the same initial conditions as already used in Sec. 2.4 and also fix the strong coupling at $g^2(\Lambda) = 4\pi \cdot 0.179$. The initial RG scale is given by $\Lambda = 10\,\mathrm{GeV}$. We refer to the preceding section for details and a discussion of the initial conditions. By including gluon-diquark interactions, we also have to specify the corresponding initial conditions. Recall that the quark-gluon interaction and the gluon-diquark interactions originate from requiring that the action is invariant under SU(3) colour transformations. Furthermore, we find that antidiquarks Δ_a transform like quarks and diquarks Δ_a^* transform like antiquarks under SU(3) colour transformations so that coupling these fields to the gluons comes with the same coupling constant, i.e., the strong coupling, at least at the initial RG scale. Therefore, we might naively argue that the initial conditions for the gluon-diquark couplings have to be initialised with the same value as the quark-gluon coupling. In addition to the coupling constants, interaction terms in the ansatz for the effective action come with a vertex renormalisation which we have tacitly absorbed into a redefinition of the couplings. Since the vertex renormalisations are

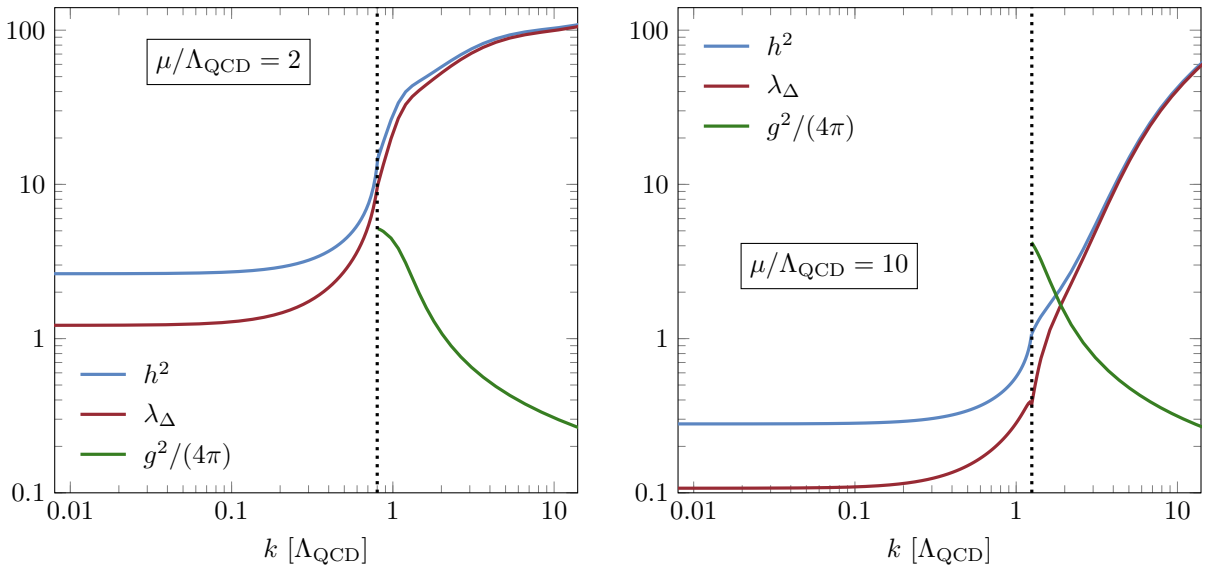

Figure 2.24: Flow of the (squared) renormalised Yukawa coupling h^2, the renormalised four-diquark coupling λ_Δ, and the renormalised strong coupling $\alpha = g^2/(4\pi)$ for $\mu/\Lambda_{\mathrm{QCD}} = 2$ (left panel) and for $\mu/\Lambda_{\mathrm{QCD}} = 10$ (right panel). The symmetry-breaking scales k_{SB} are given by vertical dashed lines. For $\mu/\Lambda_{\mathrm{QCD}} = 2$, it is given by $k_{\mathrm{SB}}/\Lambda_{\mathrm{QCD}} \approx 0.8$, and for $\mu/\Lambda_{\mathrm{QCD}} = 10$, it is given by $k_{\mathrm{SB}}/\Lambda_{\mathrm{QCD}} \approx 1.25$. The strong coupling is only shown in the symmetric phase since we decoupled the matter sector from the gauge sector in the phase below the symmetry scale. This corresponds to the approximation that we refer to as "gapped" gluons, see main text and Sec. 2.5 for details. We have used Landau gauge and fixed the strong coupling at $g^2(\Lambda) = 4\pi \cdot 0.179$.

different, also the couplings $g_{\Delta,1}$ and $g^2_{\Delta,2}$ are not equivalent to the strong coupling g. Additionally, from an analysis of the corresponding loop diagrams, we find that (excluding contributions from the dynamical bosonisation) $\partial_t g_{\Delta,1} \sim g^5$ and $\partial_t g^2_{\Delta,2} \sim g^6$ at least for large scales where diquark fluctuations are suppressed. For scales in the vicinity of the initial RG scale Λ, the running of the gluon-diquark couplings is dominated by contributions originating from the use of the dynamical bosonisation technique. Since diquark fields only become dynamic degrees of freedom along the RG flow, we expect that the interactions with gluons are parametrically suppressed at the initial RG scale and are only generated in the RG flow. Therefore, we initialise the couplings associated with gluon-diquark interactions at zero. Note that this situation is different from the ghost-gluon interaction, three-gluon interaction, and four-gluon interaction where the corresponding couplings only deviate from the strong coupling for smaller scales where nonperturbative effects start to play a role [175, 176], i.e., they are identical on the one-loop level which can be shown by employing the corresponding Ward-Takahashi identities. However, we find that this is not the case for the gluon-diquark interactions.

To update the results for the RG flows presented in Sec. 2.4, we start with the flow of the (squared) renormalised Yukawa coupling h^2, the renormalised four-diquark coupling λ_Δ, and the renormalised strong coupling $\alpha = g^2/(4\pi)$ which are all shown in Fig. 2.24. We show the couplings over a wide range of scales for two different chemical potentials, $\mu/\Lambda_{\mathrm{QCD}} = 2$ and $\mu/\Lambda_{\mathrm{QCD}} = 10$. We also show the renormalised dimensionless curvature ϵ for $k \geq k_{\mathrm{SB}}$ and the diquark gap $\Delta_{\mathrm{gap}} = hk\sqrt{\kappa}$ for $k \leq k_{\mathrm{SB}}$ in Fig. 2.25. Compared to the RG flows in Sec. 2.4, we find a shift of the couplings and the diquark gap towards lower values when considering the long-range limit $k \to 0$. However, the qualitative behaviour of the couplings as a function of the scale k is identical to the one observed in Sec. 2.4: The (squared) Yukawa coupling h^2 and the diquark coupling λ_Δ

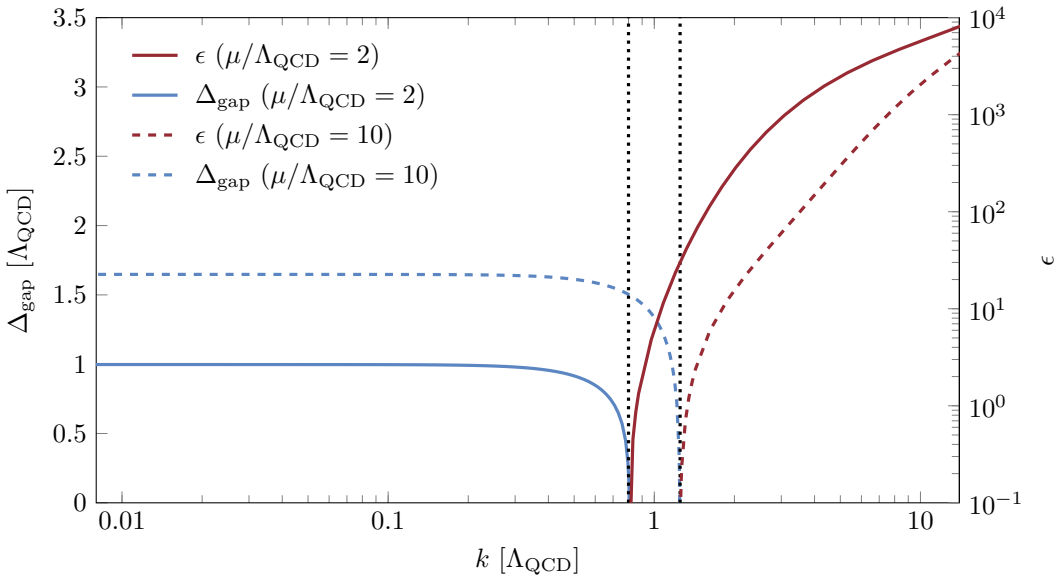

Figure 2.25: Renormalised dimensionless curvature ϵ of the diquark potential for $k \geq k_{\mathrm{SB}}$ and the diquark gap $\Delta_{\mathrm{gap}} = hk\sqrt{\kappa}$ for $k \leq k_{\mathrm{SB}}$ for $\mu/\Lambda_{\mathrm{QCD}} = 2$ (solid lines) and for $\mu/\Lambda_{\mathrm{QCD}} = 10$ (dashed lines). The vertical dashed lines are associated with the symmetry-breaking scales $k_{\mathrm{SB}}/\Lambda_{\mathrm{QCD}} \approx 0.8$ for $\mu/\Lambda_{\mathrm{QCD}} = 2$ and $k_{\mathrm{SB}}/\Lambda_{\mathrm{QCD}} \approx 1.25$ for $\mu/\Lambda_{\mathrm{QCD}} = 10$. The onset of spontaneous symmetry breaking is indicated by a vanishing curvature ϵ (red line and red dashed line).

decrease towards the long-range limit. Furthermore, coming from large values, the curvature ϵ decreases and eventually hits zero which determines the symmetry-breaking scale k_{SB}. This indicates the onset of spontaneous symmetry breaking of the $\mathrm{U}(1)_V$ symmetry. The symmetry-breaking scale is given by $k_{\mathrm{SB}}/\Lambda_{\mathrm{QCD}} \approx 0.8$ for $\mu/\Lambda_{\mathrm{QCD}} = 2$ and by $k_{\mathrm{SB}}/\Lambda_{\mathrm{QCD}} \approx 1.25$ for $\mu/\Lambda_{\mathrm{QCD}} = 10$. Comparing these values to our results from Sec. 2.4, we find that the symmetry-breaking scale is shifted towards smaller scales k compared to the results in Sec. 2.4. See the aforementioned section for a discussion about the qualitative behaviour of the RG flows and the effects of gluon screening masses which remains correct for the analysis here.

In the present section, we have also included the interactions between diquark fields and gluons that exist because diquark fields are not colour-neutral states. We show the quark-gluon interaction g^2, the one-gluon two-diquark interaction $g^2_{\Delta,1}$, and the two-gluon two-diquark interaction $g^2_{\Delta,2}$ for two different chemical potentials, namely $\mu/\Lambda_{\mathrm{QCD}} = 2$ and $\mu/\Lambda_{\mathrm{QCD}} = 10$, in Fig. 2.26 across a wide range of scales. Note that we only show them in the symmetric phase (for $k \geq k_{\mathrm{SB}}$) since we have decoupled the gauge sector from the matter sector below the symmetry-breaking scale k_{SB}. Recall that the couplings associated with gluon-diquark interactions are zero at the initial RG scale and are then generated along the RG flow towards the symmetry-breaking scale. Notably, the one-gluon two-diquark interaction $g^2_{\Delta,1}$ is generally smaller than the strong coupling and the two-gluon two-diquark coupling and becomes even smaller towards the symmetry-breaking scale. It should be noted that it does not become zero. The two-gluon two-diquark interaction $g^2_{\Delta,2}$ has a similar qualitative behaviour as the quark-gluon interaction at least for scales not too close to the symmetry-breaking scale. It increases coming from large scales but it eventually decreases again, at least for small chemical potential. For large scales but below $k = \Lambda$ and small chemical potentials, the coupling is even greater than the (squared) quark-gluon interaction g^2. However, towards the symmetry-breaking scale, the quark-gluon interaction exceeds the couplings associated with the gluon-diquark interactions for the chemical potentials considered in the present work.

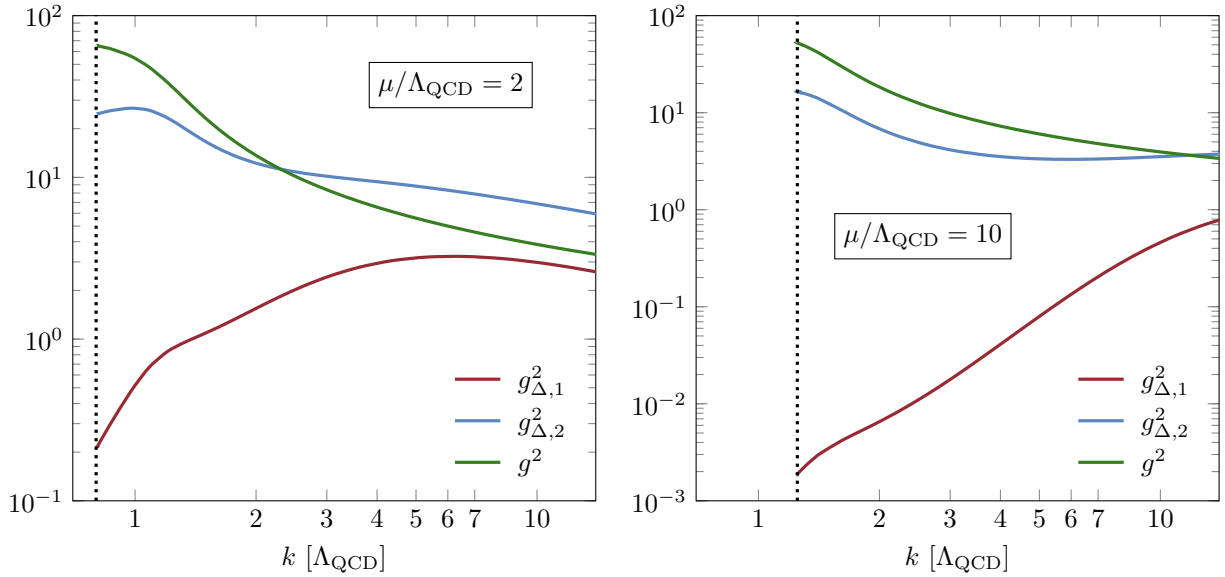

Figure 2.26: Flow of the couplings associated with gluon-matter interactions for $\mu/\Lambda_{\mathrm{QCD}} = 2$ (left panel) and $\mu/\Lambda_{\mathrm{QCD}} = 10$ (right panel) as a function of the RG scale k for $k \geq k_{\mathrm{SB}}$ where the vertical dashed lines are associated with the symmetry-breaking scale ($k = k_{\mathrm{SB}}$): We compare the strong coupling g^2 (green line) associated with quark-gluon interaction to the couplings between one gluon and two diquarks $g^2_{\Delta,1}$ (red line) and between two gluons and two diquarks $g^2_{\Delta,2}$ (blue line), respectively. Note that we use a logarithmic scale since the one-gluon two-diquark interaction $g^2_{\Delta,1}$ for $\mu/\Lambda_{\mathrm{QCD}} = 10$ becomes very small compared to the remaining couplings.

We conclude this section, by commenting on the values of the various couplings at a scale above the symmetry-breaking scale k_{SB}, namely the scale $\Lambda' = 1\,\mathrm{GeV}$. These values are shown in Fig. 2.27. The (squared) Yukawa coupling h^2, the diquark coupling λ_Δ, the curvature ϵ, and the inverse of the four-quark interaction λ_{csc} (left panel) show the same qualitative behaviour as in Fig. 2.15, see Sec. 2.4. Compared to before, the curvature and also the four-quark interaction at 1 GeV differ by about a factor of four. However, as we shall see in Sec. 2.6.3, this only leads to a mild difference in the symmetry-breaking scale and the diquark gap. This again shows that it is somewhat difficult to fix low-energy models with scheme-dependent quantities at, e.g., a scale above the symmetry-breaking scale, instead of using observables in the long-range limit. We also show the values of the (squared) strong coupling g^2, the gluon-diquark couplings $g^2_{\Delta,1}$ and $g^2_{\Delta,2}$. Notably, the dependence on the chemical potential of g^2 is small. In contrast to that, the gluon-diquark couplings decrease with an increase in the chemical potential and the two-gluon two-diquark coupling $g^2_{\Delta,2}$ even exceeds the strong coupling g^2 for lower chemical potentials.

2.6.3 Symmetry-Breaking Scale and the Diquark Gap

In the following, we provide updates for the symmetry-breaking scale k_{SB} and the diquark gap $\Delta_{\mathrm{gap}} = \bar{h}\Delta_0 = hk\sqrt{\kappa}$ for the results obtained in Sec. 2.5. By comparing the results obtained from the RG flows in Sec. 2.6.2 with those from the aforementioned section, we can estimate the effect of the approximations. In addition to that, we shall also directly analyse the influence of the choice of the gauge-fixing parameter on the results by comparing results for Landau and Feynman gauge. As already done in Sec. 2.5, we have included uncertainties arising from the experimental error of the strong coupling $g^2(\Lambda) = 4\pi \cdot (0.179 \pm 0.004)$

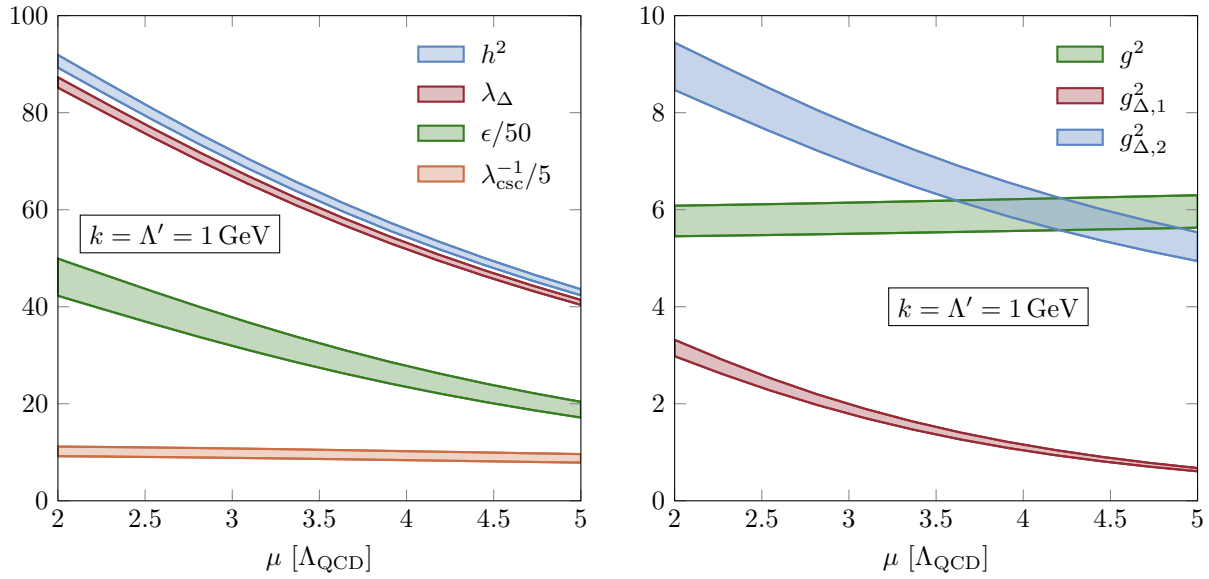

Figure 2.27: Left panel: Diquark coupling λ_Δ (green band), squared Yukawa coupling h^2 (blue band), renormalised dimensionless curvature of the diquark potential ϵ (red band), and inverse of the four-quark interaction $\lambda_{\mathrm{csc}}^{-1} = 2\epsilon/h^2$ (orange band) as a function of the chemical potential (in units of the QCD scale Λ_{QCD}). Right panel: Quark-gluon interaction g^2, one-gluon two-diquark interaction $g^2_{\Delta,1}$, and two-gluon two-diquark interaction $g^2_{\Delta,2}$ as a function of the chemical potential. The couplings have been evaluated at a scale $k = \Lambda' = 1\,\mathrm{GeV} \approx 4.8\Lambda_{\mathrm{QCD}}$ above the symmetry-breaking scale: $\Lambda' > k_{\mathrm{SB}}$. The bands represent the uncertainties arising from the experimental error of the strong coupling and a variation of the regularisation scheme. The qualitative behaviour of these quantities as a function of the chemical potential is identical to the one found in Sec. 2.4.

and uncertainties of the regularisation scheme by varying the order of the polynomial regulator used in the present work. However, the dependence of the results on the regularisation scheme is negligible compared to those from the error of the strong coupling. Since the present section only presents updates for the results in Sec. 2.5, the general statements and especially the estimates for the symmetry-breaking scale and the diquark gap, see Eqs. (2.90)–(2.94), still hold. We still set the gluon masses to zero although they are included in the flow equations in Sec. 2.6.1 and defer their inclusion to future studies. For a discussion of the possible effects of gluon screening masses, see Sec. 2.4. However, the inclusion of gluon screening masses is expected to lead to a decrease in the symmetry-breaking scale and consequently the diquark gap following the discussion in the aforementioned section.

The symmetry-breaking scale k_{SB} as a function of the chemical potential is shown in Fig. 2.28. By comparing the results obtained in Feynman gauge, we find that the inclusion of diquark fluctuations, gluon-diquark couplings, and the quark anomalous dimension as considered in the present section leads to a decrease in the symmetry-breaking scale compared to the one from Sec. 2.5. However, the influence of these contributions becomes smaller towards larger chemical potentials. We further note that the results for Feynman and Landau gauge as obtained from the RG flows in Sec. 2.6.2 scarcely overlap, with Landau gauge resulting in a smaller symmetry-breaking scale.

Considering the analytic estimate (2.94) in Sec. 2.5 relating the diquark gap Δ_{gap} and the symmetry-breaking scale k_{SB}, we expect that the discussed effects on the symmetry-breaking scale are also reflected in the diquark gap as shown in Fig. 2.29. Recall that the diquark gap corresponds to a gap in the fermionic excitation

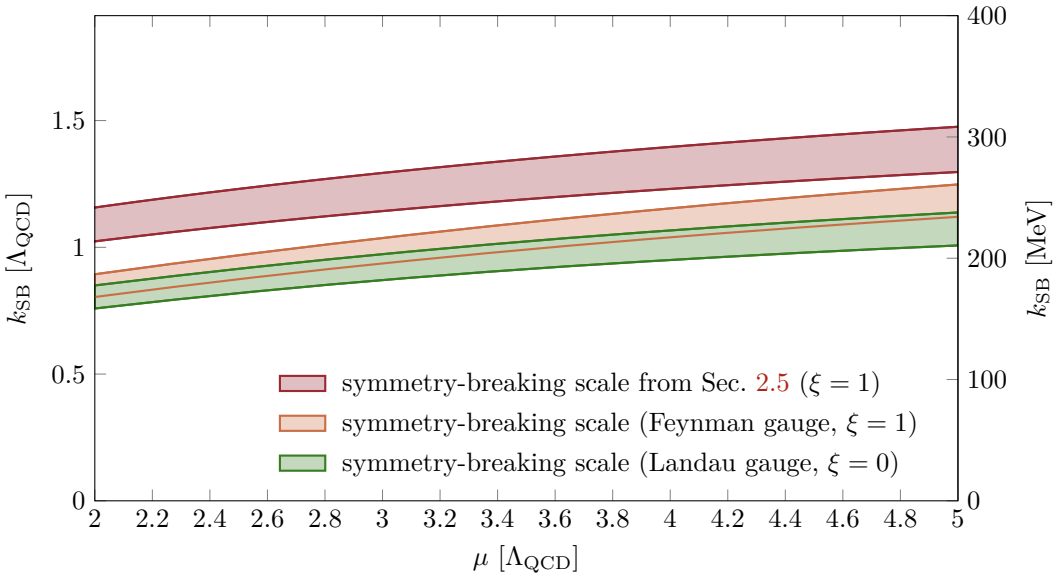

Figure 2.28: Symmetry-breaking scale k_{SB} as a function of the chemical potential in units of the QCD scale $\Lambda_{\mathrm{QCD}} = 209\,\mathrm{MeV}$. We compare the results obtained in the present section for two different gauge-fixing parameters, i.e., for Landau gauge $\xi = 0$ (green band) and Feynman gauge $\xi = 1$ (orange band), with the result for the symmetry-breaking scale from Sec. 2.5 (red band) where we have dropped diquark fluctuations, set the gluon-diquark interactions to zero, and set $Z_\psi = 1$. The bands for the symmetry-breaking scale represent the uncertainty of the strong coupling at the initial RG scale where we have used $g^2(\Lambda) = 4\pi \cdot (0.179 \pm 0.004)$. Furthermore, they include a variation of the regularisation scheme in terms of the order of the polynomial regulator. However, the dependence on the regulator scheme is negligible compared to the uncertainties arising from the strong coupling.

spectrum tightly connected to the formation of a colour-superconducting ground state. Comparing the diquark gap for Feynman gauge from Sec. 2.5 with our present results, we find that the inclusion of diquark fluctuations, gluon-diquark couplings, and the quark anomalous dimension leads to a decrease in the diquark gap. However, this decrease is smaller for the diquark gap than for the symmetry-breaking scale. Especially for larger chemical potentials, the uncertainty bands even overlap. We also find that the diquark gap for Feynman and Landau gauge, as obtained from the flow equations in Sec. 2.6.1, scarcely overlap at least towards larger chemical potentials, while the diquark gap for Landau gauge is smaller.

At this point, it should be emphasised again that we have decoupled the gauge sector from the matter sector and dropped diquark fluctuations below the symmetry-breaking scale k_{SB}. Therefore, the flow equations in the phase governed by spontaneous symmetry breaking, as used in the present section (see Sec. 2.6.1), are identical to those underlying the result for the diquark gap from Sec. 2.5 for "gapped gluons". As already discussed above in detail, we consider "gapped gluons" because gluonic contributions are expected to be at least partially suppressed below the symmetry-breaking scale due to an Anderson-Higgs-type mechanism. From the results for the diquark gap in Fig. 2.29, it also becomes apparent that the dependence of the diquark gap on the gauge-fixing parameter is comparable or even larger than the remaining improvements to the diquark gap from Sec. 2.5, i.e., the inclusion of diquark fluctuations and gluon-diquark interactions. We also note that, within the range of chemical potentials considered in the present study, the symmetry-breaking scale and the diquark gap are consistent with the standard BCS-type scaling behaviour, i.e., they increase if the chemical potential is increased [40, 82, 84–86].

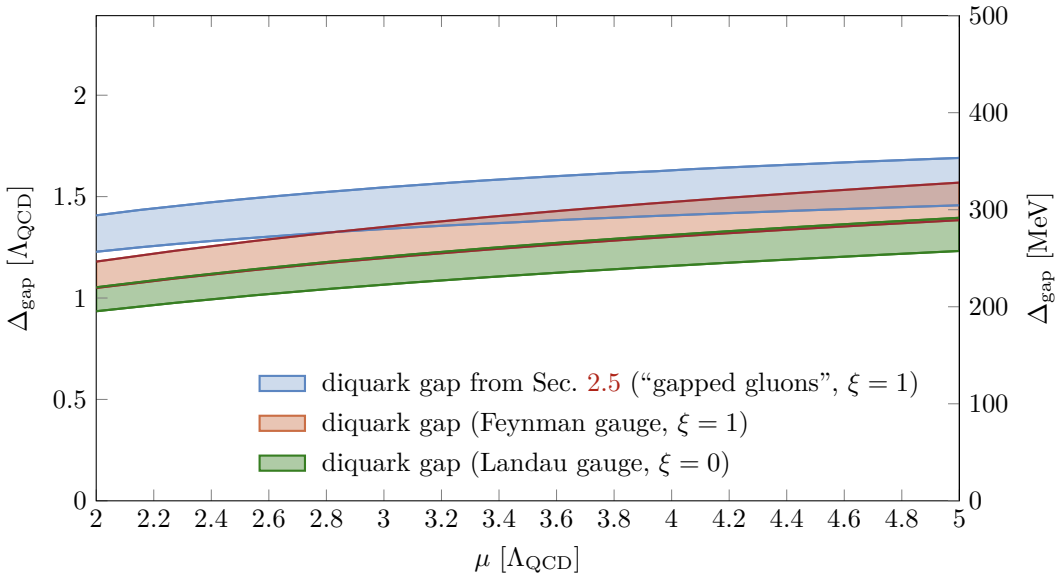

Figure 2.29: Diquark gap Δ_{gap} as a function of the chemical potential in units of the QCD scale $\Lambda_{\text{QCD}} = 209\,\text{MeV}$. We compare the results obtained in the present section for two different gauge-fixing parameters, i.e., for Landau gauge $\xi = 0$ (green band) and Feynman gauge $\xi = 1$ (orange band), to the result for the diquark gap from Sec. 2.5 (blue band) where we have dropped diquark fluctuations, set the gluon-diquark interactions to zero, and set the wavefunction renormalisation of the quarks to one ($Z_\psi = 1$). Note that we have "infinitely" gapped the gluons in the phase governed by spontaneous symmetry breaking, i.e., we have decoupled the matter sector from the gauge sector, see Sec. 2.5 for a discussion. The bands for the gap and the symmetry-breaking scale represent the uncertainty of the strong coupling at the initial RG scale where $g^2(\Lambda) = 4\pi \cdot (0.179 \pm 0.004)$. Further, they include a variation of the regularisation scheme in terms of the order of the polynomial regulator. However, the dependence on the regulator scheme is negligible compared to the uncertainties arising from the strong coupling.

To conclude the comparison of the symmetry-breaking scale and the diquark gap, we would like to comment on the effect of the gluon-diquark interactions and the diquark fluctuations so that the error from dropping these contributions can be estimated in future studies since their inclusion can considerably increase the effort. Diquark fluctuations are anyhow expected to only become important close to the symmetry-breaking scale when the curvature of the diquark potential, which enters the diquark propagators as an effective mass, becomes small. For a large effective mass, the diquark propagates are parametrically suppressed. Indeed, we find $\epsilon \gtrsim 100$ for $k \gtrsim 2k_{\text{SB}}$, see Fig. 2.25. Therefore, reasonably far away from the symmetry-breaking scale, the diquark fluctuations are suppressed because of a large curvature ϵ of the diquark potential. This is also reflected in the numerical results presented in Fig. 2.30 where results for the diquark gap for Landau gauge with and without the inclusion of diquark fluctuations in the symmetric phase are compared. Indeed, the inclusion of diquark fluctuations only leads to a small shift of the diquark gap which is negligible compared to the uncertainties arising from, e.g., the error of the strong coupling at the initial RG scale. Apparently, the small region close to the symmetry-breaking scale where diquark fluctuations become sizeable is not sufficient to have a big impact on the diquark gap.

These considerations can be used in future studies to simplify the calculations by dropping corrections from diquark fluctuations, at least in a qualitative study. In practice, dropping diquark fluctuations, i.e., contribu-

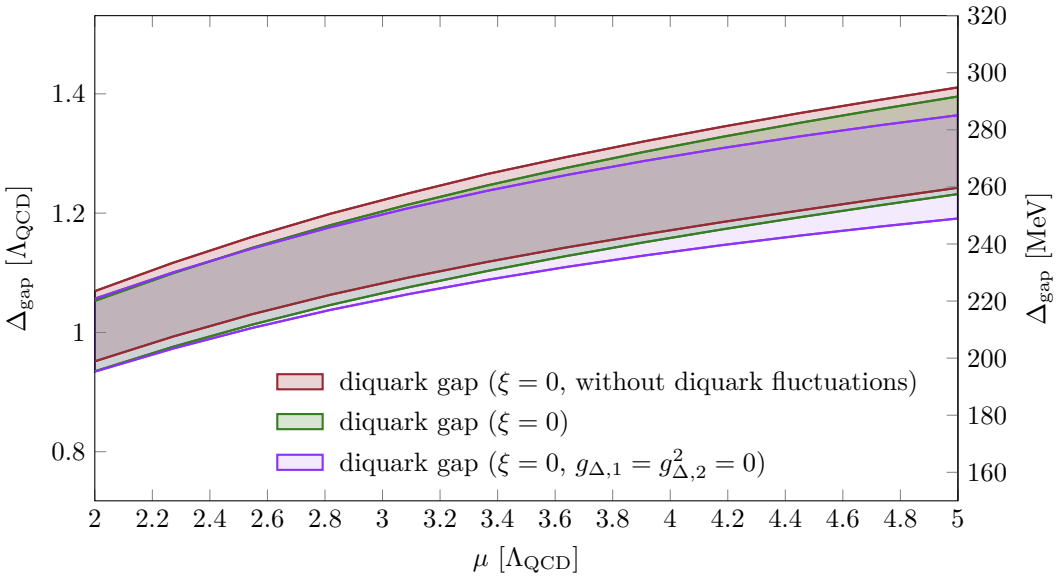

Figure 2.30: Comparison of the diquark gap Δ_{gap} for Landau gauge $\xi = 0$. We compare the diquark gap already shown in Fig. 2.29 (green band), which includes diquark fluctuations and gluon-diquark interactions in the symmetric phase, with the diquark gap where diquark fluctuations and gluon-diquark interactions have also been dropped in the symmetric phase (red band). We find that the inclusion of diquark fluctuations and gluon-diquark interactions only leads to corrections that are subleading compared to the error arising from the strong coupling as represented by the uncertainty bands.

tions from diagrams with internal diquark lines, significantly simplifies the calculation of the corresponding flow equations. For example, it reduces the diagrams that are needed for the calculation of the diquark coupling from six to two, see Fig. 2.20. From this analysis, it also follows that it can be expected that higher-order diquark self-interactions, e.g., six-diquark interactions, are subleading. Indeed, higher-order diquark self-interactions only contribute to the remaining couplings when considering diquark fluctuations and the corresponding flow equations fully decouple otherwise.

Additionally, the inclusion of gluon-diquark interactions also leads to subleading corrections compared to the effect of varying the gauge-fixing parameter and the impact of the quark anomalous dimension, see Fig. 2.30. Therefore, at least for qualitative studies, it seems reasonable to neglect gluon-diquark interactions.

We close by noting that the existence of symmetry breaking in the system considered here is very sensitive to changes in the flow equations. For example, artificially amplifying the gluon-diquark interaction, so that it is of the order of the quark-gluon strong coupling, might already influence the existence of symmetry breaking so that, consequently, no diquark gap exists. For the quark-gluon coupling we have used results for the gluon anomalous dimension from Ref. [297, 298, 311], see Eq. (2.109) and App. D for details. In contrast to that, using the one-loop strong coupling proves to be difficult to implement because the symmetry-breaking scale for chemical potentials considered in the present study is of the order of the Landau pole, which for the one-loop running is given by $\Lambda_{\text{Landau}} \approx 240...290\,\text{MeV}$. Since the dependence of the symmetry breaking on the chemical potential is small, the symmetry-breaking scale is expected to be of the order of the Landau pole up to very high densities. Therefore, although the associated chemical potentials are well-beyond the Landau pole, the dynamics close to the symmetry-breaking scale might still be dominated by nonphysical effects from the Landau pole.

2.7 Conclusions

With this chapter, starting in the high-energy regime where the dynamics is governed by the fundamental quark and gluon degrees of freedom, we analysed the dynamical formation of diquark fields in the low-energy regime. The formation of a finite expectation value of the diquark fields is associated with the emergence of a colour-superconducting ground state that governs the physics in the low-energy regime. Since we only consider two massless quark flavours, this ground state corresponds to pairing of the two-flavour colour-superconductor (2SC) type, in agreement with Refs. [40, 82–90, 92, 179].

Our study represents a first-principles study of dense strong-interaction matter with the only external input parameter being the value of the strong coupling at the initial RG scale. To continuously translate the degrees of freedom from the high-energy regime to the low-energy regime, we have used the so-called dynamical bosonisation technique. We have demonstrated that this provides a suitable method to study the dynamical generation of diquark fields over a wide range of chemical potentials. Notably, this technique allows us to achieve this without introducing an additional uncertainty, namely an additional scale Λ_0 which appears when bosonising at a specific scale instead of doing it continuously. This approach underlies the study in Ref. [126]. Additionally, we used a new class of regulators which is adapted to handle issues arising in the computations at finite chemical potential. Overall, this allowed for the calculation of the diquark gap which is at the heart of this chapter over a wide range of chemical potentials. This diquark gap corresponds to a gap in the excitation spectrum of the quarks which signals the formation of the colour-superconducting ground state. We analysed the dependence of the diquark gap on the chemical potential and the strong coupling and even found an analytic estimate for the diquark gap, see Eq. (2.94), giving an estimate for the dependences on the aforementioned quantities.

We also analysed the approximations underlying our calculation of the diquark gap. In particular, we discussed gluon-screening effects, which we have not included in the present study since we have dropped the corresponding screening masses of the gluons. According to our estimates, we expect that their inclusion may lead to a decrease in the symmetry-breaking scale, at least for high densities where the chemical potential eventually exceeds the symmetry-breaking scale. However, the effect is expected to be less sizeable towards smaller chemical potentials. Although we drop the gluon screening masses in the numerical results for the RG flows and the diquark gap, we have included them in the derived flow equations so that their inclusion is straightforward in future studies, at least in the symmetric phase.

In addition to gluon-screening effects, fluctuations of diquark fields may become important. At least in the symmetric phase, we have included them in the calculation of the diquark gap where we find that their effect is subleading. This is expected since large diquark screening masses suppress this effect in the symmetric regime as they become small only close to the symmetry-breaking scale. This suppression of fluctuation effects has already been observed in other early fRG studies, see, e.g., Refs. [259, 323, 324].

However, below the symmetry-breaking scale, the situation becomes more involved. The inclusion of diquark fluctuations requires to consider an Anderson-Higgs-type mechanism [61–66], see, e.g., Refs. [325–327] for general groundwork for studying this mechanism with the fRG method. Still, diquark fluctuation effects are expected to be suppressed as symmetry breaking does not generate Goldstone modes in this case and the diquark fields therefore remain gapped. In fact, according to this mechanism, five of the eight gluons acquire a mass by "eating up" Goldstone modes, effectively gapping the gluons and consequently suppressing gluonic contributions [50]. We analysed this effect by employing two different approximations below the symmetry-breaking scale: Firstly, we have left the gluons ungapped so that they are assumed to not acquire a mass according to the Anderson-Higgs-type mechanism. Secondly, we have infinitely gapped the gluons, effectively decoupling the matter sector from the gauge sector. We found that the diquark gap is approximately twice as big when leaving the gluons ungapped.

Since diquark fields are not colour-neutral states, they are expected to interact with the gluons. This requires to include gluon-diquark interactions. We have studied the corresponding couplings, at least in the symmetric regime where they appear to be subleading. The gluon-diquark couplings have to necessarily differ from the strong coupling, which might be naively assumed considering that the behaviour of quarks and diquark fields under SU(3) colour transformations is connected. We also analysed the dependence of the results for the diquark gap on the gauge-fixing parameter ξ. We find that using Landau gauge compared to Feynman gauge slightly reduces the size of the gap. However, the qualitative behaviour is identical.
Lastly, we would like to note that we have analysed the dependence of the results on the initial conditions of the various couplings at the initial RG scale. Recall that the only external input parameter is the strong coupling at the initial RG scale. Notably, the experimental uncertainty of this quantity represents the leading-order contribution to the error bands in the calculations while effects from a variation of the regularisation scheme are subleading. We have also checked that our results do not depend on the initial values of the remaining couplings as long as they are chosen such that they are compatible with the QCD action at high scales.
By comparing the present study with previous fRG results that take into account a Fierz-complete ansatz of gluon-induced four-quark interaction, see Ref. [126, 179], we deduced that Fierz completeness becomes more important towards lower chemical potentials, i.e., towards the nucleonic density regime. In the high-density regime where the diquark channel is dominant, only considering this single channel appears to be reasonable. While the dynamics in the intermediate density range is expected to be governed by many different interaction channels (indicating a rich and complex phase structure) [130–132, 135, 164–169], the scalar-pseudoscalar channel becomes dominant in the regime for small chemical potential [179]. However, the inclusion of additional four-quark channels is well-beyond the scope of the present work.
Still, the present study provides important field-theoretical foundations that allow to systematically improve the calculations of, e.g., the diquark gap. In particular, this paves the way for first principles studies of the equation of state of strong-interaction matter at supranuclear densities. However, already at this point, we have established an important and interesting insight into the dynamics governing dense strong-interaction matter. In the subsequent chapter, we shall demonstrate that the findings in the present chapter, especially the diquark gap as a function of the chemical potential, can be used to improve already existing low-energy models of dense QCD. In particular, this shall allow us to calculate the speed of sound as a function of the total baryon density and relate it to the size of the gap. Therefore, we show that the present chapter lays the groundwork for upcoming first-principles calculations of the equation of state and the speed of sound at supranuclear densities, which are ultimately needed for astrophysical applications.

3

Thermodynamics of Dense Strong-Interaction Matter

Investigating the thermodynamic properties of dense strong-interaction matter has become increasingly important due to recent advancements in the observation of neutron stars and the measurement of their properties. Notably, gravitational wave signals [110, 111], direct measurements of neutron-star radii [112–117], and mass measurements of heavy neutron stars [99, 100, 102, 118] provide valuable constraints for the equation of state of neutron-rich matter [119]. Consequently, quantitative theoretical results for the equation of state are necessary for astrophysical applications across a wide range of densities. At low densities, where nucleons and pions are the effective degrees of freedom and the dynamics is governed by spontaneous chiral symmetry breaking, results from chiral effective field theory provide constraints the equation of state [125–127, 211]. In this density regime, results from fRG also exist, see Ref. [130–136]. On the other hand, results from perturbative QCD provide insight into the equation of state at very high densities. However, for intermediate densities (about 10 times the nuclear saturation density), where the chiral symmetry is expected to be at least partially restored, barely any results exist for the equation of state. This density regime remains of particular interest for simulations of neutron stars.

In Chap. 2, it was demonstrated that dense strong-interaction matter is governed by the formation of a colour-superconducting ground state due to a BCS-type instability, see also Refs. [20, 46–56] for reviews. In the following, we utilise results obtained in the aforementioned chapter, particularly for the so-called diquark gap, to impose constraints on the equation of state at zero temperature. Of particular interest for astrophysical applications is the speed of sound (see e.g. Refs. [103, 119–122]), which serves as an indicator of the stiffness of the equation of state and is a highly sensitive quantity concerning changes in the density dependence of the pressure. The observation of massive neutron stars, particularly the existence of neutron stars with masses of around two solar masses suggests that the speed of sound as a function of the density reaches a maximum for intermediate densities $n/n_0 \lesssim 10$, exceeding the value associated with the noninteracting quark gas, see Ref. [103, 119–124]. In the present chapter, we pursue two (related) approaches to provide constraints for the equation of state, particularly for the speed of sound. By addressing these aspects, we aim

to provide valuable insight and constraints for the equation of state, which are essential for understanding the properties of neutron stars. Notably, in previous fRG studies, it has been found that the presence of a colour-superconducting gap leads to a maximum in the speed of sound for symmetric matter that exceeds the value of a noninteracting quark gas [126]. In addition to that, for very high densities where it is assumed that the colour-superconducting gap does not contribute significantly, it has been found that the speed of sound approaches its asymptotic value from below [154–162, 320].

The description of neutron stars requires knowledge of the equation of state including different quark species. While strange quarks are expected to already become relevant at densities relevant for astrophysical applications (see e.g. Ref. [328]), we only distinguish between up and down quarks in the following, omitting the inclusion of strange quarks. Nevertheless, even with two quark flavours, we expect that the results already provide valuable insight into the thermodynamic properties of dense strong-interaction matter which are relevant for the understanding of the properties of neutron stars. This requires the introduction of different chemical potentials for the up and down quarks, enabling us to extend the findings to finite isospin asymmetry. Our investigations so far, especially in Chap. 2, have only focused on symmetric matter, and the inclusion of isospin asymmetry in the QCD calculations performed in the aforementioned chapter exceeds the scope of the present work. However, our analysis will show that the corrections induced by this asymmetry are presumably small. In any case, in order to extend our calculations to finite isospin asymmetry and also to calculate observables relevant to astrophysical applications, such as the speed of sound or the pressure, we intend to improve an already existing low-energy model. In the first part of this chapter, see Sec. 3.1, we therefore utilise the results from Chap. 2, where constraints from fundamental quark and gluon degrees of freedom have been calculated, to constrain a low-energy model that includes isospin asymmetry. This should allow us to calculate the speed of sound at intermediate to high densities. We further analyse the zero-temperature phase structure for dense isospin-asymmetric matter with two quark flavours. This requires, for an accurate description of neutron stars, the implementation of beta equilibrium, electric-charge neutrality, and colour-charge neutrality [328, 329].

In the second part of this chapter, see Sec. 3.2, we also use the results obtained in Chap. 2, where the diquark gap has been obtained from a first-principles study, but analyse thermodynamic properties by employing an expansion of the equation of state for isospin-symmetric matter. This expansion can be deduced with relatively simple arguments. We shall focus on the speed of sound since it is a very sensitive quantity concerning changes in the density dependence of the pressure. Therefore, already small changes in the equation of state might lead to qualitative changes in the speed of sound which requires to analyse the relevant effective degrees of freedom at different densities. In order to identify the relevant degrees of freedom at different densities and to analyse the qualitative behaviour of the speed of sound, we introduce a diquark gap and include constraints from perturbative QCD in the expansion of the equation of state. Thereby, estimates for the speed of sound can be obtained for a very wide density range. We conclude our findings in Sec. 3.3.

3.1 Low-Energy Model for Dense Strong-Interaction Matter

The description of the low-energy dynamics may be more efficient in terms of suitably chosen degrees of freedom in the long-range limit (e.g., diquark fields). This can be provided by so-called low-energy models which also give reliable constraints for physical observables. By using the most relevant degrees of freedom of QCD, the low-energy regime which is governed by nonperturbative phenomena, like spontaneous symmetry breaking, can be conveniently accessed by low-energy models. For low densities, the effective degrees of freedom are nucleons and pions, whereas at intermediate to high densities (for $n \approx 10n_0$) the dynamics is dominated by diquark degrees of freedom. As we have already seen in Chap. 2, strong-interaction matter is expected to

exist in a colour-superconducting ground state even at asymptotically high densities. Without considering strange quarks, the chirally symmetric diquark condensate of the two-flavour colour-superconductor (2SC) type is expected to be the most dominant, see, e.g., Refs. [47, 56, 179]. This corresponds to the formation of the so-called diquark gap which is a gap in the excitation spectrum of the quarks that leads to the formation of a new ground state.

For the low-energy model considered in the following, we introduce Λ_{LEM} as the scale below which the description in terms of suitable degrees of freedom is feasible. This model scale is scheme dependent but only its existence matters for our discussion. One might be tempted to use the symmetry-breaking scale k_{SB} as the low-energy scale, but it is more appropriate to use a scale where spontaneous symmetry breaking has not yet set in because the symmetry-breaking scale is often unknown, dependent on external parameters, and scheme dependent. Furthermore, the scale has to be chosen in such a way that contributions from the gauge degrees of freedom (i.e., gluons) are subdominant since they are not included in the low-energy model. The existence of a scale that fulfils these requirements is indeed expected from the analysis of the relevant operators in the RG flow [126, 273, 297, 298]. General aspects of the model have already been discussed in Sec. 2.1 and shall only briefly be reviewed here. We refer the reader to the aforementioned chapter for more details. In summary, the diquark channel is most dominant for densities relevant for astrophysical applications. It indicates the formation of a chirally symmetric diquark condensate of the two-flavour colour-superconductor type. To capture the momentum dependence of the correlation functions for the calculation of thermodynamic properties, we introduce auxiliary fields, so-called diquark fields. We further rewrite the four-quark interaction by employing a Hubbard–Stratonovich transformation [299, 300]. Thereby, we replace the four-quark interaction with a suitable description of the interaction in terms of diquark fields

$$\frac{1}{2}\bar{\lambda}_{\mathrm{csc}}^{-1}\bar{\Delta}_a^*\bar{\Delta}_a + \frac{1}{2}\mathrm{i}\Big(\psi^T\mathcal{C}\gamma_5\tau_2\bar{\Delta}_a\epsilon_a\psi\Big) - \frac{1}{2}\mathrm{i}\Big(\bar{\psi}\gamma_5\tau_2\bar{\Delta}_a^*\epsilon_a\mathcal{C}\bar{\psi}^T\Big)\,, \tag{3.1}$$

where ϵ_a is a matrix in colour space and its entries are given by the Levi-Civita tensor $(\epsilon_a)_{bc} = \epsilon_{abc}$. Here, $a, b, c = 1, 2, 3$ are colour indices and ϵ_a couples the colour degrees of freedom of the quarks to the diquark fields. Note that the diquark fields carry a colour charge since they carry the quantum numbers of $(\psi^T\mathcal{C}\gamma_5\tau_2\epsilon_a\psi)$ and $(\bar{\psi}\gamma_5\tau_2\epsilon_a\mathcal{C}\bar{\psi}^T)$, respectively. For better readability, we have omitted the colour, flavour, and Dirac indices of the quark fields ψ and $\bar{\psi}$. For more details on the Hubbard-Stratonovich transformation, see Sec. 2.1. In contrast to the aforementioned section and to the definition of the effective action in Sec. 2.2, we have expressed the coefficient of the curvature term $\sim \bar{\Delta}_a^*\bar{\Delta}_a$ in terms of the inverse of the four-quark coupling $\bar{\lambda}_{\mathrm{csc}} = \bar{h}^2/(2\tilde{m}^2)$. This arises from the Hubbard-Stratonovich transformation so that it effectively enters the action as a mass of the diquark fields. By assuming that the Yukawa coupling $\bar{h}$ does not depend on the scale k in this model, we were able to absorb it by rescaling the diquark fields $\bar{\Delta}_a = \bar{h}\Delta_a$. Couplings like the Yukawa coupling are frequently assumed to be scale independent in low-energy models. Since diquark-like eight-quark interactions are already generated dynamically above the symmetry-breaking scale, as we have seen in our RG study in Sec. 2.4.2, they are also relevant at the scale Λ_{LEM}. Therefore, we include a corresponding four-diquark interaction

$$\bar{\lambda}_{\mathrm{eff}}\Big(\bar{\Delta}_a^*\bar{\Delta}_a\Big)^2 \qquad \text{with} \qquad \bar{\lambda}_{\mathrm{eff}} > 0\,. \tag{3.2}$$

Here, $\bar{\lambda}_{\mathrm{eff}}$ is the effective four-diquark coupling associated with the four-diquark interaction. Since there are presently no constraints available for higher-order interactions from the fRG study in Chap. 2, we shall not include them in the following. To include a possible isospin asymmetry in the model, we allow for different chemical potentials for the up and down quarks. For the description of neutron stars, beta equilibrium also needs to be implemented which implies that we have to include electrons with a chemical potential. Since interactions among the electrons and of quarks and electrons are much weaker than interactions generated by

QCD, we do not include such interactions in the model but only include a kinetic term so that they only appear as noninteracting spectators and provide a charged background. Note also that the action constructed from the diquark and Yukawa interaction is not confining. In order to describe neutron stars which are colourless, colour-charge neutrality needs to be enforced which requires the inclusion of chemical potentials for colour charges. We do not include a kinetic term for the auxiliary diquark fields so that they are not dynamical degrees of freedom. In doing so, we also ignore corrections that might render them dynamic which already emerge from purely fermionic loops. With this, we end up with a frequently employed low-energy model for dense strong-interaction matter (see, e.g., Refs. [46–50]), but we allow for different chemical potentials and a four-diquark interaction which is already relevant at high scales and should therefore be present at the model scale $\Lambda_{\mathrm{LEM}} \sim \mathcal{O}(1\,\mathrm{GeV})$. With these considerations, we find the following ansatz for the low-energy model employed in the present work:

$$\begin{aligned} S_{\mathrm{LEM}} = \int_x \Big\{ &\bar{\psi}\Big(\mathrm{i}\partial\!\!\!/ - \mathrm{i}\big(\hat{\mu}_{(\mathrm{f})} + \hat{\mu}_{(\mathrm{c})}\big)\Big)\psi + \frac{1}{2}\bar{\lambda}_{\mathrm{csc}}^{-1}\bar{\Delta}_a^*\bar{\Delta}_a + \bar{\lambda}_{\mathrm{eff}}\Big(\bar{\Delta}_a^*\bar{\Delta}_a\Big)^2 + \frac{1}{2}\mathrm{i}\Big(\psi^T\mathcal{C}\gamma_5\tau_2\bar{\Delta}_a\epsilon_a\psi\Big) \\ &- \frac{1}{2}\mathrm{i}\Big(\bar{\psi}\gamma_5\tau_2\bar{\Delta}_a^*\epsilon_a\mathcal{C}\bar{\psi}^T\Big) + \bar{\psi}^{(\mathrm{e})}\Big(\mathrm{i}\partial\!\!\!/ - \mathrm{i}\mu_{\mathrm{e}}\gamma_0\Big)\psi^{(\mathrm{e})}\Big\}\,. \end{aligned} \tag{3.3}$$

This action is, aside from the inclusion of different chemical potentials and electron degrees of freedom, part of the action (2.25) defined in Sec. 2.2. The quark fields are denoted by $\bar{\psi}$ and ψ, whereas electrons are given by $\psi^{(\mathrm{e})}$. The electron chemical potential is given by μ_{e}. We have also introduced different chemical potentials for the up quark μ_{u} and down quark μ_{d} combined in a flavour-chemical potential

$$\hat{\mu}_{(\mathrm{f})} = \mathrm{diag}\big(\mu_{\mathrm{u}}, \mu_{\mathrm{d}}\big)_{\mathrm{f}} \otimes \mathbb{1}_{\mathrm{c}} \otimes \gamma_0 \tag{3.4}$$

and different chemical potentials for differently coloured quarks via

$$\hat{\mu}_{(\mathrm{c})} = \mathbb{1}_{\mathrm{f}} \otimes \mathrm{diag}\big(\mu_{\mathrm{r}}, \mu_{\mathrm{g}}, \mu_{\mathrm{b}}\big)_{\mathrm{c}} \otimes \gamma_0\,, \tag{3.5}$$

where, on the right-hand side, the index 'f' refers to flavour space and 'c' to colour space. The chemical potentials μ_{r}, μ_{g}, and μ_{b} are associated with the three colour charges (red, green, and blue). They are related to the chemical potentials μ_3 and μ_8 which are associated with the colour generators T_3 and T_8 via

$$\mathrm{diag}\big(\mu_{\mathrm{r}}, \mu_{\mathrm{g}}, \mu_{\mathrm{b}}\big)_{\mathrm{c}} = \mu_3 T_3 + \mu_8 T_8 \tag{3.6}$$

with

$$\mu_{\mathrm{r}} = \frac{1}{2\sqrt{3}}\mu_8 + \frac{1}{2}\mu_3, \qquad \mu_{\mathrm{g}} = \frac{1}{2\sqrt{3}}\mu_8 - \frac{1}{2}\mu_3, \qquad \text{and} \qquad \mu_{\mathrm{b}} = -\frac{1}{\sqrt{3}}\mu_8\,. \tag{3.7}$$

The inclusion of the chemical potentials μ_3 and μ_8 is detailed in, e.g., Refs. [328–331]. Note that the chemical potentials are not independent parameters. The colour-charge chemical potentials are determined by the requirements for colour-charge neutrality which we shall introduce in Sec. 3.1.2. The chemical potential for up and down quarks and the chemical potential of the electrons reduce to a single free parameter when considering beta equilibrium and electric-charge neutrality, as we shall see in Sec. 3.1.6.

3.1.1 Calculation of the Effective Potential

The effective potential for the low-energy model can be obtained in different ways. In the following, we use the Wetterich equation introduced in Sec. 1.2 for the average effective action of the low-energy model $\Gamma_{k,\mathrm{LEM}}$ which is given by

$$\partial_t \Gamma_{k,\mathrm{LEM}} = \frac{1}{2}\mathrm{STr}\,\partial_t R_k \left(\Gamma^{(1,1)}_{k,\mathrm{LEM}} + R_k\right)^{-1} = \frac{1}{2}\mathrm{STr}\,\partial_t R_k \left(S^{(1,1)}_{\mathrm{LEM}} + R_k\right)^{-1}. \tag{3.8}$$

We compute the effective action in a one-loop approximation and, consequently, replaced the derivative of the effective action $\Gamma^{(1,1)}_{k,\mathrm{LEM}}$ appearing on the right-hand side of Eq. (3.8) with derivatives of the action $S^{(1,1)}_{\mathrm{LEM}}$. Only considering "pure" fermion loops yields

$$S^{(1,1)}_{\mathrm{LEM}} = \frac{\vec{\delta}}{\delta\varphi^T(-p)} S_{\mathrm{LEM}} \frac{\delta}{\delta\varphi(q)}\,, \qquad \text{where} \qquad \varphi(q) = \begin{pmatrix} \Psi(q) \\ \bar{\Psi}^T(-q) \end{pmatrix}. \tag{3.9}$$

Here, Ψ and $\bar{\Psi}$ are the Fourier transforms of the quark fields ψ and $\bar{\psi}$, respectively.
Note that we have restricted ourselves to quark loops for convenience. Contributions from electron degrees of freedom can be added independently since they are assumed not to interact with the quarks and simply contribute as a free electron gas. Further, we set the wavefunction renormalisation of the diquark fields to zero, which allows us to drop kinetic terms of the diquark fields in the ansatz for the effective action. Additionally, the wavefunction renormalisation of the quark fields is assumed to be constant. The regulator matrix entering the Wetterich equation is given by

$$R_k = \begin{pmatrix} 0 & R^\tau \\ R & 0 \end{pmatrix} (2\pi)^4 \delta^{(4)}\,(p-q)\,. \tag{3.10}$$

The various entries of the matrix are given by

$$R = \mathcal{R}_- P_- \gamma_0 + \mathcal{R}_+ P_+ \gamma_0 \qquad \text{with} \qquad \mathcal{R}_\pm = -\mathrm{i}\,\mathrm{diag}\left(\bar{\epsilon}^{\mathrm{u,r}}_\pm, \bar{\epsilon}^{\mathrm{u,g}}_\pm, \bar{\epsilon}^{\mathrm{u,b}}_\pm, \bar{\epsilon}^{\mathrm{d,r}}_\pm, \bar{\epsilon}^{\mathrm{d,g}}_\pm, \bar{\epsilon}^{\mathrm{d,b}}_\pm\right)_{\mathrm{f,c}}, \tag{3.11}$$

$$R^\tau = \mathcal{R}^\tau_+ \gamma_0 P^T_- + \mathcal{R}^\tau_- \gamma_0 P^T_+ \qquad \text{with} \qquad \mathcal{R}^\tau_\pm = \mathrm{i}\,\mathrm{diag}\left(\bar{\epsilon}^{\mathrm{u,r}}_\pm, \bar{\epsilon}^{\mathrm{u,g}}_\pm, \bar{\epsilon}^{\mathrm{u,b}}_\pm, \bar{\epsilon}^{\mathrm{d,r}}_\pm, \bar{\epsilon}^{\mathrm{d,g}}_\pm, \bar{\epsilon}^{\mathrm{d,b}}_\pm\right)_{\mathrm{f,c}}. \tag{3.12}$$

The index 'f,c' indicates that $\mathcal{R}_\pm$ and $\mathcal{R}^\tau_\pm$ are matrices in flavour and colour space, where we have defined $\bar{\epsilon}^{f,c}_\pm = \left(\mu_f + \mu_c \pm |\vec{p}\,|\right) r^{f,c}_\pm$. Here, $r^{f,c}_\pm$ is the regulator shape function. Recall that the projection operators $P_\pm$ have been introduced in Sec. 1.3.1.
We expand the auxiliary diquark fields around a homogeneous background field $\bar{\Delta}_3$ which we choose to point into the three-direction in colour space, for convenience. We can do so because physical observables, such as the pressure and the speed of sound, only depend on the gauge-invariant quantity $|\Delta^*_a \Delta_a|$ and consequently do not depend on the selected direction, see also Ref. [46]. Therefore, we find

$$\left(S^{(1,1)}_{\mathrm{LEM}} + R_k\right) = \begin{pmatrix} \mathrm{i}\mathcal{C}\gamma_5\tau_2\bar{\Delta}_3\epsilon_3 & P^*_\psi(p) \\ P_\psi(p) & -\mathrm{i}\gamma_5\mathcal{C}\tau_2\bar{\Delta}^*_3\epsilon_3 \end{pmatrix} (2\pi)^4\delta^{(4)}(p-q)\,. \tag{3.13}$$

For the matrix elements P_ψ and P^*_ψ, we use the quasi-particle regularisation scheme. Their derivation and definition can be found in App. C. Every entry of the latter matrix is itself a matrix in colour, flavour, and Dirac space. Solving the additional "field" trace yields

$$\partial_t \Gamma_{k,\mathrm{LEM}} = \frac{1}{2}\mathrm{STr}\left[\partial_t R_k \left(S^{(1,1)}_{\mathrm{LEM}} + R_k\right)^{-1}\right] = -\frac{1}{2}\mathrm{Tr}\left[\partial_t R^\tau \left(S^{(1,1)}_{\mathrm{LEM}} + R_k\right)^{-1}_{21} + \partial_t R \left(S^{(1,1)}_{\mathrm{LEM}} + R_k\right)^{-1}_{12}\right]. \tag{3.14}$$

Here, the minus sign arises due to the super trace 'STr' which introduces a minus sign for fermion degrees of freedom. For the upper left element of the inverse matrix, we find

$$\left(S^{(1,1)}_{\mathrm{LEM}} + R_k\right)^{-1}_{12} = \mathcal{G}_-\left(1 - |\bar{\Delta}|^2\mathcal{G}_{-,\chi}\right)P_+\gamma_0 + \mathcal{G}_+\left(1 - |\bar{\Delta}|^2\mathcal{G}_{+,\chi}\right)P_-\gamma_0 \tag{3.15}$$

and for the lower right element of the inverse matrix we find

$$\left(S^{(1,1)}_{\mathrm{LEM}} + R_k\right)^{-1}_{21} = \mathcal{G}^*_-\left(1 - |\bar{\Delta}|^2\mathcal{G}^*_{-,\chi}\right)\gamma_0 P^T_- + \mathcal{G}^*_+\left(1 - |\bar{\Delta}|^2\mathcal{G}^*_{+,\chi}\right)\gamma_0 P^T_+\,. \tag{3.16}$$

Here, we have introduced

$$\mathcal{G}_{\pm} = \mathrm{diag}\left(G_{\pm}^{\mathrm{u,r}}, G_{\pm}^{\mathrm{u,g}}, G_{\pm}^{\mathrm{u,b}}, G_{\pm}^{\mathrm{d,r}}, G_{\pm}^{\mathrm{d,g}}, G_{\pm}^{\mathrm{d,b}}\right)_{\mathrm{f,c}} \tag{3.17}$$

and

$$\mathcal{G}_{\pm,\chi} = \mathrm{diag}\left(G_{\pm,\chi}^{(\mathrm{u,r}),(\mathrm{d,g})}, G_{\pm,\chi}^{(\mathrm{u,g}),(\mathrm{d,r})}, 0, G_{\pm,\chi}^{(\mathrm{d,r}),(\mathrm{u,g})}, G_{\pm,\chi}^{(\mathrm{d,g}),(\mathrm{u,r})}, 0\right)_{\mathrm{f,c}} . \tag{3.18}$$

Note that $\mathcal{G}_{\pm,\chi}$ are matrices in flavour and colour space as indicated by the subscript 'f,c'. The elements of the matrix are given by

$$G_{\pm}^{f,c} = -\frac{1}{p_0 + \mathrm{i}\epsilon_{\pm}^{f,c}} \qquad \text{and} \qquad G_{\pm,\chi}^{(f_1,c_1),(f_2,c_2)} = \frac{1}{|\bar{\Delta}|^2 + (p_0 + \mathrm{i}\epsilon_{\pm}^{f_1,c_1})(p_0 - \mathrm{i}\epsilon_{\pm}^{f_2,c_2})} . \tag{3.19}$$

For convenience, we introduced $|\bar{\Delta}|^2 = \bar{\Delta}_3^* \bar{\Delta}_3$ and $\epsilon_{\pm}^{f,c} = (\mu_f + \mu_c \pm |\vec{p}\,|)\,(1 + r_{\pm}^{f,c})$ where $f, f_1, f_2 = \mathrm{u}, \mathrm{d}$ and $c, c_1, c_2 = \mathrm{r}, \mathrm{g}, \mathrm{b}$. In the following, we resolve the colour and flavour traces, which is tedious but straightforward. Recall that the trace also includes an integral over the momentum p. After solving the traces, we can rewrite the result and find

$$\begin{aligned}
\frac{\partial_t \Gamma_{k,\mathrm{LEM}}}{V_4} = &-2 \sum_{\sigma=\pm} \int_p \tilde{\partial}_t \ln\left((p_0 + \mathrm{i}\epsilon_{\sigma}^{\mathrm{d,b}})(p_0 - \mathrm{i}\epsilon_{\sigma}^{\mathrm{u,b}})\right) \\
&- 2 \sum_{\sigma=\pm} \int_p \tilde{\partial}_t \ln\left((p_0 + \mathrm{i}\epsilon_{\sigma}^{\mathrm{d,g}})(p_0 - \mathrm{i}\epsilon_{\sigma}^{\mathrm{u,r}}) + |\bar{\Delta}|^2\right) \\
&- 2 \sum_{\sigma=\pm} \int_p \tilde{\partial}_t \ln\left((p_0 + \mathrm{i}\epsilon_{\sigma}^{\mathrm{d,r}})(p_0 - \mathrm{i}\epsilon_{\sigma}^{\mathrm{u,g}}) + |\bar{\Delta}|^2\right) .
\end{aligned} \tag{3.20}$$

We have introduced the spacetime volume $V_4 = (2\pi)^4 \delta^{(4)}(0)$ and have started to sum over σ, for convenience. The derivative $\tilde{\partial}_t$ now only acts on the k-dependence of the regulator. Interestingly, terms that are associated with blue quarks, i.e., terms that contain a blue chemical potential, do not depend on the gap and can be separated from terms involving red and green quarks. Further, terms containing the diquark gap mix red and green quarks so that they cannot be separated from one another. This mixing arises as a consequence of the aforementioned expansion into the three-direction. By expanding in a different direction, we expect that quarks with other colours mix. However, the corresponding diquark gap is always associated with an up and a down quark coming in different colours. By expanding the diquark fields around a homogeneous background and using the fact that the Yukawa coupling is constant in our current setting, we can simply integrate Eq. (3.20) from k to Λ_{LEM} and find

$$\begin{aligned}
\frac{\Gamma_{k,\mathrm{LEM}}}{V_4} - \frac{\Gamma_{\Lambda_{\mathrm{LEM}},\mathrm{LEM}}}{V_4} = &-2 \sum_{\sigma=\pm} \int_p \ln\left((p_0 + \mathrm{i}\epsilon_{\sigma}^{\mathrm{d,b}})(p_0 - \mathrm{i}\epsilon_{\sigma}^{\mathrm{u,b}})\right)\Big|_{\Lambda_{\mathrm{LEM}}}^{k} \\
&- 2 \sum_{\sigma=\pm} \int_p \ln\left((p_0 + \mathrm{i}\epsilon_{\sigma}^{\mathrm{d,g}})(p_0 - \mathrm{i}\epsilon_{\sigma}^{\mathrm{u,r}}) + |\bar{\Delta}|^2\right)\Big|_{\Lambda_{\mathrm{LEM}}}^{k} \\
&- 2 \sum_{\sigma=\pm} \int_p \ln\left((p_0 + \mathrm{i}\epsilon_{\sigma}^{\mathrm{d,r}})(p_0 - \mathrm{i}\epsilon_{\sigma}^{\mathrm{u,g}}) + |\bar{\Delta}|^2\right)\Big|_{\Lambda_{\mathrm{LEM}}}^{k} .
\end{aligned} \tag{3.21}$$

According to the construction of our model, the initial condition is given by

$$\frac{\Gamma_{\Lambda_{\mathrm{LEM}},\mathrm{LEM}}}{V_4} = \frac{1}{2} \bar{\lambda}_{\mathrm{csc}}^{-1} |\bar{\Delta}|^2 + \bar{\lambda}_{\mathrm{eff}} |\bar{\Delta}|^4 . \tag{3.22}$$

An RG-consistent effective action can now be constructed by considering the effective action (3.21) at a new scale $\Lambda > \Lambda_{\mathrm{LEM}}$ instead of Λ_{LEM}. Then, $\Gamma_{\Lambda,\mathrm{LEM}}$ can be used to ensure RG consistency by including carefully

chosen counterterms. Consequently, Γ_Λ consists of two contributions, one that determines the effective action at the scale Λ_{LEM} and one that includes counterterms such that the effective action is RG consistent. Since we are not aiming to discuss RG consistency in the following, we simply follow the line of arguments presented in Ref. [194], where details about this aspect can be found, and adapt them to the present work, which is straightforward.
The effective potential U can then be calculated by considering the long-range limit ($k \to 0$) of the effective action (3.21): $U(|\bar{\Delta}|^2) = \Gamma_{k\to 0,\mathrm{LEM}}/V_4$. In the following, we shall use a three-dimensional sharp cutoff, for convenience.

3.1.2 Effective Potential

Including electron degrees of freedom, which only contribute as a free electron gas, the effective potential U of the low-energy model is given by

$$\begin{aligned} U(|\bar{\Delta}|^2) = \frac{1}{2}\bar{\lambda}_{\mathrm{csc}}^{-1}|\bar{\Delta}|^2 + \bar{\lambda}_{\mathrm{eff}}|\bar{\Delta}|^4 - \frac{\mu_{\mathrm{e}}^4}{12\pi^2} - \frac{\mu_{\mathrm{u,b}}^4}{12\pi^2} - \frac{\mu_{\mathrm{d,b}}^4}{12\pi^2} - 8\bar{l}(|\bar{\Delta}|^2) \\ + \frac{1}{2}\theta\big(\delta\mu_{\mathrm{gr}}^2 - |\bar{\Delta}|^2\big)\delta\bar{l}(|\bar{\Delta}|^2)\big|_{\delta\mu=\delta\mu_{\mathrm{gr}}} + \frac{1}{2}\theta\big(\delta\mu_{\mathrm{rg}}^2 - |\bar{\Delta}|^2\big)\delta\bar{l}(|\bar{\Delta}|^2)\big|_{\delta\mu=\delta\mu_{\mathrm{rg}}}\,. \end{aligned} \tag{3.23}$$

Recall that $|\bar{\Delta}|^2 = \bar{\Delta}_3^*\bar{\Delta}_3$ where $\bar{\Delta}_3$ is the homogeneous background field. The so-called diquark gap $\bar{\Delta}_{\mathrm{gap}}$ which is the gap in the excitation spectrum of the quarks can now be obtained by minimising the effective potential U with respect to $|\bar{\Delta}|^2$. The input parameters of the model are the four-quark interaction $\bar{\lambda}_{\mathrm{csc}}$ and the effective diquark interaction $\bar{\lambda}_{\mathrm{eff}}$ which can be fixed such that observables are recovered from the effective potential U. In Sec. 3.1.4, we shall see how we can use our results from the fRG study in Chap. 2 to fix the model parameters. The μ_{e}^4-term represents the electrons which only provide a charged background since they do not interact with the quarks in the present model. The $\mu_{\mathrm{u,b}}^4$ and $\mu_{\mathrm{d,b}}^4$ terms originate from blue fermion degrees of freedom that do not couple to the diquark fields, and therefore only appear as a "noninteracting contribution" which is a consequence of the choice to expand the background field in the three-direction. The contributions of the remaining quark loops are parametrised by the functions $\bar{l}$ and $\delta\bar{l}$ which depend on $|\bar{\Delta}|^2$:

$$\begin{aligned} \bar{l}(|\bar{\Delta}|^2) = \frac{1}{4\pi^2}\int_0^\Lambda \mathrm{d}p\, p^2\left(\sqrt{(p+\bar{\mu})^2+|\bar{\Delta}|^2} + \sqrt{(p-\bar{\mu})^2+|\bar{\Delta}|^2}\right) \\ - \frac{1}{2\pi^2}\int_{\Lambda_{\mathrm{LEM}}}^\Lambda \mathrm{d}p\, p^2\left(\sqrt{p^2+|\bar{\Delta}|^2} + \frac{\bar{\mu}^2|\bar{\Delta}|^2}{2(p^2+|\bar{\Delta}|^2)^{\frac{3}{2}}}\right) \end{aligned} \tag{3.24}$$

and

$$\delta\bar{l}(|\bar{\Delta}|^2) = \frac{2}{\pi^2}\int_{p_-}^{p_+}\mathrm{d}p\, p^2\left(\sqrt{(p-\bar{\mu})^2+|\bar{\Delta}|^2} - |\delta\mu|\right), \qquad \text{where} \qquad p_\pm = \bar{\mu} \pm \sqrt{\delta\mu^2 - |\bar{\Delta}|^2}\,. \tag{3.25}$$

Here, $\delta\bar{l}$ describes the shift of the effective potential U for finite isospin asymmetry. The momentum integrals in $\bar{l}$ and $\delta\bar{l}$ can be solved analytically since we have used a three-dimensional sharp cutoff. We have ensured that the potential is RG consistent by carefully introducing counterterms included in $\bar{l}$. Since the terms depending on the isospin asymmetry, in particular $\delta\bar{l}$, are not affected by the initial RG scale Λ, they do not need to be considered when constructing counterterms. Therefore, we employ counterterms already used in Ref. [194]. These counterterms are given by the second line in Eq. (3.24). If they are chosen carefully, we expect that the results for physical observables do not depend on the regulator. Nevertheless, the parameters of the model, $\bar{\lambda}_{\mathrm{csc}}$ and $\bar{\lambda}_{\mathrm{eff}}$, are affected by the regularisation scheme. In Sec. 3.1.4, we shall discuss how to properly set these parameters. By introducing counterterms, we introduce a new scale Λ

where $\Lambda \gg \Lambda_{\mathrm{LEM}} > \bar{\mu}$. RG consistency is now ensured by considering the limit $\Lambda \to \infty$. We find

$$\Lambda \partial_\Lambda U(|\bar{\Delta}|^2) = -\frac{2\bar{\mu}^4 |\Delta|^2}{\pi^2 \Lambda^2} + \mathcal{O}\left(1/\Lambda^4\right) . \tag{3.26}$$

Therefore, the Λ dependence, which results from the Λ dependence of $\bar{l}$, is removed in the limit $\Lambda \to \infty$. In the present work, we ensure this by choosing the scale Λ to be sufficiently large compared to the model scale Λ_{LEM}, i.e., $\Lambda \gg \Lambda_{\mathrm{LEM}} > \bar{\mu}$. Since we do not aim to discuss artefacts from the regularisation, we refer the reader to Ref. [194] for a detailed discussion, and simply choose $\Lambda = 10\Lambda_{\mathrm{LEM}}$ for the present work. As the low-energy scale, we choose $\Lambda_{\mathrm{LEM}} = 1\,\mathrm{GeV}$ which is larger than the symmetry-breaking scale and which allows us to cover a reasonable range of chemical potentials.

The different chemical potentials defined in the action (3.3), only appear in specific combinations in the effective potential (3.23). The chemical potentials associated with the red and green quarks have been replaced by combinations of μ_{u}, μ_{d}, μ_3, and μ_8 since red and green quarks mix in the colour-superconducting phase such that

$$\bar{\mu} = \frac{\mu_{\mathrm{u}} + \mu_{\mathrm{d}}}{2} + \frac{\mu_{\mathrm{r}} + \mu_{\mathrm{g}}}{2} = \frac{\mu_{\mathrm{u}} + \mu_{\mathrm{d}}}{2} + \frac{1}{2\sqrt{3}}\mu_8 \,, \tag{3.27}$$

$$\delta\mu_{\mathrm{rg}} = \frac{\mu_{\mathrm{u}} - \mu_{\mathrm{d}}}{2} + \frac{\mu_{\mathrm{r}} - \mu_{\mathrm{g}}}{2} = \frac{\mu_{\mathrm{u}} - \mu_{\mathrm{d}}}{2} + \frac{1}{2}\mu_3 \,, \tag{3.28}$$

$$\delta\mu_{\mathrm{gr}} = \frac{\mu_{\mathrm{u}} - \mu_{\mathrm{d}}}{2} + \frac{\mu_{\mathrm{g}} - \mu_{\mathrm{r}}}{2} = \frac{\mu_{\mathrm{u}} - \mu_{\mathrm{d}}}{2} - \frac{1}{2}\mu_3 \,. \tag{3.29}$$

Here, $\bar{\mu}$ can be interpreted as the average of the two quark flavours and $\delta\mu_{\mathrm{rg}}$ and $\delta\mu_{\mathrm{rg}}$ are a measure of the isospin asymmetry. The chemical potentials associated with the blue quarks are

$$\mu_{\mathrm{u,b}} = \mu_{\mathrm{u}} + \mu_{\mathrm{b}} = \mu_{\mathrm{u}} - \frac{1}{\sqrt{3}}\mu_8 \qquad \text{and} \qquad \mu_{\mathrm{d,b}} = \mu_{\mathrm{d}} + \mu_{\mathrm{b}} = \mu_{\mathrm{d}} - \frac{1}{\sqrt{3}}\mu_8 \,. \tag{3.30}$$

In contrast to the chemical potential of the red and green quarks, the chemical potentials associated with the blue quarks appear explicitly in the effective potential as they only appear as "noninteracting" spectators. This is a consequence of the expansion of the diquark fields in the three-direction. Therefore, only red and green quarks can obtain a gap in the fermionic excitation spectrum and the blue quarks remain "ungapped" even in the phase governed by spontaneous symmetry breaking, see Fig. 3.1.

Note that it is possible to include additional four-quark interaction channels, alongside the diquark channel used in the present approach, when constructing the low-energy model. As with the current approach, a Hubbard–Stratonovich transformation can be employed to introduce suitable effective degrees of freedom. With a fitting four-quark interaction channel, these effective degrees of freedom can be chosen such that blue quarks can obtain a gap. Specifically, these degrees of freedom also represent diquark fields but come with a symmetric colour structure so that these diquark fields always consist of quarks of the same colour, e.g., blue quarks. It is important to emphasise that the resulting gap associated with blue quarks is then different from the gap associated with red and green quarks as considered in the present work. However, these considerations are beyond the scope of the present work.

From the effective potential U, it is possible to extract and analyse thermodynamic quantities of dense strong-interaction matter. Accordingly, we define some thermodynamic properties that are calculated in the following. The pressure is given by the effective potential U evaluated at the ground state (gs):

$$P = -U(|\bar{\Delta}|^2)\big|_{\mathrm{gs},\vec{\mu}} - P_0 \,, \tag{3.31}$$

where the ground state at high densities is dominated by the emergence of the diquark gap $\bar{\Delta}_{\mathrm{gap}}$. Here, $\vec{\mu} = (\mu_{\mathrm{u}}, \mu_{\mathrm{d}}, \mu_{\mathrm{r}}, \mu_{\mathrm{g}}, \mu_{\mathrm{b}}, \mu_{\mathrm{e}})$. The vacuum constant P_0, associated with $\vec{\mu} = 0$, requires knowledge about the ground state in the vacuum. However, the vacuum is governed by spontaneous chiral symmetry breaking which cannot be reliably accessed in our current model since we only take into account diquark-like interactions. Therefore,

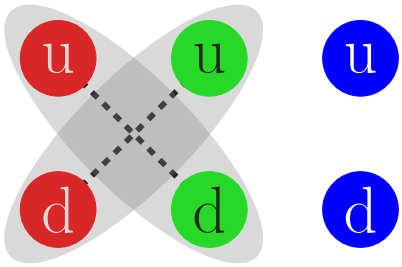

Figure 3.1: Illustration of the interactions between the quarks that form diquark fields and possible diquark condensates: Diquark fields as introduced in the present study always consist of one up and one down quark. Additionally, by expanding the diquark fields in the three-direction, only the red and green quarks interact and can therefore form diquark condensates. This leads to a gap in the fermionic excitation spectrum only for red and green quarks. The blue quarks only contribute as free quarks that remain "ungapped". By expanding in a different direction, we expect that quarks with another colour contribute as free quarks while the quarks with the remaining two colours mix.

also the pressure cannot be accessed in our current approximation. Nevertheless, in the high density regime where the ground state is dominated by colour superconductivity, derivatives of the pressure with respect to the chemical potentials are accessible so that the density for up and down quarks are given by

$$n_{\mathrm{u}} = \frac{\partial P}{\partial \mu_{\mathrm{u}}} \qquad \text{and} \qquad n_{\mathrm{d}} = \frac{\partial P}{\partial \mu_{\mathrm{d}}}\,, \tag{3.32}$$

respectively. The electron density is given by

$$n_{\mathrm{e}} = \frac{\partial P}{\partial \mu_{\mathrm{e}}}\,. \tag{3.33}$$

Note that we can define densities corresponding to each chemical potential present in the effective potential, e.g., colour-charge chemical potentials.
Another thermodynamic quantity of interest, especially for astrophysical applications, is the speed of sound. It can be thought of as a measure for the stiffness of matter or the stiffness of the equation of state and is therefore a very sensitive quantity. Consequently, it is of particular interest for astrophysical application, see Refs. [103, 119–122]. The speed of sound squared is given by the derivative of the pressure P with respect to the energy density ϵ:

$$c_{\mathrm{s}}^2 = \frac{\partial P}{\partial \epsilon}\,, \qquad \text{where} \qquad \epsilon = -P + \mu_{\mathrm{u}} n_{\mathrm{u}} + \mu_{\mathrm{d}} n_{\mathrm{d}} + \mu_{\mathrm{e}} n_{\mathrm{e}}\,. \tag{3.34}$$

As the speed of sound does not depend on the vacuum constant P_0, it can be accessed in the present work.
Before starting to discuss the phase structure, we can already enforce colour-charge neutrality. As we shall see, this allows us to immediately eliminate one colour-charge chemical potential in the effective potential with simple arguments. Macroscopic matter has to be colour-neutral, i.e., it has to be a colour singlet state and therefore, we are interested in studying colour-neutral matter. Especially, to study realistic neutron-star matter, colour-charge neutrality has to be implemented [328–330, 332]. It is important to emphasise that colour-charge neutrality is not to be confused with colour confinement. To enforce colour-charge neutrality, we have introduced the colour chemical potentials μ_{r}, μ_{g}, and μ_{b} in the ansatz for the effective action, see Eq. (3.3). Colour-charge neutrality is given if all colour densities n_r, n_g, and n_b are identical such that an equal number of red, green, and blue quarks exists. Here, n_{r}, n_{g}, and n_{b} are the densities of the red, green,

and blue quarks, respectively. We enforce this by requiring that the densities that correspond to μ_3 and μ_8 vanish simultaneously: $n_3 = n_8 = 0$. This is enforced by choosing μ_3 and μ_8 accordingly. The colour densities associated with μ_3 and μ_8 are

$$n_8 = \frac{\partial P}{\partial \mu_8} = \frac{1}{2\sqrt{3}}\frac{\partial P}{\partial \mu_\mathrm{r}} + \frac{1}{2\sqrt{3}}\frac{\partial P}{\partial \mu_\mathrm{g}} - \frac{1}{\sqrt{3}}\frac{\partial P}{\partial \mu_\mathrm{b}} = \frac{1}{2\sqrt{3}}\Big(n_\mathrm{r} + n_\mathrm{g} - 2n_\mathrm{b}\Big) \stackrel{!}{=} 0 \tag{3.35}$$

and

$$n_3 = \frac{\partial P}{\partial \mu_3} = \frac{1}{2}\frac{\partial P}{\partial \mu_\mathrm{r}} - \frac{1}{2}\frac{\partial P}{\partial \mu_\mathrm{g}} = \frac{1}{2}\Big(n_\mathrm{r} - n_\mathrm{g}\Big) \stackrel{!}{=} 0\,. \tag{3.36}$$

With the requirement that both densities vanish, we indeed find that an equal number of red, green, and blue quarks exists: $n_\mathrm{r} = n_\mathrm{g} = n_\mathrm{b}$. Note that the effective potential U is invariant under $r \leftrightarrow g$ so that $P(\mu_\mathrm{r}, \mu_\mathrm{g}) = P(\mu_\mathrm{g}, \mu_\mathrm{r})$. Therefore, the constraint for n_3 is fulfilled if $\mu_\mathrm{r} = \mu_\mathrm{g}$ from which it follows that $\mu_3 = \mu_\mathrm{r} - \mu_\mathrm{g} = 0$. This is a convenient consequence of the form of the effective potential. In general, the constraints for n_3 and n_8, see Eqs. (3.35) and (3.36), have to be fulfilled simultaneously.
With these considerations, the potential assumes the following form:

$$U(|\bar{\Delta}|^2) = \frac{1}{2}\bar{\lambda}_\mathrm{csc}^{-1}|\bar{\Delta}|^2 + \bar{\lambda}_\mathrm{eff}|\bar{\Delta}|^4 - \frac{\mu_\mathrm{e}^4}{12\pi^2} - \frac{\mu_\mathrm{u,b}^4}{12\pi^2} - \frac{\mu_\mathrm{d,b}^4}{12\pi^2} - 8\bar{l}(|\bar{\Delta}|^2) + \theta\big(\delta\mu^2 - |\bar{\Delta}|^2\big)\delta\bar{l}(|\bar{\Delta}|^2)\,, \tag{3.37}$$

and the chemical potential associated with μ_3 simplifies to

$$\delta\mu_\mathrm{gr} = \delta\mu_\mathrm{rg} = \frac{\mu_\mathrm{u} - \mu_\mathrm{d}}{2} \equiv \delta\mu\,. \tag{3.38}$$

Now, $\delta\mu$ controls the isospin asymmetry. Determining the value for μ_8 is done by solving the constraint for n_8, see Eq. (3.35). This cannot be done analytically as for μ_3 and is postponed to a later stage.

3.1.3 Qualitative Discussion of the Phase Structure

In the following, we qualitatively discuss the phase structure for isospin-asymmetric matter. For this, we set $\mu_8 = 0$, for convenience. Note that $\mu_3 = 0$ has already been implemented because of the colour constraint for n_3. Then, $\bar{\mu} = (\mu_\mathrm{u} + \mu_\mathrm{d})/2$ is the quark-chemical potential as the average of the up- and down-quark densities. The discussion shall give us insight into the dynamics that we can subsequently use to constrain the model with QCD results from our fRG study in Chap. 2. For now, we only have to assume that the parameters λ_eff and λ_csc have been tuned such that the potential has a nontrivial minimum at $|\bar{\Delta}| = \bar{\Delta}_\mathrm{gap}$. Therefore, already for vanishing isospin chemical potential, a finite gap exists for all considered $\bar{\mu}$ values. In practice, we have already tuned the model parameters according to the considerations in the subsequent section, see Sec. 3.1.4.
The effective potential is shown for $\bar{\mu} = 0.5\,\mathrm{GeV}$ and different isospin asymmetries in Fig. 3.2. Since the potential remains invariant for $\delta\mu \to -\delta\mu$, we only consider $\delta\mu > 0$ in the following. For vanishing isospin chemical potential $\delta\mu/\bar{\mu} = 0$, we find a nontrivial minimum for finite $\bar{\Delta}$, see Fig. 3.2 (blue line). As a global minimum, this represents the ground state and gives rise to a diquark gap. By increasing the isospin asymmetry to $\delta\mu/\bar{\mu} = 0.45$, we find that another minimum emerges at $\bar{\Delta} = 0$, see Fig. 3.2 (red line). However, for $\delta\mu/\bar{\mu} = 0.45$, this new minimum is still only a local minimum, and therefore, we still encounter a diquark gap which is given by the global nontrivial minimum. Interestingly, the minimum associated with the diquark gap remains in the same position as in the isospin-symmetric case. If we increase the asymmetry further to $\delta\mu/\bar{\mu} = 0.50$ (see Fig. 3.2, green line) or $\delta\mu/\bar{\mu} = 0.55$ (see Fig. 3.2, orange line) the minimum at $\bar{\Delta} = 0$ (which is a local maximum for $\delta\mu/\bar{\mu} = 0$ and a local minimum for $\delta\mu/\bar{\mu} = 0.45$) becomes a global minimum. Therefore, the new ground state is associated with the trivial minimum at $\bar{\Delta} = 0$ so that there is no diquark gap for these isospin chemical potentials.

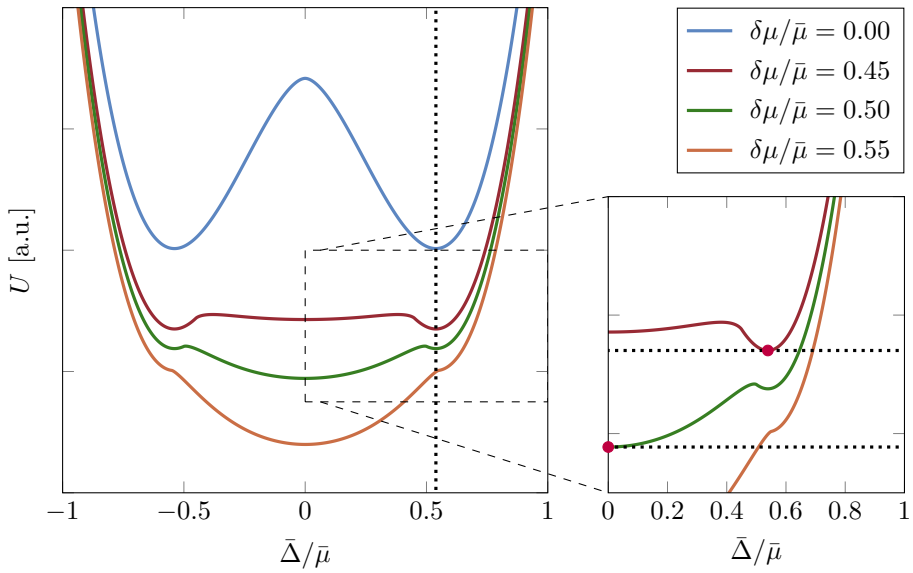

Figure 3.2: Schematic illustration of the effective potential U for fixed chemical potential $\bar{\mu} = 0.5\,\mathrm{GeV}$ as a function of $\bar{\Delta}/\mu$. We show the potential for different relative isospin chemical potentials $\delta\mu/\bar{\mu}$. The global nontrivial minimum for vanishing isospin chemical potential becomes a local minimum when increasing the asymmetry and eventually disappears altogether. The position of the nontrivial minimum remains the same. Note that we have set $\mu_\mathrm{e} = 0$ which would only lead to a global offset along the y-axis. The model parameters have been tuned according to the considerations in the subsequent section, see Sec. 3.1.4.

We can deduce two important features of the potential: Firstly, there is a critical value for the isospin chemical potential above which the diquark gap vanishes. Secondly, we find that the position of the nontrivial minimum, see vertical dashed line in Fig. 3.2, does not change for different isospin asymmetries (for fixed chemical potential $\bar{\mu}$). We shall discuss this behaviour and its origin in more detail in the following.
The behaviour of the position of the minimum can be explained by closer examining the relevance of the "quantum correction" $\delta\bar{l}$ in Eq. (3.37). Due to the θ-function, it does not contribute to the potential for $\delta\mu = 0$. More importantly, it also does not influence the form of the potential for $|\bar{\Delta}|^2 > \delta\mu^2$. In this region and since the function $\bar{l}$ does not depend on the isospin asymmetry, the potential is only shifted vertically by a constant offset due to contributions from the blue quarks which are affected by the isospin asymmetry. It immediately follows that (for fixed $\bar{\mu}$) the existence and the position of the nontrivial minimum remain unchanged provided that the isospin asymmetry is smaller than the aforementioned nontrivial minimum. From this, it follow three different scenarios: Firstly, this minimum can be a global minimum so that it can be associated with the gap $\bar{\Delta}_\mathrm{gap}$, see vertical dashed line and blue and red line in Fig. 3.2. Secondly, the nontrivial minimum still exists but only as a local minimum so that it cannot be associated with the diquark gap, see green line in Fig. 3.2. In this case, the global minimum is at $\bar{\Delta} = 0$. Thirdly, the nontrivial minimum can vanish completely, see orange line in Fig. 3.2. These findings suggest that a finite range of values for $\delta\mu$ exists where the gap $\bar{\Delta}_\mathrm{gap}$ is identical to the gap in the isospin-symmetric limit.
The existence of the critical value for the isospin asymmetry can also be explained by considering the effect of the "quantum correction" $\delta\bar{l}$ in the region where it affects the potential (for $|\bar{\Delta}|^2 < \delta\mu^2$). We find that it generates a second minimum at $\bar{\Delta} = 0$ for a sufficiently large $\delta\mu$. This minimum starts as a local one (see red line) but it eventually becomes a global minimum for a sufficiently large isospin asymmetry (see green line). Since the diquark gap is given by a nontrivial global minimum, a critical value $\delta\mu_\mathrm{cr}$ exits such that the

gap $\bar{\Delta}_{\mathrm{gap}}$ vanishes for $\delta\mu^2 > \delta\mu_{\mathrm{cr}}^2$. This transition is (at least for vanishing temperature as considered in the present work) not continuous. Therefore, we encounter a first-order phase transition at $\delta\mu = \delta\mu_{\mathrm{cr}}$ where the system transitions from a gapped phase governed by the formation of a diquark gap to an ungapped phase. The existence of such a phase transition is also discussed in, e.g., Ref. [333].

As we have stated before, we expect that a finite range of values for $\delta\mu$ exists where the gap $\bar{\Delta}_{\mathrm{gap}}(\bar{\mu}, \delta\mu)$ is given by the gap in the isospin-symmetric limit $\bar{\Delta}_{\mathrm{gap}}(\bar{\mu}, 0)$. To demonstrate this, we show the diquark gap as a function of the chemical potential $\bar{\mu}$ and the isospin asymmetry $\delta\mu$ in Fig. 3.3. We find that the gap remains unchanged throughout the entire gapped region, i.e., for $\delta\mu < \delta\mu_{\mathrm{cr}}$ (see Fig. 3.3, blue region): The isospin chemical potential only affects the potential for $\delta\mu^2 < |\bar{\Delta}|^2$. In the present study, the gap is larger than the critical isospin asymmetry $\delta\mu_{\mathrm{cr}}^2 < \Delta_{\mathrm{gap}}^2$. Therefore, in the gapped region $\delta\mu < \delta\mu_{\mathrm{cr}}$, we find that the potential can only be influenced by the "quantum correction" $\delta\bar{l}$ in the region below the gap Δ_{gap}, i.e., in the region $\delta\mu^2 < \Delta_{\mathrm{gap}}^2$. It follows that the position of the gap cannot be changed in the gapped region for a given chemical potential $\bar{\mu}$.

Above the critical value, the gap vanishes, see Fig. 3.3 (green region), and the quarks exist as a free (asymmetric) quark gas. Both regions are separated at the critical isospin asymmetry by a first-order phase transition, see Fig. 3.3 (red line). Following this figure for a given $\delta\mu$ from small chemical potential to large chemical potential, we may find trajectories (for certain $\delta\mu$-values) that cross the line for the critical isospin chemical potential such that the gap jumps from zero to a finite value. This is associated with a first-order phase transition. Inside the gapped phase (blue region), the gap does not depend on the isospin asymmetry and is given by the gap for isospin-symmetric matter. In conclusion, the gap can be written as:

$$\bar{\Delta}_{\mathrm{gap}}(\bar{\mu}, \delta\mu) = \bar{\Delta}_{\mathrm{gap}}(\bar{\mu}, 0)\theta(\delta\mu_{\mathrm{cr}} - |\delta\mu|)\,. \tag{3.39}$$

The finding that the gap remains unchanged (along the $\delta\mu$-axis) in the entire gapped phase is a consequence of our initial conditions. Therefore, the critical isospin asymmetry coincides with the first-order phase transition. There might be configurations where the gap only remains unchanged (along the $\delta\mu$-axis) for a finite part of the gapped region and varies before the phase boundary is reached. We further note that the existence of a finite range of isospin chemical potentials for which the gap remains unchanged is only valid for vanishing temperature. Indeed, the gap depends on the isospin asymmetry $\delta\mu$ in the gapped phase when considering a finite temperature. However, a phase transition to an ungapped phase still exists. For some finite temperature, we expect that this transition from the gapped region (blue region in Fig. 3.3) to the ungapped region (green region in Fig. 3.3) is smeared out so that the first-order phase transition becomes a second-order phase transition. However, fixing the initial conditions for finite temperature, with the same approach used in 3.1.4 for vanishing temperature, would require results for the temperature dependence of the diquark gap (from, e.g., fRG calculation) which are presently unavailable. Therefore, we only consider the zero temperature limit in the present work and postpone the inclusion of temperature to future work.

We close this section by comparing and extending the discussion to conventional superconductors. The existence of a critical value above which superconductivity ceases to exist has already been observed in two-component Fermi gases exhibiting a superconducting ground state [334, 335]. For example, the introduction of up and down quarks can be suitably compared to an electron gas to which a magnetic field is applied. The Zeeman coupling of the electron spin to the magnetic field induces an imbalance between spin-up and spin-down electrons leading to the polarisation of the system. In a "classical" superconductor (superconductivity in metals), pairs of electrons form so-called Cooper pairs resulting in the formation of a superconducting ground state. The attractive forces necessary for the formation of Cooper pairs are strongest between electrons with opposite spin. The decay and formation of such pairs are in equilibrium. By applying a magnetic field to the superconductor, spin polarisations aligning with the magnetic field become more favourable as the energy of the state with opposite spin alignment is higher. At the critical magnetic field, a sufficient number

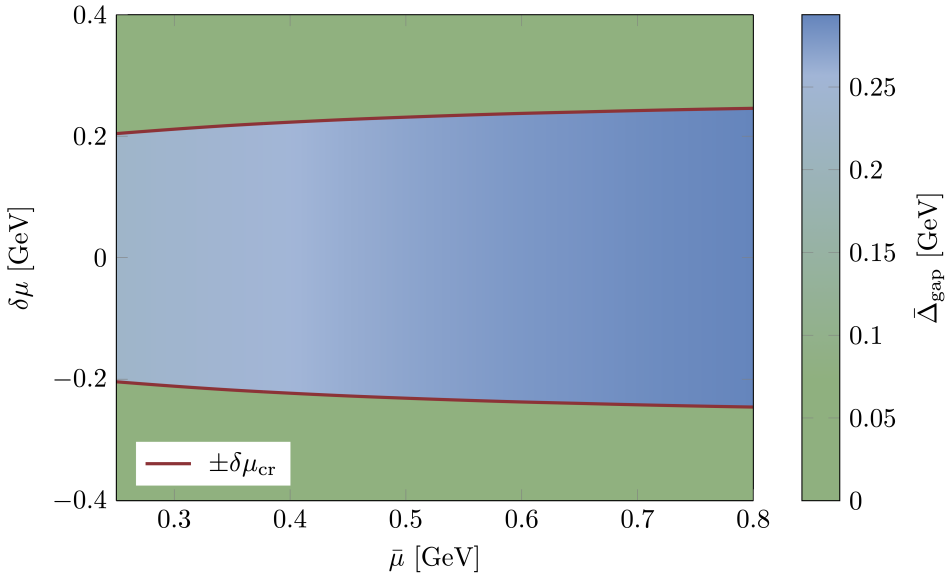

Figure 3.3: Diquark gap $\bar{\Delta}_{\mathrm{gap}}$ as a function of the chemical potential $\bar{\mu}$ and the chemical potential that measures the isospin asymmetry $\delta\mu$. The red line represents the critical value $\delta\mu_{\mathrm{cr}}$ of the isospin asymmetry as a function of the chemical potential $\bar{\mu}$. Above this value, the system is in an ungapped phase (green area) whereas a finite gap exists below this value. In the region below the critical isospin chemical potential, the gap does not depend on the isospin chemical potential (blue area). The model parameters have been tuned according to the considerations in the subsequent section but the existence of a finite range for the isospin asymmetry where the gap is unaffected is a general feature of the present model. Further, the existence of a phase transition is also unaffected by the choice of the parameters of the model as long as they are tuned such that a diquark gap exists.

of spins align in the same direction preventing the formation of enough Cooper pairs required to maintain the superconducting phase. Consequently, even at temperatures approaching zero, the superconducting phase cannot exist in a classical superconductor when subjected to a magnetic field exceeding some critical value. This critical value for the magnetic field depends on the temperature. It is worth noting that there are two types of superconductors: Type I and Type II. In Type I superconductors there exists only one critical magnetic field below which a superconducting phase exists. For Type II superconductors, on the other hand, there exist two critical magnetic fields. Below the first, the system is governed by a superconducting phase while above the second critical field, the system is not superconducting. In the region between the critical magnetic fields, a mixed phase with magnetic vortices arises. For both types of superconductors, the material expels a magnetic field as long as its magnitude is smaller than the critical value which is the so-called Meissner-Ochsenfeld effect [81]. See also, e.g., Refs. [283, 336–338] for details about these phenomena.
The critical magnetic field, beyond which superconductivity breaks down, is associated with a first-order phase transition to a normally conducting phase. Building upon the preceding discussion, it follows that a critical magnetic field corresponds to a critical spin polarisation, compared to the critical isospin asymmetry encountered in the present study. An estimate for the critical polarisation can be found by comparing the pressure of the unpolarised superconducting ground state with the partially polarised ungapped phase. The ground state is determined by the state with the highest pressure (i.e., lowest Gibbs energy). For more details, see Refs. [334, 335]. Within the QCD inspired model employed in the present work, Cooper pairs correspond to diquark fields formed by differently coloured up and down quarks. In contrast to a critical

magnetic field, there is a critical value for the difference in the number of up and down quarks, represented by $\delta\mu$. We find some critical value for $\delta\mu$ above which the diquark gap vanishes. In contrast to the magnetic field, which controls the polarisation in ordinary superconductors, the ratio of up and down quarks is not an experimental control parameter but shall, e.g., be controlled by constraints for neutron-star matter.
The analogy between ordinary superconductors and colour superconductors can be used to find an estimate for the critical isospin asymmetry. For quark matter, the formation of a diquark from two quarks gives an energy gain per quark. This energy gain is of the order of the gap in the isospin-symmetric limit: $\bar{\Delta}_{\mathrm{gap}}(\bar{\mu},0)$. If the energy gain $\delta\mu$ by adding an up quark (or a down quark) to the system exceeds the critical value $\delta\mu_{\mathrm{cr}}$, superconductivity breaks down. Comparing the pressure for isospin-asymmetric quark matter in the noninteracting limit (Stefan-Boltzmann limit)

$$P_{\mathrm{SB}}(\bar{\mu},\delta\mu)=\frac{(\bar{\mu}+\delta\mu)^2}{4\pi^2}+\frac{(\bar{\mu}-\delta\mu)^2}{4\pi^2} \tag{3.40}$$

with the estimate for the pressure for gapped isospin-symmetric matter [46, 194, 339, 340]

$$P(\bar{\mu})=P_{\mathrm{SB}}(\bar{\mu},0)\left(1+2\left(\frac{\bar{\Delta}_{\mathrm{gap}}(\bar{\mu},0)}{\bar{\mu}}\right)^2+\cdots\right), \tag{3.41}$$

we can find an estimate for the critical isospin asymmetry $\delta\mu_{\mathrm{cr}}$. The relation for the pressure (3.41) can also be obtained from the effective potential (3.37) in the weak-coupling limit for small $\bar{\Delta}_{\mathrm{gap}}(\bar{\mu},0)/\bar{\mu}$ and weak four-quark and four-diquark interactions. Notably, the estimate does not depend on the model parameters $\bar{\lambda}_{\mathrm{csc}}$ and $\bar{\lambda}_{\mathrm{eff}}$. At the critical isospin asymmetry, both expressions for the pressure have to be identical: $P(\bar{\mu})\overset{!}{=}P_{\mathrm{SB}}(\bar{\mu},\delta\mu_{\mathrm{cr}})$. Therefore, the estimate for the critical value of the isospin asymmetry becomes

$$|\delta\mu_{\mathrm{cr}}(\bar{\mu})|=\bar{\Delta}_{\mathrm{gap}}(\bar{\mu},0)/\sqrt{3}+\cdots. \tag{3.42}$$

The dots represent higher orders in the gap $\bar{\Delta}_{\mathrm{gap}}(\bar{\mu},0)$. The scale for $\delta\mu_{\mathrm{cr}}$ is, therefore, given by the diquark gap and it inherits its $\bar{\mu}$-dependence in the isospin-symmetric limit. At $\delta\mu_{\mathrm{cr}}$, the system undergoes a first-order phase transition, as already discussed in the present section, because the pressure is not continuously differentiable at $\delta\mu_{\mathrm{cr}}$ (see also Refs. [339, 341] for a similar analysis in $2+1$ quark flavours). We shall compare the analytic estimate (3.42) to the exact value obtained from the effective potential (3.37) in the subsequent section after fixing the initial conditions.

3.1.4 Constraining the Model with the Diquark Gap from an fRG Calculation

The effective potential U can be used to calculate thermodynamic properties for phenomenological applications. However, utilising it, first requires to fix the parameters, $\bar{\lambda}_{\mathrm{csc}}^{-1}$ and $\bar{\lambda}_{\mathrm{eff}}$, of the model at the scale $\Lambda_{\mathrm{LEM}}=1\,\mathrm{GeV}$. In the following section, we use the insight gained from the preceding section, see Sec. 3.1.3, to constrain the low-energy model using the results for the gap obtained in Sec. 2.5, where the diquark gap has been calculated from first principles, considering the underlying quark-gluon dynamics. It should be noted that these results were only obtained for isospin-symmetric matter.
Nevertheless, it is reasonable to utilise the findings for isospin-symmetric matter to fix the initial conditions also for isospin-asymmetric matter. This is mainly due to the fact that the gap remains unaffected by the isospin chemical potential below some critical value $\delta\mu_{\mathrm{cr}}$ and vanishes above this scale. Above the critical value (for $\delta\mu^2>\delta\mu_{\mathrm{cr}}^2$), the effective potential corresponds to that of a noninteracting asymmetric quark gas. Consequently, it is consistent to adopt the results for isospin-symmetric matter when setting the initial conditions, even for isospin-asymmetric matter. In the following, we therefore, describe how the initial conditions are adjusted such that the diquark gap from the fRG calculation obtained in Sec. 2.5 is recovered.

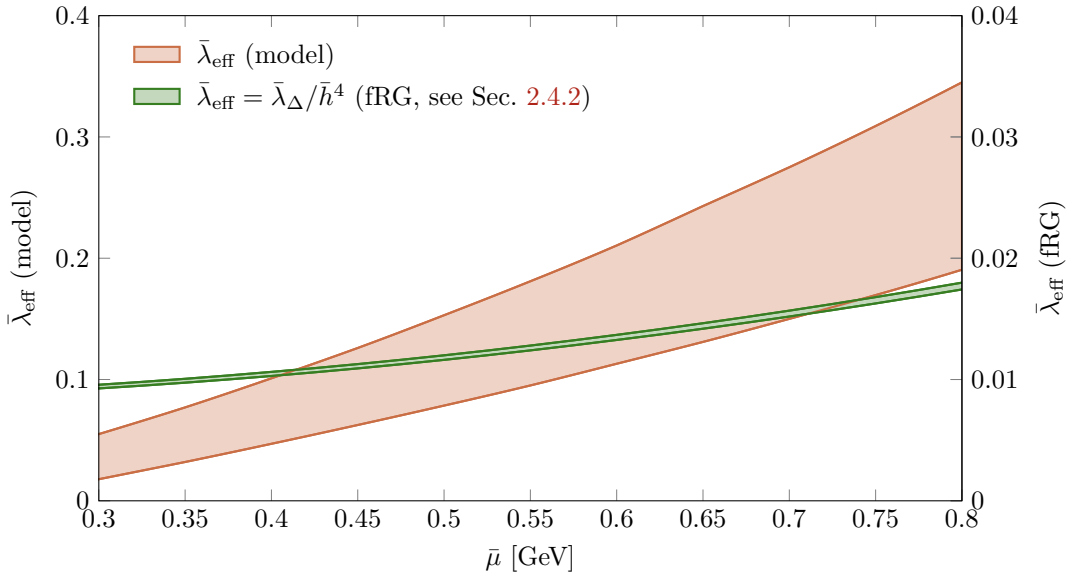

Figure 3.4: Comparison of the effective diquark coupling as a function of the chemical potential $\bar{\mu}$ obtained from the fRG calculation (see Sec. 2.4.2) $\bar{\lambda}_{\text{eff}} = \bar{\lambda}_\Delta/\bar{h}^4$ and the effective coupling used as the initial condition of the model in the present calculation $\bar{\lambda}_{\text{eff}}$. Note that the absolute values differ but the qualitative behaviour agrees. For increasing chemical potential, also the effective coupling increases. The couplings have been evaluated at the scale $k = \Lambda_{\text{LEM}} = 1\,\text{GeV}$. The uncertainty band for the fRG results (green band) results in the variation of the strong coupling at the initial RG scale. The uncertainty band for the model parameter (orange band) represents the uncertainty coming from the diquark gap used to fix the initial conditions by choosing the initial values so that we recover the diquark gap from the fRG study.

Our numerical results and the analytic estimate concerning the fRG calculation (see Sec. 2.4.2) indicate that the four-quark coupling $\bar{\lambda}_{\text{csc}}$ depends only mildly on the chemical potential at scales sufficiently larger than the symmetry-breaking scale and the chemical potential. Consequently, we assume the four-quark coupling to be constant at the scale $\Lambda_{\text{LEM}} > \bar{\mu}$. In practice, we choose $\bar{\lambda}_{\text{csc}}^{-1} = 0.197\,\text{GeV}^2$ for all chemical potentials $\bar{\mu}$. In contrast to that, the effective diquark coupling $\bar{\lambda}_{\text{eff}}$ depends on the chemical potential already at scales larger than the symmetry-breaking scale (see Fig. 3.4, green band). Therefore, we assume that the effective diquark coupling depends on the chemical potential. The actual value for $\bar{\lambda}_{\text{eff}}$ for each μ-value is then determined by tuning it (while keeping the value for $\bar{\lambda}_{\text{csc}}^{-1}$ constant) so that the value for the gap $\bar{\Delta}_{\text{gap}}$ from the fRG study is recovered when calculating the gap in the present model. The latter is achieved by minimising the effective potential. In contrast to the model parameters which are scheme dependent, the diquark gap is, as a physical observable, a scheme-independent quantity. We tune the parameters in such a way that we recover the gap in the case of "gapped" gluons. Here, "gapped" gluons refers to the approximation where the matter sector has been decoupled from the gauge sector in the phase governed by spontaneous symmetry breaking which has been done to analyse the effect of "gluon gapping" according to an Anderson-Higgs-type mechanism. For further details, we refer the reader to Sec. 2.4.2. The effect of using the gap for "ungapped" gluons can then be inferred. The gap used to fix the model parameters is shown in Fig. 3.5 (left panel, green band). The actual values of the model parameter $\bar{\lambda}_{\text{eff}}$ as used for the present model are shown in Fig. 3.4 (orange band) compared to the value obtained in the fRG calculation by evaluating at the model scale $\Lambda_{\text{LEM}} = 1\,\text{GeV}$. The specific numerical values are not meaningful because the model parameters depend on the regularisation scheme and are not scheme-independent quantities. However, the general dependence on the chemical

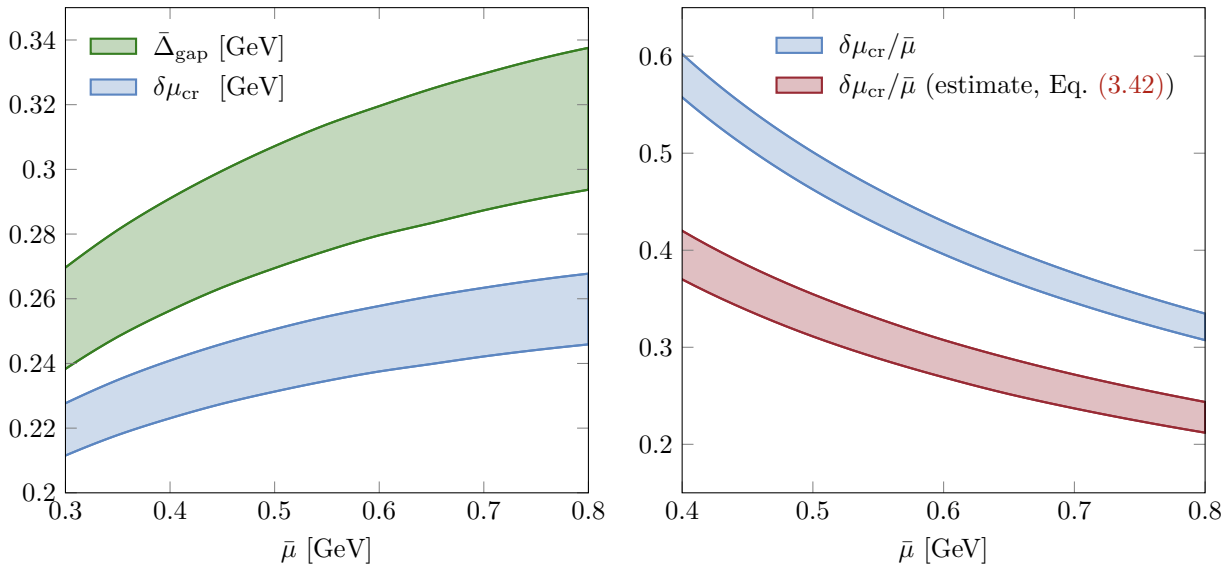

Figure 3.5: Left panel: Diquark gap for symmetric matter $\bar{\Delta}_{\mathrm{gap}}$ (green band) compared to the critical value for the isospin asymmetry $\delta\mu_{\mathrm{cr}}$ (blue band) as a function of the chemical potential $\bar{\mu}$. Below the critical value, a gapped phase is encountered and above the critical value the gap vanishes and a free quark gas is encountered. We find that $\bar{\Delta}_{\mathrm{gap}} > \delta\mu_{\mathrm{cr}}$. Right panel: Comparison of the relative critical isospin asymmetry $\delta\mu_{\mathrm{cr}}/\bar{\mu}$ as obtained by minimising the effective action compared to the qualitative analytic estimate, see Eq. (3.42), as a function of the chemical potential $\bar{\mu}$. We observe, that their qualitative behaviour is compatible. The error bands represent the uncertainties of the results for the diquark gap which have been used to fix the initial conditions.

potential $\bar{\mu}$ is consistent. In both cases, the effective diquark coupling increases with increasing chemical potential. The gap used to fix the model parameters comes with an uncertainty band which is reflected in the uncertainty band of the model parameter, see Fig. 3.4 (orange band). Note that extracting the model parameters from the RG flows in Sec. 2.4.2 evaluated at a suitably chosen low-energy scale is, in principle, also possible. For example, the couplings evaluated at 1 GeV are shown in Fig. 2.15. Since the parameters are scheme-dependent quantities, it is however not straightforward to match the couplings from the fRG results to the couplings used in the low-energy model.

After fixing the initial conditions for the low-energy model, we can go back to some of the findings discussed in the previous section regarding general aspects about the phase structure. Interestingly, the diquark gap $\bar{\Delta}_{\mathrm{gap}}$ is larger than the critical isospin asymmetry $\delta\mu_{\mathrm{cr}}$ for all considered chemical potentials, see left panel in Fig. 3.5. Only considering the gapped region $\delta\mu < \delta\mu_{\mathrm{cr}}$, we consequently find $\bar{\Delta}_{\mathrm{gap}} > \delta\mu$. Therefore, the correction $\delta\bar{l}$ does not contribute in the gapped phase. It follows that the diquark gap remains unchanged in the entire gapped region (along the $\delta\mu$-axis) and not only for some finite range as we have already discussed in the previous section, see Fig. 3.3. As a consequence, the critical value for the isospin asymmetry coincides with the position of the first-order phase transition. Consequently, it is consistent to use the gap for isospin-symmetric matter to fix the model parameters also for asymmetric matter as we have already stated at the beginning of this section. Further, we would like to comment on the analytic estimate for the critical isospin asymmetry, see Eq. (3.42). We find that the analytic estimate is compatible with the critical isospin asymmetry as obtained directly from the effective potential (3.37). Most importantly, we emphasise that the qualitative behaviour agrees.

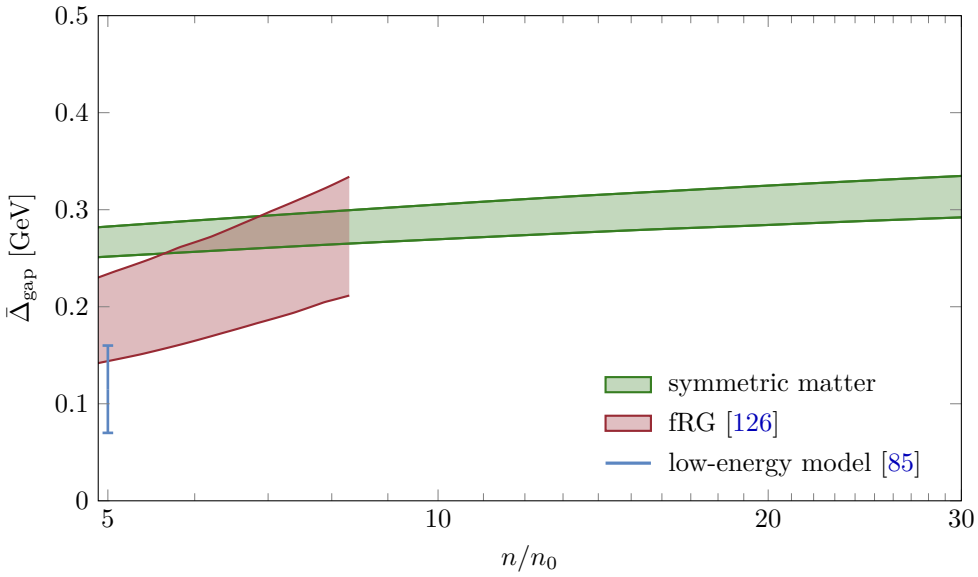

Figure 3.6: Different results for the diquark gap $\bar{\Delta}_{\text{gap}}$ as a function of the baryon density n normalised by the nuclear saturation density n_0: The results for symmetric matter (green band), from the fRG calculation for QCD in Sec. 2.5, have been used in the present section to fix the initial conditions. They are compared to previous fRG results (red band, see Ref. [126]) and, as an example, a low-energy model from Ref. [85] (blue). The error band for the green line includes a variation of the strong coupling at the initial RG scale. The nuclear saturation density n_0 is given by 0.165 nucleons per fm^3.

After fixing the model parameters, we can proceed with the computation of thermodynamic observables in Sec. 3.1.5. We conclude this section by providing additional insight on the behaviour of the diquark gap as a function of the density. While we have already discussed the diquark gap as a function of the chemical potential in Sec. 2.5, we can now consider the diquark gap as a function of the baryon density. Therefore, we show the diquark gap $\bar{\Delta}_{\text{gap}}$ as a function of the baryon density n in units of the nuclear saturation density n_0 in Fig. 3.6 for symmetric matter (green band) as obtained from the fRG calculation in Sec. 2.5. The results reveal a relatively weak dependence of the gap on the density. To obtain the gap as a function of the density, we have used the effective potential (3.37) for symmetric matter, enabling us to determine the associated pressure and subsequently calculate the density. However, it is important to note that incorporating isospin asymmetry and considering constraints from colour-charge neutrality and electric-charge neutrality which are both relevant for astrophysical applications, may quantitatively alter the diquark gap as a function of the density. Despite employing the same diquark gap to fix the initial conditions, the aforementioned constraints influence the density, and consequently, the diquark gap as a function of the density. Nevertheless, we expect these effects to be relatively minor as the leading-order contribution to the density is given by $\bar{\mu} \sim n^{1/3}$ at least for isospin chemical potentials $\delta\mu$ that are small compared to $\bar{\mu}$. Taking these considerations into account, we can derive an analytic estimate for the scaling behaviour of the diquark gap as a function of the density. With the result for the gap from Sec. 2.5, $\bar{\Delta}_{\text{gap}} \sim \exp\left(-c/(g^4\bar{\mu}^2)\right)$, and $\bar{\mu} \sim n^{1/3}$, we find

$$\bar{\Delta}_{\text{gap}} \sim \exp\left(-\frac{c}{g^4 n^{2/3}}\right), \qquad c > 0\,. \tag{3.43}$$

It is worth noting that it follows that the ground state is nonperturbative in the presence of a diquark gap. By comparing our present results for the diquark gap $\bar{\Delta}_{\text{gap}}$ (green band in Fig. 3.6) with previous fRG results,

taken from Ref. [126], where a Fierz-complete ansatz was employed (red band), we conclude that at lower densities, the inclusion of four-quark interactions other than the diquark channel becomes important. This is indeed in agreement with the results from the aforementioned Fierz-complete study of gluon-induced four-quark interactions, where it was also found that the scalar-pseudoscalar channel becomes important at lower densities [179]. Therefore, we expect that the regime $n/n_0 \gtrsim 7$ is reliably accessible in our present study. For comparison and as an example, we further show a result from a low-energy model from Ref. [85], see blue line in Fig. 3.6. We find, that the results for the diquark gap from the present work and from Ref. [126] lie above those from the low-energy model in Ref. [85]. This can already be understood from the analytic estimate for the diquark gap (3.43), where the quark-gluon dynamics leads to a rapid increase in the gap at low densities. The uncertainty from the diquark gap used to fix the initial conditions shall lead to uncertainties in the phase structure and the thermodynamics for isospin-symmetric matter. In the following, this can be used to analyse the sensitivity of the results, especially how a smaller or larger diquark gap would change the results.

3.1.5 Phase Diagram for Asymmetric Dense Strong-Interaction Matter

We start with a general discussion of the phase structure for zero-temperature dense strong-interaction matter with two quark flavours. For this, we set $\mu_8 = 0$ in this section for convenience. At the end of this section, by extending the results to finite μ_8, we obtain a phase diagram for colour-neutral matter. Note that $\mu_3 = 0$ has already been implemented because of the colour constraint for n_3. The phase diagram spanned by the down quark fraction $n_\mathrm{d}/(n_\mathrm{u}+n_\mathrm{d})$ as a function of the total baryon density $n = (n_\mathrm{u}+n_\mathrm{d})/3$ in units of the nuclear saturation density n_0 is shown in Fig. 3.7. In practice, it has been obtained by considering the pressure in the gapped and the ungapped case, respectively, and evaluating it at the phase boundary, i.e., the critical isospin asymmetry. The pressure has been obtained by evaluating the potential, see Eq. (3.37), at the ground state. The phase diagram reveals three distinct regions. The ungapped case (blue-shaded area in Fig. 3.7) corresponds to a free (asymmetric) quark gas and can also be calculated in a perturbative setting [154–160]. When attempting to calculate the density (by differentiating the potential with respect to the corresponding chemical potential) as a function of the chemical potential, we find that we cannot reach every density ratio between the up and down densities. The density is discontinuous, which is a consequence of the first-order phase transition. This region is unstable and is the so-called first-order region, see white area in Fig. 3.7. For density ratios close to symmetric matter, characterised by the ratio $n_\mathrm{d}/(n_\mathrm{u}+n_\mathrm{d}) = 0.5$, a gapped phase that is dominated by the formation of a colour superconducting ground state with spontaneous symmetry breaking is encountered, see grey-shaded area in Fig. 3.7. The three regions are separated by the phase boundaries (blue and black lines in Fig. 3.7) which come with an error band originating in the uncertainty of the gap used to fix the initial conditions. When increasing the down quark fraction from the symmetric limit $n_\mathrm{d}/(n_\mathrm{u}+n_\mathrm{d}) = 0.5$ to the limit of pure down-quark matter $n_\mathrm{d}/(n_\mathrm{u}+n_\mathrm{d}) = 1$ for fixed baryon density, we find a (strong) first-order phase transition.

In the phase diagram, we observe that the phase boundaries separating the gapped and ungapped phase from the first-order region decrease with increasing baryon density. This can already be understood by considering an analytic estimate for the behaviour of the phase boundary. With Eq. (3.42), we found an estimate for the critical isospin asymmetry which we can generalise to $|\delta\mu_\mathrm{cr}| = \bar{\Delta}_\mathrm{gap}(\bar{\mu}, \delta\mu = 0)/c_\delta + \cdots$ by introducing $c_\delta > 0$. The analytic estimate (3.42) can be recovered by setting $c_\delta = \sqrt{3}$. Note that only the sign of the constant matters for the following discussion. However, by appropriately choosing c_δ we can more closely recover the result for $\delta\mu_\mathrm{cr}$ as obtained from the effective potential, see Fig. 3.5 (right panel, blue band). Further, the down-quark fraction in the ungapped phase for $|\delta\mu|/\bar{\mu} \ll 1$ can be estimated by

$$\frac{n_\mathrm{d}}{n_\mathrm{d}+n_\mathrm{u}} = \frac{1}{2} - \frac{3}{2}\frac{\delta\mu}{\bar{\mu}} + \cdots . \tag{3.44}$$

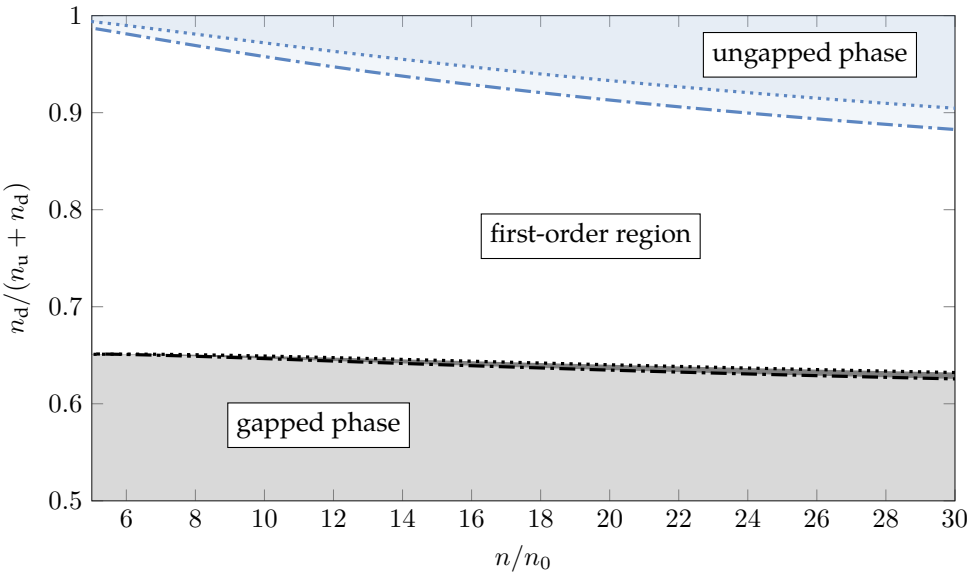

Figure 3.7: Phase diagram spanned by the down-quark fraction $n_\mathrm{d}/(n_\mathrm{u}+n_\mathrm{d})$ as a function of the baryon density n normalised by the nuclear saturation density n_0. Note that we have set $\mu_8 = 0$. The lower end of the y-axis represents symmetric matter $n_\mathrm{d}/(n_\mathrm{u}+n_\mathrm{d}) = 1/2$ and the upper end represents pure down-quark matter $n_\mathrm{d}/(n_\mathrm{u}+n_\mathrm{d}) = 1$. The error band of the transition lines (depicted by differently dashed lines) describes the error given by the uncertainty of the gap where the dotted line is the upper end and the dot-dashed line the lower end of the uncertainty band of the diquark gap. The phase transition lines have been calculated by evaluating the pressure in the gapped phase and the pressure for the ungapped phase at the critical isospin asymmetry, respectively.

By inserting the estimate for the critical isospin asymmetry $\delta\mu_\mathrm{cr}$ into the latter expression, we find the following expression for the critical down-quark fraction:

$$\left.\frac{n_\mathrm{d}}{n_\mathrm{d}+n_\mathrm{u}}\right|_\mathrm{cr} = \frac{1}{2} - \frac{3}{2c_\delta\bar{\mu}}\bar{\Delta}_\mathrm{gap}(\bar{\mu},0) + \cdots . \tag{3.45}$$

With the total baryon density in the ungapped phase which is given by

$$n = \frac{n_\mathrm{u}+n_\mathrm{d}}{3} = \frac{2\bar{\mu}^3}{3\pi^2}\left(1+3\left(\frac{\delta\mu}{\bar{\mu}}\right)^2\right) \tag{3.46}$$

and the scaling behaviour of the gap $\bar{\Delta}_\mathrm{gap} \sim \exp\left(-c'/\bar{\mu}^2\right)$ (as expected from relativistic models for the colour-superconducting gap, see Refs. [40, 82, 84–86]), where $c' > 0$, we find

$$\left.\frac{n_\mathrm{d}}{n_\mathrm{d}+n_\mathrm{u}}\right|_\mathrm{cr} - \frac{1}{2} \sim \frac{1}{n^{1/3}}\exp\left(-\frac{c''}{n^{2/3}}\right), \qquad \text{where} \qquad c'' > 0\,. \tag{3.47}$$

The analytic estimate reflects what can already be observed in the phase diagram, see Fig. 3.7. By increasing the baryon density the transition line between the ungapped phase and the first-order region decreases. By further increasing the baryon density beyond values depicted in the phase diagram, it eventually (very slowly) approaches the diquark fraction associated with isospin-symmetric matter, i.e., $n_\mathrm{d}/(n_\mathrm{u}+n_\mathrm{d}) = 0.5$, for $n \to \infty$. Therefore, also the transition line between the gapped phase and the first-order region has to approach the limit for symmetric matter so that the gapped phase shrinks to zero. In the limit $n \to \infty$, a gap then exists only for isospin-symmetric matter.

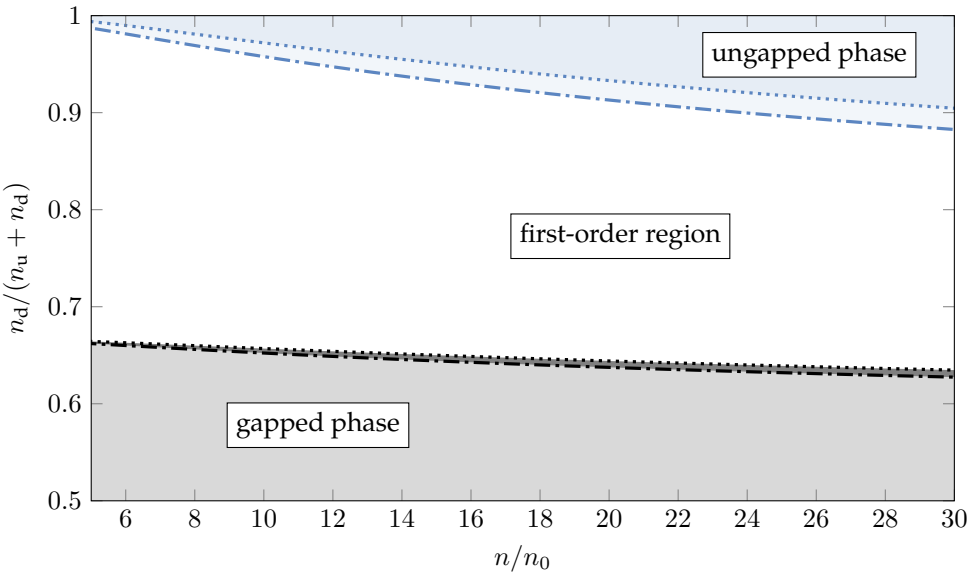

Figure 3.8: Phase diagram where colour-neutral matter undergoes a phase transition depicted by the down-quark fraction $n_\mathrm{d}/(n_\mathrm{u}+n_\mathrm{d})$ as a function of the baryon density n in units of the nuclear saturation density n_0. The black line represents the (colour-neutral) transition from the gapped phase to the first-order region which (in contrast to the one in Fig. 3.7) has been obtained by simultaneously requiring the colour-charge neutrality constraint $n_8 = n_3 = 0$ and evaluating the pressure at the critical isospin asymmetry. Note that the transition line from the first-order region into the ungapped phase remains unchanged. In addition to that, the transition line from the first-order region into the gapped phase is only slightly affected by the colour-charge neutrality constraint. As before, the error bands represent the errors originating in the uncertainty of the diquark gap.

The results can be directly extended to colour-neutral matter. Conveniently, the phase transition line between the ungapped phase and the first-order region is already colour-neutral. The (colour-neutral) transition line between the gapped phase and the first-order region can be obtained by solving the remaining colour constraint $n_8 = 0$ while simultaneously evaluating the pressure at the critical isospin asymmetry. Recall that the colour constraint $n_3 = 0$ has already been implemented in Sec. 3.1.2. The resulting phase diagram spanned by the down-quark fraction as a function of the baryon density is shown in Fig. 3.8. Note that there is only a small shift of the phase boundary depicted in the phase diagram mainly towards the lower density regime compared to Fig. 3.7.

We close this section by commenting on the extension of the phase diagram to finite temperature. In this case, we expect that the first-order phase transition, as observed in the zero-temperature limit, becomes a second-order phase transition at some finite temperature. However, a detailed study is beyond the scope of the present work because it requires results for the diquark gap at finite temperature. Additionally, at finite temperature the existence of a finite range of isospin chemical potentials for asymmetric matter for which the diquark gap remains unchanged (as observed in Sec. 3.1.3) is no longer expected to be valid any more. Indeed, the θ function appearing in the effective potential (3.37) is "smeared" out at finite temperature leading to a qualitative change compared to the vanishing temperature limit, see Sec. 3.1.3 for details on the qualitative phase structure at vanishing temperature. In order to determine the model parameters for finite temperature, results for the diquark gap are therefore required for finite temperature and for different isospin chemical potentials.

3.1.6 Towards Neutron-Star Matter

In the following, we use the results from Sec. 3.1.5 to identify trajectories in the phase diagram that are relevant for astrophysical applications and extract information about the phase structure of neutron-star matter. A realistic description of neutron-star matter in terms of a gapped quark gas requires to include neutrality constraints, i.e., colour-charge neutrality as already introduced in Sec. 3.1.2 and electric-charge neutrality. Additionally, neutron stars are in beta equilibrium [328, 329, 339]. We shall discuss these aspects in detail in the following. We only consider two quark flavours, although densities relevant to the description of neutron stars may require the inclusion of strange quarks. However, we expect that the results for only two quark flavours already provide potentially useful insight into the mechanisms relevant in neutron stars. To compare the results considering a gapped quark gas, which we expect to present a suitable description for quark matter at high densities, we shall also include the aforementioned constraints for a free quark gas.
As the name suggests, it might be tempting to describe *neutron* star matter by considering pure *neutron* matter which consists of twice as many down quarks as up quarks. Therefore, we expect that the down density is approximately twice as big as the up density. This corresponds to a trajectory in the phase diagram with $n_\mathrm{d}/(n_\mathrm{u}+n_\mathrm{d}) = 2/3$ which lies within the first-order region, see Fig. 3.8. However, in reality, the situation is more involved since neutron stars do not purely consist of neutrons but also a certain fraction of protons. Protons are positively charged, and macroscopic matter has to be charge neutral. Therefore, we also expect a certain number of electrons. Furthermore, as already stated before, neutron stars are in beta equilibrium. To describe this, we have to consider weak processes like

$$u \longleftrightarrow d + e^+ + \nu_\mathrm{e}\,. \tag{3.48}$$

Here an up quark u decays to a down quark d, a positron e^+, and an electron neutrino ν_e and vice versa. This process is in equilibrium, meaning that no preferred direction exists. Therefore, we have to include electrons that participate in the beta-equilibrium process in our discussion. We assume that enough time has passed for all neutrinos to leave the system (see Refs. [48, 328, 329, 341–343]) so that we can set the chemical potential of the neutrinos to zero. Therefore, we find in beta equilibrium that

$$\mu_\mathrm{u} = \mu_\mathrm{d} + \mu_\mathrm{Q}\,. \tag{3.49}$$

Here, μ_Q is the charge chemical potential associated with the electric charge Q. To account for the charge chemical potential μ_Q, we introduce an auxiliary chemical potential μ so that the chemical potentials for the up and down quarks are now given by

$$\mu_\mathrm{u} = \mu + \frac{2}{3}\mu_\mathrm{Q} \qquad \text{and} \qquad \mu_\mathrm{d} = \mu - \frac{1}{3}\mu_\mathrm{Q}\,. \tag{3.50}$$

The prefactors for the charge chemical potential μ_Q are determined by the electrical charge of the up and down quark, respectively. Electrons are negatively charged so that their chemical potential is given by

$$\mu_\mathrm{e} = -\mu_\mathrm{Q}. \tag{3.51}$$

Consequently, the effective potential (3.37) can be expressed in terms of

$$\bar{\mu} = \frac{\mu_\mathrm{u}+\mu_\mathrm{d}}{2} + \frac{1}{2\sqrt{3}}\mu_8 = \mu + \frac{1}{6}\mu_\mathrm{Q} + \frac{1}{2\sqrt{3}}\mu_8 \qquad \text{and} \qquad \delta\mu = \frac{\mu_\mathrm{u}-\mu_\mathrm{d}}{2} = \frac{1}{2}\mu_\mathrm{Q}\,. \tag{3.52}$$

The pressure can therefore be expressed as a function of μ_u, μ_d, and μ_8 or μ, μ_Q, and μ_8, respectively. Note that we have already set $\mu_3 = 0$ according to the considerations in Sec. 3.1.2.

A chunk of macroscopic matter has to be electric-charge neutral and colour-charge neutral. We enforce electric-charge neutrality by requiring that the charge density n_{Q} is zero

$$n_{\mathrm{Q}} = \frac{\partial P}{\partial \mu_{\mathrm{Q}}} = \frac{2}{3} n_{\mathrm{u}} - \frac{1}{3} n_{\mathrm{d}} - n_{\mathrm{e}} \stackrel{!}{=} 0 \,. \tag{3.53}$$

The electron density n_{e} for the model considered here is given by a free relativistic fermion gas $n_{\mathrm{e}} = \mu_{\mathrm{e}}^3/(3\pi^2)$. The electric-charge neutrality has to be constrained alongside the constraints for colour-charge neutrality which we have already introduced in Sec. 3.1.2 where we found that the constraint for n_3 requires to choose $\mu_3 = 0$. Therefore, we are left with constraining μ_8 by requiring that $n_8 = 0$, see Eq. (3.35). In the following, we find trajectories in the phase diagram spanned by the down-quark fraction $n_{\mathrm{d}}/(n_{\mathrm{d}} + n_{\mathrm{u}})$ as a function of the baryon density n by considering the pressure in the "gapped" phase (which is governed by the formation of the diquark gap $\bar{\Delta}_{\mathrm{gap}}$) and "ungapped" phase by evaluating the effective potential U at the ground state. The pressure then depends on μ_{u}, μ_{d}, and μ_8 (or μ, μ_{Q}, and μ_8) so that the densities also depend on these quantities. Enforcing colour- and electric-charge neutrality by solving Eqs. (3.35), (3.36) and (3.53) with the constraint from beta equilibrium (3.49), we can uniquely match the chemical potentials for up quarks μ_{u} and down quarks μ_{d} and the colour-charge chemical potential μ_8 by, e.g., effectively singling out a value for μ_{u} for each value of μ_{d} and μ_8. Alternatively, we can match μ, μ_{Q}, and μ_8. The resulting densities uniquely determine the trajectory in the phase diagram.

3.1.6.1 Free Quark Gas with Neutrality Constraints and Beta Equilibrium

Before identifying the trajectory in the phase diagram that describes what we shall refer to as "neutron-star matter", we consider the pressure of a free quark gas and a free electron gas and implement the aforementioned neutrality constraints. The combined pressure (which corresponds to the pressure obtained from the effective potential (3.37) for vanishing diquark gap) is given by

$$P_{\mathrm{free}} = \frac{\mu_{\mathrm{u,b}}^4}{12\pi^2} + \frac{\mu_{\mathrm{d,b}}^4}{12\pi^2} + \frac{\mu_{\mathrm{u,r}}^4}{12\pi^2} + \frac{\mu_{\mathrm{d,r}}^4}{12\pi^2} + \frac{\mu_{\mathrm{u,g}}^4}{12\pi^2} + \frac{\mu_{\mathrm{d,g}}^4}{12\pi^2} + \frac{\mu_{\mathrm{e}}^4}{12\pi^2} \,. \tag{3.54}$$

Here, the different chemical potentials are given by $\mu_{f,c} = \mu_f + \mu_c$. By requiring colour-charge neutrality via $n_8 = n_3 = 0$, we find $\mu_{\mathrm{r}} = \mu_{\mathrm{g}} = \mu_{\mathrm{b}}$. We also know that $\mu_{\mathrm{b}} + \mu_{\mathrm{r}} + \mu_{\mathrm{g}} = 0$ so that, in conclusion, it follows $\mu_{\mathrm{r}} = \mu_{\mathrm{g}} = \mu_{\mathrm{b}} = 0$ so that $\mu_3 = \mu_8 = 0$. Therefore, the calculation of the up and down density simplifies and we find $n_{\mathrm{u}} = \mu_{\mathrm{u}}^3/\pi^2$ and $n_{\mathrm{d}} = \mu_{\mathrm{d}}^3/\pi^2$. Since we describe beta equilibrium, we have to also consider the electron density which is $n_{\mathrm{e}} = \mu_{\mathrm{e}}^3/(3\pi^2)$ where from beta equilibrium, it follows that $\mu_{\mathrm{e}} = \mu_{\mathrm{d}} - \mu_{\mathrm{u}}$. For the charge density, we find

$$n_{\mathrm{Q}} = \frac{\partial P_{\mathrm{free}}}{\partial \mu_{\mathrm{Q}}} = \frac{2}{3} n_{\mathrm{u}} - \frac{1}{3} n_{\mathrm{d}} - n_{\mathrm{e}} = \frac{2}{3}\left(\frac{\mu_{\mathrm{u}}^3}{\pi^2}\right) - \frac{1}{3}\left(\frac{\mu_{\mathrm{d}}^3}{\pi^2}\right) - \frac{\mu_{\mathrm{e}}^3}{3\pi^2} \,. \tag{3.55}$$

Requiring that the charge density vanishes $n_{\mathrm{Q}} = 0$ yields the ratio between up and down density

$$\mu_{\mathrm{u}} \approx 0.796\,\mu_{\mathrm{d}} \quad \Rightarrow \quad \frac{n_{\mathrm{d}}}{n_{\mathrm{u}}} \approx 1.983 \quad \Rightarrow \quad \frac{n_{\mathrm{d}}}{n_{\mathrm{d}} + n_{\mathrm{u}}} \approx 0.665 \,. \tag{3.56}$$

The down-quark fraction corresponds to a trajectory in the phase diagram that we shall refer to as "non-interacting neutron-star matter", in the following. It should be noted that there is only a slight deviation from pure neutron matter, where $n_{\mathrm{d}}/(n_{\mathrm{d}} + n_{\mathrm{u}}) = 2/3$. Furthermore, we can use this result to calculate the electron density. We find that $n_{\mathrm{e}} \ll n_{\mathrm{d}}$: $n_{\mathrm{e}} \approx 0.0028\, n_{\mathrm{d}}$.

Another interesting property is the proton fraction since protons and neutrons are the most relevant degrees of freedom at low densities. Therefore, we assume that all quarks are bound in protons and neutrons: $n_{\mathrm{p}}^{\mathrm{u}}$ up quarks are bound in protons, $n_{\mathrm{p}}^{\mathrm{d}}$ down quarks are bound in protons, $n_{\mathrm{n}}^{\mathrm{u}}$ up quarks are bound in neutrons,

and $n_{\mathrm{n}}^{\mathrm{d}}$ down quarks are bound in neutrons. Since neutrons consist of two down and one up quark, we have $n_{\mathrm{n}}^{\mathrm{d}} = 2n_{\mathrm{n}}^{\mathrm{u}}$ whereas protons consist of two up and one down quark $n_{\mathrm{p}}^{\mathrm{d}} = \frac{1}{2}n_{\mathrm{p}}^{\mathrm{u}}$. The total number of up and down quarks is $n_{\mathrm{n}}^{\mathrm{d}} + n_{\mathrm{p}}^{\mathrm{d}} = n_{\mathrm{d}}$ and $n_{\mathrm{n}}^{\mathrm{u}} + n_{\mathrm{p}}^{\mathrm{u}} = n_{\mathrm{u}}$, respectively. Now, we introduce r as the ratio between the up and down quark density so that $n_{\mathrm{d}} = rn_{\mathrm{u}}$. For the proton fraction, we find

$$\frac{n_{\mathrm{p}}}{n_{\mathrm{n}}} = \frac{2-r}{2r-1}\,. \tag{3.57}$$

For the ratio that we found for a free quark gas $r \approx 1.983$, we find $n_{\mathrm{p}}/n_{\mathrm{n}} \approx 0.0057$. Therefore, more than 99% of the quarks are bound in neutrons so that $n_{\mathrm{n}} \gg n_{\mathrm{p}}$ where n_{n} is the neutron density and n_{p} is the proton density. For a free quark gas it is therefore reasonable to assume, that noninteracting quark matter in beta equilibrium mostly consists of pure neutron matter.

3.1.6.2 Gapped Quark Gas with Neutrality Constraints and Beta Equilibrium

Next, we calculate the trajectory in the phase diagram that we shall refer to as "neutron-star matter" in the following, by calculating the pressure from the effective potential (3.37), while including constraints from colour-charge neutrality, beta equilibrium, and electric-charge neutrality. Interestingly, we can find an analytical result for the trajectory by considering the pressure in the gapped phase, which is given by

$$P_{\mathrm{gap}} = \frac{\mu_{\mathrm{e}}^4}{12\pi^2} + \frac{\mu_{\mathrm{u,b}}^4}{12\pi^2} + \frac{\mu_{\mathrm{d,b}}^4}{12\pi^2} + \bar{P}(\bar{\Delta}_{\mathrm{gap}}^2) - P_0 \tag{3.58}$$

with

$$\bar{P}(\bar{\Delta}_{\mathrm{gap}}^2) = -\frac{1}{2}\bar{\lambda}_{\mathrm{csc}}^{-1}\bar{\Delta}_{\mathrm{gap}}^2 - \bar{\lambda}_{\mathrm{eff}}\bar{\Delta}_{\mathrm{gap}}^4 + 8\bar{l}(\bar{\Delta}_{\mathrm{gap}}^2)\,. \tag{3.59}$$

Note that we cannot calculate the pressure in the vacuum P_0. The function $\bar{l}$ only depends on $\bar{\mu}$, at least for vanishing temperature. Also, $\bar{\Delta}_{\mathrm{gap}}^2$ only depends on $\bar{\mu}$, see Sec. 3.1.3. The term δl drops out because of our considerations that, in the gapped region $\delta\mu < \delta\mu_{\mathrm{cr}}$, we find $\bar{\Delta}_{\mathrm{gap}} > \delta\mu$. In the ungapped phase, the pressure is given by the pressure of a noninteracting quark gas so that the total pressure becomes

$$P = P_{\mathrm{gap}}\theta(\delta\mu_{\mathrm{cr}} - |\delta\mu|) + P_{\mathrm{free}}\theta(|\delta\mu| - \delta\mu_{\mathrm{cr}})\,. \tag{3.60}$$

In the following, we only consider the gapped phase. Then, the up and down densities are given by

$$n_{\mathrm{u}} = \frac{\mu_{\mathrm{u,b}}^3}{3\pi^2} + \frac{1}{2}\frac{\partial\bar{P}}{\partial\bar{\mu}} \qquad \text{and} \qquad n_{\mathrm{d}} = \frac{\mu_{\mathrm{d,b}}^3}{3\pi^2} + \frac{1}{2}\frac{\partial\bar{P}}{\partial\bar{\mu}}\,. \tag{3.61}$$

We have already ensured that $n_3 = 0$, so that we only have to simultaneously fulfil the electric-charge neutrality constraint

$$n_{\mathrm{Q}} = \frac{\partial P_{\mathrm{gap}}}{\partial\mu_{\mathrm{Q}}} = \frac{2}{3}n_{\mathrm{u}} - \frac{1}{3}n_{\mathrm{d}} - n_{\mathrm{e}} = \frac{2}{3}\frac{\mu_{\mathrm{u,b}}^3}{3\pi^2} - \frac{1}{3}\frac{\mu_{\mathrm{d,b}}^3}{3\pi^2} - \frac{\mu_{\mathrm{e}}^4}{3\pi^2} + \frac{1}{6}\frac{\partial\bar{P}}{\partial\bar{\mu}} \overset{!}{=} 0 \tag{3.62}$$

and the remaining colour-charge neutrality constraint

$$n_8 = \frac{\partial P_{\mathrm{gap}}}{\partial\mu_8} = -\frac{1}{\sqrt{3}}\frac{\mu_{\mathrm{u,b}}^3}{3\pi^2} - \frac{1}{\sqrt{3}}\frac{\mu_{\mathrm{d,b}}^3}{3\pi^2} + \frac{1}{2\sqrt{3}}\frac{\partial\bar{P}}{\partial\bar{\mu}} \overset{!}{=} 0\,. \tag{3.63}$$

With these relations and along with the constraint from beta equilibrium $\mu_{\mathrm{e}} = \mu_{\mathrm{d}} - \mu_{\mathrm{u}}$, we can uniquely determine an up chemical potential for each down chemical potential, simultaneously fulfilling the constraints for colour- and electric-charge neutrality. Notably, we can use the latter relation to eliminate $\bar{P}$ in all remaining equations such that the up and down density become

$$n_{\mathrm{u}} = \frac{\mu_{\mathrm{u,b}}^3}{3\pi^2} + \frac{1}{2}\frac{\partial\bar{P}}{\partial\bar{\mu}} = 2\frac{\mu_{\mathrm{u,b}}^3}{3\pi^2} + \frac{\mu_{\mathrm{d,b}}^3}{3\pi^2} \qquad \text{and} \qquad n_{\mathrm{d}} = \frac{\mu_{\mathrm{d,b}}^3}{3\pi^2} + \frac{1}{2}\frac{\partial\bar{P}}{\partial\bar{\mu}} = 2\frac{\mu_{\mathrm{d,b}}^3}{3\pi^2} + \frac{\mu_{\mathrm{u,b}}^3}{3\pi^2}\,. \tag{3.64}$$

We also eliminate $\bar{P}$ in the equation for n_{Q} so that the electric-charge neutrality constraint is fulfilled if

$$\mu_{\mathrm{u,b}}^3 - \mu_{\mathrm{e}}^3 \stackrel{!}{=} 0 \qquad \Rightarrow \qquad \mu_{\mathrm{u,b}}^3 \stackrel{!}{=} \left(\mu_{\mathrm{d,b}} - \mu_{\mathrm{u,b}}\right)^3 . \tag{3.65}$$

Here, we used $\mu_{\mathrm{e}} = \mu_{\mathrm{d}} - \mu_{\mathrm{u}} = \mu_{\mathrm{d,b}} - \mu_{\mathrm{u,b}}$. With this, it follows

$$\mu_{\mathrm{u,b}} = \frac{\mu_{\mathrm{d,b}}}{2} . \tag{3.66}$$

Inserting the latter expression into the expressions for the up and down densities, we notably find an exact solution for the down-quark fraction

$$\frac{n_{\mathrm{d}}}{n_{\mathrm{u}} + n_{\mathrm{d}}} = \frac{17}{27} , \tag{3.67}$$

which yields $n_{\mathrm{d}}/n_{\mathrm{u}} = 17/10$. With this, the ratio between protons and neutrons becomes $n_{\mathrm{p}}/n_{\mathrm{n}} = 1/8$ and for the proton fraction, we find $n_{\mathrm{p}}/(n_{\mathrm{p}} + n_{\mathrm{n}}) = 1/9$. Therefore, there are 8 neutrons for each proton. Note that, by eliminating $\bar{P}$, effectively all terms that come with an uncertainty band, the diquark gap $\bar{\Delta}_{\mathrm{gap}}$ and the model parameter λ_{eff}, drop out in the calculation of the down-quark fraction so that the down-quark fraction for "neutron-star matter" does not come with an error band.

3.1.6.3 Trajectories in the Phase Diagram

Having identified the trajectories for "noninteracting neutron-star matter" and for "neutron-star matter", we can draw them into the phase diagram spanned by the down-quark fraction $n_{\mathrm{d}}/(n_{\mathrm{u}} + n_{\mathrm{d}})$ as a function of the baryon density n normalised by the nuclear saturation density n_0, see Fig. 3.9. The trajectory for "noninteracting neutron-star matter" (green dashed line in Fig. 3.9) lies in the first-order region which would also apply for a trajectory describing pure neutron matter. The trajectory representing "neutron-star matter" (red line in Fig. 3.9) lies in the gapped phase for densities below $n \approx 27 n_0$. At this density, the system undergoes a first-order phase transition from a gapped phase dominated by colour superconductivity into an ungapped phase where the system can be described as a free noninteracting quark gas.

From the general discussions in Sec. 3.1.5, it follows that, provided that a gap exists for dense symmetric matter, a phase transition from an ungapped phase described by a noninteracting quark gas and a gapped phase governed by colour superconductivity exists for asymmetric matter. Furthermore, the line describing the phase transition approaches the quark density associated with symmetric matter for $n \to \infty$. This statement is model-independent and only relies on the expansion of the pressure in the gap, see Eq. (3.41). From this, it follows that neutron-star matter eventually undergoes a first-order phase transition provided that such a trajectory lies in the gapped phase for some finite density. Note that another phase transition is expected to occur at much lower densities where a phase governed by spontaneous chiral symmetry breaking undergoes a phase transition to the chirally symmetric colour-superconducting (gapped) phase considered here. However, we shall not discuss this transition in the following.

The effects of the colour-charge neutrality constraint can be studied by considering what we shall refer to as "colour-charged neutron-star matter". For this, we ignore the colour-charge constraint and simply set $\mu_3 = \mu_8 = 0$ while still implementing constraints from beta equilibrium and electric-charge neutrality. In contrast to the trajectory for "neutron-star matter", the trajectory comes with an error band since quantities coming with an uncertainty do not drop out in the calculation. We emphasise that we only calculate this trajectory to study the dependence of the results on the charge constraints, especially the colour-charge neutrality constraints. The resulting trajectory is shown in the phase diagram depicted in Fig. 3.10. The result for "colour-charged neutron-star matter" lies in the gapped phase for densities below $n \approx 28 n_0$ and it lies close to the trajectory associated with "neutron-star matter". Notably, the results for "neutron-star matter"

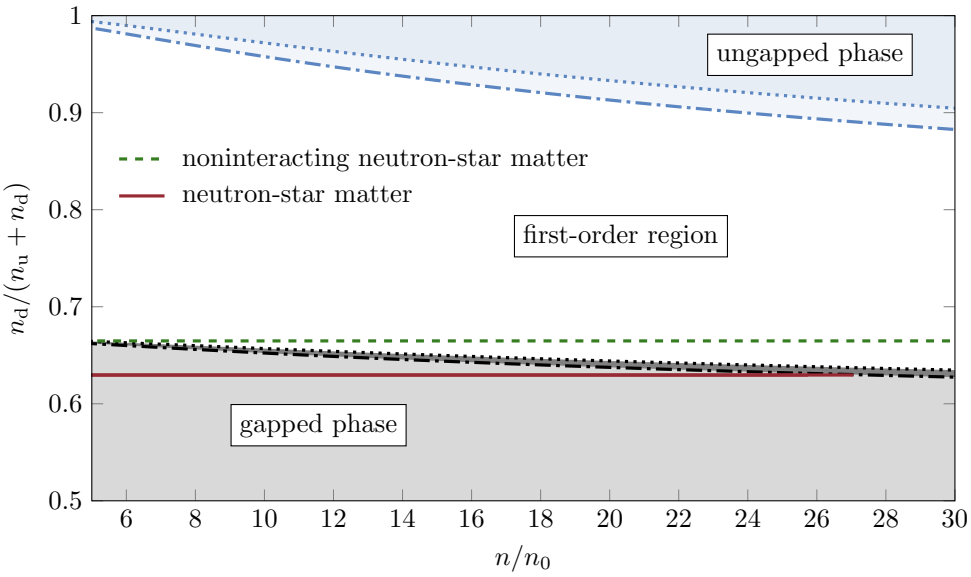

Figure 3.9: Different trajectories appearing in the phase diagram for isospin-asymmetric strong-interaction matter depicted by the down-quark fraction $n_\mathrm{d}/(n_\mathrm{u}+n_\mathrm{d})$ as a function of the baryon density n in units of the nuclear saturation density n_0: The red line represents neutron-star matter as obtained by our model where we have implemented beta equilibrium and simultaneously satisfied the colour and electric-charge neutrality constraints ($n_\mathrm{d}/(n_\mathrm{d}+n_\mathrm{u}) = 17/27$). The green dashed line represents noninteracting neutron-star matter ($n_\mathrm{d}/(n_\mathrm{d}+n_\mathrm{u}) \approx 0.665$) where the colour and charge constraints have been satisfied for a noninteracting quark gas. The phase boundaries are where colour-neutral matter undergoes a phase transition as already enforced in Fig. 3.8. As before, the uncertainties in the boundaries (depicted by differently dashed lines) originate from the uncertainty of the gap.

and "colour-charged neutron-star matter" converge towards high densities. This effect is also reflected in the electric-charge chemical potential μ_Q as depicted in Fig. 3.11 (left panel) that has been calculated in determining the corresponding trajectories. The result for "neutron-star matter" (blue band) and "colour-charged neutron-star matter" (green band) lie close to each other and converge when going to higher baryon densities. Note that μ_Q is negative which implies that $\mu_\mathrm{d} > \mu_\mathrm{u}$ as expected for matter which consists of more neutrons than protons. Further, the electron chemical potential is positive which implies that electrons instead of positrons are present in "neutron-star matter".

Furthermore, the colour-charge chemical potential μ_8 only "shifts" the chemical potential $\bar{\mu}$ (which is associated with the up and down chemical potential) by $\mu_8/(2\sqrt{3})$. Therefore, if $\mu_8/(2\sqrt{3})$ is small compared to the up and down chemical potential or $\bar{\mu}$, respectively, the difference between results with and without colour-charge neutrality are expected to be small. We show the result for the relative colour-charge chemical potential $\mu_8/\bar{\mu}$ in Fig. 3.11 as a function of the baryon density n. Indeed, we find that the relative colour-charge chemical potential is small, especially for high densities regarding the density range relevant for the trajectories in the gapped phase. This indicates that the effect of the colour-charge neutrality constraint is only subleading at least for densities close to the phase boundary.

The electron density for "colour-charged neutron-star matter" as a function of the normalised baryon density is depicted in Fig. 3.11 (right panel, blue band) and it increases towards lower densities. This is not what is expected when considering constraints from nuclear physics and observations which appear to disfavour large electron densities. Further, the electron fraction in neutron stars is not expected to increase towards

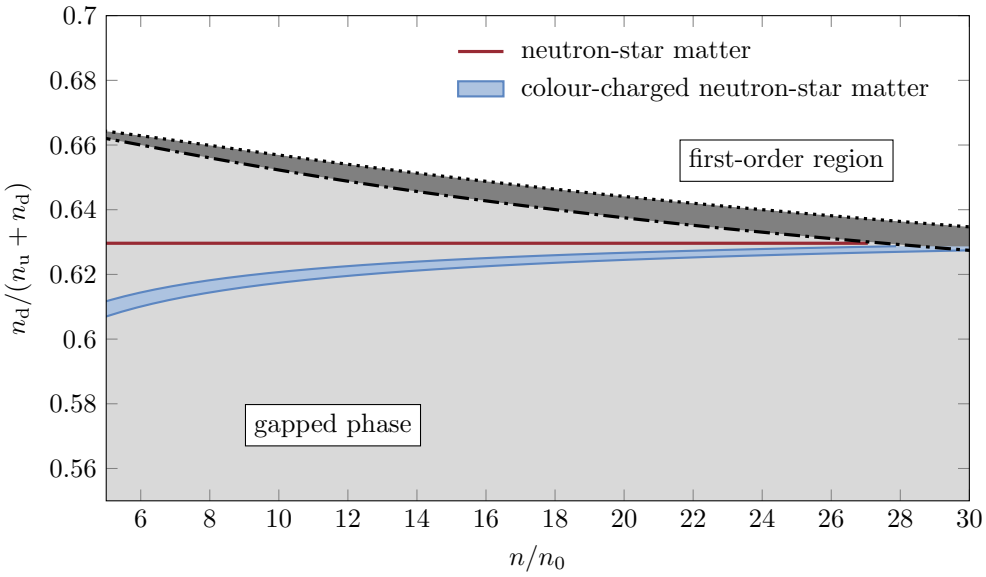

Figure 3.10: Part of the phase diagram shown in Fig. 3.9 (with a reduced y-axis) where, additionally to the line for "neutron-star matter" (red line), also the result for "colour-charged neutron-star matter" (blue line) is shown. The line for "colour-charged neutron-star matter" has been obtained by setting $\mu_3 = \mu_8 = 0$, implementing beta equilibrium, and electric-charge neutrality. Compared to the trajectory for "neutron-star matter", it comes with an error band originating in the uncertainty of the gap used to constrain the model. The transition lines (black lines) correspond to colour-neutral matter undergoing a phase transition.

lower densities [119]. However, the line associated with "neutron-star matter", see red line in Fig. 3.11 (right panel), is in accordance with the results from nuclear physics and observations. The inclusion of constraints for colour-charge neutrality is, therefore, indeed needed for qualitative results of the electron density. As we shall see in Sec. 3.1.7, the inclusion of the aforementioned constraints seems to be less important when considering the speed of sound as a function of density where the results for "colour-charged neutron-star matter" and for "neutron-star matter" are practically almost identical. Similar to before, the result the electron density for "colour-charged neutron-star matter" approaches the line associated with "neutron-star matter" but differs for lower densities. For "neutron-star matter", we again obtain an analytic result so that the electron density becomes $n_e/n = 1/9$ which is in accordance with the number of protons which is also given by $n_\mathrm{p}/n = 1/9$ and ensures that electric-charge neutrality is indeed fulfilled.

3.1.7 Speed of Sound for Neutron-Star Matter

As we have already stated at the beginning of this chapter, another quantity of interest, especially for astrophysical observations, is the speed of sound. Since we have no access to the QCD vacuum constant in our model, the pressure cannot be reliably calculated in the present model. For this reason, we focus on the speed of sound for the discussion of thermodynamic properties of dense strong-interaction matter. To calculate the speed of sound for colour- and electric-charge neutrality in beta equilibrium, we calculate the pressure and the energy density by employing Eq. (3.34) along the corresponding trajectories.
In the following, we show the speed of sound squared c_s^2 as a function of the baryon density n in units of the nuclear saturation density n_0 for three different approximations, see Fig. 3.12. Note that all approximations, "symmetric matter" (green band), "neutron-star matter" (black band), and "colour-charged neutron-star

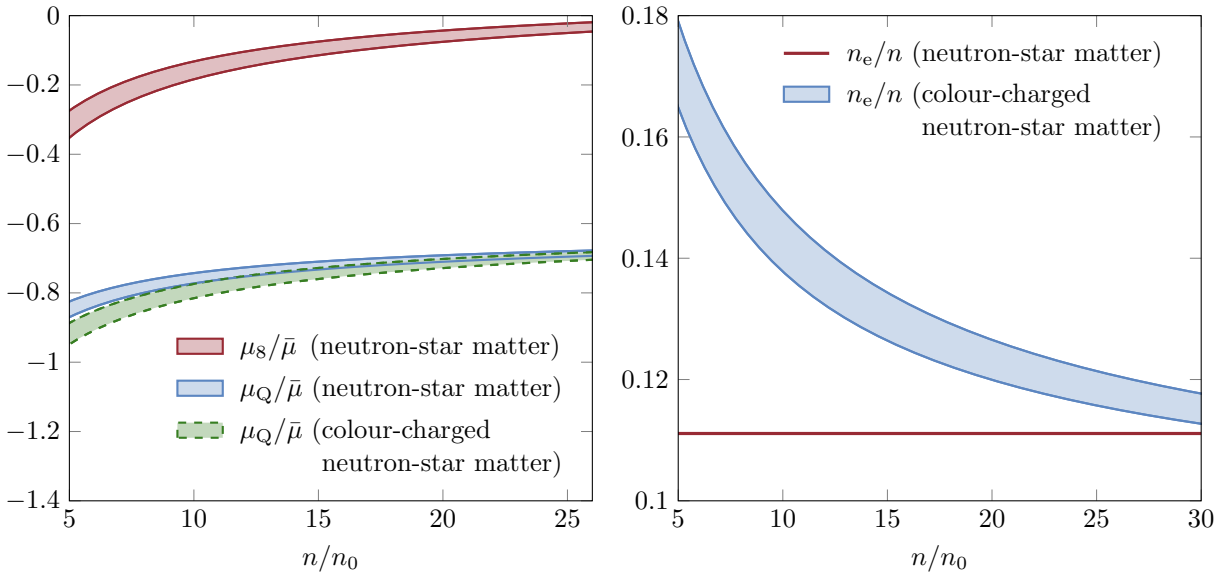

Figure 3.11: Left panel: Relative colour-chemical potential $\mu_8/\bar{\mu}$ (red band) and charge-chemical potential $\mu_Q/\bar{\mu}$ (blue band) for neutron-star matter (colour- and electric-charge neutrality in beta equilibrium) as a function of the baryon density n normalised by the nuclear saturation density n_0. The electric-charge chemical potential μ_Q comes with an error band, although we find a constant value for the ratio of down quark density to total density (and μ_Q itself has no error band) because $\bar{\mu}$ comes with an error band. We also show the electric-charge chemical potential for "colour-charged neutron-star matter" (green band). For this, we artificially set $\mu_3 = \mu_8 = 0$ and only implemented beta equilibrium and electric-charge neutrality. Right panel: Comparison of the electron fraction n_e/n as a function of the normalised density n/n_0 for "neutron-star matter" (red) and for "colour-charged neutron-star matter". The missing error band for "neutron-star matter" is a consequence of terms depending on the uncertainties dropping out in the calculation of the down-quark fraction $n_d/(n_u + n_d)$. The result for "colour-charged neutron-star matter" comes with an error band where the lower (upper) end represents the lower (upper) end of the uncertainty of the gap.

matter" (orange diamond pattern), exceed the value associated with the noninteracting quark gas which is given by $c_s^2 = 1/3$ and increase towards lower densities within the considered density regime. Notably, the bands lie close to each other and even overlap going to higher densities where they seem to converge. However, the apparent convergence of the speed of sound towards high densities has to be discussed carefully: In Fig. 3.12, we have only plotted the speed of sound in the density regime ($n/n_0 \lesssim 27$) where the trajectories for "neutron-star matter" and "colour-charged neutron-star matter" lie in the gapped phase, see Fig. 3.9 and 3.10. However, the associated trajectory in the phase diagram eventually hits the first-order phase boundary and then enters the ungapped phase, so that the system can be described by a noninteracting quark gas. At this point, the speed of sound is, in the present model, given by the value associated with the noninteracting quark gas $c_s^2 = 1/3$. In contrast to that, symmetric matter remains in the gapped phase and, for the current model, it remains above the value for the noninteracting quark gas. Still, the speed of sound for symmetric matter may also cross the line associated with the noninteracting quark gas and approach it from below at even higher densities when including higher-order corrections from QCD which are not considered in the present model. We shall come back to this in detail in Sec. 3.2. However, in contrast to asymmetric matter, a gap still exists for symmetric matter even at very high densities. For future calculations, it is interesting to note that the bands for "neutron-star matter" and "colour-charged neutron-star matter"

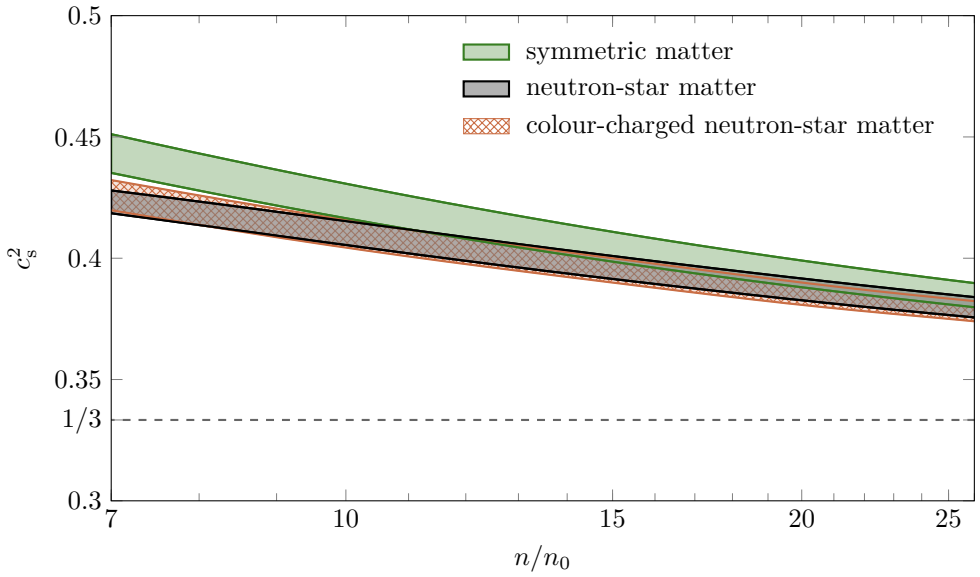

Figure 3.12: Speed of sound squared c_s^2 in units of the speed of light squared as a function of the baryon density n normalised by the nuclear saturation density n_0. We compare the results obtained in the present work for isospin-symmetric matter (green band) and for "neutron-star matter" (black band). We also show the results for "colour-charged neutron-star matter" (orange diamond pattern). The noninteracting limit, which is given by $c_s^2 = 1/3$, is illustrated by the grey dashed line. The error bands represent the uncertainty of the gap which has been used to fix the initial conditions, where the upper (lower) end corresponds to the upper (lower) end of the gap.

are almost indistinguishable from one another, at least with regards to the density dependence of the speed of sound. In comparison to that, the results for the electron fraction clearly deviate, especially for lower densities, see Fig. 3.11 (right panel). Therefore, it seems to be sufficient to only implement electric-charge neutrality and to ignore constraints from colour-charge neutrality in practice, at least if only the speed of sound is of interest. Even results for symmetric matter seem to be a good estimate for the speed of sound in "neutron-star matter", provided that the corresponding trajectory lies in the gapped phase, considering that the implementation of colour-charge and electric-charge neutrality might come at an increased numerical cost in a more advanced calculation, taking into account additional degrees of freedom. Note that the inclusion of the neutrality constraints appears to lower the speed of sound compared to symmetric matter, most notably towards lower densities.

The qualitative behaviour can also be estimated from the pressure for symmetric matter in leading order of the gap (3.41) and by assuming that the gap is given by $\bar{\Delta}_{\text{gap}} \sim \exp\left(-c'/\bar{\mu}^2\right)$ and $\bar{\mu} \sim n^{1/3}$ as done in Sec. 3.1.5. Then, the deviation of the speed of sound squared from its value in the noninteracting limit is

$$c_s^2 - \frac{1}{3} \sim \frac{1}{n^{2/3}} \exp\left(-\frac{2c''}{n^{2/3}}\right), \qquad \text{where} \qquad c'' > 0\,. \tag{3.68}$$

Here, we have dropped higher-order corrections $\sim 1/n^{1/3}$ and $\sim \bar{\Delta}_{\text{gap}}/\bar{\mu}$. Therefore, we indeed find that the speed of sound approaches the value associated with the noninteracting quark gas from above, at least for symmetric matter. This statement is insensitive to the details of the form of the gap, only relying on the expansion of the pressure (3.41) and that the gap increases monotonically as a function of $\bar{\mu}$, in particular, that $\bar{\Delta}_{\text{gap}}/\bar{\mu} \to 0$ for $\bar{\mu} \to \infty$.

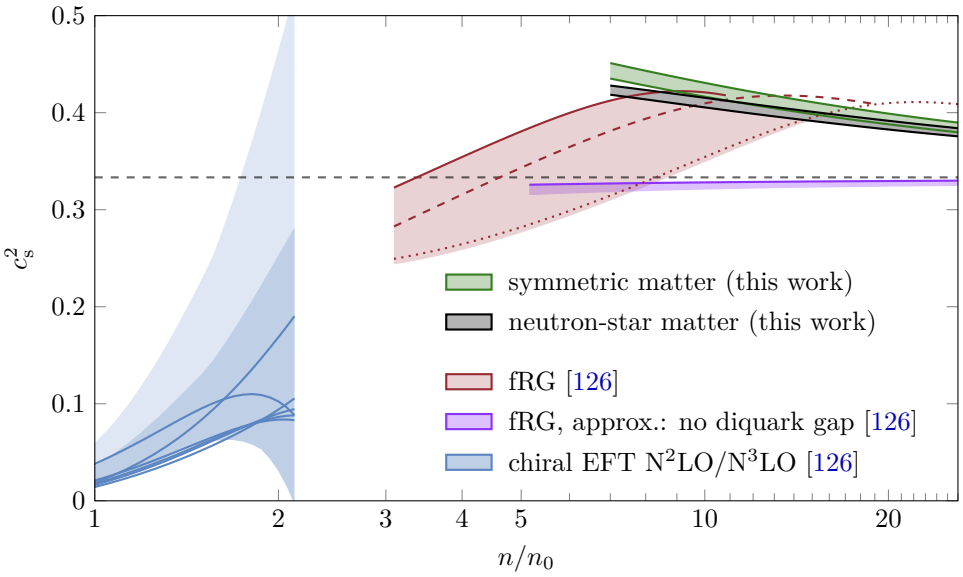

Figure 3.13: Speed of sound squared c_s^2 in units of the speed of light squared as a function of the baryon density n normalised by the nuclear saturation density n_0. The grey dashed line represents the value associated with the noninteracting quark gas $c_s^2 = 1/3$. We show the results obtained in this work for isospin-symmetric matter (green band) and for neutron-star matter (black band) that have already been shown in Fig. 3.12. For comparison, we show results for the speed of sound for isospin-symmetric matter obtained by chiral effective field theory (chiral EFT, blue band) [126], an fRG study taking into account a diquark gap (red) [126], and an fRG study where no diquark gap is included in the calculation (purple) [126].

In Fig. 3.12, we only show the speed of sound for densities above $7n_0$ because we cannot reliably constrain the speed of sound for low densities. As we have seen by comparing the diquark gap used in the present model with previous fRG results [126], see Fig. 3.6, the results agree nicely but deviate clearly when going to lower densities because the previous fRG results include a Fierz-complete set of four-quark interactions. Consequently, reliable constraints for lower densities require the inclusion of at least the scalar-pseudoscalar channel because the low-density regime is governed by the formation of a chiral condensate and is dominated by the formation of pions and nucleons. In this density regime, the speed of sound can be calculated using, e.g., chiral effective field theory (chiral EFT). In Fig. 3.13, we therefore compare results for the speed of sound squared as a function of the baryon density in units of the nuclear saturation density, as obtained from chiral EFT at low densities (blue band, [125, 126]) to results from the present work where we show the speed of sound for "neutron-star matter" (black band) and symmetric matter (green band). We further show results from the previous fRG calculations, see Ref. [126, 179], based on a Fierz-complete set of (gluon-induced) four-quark interactions (red band), which also indicates the formation of a diquark gap, and an approximation that does not take into account the existence of a diquark gap (purple band). Our results are consistent with the results employing a Fierz-complete set for $n/n_0 \gtrsim 7$. This is expected since this is the density regime where the diquark channel is expected to be dominant according to the aforementioned Fierz-complete study, see Refs. [179]. Furthermore, the speed of sound in the approximation not including a diquark gap (purple band) does not exceed the value associated with a noninteracting quark gas. This indicates that a diquark gap is essential to obtain a speed of sound that exceeds the noninteracting limit. Note that the speed of sound for lower densities is not accessible in our current approximation but requires, at least, the inclusion of chiral interaction channels. However, together with the results from chiral EFT

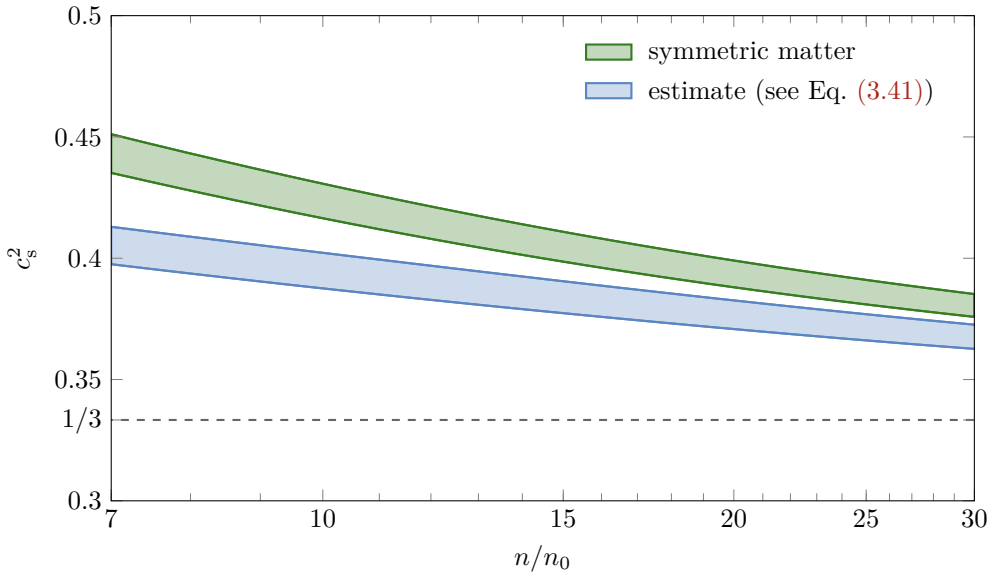

Figure 3.14: Speed of sound (squared) for gapped isospin-symmetric matter as obtained by evaluating the effective potential at the ground state (as already shown in Fig. 3.12 and Fig. 3.13) compared to an estimate for the speed of sound for isospin-symmetric matter as obtained from the expansion of the pressure (3.41) in terms of the gap (blue band). The error bands represent the uncertainties of the gap where the upper (lower) end corresponds to the upper (lower) end of the gap. Note that we consider the expansion of the pressure in more detail in the subsequent section, see Sec. 3.2. The horizontal dashed line represents the value for the speed of sound for a noninteracting quark gas.

(blue band), the results indicated that the speed of sound squared exhibits a maximum for $n/n_0 \lesssim 10$ which is also in accordance with the previously mentioned fRG result from Ref. [126]. Therefore, the existence of a maximum in the speed of sound seems to be tightly connected to the formation of a diquark gap associated with a colour-superconducting ground state. Interestingly, constraints from observations of neutron-star masses strongly suggest that the speed of sound has a maximum for neutron-rich matter [103, 119–122]. The exact position of the maximum remains unknown and indeed requires the inclusion of additional degrees of freedom such as pions and nucleons, which become relevant in this density regime [165–168, 179].

Recall that we have used the results for the diquark gap from our fRG calculation, see Sec. 2.5, and considered the result for "gapped" gluons instead of "ungapped" gluons to fix the model parameters. There, we found that the gap for "ungapped" gluons is approximately two times bigger than compared to "gapped" gluons. In principle, we can also tune the model parameters so that we recover the gap for "ungapped" gluons. The change in the size of the gap affects the speed of sound such that we find an increase of up to 70% in the speed of sound squared at least when considering the analytic estimate for the pressure (3.41). The qualitative behaviour, i.e., the increase towards lower densities, remains unaffected.

We also have the freedom to choose the model parameters $\bar{\lambda}_{\mathrm{csc}}$ and $\bar{\lambda}_{\mathrm{eff}}$. However, a variation of the model parameters only results in a mild dependence of the speed of sound squared c_{s}^2 and does not change the qualitative behaviour if the model parameters are chosen such that the gap as a function of the chemical potential does not change.

The pressure as a function of the density, which is another quantity that is of great importance for astrophysical applications, is only determined up to a constant in the present study since this constant requires knowledge about QCD in the vacuum. Different possibilities to calculate this constant have been discussed

for low-energy models in Refs. [166, 344–346]. However, as already mentioned before, the speed of sound as obtained in the present work is compatible with the result from the Fierz-complete study, see Ref. [126], that also takes into account a colour-superconducting diquark gap. There, the pressure for isospin-symmetric matter has been calculated and it has been found that the pressure is consistent with calculations that do not take into account a diquark gap. Since the speed of sound is only mildly affected by the isospin imbalance, at least in the density regime underlying the present study, we expect that the effect on the pressure is also small. Therefore, we postpone a detailed analysis of this aspect to future work.
We close this section by guiding the discussion to the subsequent section, see Sec. 3.2. The reliability of the present results can be investigated by considering the expansion of the pressure (3.41) already used for the analytic estimates throughout Sec. 3.1. We compare the speed of sound for isospin-symmetric matter with its estimate as obtained from this expansion of the pressure in Fig. 3.14. We find that the qualitative behaviour is identical, i.e., the speed of sound exceeds the value associated with the noninteracting quark gas and increases when decreasing the density. However, the estimated speed of sound is shifted towards lower values. It is noteworthy that the expansion of the pressure (3.41) does not explicitly depend on the model parameters but only depends on the chemical potential and the diquark gap. It should be emphasised that the gap implicitly depends on the model parameters. The expansion of the pressure can be associated with regimes where $\bar{\Delta}_{\mathrm{gap}}/\mu$ is sufficiently small. This aspect is also present in the results in Fig. 3.14 where the results for the speed of sound seem to converge towards higher densities (associated with a larger chemical potential). Note that in the density regime considered in the present work, we have $0.3 \lesssim |\Delta_{\mathrm{gap}}|/\mu \lesssim 0.6$.
In the following section, see Sec. 3.2, we shall extend on the idea to use an expansion of the pressure for the qualitative study of the speed of sound. As already mentioned, the calculation of the speed of sound going to even higher densities, becomes more involved. The present results indicate that the speed of sound squared for symmetric matter stays above the noninteracting limit and approaches it from above. However, results for corrections to the noninteracting quark gas, e.g., from perturbative QCD, should be taken into account when going to even higher densities than those considered in the present work. Using an extended version of the expansion of the pressure in terms of the gap by including effects from perturbative QCD should give us an insight into effects from corrections to the noninteracting quark gas.

3.2 Constraints on the Equation of State and the Speed of Sound

In the previous section, see Sec. 3.1.7, we have seen that, by including a colour-superconducting gap, the speed of sound exceeds the value associated with a noninteracting quark gas and approaches the corresponding limit from above for $n \to \infty$ at least for isospin-symmetric matter. However, constraints from perturbative QCD suggest that the speed of sound approaches the aforementioned limit from below provided that the colour-superconducting gap does not contribute significantly at very high densities [154–162, 320]. With the present section, we intend to bridge the gap between these two density regions: At intermediate densities, we expect that the speed of sound exceeds the noninteracting limit whereas, at very high densities, we expect that the noninteracting limit is approached from below. This shall allow us to identify a density where, coming from high densities, the speed of sound exceeds the noninteracting limit. In addition to that, we compare the dominance patterns for different density regimes and analyse the qualitative behaviour of the speed of sound and the underlying mechanisms. For this purpose, we again turn to symmetric matter so that the speed of sound (squared) is given by

$$c_{\mathrm{s}}^2 = \frac{1}{\mu}\left(\frac{\partial P}{\partial \mu}\right)\left(\frac{\partial^2 P}{\partial \mu \partial \mu}\right)^{-1} . \tag{3.69}$$

From this expression, it becomes clear that the speed of sound is very sensitive to changes in the density dependence of the pressure so that a qualitative description requires to include the relevant degrees of freedom. We consider density regimes which are governed by the presence of a colour-superconducting diquark gap. To not only rely on results obtained in Chap. 2, in particular for the diquark gap signalling the onset of colour superconductivity, we shall additionally use another functional form of the gap, see Sec. 3.2.1 and Sec. 3.2.2 for details.

We start with a general discussion of the expansion of the equation of state in the presence of a colour-superconducting gap in terms of the pressure in Sec. 3.2.1, relying on very general assumptions. We consider two massless quark flavours coming in three colours and concentrate on symmetric matter. In practice, this leads to an extension of the expansion of the pressure (3.41) already underlying the analytic estimates throughout Sec. 3.1. In Sec. 3.2.2, we apply the findings to a qualitative study of the speed of sound which shall allow us to identify the relevant degrees of freedom and mechanisms for different densities.

3.2.1 Expansion of the Equation of State

The pressure for the noninteracting quark gas (Stefan-Boltzmann limit) is given by

$$P_{\mathrm{SB}} = \frac{\mu^4}{2\pi^2}\,. \tag{3.70}$$

However, we consider density regimes which are expected to be governed by the presence of a colour-superconducting gap $|\bar{\Delta}_{\mathrm{gap}}|$ in the excitation spectrum of the quarks, see Chap. 2 for details. The gap depends on the chemical potential and the strong coupling which we assume to be a constant parameter for now. Since the chemical potential is the only dimensionful quantity, we can write the gap as $|\bar{\Delta}_{\mathrm{gap}}| = |\bar{\Delta}_{\mathrm{gap}}(\mu, g)| = \mu f_\Delta(g)$, where the function f_Δ only depends on the strong coupling g.

In Chap. 2, we have considered the chirally symmetric diquark gap (with $J^P = 0^+$) associated with pairing of the two-flavour colour-superconductor type (2SC). This gap is closely related to the expectation value of a quark bilinear: $\bar{\Delta}^a_{\mathrm{gap}} \sim \langle \psi^T \mathcal{C}\gamma_5\tau_2\epsilon_a\psi\rangle$. However, note that $|\bar{\Delta}_{\mathrm{gap}}|^2 = \sum_a |\bar{\Delta}^a_{\mathrm{gap}}|^2$ is a gauge-invariant quantity. In the weak-coupling limit, the aforementioned gap was calculated analytically in Refs. [82, 83, 87, 88, 90] for very high densities. There, it was found that

$$|\bar{\Delta}_{\mathrm{gap}}| \sim \mu g^{-5} \exp\left(-\frac{3\pi^2}{\sqrt{2}g}\right)\,. \tag{3.71}$$

By considering a constant strong coupling, the gap only exhibits a trivial dependence on the chemical potential since it is the only dimensionful quantity. Going towards lower densities where the weak-coupling limit is expected to break down, the functional form of the gap may deviate from Eq. (3.71) and become nontrivial, see Refs. [50, 56, 82, 84, 87, 88, 126, 321, 322, 347] for discussions.

The calculation of the pressure, as the quantum effective action Γ evaluated at its minimum, requires to take the emergence of the gap in the fermionic excitation spectrum into account, as we have already seen in Sec. 3.1. The resulting pressure is a function of the gap and the strong coupling: $P = P(g, |\bar{\Delta}_{\mathrm{gap}}|^2)$. From dimensional and symmetry arguments, we therefore find an expansion of the pressure in terms of the dimensionless quantity $|\bar{\Delta}_0|^2 = |\bar{\Delta}_{\mathrm{gap}}/\mu|^2$ so that

$$P = P_{\mathrm{SB}}\left(\gamma_0(g) + \gamma_1(g)|\bar{\Delta}_0|^2 + \frac{1}{2}\gamma_2(g)|\bar{\Delta}_0|^4 + \cdots\right)\,. \tag{3.72}$$

The coefficients depending on the strong coupling in the expansion are given by

$$\gamma_i(g) = \frac{\mu^{2i}}{P_{\mathrm{SB}}} \frac{\partial^i P(g, |\bar{\Delta}_{\mathrm{gap}}|^2)}{\partial(|\bar{\Delta}_{\mathrm{gap}}|^2)^i}\bigg|_{|\bar{\Delta}_{\mathrm{gap}}|=0}\,. \tag{3.73}$$

In the expansion, we assume the pressure to be an analytic function of the gap, which is reasonable to assume to be valid far enough away from a phase transition. For the first coefficient γ_0 that gives corrections to the pressure in the absence of a gap (gap-independent contribution to the pressure), we have

$$\gamma_0(g) = 1 + \mathcal{O}(g^2)\,. \tag{3.74}$$

Provided that the strong coupling is sufficiently small, these corrections can be extracted from perturbative calculations, see Refs. [154–162, 320].
For the coefficient describing corrections to gap-dependent contributions $\sim |\bar{\Delta}_0|^2$, we have

$$\gamma_1(g) = 2 + \mathcal{O}(g^2)\,. \tag{3.75}$$

The coefficients γ_j can be related to correlation functions with $4j$ quarks evaluated at vanishing gap. For instance, γ_1 can be obtained from a calculation of the four-quark correlation function

$$\left\langle (\bar{\psi}\tau_2\epsilon_a\gamma_5\mathcal{C}\bar{\psi}^T)(\psi^T\mathcal{C}\gamma_5\tau_2\epsilon_a\psi)\right\rangle\big|_{|\bar{\Delta}_{\mathrm{gap}}|=0}\,. \tag{3.76}$$

Correlation functions corresponding to $j > 1$ have been found to be subleading, see the discussion in Chap. 2. Considering g-dependent corrections to γ_1 is beyond the scope of the present work. However, note that the ground state at sufficiently high densities is expected to exist in a colour-superconducting state. Therefore, the pressure should be greater than the pressure without a gap. Otherwise, the system would exist in an ungapped phase since the ground state is the phase associated with the highest pressure. It follows that $\gamma_1(g) > 0$ for sufficiently high densities, where $\bar{\Delta}_0$ is small so that higher orders in the expansion can be dropped.
Up to now, the only dimensionful quantity is the chemical potential. However, taking into account the scale dependence of the strong coupling in a nonperturbative calculation, the gap may acquire a nontrivial dependence on the chemical potential since the chemical potential has to be measured in units of the scale set by the running coupling which introduces a new dimensionful quantity. Using for example the one-loop coupling and evaluating it at the scale set by the chemical, which yields $g^2(\mu/\Lambda_{\mathrm{QCD}}) = 1/(b_0\ln(\mu/\Lambda_{\mathrm{QCD}}))$, the dimensionful quantity introduced by the running of the strong coupling is Λ_{QCD}. In the expansion of the pressure, we therefore consider g as a function of the dimensionless quantity $\mu/\Lambda_{\mathrm{QCD}}$ so that

$$P = P_{\mathrm{SB}}\left(\gamma_0\big(g\left(\mu/\Lambda_{\mathrm{QCD}}\right)\big) + \gamma_1\big(g\left(\mu/\Lambda_{\mathrm{QCD}}\right)\big)|\bar{\Delta}_0|^2 + \cdots\right)\,. \tag{3.77}$$

Here, $\bar{\Delta}_0 = \bar{\Delta}_0(\mu, g(\mu/\Lambda_{\mathrm{QCD}}))$. It follows, already in the limit of vanishing gap, that the pressure acquires a nontrivial dependence on the chemical potential which already leads to a deviation of the speed of sound from the noninteracting limit $c_{\mathrm{s}}^2 = 1/3$.

3.2.2 Speed of Sound

3.2.2.1 General Considerations

In the following, we use the considerations from the previous section to conduct a qualitative study of the speed of sound. We employ Eq. (3.77) and set $\gamma_i = 0$ for $i > 1$ so that the pressure reduces to

$$P \approx P_{\mathrm{SB}}\left(\gamma_0 + \gamma_1|\bar{\Delta}_0|^2\right)\,. \tag{3.78}$$

We expect that higher-order corrections $\sim |\bar{\Delta}_0|^{2n}$ for $n > 1$ in the gap are not needed for the qualitative study considered here. Indeed, we have seen that higher-order corrections do not alter the qualitative behaviour of the speed of sound, see Fig. 3.14 and the discussion in Sec. 3.1.7. However, it is worth noting that considering the expansion of the pressure instead of solving the underlying exact expression for the pressure shifts the speed of sound towards slightly lower values.

Before showing the speed of sound, we consider and discuss two limiting cases for γ_0 and γ_1. Firstly, we set $\gamma_0 = 1$ and $\gamma_1 = 2$ which corresponds to the approximation of the pressure (3.41) underlying the analytic estimates presented throughout Sec. 3.1 and the estimate for the speed of sound shown in Fig. 3.14. This approximation also corresponds to early studies of the pressure of dense strong-interaction matter, see, e.g., Refs. [46, 339, 340]. From the estimate of the speed of sound (3.68) underlying the aforementioned expansion of the pressure, we find that the speed of sound for symmetric matter approaches the value in the noninteracting limit from above for $\mu \to \infty$ (corresponding to $n \to \infty$). The statement is insensitive to the details of the form of the gap and only relies on the expansion of the pressure (3.41) and that $\bar{\Delta}_{\mathrm{gap}}/\bar{\mu} \to 0$ for $\bar{\mu} \to \infty$. This is in accordance with the expected behaviour of the gap for at least very high densities [46, 47, 49, 50, 56, 82, 84, 87, 88, 126, 321, 322, 330]. The behaviour of the speed of sound is also reflected in the estimate in Fig. 3.14. Note that, in this setting, the γ_i's are independent of the strong coupling g.
Secondly, we include corrections (i.e., perturbative contributions) to the gap-independent contribution γ_0 to the pressure while dropping all gap-induced corrections so that $\gamma_i = 0$ for $i > 0$. To recover the perturbative QCD result for the pressure at leading order in the coupling g, see Refs. [154–156, 320], we choose

$$\gamma_0(g) = 1 - \frac{g^2}{2\pi^2} + \mathcal{O}(g^3)\,. \tag{3.79}$$

The contribution $\sim g^2$ in Eq. (3.79) is generated from a two-loop diagram. For our qualitative analysis, however, we employ the standard one-loop result [318] for the strong coupling which is given by

$$g^2(\mu/\Lambda_{\mathrm{QCD}}) = \frac{1}{b_0 \ln(\mu/\Lambda_{\mathrm{QCD}})}\,. \tag{3.80}$$

We evaluate the strong coupling at the scale set by the chemical potential. Here, the QCD scale Λ_{QCD} is given by $\Lambda_{\mathrm{QCD}} = \Lambda_0 \exp(-1/(b_0 g_0^2))$ with $b_0 = 29/(24\pi^2)$ and g_0 is the value of the strong coupling at the scale Λ_0. For $g_0^2/(4\pi) = 0.179$ at $\Lambda_0 = 10\,\mathrm{GeV}$, which is used in the following to fix the strong coupling, we have $\Lambda_{\mathrm{QCD}} \approx 0.265\,\mathrm{GeV}$. For details about the strong coupling, see App. D. Within this approximation, the speed of sound is smaller than the noninteracting limit and approaches it from below for $n \to \infty$ which we shall discuss in more detail below. This behaviour is unaffected when taking into account higher-order corrections in γ_0 [126, 160–162].
In the expansion of the pressure (3.78) gap-induced contributions appear to be suppressed, at least for small $\bar{\Delta}_{\mathrm{gap}}/\bar{\mu}$. Indeed, for $\mu \to \infty$ this contribution vanishes provided that $\bar{\Delta}_{\mathrm{gap}}/\bar{\mu} \to 0$ in this limit. Then, the pressure effectively reduces to the ungapped case so that only γ_0 has to be specified. However, while this may be an appropriate and convenient estimate for the pressure, the qualitative behaviour of the speed of sound is heavily influenced by gap-induced corrections to the pressure. This becomes apparent when considering the definition of the speed of sound as the first derivative of the pressure divided by the second derivative of the pressure each with respect to the chemical potential, see Eq. (3.69). The speed of sound is consequently very sensitive to the dependence of the pressure on the chemical potential, so that even comparatively small changes in the pressure that affect it only quantitatively can induce a qualitative change in the speed of sound.
Therefore, we combine the previous two cases by setting $\gamma_i = 0$ for $i > 1$, choosing γ_0 as introduced in Eq. (3.79), and using $\gamma_1 = 2$. Recall that choosing $\gamma_0 = 1$ and $\gamma_1 = 2$ leads to a speed of sound that exceeds the noninteracting limit which is then approached from above towards very high densities. In contrast to that, choosing γ_0 as introduced in Eq. (3.79) and $\gamma_1 = 0$ leads to a speed of sound that falls below the noninteracting limit which is then approached from below. Consequently, we expect that the size of the gap has an influence on the qualitative behaviour of the speed of sound.

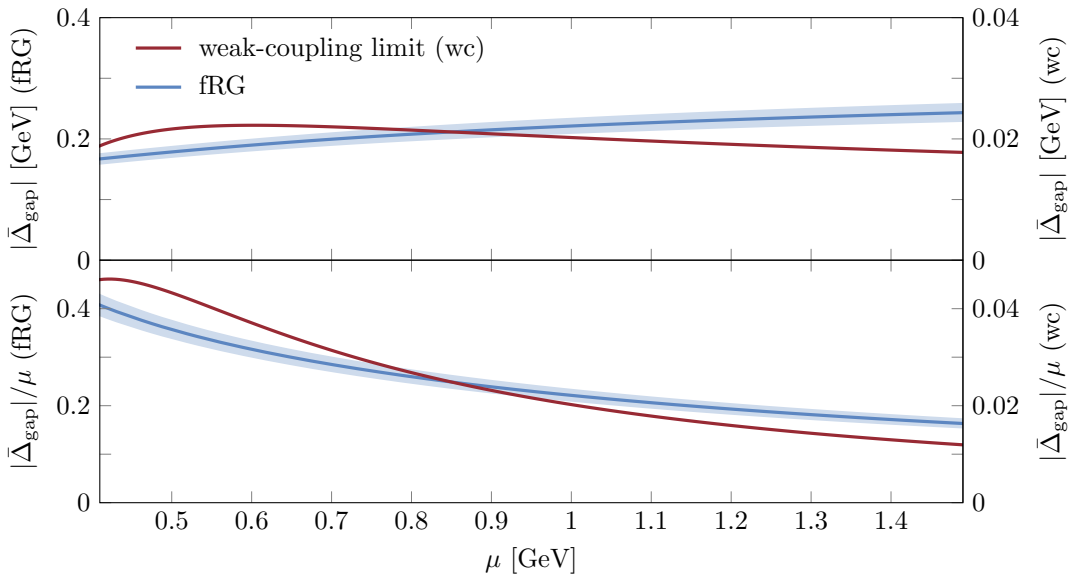

Figure 3.15: Comparison of the colour-superconducting gap $|\bar{\Delta}_{\mathrm{gap}}|$ (top panel) and the dimensionless quantity $|\bar{\Delta}_{\mathrm{gap}}/\mu|$ (bottom panel) as a function of the chemical potential μ. For the red lines, we have employed the functional form of the gap in the weak-coupling limit (red line) from Ref. [56, 82, 87, 88]. The gap is recovered by setting $s_0 = 1$ in Eq. (3.81). The blue lines represent the gap shown in Sec. 2.6.3 as obtained by the fRG calculation. More specifically, it is the gap in Landau gauge presented in Fig. 2.29, see main text for details. The error bands have also been adapted from the aforementioned calculation which include uncertainties from the experimental value of the strong coupling and a variation of the regularisation scheme.

For the dimensionless diquark gap $|\bar{\Delta}_0|^2 = |\bar{\Delta}_{\mathrm{gap}}/\mu|^2$ entering the expansion of the pressure (3.78), we employ two different results since the precise functional form of the diquark gap as a function of the density is still unknown and under ongoing investigation. In addition to that, we expect to gain a better understanding on the influence of the density dependence of the gap on the qualitative behaviour of the speed of sound. Firstly, we use the result from the aforementioned early study in the weak-coupling limit, see Refs. [56, 87, 88]. There, it has been found that

$$|\bar{\Delta}_{\mathrm{gap}}| = s\mu g^{-5} \exp\left(-\frac{3\pi^2}{\sqrt{2}g}\right) , \tag{3.81}$$

where $s = 512\pi^4 \exp(-(4+\pi^2)/8)s_0$. We have introduced s_0 to rescale the gap by a constant factor, see the following discussion for details. For $s_0 = 1$ the gap in the weak-coupling limit as found in Refs. [56, 87, 88] is recovered.

Secondly, we use the diquark gap from the fRG study discussed in Chap. 2, where the gap has been calculated at intermediate densities from first principles. In particular, we use the gap obtained from the QCD calculation in Sec. 2.6.3 in Landau gauge. Note that this gap depends implicitly on the strong coupling g, see also the analytic estimate of the gap (2.94) in Sec. 2.5. The gap from the fRG study is only available in numerical form but is consistent with the gap found in conventional low-energy model studies at least for low densities [85, 126]. We show it as a function of the chemical potential alongside the gap in the weak-coupling limit in Fig. 3.15.

To gain a better understanding of the influence of the size of the gap on the speed of sound, we shall vary the size of the gap from the fRG calculation in Sec. 2.6.3 by rescaling it with a constant factor. For the gap in the weak-coupling limit, we shall rescale the gap by varying the factor s_0. Since we vary the size of the gap

anyway, we do not use the error band depicted in Fig. 3.15 but use the gap as obtained by fixing the strong coupling with $g_0^2/(4\pi) = 0.179$ at $\Lambda_0 = 10\,\mathrm{GeV}$ (blue line in Fig. 3.15). It should be noted that rescaling the gaps employed in the present work slightly changes the respective density dependences.

3.2.2.2 Numerical Results

With Eq. (3.69) and the expansion of the pressure (3.78), we can calculate the speed of sound underlying the aforementioned considerations, i.e., by choosing γ_0 as introduced in Eq. (3.79) and $\gamma_1 = 2$. The speed of sound (squared) as a function of the baryon density $n = (\partial P/\partial\mu)/3$ employing the gap in the weak-coupling limit, see Eq. (3.81), is shown in Fig. 3.16. Utilising the gap from the fRG study leads to the speed of sound shown in Fig. 3.17. The qualitative behaviour of the speed of sound as a function of the density remains consistent in both cases. We show the speed of sound (squared) for different values of the gap at $n/n_0 = 10$: $\Delta_* = |\bar{\Delta}_{\mathrm{gap}}(n/n_0 = 10)|$. Note that $n/n_0 = 10$ is roughly associated with a chemical potential $\mu \approx 0.6\,\mathrm{GeV}$. The different values of the gap at $n/n_0 = 10$ have been obtained by artificially varying the size of the gap according to the discussion above. We find that for small values of the gap (associated with $\Delta_\star = 0.022\,\mathrm{GeV}$, red lines), the speed of sound approaches the noninteracting limit from below and is almost identical to the perturbative QCD result (blue dashed lines). However, by increasing the size of the gap, we find a change in the qualitative behaviour of the speed of sound. This effect of the diquark gap becomes larger for smaller densities where the speed of sound eventually exceeds the value in the noninteracting limit. Going to higher densities, the speed of sound decreases so that it eventually crosses the line associated with the noninteracting limit. We shall refer to this density as the "crossing density" $n_{c_\mathrm{s}}^*$ in the following (coloured dots and dotted lines in Fig. 3.16 and Fig. 3.17). In calculations where the crossing density is located at $n_{c_\mathrm{s}}^*/n_0 = 10$, the size of the gap at the crossing density is given by $\Delta_* \approx 0.175\,\mathrm{GeV}$ for the gap in the weak-coupling limit and $\Delta_* \approx 0.215\,\mathrm{GeV}$ for the gap from the fRG calculation. Going to higher densities beyond the crossing density, we eventually find a local minimum in the speed of sound at $n = n_{\mathrm{min}}$. In the limit $n \to \infty$, the speed of sound then approaches the noninteracting limit from below and lies close to the aforementioned limit for high densities. This behaviour for $n \to \infty$ is present for all sizes of the gaps whereas the increase in the speed of sound towards lower densities only exists for sufficiently large values of the gap.
With these considerations, we can split the density range into two distinct regions: For $n > n_{\mathrm{min}}$ gap-induced corrections are subleading and can therefore be dropped in the calculation of the pressure and the speed of sound. For $n < n_{\mathrm{min}}$ gap-induced corrections become dominant and lead to a qualitative change of the speed of sound so that it even exceeds the noninteracting limit at the crossing density $n_{c_\mathrm{s}}^*$. However, these values for n_{min} and the crossing density $n_{c_\mathrm{s}}^*$ depend on the size of the gap and the functional form. By considering the same functional form, an increase in the size of the gap leads to a shift of the crossing density $n_{c_\mathrm{s}}^*$ and the minimum n_{min} towards higher densities. Comparing the speed of sound as obtained from the gap in the weak-coupling limit and the one from the fRG calculation, we find that a larger gap is needed to exceed the noninteracting limit demonstrating the dependence of the speed of sound on the functional form of the gap. Recall, that the estimate for the speed of sound (as obtained from an expansion of the pressure) shown in Fig. 3.14 is smaller compared to a calculation taking into account arbitrary orders in the gap. Therefore, we expect that the current calculation rather underestimates the speed of sound.
We analyse the dependence of the crossing density on the gap and its functional form in more detail in Fig. 3.18. There, we show the crossing density $n_{c_\mathrm{s}}^*$ as a function of the value of the gap at the crossing density $|\bar{\Delta}_{\mathrm{gap}}(n_{c_\mathrm{s}}^*)|$ (left panel) and the value of the gap at $n/n_0 = 10$: $|\bar{\Delta}_{\mathrm{gap}}(n/n_0 = 10)|$ (right panel). We again find that increasing the size of the gap leads to an increase in the crossing density. Considering a large gap, the speed of sound exceeds the noninteracting limit already for very high densities. As we have already seen in Fig. 3.16 and Fig. 3.17, the crossing density also depends on the functional form of the

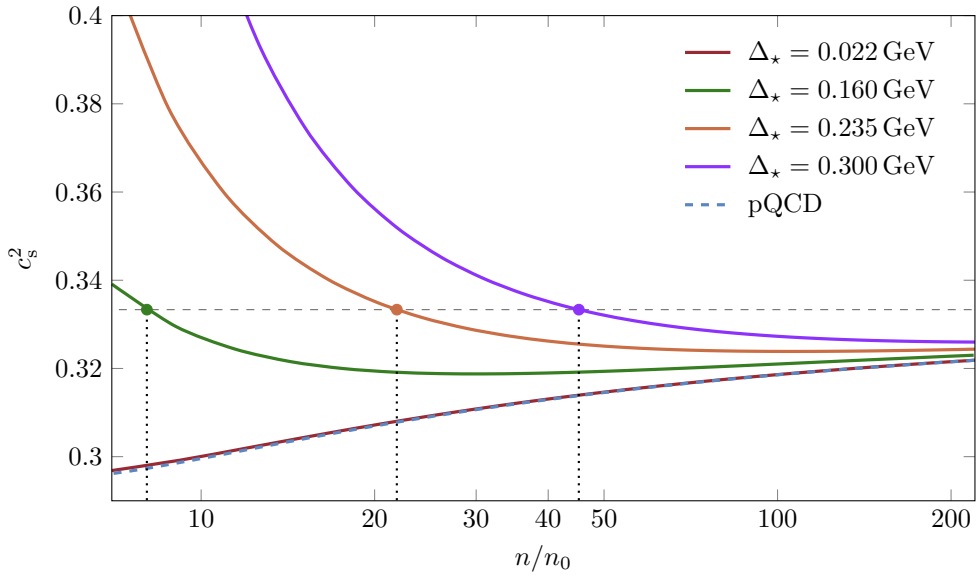

Figure 3.16: Speed of sound (squared) as a function of the baryon density n normalised by the nuclear saturation density n_0 for different values Δ_* as obtained from the gap in the weak-coupling limit, see Eq. (3.81). Here, Δ_* corresponds to the value of the gap at $n/n_0 = 10$: $\Delta_* = |\bar{\Delta}_{\mathrm{gap}}(n/n_0 = 10)|$. In practice, the parameter s_0 in Eq. (3.81) has been tuned such that we recover $\Delta_* = 0.022\,\mathrm{GeV}, 0.160\,\mathrm{GeV}, 0.235\,\mathrm{GeV}, 0.300\,\mathrm{GeV}$, where $\Delta_\star = 0.022\,\mathrm{GeV}$ corresponds to $s_0 = 1$. In an early low-energy model, it has been found that $|\bar{\Delta}_{\mathrm{gap}}| \approx 0.07 \ldots 0.16\,\mathrm{GeV}$ at $n/n_0 = 5$ [85]. For a comparison, we show the perturbative QCD (pQCD) result (dashed blue line) which has been obtained by setting the gap to zero (or $\gamma_i = 0$ for $i > 0$) in the expansion of the pressure (3.78) and choosing γ_0 as given in Eq. (3.79). Note that it lies very close to the line for $\Delta_* = 0.022\,\mathrm{GeV}$. The density where the speed of sound for the different gap sizes crosses the line associated with the noninteracting quark gas is given by coloured dots and dotted vertical lines and the speed of sound of the noninteracting quark gas is given by the dashed horizontal line.

gap. Indeed, when comparing the crossing density for the gap in the weak-coupling limit with that from the fRG calculation, we find that it differs for the same value of the gap at $|\bar{\Delta}_{\mathrm{gap}}(n^*_{c_s})|$ or $|\bar{\Delta}_{\mathrm{gap}}(n/n_0 = 10)|$, respectively. Keeping the size of the gap $|\bar{\Delta}_{\mathrm{gap}}(n/n_0 = 10)|$ fixed and comparing the crossing density as obtained from the gap in the weak-coupling limit to the one from the fRG calculations, we find that the crossing density eventually becomes larger for the fRG calculation (right panel). Nevertheless, by considering the crossing density as a function of the gap at the crossing density $|\bar{\Delta}_{\mathrm{gap}}(n^*_{c_s})|$ (left panel) instead of the gap at $n/n_0 = 10$ ($|\bar{\Delta}_{\mathrm{gap}}(n/n_0 = 10)|$, right panel), the aforementioned difference in the crossing density is smaller. For a given crossing density $n^*_{c_s}$, the value of the gap at the crossing density is smaller employing the functional form of the weak-coupling limit. This effect is stronger for densities $n^*_{c_s} \lesssim 40$. However, the qualitative behaviour of the crossing density in the two cases is similar.

3.2.2.3 Analytic Analysis

The qualitative behaviour of the speed of sound and the crossing density can already be understood by considering an analytic estimate for the speed of sound. Inserting the expansion of the pressure (3.78) into the definition of the speed of sound (3.69) and only considering terms up to the order $|\bar{\Delta}_0|^2$ leads to

$$c_{\mathrm{s}}^2 = \frac{1}{3} + \frac{\pi^2}{6\mu^3}\frac{\partial}{\partial\mu} P_{\mathrm{SB}}\left(\gamma_0 - 1 + \gamma_1 |\bar{\Delta}_0|^2\right) + \ldots \,. \tag{3.82}$$

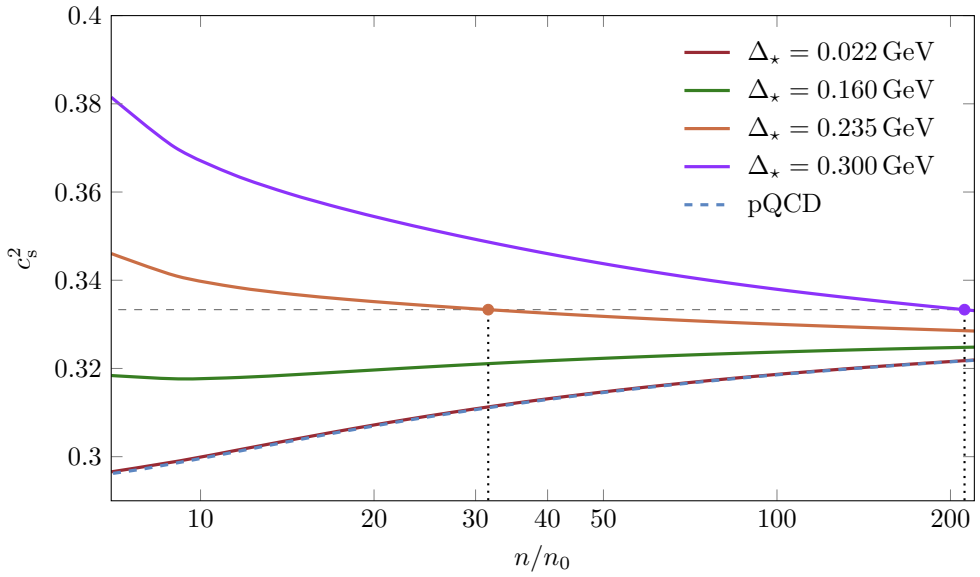

Figure 3.17: Speed of sound (squared) as a function of the baryon density n normalised by the nuclear saturation density n_0 for different values Δ_* as obtained by employing the gap with a functional as obtained in the fRG study and as shown in Fig. 3.15. Here, Δ_* corresponds to the value of the gap evaluated at $n/n_0 = 10$: $\Delta_* = |\bar{\Delta}_{\mathrm{gap}}(n/n_0 = 10)|$. In practice, we have simply rescaled the gap as already done for the gap in the weak-coupling limit in Fig. 3.16 such that we recover $\Delta_* = 0.022\,\mathrm{GeV}, 0.160\,\mathrm{GeV}, 0.235\,\mathrm{GeV}, 0.300\,\mathrm{GeV}$, where $\Delta_\star = 0.235\,\mathrm{GeV}$ corresponds to the gap as shown in Fig. 3.15 without any scaling. As before, for a comparison, we show the perturbative QCD (pQCD) result (dashed blue line), which was obtained by setting the gap to zero (or $\gamma_i = 0$ for $i > 0$) in the expansion of the pressure (3.78) and choosing γ_0 as given in Eq. (3.79). The density where the speed of sound for the different gap sizes crosses the line associated with the noninteracting quark gas is given by coloured dots and dotted vertical lines where the speed of sound of the noninteracting quark gas is given by the dashed horizontal line.

Note that we have assumed that corrections to the noninteracting quark gas are small so that they can be dropped in the denominator of Eq. (3.69). From the expansion (3.82) of the speed of sound, we can read off that the speed of sound exceeds the value of the noninteracting quark gas provided that

$$\frac{\partial}{\partial\mu} P_{\mathrm{SB}} \gamma_1 |\bar{\Delta}_0|^2 > \frac{\partial}{\partial\mu} P_{\mathrm{SB}} \left(1 - \gamma_0\right) . \tag{3.83}$$

Without taking into account corrections to the gap-independent contribution γ_0 to the pressure, i.e., setting $\gamma_0 = 1$, it follows that $c_{\mathrm{s}} > 1/3$ provided that $P_{\mathrm{SB}} \gamma_1 |\bar{\Delta}_0|^2$ increases as a function of the chemical potential. With γ_0 as introduced in Eq. (3.79) (i.e., with perturbative corrections included), we find that the μ dependence of the right-hand side of Eq. (3.83) is given by

$$P_{\mathrm{SB}} \left(1 - \gamma_0\right) \sim \frac{\mu^4}{\ln(\mu/\Lambda_{\mathrm{QCD}})} . \tag{3.84}$$

The left-hand side of Eq. (3.83) depends on the diquark gap and its dependence on the chemical potential. In the following, we assume that the μ dependence of the left-hand side of Eq. (3.83) can be written as follows

$$P_{\mathrm{SB}} \gamma_1 |\bar{\Delta}_0|^2 \sim \mu^{2(1+\sigma)} . \tag{3.85}$$

A fit to the latter equation (for $0.5\,\mathrm{GeV} \lesssim \mu \lesssim 1.5\,\mathrm{GeV}$) gives $\sigma \approx 0.3$ for the gap from the fRG calculation and $\sigma \approx -0.2$ for the gap obtained in the weak-coupling limit. This approximately corresponds to a μ dependence of the gap $|\bar{\Delta}_{\mathrm{gap}}| \sim \mu^\sigma$ where σ is an effective scaling exponent.

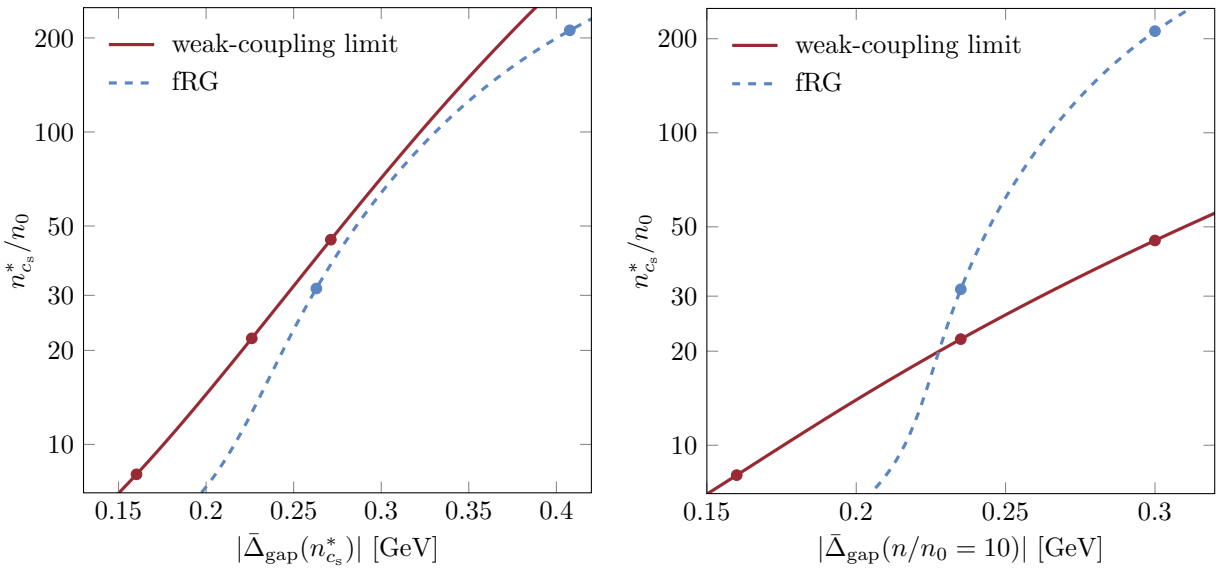

Figure 3.18: Density where the speed of sound crosses the line associated with the speed of sound associated with the noninteracting quark gas (crossing density) $n^*_{c_s}$ normalised by the nuclear saturation density n_0 as a function of the value of the gap at the crossing density $|\bar{\Delta}_{\rm gap}(n^*_{c_s})|$ (left panel) and as a function of the value of the gap at $n/n_0 = 10$, $|\bar{\Delta}_{\rm gap}(n/n_0 = 10)|$ (right panel). We compare the results from employing the gap in the weak-coupling limit (red lines), see Eq. (3.81), with the ones from employing the gap from the fRG calculation (dashed blue lines). See Fig. 3.15 for the functional form of the gaps as a function of the chemical potential. The dots are associated with the dotted lines and coloured dots in Fig. 3.16 and Fig. 3.17, respectively.

With these considerations, it is in principle possible to obtain an estimate for the value of the chemical potential $\mu^*_{c_s}$ where the speed of sound exceeds the value in the noninteracting limit. This chemical potential is associated with the crossing density $n^*_{c_s}$. It follows that this value depends on the size of the colour-superconducting diquark gap and its functional form. Moreover, it is also possible to find an analytic estimate for the speed of sound. Employing Eqs. (3.82), (3.84) and (3.85), we find

$$c_s^2 \approx \frac{1}{3} + \bar{c}_0(1+\sigma)n^{\frac{2(\sigma-1)}{3}} - \frac{\bar{c}_1}{\ln(\bar{c}_2 n^{\frac{1}{3}})}\,. \tag{3.86}$$

Here, $\bar{c}_0$, $\bar{c}_1$, and $\bar{c}_2$ are positive constants and $\bar{c}_2 n^{\frac{1}{3}} > 1$ within the considered density range. In addition to that, σ measures the functional form of the gap. For $\sigma < -1$, we do not expect that the speed of sound exceeds the noninteracting limit, at least at this order of our approximation. However, for $\sigma > -1$ it is possible that the speed of sound exceeds the noninteracting limit, at least if the gap-independent contributions (corresponding to $\bar{c}_1$) are small compared to gap-induced contributions (corresponding to $\bar{c}_0$).
The influence of the size of the diquark gap and its functional form can also be illustrated by comparing the leading-order gap-induced contribution to the pressure of a noninteracting quark gas, given by $\gamma_1|\bar{\Delta}_0|^2$, with the leading order perturbative correction to the gap-independent contribution to the pressure, given by $(1-\gamma_0)$. We show this ratio in Fig. 3.19 for different values of the gap Δ_* at $n/n_0 = 10$. As expected, the impact of the gap-induced contribution increases by increasing the gap. However, already comparatively small gap-induced corrections might alter the qualitative behaviour of the speed of sound. For this, we consider, e.g., the ratio associated with $\Delta_\star = 0.160\,\text{GeV}$ employing the gap as obtained in the weak-coupling limit (solid green line in Fig. 3.16 and Fig. 3.19), where the crossing density is given by $n^*_{c_s} \approx 8$. At this density,

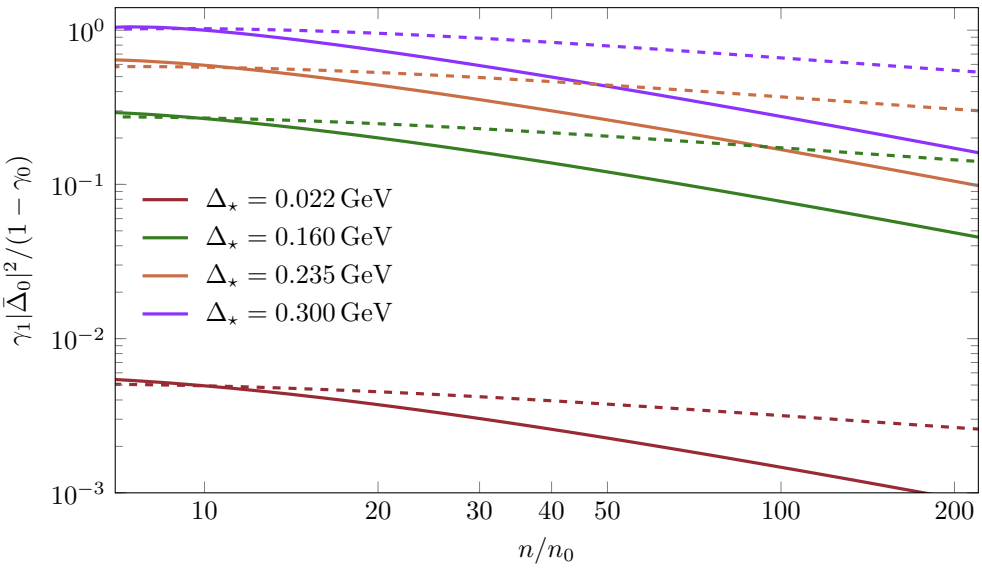

Figure 3.19: Comparison of the leading-order gap-induced correction, given by $\gamma_1|\bar{\Delta}_0|^2$, to the pressure with the size of the leading order perturbative contribution, given by $(1-\gamma_0)$, as a function of the baryon density n in units of the nuclear saturation density n_0. The solid lines have been obtained by employing the gap from the weak-coupling limit, see Eq. (3.81), while the dashed lines represent results obtained with the gap from the fRG calculation. To examine the effect of the size of the gaps, they have been rescaled so that $\Delta_\star$ corresponds to their respective values at $n/n_0 = 10$, see main text for details. Here, $\Delta_\star = 0.022\,\mathrm{GeV}$ corresponds to the value of the gap in the weak-coupling limit without rescaling and $\Delta_\star = 0.235\,\mathrm{GeV}$ to the value of the gap from the fRG calculation without rescaling.

the perturbative contribution is four times larger than the gap-induced corrections. Going to $n/n_0 \approx 28$ where the speed of sound has a local minimum, we find that perturbative contributions are about six times bigger than gap-induced corrections. In this density range, the gap-induced contribution to the pressure corresponds to approximately 5% of the pressure. Similar to this, we can consider $\Delta_\star = 0.350\,\mathrm{GeV}$ and use the gap from the fRG calculation (solid orange line in Fig. 3.17 and dashed orange line in Fig. 3.19) so that the crossing density is $n^*_{c_s} \approx 32$. We again find that perturbative contributions are roughly twice as big as gap-induced corrections. In this density range, the gap-induced contribution to the pressure corresponds to approximately 20% of the pressure. Therefore, we can conclude that even if gap-induced contributions are small compared to the gap-independent corrections and the change in the pressure might seem small, the inclusion of gap-induced contributions might still lead to a qualitative and sizeable change in the speed of sound. This behaviour has already been observed in a previous fRG calculation, see Ref. [126]. There, it has been found that the pressure including a diquark gap, is consistent with calculations that do not take into account a gap. In contrast to that, the presence of the diquark gap makes a significant difference in the speed of sound and leads to a maximum at supranuclear densities.

We conclude this section by comparing the speed of sound as obtained from the expansion of the pressure with results from the previous fRG calculation [126] and chiral EFT at low densities [125, 126] already shown in Fig. 3.13 in Sec. 3.1.7. The speed of sound squared c_s^2 as a function of the total baryon density n is shown in Fig. 3.20. Note that the results in the present section only present qualitative estimates for the speed of sound. However, since the error band includes the variation of the size of the gap and its functional form as considered in the present section, we expect that it is useful to at least test the robustness of the results

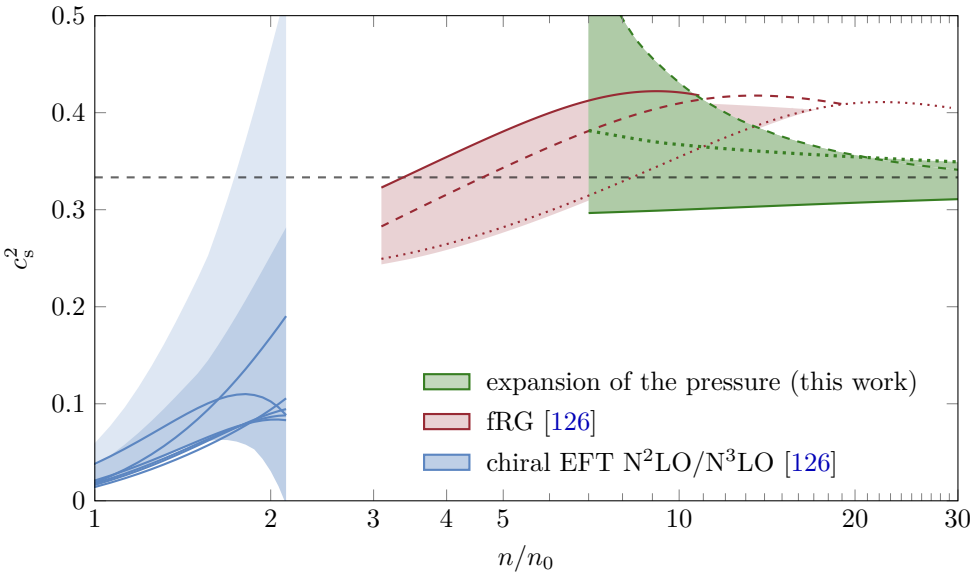

Figure 3.20: Speed of sound squared c_s^2 in units of the speed of light squared as a function of the baryon density n normalised by the nuclear saturation density n_0. The grey dashed line represents the value associated with the noninteracting quark gas $c_s^2 = 1/3$. We show the results obtained from the expansion of the pressure (green band) as considered in the present section. The error band includes a variation of the size of the gap (by rescaling it) and the functional form of the gap, see main text for details. The size of the gap has been tuned such that $\Delta_\star = 0.022\,\mathrm{GeV} \ldots 0.300\,\mathrm{GeV}$ where $\Delta_\star$ corresponds to the value of the gap at $n/n_0 = 10$: $\Delta_\star = |\bar{\Delta}_{\mathrm{gap}}(n/n_0 = 10)|$. For the functional form, we used the gap in the weak-coupling limit (3.81) and the gap from the fRG calculation, see main text for details. For comparison, we show results for the speed of sound for isospin-symmetric matter obtained by chiral EFT (blue band, [126]) and an fRG study taking into account a diquark gap (red, [126]).

presented in Sec. 3.1. Still, some remarks are in order: The speed of sound (squared) as obtained from the considerations in the present section is shown as the green band in Fig. 3.20. The lower end of the error band (associated with $\Delta_* = 0.022\,\mathrm{GeV}$, green solid line) represents the speed of sound as obtained from the gap in the weak-coupling limit and the gap from the fRG calculation alike because they are practically indistinguishable. For the upper end of the error band (which corresponds to $\Delta_* = 0.300\,\mathrm{GeV}$), we show the results for both functional forms of the gap as dashed and dotted green lines. The dotted line was obtained from the fRG gap calculation while the dashed line (corresponding to a larger value for the speed of sound at $n/n_0 = 10$) was obtained from the gap in the weak-coupling limit. Note also that the lower end of the error band (which corresponds to $\Delta_* = 0.022\,\mathrm{GeV}$) coincides with the pure perturbative QCD result, i.e., the speed of sound without the inclusion of a diquark gap in the expansion of the pressure (3.78). It follows that, without a diquark gap, the speed of sound does not exceed the noninteracting limit and approaches it from below for very high densities. For small gap sizes, the situation is similar. This aspect should, however, be considered carefully since, if the gap is large enough, the speed of sound exceeds the noninteracting limit. Considering for example the size of the gap from the fRG calculation, the speed of sound exceeds the noninteracting limit, see orange line in Fig. 3.17. In addition to that, we expect (from the results in Sec. 3.1.7) that the expansion of the pressure rather underestimates the speed of sound. As we have already discussed throughout the present section, going to higher densities, the speed of sound approaches the noninteracting limit from below, regardless of the existence or the size of the gap.

3.3 Conclusions

In this chapter, we demonstrated that our results from the fRG study presented in Chap. 2 can be used to improve already existing low-energy models of dense QCD matter. In particular, we have shown that the results allow us to calculate the speed of sound in the phase governed by the formation of a colour-superconducting ground state. Interestingly, for this region in the phase diagram, barely any results exist for the equation of state, although it is of particular interest for astrophysical applications, e.g., for the description of neutron stars [103, 119–122]. We laid the groundwork for the analysis of the equation of state and the speed of sound over a wide range of densities while we expect that our results in their present form already provide an important insight into the dynamics of dense strong-interaction matter. In this chapter particularly, we employed two different approaches to gain insight into the underlying thermodynamics: Firstly, we considered a low-energy model including the relevant low-energy degrees of freedom of dense QCD, and secondly, an expansion of the equation of state in the presence of a colour-superconducting gap.

To begin with, we used the low-energy model employed in the first part of the present chapter to analyse the zero-temperature phase diagram of dense strong-interaction matter with two quark flavours. Note that the construction of the model was based on the findings of the previous chapter. In particular, it includes the most relevant degrees of freedom of dense QCD. In addition to that, we included different chemical potentials, namely chemical potentials for up and down quarks, effectively allowing for different up and down quark densities, and different colour chemical potentials. Since we consider the density regime where, at least for symmetric matter, the ground state is governed by colour superconductivity (see Refs. [20, 46–56] for reviews), we used the diquark gap from the fRG study employed in Chap. 2 to constrain the model with the gap values in the low-energy limit. Although we only calculated the diquark gap for symmetric matter, the details of the model allowed us to conveniently use the diquark gap in the symmetric limit to also constrain the model for finite isospin asymmetry.

In the phase diagram spanned by the down-quark fraction and the total baryon density, we encountered a (strong) first-order phase transition from a colour-superconducting ground state to an ungapped quark-matter phase. By increasing the total baryon density, we found that the line associated with the phase transition decreases and approaches the line associated with the isospin-symmetric limit. However, isospin-symmetric matter does not undergo a phase transition while isospin-asymmetric matter eventually enters the ungapped quark-matter phase if the total baryon density has become large enough. Colour superconductivity exists over a wide range of total baryon densities at least for small down quark fractions. By including constraints from beta equilibrium, colour-charge neutrality, and electric-charge neutrality, we identified a trajectory in the phase diagram that represents neutron-star matter. This trajectory lies in the gapped phase for densities $n/n_0 \lesssim 27$ where it eventually crosses the phase boundary and enters the first-order region. In contrast to that, the line associated with noninteracting neutron-star matter (corresponding to almost pure neutron matter with only a negligible fraction of protons and electrons) lies in the first-order region for all densities considered in the present work.

In the region of the phase diagram that is governed by the colour-superconducting ground state, we calculated two observables that are relevant for astrophysical applications, namely the electron fraction and the speed of sound. We found that the electron fraction for neutron-star matter is in accordance with results from nuclear physics and observations [119]. Concerning the speed of sound, we observed that it exceeds the value in the noninteracting limit and increases towards lower densities. We find the qualitatively same behaviour for symmetric matter and neutron-star matter. However, it should be noted that neutron-star matter eventually undergoes a first-order phase transition going towards high densities. It eventually enters the phase associated with ungapped quark matter. In this ungapped region, the speed of sound is expected to be given by the speed of sound as computed within perturbative QCD.

In the second part of this chapter, we extended the investigation of the speed of sound and the influence of a gap in the fermionic excitation spectrum by employing an expansion of the equation of state in the presence of a colour-superconducting gap. As before, we studied two massless quark flavours but only considered symmetric matter. The leading order in the expansion can be identified with the pressure in the absence of a colour-superconducting gap corresponding to results from, e.g., perturbative studies of QCD [154–162, 320]. The next-to-leading orders in the expansion are gap-induced contributions to the pressure. Notably, this expansion only relied on the assumption that dense strong-interaction matter is a colour superconductor at sufficiently low temperatures. Since higher-order gap-induced contributions appear to be suppressed, we only considered the first gap-induced contribution to the pressure.

Utilising the expansion of the pressure, we analysed the speed of sound. Starting from the infinite density limit, where the speed of sound is expected to be given by the noninteracting limit, we find that the speed of sound first decreases even in the presence of a gap. This decrease results from perturbative corrections to the gap-independent contributions to the pressure and, therefore, also agrees with calculations where a gap is not taken into account [157–162]. Going towards lower densities, gap-induced contributions become important, leading to an increase in the speed of sound. Consequently, a local minimum in the speed of sound emerges. Above the local minimum gap-induced contributions to thermodynamic quantities may be neglected. However, below the minimum gap-induced contributions become important which eventually leads to the speed of sound crossing the line associated with the noninteracting quark gas. The associated crossing density and the local minimum not only depend on the size of the gap but also its functional form, i.e., its dependence on the chemical potential. We showed that already small gap-induced contributions to the pressure may significantly influence the speed of sound since the included derivatives with respect to the chemical potential become sizeable. However, a quantitative calculation of the crossing density and the minimum requires higher-order corrections in the expansion which is beyond the scope of the present work. Still, we believe that the present work already helps to understand mechanisms underlying the dynamics of dense strong-interaction matter.

Both approaches to calculate the speed of sound predict that the speed of sound exceeds the value in the noninteracting limit at supranuclear densities, in accordance with Ref. [126]. Together with results from chiral EFT [125, 126], these findings suggest the existence of a global maximum in the speed of sound. However, determining the position and value of this maximum is challenging since many interaction channels become relevant towards the nucleonic density regime (see, e.g., Refs. [130–132, 135, 164–169]) where the position of the maximum is expected. The increase in the speed of sound has not been observed in fRG calculations that do not take into account the existence of a diquark gap [126]. Interestingly, the existence of a maximum in the speed of sound is also expected from the analysis of constraints from neutron-star masses for neutron-rich matter [103, 119–124]. Since the height of maximum is related to the size of the diquark gap, this may possibly allow to infer information about the size of the gap from neutron-star measurements.

Finally, we should point out again that we have only considered two massless quark flavours. Strange quarks may potentially contribute at densities considered in the present work which are relevant for astrophysical applications. Then pairing of the two-flavour colour-superconductivity type, underlying the calculations in the present work, may no longer be favoured [328]. Studies of QCD with two massless and one massive quark flavours appear to be much more challenging since, for example, a phase with pairing of the colour-flavour locking type may become relevant [47, 56, 328, 329]. However, the general considerations, particularly regarding the expansion of the equation of state do not rely on the origin or type of the gap but only on its existence. Therefore, we expect that our general considerations about the density dependence of the speed of sound also hold for a situation where the gap originates from a different type of colour superconductivity. Additionally, we expect that the present work provides a useful insight into dense strong-interaction matter, helping to understand its dynamics and the emergence of different phases.

Summary and Outlook

With the present work, we aim to analyse the phase diagram and the thermodynamics of dense strong-interaction matter which have been the subject of intensive research in recent years. Note that we only highlight the most important results of the present work here. More detailed conclusions and discussions, including comments on the underlying approximations, can be found in the conclusions of the corresponding chapters, see Secs. 2.7 and 3.3.

Using a newly constructed class of regulators, we studied the dynamical formation of diquarks in the low-energy regime from the fundamental quark and gluon degrees of freedom employing the fRG approach. We have thereby shown that the use of the aforementioned class of regulators is well-suited for studies of relativistic theories in the presence of a Cooper instability. Considering two massless quark flavours, namely up and down quarks, we find the formation of a ground state characterised by the pairing of a chirally symmetric two-flavour colour superconducting type at intermediate to high densities in accordance with, e.g., Refs. [40, 84–86]. We computed the corresponding gap in the excitation spectrum of the quarks over a wide range of chemical potentials and towards (very) high chemical potentials. For the scaling behaviour of the gap as a function of the strong coupling g and the chemical potential μ, we found an analytic estimate at intermediate densities which is given by $\Delta_{\mathrm{gap}} \sim \exp(-\bar{c}/(g^4\mu^2))$, where $\bar{c}$ is a positive constant, see Sec. 2.5. We discussed possible extensions of our present study. In particular, we analysed the effect of fluctuations of the diquark fields which we have at least included above the symmetry-breaking scale where they appear to be subleading as already observed for other fluctuation effects in early fRG studies [259, 323, 324]. In addition to that, we discussed effects from gluon-screening masses and an Anderson-Higgs-type mechanism [61–66] in the phase governed by spontaneous symmetry breaking. The Anderson-Higgs-type mechanism is expected to lead to a suppression of gluonic contributions in the infrared regime.

We have demonstrated that our approach is capable of investigating dense strong-interaction matter over a wide range of densities, including the possibility of systematic improvements by implementing the aforementioned extensions to our present study. In particular, our fRG approach allows us to connect the high-energy regime associated with quarks and gluons with the low-energy regime associated with the emergence of a colour-superconducting ground state at high densities.

Based on our first-principles RG flows, we demonstrated that our results can be used to constrain already existing low-energy models of QCD. In particular, we constructed a low-energy model of dense strong-interaction matter to analyse the thermodynamics and phase structure of dense strong-interaction matter. By including isospin asymmetry with two quark flavours, we found a (strong) first-order phase transition from a phase governed by a superconducting ground state to an ungapped phase. We were able to identify trajectories in the corresponding phase diagram spanned by the total baryon density and the down quark fraction. By computing a trajectory representing neutron-star matter in this phase diagram, we found that this trajectory lies in the phase governed by a superconducting ground state for up to a density of $n/n_0 \lesssim 27$ where n is the total baryon density and n_0 is the nuclear saturation density. At this density, neutron-star matter undergoes

a first-order phase transition to an ungapped phase. Interestingly, we found that this phase transition does not occur in isospin-symmetric matter.

We then calculated the speed of sound at supranuclear densities using the low-energy model and, alternatively, employing a systematic expansion of the equation of state of isospin-symmetric matter in the presence of a superconducting gap. In doing so, we provided updates to a recent computation of the speed of sound of dense strong-interaction matter [126]. Our results are in accordance with constraints from nuclear physics and observations [119]. By including perturbative corrections in the expansion of the equation of state, we found that, coming from asymptotically high densities, the speed of sound as a function of the total baryon density decreases. This decrease is in agreement with, e.g., Refs. [126, 157–162], where a gap in the excitation spectrum of the quarks was not taken into account. At lower densities, however, contributions to the equation of state from the superconducting gap become relevant and lead to an increase in the speed of sound, so that it eventually exceeds the value of the speed of sound in the noninteracting limit. Together with results from chiral effective field theory at low densities [125, 126], we conclude that the speed of sound exhibits a maximum at supranuclear densities as already observed and discussed in Ref. [126]. We would like to add that, by including isospin asymmetry in the aforementioned low-energy model, we found that the density dependence of the speed of sound, in the density regime considered in the present work (i.e., $n/n_0 \gtrsim 7$), for neutron-star matter differs only slightly from that for symmetric matter, as long as the dynamics is governed by a colour-superconducting ground state.

Interestingly, the existence of a maximum in the speed of sound is also supported by constraints from neutron-star masses [103, 119–124]. In fact, the present study provides a possible explanation for this maximum with the formation of a superconducting ground state, which is expected to govern the dynamics in the core of neutron stars. Therefore, the insight gained in the present work may be used to improve already existing constraints on the equation of state used as an input for astrophysical calculations, in particular, for neutron-star simulations.

By comparing our present work with previous fRG studies [126, 179], we also analysed the reliability of our present results, in particular for the speed of sound. From this, we concluded that our results are reliable in the high-density regime where the diquark channel is dominant [179]. However, the approximation to only include the diquark channel becomes less reliable as we move towards the nucleonic low-density regime, where the use of a Fierz-complete basis of gluon-induced four-quark interactions becomes more important. Therefore, we expect our present study to be limited to densities $n/n_0 \gtrsim 7$. In particular, the calculation of the pressure within the fRG study requires at least the inclusion of the chiral dynamics by including the chiral scalar-pseudoscalar channel as a four-quark interaction induced by the fundamental quark-gluon dynamics in addition to the diquark channel. Recall that the scalar-pseudoscalar interaction channel is associated with the formation of a chiral condensate which governs the dynamics of QCD for low densities [179]. For a first analysis of the dependence of the symmetry-breaking scale on the scalar-pseudoscalar channel, it may be interesting to include this channel only above the symmetry-breaking scale without bosonising it. Ultimately, however, the dynamical bosonisation of the scalar-pseudoscalar channel alongside the diquark channel (associated with the formation of a colour-superconducting ground state) is required. In this way, the momentum dependence of two interaction channels can be at least partially resolved, allowing access to the low-energy degrees of freedom and the formation of bound states and condensates in the infrared regime. Note that the dynamical bosonisation technique used in our studies has already been used in other studies in the low-density regime for the scalar-pseudoscalar channel, see, e.g., Refs. [146, 175, 176, 316].

Moreover, between the regime where the dynamics is governed by the scalar-pseudoscalar channel and the region where the diquark channel becomes dominant, a regime opens up in which many interaction channels become sizeable, indicating a rich phase structure [130–132, 135, 164–169]. Therefore, the inclusion of additional quark-pairing channels other than the two discussed above is ultimately required to bridge the

gap between the high- and low-density regime. However, the inclusion of additional pairing channels comes with a significant cost since a certain number of additional four-quark interactions not only requires the inclusion of the same number of additional flow equations, but also additionally couples the corresponding quark-interaction channels, as already observed in Ref. [179]. Nevertheless, the inclusion of additional quark-pairing channels should eventually allow us to obtain quantitative estimates for the density regime $n/n_0 \lesssim 7$, i.e., the regime excluded in the present work. It will be interesting to see how this affects the position and height of the maximum of the speed of sound.

Given our goal to determine an equation of state relevant to astrophysical applications, especially for neutron stars, an extension of our analysis to finite temperature is eventually required, especially for simulations concerning neutron-star mergers. In addition to that, strange quarks may become relevant for densities reached in the core of neutron stars. Taking strange quarks into account, so-called colour-flavour locking is expected to be the most dominant pairing channel, in contrast to the pairing of the two-flavour colour-superconducting type [47, 50, 56, 85, 328, 329]. The inclusion of colour-flavour locking is, in principle, also possible. However, this requires to first study the dominance pattern of gluon-induced four-quark interactions for three quark flavours. This analysis is expected to be much more challenging than the corresponding one for two quark flavours in Ref. [179] preceding our present work, because the number of channels in a corresponding Fierz-complete study increases significantly because the flavour symmetry is explicitly broken [348].

In conclusion, the present work provides a framework for the analysis of dense strong-interaction matter over a wide range of densities and presents field-theoretical foundations for the calculation of the superconducting gap and the thermodynamics with the fRG approach. It thus provides the basis for future systematic nonperturbative studies of the equation of state and speed of sound of dense strong-interaction matter.

A

Notation and Convention

In the following, we introduce our conventions for the Fourier transformations in App. A.1, for the matrices used for colour degrees of freedom in App. A.2, for the matrices used for flavour degrees of freedom in App. A.3, and for the Dirac matrices in App. A.4. We present the so-called Fierz transformations in App. A.5 which we use in the present work to rewrite products of bilinears consisting of spinors. Throughout the present work, we work in natural units. We show how to convert them into SI units in App. A.6.

A.1 Fourier Conventions

For integrals as used in Sec. 1.2, we use the abbreviated form for n spacetime dimensions

$$\int_x \equiv \int \mathrm{d}^n x \qquad \text{and} \qquad \int_p \equiv \int \frac{\mathrm{d}^n p}{(2\pi)^n} \,. \tag{A.1}$$

For the remainder of the present work, we work in four spacetime dimensions so that

$$\int_x \equiv \int \mathrm{d}^4 x \qquad \text{and} \qquad \int_p \equiv \int \frac{\mathrm{d}^4 p}{(2\pi)^4} \,. \tag{A.2}$$

Here, x is the coordinate vector in Euclidean spacetime and p is the momentum vector. When using four spacetime dimensions, we sometimes split the four-momentum vector p into its time (energy) component p_0 and the spatial component, the three-momentum $\vec{p}$. The Fourier convention used in the present work reads

$$\begin{aligned} \bar{\psi}(x) &= \int_p \mathrm{e}^{-\mathrm{i}px} \bar{\Psi}(p) \,, \qquad \psi(x) = \int_p \mathrm{e}^{\mathrm{i}px} \Psi(p) \,, \qquad A^a_\mu(x) = \int_p \mathrm{e}^{\mathrm{i}px} \mathbf{A}^a_\mu(p) \,, \\ \Delta^*_a(x) &= \int_p \mathrm{e}^{\mathrm{i}px} \boldsymbol{\Delta}^*_a(p) \,, \qquad \text{and} \qquad \Delta_a(x) = \int_p \mathrm{e}^{-\mathrm{i}px} \boldsymbol{\Delta}_a(p) \,. \end{aligned} \tag{A.3}$$

Here, $\bar{\Psi}$, Ψ, $\mathbf{A}^a_\mu$, $\boldsymbol{\Delta}^*_a$, and $\boldsymbol{\Delta}_a$ are the Fourier transforms of the fields $\bar{\psi}$, ψ, A^a_μ, Δ^*_a, and Δ_a, respectively.

A.2 Colour Matrices

The gauge group for three colours $N_\mathrm{c} = 3$ is the special unitary group SU(3). The generators of the group SU(3) are the eight Hermitian Gell-Mann matrices λ_i $(i = 1, \ldots, 8)$ which are given by

$$\lambda_1 = \begin{pmatrix} 0 & 1 & 0 \\ 1 & 0 & 0 \\ 0 & 0 & 0 \end{pmatrix}, \quad \lambda_2 = \begin{pmatrix} 0 & -\mathrm{i} & 0 \\ \mathrm{i} & 0 & 0 \\ 0 & 0 & 0 \end{pmatrix}, \quad \lambda_3 = \begin{pmatrix} 1 & 0 & 0 \\ 0 & -1 & 0 \\ 0 & 0 & 0 \end{pmatrix},$$

$$\lambda_4 = \begin{pmatrix} 0 & 0 & 1 \\ 0 & 0 & 0 \\ 1 & 0 & 0 \end{pmatrix}, \quad \lambda_5 = \begin{pmatrix} 0 & 0 & -\mathrm{i} \\ 0 & 0 & 0 \\ \mathrm{i} & 0 & 0 \end{pmatrix}, \quad \lambda_6 = \begin{pmatrix} 0 & 0 & 0 \\ 0 & 0 & 1 \\ 0 & 1 & 0 \end{pmatrix}, \tag{A.4}$$

$$\lambda_7 = \begin{pmatrix} 0 & 0 & 0 \\ 0 & 0 & -\mathrm{i} \\ 0 & \mathrm{i} & 0 \end{pmatrix}, \quad \lambda_8 = \frac{1}{\sqrt{3}} \begin{pmatrix} 1 & 0 & 0 \\ 0 & 1 & 0 \\ 0 & 0 & -2 \end{pmatrix}.$$

Note that $\lambda_i^\dagger = \lambda_i$. As the colour generators, instead of the Gell-Mann matrices, we use the colour matrices

$$T^a = \frac{\lambda_a}{2}, \qquad \text{where} \qquad a = 1, \ldots 8\,. \tag{A.5}$$

To avoid confusion, we always use upper indices (e.g., a) to specify the generators (e.g., T^a) so that we can use lower indices to refer to the entries of the corresponding matrices, i.e., T^a_{ab} represents the element at the a-th row and the b-th column of the matrix T^a. The generators T^a satisfy the commutation and anticommutation relations

$$\left[T^a, T^b\right] = \mathrm{i} f^{abc} T^c \qquad \text{and} \qquad \left\{T^a, T^b\right\} = \frac{1}{3}\mathbb{1}_\mathrm{c}\delta^{ab} + d^{abc}T^c\,, \tag{A.6}$$

where $\mathbb{1}_\mathrm{c}$ is a 3×3 identity matrix that acts as a 'one' in colour space. Furthermore, the structure constants are f^{abc} (totally antisymmetric), d^{abc} (totally symmetric), and h^{abc}. They are given by

$$f^{abc} = -2\mathrm{i}\mathrm{Tr}\left(\left[T^a, T^b\right] T^c\right), \qquad d^{abc} = 2\mathrm{Tr}\left(\left\{T^a, T^b\right\} T^c\right), \qquad \text{and} \qquad h^{abc} = d^{abc} + \mathrm{i} f^{abc}\,. \tag{A.7}$$

From these definitions follow the relations

$$f^{abc}d^{abd} = 0\,, \qquad f^{abc}f^{abd} = 3\delta^{cd}\,, \qquad d^{abc}d^{abd} = \frac{5}{3}\delta^{cd}\,, \qquad h^{abc}h^{abd} = -\frac{4}{3}\delta^{cd}\,, \tag{A.8}$$

$$h^{aab} = d^{aab} = f^{aab} = 0\,, \qquad \text{and} \qquad h^{abc} = h^{cab} = h^{bca}\,. \tag{A.9}$$

The product of two colour generators is given by

$$T^a T^b = \frac{1}{6}\delta^{ab}\mathbb{1}_\mathrm{c} + \frac{1}{2}h^{abc}T^c\,, \tag{A.10}$$

which yields

$$T^a T^a = \frac{4}{3}\mathbb{1}_\mathrm{c} \qquad \text{and} \qquad T^a T^b T^a = -\frac{1}{6}T^b. \tag{A.11}$$

The first traces of the generators T^a are given by

$$\mathrm{Tr}(T^a) = 0\,, \tag{A.12}$$

$$\mathrm{Tr}\left(T^a T^b\right) = \frac{1}{2}\delta^{ab}\,, \tag{A.13}$$

$$\mathrm{Tr}\left(T^a T^b T^c\right) = \frac{1}{4}\left(d^{abc} + \mathrm{i} f^{abc}\right) = \frac{1}{4}h^{abc}\,, \tag{A.14}$$

$$\mathrm{Tr}\left(T^a T^b T^c T^d\right) = \frac{1}{12}\delta^{ab}\delta^{cd} + \frac{1}{8}h^{abe}h^{ecd}\,. \tag{A.15}$$

To represent the antisymmetric colour structure in the diquark channel, we have introduced matrices that are totally antisymmetric via the Levi-Civita tensor ϵ_{abc}. Here, the lower indices refer to the colour indices $a, b, c = 1, 2, 3$ (or alternatively $a, b, c = \mathrm{r}, \mathrm{g}, \mathrm{b}$ referring to the three colour charges red (r), green (g), and blue (b)). With this, we define the three antisymmetric matrices ϵ_a where the entries of the matrices are given by the Levi-Civita tensor: $(\epsilon_a)_{bc} = \epsilon_{abc}$. The resulting matrices are closely related to the antisymmetric Gell-Mann matrices and are given by

$$\epsilon_1 = \mathrm{i}\lambda_7 = \begin{pmatrix} 0 & 0 & 0 \\ 0 & 0 & 1 \\ 0 & -1 & 0 \end{pmatrix}, \quad \epsilon_2 = -\mathrm{i}\lambda_5 = \begin{pmatrix} 0 & 0 & -1 \\ 0 & 0 & 0 \\ 1 & 0 & 0 \end{pmatrix}, \quad \epsilon_3 = \mathrm{i}\lambda_2 = \begin{pmatrix} 0 & 1 & 0 \\ -1 & 0 & 0 \\ 0 & 0 & 0 \end{pmatrix}. \tag{A.16}$$

The product of two Levi-Civita tensors is given by

$$\epsilon_{ijk}\epsilon_{lmn} = \delta_{il}\delta_{jm}\delta_{kn} + \delta_{im}\delta_{jn}\delta_{kl} + \delta_{in}\delta_{jl}\delta_{km} - \delta_{in}\delta_{jm}\delta_{kl} - \delta_{il}\delta_{jn}\delta_{km} - \delta_{im}\delta_{jl}\delta_{kn} \tag{A.17}$$

so that the product of two ϵ_a matrices is given by

$$(\epsilon_a\epsilon_b)_{ik} = (\epsilon_a)_{ij}(\epsilon_b)_{jk} = \delta_{ak}\delta_{bi} - \delta_{ab}\delta_{ik}\,. \tag{A.18}$$

From this, it follow

$$\epsilon_a\epsilon_a = -2\mathbb{1}_\mathrm{c} \qquad \text{and} \qquad \epsilon_a\epsilon_b\epsilon_a = -\epsilon_b\,. \tag{A.19}$$

The first traces of the matrices ϵ_a are given by

$$\mathrm{Tr}(\epsilon_a) = 0\,, \tag{A.20}$$

$$\mathrm{Tr}(\epsilon_a\epsilon_b) = -2\delta_{ab}\,, \tag{A.21}$$

$$\mathrm{Tr}(\epsilon_a\epsilon_b\epsilon_c) = \epsilon_{abc}\,, \tag{A.22}$$

$$\mathrm{Tr}(\epsilon_a\epsilon_b\epsilon_c\epsilon_d) = \delta_{ad}\delta_{cb} + \delta_{ab}\delta_{cd}\,. \tag{A.23}$$

A.3 Flavour Matrices

The gauge group for two flavours $N_\mathrm{f} = 2$ is the special unitary group SU(2) of unitary matrices with determinant 1. The generators of SU(2) are given by the Hermitian Pauli matrices τ_i $(i = 1, 2, 3)$ which are

$$\tau_1 = \begin{pmatrix} 0 & 1 \\ 1 & 0 \end{pmatrix}, \qquad \tau_2 = \begin{pmatrix} 0 & -\mathrm{i} \\ \mathrm{i} & 0 \end{pmatrix}, \qquad \tau_3 = \begin{pmatrix} 1 & 0 \\ 0 & -1 \end{pmatrix}. \tag{A.24}$$

The only antisymmetric Pauli matrix is τ_2. Note that the Pauli matrices are traceless, $\tau_i^\dagger = \tau_i$, and that $\det\tau_i = -1$. The commutation and anticommutation relations for the Pauli matrices read

$$\big[\tau_i, \tau_j\big] = 2\mathrm{i}\epsilon_{ijk}\tau_k \qquad \text{and} \qquad \big\{\tau_i, \tau_j\big\} = 2\delta_{ij}\mathbb{1}_\mathrm{f}\,. \tag{A.25}$$

Here, ϵ_{ijk} is the three-dimensional Levi-Civita symbol and $\mathbb{1}_\mathrm{f}$ is a 2×2 identity matrix which acts as a 'one' in flavour space. Furthermore, it is

$$\tau_i\tau_j = \delta_{ij}\mathbb{1}_\mathrm{f} + \mathrm{i}\epsilon_{ijk}\tau_k \qquad \text{and} \qquad \tau_1\tau_1 = \tau_2\tau_2 = \tau_3\tau_3 = \mathbb{1}_\mathrm{f}\,. \tag{A.26}$$

The first traces of the Pauli matrices are given by

$$\mathrm{Tr}\big(\tau_i\big) = 0\,, \tag{A.27}$$

$$\mathrm{Tr}\big(\tau_i\tau_j\big) = 2\delta_{ij}\,, \tag{A.28}$$

$$\mathrm{Tr}\big(\tau_i\tau_j\tau_k\big) = 2\mathrm{i}\epsilon_{ijk}\,, \tag{A.29}$$

$$\mathrm{Tr}\big(\tau_i\tau_j\tau_k\tau_l\big) = 2\big(\delta_{ij}\delta_{kl} + \delta_{il}\delta_{jk} - \delta_{ik}\delta_{jl}\big)\,. \tag{A.30}$$

A.4 Euclidean Dirac Matrices

Throughout the entire work, we use Euclidean spacetime. For the γ-matrices (also referred to as Dirac matrices named after physicist Paul Dirac), we use the following convention:

$$\gamma_0 = \begin{pmatrix} 0 & 0 & 1 & 0 \\ 0 & 0 & 0 & 1 \\ 1 & 0 & 0 & 0 \\ 0 & 1 & 0 & 0 \end{pmatrix}, \qquad \gamma_1 = \begin{pmatrix} 0 & 0 & 0 & -\mathrm{i} \\ 0 & 0 & -\mathrm{i} & 0 \\ 0 & \mathrm{i} & 0 & 0 \\ \mathrm{i} & 0 & 0 & 0 \end{pmatrix}, \tag{A.31}$$

$$\gamma_2 = \begin{pmatrix} 0 & 0 & 0 & -1 \\ 0 & 0 & 1 & 0 \\ 0 & 1 & 0 & 0 \\ -1 & 0 & 0 & 0 \end{pmatrix}, \qquad \gamma_3 = \begin{pmatrix} 0 & 0 & -\mathrm{i} & 0 \\ 0 & 0 & 0 & \mathrm{i} \\ \mathrm{i} & 0 & 0 & 0 \\ 0 & -\mathrm{i} & 0 & 0 \end{pmatrix}. \tag{A.32}$$

The γ-matrices obey the Clifford algebra

$$\left\{\gamma_\mu, \gamma_\nu\right\} = 2\delta_{\mu\nu}\,. \tag{A.33}$$

Since we work in Euclidean spacetime, there is no difference between matrices with upper and lower indices so that we write all Dirac matrices with lower indices. Additionally, in Euclidean spacetime, the γ-matrices are Hermitian matrices: $\gamma_\mu^\dagger = \gamma_\mu$. Some products of γ-matrices are given by

$$\gamma_\mu\gamma_\mu = 4\mathbb{1}_\mathrm{D}\,, \qquad \gamma_\mu\gamma_\nu\gamma_\mu = -2\gamma_\nu\,, \qquad \text{and} \qquad \gamma_\mu\gamma_\alpha\gamma_\beta\gamma_\mu = 4\delta_{\alpha\beta}\,. \tag{A.34}$$

Here, $\mathbb{1}_\mathrm{D}$ is a 4×4 identity matrix that acts as a 'one' in Dirac space. We further define the γ_5-matrix via

$$\gamma_5 = \gamma_1\gamma_2\gamma_3\gamma_0 = -\frac{1}{4!}\epsilon_{\alpha\beta\mu\nu}\gamma_\alpha\gamma_\beta\gamma_\mu\gamma_\nu\,. \tag{A.35}$$

The γ_5-matrix is not one of *the* γ-matrices, i.e., the indices of the γ-matrices are given by $\mu = 0, 1, 2, 3$. The γ_5-matrix is its own inverse $\gamma_5\gamma_5 = \mathbb{1}_\mathrm{D}$ and anticommutes with the γ-matrices: $\gamma_5\gamma_\mu = -\gamma_\mu\gamma_5$. Therefore, terms that contain γ_5 change their sign under parity transformations so that a scalar becomes a pseudoscalar and vectors become pseudovectors. For example, $\bar\psi\psi$ transforms like a scalar but $\bar\psi\gamma_5\psi$ transforms like a pseudoscalar. In addition to γ_5, we also introduce the charge conjugation matrix $\mathcal{C}$ via

$$\mathcal{C} = \mathrm{i}\gamma_2\gamma_0\,. \tag{A.36}$$

It is also its own inverse: $\mathcal{C}\mathcal{C} = \mathbb{1}_\mathrm{D}$. Note that γ_5 and $\mathcal{C}$ commute: $\gamma_5\mathcal{C} = \mathcal{C}\gamma_5$. The introduction of these matrices leads to some useful relations:

$$\mathcal{C}\gamma_\mu^T = -\gamma_\mu\mathcal{C}\,, \qquad \gamma_5\mathcal{C}\gamma_\mu^T = \gamma_\mu\gamma_5\mathcal{C}\,, \qquad \mathcal{C}\gamma_\mu^T\mathcal{C} = -\gamma_\mu\,, \qquad \text{and} \qquad \gamma_5\mathcal{C}\gamma_\mu^T\mathcal{C}\gamma_5 = \gamma_\mu\,. \tag{A.37}$$

We also define the commutator of γ-matrices via

$$\sigma_{\mu\nu} = \frac{\mathrm{i}}{2}\left[\gamma_\mu, \gamma_\nu\right] = -\mathrm{i}\delta_{\mu\nu} + \mathrm{i}\gamma_\mu\gamma_\nu\,. \tag{A.38}$$

Some traces of products of γ-matrices and possibly γ_5 are given by

$$\mathrm{Tr}(\gamma_\mu) = 0\,, \tag{A.39}$$

$$\mathrm{Tr}(\gamma_\mu\gamma_\nu) = 4\delta_{\mu\nu}\,, \tag{A.40}$$

$$\mathrm{Tr}(\gamma_\mu\gamma_\nu\gamma_\rho\gamma_\sigma) = 4\left(\delta_{\mu\nu}\delta_{\rho\sigma} - \delta_{\mu\rho}\delta_{\nu\sigma} + \delta_{\mu\sigma}\delta_{\rho\nu}\right)\,, \tag{A.41}$$

$$\mathrm{Tr}(\gamma_5) = \mathrm{Tr}(\gamma_\mu\gamma_\nu\gamma_5) = 0\,. \tag{A.42}$$

The trace of a product of an odd number of γ-matrices yields zero. In addition to that, γ_5 times a product of an odd number of γ-matrices also yields zero.

A.5 Fierz Transformations

In the following, we introduce the so-called Fierz transformations [349], see also Refs. [350–352]. They are frequently used to rewrite Dirac bilinears, which are products of Dirac matrices taken between two spinors. For instance, in calculations in quantum field theory, products of two Dirac bilinears often appear, which then consist of four Dirac spinors in total. In these cases, the order of the appearance of the individual spinors is critical. Fierz transformations can then be used to reorder the order of appearance of the spinors, as we shall see in the following. In the present work, we use Fierz transformations for Dirac bilinears and for colour and flavour matrices taken between two spinors. Therefore, we begin with the derivation of general Fierz identities by considering $N \times N$ matrices and show the explicit Fierz transformations for colour, flavour, and Dirac matrices in Apps. A.5.1–A.5.3.

The $N \times N$ (square) matrices form an N^2-dimensional vector space. Let Γ^a and Γ^b be basis elements of this vector space with $\mathrm{Tr}\left(\Gamma^a\Gamma^b\right) = \zeta\,\delta^{ab}$ where ζ is a normalisation factor which depends on the choice for the basis elements. Then, any $N \times N$ matrix M in the vector space can be expanded in the basis elements by considering $M = \sum_a \mathrm{Tr}\left(M\Gamma^a\right)\Gamma^a/\zeta$. From these general aspects, we can infer a so-called completeness relation. For this, we expand the basis element Γ^b itself in the basis, so that the entries of this matrix are given by $\Gamma^b_{ij} = \sum_a \Gamma^b_{lk}\Gamma^a_{kl}\Gamma^a_{ij}/\zeta$. However, we can also write $\Gamma^b_{ij} = \Gamma^b_{lk}\delta_{il}\delta_{jk}$. By comparing the two expressions for Γ^b_{ij}, we find the completeness relation

$$\sum_a \left(\Gamma^a\right)_{ij}\left(\Gamma^a\right)_{kl} = \zeta\delta_{il}\delta_{jk}\,. \tag{A.43}$$

We consider two $N \times N$ matrices M and M' in the vector space. Using the completeness relation, we find

$$\begin{aligned}\left(M\right)_{ij}\left(M'\right)_{kl} &= \left(M\right)_{mn}\left(M'\right)_{rs}\delta_{im}\delta_{nj}\delta_{kr}\delta_{ls} = \zeta^{-2}\sum_{cd}\left(M\right)_{mn}\left(\Gamma^d\right)_{nr}\left(M'\right)_{rs}\left(\Gamma^c\right)_{sm}\left(\Gamma^c\right)_{il}\left(\Gamma^d\right)_{kj}\\ &= \zeta^{-2}\sum_{cd}\mathrm{Tr}\left(M\Gamma^dM'\Gamma^c\right)\left(\Gamma^c\right)_{il}\left(\Gamma^d\right)_{kj} = \sum_{cd}c^{cd}\left(\Gamma^c\right)_{il}\left(\Gamma^d\right)_{kj}\,.\end{aligned} \tag{A.44}$$

Here, the coefficients are given by $c^{cd} = \zeta^{-2}\mathrm{Tr}\left(M\Gamma^dM'\Gamma^c\right)$. This relation can conveniently be used to rearrange spinors representing fermionic fields to find relations between different four-quark interaction channels. When including fermionic fields, we have to account for an uneven permutation of Grassmann-valued fields and include a minus sign. Therefore, mapping onto a quark-antiquark interaction yields

$$\bar\psi_i\left(M\right)_{ij}\psi_j\,\bar\psi_k\left(M'\right)_{kl}\psi_l = -\sum_{cd}c^{cd}\bar\psi_i\left(\Gamma^c\right)_{il}\psi_l\,\bar\psi_k\left(\Gamma^d\right)_{kj}\psi_j\,. \tag{A.45}$$

Here, $\bar\psi$ and ψ are Dirac spinors. Note that the order of the appearance of the spinors changes from $ijkl$ to $ilkj$. We can also find a second relation by again considering two $N \times N$ matrices M and M' in the vector space and by using the completeness relation, which yields

$$\begin{aligned}\left(M\right)_{ij}\left(M'\right)_{kl} &= \left(M\right)_{mn}\left(M'\right)_{rs}\delta_{im}\delta_{nj}\delta_{kr}\delta_{ls} = \zeta^{-2}\sum_{cd}\left(M\right)_{mn}\left(\Gamma_d\right)_{ns}\left(M'\right)_{rs}\left(\Gamma^c\right)_{rm}\left(\Gamma^c\right)_{ik}\left(\Gamma^d\right)_{lj}\\ &= \zeta^{-2}\sum_{cd}\mathrm{Tr}\left(M\Gamma^dM'^T\Gamma^c\right)\left(\Gamma^c\right)_{ik}\left(\Gamma^d\right)_{lj} = \sum_{cd}d^{cd}\left(\Gamma^c\right)_{ik}\left(\Gamma^d\right)_{lj}\,.\end{aligned} \tag{A.46}$$

Here, the coefficients are given by $d^{cd} = \zeta^{-2}\mathrm{Tr}\left(M\Gamma^dM'^T\Gamma^c\right)$. When including fermionic fields in this expression, we now have to account for an even permutation of Grassmann-valued fields and, therefore, not include a minus sign. The Fierz transformation used for the quark-quark interaction reads

$$\bar\psi_i\left(M\right)_{ij}\psi_j\,\bar\psi_k\left(M'\right)_{kl}\psi_l = \sum_{cd}d^{cd}\bar\psi_i\left(\Gamma^c\right)_{ik}\bar\psi_k\,\psi_l\left(\Gamma^d\right)_{lj}\psi_j. \tag{A.47}$$

In contrast to before, the order of appearance of the spinors changes from $ijkl$ to $iklj$.

A.5.1 Colour Matrices

The colour matrices for three colours $N_\mathrm{c} = 3$ as the generators of SU(3) have been introduced in App. A.2. Together with the 'one element' in colour space $\mathbb{1}_\mathrm{c}$ they span the vector space of all 3×3 matrices: $\Gamma = \{T^0, T^a\} = \{T^S, T^A\}$. Here, the uppercase index A refers to the antisymmetric subset of Γ given by the antisymmetric colour matrices, i.e., $A = 2, 5, 7$, while S indicates the symmetric subset, i.e., $S = 0, 1, 3, 4, 6, 8$. Note that S includes the symmetric colour matrices and the normalised 'one element' which is given by $T^0 = \mathbb{1}_\mathrm{c}/\sqrt{2N_\mathrm{c}}$. The lowercase index a corresponds to all colour matrices, i.e., $a = 1, \ldots, 8$. Recall that $\mathrm{Tr}[T^a T^b] = \delta^{ab}/2$ and that we have normalised the 'one element' according to $\mathrm{Tr}[T^0 T^0] = 1/2$ and $\mathrm{Tr}[T^0 T^a] = 0$ so that the normalisation factor is given by $\zeta = 1/2$. The Fierz transformation can be applied for any product of two matrices. However, we only show the Fierz transformations for the basis elements.

The Fierz transformations for the basis elements corresponding to the **quark-antiquark interaction** can be obtained from Eq. (A.44) which yields

$$\begin{pmatrix} (\mathbb{1}_\mathrm{c})_{ij}(\mathbb{1}_\mathrm{c})_{kl} \\ (T^a)_{ij}(T^a)_{kl} \end{pmatrix} = \begin{pmatrix} \frac{1}{3} & 2 \\ \frac{4}{9} & -\frac{1}{3} \end{pmatrix} \cdot \begin{pmatrix} (\mathbb{1}_\mathrm{c})_{il}(\mathbb{1}_\mathrm{c})_{kj} \\ (T^a)_{il}(T^a)_{kj} \end{pmatrix} . \tag{A.48}$$

The Fierz transformations for the basis elements corresponding to the **quark-quark interaction** can be obtained from Eq. (A.46) which yields

$$\begin{pmatrix} (\mathbb{1}_\mathrm{c})_{ij}(\mathbb{1}_\mathrm{c})_{kl} \\ (T^a)_{ij}(T^a)_{kl} \end{pmatrix} = \begin{pmatrix} 2 & 2 \\ -\frac{4}{3} & \frac{2}{3} \end{pmatrix} \cdot \begin{pmatrix} (T^A)_{ik}(T^A)_{lj} \\ (T^S)_{ik}(T^S)_{lj} \end{pmatrix} . \tag{A.49}$$

Here, it is useful to split the matrices on the right-hand side into symmetric and antisymmetric matrices.

A.5.2 Flavour Matrices

The flavour matrices for two flavours $N_\mathrm{f} = 2$ as the generators of SU(2) have been introduced in App. A.3. Together with the 'one element' in flavour space $\tau_0 = \mathbb{1}_\mathrm{f}$, they span the vector space of all 2×2 matrices: $\Gamma = \{\tau_0, \tau_a\} = \{\tau_S, \tau_2\}$. Here, the uppercase index S refers to the symmetric matrices of Γ, i.e., $S = 0, 1, 3$, which includes the symmetric Pauli matrices and the 'one element'. The only antisymmetric matrix in the set is the second Pauli matrix τ_2. The lowercase index a refers to the three Pauli matrices $a = 1, 2, 3$. The 'one element' $\tau_0 = \mathbb{1}_\mathrm{f}$ is already properly normalised in the sense that $\mathrm{Tr}\,[\tau_0 \tau_0] = 2$ and $\mathrm{Tr}\,[\tau_0 \tau_a] = 0$. Recall that $\mathrm{Tr}\,[\tau_a \tau_b] = 2\delta_{ab}$ so that the normalisation factor is given by $\zeta = 2$. Note that the Fierz transformation can be applied to any product of two matrices. However, we only show the Fierz transformations for the basis elements.

The Fierz transformations for the basis elements corresponding to the **quark-antiquark interaction** can be obtained from Eq. (A.44) which yields

$$\begin{pmatrix} (\mathbb{1}_\mathrm{f})_{ij}(\mathbb{1}_\mathrm{f})_{kl} \\ (\tau_a)_{ij}(\tau_a)_{kl} \end{pmatrix} = \begin{pmatrix} \frac{1}{2} & \frac{1}{2} \\ \frac{3}{2} & -\frac{1}{2} \end{pmatrix} \cdot \begin{pmatrix} (\mathbb{1}_\mathrm{f})_{il}(\mathbb{1}_\mathrm{f})_{kj} \\ (\tau_a)_{il}(\tau_a)_{kj} \end{pmatrix} . \tag{A.50}$$

The Fierz transformations for the basis elements corresponding to the **quark-quark interaction** can be obtained from Eq. (A.46) which yields

$$\begin{pmatrix} (\mathbb{1}_\mathrm{f})_{ij}(\mathbb{1}_\mathrm{f})_{kl} \\ (\tau_a)_{ij}(\tau_a)_{kl} \end{pmatrix} = \begin{pmatrix} \frac{1}{2} & \frac{1}{2} \\ -\frac{3}{2} & \frac{1}{2} \end{pmatrix} \cdot \begin{pmatrix} (\tau_2)_{ik}(\tau_2)_{lj} \\ (\tau_S)_{ik}(\tau_S)_{lj} \end{pmatrix} . \tag{A.51}$$

Note that it is again useful to split the matrices on the right-hand side into symmetric and antisymmetric matrices.

A.5.3 Dirac Matrices

Along with the Dirac matrices that have been introduced in Sec. A.4, a set of in total 16 matrices can be introduced that span the 16-dimensional space of all 4×4 matrices. The remaining matrices that are needed have also been introduced in the aforementioned section. It follow the basis elements which are given by

$$\Gamma = \left\{\mathbb{1}_\mathrm{D}, \gamma_5, \gamma_0, \gamma_i, \mathrm{i}\gamma_5\gamma_0, \mathrm{i}\gamma_5\gamma_i, \sigma_{0i}, \sigma_{12}, \sigma_{13}, \sigma_{23}\right\}. \tag{A.52}$$

Note that we consider the zeroth and i-th components of the matrices separately where $i = 1,2,3$. The normalisation is given by $\mathrm{Tr}\big(\Gamma_a\Gamma_b\big) = 4\delta_{ab}$ so that the normalisation factor is $\zeta = 4$. The inclusion of the imaginary unit i in the definition of some of the basis elements is important so that the normalisation holds for all basis elements as required.

The Fierz transformations for the basis elements corresponding to the **quark-antiquark interaction** can be obtained from Eq. (A.44) which yields

$$\begin{pmatrix} (\mathbb{1}_\mathrm{D})_{ij}(\mathbb{1}_\mathrm{D})_{kl} \\ (\gamma_5)_{ij}(\gamma_5)_{kl} \\ (\gamma_0)_{ij}(\gamma_0)_{kl} \\ (\gamma_i)_{ij}(\gamma_i)_{kl} \\ (\mathrm{i}\gamma_5\gamma_0)_{ij}(\mathrm{i}\gamma_5\gamma_0)_{kl} \\ (\mathrm{i}\gamma_5\gamma_i)_{ij}(\mathrm{i}\gamma_5\gamma_i)_{kl} \\ (\sigma_{0i})_{ij}(\sigma_{0i})_{kl} \\ (\sigma_{nm})_{ij}(\sigma_{nm})_{kl} \end{pmatrix} = \frac{1}{4}\begin{pmatrix} 1 & 1 & 1 & 1 & 1 & 1 & 1 & \frac{1}{2} \\ 1 & 1 & -1 & -1 & -1 & -1 & 1 & \frac{1}{2} \\ 1 & -1 & 1 & -1 & -1 & 1 & -1 & \frac{1}{2} \\ 3 & -3 & -3 & -1 & 3 & 1 & 1 & -\frac{1}{2} \\ 1 & -1 & -1 & 1 & 1 & -1 & -1 & \frac{1}{2} \\ 3 & -3 & 3 & 1 & -3 & -1 & 1 & -\frac{1}{2} \\ 3 & 3 & -3 & 1 & -3 & 1 & -1 & -\frac{1}{2} \\ 6 & 6 & 6 & -2 & 6 & -2 & -2 & -1 \end{pmatrix} \cdot \begin{pmatrix} (\mathbb{1}_\mathrm{D})_{il}(\mathbb{1}_\mathrm{D})_{kj} \\ (\gamma_5)_{il}(\gamma_5)_{kj} \\ (\gamma_0)_{il}(\gamma_0)_{kj} \\ (\gamma_i)_{il}(\gamma_i)_{kj} \\ (\mathrm{i}\gamma_5\gamma_0)_{il}(\mathrm{i}\gamma_5\gamma_0)_{kj} \\ (\mathrm{i}\gamma_5\gamma_i)_{il}(\mathrm{i}\gamma_5\gamma_i)_{kj} \\ (\sigma_{0i})_{il}(\sigma_{0i})_{kj} \\ (\sigma_{nm})_{il}(\sigma_{nm})_{kj} \end{pmatrix}. \tag{A.53}$$

For the **quark-quark interaction**, instead of applying Eq. (A.46), we consider a slightly different approach in the following. For this approach, we consider the two 4×4 matrices M and $\tilde{M}$ in the vector space spanned by the matrices in Γ. By transposing the matrix $\tilde{M}$, rewriting it in terms of $\tilde{M}^T = \mathcal{C}M'\mathcal{C}$, and by using the Fierz transformation for the quark-antiquark interaction (A.44), we find the following relation:

$$\begin{aligned}(M)_{ij}(\tilde{M})_{kl} &= (M)_{ij}(\tilde{M}^T)_{lk} = (M)_{ij}(\mathcal{C}M'\mathcal{C})_{lk} = (M)_{ij}(\mathcal{C})_{lm}(M')_{mn}(\mathcal{C})_{nk} \\ &= (\mathcal{C})_{lm}(\mathcal{C})_{nk}\sum_{cd} d^{cd}(\Gamma_c)_{in}(\Gamma_d)_{mj} = \sum_{cd} d^{cd}(\Gamma_c\mathcal{C})_{ik}(\mathcal{C}\Gamma_d)_{lj}\,.\end{aligned} \tag{A.54}$$

Here, we defined the coefficients d_{cd} and reintroduced the initial matrix $\tilde{M}$ so that

$$d_{cd} = \frac{1}{16}\mathrm{Tr}\left[M\Gamma^d M'\Gamma^c\right] = \frac{1}{16}\mathrm{Tr}\left[M\Gamma^d\mathcal{C}\tilde{M}^T\mathcal{C}\Gamma^c\right]. \tag{A.55}$$

With this approach, we have managed to introduce the charge conjugation operator $\mathcal{C}$ in the Fierz transformation so that it also appears in the product of two Dirac bilinears associated with a quark-quark interaction. We have done this because it is, e.g., for the study of diquark condensates, often convenient and common to write the Dirac spinors in terms of so-called Nambu-Gorkov spinors $(\psi, \psi^\mathcal{C})^T$ by introducing the charge conjugated fields $\psi^\mathcal{C} = \mathcal{C}\bar{\psi}^T$ and $\bar{\psi}^\mathcal{C} = \psi^T\mathcal{C}$, respectively. Recall that $\mathcal{C} = \mathrm{i}\gamma_2\gamma_0$ so that $\mathcal{C}$ switches particle and antiparticle states in the Dirac spinor, i.e., it complex conjugates and switches the upper two and lower two components of the Dirac spinor and also the two elements of the upper and lower two components. In addition to that, the energy and spin change their sign. Note that $\psi^\mathcal{C}$ is also a solution of the Dirac equation, as is ψ.

The Fierz transformations for the basis elements corresponding to the **quark-quark interaction** can be obtained from Eq. (A.54) which yields

$$\begin{pmatrix} (\mathbb{1}_{\mathrm{D}})_{ij}(\mathbb{1}_{\mathrm{D}})_{kl} \\ (\gamma_5)_{ij}(\gamma_5)_{kl} \\ (\gamma_0)_{ij}(\gamma_0)_{kl} \\ (\gamma_i)_{ij}(\gamma_i)_{kl} \\ (\mathrm{i}\gamma_5\gamma_0)_{ij}(\mathrm{i}\gamma_5\gamma_0)_{kl} \\ (\mathrm{i}\gamma_5\gamma_i)_{ij}(\mathrm{i}\gamma_5\gamma_i)_{kl} \\ (\sigma_{0i})_{ij}(\sigma_{0i})_{kl} \\ (\sigma_{nm})_{ij}(\sigma_{nm})_{kl} \end{pmatrix} = \frac{1}{4} \begin{pmatrix} 1 & 1 & 1 & 1 & 1 & 1 & 1 & \frac{1}{2} \\ 1 & 1 & -1 & -1 & -1 & -1 & 1 & \frac{1}{2} \\ -1 & 1 & -1 & 1 & 1 & -1 & 1 & -\frac{1}{2} \\ -3 & 3 & 3 & 1 & -3 & -1 & -1 & \frac{1}{2} \\ 1 & -1 & -1 & 1 & 1 & -1 & -1 & \frac{1}{2} \\ 3 & -3 & 3 & 1 & -3 & -1 & 1 & -\frac{1}{2} \\ -3 & -3 & 3 & -1 & 3 & -1 & 1 & \frac{1}{2} \\ -6 & -6 & -6 & 2 & -6 & 2 & 2 & 1 \end{pmatrix} \cdot \begin{pmatrix} (\mathcal{C})_{ik}(\mathcal{C})_{lj} \\ (\gamma_5\mathcal{C})_{ik}(\mathcal{C}\gamma_5)_{lj} \\ (\gamma_0\mathcal{C})_{ik}(\mathcal{C}\gamma_0)_{lj} \\ (\gamma_i\mathcal{C})_{ik}(\mathcal{C}\gamma_i)_{lj} \\ (\mathrm{i}\gamma_5\gamma_0\mathcal{C})_{ik}(\mathcal{C}\mathrm{i}\gamma_5\gamma_0)_{lj} \\ (\mathrm{i}\gamma_5\gamma_i\mathcal{C})_{ik}(\mathcal{C}\mathrm{i}\gamma_5\gamma_i)_{lj} \\ (\sigma_{0i}\mathcal{C})_{ik}(\mathcal{C}\sigma_{0i})_{lj} \\ (\sigma_{nm}\mathcal{C})_{ik}(\mathcal{C}\sigma_{nm})_{lj} \end{pmatrix} . \tag{A.56}$$

By using the transformation (A.54), the charge conjugation operator appears in the elements on the right-hand side.

A.6 Natural Units

Throughout the present work, we work in natural units so that $\hbar = c = k_{\mathrm{B}} = 1$. Therefore, the dimensions of all quantities are measured in the dimension of energy: [temperature] = [length]$^{-1}$ = [time]$^{-1}$ = [mass] = [energy]. Natural units can be translated into SI units by suitably multiplying with and dividing by $\hbar$, c, and k_{B} that are set to one when working in natural units.

For converting **length**, we find

$$1\,\mathrm{m}\Big(\times 1/(\hbar c)\Big) = 10^{15}\,\mathrm{fm}\Big(\times 1/(\hbar c)\Big) = 5.06773\times 10^{12}/\mathrm{MeV}\,, \tag{A.57}$$

$$1/\mathrm{MeV}\Big(\times \hbar c\Big) = 1.97327\times 10^{-13}\,\mathrm{m}\,. \tag{A.58}$$

For converting **temperature**, we find

$$1\,\mathrm{K}\Big(\times k_{\mathrm{B}}\Big) = 8.61733\times 10^{-11}\,\mathrm{MeV}\,, \tag{A.59}$$

$$1\,\mathrm{MeV}\Big(\times 1/k_{\mathrm{B}}\Big) = 1.16045\times 10^{10}\,\mathrm{K}\,. \tag{A.60}$$

For converting **time**, we find

$$1\,\mathrm{s}\Big(\times 1/\hbar\Big) = 1.51927\times 10^{21}/\mathrm{MeV}\,, \tag{A.61}$$

$$1/\mathrm{MeV}\Big(\times \hbar\Big) = 6.58212\times 10^{-22}\,\mathrm{s}\,. \tag{A.62}$$

For converting **mass**, we find

$$1\,\mathrm{MeV}\Big(\times 1/c^2\Big) = 1.78266192\times 10^{-30}\,\mathrm{kg}\,, \tag{A.63}$$

$$1\,\mathrm{kg}\Big(\times c^2\Big) = 5.60959\times 10^{29}\,\mathrm{MeV}\,. \tag{A.64}$$

For the nuclear saturation density n_0 used throughout the present work, we have 0.165 nucleons per fm^3 which is given by $n_0 = 0.00127\,\mathrm{GeV}^3$ in natural units.

B

Regularisation Scheme

Recall that we have introduced a so-called regulator term in the derivation of the Wetterich equation in Sec. 1.2. We have extended the discussion about the regularisation scheme in Sec. 1.3 by introducing a regularisation scheme that is suitable to handle systems that exhibit a BCS-type instability. We refer to this scheme as the quasi-particle regularisation scheme. However, the calculations in Chap. 3.1 require the inclusion of different chemical potentials for up and down quarks and different colour chemical potentials. Therefore, we shall extend the aforementioned regularisation scheme to account for these different chemical potentials in App. B.1. In introducing the regularisation scheme and also in the discussion of the Wetterich equation in Sec. 1.2, we write the regulator term in terms of dimensionless regulator shape functions. The specific functional forms of different regulator shape functions, mainly those used throughout the present work, are defined in App. B.2. In the calculation of loop diagrams especially throughout Chap. 2, we encounter so-called threshold functions that depend on the regularisation scheme. The threshold functions used in the present work are defined in App. B.3.

B.1 Extension of the Quasi-Particle Regularisation Scheme

In the following, we introduce the quasi-particle regularisation scheme for isospin-asymmetric matter with different chemical potentials for differently coloured quarks. Note that we explicitly consider two flavours $N_{\mathrm{f}} = 2$ and three colours $N_{\mathrm{c}} = 3$. The following should only be considered as an extension of the regularisation scheme introduced in Sec. 1.3.1 where a detailed discussion of the aspects of the quasi-particle regularisation scheme can be found. The kinetic term for the fermions (as, e.g., used in the action for the low-energy model employed in Sec. 3.1) including different chemical potentials reads

$$S_{\bar{\psi}\psi} = \int_p \Big\{ \bar{\Psi}(p) \Big(-p_0\gamma_0 - \mathrm{i}\big(\hat{\mu}_{(\mathrm{f})} + \hat{\mu}_{(\mathrm{c})}\big) - \vec{p} \Big) \Psi(p) \,. \tag{B.1}$$

Recall that $\bar{\Psi}$ and Ψ are the Fourier transforms of the fermionic fields $\bar{\psi}$ and ψ, respectively. The kinetic term suggests to introduce the kinetic operator

$$T = -p_0\gamma_0 - \mathrm{i}\big(\hat{\mu}_{(\mathrm{f})} + \hat{\mu}_{(\mathrm{c})}\big) - \vec{p} = -p_0\gamma_0 - \mathrm{i}\big(\mathrm{diag}\big(\mu_\mathrm{u},\mu_\mathrm{d}\big)_\mathrm{f} + \mathrm{diag}\big(\mu_\mathrm{r},\mu_\mathrm{g},\mu_\mathrm{b}\big)_\mathrm{c}\big)\gamma_0 - \vec{p}\,. \tag{B.2}$$

Indeed, this definition is convenient in the calculation of loop diagrams and for calculations using the Wetterich equation where the inverse of T appears. Here, the kinetic operator includes different chemical potentials for the up μ_u and down quark μ_d combined in a flavour chemical potential $\hat{\mu}_{(\mathrm{f})} = \mathrm{diag}\big(\mu_\mathrm{u},\mu_\mathrm{d}\big)_\mathrm{f} \otimes \mathbb{1}_\mathrm{c} \otimes \gamma_0$ and it introduces different chemical potentials for differently coloured quarks via $\hat{\mu}_{(\mathrm{c})} = \mathbb{1}_\mathrm{f} \otimes \mathrm{diag}\big(\mu_\mathrm{r},\mu_\mathrm{g},\mu_\mathrm{b}\big)_\mathrm{c} \otimes \gamma_0$. Here, the index 'f' refers to flavour space while 'c' refers to colour space. For convenience, we do not show the unit matrices in colour and flavour space. The chemical potentials μ_r, μ_g, and μ_b correspond to the three colour charges (red, green, and blue). For further details about the chemical potentials, see Sec. 3.1.
With the projectors $P_\pm$ defined at the beginning of Sec. 1.3.1, the kinetic operator can conveniently be split into two parts so that it can be rewritten to read

$$T = T\big(P_+ + P_-\big) = \mathcal{T}_- P_- \gamma_0 + \mathcal{T}_+ P_+ \gamma_0\,. \tag{B.3}$$

Here, we have introduced

$$\begin{aligned}\mathcal{T}_\pm &= -\Big(p_0 + \mathrm{i}\big(\mathrm{diag}\big(\mu_\mathrm{u},\mu_\mathrm{d}\big)_\mathrm{f} + \mathrm{diag}\big(\mu_\mathrm{r},\mu_\mathrm{g},\mu_\mathrm{b}\big)_\mathrm{c} \pm |\vec{p}\,|\big)\Big) \\ &= -\Big(p_0 + \mathrm{i}\big(\mathrm{diag}\big(\mu_\mathrm{u}+\mu_\mathrm{r},\mu_\mathrm{u}+\mu_\mathrm{g},\mu_\mathrm{u}+\mu_\mathrm{b},\mu_\mathrm{d}+\mu_\mathrm{r},\mu_\mathrm{d}+\mu_\mathrm{g},\mu_\mathrm{d}+\mu_\mathrm{b}\big)_{\mathrm{c,f}} \pm |\vec{p}\,|\big)\Big)\,.\end{aligned} \tag{B.4}$$

Note that $\mathcal{T}_\pm$ are matrices in colour and flavour space and that they are diagonal. This diagonal structure allows, together with the properties of the projectors, for a straightforward calculation of the inverse of the kinetic operator T. However, before calculating the inverse, we shall introduce a regulator term. Recall from Sec. 1.3.1 that the inverse of the kinetic operator suffers from poles at the Fermi surface so that, in general, it is not invertible. To handle these poles, we introduced a suitable regulator which resulted in handling positive and negative energy solutions of the quasi-particle dispersion relations differently. The inclusion of different chemical potentials for differently coloured up and down quarks requires to suitably adapt the regulator term. As before, we require that the different energy solutions are only supposed to be treated differently in the presence of chemical potentials but are still supposed to be treated in the same way in the limit of vanishing chemical potentials. In addition to that, for $\mu_\mathrm{u} = \mu_\mathrm{d} = \mu$ and $\mu_\mathrm{r} = \mu_\mathrm{g} = \mu_\mathrm{b} = 0$, we require to recover the regularisation scheme as introduced in Sec. 1.3.1. This results in a regulator that treats the dispersion relations associated with positive and negative energy solutions and the terms with different chemical potentials differently. A general regulator term that fulfils these requirements is given by

$$R_k^\psi = \mathcal{R}_- P_- \gamma_0 + \mathcal{R}_+ P_+ \gamma_0\,. \tag{B.5}$$

Here, we have introduced $\mathcal{R}_\pm$, matrices in colour and flavour space (as indicated by the subscript c, f), which are given by

$$\mathcal{R}_\pm = -\mathrm{i}\,\mathrm{diag}\left(\bar{\epsilon}_\pm^{\mathrm{u,r}}, \bar{\epsilon}_\pm^{\mathrm{u,g}}, \bar{\epsilon}_\pm^{\mathrm{u,b}}, \bar{\epsilon}_\pm^{\mathrm{d,r}}, \bar{\epsilon}_\pm^{\mathrm{d,g}}, \bar{\epsilon}_\pm^{\mathrm{d,b}}\right)_{\mathrm{c,f}} \qquad \text{with} \qquad \bar{\epsilon}_\pm^{f,c} = \big(\mu_f + \mu_c \pm |\vec{p}\,|\big)\, r_\pm^{f,c}\,. \tag{B.6}$$

To deal with the positive and negative energy solutions as well as the different chemical potentials, we have introduced 12 different dimensionless regulator shape functions $r_\pm^{f,c}$ where $f = \mathrm{u},\mathrm{d}$ and $c = \mathrm{r},\mathrm{g},\mathrm{b}$. The subscript '$\pm$' indicates that we regularise the solutions associated with positive and negative energy values separately. The different regulator shape functions only differ by the argument since we use regulator shape functions of the form

$$r_\pm^{f,c} \equiv r\big(x_\pm^{f,c}\big) \qquad \text{with} \qquad x_\pm^{f,c} = \big(\mu_f + \mu_c \pm |\vec{p}\,|\big)^2/k^2\,. \tag{B.7}$$

Properties of the regulator shape functions have already been discussed in Sec. 1.3.1. Some regulator shape functions, mainly those used in the present work, are introduced in App. B.2.

Adding the regulator term R_k^ψ to the kinetic operator T yields the regulated kinetic operator

$$T + R_k^\psi = \big(\mathcal{T}_- + \mathcal{R}_-\big) P_- \gamma_0 + \big(\mathcal{T}_+ + \mathcal{R}_+\big) P_+ \gamma_0 \,, \tag{B.8}$$

where

$$\mathcal{T}_\pm + \mathcal{R}_\pm = -\mathrm{diag}\Big(p_0 + \mathrm{i}\epsilon_\pm^{\mathrm{u,r}}, p_0 + \mathrm{i}\epsilon_\pm^{\mathrm{u,g}}, p_0 + \mathrm{i}\epsilon_\pm^{\mathrm{u,b}}, p_0 + \mathrm{i}\epsilon_\pm^{\mathrm{d,r}}, p_0 + \mathrm{i}\epsilon_\pm^{\mathrm{d,g}}, p_0 + \mathrm{i}\epsilon_\pm^{\mathrm{d,b}}\Big)_{\mathrm{c,f}} \,. \tag{B.9}$$

We have introduced a generalised version of $\epsilon_\pm$ from the one employed in Sec. 1.3.1 representing the regularised quasi-particle dispersion relations. In contrast to before, it includes different chemical potentials:

$$\epsilon_\pm^{f,c} = \left(\mu_f + \mu_c \pm |\vec{p}\,|\right)\left(1 + r_\pm^{f,c}\right) . \tag{B.10}$$

With the properties of the projectors $P_\pm$ and utilising that $\mathcal{T}_\pm + \mathcal{R}_\pm$ are diagonal matrices in colour and flavour space, we can simply invert the regulated kinetic operator $T + R_k^\psi$ and find

$$\big(T + R_k^\psi\big)^{-1} = \big(\mathcal{T}_- + \mathcal{R}_-\big)^{-1} P_+ \gamma_0 + \big(\mathcal{T}_+ + \mathcal{R}_+\big)^{-1} P_- \gamma_0 \,, \tag{B.11}$$

where

$$\big(\mathcal{T}_\pm + \mathcal{R}_\pm\big)^{-1} = -\mathrm{diag}\left(\frac{1}{p_0 + \mathrm{i}\epsilon_\pm^{\mathrm{u,r}}}, \frac{1}{p_0 + \mathrm{i}\epsilon_\pm^{\mathrm{u,g}}}, \frac{1}{p_0 + \mathrm{i}\epsilon_\pm^{\mathrm{u,b}}}, \frac{1}{p_0 + \mathrm{i}\epsilon_\pm^{\mathrm{d,r}}}, \frac{1}{p_0 + \mathrm{i}\epsilon_\pm^{\mathrm{d,g}}}, \frac{1}{p_0 + \mathrm{i}\epsilon_\pm^{\mathrm{d,b}}}\right)_{\mathrm{c,f}} . \tag{B.12}$$

We note that the inverse is now well-defined for all p_0 and $\vec{p}$. As before, the effect of the regularisation can be visualised by considering the effect of the regulator on the "quasi-particle dispersion relation" (including different chemical potentials) associated with the negative energy mode $\epsilon_-^{f,c}$. We find that $\epsilon_- > 0$ for $\mu_f + \mu_c > |\vec{p}\,|$ and $\epsilon_-^{f,c} < 0$ for $\mu_f + \mu_c < |\vec{p}\,|$. Therefore, it changes its sign at $\mu_f + \mu_c = |\vec{p}\,|$ where it is given by $\epsilon_-^{f,c} = k\,\mathrm{sgn}(\mu_f + \mu_c - |\vec{p}\,|) + \cdots$. Consequently, fluctuations around this point are gapped by the regulator with a gap given by $\sim k$. In contrast to that, we find $\epsilon_+^{f,c} > 0$, where the chemical potential effectively acts as a regulator even for $k \to 0$.

The results for symmetric matter and without the inclusion of any colour chemical potentials, as considered in Sec. 1.3.1, can be straightforwardly recovered by setting $\mu_{\mathrm{u}} = \mu_{\mathrm{d}} = \mu$ and $\mu_{\mathrm{r}} = \mu_{\mathrm{g}} = \mu_{\mathrm{b}} = 0$. For terms appearing in the application of the Wetterich equation, we find

$$\mathrm{Tr}\left\{\left(T + R_k^\psi\right)^{-1} \partial_t R_k^\psi\right\} = 2\mathrm{i} \sum_{f=\mathrm{u,d}} \sum_{c=\mathrm{r,g,b}} \left(\frac{\left(\mu_f + \mu_c + |\vec{p}\,|\right) r_+^{f,c}}{p_0 + \mathrm{i}\epsilon_+^{f,c}} + \frac{\left(\mu_f + \mu_c - |\vec{p}\,|\right) r_-^{f,c}}{p_0 + \mathrm{i}\epsilon_-^{f,c}}\right) . \tag{B.13}$$

The trace runs over Dirac, flavour, and colour space. Interestingly, the derivatives with respect to the regulator only appear together with the corresponding energy modes, i.e., the quasi-particle dispersion relations. More precisely, the scale derivative of the regulator $r_\pm^{f,c}$ appears together with the corresponding dispersion relation $\epsilon_\pm^{f,c}$. We thus find 12 contributions, each with different combinations of up- and down-quark chemical potentials, colour chemical potentials, and positive and negative energy solutions. These contributions are conveniently split into twelve terms that can be handled separately. For applications of the Wetterich equation, it is also useful to consider the complex conjugate of the kinetic operator which is given by

$$\big(T\big)^* = -p_0 \gamma_0^T + \mathrm{i}\big(\hat{\mu}_{(\mathrm{f})} + \hat{\mu}_{(\mathrm{c})}\big) - \not{p}^T = \mathcal{T}_-^* \gamma_0 P_+^T + \mathcal{T}_+^* \gamma_0 P_-^T \,. \tag{B.14}$$

With the complex conjugate of the regulator term $(R_k^\psi)^*$, the inverse of the regulated kinetic operator becomes

$$\Big(\big(T\big)^* + \big(R_k^\psi\big)^*\Big)^{-1} = \big(\mathcal{T}_-^* + \mathcal{R}_-^*\big)^{-1} \gamma_0 P_-^T + \big(\mathcal{T}_+^* + \mathcal{R}_+^*\big)^{-1} \gamma_0 P_+^T \,, \tag{B.15}$$

where

$$\big(\mathcal{T}_\pm^* + \mathcal{R}_\pm^*\big)^{-1} = -\mathrm{diag}\left(\frac{1}{p_0 - \mathrm{i}\epsilon_\pm^{\mathrm{u,r}}}, \frac{1}{p_0 - \mathrm{i}\epsilon_\pm^{\mathrm{u,g}}}, \frac{1}{p_0 - \mathrm{i}\epsilon_\pm^{\mathrm{u,b}}}, \frac{1}{p_0 - \mathrm{i}\epsilon_\pm^{\mathrm{d,r}}}, \frac{1}{p_0 - \mathrm{i}\epsilon_\pm^{\mathrm{d,g}}}, \frac{1}{p_0 - \mathrm{i}\epsilon_\pm^{\mathrm{d,b}}}\right)_{\mathrm{c,f}} . \tag{B.16}$$

The expressions for the inverse of the kinetic operators, see Eqs. (B.11) and (B.16), can be directly transferred to define the so-called propagator matrix, see App. C.3, which we use in our fRG studies.

B.2 Regulator Shape Functions

In Sec. 1.2, we have introduced the Wetterich equation which introduces a regulator term. The regulator term can be written in terms of dimensionless regulator shape functions. These functions have to ensure that the properties required of the regulator terms, as introduced in Sec. 1.2, are fulfilled. Note that we have slightly adapted these requirements to account for the presence of a chemical potential in Sec. 1.3.1 by introducing the quasi-particle regularisation scheme. In addition to that, a suitable choice of shape functions may simplify calculations especially considering possibly appearing numerical problems. In the following, we introduce regulator shape functions for bosonic and fermionic degrees of freedom, mostly those used throughout the present work. For further details and definitions of regulator shape functions, see, e.g., [172, 259, 262, 263, 278, 279, 323, 324, 353–355], from which the following definitions are adapted.
For the present studies, we mainly use polynomial regulator shape functions. The fermionic version of this shape function $r^{\mathrm{pol}}_{\psi,N}$ is given by

$$r^{\mathrm{pol}}_{\psi,N}(x) = -1 + \frac{1}{\sqrt{1 - \left(\sum_{n=0}^{N} \frac{1}{n!} x^n\right)^{-1}}} \qquad \text{with} \qquad N > 2\,. \tag{B.17}$$

Here, the order of the polynomial in $r^{\mathrm{pol}}_{\psi,N}$ is given by N. This function fulfils the necessary requirements since it has the following properties: (i) It does not introduce any artificial divergences, which is ensured by $(1 + r^{\mathrm{pol}}_{\psi,N}) \geq 0$, (ii) it vanishes in the long-range limit $k \to 0$ for fixed momentum and in the limit $|\vec{p}| \to \infty$ for fixed k so that $\lim_{x\to\infty} r^{\mathrm{pol}}_{\psi,N}(x) = 0$, and (iii) it ensures infrared regularisation by satisfying $\lim_{x\to 0} \sqrt{x}\, r^{\mathrm{pol}}_{\psi,N}(x) = 1 > 0$. Considering the quasi-particle regularisation scheme, the argument of the shape function is given by $x = x_{\pm} = (\mu \pm |\vec{p}|)^2/k^2$. Therefore, property (iii) yields that, for $x \to 0$, the shape function is $r^{\mathrm{pol}}_{\psi,N}(x_{\pm}) = k/(|\mu \pm |\vec{p}||) + \cdots$. The polynomial regulator shape function $r^{\mathrm{pol}}_{\psi,N}$ has been defined such that the exponential regulator shape function r^{exp}_{ψ} is recovered for $N \to \infty$:

$$r^{\mathrm{exp}}_{\psi}(x) = r^{\mathrm{pol}}_{\psi,N\to\infty}(x) = -1 + \frac{1}{\sqrt{1 - \exp(x)^{-1}}}\,. \tag{B.18}$$

The bosonic version of the polynomial regulator shape function $r^{\mathrm{pol}}_{\mathrm{B},N}$ is given by

$$r^{\mathrm{pol}}_{\mathrm{B},N}(x) = \frac{1}{-1 + \sum_{n=0}^{N} \frac{1}{n!} x^n} = \frac{1}{\sum_{n=1}^{N} \frac{1}{n!} x^n} \qquad \text{with} \qquad N > 2\,. \tag{B.19}$$

Again, the order of the polynomial in $r^{\mathrm{pol}}_{\mathrm{B},N}$ is given by N. This function fulfils the necessary requirements since it has the following properties: (i) It does not introduce any artificial divergences which is ensured by $(1+r^{\mathrm{pol}}_{\mathrm{B},N}) \geq 0$, (ii) it vanishes in the long-range limit $k \to 0$ for fixed momentum and in the limit $|\vec{p}| \to \infty$ for fixed k: $\lim_{x\to\infty} r^{\mathrm{pol}}_{\mathrm{B},N}(x) = 0$, (iii) it ensures infrared regularisation by satisfying $\lim_{x\to 0} x\, r^{\mathrm{pol}}_{\mathrm{B},N}(x) = 1 > 0$. The argument of the shape function is given by $x = \vec{p}^{\,2}/k^2$. Property (iii) yields that, for $x \to 0$, the shape function is $r^{\mathrm{pol}}_{\mathrm{B},N}(x) = k/|\vec{p}| + \cdots$. The polynomial regulator shape function $r^{\mathrm{pol}}_{\mathrm{B},N}$ has been defined so that the exponential regulator shape function $r^{\mathrm{exp}}_{\mathrm{B}}$ is recovered for $N \to \infty$:

$$r^{\mathrm{exp}}_{\mathrm{B}}(x) = r^{\mathrm{pol}}_{\mathrm{B},N\to\infty} = \frac{1}{-1 + \exp(x)}\,. \tag{B.20}$$

Note that the exponential shape functions r^{exp}_{ψ} and $r^{\mathrm{exp}}_{\mathrm{B}}$ fulfil the same properties as the corresponding polynomial shape functions. To study how the results in the present work depend on the regulator term, we use different orders N for the polynomial in $r^{\mathrm{pol}}_{\psi,N}$ and $r^{\mathrm{pol}}_{\mathrm{B},N}$. However, we always use the same order for the bosonic and fermionic degrees of freedom.

As we shall see in the subsequent section, the scale derivative $\partial_t r$ of the regulator functions appears in the calculation of the threshold functions. Recalling that $\partial_t = k\partial_k$ and using that $x = (\mu \pm |\vec{p}\,|)^2/k^2$ or $x = \vec{p}^{\,2}/k^2$, respectively, the scale derivative is generally given by

$$\partial_t r(x) = -2x\partial_x r(x)\,. \tag{B.21}$$

Therefore, for the fermionic version of the polynomial shape function defined in Eq. (B.17), we find

$$\partial_t r^{\mathrm{pol}}_{\psi,N}(x) = \frac{x\left(\sum_{n=0}^{N}\frac{1}{n!}x^n - \frac{1}{N!}x^N\right)}{\left(-1+\sum_{n=0}^{N}\frac{1}{n!}x^n\right)^{3/2}\sqrt{\sum_{n=0}^{N}\frac{1}{n!}x^n}}\,. \tag{B.22}$$

The scale derivative of the bosonic version of the polynomial shape function defined in Eq. (B.19) yields

$$\partial_t r^{\mathrm{pol}}_{\mathrm{B},N}(x) = \frac{2x\left(\sum_{n=0}^{N}\frac{1}{n!}x^n - \frac{1}{N!}x^N\right)}{\left(-1+\sum_{n=0}^{N}\frac{1}{n!}x^n\right)^{2}}\,. \tag{B.23}$$

Another possible regulator shape function, which often allows to calculate the corresponding threshold functions analytically, is the sharp regulator. The fermionic r_ψ^{sharp} and the bosonic version $r_{\mathrm{B}}^{\mathrm{sharp}}$ are given by

$$r_\psi^{\mathrm{sharp}}(x) = \sqrt{\frac{1}{\theta(x-1)}} - 1 \qquad \text{and} \qquad r_{\mathrm{B}}^{\mathrm{sharp}}(x) = \frac{1}{\theta(x-1)} - 1\,. \tag{B.24}$$

B.3 Threshold Functions

In the following, we define the threshold functions used throughout the present work. Since threshold functions correspond to loop diagrams, they can be classified by the type of internal lines the associated loop diagrams have. The internal lines correspond to different propagators which entail the regularisation scheme. For the fermionic contributions, we use the quasi-particle regularisation scheme, a three-dimensional regularisation scheme that has been adapted to integrate out fluctuations around the Fermi surface. Recall that the regulated quasi-particle dispersion relations are given by $\epsilon_\pm = (\mu \pm |\vec{p}\,|)(1 + r_\pm)$ where $r_\pm \equiv r_\psi(x_\pm)$ and $x_\pm = (\mu \pm |\vec{p}\,|)^2/k^2$. For bosonic degrees of freedom, we use a three-dimensional regulator function which is given by $r_{\mathrm{B}} \equiv r_{\mathrm{B}}(x)$ where $x = \vec{p}^{\,2}/k^2$. For calculations with the Wetterich equation, see App. C for details, we introduce the derivative $\tilde{\partial}_t$ which only affects the scale dependence of the regulator term. In addition to the scale dependence of the regulator shape function, the derivative $\tilde{\partial}_t$ also acts on the wavefunction renormalisations of the fields that are included in the regulator term. Therefore, the anomalous dimension of the corresponding fields enters via this derivative. It follows that the derivative $\tilde{\partial}_t$, by including fermionic degrees of freedom regularised according to the quasi-particle regularisation scheme and bosonic degrees of freedom, is given by

$$\tilde{\partial}_t = f_+\partial_{r_+} + f_-\partial_{r_-} + \sum\nolimits_l f_l\partial_{r_l}\big|_{r_l = r_{\mathrm{B}}}\,. \tag{B.25}$$

Here, we have defined

$$f_\pm \equiv f_\pm(x_\pm) = \partial_t r_\psi(x_\pm) - r_\psi(x_\pm)\eta_\psi\,, \tag{B.26}$$

$$f_l \equiv f_l(x) = \partial_t r_l(x) - r_l(x)\eta_l\,. \tag{B.27}$$

The sum over l runs over all bosonic degrees of freedom. Using different r_l for bosonic degrees of freedom is only a technical trick. We need it so that we can consider different anomalous dimensions for different types

of bosonic fields and still rewrite the dimensionless derivative via Eq. (B.25). After taking the derivative with respect to r_l, we can set $r_l = r_\mathrm{B}$. For bosonic degrees of freedom, we also define

$$\gamma_l = p_0^2 + \vec{p}^{\,2}\,(1 + r_l) + k^2 m_l^2\,. \tag{B.28}$$

Here, m_i^2 is a renormalised and dimensionless bosonic mass (i.e., gluon or diquark mass).
Before turning to the definitions of the threshold functions, we also have to note that we define "collective" arguments. The argument ρ_ψ includes all possible arguments from fermionic propagators. Although the diquark gap is also an argument of the fermion propagator, in order to better distinguish the threshold functions in the symmetric phase and the regime governed by spontaneous symmetry breaking, we do not include the diquark gap in ρ_ψ but keep it as a separate argument in the threshold functions. In the following, the diquark gap Δ_gap^2 enters the threshold functions via $\chi/k^2 = h^2\kappa = \Delta_\mathrm{gap}^2/k^2$. In addition to that, we do not consider any fermion masses. Therefore, the only argument of the fermion propagator in the present study is the anomalous dimension η_ψ such that $\rho_\psi = [\eta_\psi]$. Note that we only consider one fermion species. The argument ρ_l collects all possible arguments coming from bosonic propagators. In the present work, we consider gluon propagators and diquark propagators which come with a mass. In addition to that, diquark fields have a nonvanishing fermion number F, while gluons have a fermion number of zero. Therefore, the general version of the argument for bosonic propagators includes the fermion number, a renormalised and dimensionless mass m^2, and the corresponding anomalous dimension η so that $\rho_l = \{F_l, m_l^2, \eta_l\}$.
Some threshold functions are only needed in the symmetric phase where a gap is absent. Therefore, some threshold functions are defined only for vanishing gap. All threshold functions defined here only depend on dimensionless (and renormalised) quantities and are dimensionless themselves. In the following, we distinguish between threshold functions corresponding to loop diagrams with only bosonic lines, with only fermionic lines, and with a combination of fermionic and bosonic internal lines.
All purely bosonic threshold functions used throughout the present work can be summarised by

$$\mathcal{L}_{m\times\mathrm{b}}^{(n_1,n_2)}\Big(\mu/k, \rho_1, \ldots, \rho_m\Big) = k^{2m-4}\int_p \tilde{\partial}_t \prod_{l=1}^{m}\left(\frac{1}{\gamma_l + 2\mathrm{i}(F_l\mu)p_0}\right)\left(\frac{\vec{p}^{\,2}}{p^2}\right)^{n_1}\left(\frac{p_0^2}{p^2}\right)^{n_2}. \tag{B.29}$$

In this case, the derivative $\tilde{\partial}_t$ simplifies to $\tilde{\partial}_t = \sum_{l=1}^m f_l \partial_{r_l}|_{r_l=r_\mathrm{B}}$. This threshold function corresponds to loop diagrams with m internal bosonic lines.
The threshold functions involving only fermion propagators are given by

$$\mathcal{L}_\mathrm{ff}^{(2)}\Big(\mu/k, \chi/k^2, \rho_\psi\Big) = \frac{1}{2}k^{-2}\int_p \tilde{\partial}_t\left(\frac{1}{p_0^2 + \epsilon_-^2 + \chi} + \frac{1}{p_0^2 + \epsilon_+^2 + \chi}\right), \tag{B.30}$$

$$\mathcal{L}_\mathrm{fff}^{(2)}\Big(\mu/k, \chi/k^2, \rho_\psi\Big) = \frac{1}{2}\int_p \tilde{\partial}_t\left(\frac{1}{(p_0^2 + \epsilon_-^2 + \chi)^2} + \frac{1}{(p_0^2 + \epsilon_+^2 + \chi)^2}\right), \tag{B.31}$$

and

$$\mathcal{L}_\mathrm{fff}^{(2)}\Big(\mu/k, 0, \rho_\psi\Big) = \mathrm{i}k^{-1}\int_p \tilde{\partial}_t\left(-\frac{1}{p_0 + \mathrm{i}\epsilon_-}\frac{1}{p_0^2 + \epsilon_-^2} - \frac{1}{p_0 + \mathrm{i}\epsilon_+}\frac{1}{p_0^2 + \epsilon_+^2}\right), \tag{B.32}$$

$$\mathcal{L}_\mathrm{fff}^{(1)}\Big(\mu/k, 0, \rho_\psi\Big) = \int_p \tilde{\partial}_t \frac{1}{p_0 + \mathrm{i}\epsilon_+}\frac{1}{p_0 + \mathrm{i}\epsilon_-}\left(\frac{1}{p_0^2 + \epsilon_+^2} + \frac{1}{p_0^2 + \epsilon_-^2}\right), \tag{B.33}$$

$$\mathcal{L}_\mathrm{fff}^{(3)}\Big(\mu/k, 0, \rho_\psi\Big) = \int_p \tilde{\partial}_t\left(\frac{1}{p_0^2 + \epsilon_+^2}\frac{1}{p_0^2 + \epsilon_-^2}\right). \tag{B.34}$$

The last three functions have only been defined in the symmetric regime where there is no finite diquark gap so that $\chi/k^2 = 0$.

The threshold functions including fermionic and bosonic propagators are given by

$$\mathcal{L}^{(2)}_{\mathrm{bff}}\Big(\mu/k,\chi/k^2,\rho_\psi,\rho_1\Big)=\frac{1}{2}\int_p\tilde{\partial}_t\bigg(\frac{1}{\gamma_1+2\mathrm{i}(F_1\mu)p_0}\bigg)\bigg(\frac{1}{p_0^2+\epsilon_-^2+\chi}+\frac{1}{p_0^2+\epsilon_+^2+\chi}\bigg), \tag{B.35}$$

$$\mathcal{L}^{(2)}_{\mathrm{bbff}}\Big(\mu/k,\chi/k^2,\rho_\psi,\rho_1,\rho_2\Big)=\frac{1}{2}k^2\int_p\tilde{\partial}_t\prod_{l=1}^{2}\bigg(\frac{1}{\gamma_l+2\mathrm{i}(F_l\mu)p_0}\bigg)\bigg(\frac{1}{p_0^2+\epsilon_+^2+\chi}+\frac{1}{p_0^2+\epsilon_-^2+\chi}\bigg), \tag{B.36}$$

$$\begin{aligned}\mathcal{L}^{(1)}_{\mathrm{bbff}}\Big(\mu/k,\chi/k^2,\rho_\psi,\rho_1,\rho_2\Big)&=k^2\int_p\tilde{\partial}_t\prod_{l=1}^{2}\bigg(\frac{1}{\gamma_l+2\mathrm{i}(F_l\mu)p_0}\bigg)\frac{1}{p_0+\mathrm{i}\epsilon_+}\frac{1}{p_0+\mathrm{i}\epsilon_-}\times\\&\quad\times\bigg(1-\frac{29}{40}\bigg(\frac{\chi}{p_0^2+\epsilon_-^2+\chi}+\frac{\chi}{p_0^2+\epsilon_+^2+\chi}\bigg)+\frac{3}{4}\frac{\chi}{p_0^2+\epsilon_+^2+\chi}\frac{\chi}{p_0^2+\epsilon_-^2+\chi}\bigg),\end{aligned} \tag{B.37}$$

$$\begin{aligned}\mathcal{L}^{(4)}_{\mathrm{bbff}}\Big(\mu/k,\chi/k^2,\rho_\psi,\rho_1,\rho_2\Big)&=k^2\int_p\tilde{\partial}_t\prod_{l=1}^{2}\bigg(\frac{1}{\gamma_l+2\mathrm{i}(F_l\mu)p_0}\bigg)\times\\&\quad\times\bigg(\frac{1}{(p_0^2+\epsilon_-^2+\chi)^2}+6\frac{1}{p_0^2+\epsilon_-^2+\chi}\frac{1}{p_0^2+\epsilon_+^2+\chi}+\frac{1}{(p_0^2+\epsilon_+^2+\chi)^2}\bigg)\chi\,.\end{aligned} \tag{B.38}$$

Threshold functions that mix fermionic and bosonic propagators that have only been defined in the symmetric phase are given by

$$\mathcal{L}^{(1)}_{\mathrm{bbf}}\Big(\mu/k,0,\rho_\psi,\rho_1,\rho_2\Big)=k\int_p\tilde{\partial}_t\prod_{l=1}^{2}\bigg(\frac{1}{\gamma_l+2\mathrm{i}(F_l\mu)p_0}\bigg)\bigg(-\frac{\mathrm{i}\vec{p}^{\,2}+|\vec{p}|p_0}{(p_0+\mathrm{i}\epsilon_+)p^2}-\frac{\mathrm{i}\vec{p}^{\,2}-|\vec{p}|p_0}{(p_0+\mathrm{i}\epsilon_-)p^2}\bigg), \tag{B.39}$$

$$\mathcal{L}^{(3)}_{\mathrm{bbf}}\Big(\mu/k,0,\rho_\psi,\rho_1,\rho_2\Big)=k\int_p\tilde{\partial}_t\prod_{l=1}^{2}\bigg(\frac{1}{\gamma_l+2\mathrm{i}(F_l\mu)p_0}\bigg)\bigg(-\frac{\mathrm{i}p_0^2-|\vec{p}|p_0}{(p_0+\mathrm{i}\epsilon_+)p^2}-\frac{\mathrm{i}p_0^2+|\vec{p}|p_0}{(p_0+\mathrm{i}\epsilon_-)p^2}\bigg), \tag{B.40}$$

$$\mathcal{L}^{(3)}_{\mathrm{bbff}}\Big(\mu/k,0,\rho_\psi,\rho_1,\rho_2\Big)=\frac{1}{2}k^2\int_p\tilde{\partial}_t\prod_{l=1}^{2}\bigg(\frac{1}{\gamma_l+2\mathrm{i}(F_l\mu)p_0}\bigg)\bigg(\frac{(p_0+\mathrm{i}|\vec{p}|)^2}{(p_0+\mathrm{i}\epsilon_+)^2p^2}+\frac{(p_0-\mathrm{i}|\vec{p}|)^2}{(p_0+\mathrm{i}\epsilon_-)^2p^2}\bigg). \tag{B.41}$$

Lastly, we turn to the threshold functions that enter the flow equations of the anomalous dimensions so that they generally (at least implicitly) include a differentiation with respect to the external momenta. Where possible, we differentiate with respect to the external momentum appearing in fermion propagators, in particular the time component of the four-momentum. To distinguish these threshold functions from those without the inclusion of a derivative with respect to external momenta, we refer to them as $\mathcal{D}$ instead of $\mathcal{L}$. The first purely fermionic threshold function of this type is given by

$$\begin{aligned}\mathcal{D}^{(1)}_{\mathrm{ff}}\Big(\mu/k,\chi/k^2,\rho_\psi\Big)=\frac{1}{4}\int_p\tilde{\partial}_t\bigg(&\frac{1+b_1(\epsilon_-)}{(p_0+\mathrm{i}\epsilon_-)^4}+\frac{2(1+b_2(\epsilon_-,\epsilon_+))}{(p_0+\mathrm{i}\epsilon_-)(p_0+\mathrm{i}\epsilon_+)^3}\\&+\frac{2(1+b_2(\epsilon_+,\epsilon_-))}{(p_0+\mathrm{i}\epsilon_+)(p_0+\mathrm{i}\epsilon_-)^3}+\frac{1+b_1(\epsilon_+)}{(p_0+\mathrm{i}\epsilon_+)^4}\bigg).\end{aligned} \tag{B.42}$$

Note that the diquark gap in terms of the parameter χ only enters via the functions b_1 and b_2 which vanish when the gap is set to zero, i.e., $\chi=0$. These functions are given by

$$\begin{aligned}b_1(\epsilon)=\frac{\chi}{12(p_0^2+\chi+\epsilon^2)^4}\Big(&-41\chi^2(p_0^2+\epsilon^2)-8(p_0-\mathrm{i}\epsilon)(p_0+\mathrm{i}\epsilon)^3(-6\mathrm{i}p_0\epsilon+7p_0^2-3\epsilon^2)\\&-6\chi(16p_0^2\epsilon^2+4\mathrm{i}p_0^3\epsilon+11p_0^4+9\epsilon^4)-11\chi^3\Big)\end{aligned} \tag{B.43}$$

and

$$\begin{aligned}b_2(\epsilon_1,\epsilon_2)=-\frac{\chi}{12(p_0^2+\epsilon_1^2+\chi)(p_0^2+\epsilon_2^2+\chi)^3}\Big(&p_0^2(41\chi^2+24\chi(\epsilon_1^2+3\epsilon_2^2)+40\epsilon_2^4)+6p_0^4(11\chi+8\epsilon_1^2+4\epsilon_2^2)\\&+8\mathrm{i}p_0^3\epsilon_2(3\chi+8\epsilon_1^2)+64\mathrm{i}p_0^5\epsilon_2+56p_0^6+(\chi+\epsilon_2^2)(2\epsilon_2^2(11\chi+8\epsilon_1^2)\\&+\chi(11\chi+8\epsilon_1^2)+8\epsilon_2^4)\Big).\end{aligned} \tag{B.44}$$

The next purely fermionic threshold function is given by

$$\mathcal{D}_{\mathrm{ff}}^{(2)}\Big(\mu/k,\chi/k^2,\rho_\psi\Big)=\frac{1}{2}\int_p\tilde{\partial}_t\bigg(\frac{1+b_3(\epsilon_+)}{(p_0^2+\epsilon_+^2)(p_0-\mathrm{i}\epsilon_+)^2}+\frac{1+b_3(\epsilon_-)}{(p_0^2+\epsilon_-^2)(p_0-\mathrm{i}\epsilon_-)^2}\bigg)\,, \tag{B.45}$$

where the diquark gap in terms of the parameter χ only enters via the function b_3 which vanishes when the gap is set to zero, i.e., $\chi=0$. This function is given by

$$b_3(\epsilon)=-\chi\frac{p_0^2(7p_0^2+5\chi+2\epsilon^2-8\mathrm{i}p_0\epsilon)+(\chi+\epsilon^2)(2\chi+3\epsilon^2)}{2(p_0^2+\epsilon^2+\chi)^3}\,. \tag{B.46}$$

The last purely fermionic threshold function is given by

$$\begin{aligned}\mathcal{D}_{\mathrm{ff}}^{(3)}\Big(\mu/k,\chi/k^2,\rho_\psi\Big)=\int_p\tilde{\partial}_t\frac{1}{24}\chi\bigg(&\frac{16p_0^2}{(p_0^2+\chi+\epsilon_-^2)^3(p_0^2+\chi+\epsilon_+^2)}+\frac{16p_0^2}{(p_0^2+\chi+\epsilon_-^2)(p_0^2+\chi+\epsilon_+^2)^3}\\&+\frac{8p_0^2}{(p_0^2+\chi+\epsilon_-^2)^4}+\frac{8p_0^2}{(p_0^2+\chi+\epsilon_+^2)^4}-\frac{4}{(p_0^2+\chi+\epsilon_-^2)^2(p_0^2+\chi+\epsilon_+^2)}\\&-\frac{4}{(p_0^2+\chi+\epsilon_-^2)(p_0^2+\chi+\epsilon_+^2)^2}-\frac{2}{(p_0^2+\chi+\epsilon_-^2)^3}-\frac{2}{(p_0^2+\chi+\epsilon_+^2)^3}\bigg)\,.\end{aligned} \tag{B.47}$$

The threshold functions, which (implicitly) include a differentiation with respect to external momenta that mix fermionic and bosonic propagators, are only needed in the symmetric phase. They are given by

$$\mathcal{D}_{\mathrm{bf}}^{(1)}\Big(\mu/k,0,\rho_\psi,\rho_1\Big)=\int_p\tilde{\partial}_t\bigg(\frac{1}{\gamma_1+2\mathrm{i}(F_1\mu)p_0}\bigg)\bigg(\frac{1}{(p_0+\mathrm{i}\epsilon_+)^2}+\frac{1}{(p_0+\mathrm{i}\epsilon_-)^2}\bigg)\,, \tag{B.48}$$

$$\mathcal{D}_{\mathrm{bf}}^{(3)}\Big(\mu/k,0,\rho_\psi,\rho_1\Big)=\int_p\tilde{\partial}_t\bigg(\frac{1}{\gamma_1+2\mathrm{i}(F_1\mu)p_0}\bigg)\bigg(\frac{\vec{p}^{\,2}-\mathrm{i}|\vec{p}|p_0}{(p_0+\mathrm{i}\epsilon_+)^2p^2}+\frac{\vec{p}^{\,2}+\mathrm{i}|\vec{p}|p_0}{(p_0+\mathrm{i}\epsilon_-)^2p^2}\bigg)\,. \tag{B.49}$$

Lastly, we define the threshold functions that include a differentiation with respect to the external momenta and that only include bosonic propagators. We have

$$\mathcal{D}_{2\times\mathrm{b}}^{(1,0)}\Big(\mu/k,\rho_1,\rho_2\Big)=\frac{1}{2}k^2\int_p\tilde{\partial}_t\bigg(\frac{1}{\gamma_2+2\mathrm{i}(F_2\mu)p_0}\frac{\vec{p}^{\,2}}{p^2}\bigg)\frac{\partial^2}{\partial p_0^2}\bigg(\frac{1}{\gamma_1+2\mathrm{i}(F_1\mu)p_0}\bigg)\,, \tag{B.50}$$

$$\mathcal{D}_{2\times\mathrm{b}}^{(0,1)}\Big(\mu/k,\rho_1,\rho_2\Big)=\frac{1}{2}k^2\int_p\tilde{\partial}_t\bigg(\frac{1}{\gamma_2+2\mathrm{i}(F_2\mu)p_0}\frac{p_0^2}{p^2}\bigg)\frac{\partial^2}{\partial p_0^2}\bigg(\frac{1}{\gamma_1+2\mathrm{i}(F_1\mu)p_0}\bigg)\,. \tag{B.51}$$

It is important to note that the differentiation with respect to p_0 acts only on the bosonic propagator corresponding to ρ_1 and that the differentiation with respect to an external momentum was rewritten as a differentiation with respect to an internal momentum. Finally, we consider a threshold function contributing to the anomalous dimension of the gluons which is given by

$$\mathcal{D}_{2\times\mathrm{b}}^{(2)}\Big(\frac{\mu}{k},\rho_1,\rho_2\Big)=-\frac{k^2}{3}\frac{\partial}{\partial\vec{P}^2}\bigg(\frac{\vec{P}^{\,2}}{P^2}\bigg)\int_p\tilde{\partial}_t\Big(G_{\Delta,1}(p)G_{\Delta,2}(p-P)+G_{\Delta,1}(p)G_{\Delta,2}(p+P)\Big)\Big|_{P_0\to0,\vec{P}\to0}\,. \tag{B.52}$$

Here, we have defined

$$G_{\Delta,l}(p)=\bigg(\frac{1}{p_0^2+\vec{p}^{\,2}(1+r_l(\vec{p}^{\,2}/k^2))+k^2m_l^2+2\mathrm{i}(F_l\mu)p_0}\bigg)\,. \tag{B.53}$$

It should be noted that we have defined the latter threshold function with a derivative with respect to the external spatial momentum $\vec{P}$ because we encounter numerical problems when differentiating with respect to the external momentum P_0. We do not aim to resolve these issues here. After differentiation, we consider the static limit, i.e., we first take the limit $P_0\to0$ and then the limit $\vec{P}\to0$.

C

Expansion of the Wetterich Equation

In this appendix, we show details underlying the calculations in Chaps. 2 and 3, in particular calculations with the Wetterich equation. However, we only consider the Wetterich equation without contributions from the consideration of k-dependent fields, i.e., we do not consider any contributions used for the dynamical bosonisation technique. See Sec. 2.3 for details on this aspect and Sec. 1.2 for a derivation of the Wetterich equation. The conventionally used Wetterich equation in momentum space is then given by

$$\partial_t \Gamma_k[\varphi] = \frac{1}{2}\mathrm{STr}\left\{\left(\partial_t \tilde{R}_k(q,p)\right)\left[\Gamma_k^{(1,1)}[\varphi,p,q) + \tilde{R}_k(p,q)\right]^{-1}\right\}. \tag{C.1}$$

The $(1+1)$-point function is given by

$$\left(\Gamma_k^{(1,1)}[\varphi,p,q)\right)_{\mathbf{ab}} = \frac{\vec{\delta}}{\delta\varphi_{\mathbf{a}}^T(-p)}\Gamma_k[\varphi]\frac{\delta}{\delta\varphi_{\mathbf{b}}(q)}\,. \tag{C.2}$$

The regulator matrix $\tilde{R}_k$ is given by

$$\left(\tilde{R}_k(p,q)\right)_{\mathbf{ab}} = \begin{pmatrix} (R_A)_{\mu\nu}^{ab}(p) & 0 & 0 & 0 & 0 \\ 0 & 0 & (R_\Delta)_{ab}(p) & 0 & 0 \\ 0 & (R_\Delta)_{ab}(p) & 0 & 0 & 0 \\ 0 & 0 & 0 & 0 & -R_\psi^T(-p) \\ 0 & 0 & 0 & R_\psi(p) & 0 \end{pmatrix} (2\pi)^4\delta^{(4)}(p-q)\,. \tag{C.3}$$

The entries of this matrix are given by

$$(R_A)_{\mu\nu}^{ab}(p) = Z_A\vec{p}^{\,2}r_{\mathrm{B}}(\vec{p}^{\,2}/k^2)\left(A_{\mu\nu} + B_{\mu\nu} + P_{\mu\nu}^L/\xi\right)\delta^{ab}\,, \tag{C.4}$$

$$(R_\Delta)_{ab}(p) = Z_\Delta\vec{p}^{\,2}r_{\mathrm{B}}(\vec{p}^{\,2}/k^2)\delta_{ab}\,, \tag{C.5}$$

$$R_\psi(p) = -Z_\psi \mathrm{i}(\mu - |\vec{p}\,|)P_-\gamma_0 r_\psi\big((\mu-|\vec{p}\,|)^2/k^2\big) - Z_\psi\mathrm{i}(\mu+|\vec{p}\,|)P_+\gamma_0 r_\psi\big((\mu+|\vec{p}\,|)^2/k^2\big)\,. \tag{C.6}$$

The regulator shape functions r_B and r_ψ can be found in App. B.2. In addition to that, we have

$$A_{ij} = \delta_{ij} - \frac{p_i p_j}{\vec{p}^2}\,, \qquad A_{00} = A_{0i} = A_{i0} = 0\,, \qquad B_{\mu\nu} = P^T_{\mu\nu} - A_{\mu\nu}\,, \tag{C.7}$$

$$P^T_{\mu\nu} = \delta_{\mu\nu} - \frac{p_\mu p_\nu}{p^2}\,, \qquad \text{and} \qquad P^L_{\mu\nu} = \frac{p_\mu p_\nu}{p^2}\,. \tag{C.8}$$

We have introduced the generalised field φ and the "super" indices $\mathbf{a}$ and $\mathbf{b}$ which include all possible indices of the fields in φ. In the present work, the field φ includes gluons, diquark fields, and quark fields and is given by $\varphi^T_\mathbf{a}(-p) = \big(\mathbf{A}^a_\mu(-p), \mathbf{\Delta}^*_a(-p), \mathbf{\Delta}_a(p), \Psi^T(-p), \bar{\Psi}(p)\big)$ and $\varphi_\mathbf{b}(q) = \big(\mathbf{A}^b_\nu(q), \mathbf{\Delta}^*_b(q), \mathbf{\Delta}_b(-q), \Psi(q), \bar{\Psi}^T(-q)\big)^T$. Therefore, the indices $\mathbf{a}$ and $\mathbf{b}$ include Lorentz indices and adjoint colour indices coming from the gluons and colour indices coming from the diquarks. Note that the quark fields have flavour, Dirac, and also colour indices. However, for convenience and better readability, we suppress them and consider the quark fields to be vectors in colour, flavour, and Dirac space. In conclusion, the indices are given by $\mathbf{a} = \mu, a, a$ and $\mathbf{b} = \mu, b, b$, where the first entry is the Lorentz index, the second is the adjoint colour index, and the third is the colour index. To distinguish between colour and adjoint colour indices, we always write colour indices as lower Roman letters and adjoint colour indices as upper Roman letters.
It is often useful to rewrite the Wetterich equation by introducing the derivative $\tilde{\partial}_t$ which only acts on the k-dependence of the regulator term. This yields

$$\partial_t \Gamma_k[\varphi] = \frac{1}{2}\mathrm{STr}\Big\{\tilde{\partial}_t \ln\Big[\Gamma_k^{(1,1)}[\varphi, p, q) + \tilde{R}_k(p,q)\Big]\Big\} = \frac{1}{2}\mathrm{STr}\Big\{\tilde{\partial}_t \ln\Big[\mathcal{P}_k(p,q) + \mathcal{F}_k[\varphi, p, q)\Big]\Big\}\,. \tag{C.9}$$

In the last step, we have also split $\Gamma_k^{(1,1)} + \tilde{R}_k$ into field-independent parts $\mathcal{P}_k$ and field-dependent parts $\mathcal{F}_k$. In general, $\mathcal{F}_k$ and $\mathcal{P}_k$ are matrix-valued and, therefore, $\mathcal{P}_k$ is often called propagator matrix and $\mathcal{F}_k$ is called fluctuation matrix. This splitting allows to expand the Wetterich equation in powers of the fields, which is called the $\mathcal{PF}$-expansion. The Wetterich equation then becomes

$$\partial_t \Gamma_k[\varphi] = \frac{1}{2}\mathrm{STr}\Big\{\tilde{\partial}_t \ln \mathcal{P}_k\Big\} - \frac{1}{2}\mathrm{STr}\Big\{\tilde{\partial}_t \sum_{n=1}^{\infty} \frac{1}{n}\Big(-\mathcal{P}_k^{-1}\mathcal{F}_k\Big)^n\Big\}\,. \tag{C.10}$$

For more details on this expansion and for applications, see, e.g., Refs. [170, 273, 323]. The trace is performed not only over the matrix structure of the propagator matrix and the fluctuation matrix but also over the "super" indices $\mathbf{a}$ and $\mathbf{b}$ which $\mathcal{P}_k$ and $\mathcal{F}_k$ inherit from the $(1+1)$-point function. Therefore, the trace yields

$$\begin{aligned}\mathrm{Tr}\Big\{\big(\mathcal{P}_k^{-1}\mathcal{F}_k\big)^n\Big\} = \mathrm{Tr}\Big\{&\big(\mathcal{P}_k^{-1}\big)_{\mathbf{a}_1\mathbf{b}_1}(p_1,q_1)\big(\mathcal{F}_k\big)_{\mathbf{b}_1\mathbf{a}_2}[\varphi, q_1, p_2)\\ &\cdots\big(\mathcal{P}_k^{-1}\big)_{\mathbf{a}_m\mathbf{b}_m}(p_m,q_m)\big(\mathcal{F}_k\big)_{\mathbf{b}_m\mathbf{a}_{m+1}}[\varphi, q_m, p_{m+1})\\ &\cdots\big(\mathcal{P}_k^{-1}\big)_{\mathbf{a}_n\mathbf{b}_n}(p_n,q_n)\big(\mathcal{F}_k\big)_{\mathbf{b}_n\mathbf{a}_1}[\varphi, q_n, p_1)\Big\}\,.\end{aligned} \tag{C.11}$$

The remaining trace on the right-hand side represents the trace over the propagator matrix, the fluctuation matrix and the quark degrees of freedom. Notably, propagator and fluctuation matrices always alternate so that each entry of the fluctuation matrix couples to a specific entry of the propagator matrix.
In App. C.1, we show the fluctuation matrix resulting from the action defined in Chap. 2 which is given by Eq. (2.25). Recall that we drop gluon self-interactions since the gauge sector enters our study only via the running of the strong gauge coupling. In addition to that, we set $\bar{\lambda}_\mathrm{csc} = 0$, which is a simplification resulting from the dynamical bosonisation technique, and we drop terms depending on derivatives of a field, except for kinetic terms. The resulting propagator matrix is shown in App. C.2. In Chap. 3, we have included different chemical potentials for differently coloured up and down quarks to study the effect of isospin asymmetry. We extend the propagator matrix to include these chemical potentials in App. C.3.

C.1 Fluctuation Matrix

The fluctuation matrix $\mathcal{F}_k$ is given by

$$\left(\mathcal{F}_k\right)_{\mathbf{ab}}[\varphi,p,q) = \begin{pmatrix} \left(F_{11}\right)^{ab}_{\mu\nu}(p,q) & \left(F_{12}\right)^{a}_{\mu,b}(p,q) & \left(F_{13}\right)^{a}_{\mu,b}(p,q) & \left(F_{14}\right)^{a}_{\mu}(p,q) & \left(F_{15}\right)^{a}_{\mu}(p,q) \\ \left(F_{21}\right)^{b}_{\nu,a}(p,q) & \left(F_{22}\right)_{ab}(p,q) & \left(F_{23}\right)_{ab}(p,q) & \left(F_{24}\right)_{a}(p,q) & \left(F_{25}\right)_{a}(p,q) \\ \left(F_{31}\right)^{b}_{\nu,a}(p,q) & \left(F_{32}\right)_{ab}(p,q) & \left(F_{33}\right)_{ab}(p,q) & \left(F_{34}\right)_{a}(p,q) & \left(F_{35}\right)_{a}(p,q) \\ \left(F_{41}\right)^{b}_{\nu}(p,q) & \left(F_{42}\right)_{b}(p,q) & \left(F_{43}\right)_{b}(p,q) & \left(F_{44}\right)(p,q) & \left(F_{45}\right)(p,q) \\ \left(F_{51}\right)^{b}_{\nu}(p,q) & \left(F_{52}\right)_{b}(p,q) & \left(F_{53}\right)_{b}(p,q) & \left(F_{54}\right)(p,q) & \left(F_{55}\right)(p,q) \end{pmatrix} . \tag{C.12}$$

The entries of this matrix are given in the following: The term that only couples to gluon propagators is

$$\left(F_{11}\right)^{ab}_{\mu\nu}(p,q) = \bar{g}^2_{\Delta,2}\int_{p'}\int_{q'} \delta_{\mu\nu}\mathbf{\Delta}^*_b(q')\Big(T^b_{bc}T^a_{ca} + T^a_{bc}T^b_{ca}\Big)\mathbf{\Delta}_a(p')(2\pi)^4\delta^{(4)}\left(p-q+p'-q'\right) . \tag{C.13}$$

Terms that couple to gluon propagators from one side and to diquark propagators from the other side are

$$\begin{aligned}\left(F_{21}\right)^{b}_{a,\nu}(p,q) = \left(F_{12}\right)^{b}_{a,\nu}(p,q) = \bar{g}^2_{\Delta,2}\int_{p'}\int_{q'} \mathbf{A}^a_\nu(q')\Big(T^a_{ac}T^b_{cb} + T^b_{ac}T^a_{cb}\Big)\mathbf{\Delta}_b(p')(2\pi)^4\delta^{(4)}\left(p-q+p'-q'\right) \\ + 4\mathrm{i}\mu\bar{g}_{\Delta,1}\int_{p'}\delta_{\nu 0}T^b_{ab}\mathbf{\Delta}_b(p')(2\pi)^4\delta^{(4)}\left(p-q+p'\right) , \end{aligned} \tag{C.14}$$

$$\begin{aligned}\left(F_{13}\right)^{a}_{b,\mu}(p,q) = \left(F_{31}\right)^{a}_{b,\mu}(p,q) = \bar{g}^2_{\Delta,2}\int_{p'}\int_{q'} \mathbf{A}^b_\mu(p')\mathbf{\Delta}^*_a(q')\Big(T^b_{ac}T^a_{cb} + T^a_{ac}T^b_{cb}\Big)(2\pi)^4\delta^{(4)}\left(p-q-q'-p'\right) \\ + 4\mathrm{i}\mu\bar{g}_{\Delta,1}\int_{p'}\delta_{\mu 0}\mathbf{\Delta}^*_a(p')T^a_{ab}(2\pi)^4\delta^{(4)}\left(p-q-p'\right) . \end{aligned} \tag{C.15}$$

Terms only coupling to diquark propagators from both sides are given by

$$\begin{aligned}\left(F_{32}\right)_{ab}(p,q) = \left(F_{23}\right)_{ba}(p,q) = \bar{g}^2_{\Delta,2}\int_{p'}\int_{q'} \mathbf{A}^a_\mu(p')\mathbf{A}^b_\mu(q')T^b_{bc}T^a_{ca}(2\pi)^4\delta^{(4)}\left(p-q-p'-q'\right) \\ + 2\bar{\lambda}_\Delta\int_{p'}\int_{q'}\Big(\delta_{ab}\mathbf{\Delta}^*_c(p')\mathbf{\Delta}_c(q') + \mathbf{\Delta}^*_a(p')\mathbf{\Delta}_b(q')\Big)(2\pi)^4\delta^{(4)}\left(p-q-p'+q'\right) \\ + 4\mathrm{i}\mu\bar{g}_{\Delta,1}\int_{p'}\mathbf{A}^a_0(p')T^a_{ba}(2\pi)^4\delta^{(4)}\left(p-q-p'\right) , \end{aligned} \tag{C.16}$$

$$\left(F_{22}\right)_{ab}(p,q) = \left(F_{33}\right)^*_{ab}(-p,-q) = 2\bar{\lambda}_\Delta\int_{p'}\int_{q'}\mathbf{\Delta}_a(p')\mathbf{\Delta}_b(q')(2\pi)^4\delta^{(4)}(p-q+p'+q') . \tag{C.17}$$

Recall that we have kept the quark fields as vectors in colour, flavour, and Dirac space. Therefore, terms in the fluctuation matrix that couple to a quark propagator and either a gluon or diquark propagator from the other side are also given by a vector in colour, flavour, and Dirac space. Terms coupling to a quark propagator from one side and a gluon propagator from the other side are thus given by

$$\left(F_{14}\right)^{a}_{\mu}(p,q) = -\Big(\left(F_{41}\right)^{a}_{\mu}(p,q)\Big)^T = \bar{g}\int_{p'}\bar{\Psi}(p')\gamma_\mu T^a(2\pi)^4\delta^{(4)}\left(p-q+p'\right) , \tag{C.18}$$

$$\left(F_{51}\right)^{b}_{\nu}(p,q) = -\Big(\left(F_{15}\right)^{b}_{\nu}(p,q)\Big)^T = \bar{g}\int_{p'}\gamma_\nu T^b\Psi(p')(2\pi)^4\delta^{(4)}\left(p-q-p'\right) . \tag{C.19}$$

Similarly, the terms coupling to a quark propagator and a diquark propagator are

$$\big(F_{42}\big)_a(p,q) = \big(F_{53}\big)_a(p,q) = \big(F_{24}\big)_a(p,q) = \big(F_{35}\big)_a(p,q) = 0\,, \tag{C.20}$$

$$\big(F_{43}\big)_b(p,q) = -\Big(\big(F_{34}\big)_b(p,q)\Big)^T = \mathrm{i}\bar{h}\int_{p'}\Big(\mathcal{C}\gamma_5\tau_2\epsilon_b\Psi(p')\Big)(2\pi)^4\delta^{(4)}\left(p-q-p'\right)\,, \tag{C.21}$$

$$\big(F_{25}\big)_a(p,q) = -\Big(\big(F_{52}\big)_a(p,q)\Big)^T = -\mathrm{i}\bar{h}\int_{p'}\Big(\bar{\Psi}(p')\gamma_5\tau_2\epsilon_a\mathcal{C}\Big)(2\pi)^4\delta^{(4)}\left(p-q+p'\right)\,. \tag{C.22}$$

Since we keep the vector structure of the quark fields, the terms in the fluctuation matrix that couple to quark propagators from both sides are matrices in colour, flavour, and Dirac space. These terms are given by

$$\big(F_{44}\big)(p,q) = \big(F_{55}\big)^*(-p,-q) = \mathrm{i}\bar{h}\int_{p'}\Big(\mathcal{C}\gamma_5\tau_2\mathbf{\Delta}_a(p')\epsilon_a\Big)(2\pi)^4\delta^{(4)}\left(p-q+p'\right)\,, \tag{C.23}$$

$$\big(F_{54}\big)(p,q) = -\Big(\big(F_{45}\big)(p,q)\Big)^T = \bar{g}\int_{p'}\gamma_\mu T^a\mathbf{A}^a_\mu(p')(2\pi)^4\delta^{(4)}\left(p-q-p'\right)\,. \tag{C.24}$$

C.2 Propagator Matrix

For the propagator matrix, we distinguish between the symmetric phase and the regime governed by spontaneous symmetry breaking. In the symmetric phase, the propagator matrix $\mathcal{P}_k$ is given by

$$\big(\mathcal{P}_k\big)_{\mathbf{ab}}(p,q) = \begin{pmatrix} \big(P_A\big)^{ab}_{\mu\nu}(p) & 0 & 0 & 0 & 0 \\ 0 & 0 & \big(P^*_\Delta\big)_{ab}(p) & 0 & 0 \\ 0 & \big(P_\Delta\big)_{ab}(p) & 0 & 0 & 0 \\ 0 & 0 & 0 & 0 & \big(P^*_\psi\big)(p) \\ 0 & 0 & 0 & \big(P_\psi\big)(p) & 0 \end{pmatrix}(2\pi)^4\delta^{(4)}\left(p-q\right)\,. \tag{C.25}$$

The entries of this matrix are given by

$$\big(P_A\big)^{ab}_{\mu\nu}(p) = Z_A\big((p^2_{\mathrm{R}}+\bar{m}^2_{\mathrm{D}}/Z_A)B_{\mu\nu} + (p^2_{\mathrm{R}}+\bar{m}^2_{\mathrm{M}}/Z_A)A_{\mu\nu} + 1/\xi(p^2_{\mathrm{R}}+\xi\bar{m}^2_{\mathrm{L}}/Z_A)P^L_{\mu\nu}\big)\delta^{ab}\,, \tag{C.26}$$

$$\big(P_\Delta\big)_{ab}(p) = Z_\Delta\big(p^2_{\mathrm{R}} + 4\mathrm{i}\mu p_0 + \tilde{m}^2/Z_\Delta\big)\delta_{ab}\,, \tag{C.27}$$

$$\big(P_\psi\big)(p) = Z_\psi\big(-(p_0+\mathrm{i}\epsilon_-)P_-\gamma_0 - (p_0+\mathrm{i}\epsilon_+)P_+\gamma_0\big)\,. \tag{C.28}$$

Recall that we use the quasi-particle regularisation scheme for quark degrees of freedom where the regularised quasi-particle dispersion relation is given by $\epsilon_\pm = (\mu \pm |\vec{p}|)(1+r_\pm)$ with $r_\pm \equiv r_\psi(x_\pm)$ and $x_\pm = (\mu\pm|\vec{p}|)^2/k^2$. In addition to that, we have introduced $p^2_{\mathrm{R}} = p_0^2 + \vec{p}^{\,2}(1+r_{\mathrm{B}})$ where $r_{\mathrm{B}} = r_{\mathrm{B}}(x)$ and $x = \vec{p}^{\,2}/k^2$. For the $\mathcal{PF}$-expansion, the inverse of $\mathcal{P}_k$ is required which is given by

$$\big(\mathcal{P}_k\big)^{-1}_{\mathbf{ab}}(p,q) = \begin{pmatrix} \Big(\big(P_A\big)^{ab}_{\mu\nu}(p)\Big)^{-1} & 0 & 0 & 0 & 0 \\ 0 & 0 & \Big(\big(P_\Delta\big)_{ab}(p)\Big)^{-1} & 0 & 0 \\ 0 & \Big(\big(P^*_\Delta\big)_{ab}(p)\Big)^{-1} & 0 & 0 & 0 \\ 0 & 0 & 0 & 0 & \Big(\big(P_\psi\big)(p)\Big)^{-1} \\ 0 & 0 & 0 & \Big(\big(P^*_\psi\big)(p)\Big)^{-1} & 0 \end{pmatrix}\times$$

$$\times\,(2\pi)^4\delta^{(4)}\left(p-q\right)\,. \tag{C.29}$$

The entries of this matrix are given by

$$\Big(\big(P_A\big)^{ab}_{\mu\nu}(p)\Big)^{-1} = Z_A^{-1}\big(G_A^{\mathrm{D}}B_{\mu\nu} + G_A^{\mathrm{M}}A_{\mu\nu} + \xi G_A^{\mathrm{L}}P^L_{\mu\nu}\big)\delta^{ab}\,, \tag{C.30}$$

$$\Big(\big(P_\Delta\big)_{ab}(p)\Big)^{-1} = Z_\Delta^{-1}G_\Delta\delta_{ab}\,, \tag{C.31}$$

$$\Big(\big(P_\psi\big)(p)\Big)^{-1} = Z_\psi^{-1}\big(G_-P_+\gamma_0 + G_+P_-\gamma_0\big)\,. \tag{C.32}$$

Here, we have defined

$$\begin{gathered} G_A^{\mathrm{D}} = \frac{1}{p_{\mathrm{R}}^2 + \bar{m}_{\mathrm{D}}^2/Z_A}\,, \qquad G_A^{\mathrm{M}} = \frac{1}{p_{\mathrm{R}}^2 + \bar{m}_{\mathrm{M}}^2/Z_A}\,, \qquad G_A^{\mathrm{L}} = \frac{1}{p_{\mathrm{R}}^2 + \xi\bar{m}_{\mathrm{L}}^2/Z_A}\,, \\ G_\pm = -\frac{1}{p_0 + \mathrm{i}\epsilon_\pm}\,, \qquad \text{and} \qquad G_\Delta = \frac{1}{p_{\mathrm{R}}^2 + \tilde{m}^2/Z_\Delta + 4\mathrm{i}\mu p_0}\,. \end{gathered} \tag{C.33}$$

The gluon masses are given by $\bar{m}_{\mathrm{D}}^2$ (Debye mass), $\bar{m}_{\mathrm{M}}^2$ (Meissner mass), and $\bar{m}_{\mathrm{L}}^2$ (longitudinal mass) and the curvature of the diquark potential is given by $\tilde{m}^2$.

Turning to the phase governed by spontaneous symmetry breaking, we note that the existence of a finite expectation value of the diquark fields leads to an Anderson-Higgs-type mechanism that effectively gaps the gluons. However, we do not aim to resolve this aspect in the present work and simply leave the gluons ungapped (i.e., using the same propagator for the gluons as in the symmetric phase) or "infinitely" gap them (i.e., drop the gluon propagator). In addition to that, we drop diquark fluctuations below the symmetry-breaking scale by effectively dropping the diquark propagators. Therefore, we only consider the quark part of the propagator matrix in the following, which is given by

$$\big(\mathcal{P}_k^\psi\big)_{\mathbf{ab}}(p,q) = \begin{pmatrix} \big(\mathrm{i}\bar{h}\mathcal{C}\gamma_5\tau_2\bar{\Delta}_3\epsilon_3\big) & \big(P_\psi^*\big)(p) \\ \big(P_\psi\big)(p) & \big(-\mathrm{i}\bar{h}\gamma_5\mathcal{C}\tau_2\bar{\Delta}_3^*\epsilon_3\big) \end{pmatrix}(2\pi)^4\delta^{(4)}\left(p-q\right)\,. \tag{C.34}$$

Recall that we use a homogeneous background for the expansion of the diquark fields. In the phase governed by spontaneous symmetry breaking, we choose the background field $\bar{\Delta}_3$ to point in the three-direction so that $\Delta_a \mapsto \Delta_a + \delta_{a3}\bar{\Delta}_3$. Notably, this background field appears on the diagonals of the propagator matrix. The resulting inverse of the propagator matrix $\mathcal{P}_k^\psi$ is given by

$$\big(\mathcal{P}_k^\psi\big)^{-1}_{\mathbf{ab}}(p,q) = \begin{pmatrix} \Big(Q^*_{\psi,\chi}(p)\Big)^{-1} & \Big(P_{\psi,\chi}(p)\Big)^{-1} \\ \Big(P^*_{\psi,\chi}(p)\Big)^{-1} & \Big(Q_{\psi,\chi}(p)\Big)^{-1} \end{pmatrix}(2\pi)^4\delta^{(4)}\left(p-q\right)\,. \tag{C.35}$$

The entries of this matrix are given by

$$\Big(P_{\psi,\chi}(p)\Big)^{-1} = Z_\psi^{-1}G_-\big(1+\chi G_{-,\chi}\epsilon_3\epsilon_3\big)P_+\gamma_0 + Z_\psi^{-1}G_+\big(1+\chi G_{+,\chi}\epsilon_3\epsilon_3\big)P_-\gamma_0\,, \tag{C.36}$$

$$\Big(Q_{\psi,\chi}(p)\Big)^{-1} = -\mathrm{i}\bar{h}\bar{\Delta}_3 Z_\psi^{-2}\mathcal{C}\gamma_5\tau_2\epsilon_3\big(G_{-,\chi}P_- + G_{+,\chi}P_+\big)\,. \tag{C.37}$$

Here, we have introduced

$$G_{\pm,\chi} = \frac{1}{p_0^2 + \epsilon_\pm^2 + \chi}\,. \tag{C.38}$$

Note that the diquark gap is related to the parameter $\chi = \bar{h}^2|\Delta_3|^2Z_\psi^{-2}$ since, by evaluating the background field at the minimum of the diquark potential $|\bar{\Delta}_3|^2 = |\bar{\Delta}_0|^2$ as done when calculating the flow equations for the different couplings, we find $\chi = \Delta_{\mathrm{gap}}^2$.

C.3 Inverse of the Propagator Matrix with Isospin Asymmetry

In the following, we show the propagator matrix including different chemical potentials, in particular different chemical potentials for up and down quarks, namely μ_{u} and μ_{d}, and different chemical potentials for colours, namely red μ_{r}, green μ_{g}, and blue μ_{b}. For details on the inclusion, see Sec. 3.1. Here, we only consider quark degrees of freedom so that the propagator matrix $\mathcal{P}_k^{\psi}$ is given by

$$\left(\mathcal{P}_k^{\psi}\right)_{\mathbf{ab}}(p,q) = \begin{pmatrix} \left(\mathrm{i}\bar{h}\mathcal{C}\gamma_5\tau_2\bar{\Delta}_3\epsilon_3\right) & P_{\psi}^{*}(p) \\ P_{\psi}(p) & \left(-\mathrm{i}\bar{h}\gamma_5\mathcal{C}\tau_2\bar{\Delta}_3^{*}\epsilon_3\right) \end{pmatrix} (2\pi)^4\delta^{(4)}(p-q)\,. \tag{C.39}$$

As before, $\bar{\Delta}_3$ is the background field which we choose to point in the three-direction such that $\Delta_a \to \Delta_a + \delta_{a3}\bar{\Delta}_3$. The entries of the propagator matrix $\mathcal{P}_k^{\psi}$ are given by

$$P_{\psi}(p) = Z_{\psi}\left(\mathcal{P}_- P_-\gamma_0 + \mathcal{P}_+ P_+\gamma_0\right), \tag{C.40}$$

where

$$\mathcal{P}_{\pm} = -\mathrm{diag}\Big(p_0 + \mathrm{i}\epsilon_{\pm}^{\mathrm{u,r}}, p_0 + \mathrm{i}\epsilon_{\pm}^{\mathrm{u,g}}, p_0 + \mathrm{i}\epsilon_{\pm}^{\mathrm{u,b}}, p_0 + \mathrm{i}\epsilon_{\pm}^{\mathrm{d,r}}, p_0 + \mathrm{i}\epsilon_{\pm}^{\mathrm{d,g}}, p_0 + \mathrm{i}\epsilon_{\pm}^{\mathrm{d,b}}\Big)_{\mathrm{c,f}}. \tag{C.41}$$

Note that $\mathcal{P}_{\pm}$ are matrices in colour and flavour space, as indicated by the subscript 'c,f'. The regularised quasi-particle dispersion relations entering this expression including different flavour and colour chemical potentials are given by $\epsilon_{\pm}^{f,c} = (\mu_f + \mu_c \pm |\vec{p}\,|)\,(1 + r_{\pm}^{f,c})$ where $r_{\pm}^{f,c} \equiv r\big(x_{\pm}^{f,c}\big)$ with $x_{\pm}^{f,c} = (\mu_f + \mu_c \pm |\vec{p}\,|)^2/k^2$. Inverting the propagator matrix $\mathcal{P}_k^{\psi}$ yields

$$\left(\mathcal{P}_k^{\psi}\right)^{-1}_{\mathbf{ab}}(p,q) = \begin{pmatrix} \Big(Q_{\psi,\chi}^{*}(p)\Big)^{-1} & \Big(P_{\psi,\chi}(p)\Big)^{-1} \\ \Big(P_{\psi,\chi}^{*}(p)\Big)^{-1} & \Big(Q_{\psi,\chi}(p)\Big)^{-1} \end{pmatrix} (2\pi)^4\delta^{(4)}\left(p-q\right). \tag{C.42}$$

The entries are given by

$$\Big(P_{\psi,\chi}(p)\Big)^{-1} = Z_{\psi}^{-1}\mathcal{G}_-\big(1-\chi\mathcal{G}_{-,\chi}\big)P_+\gamma_0 + Z_{\psi}^{-1}\mathcal{G}_+\big(1-\chi\mathcal{G}_{+,\chi}\big)P_-\gamma_0\,, \tag{C.43}$$

$$\Big(Q_{\psi,\chi}(p)\Big)^{-1} = -\mathrm{i}\bar{h}\bar{\Delta}_3 Z_{\psi}^{-2}\mathcal{C}\gamma_5\tau_2\epsilon_3\Big(\mathcal{G}_{-,\chi}P_- + \mathcal{G}_{+,\chi}P_+\Big). \tag{C.44}$$

Here, we have defined

$$\mathcal{G}_{\pm} = \mathrm{diag}\left(G_{\pm}^{\mathrm{u,r}}, G_{\pm}^{\mathrm{u,g}}, G_{\pm}^{\mathrm{u,b}}, G_{\pm}^{\mathrm{d,r}}, G_{\pm}^{\mathrm{d,g}}, G_{\pm}^{\mathrm{d,b}}\right)_{\mathrm{c,f}}, \tag{C.45}$$

$$\mathcal{G}_{\pm,\chi} = \mathrm{diag}\left(G_{\pm,\chi}^{(\mathrm{u,r}),(\mathrm{d,g})}, G_{\pm,\chi}^{(\mathrm{u,g}),(\mathrm{d,r})}, 0, G_{\pm,\chi}^{(\mathrm{d,r}),(\mathrm{u,g})}, G_{\pm,\chi}^{(\mathrm{d,g}),(\mathrm{u,r})}, 0\right)_{\mathrm{c,f}}. \tag{C.46}$$

Note that $\mathcal{G}_{\pm}$ and $\mathcal{G}_{\pm,\chi}$ are matrices in colour and flavour space as indicated by the subscript 'c,f'. In addition to that, we have defined

$$G_{\pm,\chi}^{(f_1,c_1),(f_2,c_2)} = \frac{1}{\chi + (p_0 + \mathrm{i}\epsilon_{\pm}^{f_1,c_1})(p_0 - \mathrm{i}\epsilon_{\pm}^{f_2,c_2})} \qquad \text{and} \qquad G_{\pm}^{f,c} = -\frac{1}{p_0 + \mathrm{i}\epsilon_{\pm}^{f,c}}\,. \tag{C.47}$$

We have only considered the phase governed by the emergence of a diquark gap. However, the result for the symmetric phase can straightforwardly be obtained by setting $\chi = 0$ (i.e., setting the background field to zero $\bar{\Delta}_3 = 0$). This yields

$$\Big(P_{\psi}(p)\Big)^{-1} = Z_{\psi}^{-1}\left(\mathcal{G}_- P_+\gamma_0 + \mathcal{G}_+ P_-\gamma_0\right) \qquad \text{and} \qquad \Big(Q_{\psi,\chi}(p)\Big)^{-1} = 0\,. \tag{C.48}$$

D

Strong Coupling

In the following, we give some details about the strong coupling g used throughout the present work. In particular, in the first-principles study in Chap. 2, the gauge sector enters the calculation only via the strong coupling. Its value at the initial RG scale Λ is the only external input parameter entering this study.
The calculations in the aforementioned chapter rely on the background-field formalism [304, 305]. Then, the beta function β_{g^2} of the (squared) strong coupling is given by

$$\beta_{g^2} = k\partial_k g^2 = \eta_A g^2 \,. \tag{D.1}$$

Here, η_A is the gluon anomalous dimension which consists of a pure gluonic contribution η_A^{glue} and a quark contribution η_A^{quark} [296–298]. By including diquark fluctuations in Sec. 2.6, we obtain an additional diquark contribution η_A^{diquark}. However, as we have shown in Sec. 2.6, diquark fluctuations are subleading, at least in the phase that is not governed by spontaneous symmetry breaking. In addition to that, diquark fields enter our calculation only as effective low-energy degrees of freedom that are purely generated from the quark-gluon dynamics. For the following discussion, we therefore drop this contribution so that the gluon anomalous dimension is given by

$$\eta_A = -Z_A^{-1}\partial_t Z_A = \eta_A^{\text{glue}} + \eta_A^{\text{quark}} \,. \tag{D.2}$$

For the gluon contribution, we employ results from previous fRG studies where η_A^{glue} was calculated nonperturbatively within the background-field formalism [297, 298, 311]. This contribution does not depend on the chemical potential. For the quark contribution, we find

$$\eta_A^{\text{quark}} = \frac{4}{3} g^2 N_{\text{f}} \mathcal{D}_{\text{ff}}^{(1)}\left(\frac{\mu}{k}, \rho_\psi\right) \,. \tag{D.3}$$

Here, $N_{\text{f}} = 2$ is the number of flavours. The threshold function $\mathcal{D}_{\text{ff}}^{(1)}$ corresponds to a loop diagram with two internal fermionic lines and its definition can be found in App. B.3. In particular, this contribution depends

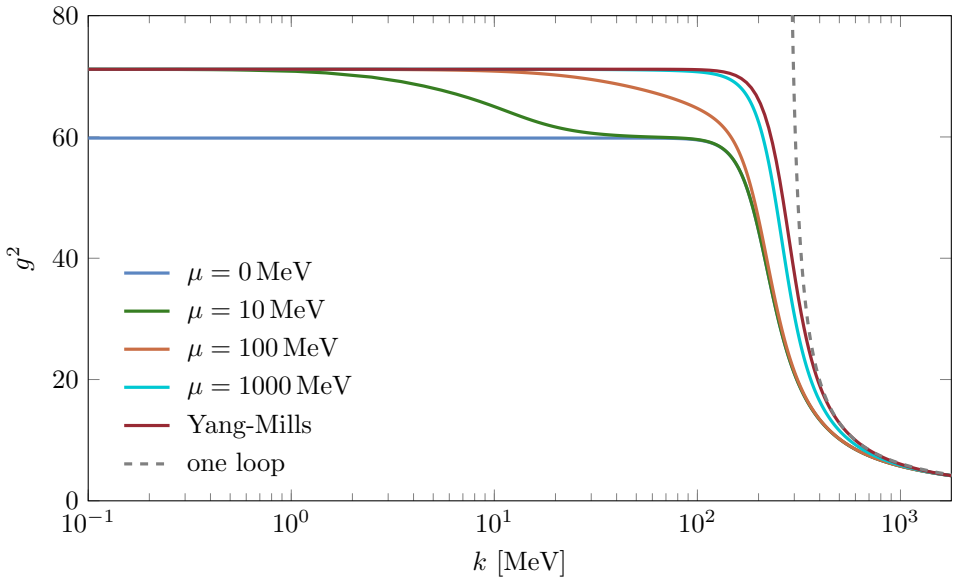

Figure D.1: Strong coupling g^2 for four different chemical potentials, namely $\mu = 0, 10, 100, 1000\,\mathrm{MeV}$, compared to the pure Yang-Mills coupling (red line) associated with $N_\mathrm{f} = 0$. For a comparison, we also show the result for the strong coupling in a one-loop approximation (dashed grey line) according to Eq. (D.5). We have fixed the strong coupling with $g^2(\Lambda) = 4\pi \cdot 0.179$ at $\Lambda = 10\,\mathrm{GeV}$.

on the chemical potential. Note that, in the phase governed by spontaneous symmetry breaking, the strong coupling also depends on the diquark gap. However, we drop the diquark gap for the purpose of the present illustration. For the effects of the diquark gap on the strong coupling, see Sec. 2.4, where the diquark gap enters the strong coupling via the quark contribution to the anomalous dimensions η_A.

In Fig. D.1, we show the strong coupling for different chemical potentials and compare it to the pure Yang-Mills coupling (associated with $N_\mathrm{f} = 0$). We have fixed the strong coupling with $g^2(\Lambda) = 4\pi \cdot 0.179$ at $\Lambda = 10\,\mathrm{GeV}$. This corresponds to the experimental value $g^2(m_\tau) = 4\pi \cdot 0.330$ at the τ-mass scale $m_\tau = 1.78\,\mathrm{GeV}$ [318]. As the only input parameter, the strong coupling sets the scale for all dimensionful quantities. Therefore, we define Λ_QCD as the deflection point of the strong coupling which we use to express all dimensionful quantities. We find $\Lambda_\mathrm{QCD} \approx 209\,\mathrm{MeV}$ in the vacuum limit.

In Sec. 3.2, we use the one-loop result for the strong coupling, which is also shown in Fig. D.1 for a comparison. The corresponding beta function in a one-loop approximation reads, see, e.g., [215, 218, 318],

$$k\partial_k g^2 = -b_0 g^4 \,. \tag{D.4}$$

For $N_\mathrm{c} = 3$ colours and $N_\mathrm{f} = 2$ flavours, b_0 is given by $b_0 = (11N_\mathrm{c} - 2N_\mathrm{f})/(24\pi^2) = 29/(24\pi^2)$. The beta function can be solved analytically resulting in

$$g^2 = \frac{1}{b_0 \ln(k/\Lambda_\mathrm{QCD})} \,. \tag{D.5}$$

For the one-loop result, the characteristic energy scale of QCD Λ_QCD is defined as the location of the divergence of the strong coupling and is given by $\Lambda_\mathrm{QCD} = \Lambda \exp(-1/(b_0 g_0^2))$. Here, g_0 is the value of the strong coupling at the scale Λ. For $g_0^2 = g^2(\Lambda) = 4\pi \cdot 0.179$ at $\Lambda = 10\,\mathrm{GeV}$, we find $\Lambda_\mathrm{QCD} \approx 265\,\mathrm{MeV}$. With the one-loop expression for the strong coupling (D.5), we find that QCD is asymptotically free if $b_0 > 0$ which is fulfilled for $11N_\mathrm{c} > 2N_\mathrm{f}$. Therefore, the strong coupling decreases towards higher scales while it increases towards lower scales.

Bibliography

[1] S. L. Glashow, "The renormalizability of vector meson interactions", Nucl. Phys. **10**, 107–117 (1959).

[2] A. Salam and J. C. Ward, "Weak and electromagnetic interactions", Nuovo Cim. **11**, 568–577 (1959).

[3] S. Weinberg, "A model of leptons", Phys. Rev. Lett. **19**, 1264–1266 (1967).

[4] M. Gell-Mann, "A schematic model of baryons and mesons", Phys. Lett. **8**, 214–215 (1964).

[5] G. Zweig, *An SU_3 model for strong interaction symmetry and its breaking; Version 1*, CERN-TH-401 (1964).

[6] G. Zweig, *An SU_3 model for strong interaction symmetry and its breaking; Version 2*, CERN-TH-412 (1964).

[7] M. Gell-Mann, *The eightfold way: A theory of strong interaction symmetry*, CTSL-20, TID-12608 (1961).

[8] Y. Ne'eman, "Derivation of strong interactions from a gauge invariance", Nucl. Phys. **26**, 222–229 (1961).

[9] W. A. Bardeen, H. Fritzsch, and M. Gell-Mann, "Light-cone current algebra, π^0 decay, and e^+e^- annihilation", in *Scale and Conformal Symmetry in Hadron Physics*, edited by R. Gatto (John Wiley and Sons, 1973), p. 139, arXiv:hep-ph/0211388.

[10] O. W. Greenberg, "Spin and unitary-spin independence in a paraquark model of baryons and mesons", Phys. Rev. Lett. **13**, 598–602 (1964).

[11] M. Y. Han and Y. Nambu, "Three-triplet model with double SU(3) symmetry", Phys. Rev. **139**, B1006–B1010 (1965).

[12] C. Burgess and G. Moore, *The Standard Model: A Primer* (Cambridge University Press, 2007).

[13] J. Greensite, *An Introduction to the Confinement Problem* (Springer Berlin Heidelberg, 2011).

[14] K. G. Wilson, "Confinement of quarks", Phys. Rev. D **10**, 2445–2459 (1974).

[15] H. Fritzsch, M. Gell-Mann, and H. Leutwyler, "Advantages of the color octet gluon picture", Phys. Lett. B **47**, 365–368 (1973).

[16] C.-N. Yang and R. L. Mills, "Conservation of isotopic spin and isotopic gauge invariance", Phys. Rev. **96**, 191–195 (1954).

[17] R. Mills, "Gauge fields", Am. J. Phys. **57**, 493–507 (1989).

[18] D. J. Gross and F. Wilczek, "Ultraviolet behavior of non-Abelian gauge theories", Phys. Rev. Lett. **30**, 1343–1346 (1973).

[19] H. D. Politzer, "Reliable perturbative results for strong interactions?", Phys. Rev. Lett. **30**, 1346–1349 (1973).

[20] K. Fukushima and T. Hatsuda, "The phase diagram of dense QCD", Rep. Prog. Phys. **74**, 014001 (2011).

[21] P. Braun-Munzinger and J. Wambach, "Colloquium: Phase diagram of strongly interacting matter", Rev. Mod. Phys. **81**, 1031–1050 (2009).

[22] M. A. Stephanov, "QCD phase diagram: An overview", PoS **LAT2006**, 024 (2006).

[23] S. Sharma, "Recent progress on the QCD phase diagram", PoS **LATTICE2018**, 009 (2019).

[24] L. Van Hove, "Theoretical prediction of a new state of matter, the "quark-gluon plasma" (also called "quark matter")", in 17th International Symposium on Multiparticle Dynamics, edited by J. N. MacNaughton, W. Majerotto, and M. Markytan (1986), pp. 801–818.

[25] E. V. Shuryak and I. Zahed, "Rethinking the properties of the quark-gluon plasma at $T_c < T < 4T_c$", Phys. Rev. C **70**, 021901 (2004).

[26] E. V. Shuryak, "Quark-gluon plasma and hadronic production of leptons, photons and psions", Phys. Lett. B **78**, 150–153 (1978).

[27] B. Müller, "Investigation of hot QCD matter: Theoretical aspects", Phys. Scr. **2013**, 014004 (2013).

[28] E. Iancu, "QCD in heavy ion collisions", in 2011 European School of High-Energy Physics, edited by C. Grojean and M. Mulders (2014), pp. 197–266.

[29] J. I. Kapusta, "Quark-gluon plasma in the early Universe", in *Phase Transitions in the Early Universe: Theory and Observations*, edited by H. J. De Vega, I. M. Khalatnikov, and N. G. Sànchez (Springer Dordrecht, 2001), pp. 103–121.

[30] B. Müller, J. Schukraft, and B. Wysłouch, "First results from Pb+Pb collisions at the LHC", Ann. Rev. Nucl. Part. Sci. **62**, 361–386 (2012).

[31] B. Müller and J. L. Nagle, "Results from the Relativistic Heavy Ion Collider", Ann. Rev. Nucl. Part. Sci. **56**, 93–135 (2006).

[32] P. Jacobs and X.-N. Wang, "Matter in extremis: Ultrarelativistic nuclear collisions at RHIC", Prog. Part. Nucl. Phys. **54**, 443–534 (2005).

[33] J. B. Kogut, M. Stone, H. W. Wyld, W. R. Gibbs, J. Shigemitsu, S. H. Shenker, and D. K. Sinclair, "Deconfinement and chiral symmetry restoration at finite temperatures in SU(2) and SU(3) gauge theories", Phys. Rev. Lett. **50**, 393–396 (1983).

[34] F. Xu and M. Huang, "The chiral and deconfinement phase transitions", Cent. Eur. J. Phys. **10**, 1357–1360 (2012).

[35] V. Koch, "Introduction to chiral symmetry", (1995), arXiv:nucl-th/9512029.

[36] R. D. Pisarski and F. Wilczek, "Remarks on the chiral phase transition in chromodynamics", Phys. Rev. D **29**, 338–341 (1984).

[37] T. Schäfer, "The chiral phase transition", Nucl. Phys. A **610**, 13–25 (1996).

[38] A. Barducci, R. Casalbuoni, S. De Curtis, R. Gatto, and G. Pettini, "Chiral phase transitions in QCD for finite temperature and density", Phys. Rev. D **41**, 1610–1619 (1990).

[39] F. Wilczek, "Application of the renormalization group to a second-order QCD phase transition", Int. J. Mod. Phys. A **7**, 3911–3925 (1992), [Erratum: Int. J. Mod. Phys. A 7, 6951 (1992)].

[40] J. Berges and K. Rajagopal, "Color superconductivity and chiral symmetry restoration at non-zero baryon density and temperature", Nucl. Phys. B **538**, 215–232 (1999).

[41] G. Bertsch and P. J. Siemens, "Nuclear fragmentation", Phys. Lett. B **126**, 9–12 (1983).

[42] P. J. Siemens, "Liquid–gas phase transition in nuclear matter", Nature **305**, 410–412 (1983).

[43] A. D. Panagiotou, M. W. Curtin, H. Toki, D. K. Scott, and P. J. Siemens, "Experimental evidence for a liquid-gas phase transition in nuclear systems", Phys. Rev. Lett. **52**, 496–499 (1984).

[44] K. Fukushima, J. Horak, J. M. Pawlowski, N. Wink, and C. P. Zelle, "The nuclear liquid-gas transition in QCD", (2023), arXiv:2308.16594 [nucl-th].

[45] B. Borderie and J. D. Frankland, "Liquid–Gas phase transition in nuclei", Prog. Part. Nucl. Phys. **105**, 82–138 (2019).

[46] K. Rajagopal and F. Wilczek, "The condensed matter physics of QCD", in *At The Frontier of Particle Physics*, edited by M. Shifman (World Scientific, 2001), pp. 2061–2151.

[47] M. G. Alford, "Color-superconducting quark matter", Ann. Rev. Nucl. Part. Sci. **51**, 131–160 (2001).

[48] M. Buballa, "NJL-model analysis of dense quark matter", Phys. Rept. **407**, 205–376 (2005).

[49] I. A. Shovkovy, "Two lectures on color superconductivity", Found. Phys. **35**, 1309–1358 (2005).

[50] M. G. Alford, A. Schmitt, K. Rajagopal, and T. Schäfer, "Color superconductivity in dense quark matter", Rev. Mod. Phys. **80**, 1455–1515 (2008).

[51] K. Fukushima, "QCD matter in extreme environments", J. Phys. G: Nucl. Part. Phys. **39**, 013101 (2012).

[52] R. Anglani, R. Casalbuoni, M. Ciminale, N. Ippolito, R. Gatto, M. Mannarelli, and M. Ruggieri, "Crystalline color superconductors", Rev. Mod. Phys. **86**, 509–561 (2014).

[53] A. Schmitt, *Introduction to Superfluidity: Field-theoretical Approach and Applications* (Springer Cham, 2015).

[54] G. Baym, T. Hatsuda, T. Kojo, P. D. Powell, Y. Song, and T. Takatsuka, "From hadrons to quarks in neutron stars: A review", Rep. Prog. Phys. **81**, 056902 (2018).

[55] D. Bailin and A. Love, "Superfluidity and superconductivity in relativistic fermion systems", Phys. Rept. **107**, 325–385 (1984).

[56] D. H. Rischke, "The quark–gluon plasma in equilibrium", Prog. Part. Nucl. Phys. **52**, 197–296 (2004).

[57] Y. Nambu and G. Jona-Lasinio, "Dynamical model of elementary particles based on an analogy with superconductivity. I.", Phys. Rev. **122**, 345–358 (1961).

[58] Y. Nambu and G. Jona-Lasinio, "Dynamical model of elementary particles based on an analogy with superconductivity. II.", Phys. Rev. **124**, 246–254 (1961).

[59] D. Griffiths, *Introduction to Elementary Particles* (John Wiley & Sons, Ltd, 1987).

[60] M. Tanabashi et al. (Particle Data Group), "Review of particle physics", Phys. Rev. D **98**, 030001 (2018).

[61] F. Englert and R. Brout, "Broken symmetry and the mass of gauge vector mesons", Phys. Rev. Lett. **13**, 321–323 (1964).

[62] P. W. Higgs, "Broken symmetries, massless particles and gauge fields", Phys. Lett. **12**, 132–133 (1964).

[63] P. W. Higgs, "Broken symmetries and the masses of gauge bosons", Phys. Rev. Lett. **13**, 508–509 (1964).

[64] G. S. Guralnik, C. R. Hagen, and T. W. B. Kibble, "Global conservation laws and massless particles", Phys. Rev. Lett. **13**, 585–587 (1964).

[65] P. W. Higgs, "Spontaneous symmetry breakdown without massless bosons", Phys. Rev. **145**, 1156–1163 (1966).

[66] P. W. Anderson, "Plasmons, gauge invariance, and mass", Phys. Rev. **130**, 439–442 (1963).

[67] P. W. Anderson, "Random-phase approximation in the theory of superconductivity", Phys. Rev. **112**, 1900–1916 (1958).

[68] Y. Nambu, "Quasi-particles and gauge invariance in the theory of superconductivity", Phys. Rev. **117**, 648–663 (1960).

[69] F. London and H. London, "The electromagnetic equations of the supraconductor", Proc. R. Soc. Lond. A **149**, 71–88 (1935).

[70] V. L. Ginzburg and L. D. Landau, "On the theory of superconductivity", Zh. Eksp. Teor. Fiz. **20**, 1064–1082 (1950).

[71] L. N. Cooper, "Bound electron pairs in a degenerate Fermi gas", Phys. Rev. **104**, 1189–1190 (1956).

[72] J. Bardeen, L. N. Cooper, and J. R. Schrieffer, "Theory of superconductivity", Phys. Rev. **108**, 1175–1204 (1957).

[73] J. Bardeen, L. N. Cooper, and J. R. Schrieffer, "Microscopic theory of superconductivity", Phys. Rev. **106**, 162–164 (1957).

[74] H. Fröhlich, "Theory of the superconducting state. I. The ground state at the absolute zero of temperature", Phys. Rev. **79**, 845–856 (1950).

[75] H. Fröhlich, "Interaction of electrons with lattice vibrations", Proc. R. Soc. Lond. A **215**, 291–298 (1952).

[76] D. D. Osheroff, R. C. Richardson, and D. M. Lee, "Evidence for a new phase of solid He^3", Phys. Rev. Lett. **28**, 885–888 (1972).

[77] D. D. Osheroff, W. J. Gully, R. C. Richardson, and D. M. Lee, "New magnetic phenomena in liquid He^3 below 3 mK", Phys. Rev. Lett. **29**, 920–923 (1972).

[78] B. DeMarco and D. S. Jin, "Onset of Fermi degeneracy in a trapped atomic gas", Science **285**, 1703–1706 (1999).

[79] J. Goldstone, "Field theories with superconductor solutions", Nuovo Cim. **19**, 154–164 (1961).

[80] J. Goldstone, A. Salam, and S. Weinberg, "Broken symmetries", Phys. Rev. **127**, 965–970 (1962).

[81] W. Meissner and R. Ochsenfeld, "Ein neuer Effekt bei Eintritt der Supraleitfähigkeit", Naturwiss. **21**, 787–788 (1933).

[82] D. T. Son, "Superconductivity by long-range color magnetic interaction in high-density quark matter", Phys. Rev. D **59**, 094019 (1999).

[83] T. Schäfer and F. Wilczek, "Superconductivity from perturbative one-gluon exchange in high density quark matter", Phys. Rev. D **60**, 114033 (1999).

[84] T. Schäfer and F. Wilczek, "High density quark matter and the renormalization group in QCD with two and three flavors", Phys. Lett. B **450**, 325–331 (1999).

[85] M. G. Alford, K. Rajagopal, and F. Wilczek, "QCD at finite baryon density: Nucleon droplets and color superconductivity", Phys. Lett. B **422**, 247–256 (1998).

[86] R. Rapp, T. Schäfer, E. V. Shuryak, and M. Velkovsky, "Diquark bose condensates in high density matter and instantons", Phys. Rev. Lett. **81**, 53–56 (1998).

[87] R. D. Pisarski and D. H. Rischke, "Color superconductivity in weak coupling", Phys. Rev. D **61**, 074017 (2000).

[88] R. D. Pisarski and D. H. Rischke, "Gaps and critical temperature for color superconductivity", Phys. Rev. D **61**, 051501 (2000).

[89] W. E. Brown, J. T. Liu, and H.-c. Ren, "Perturbative nature of color superconductivity", Phys. Rev. D **61**, 114012 (2000).

[90] D. K. Hong, V. A. Miransky, I. A. Shovkovy, and L. C. R. Wijewardhana, "Schwinger-Dyson approach to color superconductivity in dense QCD", Phys. Rev. D **61**, 056001 (2000), [Erratum: Phys. Rev. D **62**, 059903 (2000)].

[91] S. D. Hsu and M. Schwetz, "Magnetic interactions, the renormalization group and color superconductivity in high density QCD", Nucl. Phys. B **572**, 211–226 (2000).

[92] N. J. Evans, J. Hormuzdiar, S. D. H. Hsu, and M. Schwetz, "On the QCD ground state at high density", Nucl. Phys. B **581**, 391–408 (2000).

[93] M. Baldo, M. Buballa, F. Burgio, F. Neumann, M. Oertel, and H. J. Schulze, "Neutron stars and the transition to color superconducting quark matter", Phys. Lett. B **562**, 153–160 (2003).

[94] E. S. Fraga, A. Kurkela, and A. Vuorinen, "Neutron star structure from QCD", Eur. Phys. J. A **52**, 49 (2016).

[95] H. Heiselberg and M. Hjorth-Jensen, "Phases of dense matter in neutron stars", Phys. Rept. **328**, 237–327 (2000).

[96] J. M. Lattimer and M. Prakash, "The physics of neutron stars", Science **304**, 536–542 (2004).

[97] A. W. Alsabti and P. Murdin, eds., *Handbook of Supernovae* (Springer Cham, 2017).

[98] A. Schmitt, *Dense Matter in Compact Stars: A Pedagogical Introduction* (Springer Berlin Heidelberg, 2010).

[99] P. Demorest, T. Pennucci, S. Ransom, M. Roberts, and J. Hessels, "A two-solar-mass neutron star measured using Shapiro delay", Nature **467**, 1081–1083 (2010).

[100] J. Antoniadis et al., "A massive pulsar in a compact relativistic binary", Science **340**, 1233232 (2013).

[101] E. Fonseca et al., "Refined mass and geometric measurements of the high-mass PSR J0740+6620", Astrophys. J. Lett. **915**, L12 (2021).

[102] H. T. Cromartie et al. (NANOGrav), "Relativistic Shapiro delay measurements of an extremely massive millisecond pulsar", Nature Astron. **4**, 72–76 (2020).

[103] E. Annala, T. Gorda, A. Kurkela, J. Nättilä, and A. Vuorinen, "Evidence for quark-matter cores in massive neutron stars", Nature Phys. **16**, 907–910 (2020).

[104] E. Annala, T. Gorda, J. Hirvonen, O. Komoltsev, A. Kurkela, J. Nättilä, and A. Vuorinen, "Strongly interacting matter exhibits deconfined behavior in massive neutron stars", Nature Commun. **14**, 8451 (2023).

[105] J. C. Collins and M. J. Perry, "Superdense matter: Neutrons or asymptotically free quarks?", Phys. Rev. Lett. **34**, 1353–1356 (1975).

[106] A. Gal, E. V. Hungerford, and D. J. Millener, "Strangeness in nuclear physics", Rev. Mod. Phys. **88**, 035004 (2016).

[107] N. K. Glendenning, "Neutron stars are giant hypernuclei?", Astrophys. J. **293**, 470–493 (1985).

[108] J. Schaffner-Bielich, M. Hanauske, H. Stöcker, and W. Greiner, "Phase transition to hyperon matter in neutron stars", Phys. Rev. Lett. **89**, 171101 (2002).

[109] I. Bombaci, "The hyperon puzzle in neutron stars", JPS Conf. Proc. **17**, 101002 (2017).

[110] B. P. Abbott et al. (LIGO Scientific Collaboration and Virgo Collaboration), "GW170817: Observation of gravitational waves from a binary neutron star inspiral", Phys. Rev. Lett. **119**, 161101 (2017).

[111] B. P. Abbott et al. (LIGO Scientific Collaboration and Virgo Collaboration), "Properties of the binary neutron star merger GW170817", Phys. Rev. X **9**, 011001 (2019).

[112] A. L. Watts et al., "Colloquium : Measuring the neutron star equation of state using x-ray timing", Rev. Mod. Phys. **88**, 021001 (2016).

[113] Z. Arzoumanian et al., "The Neutron Star Interior Composition Explorer (NICER): Mission definition", in Space Telescopes and Instrumentation 2014: Ultraviolet to Gamma Ray, Vol. 9144, Proc. SPIE (2014), p. 914420.

[114] K. C. Gendreau et al., "The Neutron Star Interior Composition Explorer (NICER): Design and development", in Space Telescopes and Instrumentation 2016: Ultraviolet to Gamma Ray, Vol. 9905, Proc. SPIE (2016), 99051H.

[115] M. C. Miller et al., "The radius of PSR J0740+6620 from NICER and XMM-Newton data", Astrophys. J. Lett. **918**, L28 (2021).

[116] T. E. Riley et al., "A NICER view of the massive pulsar PSR J0740+6620 informed by radio timing and XMM-Newton spectroscopy", Astrophys. J. Lett. **918**, L27 (2021).

[117] G. Raaijmakers, S. K. Greif, K. Hebeler, T. Hinderer, S. Nissanke, A. Schwenk, T. E. Riley, A. L. Watts, J. M. Lattimer, and W. C. G. Ho, "Constraints on the dense matter equation of state and neutron star properties from NICER's mass–radius estimate of PSR J0740+6620 and multimessenger observations", Astrophys. J. Lett. **918**, L29 (2021).

[118] E. Fonseca et al., "The NANOGrav nine-year data set: Mass and geometric measurements of binary millisecond pulsars", Astrophys. J. **832**, 167 (2016).

[119] S. Huth, C. Wellenhofer, and A. Schwenk, "New equations of state constrained by nuclear physics, observations, and QCD calculations of high-density nuclear matter", Phys. Rev. C **103**, 025803 (2021).

[120] P. Bedaque and A. W. Steiner, "Sound velocity bound and neutron stars", Phys. Rev. Lett. **114**, 031103 (2015).

[121] I. Tews, J. Carlson, S. Gandolfi, and S. Reddy, "Constraining the speed of sound inside neutron stars with chiral effective field theory interactions and observations", Astrophys. J. **860**, 149 (2018).

[122] S. K. Greif, G. Raaijmakers, K. Hebeler, A. Schwenk, and A. L. Watts, "Equation of state sensitivities when inferring neutron star and dense matter properties", Mon. Not. Roy. Astron. Soc. **485**, 5363–5376 (2019).

[123] S. Altiparmak, C. Ecker, and L. Rezzolla, "On the sound speed in neutron stars", Astrophys. J. Lett. **939**, L34 (2022).

[124] T. Gorda, O. Komoltsev, and A. Kurkela, "Ab-initio QCD calculations impact the inference of the neutron-star-matter equation of state", Astrophys. J. **950**, 107 (2023).

[125] K. Hebeler, J. M. Lattimer, C. J. Pethick, and A. Schwenk, "Equation of state and neutron star properties constrained by nuclear physics and observation", Astrophys. J. **773**, 11 (2013).

[126] M. Leonhardt, M. Pospiech, B. Schallmo, J. Braun, C. Drischler, K. Hebeler, and A. Schwenk, "Symmetric nuclear matter from the strong interaction", Phys. Rev. Lett. **125**, 142502 (2020).

[127] K. Hebeler, "Three-nucleon forces: Implementation and applications to atomic nuclei and dense matter", Phys. Rept. **890**, 1–116 (2021).

[128] J. Keller, K. Hebeler, and A. Schwenk, "Nuclear equation of state for arbitrary proton fraction and temperature based on chiral effective field theory and a Gaussian process emulator", Phys. Rev. Lett. **130**, 072701 (2023).

[129] J. Keller, C. Wellenhofer, K. Hebeler, and A. Schwenk, "Neutron matter at finite temperature based on chiral effective field theory interactions", Phys. Rev. C **103**, 055806 (2021).

[130] J. Berges, D. U. Jungnickel, and C. Wetterich, "Quark and nuclear matter in the linear chiral meson model", Int. J. Mod. Phys. A **18**, 3189–3220 (2003).

[131] M. Drews and W. Weise, "Functional renormalization group approach to neutron matter", Phys. Lett. B **738**, 187–190 (2014).

[132] M. Drews and W. Weise, "From asymmetric nuclear matter to neutron stars: A functional renormalization group study", Phys. Rev. C **91**, 035802 (2015).

[133] R.-A. Tripolt, B.-J. Schaefer, L. von Smekal, and J. Wambach, "Low-temperature behavior of the quark-meson model", Phys. Rev. D **97**, 034022 (2018).

[134] K. Otto, M. Oertel, and B.-J. Schaefer, "Hybrid and quark star matter based on a nonperturbative equation of state", Phys. Rev. D **101**, 103021 (2020).

[135] K. Otto, M. Oertel, and B.-J. Schaefer, "Nonperturbative quark matter equations of state with vector interactions", Eur. Phys. J. ST **229**, 3629–3649 (2020).

[136] K. Kamikado, N. Strodthoff, L. von Smekal, and J. Wambach, "Fluctuations in the quark-meson model for QCD with isospin chemical potential", Phys. Lett. B **718**, 1044–1053 (2013).

[137] G. D. Moore and T. Gorda, "Bounding the QCD equation of state with the lattice", J. High Energ. Phys. **2023**, 133 (2023).

[138] S. Borsányi, Z. Fodor, C. Hoelbling, S. D. Katz, S. Krieg, and K. K. Szabó, "Full result for the QCD equation of state with 2+1 flavors", Phys. Lett. B **730**, 99–104 (2014).

[139] A. Bazavov et al. (HotQCD Collaboration), "Equation of state in (2+1)-flavor QCD", Phys. Rev. D **90**, 094503 (2014).

[140] O. Philipsen, "Lattice QCD at finite temperature and density", Eur. Phys. J. Spec. Top. **152**, 29–60 (2007).

[141] C. Ratti, "Lattice QCD and heavy ion collisions: A review of recent progress", Rep. Prog. Phys. **81**, 084301 (2018).

[142] J. Braun, "The QCD phase boundary from quark-gluon dynamics", Eur. Phys. J. C **64**, 459–482 (2009).

[143] J. Braun, L. M. Haas, F. Marhauser, and J. M. Pawlowski, "Phase structure of two-flavor QCD at finite chemical potential", Phys. Rev. Lett. **106**, 022002 (2011).

[144] L. Fister and J. M. Pawlowski, "Yang-Mills correlation functions at finite temperature", (2011), arXiv:1112.5440 [hep-ph].

[145] W.-j. Fu, J. M. Pawlowski, F. Rennecke, and B.-J. Schaefer, "Baryon number fluctuations at finite temperature and density", Phys. Rev. D **94**, 116020 (2016).

[146] W.-j. Fu, J. M. Pawlowski, and F. Rennecke, "QCD phase structure at finite temperature and density", Phys. Rev. D **101**, 054032 (2020).

[147] F. Gao and J. M. Pawlowski, "QCD phase structure from functional methods", Phys. Rev. D **102**, 034027 (2020).

[148] P. Isserstedt, C. S. Fischer, and T. Steinert, "QCD's equation of state from Dyson-Schwinger equations", PoS **FAIRness2022**, 024 (2023).

[149] P. Isserstedt, M. Buballa, C. S. Fischer, and P. J. Gunkel, "Baryon number fluctuations in the QCD phase diagram from Dyson-Schwinger equations", Phys. Rev. D **100**, 074011 (2019).

[150] P. Isserstedt, C. S. Fischer, and T. Steinert, "Thermodynamics from the quark condensate", Phys. Rev. D **103**, 054012 (2021).

[151] P. de Forcrand, "Simulating QCD at finite density", PoS **LAT2009**, 010 (2009).

[152] K. Nagata, "Finite-density lattice QCD and sign problem: Current status and open problems", Prog. Part. Nucl. Phys. **127**, 103991 (2022).

[153] V. A. Goy, V. Bornyakov, D. Boyda, A. Molochkov, A. Nakamura, A. Nikolaev, and V. Zakharov, "Sign problem in finite density lattice QCD", Prog. Theor. Exp. Phys. **2017**, 031D01 (2017).

[154] B. A. Freedman and L. D. McLerran, "Fermions and gauge vector mesons at finite temperature and density. I. Formal techniques", Phys. Rev. D **16**, 1130–1146 (1977).

[155] B. A. Freedman and L. D. McLerran, "Fermions and gauge vector mesons at finite temperature and density. III. The ground state energy of a relativistic quark gas", Phys. Rev. D **16**, 1169–1185 (1977).

[156] V. Baluni, "Non-Abelian gauge theories of Fermi systems: Quantum-chromodynamic theory of highly condensed matter", Phys. Rev. D **17**, 2092–2121 (1978).

[157] A. Kurkela, P. Romatschke, and A. Vuorinen, "Cold quark matter", Phys. Rev. D **81**, 105021 (2010).

[158] E. S. Fraga, A. Kurkela, and A. Vuorinen, "Interacting quark matter equation of state for compact stars", Astrophys. J. Lett. **781**, L25 (2014).

[159] E. S. Fraga, A. Kurkela, J. Schaffner-Bielich, and A. Vuorinen, "QCD constraints on the equation of state for compact stars", Nucl. Phys. A **956**, 813–816 (2016).

[160] T. Gorda, A. Kurkela, P. Romatschke, M. Säppi, and A. Vuorinen, "Next-to-next-to-next-to-leading order pressure of cold quark matter: Leading logarithm", Phys. Rev. Lett. **121**, 202701 (2018).

[161] T. Gorda, A. Kurkela, R. Paatelainen, S. Säppi, and A. Vuorinen, "Soft interactions in cold quark matter", Phys. Rev. Lett. **127**, 162003 (2021).

[162] T. Gorda, A. Kurkela, R. Paatelainen, S. Säppi, and A. Vuorinen, "Cold quark matter at $\mathrm{N^3LO}$: Soft contributions", Phys. Rev. D **104**, 074015 (2021).

[163] O. Komoltsev, R. Somasundaram, T. Gorda, A. Kurkela, J. Margueron, and I. Tews, "Equation of state at neutron-star densities and beyond from perturbative QCD", (2023), arXiv:2312.14127 [nucl-th].

[164] S. Floerchinger and C. Wetterich, "Chemical freeze-out in heavy ion collisions at large baryon densities", Nucl. Phys. A **890-891**, 11–24 (2012).

[165] J. Braun, M. Leonhardt, and M. Pospiech, "Fierz-complete NJL model study. II. Toward the fixed-point and phase structure of hot and dense two-flavor QCD", Phys. Rev. D **97**, 076010 (2018).

[166] L. McLerran and S. Reddy, "Quarkyonic matter and neutron stars", Phys. Rev. Lett. **122**, 122701 (2019).

[167] Y. Song, G. Baym, T. Hatsuda, and T. Kojo, "Effective repulsion in dense quark matter from non-perturbative gluon exchange", Phys. Rev. D **100**, 034018 (2019).

[168] R. D. Pisarski, "Remarks on nuclear matter: How an ω_0 condensate can spike the speed of sound, and a model of $Z(3)$ baryons", Phys. Rev. D **103**, L071504 (2021).

[169] R.-A. Tripolt, C. Jung, L. von Smekal, and J. Wambach, "Vector and axial-vector mesons in nuclear matter", Phys. Rev. D **104**, 054005 (2021).

[170] H. Gies and C. Wetterich, "Renormalization flow of bound states", Phys. Rev. D **65**, 065001 (2002).

[171] H. Gies and C. Wetterich, "Universality of spontaneous chiral symmetry breaking in gauge theories", Phys. Rev. D **69**, 025001 (2004).

[172] J. M. Pawlowski, "Aspects of the functional renormalisation group", Ann. Phys. **322**, 2831–2915 (2007).

[173] H. Gies, "Introduction to the functional RG and applications to gauge theories", in *Renormalization Group and Effective Field Theory Approaches to Many-Body Systems*, edited by A. Schwenk and J. Polonyi (Springer Berlin Heidelberg, 2012), pp. 287–348.

[174] S. Floerchinger and C. Wetterich, "Exact flow equation for composite operators", Phys. Lett. B **680**, 371–376 (2009).

[175] J. Braun, L. Fister, J. M. Pawlowski, and F. Rennecke, "From quarks and gluons to hadrons: Chiral symmetry breaking in dynamical QCD", Phys. Rev. D **94**, 034016 (2016).

[176] M. Mitter, J. M. Pawlowski, and N. Strodthoff, "Chiral symmetry breaking in continuum QCD", Phys. Rev. D **91**, 054035 (2015).

[177] A. K. Cyrol, M. Mitter, J. M. Pawlowski, and N. Strodthoff, "Nonperturbative quark, gluon, and meson correlators of unquenched QCD", Phys. Rev. D **97**, 054006 (2018).

[178] K. Fukushima, J. M. Pawlowski, and N. Strodthoff, "Emergent hadrons and diquarks", Ann. Phys. **446**, 169106 (2022).

[179] J. Braun, M. Leonhardt, and M. Pospiech, "Fierz-complete NJL model study III: Emergence from quark-gluon dynamics", Phys. Rev. D **101**, 036004 (2020).

[180] N. Strodthoff, B.-J. Schaefer, and L. von Smekal, "Quark-meson-diquark model for two-color QCD", Phys. Rev. D **85**, 074007 (2012).

[181] N. Strodthoff and L. von Smekal, "Polyakov-quark-meson-diquark model for two-color QCD", Phys. Lett. B **731**, 350–357 (2014).

[182] K. Morita, B. Friman, K. Redlich, and V. Skokov, "Net quark number probability distribution near the chiral crossover transition", Phys. Rev. C **88**, 034903 (2013).

[183] K.-I. Aoki, S.-I. Kumamoto, and D. Sato, "Weak solution of the non-perturbative renormalization group equation to describe dynamical chiral symmetry breaking", Prog. Theor. Exp. Phys. **2014**, 043B05 (2014).

[184] N. Khan, J. M. Pawlowski, F. Rennecke, and M. M. Scherer, "The phase diagram of QC2D from functional methods", (2015), arXiv:1512.03673 [hep-ph].

[185] C. Jung, F. Rennecke, R.-A. Tripolt, L. von Smekal, and J. Wambach, "In-medium spectral functions of vector- and axial-vector mesons from the functional renormalization group", Phys. Rev. D **95**, 036020 (2017).

[186] T. Yokota, T. Kunihiro, and K. Morita, "Functional renormalization group analysis of the soft mode at the QCD critical point", Prog. Theor. Exp. Phys. **2016**, 073D01 (2016).

[187] F. Rennecke and B.-J. Schaefer, "Fluctuation-induced modifications of the phase structure in (2+1)-flavor QCD", Phys. Rev. D **96**, 016009 (2017).

[188] G. A. Almási, B. Friman, and K. Redlich, "Baryon number fluctuations in chiral effective models and their phenomenological implications", Phys. Rev. D **96**, 014027 (2017).

[189] W.-j. Fu, J. M. Pawlowski, and F. Rennecke, "Strangeness neutrality and baryon-strangeness correlations", Phys. Rev. D **100**, 111501 (2019).

[190] R.-A. Tripolt, D. H. Rischke, L. von Smekal, and J. Wambach, "Fermionic excitations at finite temperature and density", Phys. Rev. D **101**, 094010 (2020).

[191] J. Braun, W.-j. Fu, J. M. Pawlowski, F. Rennecke, D. Rosenblüh, and S. Yin, "Chiral susceptibility in (2+1)-flavor QCD", Phys. Rev. D **102**, 056010 (2020).

[192] N. Dupuis, L. Canet, A. Eichhorn, W. Metzner, J. M. Pawlowski, M. Tissier, and N. Wschebor, "The nonperturbative functional renormalization group and its applications", Phys. Rept. **910**, 1–114 (2021).

[193] J. Braun, M. Leonhardt, and M. Pospiech, "Fierz-complete NJL model study: Fixed points and phase structure at finite temperature and density", Phys. Rev. D **96**, 076003 (2017).

[194] J. Braun, M. Leonhardt, and J. M. Pawlowski, "Renormalization group consistency and low-energy effective theories", SciPost Phys. **6**, 056 (2019).

[195] J. Braun, T. Dörnfeld, B. Schallmo, and S. Töpfel, "Renormalization group studies of dense relativistic systems", Phys. Rev. D **104**, 096002 (2021).

[196] J. Braun and B. Schallmo, "From quarks and gluons to color superconductivity at supranuclear densities", Phys. Rev. D **105**, 036003 (2022).

[197] J. Braun and B. Schallmo, "Zero-temperature thermodynamics of dense asymmetric strong-interaction matter", Phys. Rev. D **106**, 076010 (2022).

[198] J. Braun, A. Geißel, and B. Schallmo, "Speed of sound in dense strong-interaction matter", SciPost Phys. Core **7**, 015 (2024).

[199] S. R. Coleman and D. J. Gross, "Price of asymptotic freedom", Phys. Rev. Lett. **31**, 851–854 (1973).

[200] J. I. Kapusta and C. Gale, *Finite-Temperature Field Theory: Principles and Applications* (Cambridge University Press, 2006).

[201] M. Laine and A. Vuorinen, *Basics of Thermal Field Theory: A Tutorial on Perturbative Computations* (Springer Cham, 2016).

[202] A. Rebhan, "Hard thermal loops and QCD thermodynamics", (2001), arXiv:hep-ph/0111341.

[203] U. Kraemmer and A. Rebhan, "Advances in perturbative thermal field theory", Rep. Prog. Phys. **67**, 351–431 (2004).

[204] K. G. Wilson, "The origins of lattice gauge theory", Nucl. Phys. B Proc. Suppl. **140**, 3–19 (2005).

[205] C. Gattringer and C. B. Lang, *Quantum Chromodynamics on the Lattice: An Introductory Presentation* (Springer Berlin Heidelberg, 2010).

[206] O. Philipsen, "The QCD equation of state from the lattice", Prog. Part. Nucl. Phys. **70**, 55–107 (2013).

[207] I. Montvay and G. Munster, *Quantum Fields on a Lattice* (Cambridge University Press, 1994).

[208] S. Weinberg, "Nuclear forces from chiral Lagrangians", Phys. Lett. B **251**, 288–292 (1990).

[209] S. Weinberg, "Effective chiral Lagrangians for nucleon - pion interactions and nuclear forces", Nucl. Phys. B **363**, 3–18 (1991).

[210] S. Weinberg, "Three body interactions among nucleons and pions", Phys. Lett. B **295**, 114–121 (1992).

[211] E. Epelbaum, H.-W. Hammer, and U.-G. Meißner, "Modern theory of nuclear forces", Rev. Mod. Phys. **81**, 1773–1825 (2009).

[212] R. Machleidt and D. R. Entem, "Chiral effective field theory and nuclear forces", Phys. Rept. **503**, 1–75 (2011).

[213] E. Epelbaum, "Nuclear forces from chiral effective field theory: A primer", (2010), arXiv:1001.3229 [nucl-th].

[214] T. Kugo, *Eichtheorie* (Springer Berlin Heidelberg, 1997).

[215] M. E. Peskin and D. V. Schroeder, *An Introduction to Quantum Field Theory* (Addison-Wesley, 1995).

[216] M. D. Schwartz, *Quantum Field Theory and the Standard Model* (Cambridge University Press, 2014).

[217] E. B. Manoukian, *Quantum Field Theory I: Foundations and Abelian and Non-Abelian Gauge Theories* (Springer Cham, 2016).

[218] S. Pokorski, *Gauge Field Theories* (Cambridge University Press, 1987).

[219] L. H. Ryder, *Quantum Field Theory* (Cambridge University Press, 1996).

[220] M. L. Bellac, *Thermal Field Theory* (Cambridge University Press, 1996).

[221] J. Zinn-Justin, *Quantum Field Theory and Critical Phenomena* (Oxford University Press, 2002).

[222] J. Zinn-Justin, *Path Integrals in Quantum Mechanics* (Oxford University Press, 2004).

[223] W. Greiner and J. Reinhardt, *Field Quantization* (Springer Berlin Heidelberg, 1996).

[224] L. D. Faddeev and V. N. Popov, "Feynman diagrams for the Yang-Mills field", Phys. Lett. B **25**, 29–30 (1967).

[225] C. Becchi, A. Rouet, and R. Stora, "Renormalization of gauge theories", Ann. Phys. **98**, 287–321 (1976).

[226] C. Becchi, A. Rouet, and R. Stora, "Renormalization of the Abelian Higgs-Kibble model", Commun. Math. Phys. **42**, 127–162 (1975).

[227] C. Becchi, A. Rouet, and R. Stora, "The Abelian Higgs-Kibble model. Unitarity of the S-operator", Phys. Lett. B **52**, 344–346 (1974).

[228] I. V. Tyutin, "Gauge invariance in field theory and statistical physics in operator formalism", Lebedev Physics Institute **39** (1975), arXiv:0812.0580 [hep-th].

[229] S. Weinberg, *The Quantum Theory of Fields. Vol. 2: Modern Applications* (Cambridge University Press, 1996).

[230] N. Goldenfeld, *Lectures On Phase Transitions And The Renormalization Group* (CRC Press, 1992).

[231] S. Weinberg, *The Quantum Theory of Fields. Vol. 1: Foundations* (Cambridge University Press, 1995).

[232] T. Lancaster and S. J. Blundell, *Quantum Field Theory for the Gifted Amateur* (Oxford University Press, 2014).

[233] A. Altland and B. D. Simons, *Condensed Matter Field Theory* (Cambridge University Press, 2010).

[234] J. Maddox, "Making the electron mass finite", Nature **353**, 497 (1991).

[235] H. A. Bethe, "The electromagnetic shift of energy levels", Phys. Rev. **72**, 339–341 (1947).

[236] J. S. Schwinger, "On quantum-electrodynamics and the magnetic moment of the electron", Phys. Rev. **73**, 416–417 (1948).

[237] J. S. Schwinger, "Quantum electrodynamics. I. A covariant formulation", Phys. Rev. **74**, 1439–1461 (1948).

[238] J. S. Schwinger, "Quantum electrodynamics. II. Vacuum polarization and self-energy", Phys. Rev. **75**, 651–679 (1948).

[239] J. S. Schwinger, "Quantum electrodynamics. III: The electromagnetic properties of the electron: Radiative corrections to scattering", Phys. Rev. **76**, 790–817 (1949).

[240] R. P. Feynman, "A relativistic cut-off for classical electrodynamics", Phys. Rev. **74**, 939–946 (1948).

[241] R. P. Feynman, "Relativistic cut-off for quantum electrodynamics", Phys. Rev. **74**, 1430–1438 (1948).

[242] S. Tomonaga, "On a relativistically invariant formulation of the quantum theory of wave fields", Prog. Theor. Phys. **1**, 27–42 (1946).

[243] F. J. Dyson, "The radiation theories of Tomonaga, Schwinger, and Feynman", Phys. Rev. **75**, 486–502 (1949).

[244] L. P. Kadanoff, W. Götze, D. Hamblen, R. Hecht, E. A. S. Lewis, V. V. Palciauskas, M. Rayl, J. Swift, D. Aspnes, and J. Kane, "Static phenomena near critical points: Theory and experiment", Rev. Mod. Phys. **39**, 395–431 (1967).

[245] L. P. Kadanoff, "Scaling laws for Ising models near T_c", Physics Physique Fizika **2**, 263–272 (1966).

[246] R. Shankar, "Renormalization-group approach to interacting fermions", Rev. Mod. Phys. **66**, 129–192 (1994).

[247] M. Salmhofer, C. Honerkamp, W. Metzner, and O. Lauscher, "Renormalization group flows into phases with broken symmetry", Prog. Theor. Phys. **112**, 943–970 (2004).

[248] S. Diehl, S. Floerchinger, H. Gies, J. M. Pawlowski, and C. Wetterich, "Functional renormalization group approach to the BCS-BEC crossover", Ann. Phys. **522**, 615–656 (2010).

[249] W. Metzner, M. Salmhofer, C. Honerkamp, V. Meden, and K. Schönhammer, "Functional renormalization group approach to correlated fermion systems", Rev. Mod. Phys. **84**, 299–352 (2012).

[250] K. G. Wilson, "Renormalization group and critical phenomena. I. Renormalization group and the Kadanoff scaling picture", Phys. Rev. B **4**, 3174–3183 (1971).

[251] K. G. Wilson, "Renormalization group and critical phenomena. II. Phase-space cell analysis of critical behavior", Phys. Rev. B **4**, 3184–3205 (1971).

[252] K. G. Wilson and J. B. Kogut, "The renormalization group and the ϵ expansion", Phys. Rept. **12**, 75–199 (1974).

[253] M. Gell-Mann and F. E. Low, "Quantum electrodynamics at small distances", Phys. Rev. **95**, 1300–1312 (1954).

[254] T. R. Morris, "The exact renormalization group and approximate solutions", Int. J. Mod. Phys. A **9**, 2411–2450 (1994).

[255] C. Wetterich, "Exact evolution equation for the effective potential", Phys. Lett. B **301**, 90–94 (1993).

[256] F. Rennecke, "The Chiral Phase Transition of QCD", PhD thesis (Heidelberg University, 2015).

[257] H. Gies, J. Jaeckel, and C. Wetterich, "Towards a renormalizable standard model without a fundamental Higgs scalar", Phys. Rev. D **69**, 105008 (2004).

[258] B. Delamotte, "An introduction to the nonperturbative renormalization group", in *Renormalization Group and Effective Field Theory Approaches to Many-Body Systems*, edited by A. Schwenk and J. Polonyi (Springer Berlin Heidelberg, 2012), pp. 49–132.

[259] J. Berges, N. Tetradis, and C. Wetterich, "Non-perturbative renormalization flow in quantum field theory and statistical physics", Phys. Rept. **363**, 223–386 (2002).

[260] J. Braun, K. Schwenzer, and H.-J. Pirner, "Linking the quark meson model with QCD at high temperature", Phys. Rev. D **70**, 085016 (2004).

[261] B.-J. Schaefer and J. Wambach, "The phase diagram of the quark-meson model", Nucl. Phys. A **757**, 479–492 (2005).

[262] J.-P. Blaizot, A. Ipp, R. Méndez-Galain, and N. Wschebor, "Perturbation theory and non-perturbative renormalization flow in scalar field theory at finite temperature", Nucl. Phys. A **784**, 376–406 (2007).

[263] D. F. Litim and J. M. Pawlowski, "Non-perturbative thermal flows and resummations", J. High Energy Phys. **11**, 026 (2006).

[264] T. D. Cohen, "Functional integrals for QCD at nonzero chemical potential and zero density", Phys. Rev. Lett. **91**, 222001 (2003).

[265] G. Markó, U. Reinosa, and Z. Szép, "Bose-Einstein condensation and Silver Blaze property from the two-loop Φ-derivable approximation", Phys. Rev. D **90**, 125021 (2014).

[266] W.-j. Fu and J. M. Pawlowski, "Relevance of matter and glue dynamics for baryon number fluctuations", Phys. Rev. D **92**, 116006 (2015).

[267] T. R. Morris, "Properties of derivative expansion approximations to the renormalization group", Int. J. Mod. Phys. B **12**, 1343–1354 (1998).

[268] T. R. Morris, "Derivative expansion of the exact renormalization group", Phys. Lett. B **329**, 241–248 (1994).

[269] G. R. Golner, "Nonperturbative renormalization-group calculations for continuum spin systems", Phys. Rev. B **33**, 7863–7866 (1986).

[270] C. Bagnuls and C. Bervillier, "Exact renormalization group equations: An introductory review", Phys. Rept. **348**, 91–157 (2001).

[271] M. C. Birse, B. Krippa, J. A. McGovern, and N. R. Walet, "Pairing in many-fermion systems: An exact renormalisation group treatment", Phys. Lett. B **605**, 287–294 (2005).

[272] S. Friederich, H. C. Krahl, and C. Wetterich, "Functional renormalization for spontaneous symmetry breaking in the Hubbard model", Phys. Rev. B **83**, 155125 (2011).

[273] J. Braun, "Fermion interactions and universal behavior in strongly interacting theories", J. Phys. G: Nucl. Part. Phys. **39**, 033001 (2012).

[274] D. Roscher, J. Braun, and J. E. Drut, "Phase structure of mass- and spin-imbalanced unitary Fermi gases", Phys. Rev. A **91**, 053611 (2015).

[275] J. Braun, H. Gies, L. Janssen, and D. Roscher, "Phase structure of many-flavor QED_3", Phys. Rev. D **90**, 036002 (2014).

[276] J. D. Bjorken and S. D. Drell, *Relativistic Quantum Mechanics* (McGraw-Hill, 1965).

[277] T. Schäfer, "Hard loops, soft loops, and high density effective field theory", Nucl. Phys. A **728**, 251–271 (2003).

[278] D. F. Litim, "Optimised renormalisation group flows", Phys. Rev. D **64**, 105007 (2001).

[279] D. F. Litim, "Derivative expansion and renormalization group flows", J. High Energy Phys. **11**, 059 (2001).

[280] S. P. Klevansky, "The Nambu-Jona-Lasinio model of quantum chromodynamics", Rev. Mod. Phys. **64**, 649–708 (1992).

[281] L. Ballentine, *Quantum Mechanics: A Modern Development* (World Scientific, 1998).

[282] J. R. Schrieffer, *Theory of Superconductivity* (CRC Press, 1999).

[283] M. Tinkham, *Introduction to Superconductivity* (Dover Publications, 1975).

[284] J. R. Schrieffer and M. Tinkham, "Superconductivity", Rev. Mod. Phys. **71**, S313–S317 (1999).

[285] S. Elitzur, "Impossibility of spontaneously breaking local symmetries", Phys. Rev. D **12**, 3978–3982 (1975).

[286] S. Friederich, "Gauge symmetry breaking in gauge theories: In search of clarification", Eur. J. Phil. Sci. **3**, 157–182 (2013).

[287] W. Caudy and J. Greensite, "Ambiguity of spontaneously broken gauge symmetry", Phys. Rev. D **78**, 025018 (2008).

[288] A. Schmitt, Q. Wang, and D. H. Rischke, "Electromagnetic Meissner effect in spin-one color superconductors", Phys. Rev. Lett. **91**, 242301 (2003).

[289] M. Iwasaki and T. Iwado, "Superconductivity in quark matter", Phys. Lett. B **350**, 163–168 (1995).

[290] X. Wang and I. A. Shovkovy, "Bulk viscosity of spin-one color superconducting strange quark matter", Phys. Rev. D **82**, 085007 (2010).

[291] M. G. Alford, J. A. Bowers, J. M. Cheyne, and G. A. Cowan, "Single color and single flavor color superconductivity", Phys. Rev. D **67**, 054018 (2003).

[292] A. Schmitt, "The ground state in a spin-one color superconductor", Phys. Rev. D **71**, 054016 (2005).

[293] A. Schmitt, "Spin-one color superconductivity in neutron stars", in *Structure and Dynamics of Elementary Matter*, edited by W. Greiner, M. G. Itkis, J. Reinhardt, and M. C. Güçlü (Springer Dordrecht, 2004), pp. 321–328.

[294] M. G. Alford, K. Rajagopal, and F. Wilczek, "Color-flavor locking and chiral symmetry breaking in high density QCD", Nucl. Phys. B **537**, 443–458 (1999).

[295] G. Nardulli, "Introduction to color superconductivity", Proc. Int. Sch. Phys. Fermi **164**, 797–815 (2007).

[296] H. Gies and J. Jaeckel, "Chiral phase structure of QCD with many flavors", Eur. Phys. J. C **46**, 433–438 (2006).

[297] J. Braun and H. Gies, "Running coupling at finite temperature and chiral symmetry restoration in QCD", Phys. Lett. B **645**, 53–58 (2007).

[298] J. Braun and H. Gies, "Chiral phase boundary of QCD at finite temperature", J. High Energy Phys. **06**, 024 (2006).

[299] J. Hubbard, "Calculation of partition functions", Phys. Rev. Lett. **3**, 77–80 (1959).

[300] R. L. Stratonovich, "On a method for the computation of quantum distribution functions", Russian, Proc. USSR Acad. Sci. **115**, 1097–1100 (1957), Translation: Soviet Physics Doklady. 2: 416 (1958).

[301] P. Kopietz, *Bosonization of Interacting Fermions in Arbitrary Dimensions* (Springer Berlin Heidelberg, 1997).

[302] W. Heisenberg, "Über den Bau der Atomkerne. I.", Z. Phys. **77**, 1–11 (1932).

[303] M. Thomson, *Modern Particle Physics* (Cambridge University Press, 2013).

[304] L. F. Abbott, "The background field method beyond one loop", Nucl. Phys. B **185**, 189–203 (1981).

[305] L. F. Abbott, "Introduction to the background field method", Acta Phys. Pol. B **13**, 33–50 (1982).

[306] M. Reuter and C. Wetterich, "Effective average action for gauge theories and exact evolution equations", Nucl. Phys. B **417**, 181–214 (1994).

[307] M. Reuter and C. Wetterich, "Gluon condensation in nonperturbative flow equations", Phys. Rev. D **56**, 7893–7916 (1997).

[308] D. F. Litim and J. M. Pawlowski, "On gauge invariant Wilsonian flows", in *The Exact Renormalization Group*, edited by A. Krasnitz, Y. A. Kubyshin, R. Potting, and P. Sá (World Scientific, 1999), pp. 168–185.

[309] F. Freire, D. F. Litim, and J. M. Pawlowski, "Gauge invariance and background field formalism in the exact renormalisation group", Phys. Lett. B **495**, 256–262 (2000).

[310] D. F. Litim and J. M. Pawlowski, "Wilsonian flows and background fields", Phys. Lett. B **546**, 279–286 (2002).

[311] H. Gies, "Running coupling in Yang-Mills theory: A flow equation study", Phys. Rev. D **66**, 025006 (2002).

[312] J. Braun, H. Gies, and J. M. Pawlowski, "Quark confinement from color confinement", Phys. Lett. B **684**, 262–267 (2010).

[313] J. Braun, A. Eichhorn, H. Gies, and J. M. Pawlowski, "On the nature of the phase transition in SU(N), Sp(2) and E(7) Yang-Mills theory", Eur. Phys. J. C **70**, 689–702 (2010).

[314] U. Reinosa, J. Serreau, M. Tissier, and N. Wschebor, "Deconfinement transition in SU(N) theories from perturbation theory", Phys. Lett. B **742**, 61–68 (2015).

[315] U. Reinosa, J. Serreau, M. Tissier, and N. Wschebor, "Deconfinement transition in SU(2) Yang-Mills theory: A two-loop study", Phys. Rev. D **91**, 045035 (2015).

[316] F. Rennecke, "Vacuum structure of vector mesons in QCD", Phys. Rev. D **92**, 076012 (2015).

[317] J. Braun, "Thermodynamics of QCD low-energy models and the derivative expansion of the effective action", Phys. Rev. D **81**, 016008 (2010).

[318] S. Bethke, "The 2009 world average of α_s", Eur. Phys. J. C **64**, 689–703 (2009).

[319] J. I. Kapusta, "Infrared properties of quark gas", Phys. Rev. D **20**, 989–995 (1979).

[320] T. Toimela, "Perturbative QED and QCD at finite temperatures and densities", Int. J. Theor. Phys. **24**, 901 (1985), [Erratum: Int. J. Theor. Phys. 26, 1021 (1987)].

[321] N. J. Evans, S. D. H. Hsu, and M. Schwetz, "An effective field theory approach to color superconductivity at high quark density", Nucl. Phys. B **551**, 275–289 (1999).

[322] N. J. Evans, S. D. H. Hsu, and M. Schwetz, "Non-perturbative couplings and color superconductivity", Phys. Lett. B **449**, 281–287 (1999).

[323] D. U. Jungnickel and C. Wetterich, "Effective action for the chiral quark-meson model", Phys. Rev. D **53**, 5142–5175 (1996).

[324] J. Berges, D. U. Jungnickel, and C. Wetterich, "Two flavor chiral phase transition from nonperturbative flow equations", Phys. Rev. D **59**, 034010 (1999).

[325] M. Reuter and C. Wetterich, "Average action for the Higgs model with Abelian gauge symmetry", Nucl. Phys. B **391**, 147–175 (1993).

[326] D. F. Litim, "On the Renormalization of the Abelian Higgs Model and the Phase Transition of Superconductors", PhD thesis (Heidelberg University, 1995).

[327] H. Gies, S. Rechenberger, M. M. Scherer, and L. Zambelli, "An asymptotic safety scenario for gauged chiral Higgs-Yukawa models", Eur. Phys. J. C **73**, 2652 (2013).

[328] M. Alford and K. Rajagopal, "Absence of two-flavor color-superconductivity in compact stars", J. High Energy Phys. **06**, 031 (2002).

[329] A. W. Steiner, S. Reddy, and M. Prakash, "Color-neutral superconducting quark matter", Phys. Rev. D **66**, 094007 (2002).

[330] M. Buballa and I. A. Shovkovy, "Note on color neutrality in Nambu-Jona-Lasinio-type models", Phys. Rev. D **72**, 097501 (2005).

[331] I. Shovkovy and M. Huang, "Gapless two-flavor color superconductor", Phys. Lett. B **564**, 205–211 (2003).

[332] P. Amore, M. C. Birse, J. A. McGovern, and N. R. Walet, "Color superconductivity in finite systems", Phys. Rev. D **65**, 074005 (2002).

[333] P. F. Bedaque, "Color superconductivity in asymmetric matter", Nucl. Phys. A **697**, 569–577 (2002).

[334] B. S. Chandrasekhar, "A note on the maximum critical field of high-field superconductors", Appl. Phys. Lett. **1**, 7–8 (1962).

[335] A. M. Clogston, "Upper limit for the critical field in hard superconductors", Phys. Rev. Lett. **9**, 266–267 (1962).

[336] W. Buckel and R. Kleiner, *Supraleitung* (John Wiley & Sons, Ltd, 2012).

[337] H. Ibach and H. Lüth, *Festkörperphysik: Einführung in die Grundlagen* (Springer Berlin Heidelberg, 2009).

[338] G. Sarma, "On the influence of a uniform exchange field acting on the spins of the conduction electrons in a superconductor", J. Phys. Chem. Solids **24**, 1029–1032 (1963).

[339] K. Rajagopal and F. Wilczek, "Enforced electrical neutrality of the color-flavor locked phase", Phys. Rev. Lett. **86**, 3492–3495 (2001).

[340] I. A. Shovkovy and P. J. Ellis, "Thermal conductivity of dense quark matter and cooling of stars", Phys. Rev. C **66**, 015802 (2002).

[341] M. G. Alford, K. Pangeni, and A. Windisch, "Color superconductivity and charge neutrality in Yukawa theory", Phys. Rev. Lett. **120**, 082701 (2018).

[342] D. Ebert and K. G. Klimenko, "Pion condensation in electrically neutral cold matter with finite baryon density", Eur. Phys. J. C **46**, 771–776 (2006).

[343] J. O. Andersen and L. Kyllingstad, "Pion condensation in a two-flavor NJL model: The role of charge neutrality", J. Phys. G: Nucl. Part. Phys. **37**, 015003 (2009).

[344] G. A. Contrera, D. Blaschke, J. P. Carlomagno, A. G. Grunfeld, and S. Liebing, "Quark-nuclear hybrid equation of state for neutron stars under modern observational constraints", Phys. Rev. C **105**, 045808 (2022).

[345] O. Ivanytskyi and D. Blaschke, "Density functional approach to quark matter with confinement and color superconductivity", Phys. Rev. D **105**, 114042 (2022).

[346] T. Kojo, D. Hou, J. Okafor, and H. Togashi, "Phenomenological QCD equations of state for neutron star dynamics: Nuclear-2SC continuity and evolving effective couplings", Phys. Rev. D **104**, 063036 (2021).

[347] D. Nickel, J. Wambach, and R. Alkofer, "Color-superconductivity in the strong-coupling regime of Landau gauge QCD", Phys. Rev. D **73**, 114028 (2006).

[348] J. Braun, M. Leonhardt, J. M. Pawlowski, and D. Rosenblüh, "Chiral and effective $U(1)_{\mathrm{A}}$ symmetry restoration in QCD", (2020), arXiv:2012.06231 [hep-ph].

[349] M. Fierz, "Zur Fermischen Theorie des β-Zerfalls", Z. Phys. **104**, 553–565 (1937).

[350] J. F. Nieves and P. B. Pal, "Generalized Fierz identities", Am. J. Phys. **72**, 1100–1108 (2004).

[351] C. C. Nishi, "Simple derivation of general Fierz-type identities", Am. J. Phys. **73**, 1160–1163 (2005).

[352] P. B. Pal, "Representation-independent manipulations with Dirac spinors", (2007), arXiv:physics/0703214.

[353] D. F. Litim, "Mind the gap", Int. J. Mod. Phys. A **16**, 2081–2088 (2001).

[354] D. F. Litim, "Optimisation of the exact renormalisation group", Phys. Lett. B **486**, 92–99 (2000).

[355] S. Floerchinger, "Analytic continuation of functional renormalization group equations", J. High Energy Phys. **2012**, 21 (2012).

Erklärung laut Promotionsordnung

§ 8 Abs. 1 lit. c PromO

Ich versichere hiermit, dass die elektronische Version meiner Dissertation mit der schriftlichen Version übereinstimmt.

§ 8 Abs. 1 lit. d PromO

Ich versichere hiermit, dass zu einem vorherigen Zeitpunkt noch keine Promotion versucht wurde. In diesem Fall sind nähere Angaben über Zeitpunkt, Hochschule, Dissertationsthema und Ergebnis dieses Versuchs mitzuteilen.

§ 9 Abs. 1 PromO

Ich versichere hiermit, dass die vorliegende Dissertation selbstständig und nur unter Verwendung der angegebenen Quellen verfasst wurde.

§ 9 Abs. 2 PromO

Die Arbeit hat bisher noch nicht zu Prüfungszwecken gedient.

Darmstadt, den

Benedikt Paul Schallmo